Issa Elfergani
Abubakar Sadiq Hussaini
Jonathan Rodriguez
Raed Abd-Alhameed *Editors*

Antenna Fundamentals for Legacy Mobile Applications and Beyond

Springer

Antenna Fundamentals for Legacy Mobile Applications and Beyond

Issa Elfergani • Abubakar Sadiq Hussaini
Jonathan Rodriguez • Raed Abd-Alhameed
Editors

Antenna Fundamentals for Legacy Mobile Applications and Beyond

Springer

Editors
Issa Elfergani
Instituto de Telecomunicações
Campus Universitário de Santiago
Aveiro, Portugal

Abubakar Sadiq Hussaini
Instituto de Telecomunicações
Campus Universitário de Santiago
Aveiro, Portugal

Jonathan Rodriguez
Instituto de Telecomunicações
Campus Universitário de Santiago
Aveiro, Portugal

Raed Abd-Alhameed
School of Engineering and Informatics
University of Bradford
Bradford, UK

University of South Wales
Pontypridd, UK

ISBN 978-3-319-63966-6 ISBN 978-3-319-63967-3 (eBook)
DOI 10.1007/978-3-319-63967-3

Library of Congress Control Number: 2017952345

This Springer imprint is published by Springer Nature
The registered company is Springer International Publishing AG
The registered company address is: Gewerbestrasse 11, 6330 Cham, Switzerland

Preface

This is the first book to really present a concerted technology road map on antenna advancements for mobile communications ranging from 3G to 5G and beyond, including design requirements, practical performance, and future market trends. This provides a concrete platform for discussing the requirements for legacy and 5G antennas, and candidate designs that are actively investigated on this topic, including design considerations, engineering design, measurement setup and methodology, and practical applications, are all covered in depth.

This book is a result of the editor's vast experience in RF and antenna design, who has collaborated in research projects at the European level designing antennas for 3G and 4G systems, as well as working closely with the industry on designs that have resulted in real products. Key examples include dual-band, broadband, and ultra-wideband antennas for UK industry such as Yorkshire Water plc, Harvard Engineering PLC, Seven Technologies Group Ltd, Two World Ltd, Hawkeye Industrial IETG Ltd, Pace plc (now known as Arris PLC), and Quadrifilar helices for satellite applications in collaboration with the former Surrey Satellite Technology Centre, UK. Moreover, the editorial team are now training tomorrow's researchers on antenna design at the international level, where they are coordinating a major training network under the MCSA (Marie Curie) instrument. The SECRET project (Project ID: 722,424) aims to develop young talents in the field of antenna design toward developing miniature antennas for 5G applications.

This book aims to provide a good reference for practicing engineers and under-/postgraduate students working in this field. The book will include simple fundamental concepts, as well as current market applications in order to provide a base on which the interested reader can either acquire new knowledge on antenna design or provide a platform for developing practical antennas for modern-day mobile applications. This book will serve as a useful tool for researchers (academia and industry) to draw inspiration toward the design of innovative antennas for next-generation systems targeting 5G and beyond. This book provides the inspiration for stakeholders (academia and vendors) to build new project proposals on this highly evolving field. Antenna design requirements in legacy and future emerging communication technologies are given, including practical prototype examples

with performance analysis. This can provide an insight on the current state of the art and help identify the missing gaps in order to develop innovations.

The scope of the book will highlight technology trends and challenges to trace the evolution of antenna design starting from third-generation phones toward the latest release of LTE-A and 5G. We will understand how the simple monopole and whip antenna from the GSM years have evolved toward what we have today, an antenna design that is compact and multiband in nature and caters for multiple elements on the same patch to provide high-throughput connectivity. Therefore, the book targets a broad range of subjects, including the microstrip antenna, PIFA antenna, and the dipole and printed monopole antenna. The book discusses basic and advanced concepts of the abovementioned antennas, including design procedure, requirements, challenges, and recent applications targeting 3G and 4G mobile systems. Beyond that, we then take a step into the future and look at antenna requirements for 5G communications. The 5G drive is in place, with prominent scenarios and use cases emerging. We examine these and put in place the challenges that lie ahead for antenna design, particularly in mm-wave design.

The key technology trends in antenna design as part of the mobile communication evolution have mainly focused on multiband, wideband, and MIMO antennas, accompanied by balanced designs, and the organization of the book is such, where the editors provide 16 self-contained chapters that guide the reader through the evolution of antenna design, initiated by GSM, driven by legacy 3G and now 4G systems, and a forecast as to where the next step in antenna design will take us, in particular:

Chapter 1 ("Fundamentals of Antenna Design, Technologies, and Applications") reviews the concepts, requirements, challenges, and the evolution of antenna technologies, driven by subsequent releases of mobile generations from legacy 3G (third-generation mobile systems) toward the latest release in LTE-A. In particular, we provide concrete and practical examples of widely adopted multiband, wideband, MIMO, balanced, and mm-wave antenna technologies for current 3G and 4G mobile systems. Issues including design considerations, engineering design, measurement setup and methodology, and practical applications are all covered in depth.

Chapter 2 ("Dual-Band Planar Inverted F-L Antenna Structure for Bluetooth and Zigbee Applications") presents and analyses low profile and dual-frequency inverted L-F antennas for the operating frequency bands related to IEEE 802.11a/b/g, Bluetooth, and ZigBee standards and the optimal design providing a compromise between size reduction and attainable bandwidth. The antenna consists of an F-shaped radiator and L-shaped parasitic element with the optimum (minimized) volume of 30× 30 × 8 mm^3, thus making it compatible with installation on portable wireless electronic devices. By controlling the geometry parameters of the radiator, the lower resonant operating band can be tuned to achieve 8% bandwidth. Likewise, by optimizing the geometry parameters of the parasitic element, the upper operating frequency band can reach the required 12.2% bandwidth. Both the simulated and measured characteristics of the proposed antenna are in good agreement.

Chapter 3 ("Double-Monopole Crescent-Shaped Antennas with High Isolation for WLAN and WiMAX Applications") provides planar double-antenna design layouts,

where we demonstrate potential use cases for WLAN and WiMAX. Each antenna has the form of a crescent-shaped monopole structure fed by a microstrip line. The lengths of the two arcs are designed to resonate at 2.45GHz and 3.5GHz to comply with the WLAN and WiMAX standards, respectively. The two monopoles have a small separation of 9 mm ($0.0735\lambda_o$ at 2.45GHz). Various techniques are proposed for the reduction of the mutual coupling between the two closely spaced antennas by etching a slot in each of the microstrip line feeding them. The slots are folded to the shape of either two interlaced U letters or an S letter to conserve length of the feed lines. In each antenna, the slot is tuned to resonate at the operating frequency of the other antenna, so that the other frequency is notched out. Four configurations are investigated to obtain increased isolation between the two antennas. The antenna performance was investigated by simulation using CST Microwave Studio software. The results show that the proposed methods can reduce the envelope correlation coefficient by 35-fold at the 2.45 GHz and 21-fold at the 3.5GHz frequency bands. Measured S-parameters verified the simulated results.

Chapter 4 ("Electrically Small Planar Antennas Based on Metamaterial") addresses a number of planar antennas with several shapes, which are loaded with different types of metamaterial such as SRRs, ZOR, and ZOR-TL. These approaches were used and studied in order to exhibit the miniaturization effect. The proposed antennas can provide dual-band operation, the first one is a Wi-Fi band at 2.45 GHz having an impedance bandwidth of 150 MHz, and the second one is an ultra-wide band extended from 4.2 to 6.5 GHz. All the proposed antennas have demonstrated and proved that the presence of metamaterial and EBG in the antenna can produce miniaturization effect from 10 to 25% and can produce a radiation pattern gain from 47 to 68.9% (in the case of SRR inclusion). These antennas are generally applied for wireless communication (WLAN and WiMAX).

Chapter 5 ("Impact of Microstrip-Line Defected Ground Plane on Aperture-Coupled Asymmetric DRA for Ultra-Wideband Applications") presents a compact dielectric resonator antenna (DRA) for shifting wideband applications with microstrip line antenna on a defected ground plan. One to five cylindrical dielectric resonators, which are asymmetrically located with respect to the center of a rectangular coupling aperture, are fed through the aperture of the defected ground plan. By optimizing the design parameters, a design has been proposed with an impedance bandwidth covering the frequency range from 2.92 to12 GHz, with a simulated gain of 10 dBi. The simulated design details of the proposed antennas and results are presented and discussed, with emphasis on the defected ground structure technique to enhance the impedance bandwidth of the patch antennas and overall circuit performance.

Chapter 6 ("Simple and Compact Planar Ultra-Wideband Antenna with Band-Notched Characteristics") discusses the phenomena of frequency interference that is faced in UWB antennas. A printed monopole ultra-wideband (UWB) antenna with frequency band-notched characteristics is proposed and investigated. The antenna consists of a hexagonal patch structure with a small stub. To achieve the frequency band-notched characteristics, slot etching on the surface of the radiator was proposed. Multiple slits can be employed to realize multiple frequency

band-notched characteristics. Two models are designed and tested. The first is a single band-notched UWB antenna, whereas the second is a dual-band-notched UWB antenna. The results also confirm the proposed UWB antenna design can achieve superior dual-band-notched performance at desired frequency bands.

Chapter 7 ("Miniaturized Monopole Wideband Antenna with Tunable Notch for WLAN/WiMAX Applications") introduces the concept of frequency tuning. A tunable band-notched printed monopole antenna is presented, exhibiting a wide impedance bandwidth from 1.5 to 5.5 GHz with good impedance matching (VSWR_2) and a tunable rejected frequency band from to 3.87 GHz. The band notching is achieved by adding an inner chorded crescent element within a driven element of similar shape. By varying the value of the varactor, which is placed between the inner and outer arcs, the desired variable rejected can be obtained. Simulated and measured results show wide impedance bandwidth with a tunable band notch, stable radiation patterns, and almost constant gain. The antenna is suitable for mobile and portable applications.

Chapter 8 ("Miniature EBG Two U-Shaped Slot PIFA MIMO Antennas for WLAN Applications") proposes a compact dual U-shaped slot PIFA antenna with electromagnetic bandgap (EBG) material on a relatively low dielectric constant substrate. Periodic structures have found to reduce mutual coupling and the separation of the antenna and ground plane. In this chapter, a design with EGB material suitable for a small terminal mobile handset operating at 2.4 GHz was studied. Simulated and measured scattering parameters are compared for U-shaped slot PIFA antenna with and without EBG structures. An evaluation of MIMO antennas is presented, with analysis of the mutual coupling, correlation coefficient, total active reflection coefficient (TARC), channel capacity, and capacity loss. The proposed antenna meets the requirements for practical application within a mobile handset.

Chapter 9 ("Compact MIMO Antenna Array Design for Wireless Applications") introduces an alternative approach to design a small MIMO antenna by exploiting multiple polarizations in the signal pathways (for a single conventional channel covering a limited range of frequencies). Discrimination of the different polarizations then requires antenna elements responding principally to each of the orthogonal polarizations, but these elements can be physically very closely located, in contrast to the spatial diversity approach, leading to the possibility that they could be integrated in a handset without a significant increase in its volume. Within this chapter, a concept will be developed by investigating the possibility of discriminating magnetic-field components as well as electric-field components and developing antennas that are very compact and amenable to production by modern printing methods. The theory and results from prototype studies of this work are presented.

Chapter 10 ("Compact Wideband Printed MIMO/Diversity Monopole Antenna for GSM/UMTS and LTE Applications") presents a printed crescent-shaped monopole MIMO diversity antenna for future wireless communication systems. The port-to-port isolation is increased by introducing an I-shaped conductor symmetrically between the two antenna elements and modifying the ground plane shape. Both the computed and experimental results confirm that the antenna possesses a wide impedance bandwidth of 54.5% across 1.6–2.8 GHz, with a reflection coefficient

and mutual coupling better than −10 and −14 dB, respectively. By further validating the simulated and the measured radiation and MIMO characteristics, including the far-field, gain, envelope correlation, and channel capacity loss, the results show that the antenna can offer effective MIMO/diversity operation to alleviate multipath environments.

Chapter 11 ("Compact Wideband Balanced Antenna Structure for 3G Mobile Handsets") introduces a wideband balanced antenna for mobile handsets covering three bands—GSM1800, GSM1900, and UMTS. Balanced antennas have advantages in handset applications as they are less affected by juxtaposition with human tissue than unbalanced types. The antenna is a slotted planar dipole with its arms folded and not connected at their ends. The antenna is fed by a balanced voltage source. The antenna impedance will be investigated. For the purpose of antenna stability evaluation and power gain measurement, a wide bandwidth planar balun would be adopted and modified to feed the antenna from an unbalanced source. For validation, prototypes of the antenna are fabricated and tested.

Chapter 12 ("Coplanar-Fed Miniaturized Folded Loop Balanced Antenna for WLAN Applications") presents a novel balanced rectangular loop antenna, having an ungrounded coplanar waveguide (CPW) feed configuration and a folded structure at both ends. This antenna is designed for operation over the 2.4 GHz and 5 GHz WLAN frequency bands. Bond-wire bridges are used along the CPW feed line to ensure the same potential across the CPW ground planes. The self-balancing structure that can be realized in a loop antenna offers operation without the need of a separate balun for connection to an RF source.

Chapter 13 ("Performance of Dual-Band Balanced Antenna Structure for LTE Applications") studies the balanced structures, which are a good choice because of their property to mitigate the degradation caused by the human body and reduced SAR effect. Furthermore, current in the ground plane is remarkably reduced because of the differential current flow in the dipole antenna arms. Most of the state of the art pertaining to balanced antennas covers either the GSM 900, GSM1800, GSM900/1800 and WLAN, or GSM and WLAN. This means that none of aforementioned balanced antennas have met the objective of this work, especially at the lower band of LTE (700 MHz). Thus, this chapter presents an antenna design that can cover the lower and higher bands of LTE, namely, 700/2600 MHz, while maintaining a compact volume and good performance.

Chapter 14 ("Millimeter-Wave Pattern Reconfigurable Antenna") focuses on pattern reconfigurable antenna array operating at 60 GHz. The radiation pattern from the proposed antenna array is controlled by activating each element in the antenna array one by one, resulting in a unique predefined radiation pattern associated with each antenna element in the array. The design process starts with a conventional microstrip patch antenna (MPA) on Roger RT/duroid 5880 substrate. The performance of the conventional MPA is enhanced in terms of bandwidth and gain by integrating an extended hemispherical Teflon lens to MPA geometry. Finally, the modified MPA with lens is utilized to construct a 15-element array having a wide-angle beam scanning capability in the azimuth plane.

The array covers 5 GHz (57.5 –62.5 GHz) bandwidth with similar radiation pattern characteristics. The 3 dB beamwidth of each array element is found to be 24° with gain higher than 15 dB. By activating each array element, one by one, while all others are terminated by 50 Ω matched load, the antenna beam can be switched, resulting in a beam scanning capability with full 360° coverage in the azimuth plane ($\theta = 90°$). The design is validated by developing and testing a prototype. The comparison between the simulated and measured results is presented which are found to be in good agreement. The presented design is a possible candidate for some communication and radar systems, especially in the area where beam steering and anti-interference capabilities are required.

Chapter 15 ("Wide-Angle Beam Scanning Antenna at 79 GHz for Short-Range Automotive Radar Applications") emphasizes on antenna array integrated with cylindrical dielectric lens operating at 79 GHz. The element in the antenna array consists of planar log periodic dipole antenna (PLPDA) implemented on quartz substrate. The gain of PLPDA is enhanced by integrating it with cylindrical dielectric lens, and beam switching is achieved by activating each element in the antenna array one by one, resulting in a unique predefined radiation pattern associated with each antenna element in the array. The array covers 4 GHz (77 –81 GHz) bandwidth with similar radiation pattern characteristics. The 3 dB beamwidth of each array element is found to be 10° with gain higher than 15 dB. By activating each array element, one by one, while all others are terminated by 50 Ω matched load, the antenna beam can be switched, resulting in a beam scanning capability of full 180° in the azimuth plane ($\theta = 90°$). The design is validated by developing and testing a prototype. The comparison between the simulated and measured results is presented which are found to be in good agreement.

Chapter 16 ("Terahertz Communications for 5G and Beyond") explains the definition of the terahertz frequency spectrum, which has been extended over a wide frequency bandwidth between 0.1 and 10 THz; however, generally, it is confined by the ITU regulation between 300 GHz and 3 THz bandwidth. This concluding chapter will not only address the practical applications of terahertz communications but also identify the research challenges that lie ahead in terms of THz antenna design.

Acknowledgments

The editors would like to thank not only the collaborators who have contributed with chapters to this book but also the 4TELL Research Group at the Instituto de Telecomunicações, Aveiro, who have provided valuable comments and contributions toward its compilation. Also, the editors would like to thank the Antennas, Propagation and Computational Electromagnetics Research Group, at the University of Bradford, UK, for their endless time and support during the fabrication and measurement setup.

The editors would also like to acknowledge the Fundacão para a Ciência e Tecnologia (FCT, Portugal) that partly sponsored this work (postdoc scholarship award with reference number: SFRH/BPD/95,110/2013) and provided valuable results, namely, to Chaps. 1, 6, 7, and 13. A special appreciation also goes to the Fundacão para a Ciência e Tecnologia and the ENIAC JU (THINGS2DO–GA n. 621,221) project for providing contributions toward the mitigation approaches of interference within the UWB spectrum in Chap. 7.

Contents

About the Editors

Issa Elfergani received his M.Sc. and Ph.D. in electrical engineering with power electronics (EEPE) from the University of Bradford (UK) in 2008 and 2012, with a specialization in tunable antenna design for mobile handset and UWB applications. He is now a senior researcher at the Instituto de Telecomunicações, Aveiro (Portugal), working with European research-funded projects, while serving as technical manager for ENIAC ARTEMIS and EUREKA BENEFIC. He is a member of the IEEE and the American Association for Science and Technology (AASCIT). He is a TPC member and reviewer for several IEEE international conferences. He has published over 70 academic journal and conference papers; in addition, he is the author of one book editorial and seven book chapters. His research interests are multidisciplinary and have a number of crosscutting themes that include research in various antenna designs such as MIMO, UWB, and balanced and unbalanced mobile phone antennas with application of theoretical, computational, and analytical approaches; RF-MEMS filter technologies; and power amplifiers.

Abubakar Sadiq Hussaini, MSc, PhD Head of Programmes/Director at Common wealth ITU Group (CIG), actively participating in the ITU activities of the radiocommunication, telecommunication standardization and the telecommunication development sections. He is Senior Researcher and project development manager with the 4TELL research group at Instituto de Telecomunicações, Aveiro, Portugal; Visiting Researcher at University of Bradford, UK; Assistant Professor at American University of Nigeria; and Visiting Assistant Professor at Modibbo Adama

University of Technology, Yola, Nigeria. He was microwave radio transmission operations and maintenance senior engineer with Nigerian Telecommunication Limited (NITEL), Abuja, Nigeria (10 years). He was Senate Committee of the University of Bradford, UK, received his M.Sc. in Radio Frequency Communication Engineering from the University of Bradford (UK) in 2007 and his Ph.D. in Telecommunications Engineering from University of Bradford, UK in 2012. He is a member of IEEE, IET, Optical Society of America and has contributed to numerous publications and is involved in European and CELTIC research projects. His research interests include radiofrequency system design and high-performance RF-MEMS tunable filters with specific emphasis on energy efficiency and linearity and his achievements comprise the participation in the design of energy efficient power amplifier at 3.5 GHz (mobile WiMAX frequency); the design of high-performance RF-MEMS tunable filters with tuning range from GSM 1.8 GHZ to LTE 2.6 GHz; the design and development of a "radio over fiber" optical transmitter and an optical receiver (1550 nm wavelength) in which the frequency limitations of quantum well lasers in direct RF to light transponding was investigated. He successfully attained several European projects among which are MOBILIA (2009–2011), ARTEMOS (2011–2014) and THINGS2DO (2014–2018). He has participated actively in events, conferences and seminars organized by the Information Society Technology (IST) research program, Institute of Electrical and Electronics Engineers (IEEE), Institute of Engineering and Technology (IET), and European Nano Electronics Forum. He participated in several annual European project reviews. His collective role is to defend the project objectives and results to a panel of examiners that are considered European experts in their respective technical fields. He served as a workshop organizer and a workshop chair. He is a TPC member and reviewer for many international conferences and journals. He is a guest editor for an *IET Science, Measurement & Technology* special issue.

Jonathan Rodriguez received his Masters degree in Electronic and Electrical Engineering and Ph.D from the University of Surrey (UK), in 1998 and 2004 respectively. In 2005, he became a researcher at the Instituto de Telecomunicações (Portugal) where he was a member of the Wireless Communications Scientific Area. In 2008, he became a Senior Researcher where he established the 4TELL Research Group targeting next generation mobile systems. He has served as project coordinator for major international research projects, including Eureka LOOP and FP7 C2POWER whilst serving as technical manager for FP7 COGEU and FP7 SALUS. He is currently the coordinator of the H2020-SECRET Innovative Training Network. Since 2009 he has served as Invited Assistant Professor at the University of Aveiro (Portugal), and attained Associate Level in 2015. In 2017 he was appointed Professor of Mobile

Communications at the University of South Wales (UK). He is author of more than 400 scientific works, including 10 book editorials. His professional affiliations include: Senior Member of the IEEE and Chartered Engineer (CEng) since 2013, and Fellow of the IET (2015).

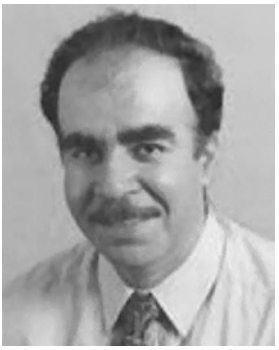

Raed A. Abd-Alhameed is professor of electromagnetic and radio frequency engineering at the University of Bradford, UK. He received his B.Sc. and M.Sc. degrees from Basrah University, in 1982 and 1985, respectively, and his Ph.D. degree from the University of Bradford, UK, in 1997, all in electrical engineering. He has many years' research experience over 25 years in the areas of radio frequency, antennas, and electromagnetic computational techniques and has published over 500 academic journal and conference papers; in addition, he is coauthor of three books and several book chapters. He is the senior academic responsible for electromagnetic research in the communications research group, in which new antenna design configurations and computational techniques have been developed including several patents which were considered and filed. Jointly with Prof. Excell (now, he is the dean of the Engineering School in Wrexham University), he has developed the principle of the "hybrid" method for electromagnetic field computation, which is able to combine the most appropriate method for differing regions of a problem (e.g., the human head and a mobile telephone). This method is recognized as being a leading area of research in bioelectromagnetic field computation. He also investigates the reduction of the size of antennas for personal mobile communications. The development of this kind of antenna is under active investigation (three patent applications submitted). He has also developed the mathematical tools needed for the simulation of nonlinear circuits, including energy-storing devices. Moreover, he has written three different programs for electromagnetic scattering problems (wire antenna design, dielectrically loaded antennas, and microstrip wire antennas) and one code for analysis of nonlinear circuits using Volterra series. Interest has been shown by publishing houses in finding ways of disseminating this work.

Part I
Evolution of the Mobile Antenna: 3G, 4G and Beyond

Chapter 1
Fundamentals of Antenna Design, Technologies and Applications

Issa Elfergani, Abubakar Sadiq Hussaini, and Jonathan Rodriguez

1.1 Introduction

In recent years, the development of telecommunication technology has brought many challenges to wireless systems, especially in the antenna domain. The significant role of the antenna development has to be considered carefully and extensively since the antenna is a very important part of the wireless system. Nowadays many different frequency bands in telecommunication systems are emerging; thus multiband antennas are becoming the standard to cover mobile technologies ranging from 2nd to 4th generation and including wireless fidelity (Wi-Fi). However, the new future releases of long-term evolution (LTE) are heading towards the lower frequency bands, providing the impetus for new antenna design requirements that can operate over a wider frequency band, and be integrated within the typically confinements of mobile handsets. In the first generation of mobile phones, the majority of global system mobile (GSM) handsets used an external antenna such as a helix, monopole (also called a whip) or a helix-plus-whip combination. However, internal antennas were gradually introduced to facilitate more flexibility in the industrial design as well as to reduce the specific absorption rate (SAR). Typically,

I. Elfergani (✉)
Instituto de Telecomunicações, Campus Universitário de Santiago, Aveiro, Portugal
e-mail: i.t.e.elfergani@av.it.pt

A.S. Hussaini
Instituto de Telecomunicações, Campus Universitário de Santiago, Aveiro, Portugal

School of Information Technology & computing, American University of Nigeria, Yola, Adamawa, Nigeria

J. Rodriguez
Instituto de Telecomunicações, Campus Universitário de Santiago, Aveiro, Portugal

University of South Wales, Pontypridd, UK

I. Elfergani et al. (eds.), *Antenna Fundamentals for Legacy Mobile Applications and Beyond*, DOI 10.1007/978-3-319-63967-3_1

there are now mainly two kinds of internal antennas used in mobile phones: the planar inverted-F antenna (PIFA), microstrip antenna and the ungrounded monopole type.

Very recently, mobile stakeholders have been investing significant research effort towards LTE Advanced (4G plus) that is able to provide higher data rates to end users by improving spectral efficiency, deploying more base stations and/or aggregating more spectra. While some of the LTE enhancements, such as advanced multiple-input multiple-output (MIMO), coordinated multipoint (CoMP), heterogeneous networks (HetNets) and carrier aggregation (CA), have the capacity to deliver additional capacity needed to sustain the traffic surge for the next few years, none of them is seen as a viable solution to support the huge influx of traffic that is forecasted for the mobile market in 2020. This provided a trigger towards the 5th generation era and yet again a new perspective to antenna design. In 5G, the research community is scanning the already congested spectrum for new slots that is able to accommodate the foreseen surge in traffic demand and has identified the underutilised millimetre-wave (mm-wave) frequency bands as a viable option. Historically, mm-wave bands were ruled out for cellular usage mainly due to concerns regarding short-range and non-line-of-sight coverage issues. However, with 5G tending towards the deployment of small cells to provide islands of high-speed connectivity, mm-wave seems to be in fashion again.

Recently, antennas are needed in almost every application related to radio engineering. A high growth in applications at different radio frequencies or radio interfaces (future emerging 5G paradigm) is providing strict design requirements on the antenna structure; the shape and size are strongly dependent on the frequency and the purpose of use. Therefore, within this chapter we introduce each antenna design driven by the concept, requirements, challenges and application, which will be reflected in the organisation of this book according to the following sections.

1.2 Multi-Band Antennas

The remarkable progress in mobile communication systems has proportionally led to the advancement of antenna systems in the recent decade. The typical mobile communication system has rapidly evolved, emerging from analogue systems to integrated digital systems fully capable of multimedia transmission over several frequency bands.

The evolution in mobile systems was paralleled by the rapid evolution in the semiconductor industry leading to advancements in mobile handset devices. In addition, keeping these devices look visually eye-catching, they must be ergonomically sound. In another words, such devices are necessary/required to be designed as slim as possible, i.e. not only in the plane parallel to the screen but also in the thickness. These design requirements had greatly influenced prevailing internal antennas over external application. Therefore, the trend was towards developing new-generation antennas suitable not only for supporting heterogeneous systems

operating on multiple frequencies but also to have conveniently small antennas integrated onto your mobile handset leading the way towards the notion of multi-band antennas.

1.2.1 Multi-Band Antenna Concept, Requirements and Techniques

Lately, the wireless technology has witnessed rapid and massive alterations/modification in terms of spectrum allocation, policies and methods of operations and approaches with the purpose of improving the performance of the wireless system as whole. Due to the enormous sophisticated studies and investigations, several wired applications have been switched into wireless, for instance, wired local access network (LAN) is converted into a wireless counterpart. Moreover, recently and due to the remarkable progress in integrated technology, it has become feasible to bring together numerous different applications operating at different channels within only one single wireless device. Accordingly, having multi-band antennas capable of covering several wireless signal standards is now a pivotal design requirement.

Wireless device terminology considers the antenna that covers more than one of the wireless communication bands as a multi-band antenna. For instance, an antenna that simultaneously covers two distinct bands encompassing frequencies of 170–2020 MHz and 2100–2700 MHz is considered a four-band or quad-band antenna because it provides coverage of International Mobile Telecommunications (IMT) 2.1 GHz (2.110–2.170, 1.920–1.980), DCS 1800 (1.805–1.880, 1.710–1.785), 2.6 GHz (2.620–2.690, 2.500–2.570) and 2 GHz S-band (2.180–2.200, 2.000–2.020). Therefore, antenna designers are recently facing huge challenges to design a single antenna element that can cover several wireless communication bands.

Multi-band antennas have drawn the attention of many operators for use in their network, due to the requirements and challenges of 2G/3G/4G co-existence. To design a single element antenna that operates over varied mobile channels such as LTE700MHZ, GSM900/1900MHZ, UMTS2100MHz, WLAN2400MHz and LTE2600MHz, antenna companies are required to come up with multi-band antennas to match different customers' requirements. For example, to model and design a 790–960/1710–2690 MHz wideband antenna, it must work over the main applications of 2G, 3G and FDD LTE. Also, to construct a 1880–2690 MHz antenna, it should operate at TD-SCDMA and TDD LTE applications to meet the multi-operator demands.

In recent times, many interesting and novel concepts and techniques have been developed to achieve multi-band antenna design to cover many wireless communication standards such as GSM, DCS, CDMA and PCS [1, 2]. Due to the quite high number of work devoted to proposing novel, beneficial avenues/techniques towards multi-band design, a detailed overview can hardly be done, and any layout can be hardly proven as the original one. For illustration, we have selected most recent published works with common methods.

For example, by simply creating slots within the radiator structure such as the U-slot patch antenna [3], multi-band function was achieved, by etching the asymmetric U-slot patch antenna with a narrow probe. This antenna layout has advantages of size reduction as well as enhanced bandwidth compared to the symmetric U-slot patch antenna.

In [4], multifunctional operation within this antenna was accomplished by creating a rectangular slot over the top of the radiator along with a T-shaped feed patch, an inverted T-shaped stub and two E-shaped stubs. Constructing an antenna with the above-mentioned procedures was sufficient to generate four bands within only one antenna element for use in GPS/WiMAX/WLAN application.

Employment of fractal shape antenna in [5] contributed towards generating multi-band frequencies. The proposed antenna with the fractal techniques was made to operate at six different resonant frequencies in X, Ku, K and V bands.

An investigation carried out in [6] was to show a new parasitic-element design for multi-band antenna, which employs the parasitic stub as the main radiator and the driven stub as a choker. This antenna structure operates over several mobile services such as GSM, GPS, DCS, PCS, UMTS and LTE 2300/2500.

Authors in [7] exploited the benefits of using metamaterial to achieve the desired negative permeability bands, which helps towards converging triple different frequency bands within a single device. Moreover, this technique has led to the significant reduction of the device structure. This design satisfies the demands of WLAN/WiMAX applications in a single device.

Exploiting the gridded ground plane [8] can be an effective way to accomplish multiple functions within one PIFA without modifying the antenna geometry and increasing the handset volume. Such a gridded ground plane was used for both size reduction and multi-band operation. This PIFA antenna can be integrated to operate for several mobile applications such as Bluetooth/WLAN, WIMAX and 4G (UMTS2100, LTE).

Antenna with different hybrid modes [9], a hybrid cylindrical dielectric resonator antenna (CDRA) was designed and implanted within this work. The radiator was designed to form a ring-shaped patch. In addition, an inverted-L strip was utilised to excite two different hybrid modes. This helped the proposed antenna to operate in several bands for use in 2400 MHz of the lower WLAN and 3600 MHz of WiMAX applications.

The entire antennas with several techniques in [1–9] have fixed multi-band operation, in which antenna cannot be altered once fabricated. However, some other adaptive techniques such as the use of PIN diodes, MEMS switches and varactor diodes are used for multi-band operation [10–13]. By using these methods, the frequency bands can be electronically tuned/modified according to the desired band without changing the antenna geometry or structure. For instance, in [10] a switchable frequency response (multi-frequency bands) was accomplished by attaching a PIN diode within the antenna ground plane. By altering the state of this diode between OFF and ON modes, the proposed antenna is capable to seamlessly tune between WLAN and a tri-band at Bluetooth, WiMAX and upper WLAN applications.

Another electronic tuning avenue is to use RF MEMS switches. In [11], the authors have designed C-shaped patches loaded with a dipole antenna. The pro-

posed antenna without the loaded RF MEMS can operate at the 1.2275 GHz for GPS applications, while it can be considered a dual-band antenna when it is being loaded with an RF MEMS switch to meet the UHF band (850 MHz–930 MHz) and ISM band (2.41–2.54 GHz) required in RFID applications. The RF MEMS are used to switch the slots ON and OFF for different frequency bands. This provides tri-band response in the reported frequency range.

Both ways of tuning the aforementioned antenna designs (PIN and RF MEMS) are said to be under the category of discrete tuning option. However, there is another complementary approach based on continuous tuning using a varactor diode. Works in [12] show that by tuning the attached varactor diode, a wide continuous frequency range from 1.7 to 2.05 GHz can be achieved. This will cover multiple frequency bands for use in various applications.

1.3 Wideband Antennas

In recent times, due to the enormous progress and growth of the mobile market, this has led to a competitive global market, which in turn has been driven by huge demand for a rich set of wireless communication services and that places stringent design requirements on the antenna layout with emphasis on key features such as compactness, wideband and good radiation performances. The broadband antennas have the capability to cover different frequency bands to allow compatibility with modern-day communication platforms and future emerging technologies. For this reason, wideband antennas are favoured since they are able to reduce the complexity, as well as the cost and size of the whole system, in contrast to traditionally deploying multiple antennas for different applications. Moreover, compact and slim wideband internal antennas are favoured in the modern mobile handset industry. In fact, the preferred antenna for contemporary wireless communications is required to operate over different services such as DVB band (530 ~ 860 MHz) [13–15], GSM band (890 ~ 960 MHz), DCS band (1710 ~ 1880 MHz) [16, 17], PCS band (1850 ~ 1990 MHz), UMTS band (1920 ~ 2170 MHz), WLAN band (2400 ~ 2484 MHz) [18, 19] and WiMAX band [3600-3800 MHz]. This type of antenna called a wideband antenna.

1.3.1 Wideband Antenna Design, Requirement and Challenges for Mobile Applications

Nowadays, to meet the customers' demand, several wireless communication services such as GSM, CDMA, GPS, WCDMA, Wi-Fi and LTE have been swiftly deployed. On the other hand, the key challenge for the wireless devices, such as mobile handsets to support all the above-mentioned services, is to incorporate more than one antenna on the same device to cater for the different frequency spectrums.

Moreover, such antennas are required to be as small as possible due the size constraints of the modern mobile device. In this context, the number and the size of the antennas affect the miniaturisation of wireless communication devices. Consequently, antennas for mobile devices should be able to operate over multi-bands or have inherent wide bandwidth characteristics, while keeping the compact size.

At the present time, portable devices, such as mobile handsets, have been profoundly integrated into our life in the first instance; 3G platform was the 'new boy on the block' providing a real choice to GSM. However, now 4G is a reality, providing higher connectivity speeds and more efficient communication in terms of spectral efficiency while also enhancing the use cases to relaying and group mobility. Therefore, it is important for wireless devices to follow evolutionary trends and to remain practical. In this context, a key challenge is focused on handset design and compatibility between generations, and beyond that between diverse wireless technologies, this means that antenna technologies should not only cover the bands of LTE700/2300/2500 but also operate over the existing mobile services of GSM850/900/1800/1900, UMTS2100 and WLAN2400MHz. The ideal sense calls for a single and simple antenna to cover all these frequencies, but practically this leads to a drop in antenna performance that was originally engineered to operate at targeted frequencies, while meeting the small size requirement also appears a challenging task (LTE700/2600/GSM900.1800/UMTS [20–26].

For example, the antenna in [20] operates over GSM900/1800, in [21] an antenna structure is capable to operate over GSM850/900 and GSM1800/1900/UMTS operations, while another antenna was proposed to cover the GSM system GSM-900/DCS-1800/PCS-1900/IMT-2000 in [22]. In [23], the antenna structure covering the GSM850/900/DCS/PCS operation was designed, and effort to generate a wide impedance band antenna to support GSM 850, GSM 900, DCS, PCS, UMTS and 2.4-GHz WLAN operations was proposed in [24]. A compact multi-band able to cover the GSM/DCS/PCS/UMTS/Bluetooth/WLANs/Wi-MAX band was investigated in [25]; another idea to design a single antenna that operates over the bands of GSM/UMTS/LTE was indicted in [26].

Therefore, the main challenge faced by antenna designers is to come up with a compact wideband mobile handset antenna for operating in the spectrum of legacy GSM, UMTS and the newly deployed long-term evolution (LTE) systems. Therefore, designing an antenna to secure the performance in the targeted bands still requires investment.

1.3.2 Wideband Antenna Techniques

Antennas for modern smart mobile phones are characterised by a low profile and wide frequency bands. The widely used frequency bands for mobile communication include LTE700 (698–787 MHz), GSM850 (824–894 MHz), GSM900 (880–960 MHz), GSM1800 (1710–1880 MHz), GSM1900 (1850–1990 MHz), UMTS

(1920–2170 MHz), LTE2300 (2305– 2400 MHz) and LTE2500 (2500–2690 MHz). The conventional mobile phone antennas mainly include three basic types: PIFAs (planar inverted-F antennas), printed monopole antennas and printed slot antennas.

Nevertheless, due to the room constraints of the antenna within the smart mobile handsets, it has become very challenging for the traditional above-mentioned antennas to operate in a wide frequency range, particularly in the lower frequency channel where it is very demanding to obtain the targeted broad bandwidth compared to the higher frequency band.

Although several approaches were reported in [13–26] to improve the bandwidth of mobile antenna, they are still not sufficient to cover all the existing services, including the GPS band, which is broadly exploited in the contemporary smartphones and tablets.

For the above case, studies have been carried out on how to achieve the GPS/GSM/UMTS/LTE wideband mobile phone antennas with emphasis on accomplishing compact volume by using several wideband techniques.

For example in [27], an antenna design procedure to cover a wide range of frequency from 700 MHz to 2600 MHz was proposed. This antenna is a type of printed monopole design. The large patch along with the matching network was responsible for the higher frequencies, i.e. GSM1800/1900/UMTS2100/LTE2300/2500. On the other hand, the ground planes of both the USB dongle and circuit board created the lower frequency bands operating over the LTE700/GSM850/900.

In [28], another printed monopole antenna paradigm was investigated. The antenna design is printed over a ground plane that was slotted exactly underneath the radiator patch strips. Wide operating bandwidths of 698–2690 MHz can be realised by the radiating arms that were capable of generating several resonant modes at about 750, 1000, 1750, 2300 and 2900 MHz. To be more explicit, the double-branch feeding line was responsible to produce triple resonant modes at around 1700, 2300 and 2900 MHz to cover the 1710–2690 MHz, whereas two-resonance modes around the 750 and 1000 MHz to cover the 698–960 MHz were generated with the aid of the long coupling strip. The proposed small antenna design can operate over LTE700, GSM850/900, DCS1800, PCS1900, UMTS2100 and LTE2300/2500 systems.

In [29], this antenna design is based on a printed PIFA shape radiator structure over the ground plane. The proposed antenna has come up with an idea of having two patches printed on both sides of a common substrate. These two patches were joined together by means of two vias. Each of these aims to contribute to impedance matching at both the upper frequency and lower frequency. The SMA connector is connected to the top radiating patch. The bottom patch is connected to the ground through a microstrip line. By exploiting such an effective technique, the proposed antenna was able to cover a wide range of bandwidth from 1.2 to 2 GHz, which was suitable to meet different applications such as GPS/DCS/GSM1800/PCS/WLAN/Bluetooth/WiMAX/LTE.

In [30], the main layout configuration of the examined antenna constitutes two strips: the top strips printed over the substrate are the combination of a coupling strip and a shorted radiating strip, while the meandered line strip was located at the

bottom side of the dielectric. The bottom meandered strip helps in widening the overall operating bands by increasing the capacitance between the main radiating strip and the meandered parasitic strip. Using the joint approaches ensures the antenna operates over a wide frequency range from 700 to 37,200 MHz, which is suitable for smart mobile handset applications.

In [31], an antenna with different configuration was proposed. This antenna is a type of radiator based on a suspended PIFA over the ground plane. The antenna is placed at the hinge position between the main and upper ground planes of the folder-type mobile phone. To excite the antenna, a capacitive feed is utilised. With the aid of this type of feeding technique, a very wide operating bandwidth from 820 to 2345 MHz is achieved. This makes such an antenna structure cover GSM850/900/1800/1900/UMTS penta-band operation for the mobile phone.

In [32], a wideband antenna is proposed whose configuration is based on an inverted F-antenna (PIFA) structure along with a coupled feeding approach. The operating bandwidth of the proposed antenna is from 820 MHz to 3 GHz, and this antenna covers the entire bands of wireless communication applications (GSM850/GSM900/GPS/DCS1800/PCS1900/WCDMA1700/WCDMA2100/WiBro2350/Bluetooth (BT)/Wi-Fi/WiMAX2500 and long-term evolution (LTE) 2600). Therefore, this makes it as an attractive option for current 2G/3G/4G and GPS services for portable devices.

1.3.3 Ultra-Wideband Antenna Requirements and Classifications

The emergence of the Internet had provided a communication platform for a great variety of services, each one of them with a specific QoS requirement and inherent mobility through access networks such as GSM, UMTS, WLAN, WiMAX and LTE. However, services like GPS and Bluetooth communications also provide very interesting use cases to be supported on portable devices. However, every service has different requirements in terms of frequency band or even polarisation and radiation, that in theory requires different antenna structures to be integrated onto a common handset. Achieving this is not an easy task, considering that the new smartphones demand more space for the electronics associated to multiple functionalities that these terminals offer, reducing the space to accommodate the antenna system. The solution is to integrate a wideband antenna that does not only operate in the above-mentioned mobile existing channels but also in synergy with the ultra-wideband (UWB) spectrum within one antenna design. This kind of UWB antenna can be used for mobile applications.

One of the main challenges for the implementation of UWB systems is the development of a suitable or optimal antenna that meets the UWB spectrum. UWB antenna is a type of antenna that covers a bandwidth greater than 500 MHz (FCC) at – 10 dB of the reflection coefficient. UWB antennas gained importance in 2002 when the US Federal Communication Commission (FCC) provided authorisation to

UWB systems to be commercially used. The FCC allocated the bandwidth of 3.1–10.6 GHz, which is one of the largest bands allocated by the FCC for unlicensed use [33]. Owing to this large bandwidth and certain important characteristics, UWB antennas have attracted a lot of attention to be used for several applications such communication, medical imaging systems and security systems. The design requirements for UWB include:

- Tremendously broad bandwidth requiring up to 7.5 GHz of bandwidth for a workable UWB antenna.
- UWB antennas are engineered for indoor use and short range, which requires an omnidirectional UWB antenna in order to provide a promising communication link between transmitters and receivers.
- High radiation efficiency. Broadly speaking, the power transmitted into space is very low, thus the radiation efficiency should be as high as possible (70% and above).
- UWB antenna requires constant group delay. When the UWB antenna is being analysed in the time domain, the linear phase benefits UWB applications. This is due to the fact that a linear phase will generate a constant group delay which in turn assures the transmitted signals and in the case of extremely short pulses will not impair the signal. This will lead to an effective system performance [33].

In terms of classifications, antennas generally can be classified based on their radiation pattern and bandwidth. UWB antenna can be categorised as omnidirectional and directional [34, 35]. Omnidirectional antennas, as the name suggests, have its radiation pattern distributed in all directions, while directional antennas have concentrated radiation patterns, thus having a high gain in the pointing direction. Another angle on classifying the UWB antennas is the determination of devices the antenna should be used for. In practice, antennas for use in base station should have high gain, while antennas for use in mobile handsets are required to compromise both size and omnidirectional features [36–39].

By investigating the antenna designs in [13–32, 34–39], it was found that they are either able to operate only over the existing mobile services such as GSM, GPS, UMTS, WLAN, WiMAX and LTE or only capable to work over the UWB spectrum from 3.1 to 10.6 GHz. Moreover, due to the constraints pertaining to the room within the mobile device, it has become unmanageable and impractical to have devices with several integrated antennas to address the entire spectrum. To address this limitation, techniques are required that can deliver a compact antenna design that can work on both existing mobile platforms and extended to UWB frequencies.

1.3.4 Methodology to Join Mobile Services and UWB Services Antenna for Mobile Application

In many applications, an antenna needs to operate efficiently with wide bandwidth characteristics. Wideband antennas refer to a classification of antennas with a relatively constant performance over a wide frequency band. Recent trends have seen

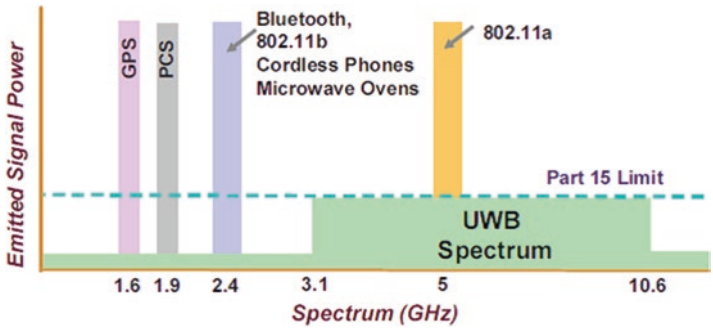

Fig. 1.1 UWB spectrum allocation

the development of wideband antennas receiving much attention to fulfil different applications in just one single terminal. Single terminals or devices could have many applications such as GPS, GSM, WLAN, Bluetooth, WiMAX, LTE and UWB spectrum. The spectrum allocation for UWB is depicted in Fig. 1.1.

However, conventional wideband antennas mentioned in [13–32] may not meet the full requirements to cover the full host of services such as GPS, GSM, WLAN, Bluetooth, WiMAX, LTE and UWB spectrum. In fact, the hypothetical single antenna will struggle to deliver the required performance over the entire frequency range, and therefore a balancing act is required to trade-off the number of antennas against performance.

Wideband antennas such as the Vivaldi [40], horn [41], log periodic [42], dipoles [43] or monopoles [44, 45] are usually found in wideband systems. However, the monopole antennas are the most common among these types; this is due to their low profile, light weight and low manufacturing costs that printed monopole antennas are very common in small wireless devices such as mobile handsets. Monopole antennas (metal-plate and printed) [44, 45] can be modified to provide wide bandwidth and omnidirectional features. Popular monopole antenna shapes with microstrip line and coplanar wave guide feeding approaches are depicted in Figs. 1.2 and 1.3.

Fundamentally, monopole antennas are composed of two major parts, namely, the radiator and the ground plane. Generally, the most common avenues to improving the impedance bandwidth of these antennas are based on optimising either the antenna's radiator, ground plane or its feeding structure, whether independently or in combination.

Thus, several techniques that may contribute towards enhancing the bandwidth of the printed and metal-plate monopole antenna were reported in [46–51]. This section will describe the conceptual study on different types of antenna using various techniques adopted to achieve ultra-wideband characteristics in the most common UWB antennas.

In [46], a novel procedure to design a metal-plate monopole antenna which operates from 1.98 to 10.14 GHz was presented. The proposed antenna mostly consists

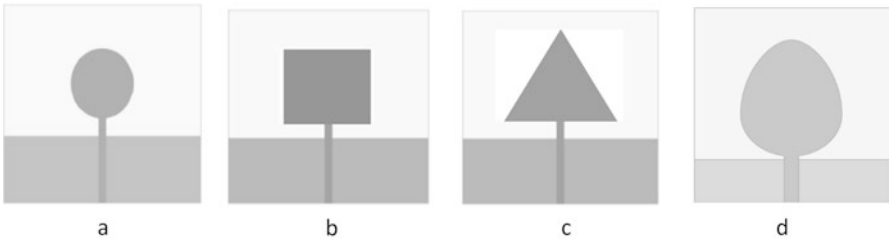

Fig. 1.2 Popular shape of monopole radiators with microstrip feeding technique, (**a**) circle, (**b**) rectangular, (**c**) triangular, (**d**) elliptical

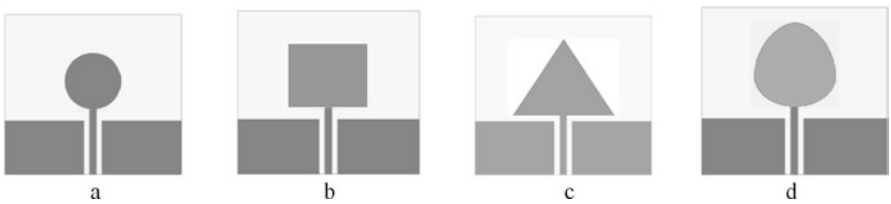

Fig. 1.3 Popular shape of monopole radiators with coplanar waveguide feeding technique, (**a**) circle, (**b**) rectangular, (**c**) triangular, (**d**) elliptical

of two parts, namely, the folded monopole portion and the matching tuning portion. The folded monopole part was accomplished by bending the rectangular planar monopole, which helped in improving the bandwidth. The part of the matching tuning was largely contributed in enhancing and controlling the impedance bandwidth by the very wide frequency range achieved; the proposed metal-plate monopole structure will be capable to operate over the existing mobile services of GSM1900, UTMS, WLAN, WiMAX, LTE as well as UWB services at the same time.

A PIFA monopole antenna configuration was presented in [47]. This antenna was printed over RF4 substrate and then mounted over a ground plane via a shorting post to form the PIFA structure. The lower frequency band was generated by a patterned ground plane with special slots as well as using stubs, while the UWB frequency was accomplished by means of utilising the taper feeding line. The proposed PIFA antenna obtained a wide frequency range from 0.8 to 11 GHz, which is suitable for GSM 900, GSM 1800, WLAN 2400 MHz, Bluetooth, WiMAX, 3G, 4G and UWB frequency from 3.1 to 10.6 GHz, making it a viable candidate for mobile and UWB applications.

Another monopole antenna based on the PIFA technique was proposed in [48]. The proposed candidate design achieved an extreme wide bandwidth from 0.8 to 11.5 GHz, recommended to work over the intended mobile phones channels as well as in the ultra-wideband (UWB) frequency range. As one can note, the feeding plate of the proposed antenna is reasonably thick compared to the normal feeding plate used with the PIFA structure. This helps the proposed PIFA to come up with a very wide bandwidth, namely, from 1.6 to 11.5 GHz. The only issues related to this kind

of feeding, where the S11 was measured to be less than 6 dB. However, the last figure of 6 dB has been used in some mobile device antenna. Since the antenna was intended to be used within the mobile device, the expectation is for the antenna to cover other existing mobile services such as GSM and GPS. Thus, to use the aforementioned wide frequency range with those mobile services within the same antenna and at the same time, an additional set of slots over the ground plane was required. This led to the creation of new low frequency modes, making this candidate antenna suitable to work at the lower spectrum of the mobile phone frequencies (GSM and GPS).

The design in [49] suggested a different type of monopole antenna that is based on the 2D printed monopole. This printed monopole antenna was designed to operate from 1.7 to 10.6 GHz frequency band, covering the services UMTS (1.9 and 2.1 GHz), WLAN (2.45 GHz) and UWB (3.1–10.6 GHz). This wide frequency range was met by introducing two high dielectric substrates on both sides. Employing such approach helps to generate the low frequency mode, while the higher resonant frequency for UWB operation is produced by feeding the antenna with a wideband microstrip feeding line.

An idea of designing a compact metal-plate monopole antenna was given in [50]. The antenna comprises two major segments, the upper hollow cylinder and a lower hollow cone. By carefully selecting the length of both parts, the cylinder and cone, the antenna was able to work over a very wide bandwidth from 1.8 to 10.6 GHz that covers the services of the UMTS (Universal Mobile Telecommunication System) band (1920 2170 MHz) and the 2.4/5.2/5.8 GHz WLAN (wireless local area network) bands for mobile/WLAN dual-mode operation together with the UWB frequency, making the proposed structure a promising candidate for mobile phone applications.

A compact internal wideband metal-plate monopole antenna suitable for mobile phone and upper UWB spectrums was presented [51]. Two basic and effective techniques were implemented to achieve the wide bandwidth characteristics. These techniques lie in using a bending radiator and asymmetrical two-branch feeding strip. This in turn will lead to create the desired impedance bandwidth over a large-scale frequency from 1.8 to 6.7 GHz, making the antenna capable to cover several bands such as the UMTS band (1920–2170 MHz), 2.4 GHz (2400–2484 MHz) and the 5.2/5.8 GHz (5150–5350/5725–5825 MHz) WLAN bands for mobile/WLAN dual-mode operation of a mobile phone. To conclude, such metal-plate antenna design can be embedded within the casing of a mobile phone as an internal antenna.

1.3.5 Notch Techniques for UWB Antenna

As mentioned before UWB technology has gained great popularity in the field of research and industrial applications due to its higher data rate and large BW. Within this section, many UWB antennas with different structure types have been

investigated [34–51]. These UWB antenna designs have overcome the main challenge of designing UWB antennas that are able to satisfy huge bandwidth, since the matching and energy transmission require to be verified over the entire bandwidth. However, in wideband applications, interference is a serious problem because of the low emitted power of the UWB system compared with major narrowband wireless standards, such as wireless local area network (WLAN) 2.4/5.2/5.8 and worldwide interoperability for microwave access (WiMAX) 2.5/3.5/5.5. Thus, the UWB antenna requires a band-suppression feature. Several techniques to create single, dual or/and triple rejected bands have been introduced [52–60]. In this section, some of those techniques that were applied to the most common UWB designs mentioned in previous section will be reviewed.

In [52], the investigation proposed a chorded crescent-shaped printed wideband antenna suitable for both mobile/wireless and low-band ultra-wide band (UWB) applications, in which the antenna operates over a wide frequency range from 1.5 to 5.5 GHz, with rejection band generated to suppress the WiMAX 3.5 GHz band. This notched band was created by etching a tapered sickle-shaped slot in the crescent element, and carefully optimising the slot locations and dimensions; the final optimum design was able to work over a wideband covering the existing wireless standards including GPS, iridium satellite band, PCS, DCS, UMTS, WLAN and lower band UWB (3.1–4.8 GHz), with a notched band feature to suppress the WiMAX sub-band (3.4–3.69 GHz).

In [53], the authors showed a new study to design a wideband antenna, including two rejection bands. The first rejection band at the higher frequency was generated by introducing an inverted strip L, while the second rejection band was produced at the lower frequency by inserting a U-shape slot. The final optimised antenna covers the frequency range from 2 to 6 GHz, with dual-band rejection at 3.5 GHz WiMAX and 5 GHz WLAN.

Another analysis of designing a wideband antenna with dual notched bands was studied in [54]. The band-rejected function has been produced by inserting strips on the wideband printed open slot antenna. By wisely selecting the optimum dimensions and positions of the two strips, both single and dual rejected bands can be easily achieved. The process started by initially introducing one strip over the printed open slot antenna that was responsible for the first notch to cover the 2.4 GHz WLAN. An additional strip was then inserted with different length, and in synergy with the previous strip, the second notch was created at 3.5 GHz WiMAX. This has enabled the proposed antenna to operate over a large bandwidth from 2 to 6 GHz, except at 2.4 and 3.5 GHz.

The most widely used methods to design notched band printed monopole antenna involve, for example, [55], which is based on the idea of proposing a compact printed monopole ultra-wideband (UWB) antenna with a single rejection band. The design involves a two-step bevelled radiant patch and a truncated ground plane, in synergy creating wide bandwidth characteristics. Moreover, by etching two symmetrical slots along with the microstrip feeding line, the rejection band was generated at the higher WLAN frequency of 5.8 GHz.

Another work in [56] presented printed monopole antennas for dual-band operating modes, namely, 2.4–2.484 GHz for use in Bluetooth applications and 3.1–10.6 GHz which is suitable for UWB. Afterwards, a stop band at the wireless local area network frequency (WLAN; 5.15–5.825 GHZ) was generated by placing a mushroom-like structure near the feed line.

To produce dual-band notches, the authors in [57] have proposed a compact triangular printed shape UWB antenna with dual rejection bands. Two procedures were implemented within this study: firstly, by creating a big C-shaped slot at the bottom side of the radiator and near to the feeding strip, a single stop band at the WiMAX (3.38–3.82 GHz) was generated, and, secondly, by etching another smaller C-shaped slot at the top of the radiating patch along with the primary bigger C-shaped slot, another filtering band at the WLAN frequencies (5.3–5.8 GHz) was realised. This has led to design of an UWB monopole antenna with two rejection bands: 3.38–3.82 GHz and 5.3–5.8 GHz for filtering the WiMAX and WLAN signals, respectively.

Another printed monopole UWB antenna with dual-band notches was presented in [58]. In this investigation, an elliptical printed shape antenna fed by a coplanar waveguide for use in UWB application was designed and implemented. Moreover, dual-band notches were created, the first rejected band was made by embedding an elliptic arc-shaped slot in the elliptical shape radiator. This will be responsible for the stop band pertaining to WiMAX 3.5 GHz. The second one was generated by inserting a compact coplanar waveguide resonant cell (CCRC) over the feeding line. The rejected band will cover the 5 GHz WLAN band. This concludes that both rejection bands were designed separately.

However, most of the UWB printed antenna stated above may face some limitations. On one aspect, increasing the size of the antenna may be needed in order to combine more band-notched elements; this does not comply with the antenna size reduction requirements for UWB systems. Moreover, some difficulties of UWB antenna design may be increased if the mutual coupling among band-notched elements takes place. Lastly, spurious resonance leads to a limited operating bandwidth which does not cover the whole UWB band from 3.1 to 10.6 GHz. Therefore, an effective approach should be provided to adjust the characteristic of each notched band according to the specification.

Thus, several attempts have been reported to design an UWB monopole printed antenna that includes going beyond dual-band notches [59, 60]. For instance, an effort in [59] was to create triple rejection bands. This involves manipulating the normal uniform width L-slots and converting these into a pair of non-uniform width L-slots that are symmetrically introduced over the stair shape radiating patch. This method results in accomplishing dual notched bands at 3.5 and 8.1 GHz, while on the other hand, another band notch was generated at 5.5 GHz by etching again two non-uniform width L-slots into the ground.

The challenge of creating a printed monopole antenna operating over the UWB range incorporating triple rejection bands was reported in [60]. This involves truncating both ends of the ground plane to create a defected ground structure (DGS) that influences the reactance of the proposed antenna and in turn leads to extending

the bandwidth by up to 160%. The triple rejection bands, namely, at 3.8, 5.5 and 7.5 GHz, were obtained simply by introducing two L-slits on the antenna PCB with two pairs of modified bow-shaped slits on the patch.

1.4 MIMO Antenna

The demand for higher data rates in wireless communications due to multimedia applications and video streaming is always on the rise. With the limited spectrum and power levels available for current wireless standards, the multiple-input multiple-output (MIMO) technology was adopted to provide a significant increase in such data rates via the use of multiple antennas on the user and base station terminals. The design of MIMO antenna systems on the user handset has many challenges due to the limited size and complexity (price). These challenges become even more profound when antenna systems are to cover the lower frequency bands supported by the latest LTE standards with multi-band coverage. Also, challenges dealing with mutual coupling and field correlation must be addressed.

1.4.1 Multiple-Input Multiple-Output (MIMO) Technology

The tremendous demands for high-speed connectivity seem endless and have been the driving force behind the evolution of wireless technology. Wireless communication systems are continuously involving, from the early analogue systems (1G, first-generation systems), taking a step to the digital world (2G, second-generation systems), 3G (3rd generation mobile communication) to support data services and voices through integrated architecture and more recently 4G (4th generation mobile communication) systems that involve high-speed data connectivity services and provisioning for future emerging use cases such as proximity-based services and Internet of Things (IoT).

However, to significantly enhance the data transmission rate, multiple-input multiple-output (MIMO) technology has been considered as a vital feature of 4G systems. As 'a key to gigabit wireless' [61], multiple-input multiple-output (MIMO) technology has been regarded as a practical approach to achieve significant increase in wireless channel capacity and reliability due to its high data rate and high spectrum efficiency without the need for additional power or spectrum in rich scattering environments [62–64].

The MIMO paradigm is playing a pivotal role in a wireless technology. It obviously can be inferred from the name that it constitutes multiple transmitters and receivers to simultaneously transfer data streams, either in space multiplexing mode for increasing data rate transmission or employing space time coding approaches for data reliability. MIMO technology takes advantage of a radio-wave phenomenon called multipath where transmitted information bounces off walls, ceilings and

Fig. 1.4 MIMO technology uses multiple radios to transfer more data at the same time

other objects, reaching the receiving antenna multiple times via different angles and at slightly different times. The paradigm of MIMO technology is illustrated in Fig. 1.4.

MIMO technology deals with issue of multipath by employing multiple, 'smart' transmitters and receivers with an added 'spatial' dimension to significantly improve performance and range. MIMO technology simultaneously allows multiple antennas to send and receive multiple spatial streams.

MIMO helps the antenna to work in a smart way. This occurs by allowing them to put together data streams arriving from many different paths and at different times to effectively increase receiver signal-capturing power. Antennas using the MIMO technology are also referred to as smart antenna. Smart antennas use spatial diversity technology. In the case of more antennas than spatial streams, the added antennas will add receiver diversity and improve coverage range.

To sum up, exploiting the MIMO antenna will noticeably enhance the capacity of a given channel. To be more realistic, increasing the number of antennas at both the receive and transmit sides will lead to linearly enhance the throughput of the channel, each time a couple of antennas (receiver/transmitter) are added to the system.

1.4.2 MIMO Antenna Concept, Requirements and Challenges

The requirements and challenges in MIMO antenna designs towards their exploitation in portable wireless communication device are focused on how to enhance the isolation between the antenna elements. Commonly, it is more challenging for engineers to design a MIMO antenna for handset applications than for the base station; this is mainly due to the size limitations in handheld devices [65, 66].

The mutual coupling takes place due to a common/shared ground plane as well as the spacing of the antenna elements. When the mutual coupling is strong, a large portion of the power fed into one port will be coupled to the other port rather than radiating to free space; consequently, destructive interference is accomplished. This entirely depends on the spacing between the antenna elements. In theory, the power gain is in proportional to the antenna elements; however, the isolation between those antenna elements decreases when the number of antenna increases. This in turn leads to high coupling coefficient, which negatively contributes towards lowering the data rates [67].

The obtained channel capacity from the MIMO antenna system offers numerous advantages compared to the traditional wireless communication system [68, 69]. However, placing multiple antennas within the area of the small, compact and slim wireless terminal device has become the key challenge due to mutual coupling. Thus, a key area of research is decoupling strategies to compensate the performance degradation in MIMO antennas, while keeping the antenna size as small as possible.

1.4.3 Decoupling Techniques for Compact MIMO Antennas

Adjacently placed antennas of distance less than λ/4 cause high coupling. Mutual coupling can be minimised by employing the antennas with some separation distance within the mobile terminal. It can be placed either on the top two edges or one on the upper part and the other on the lower part. The positioning of the antennas also disturbs the phase of the coupling currents along with the polarisation of the radiated fields. The ground coupling and field coupling can be decreased if the adjacent antennas are oriented perpendicularly to each other (i.e. 90°). Linearly polarised antennas located orthogonally to each other increase the isolation and provide polarisation diversity. However, they require a large antenna space and ground. Generally, the decoupling techniques have been classified into four classes [70], namely: the eigenmode decomposition scheme, which will identify the scattering matrix of array antenna structure by using 90° and 180°; inserted component scheme, which works on the concept of inserting a section of transmission line between the coupled antenna ports; the third scheme is the artificial structure decoupling scheme, which uses sub-wavelength EM structures such as electromagnetic band gap (EBG) structure, defected ground structures (DGS) and magnetic metamaterials; and, finally, the forth one is the coupled resonator decoupling scheme, which is based on the concept of decoupling the pair of coupled elements using coupled resonators.

The following section will focus more on the main decoupling approaches and strategies used within the MIMO mobile handset antennas. Thus, several approaches and/or leading technologies to reduce the mutual coupling within the single-band, dual-band, multi-band and wideband mobile handset MIMO antennas have been reported [71–82].

For example, the authors in [71] have shown a simple technique to reduce the mutual coupling between the antenna elements. In most cases to mitigate the coupling between the antennas, branches, elements and some other components may be added which in turn will take up costly space in mobile handsets. However, within this study the isolation was enhanced by implementing the PIFA antenna together with the coupling antenna with loop configuration. This has shown better isolation (does not exceed 220 dB, ECC is smaller than 0.02 in all considered bands) compared with the traditional way of using two PIFA antennas and exploiting other methods to reduce the coupling. The proposed antenna was found to be suitable for GSM mobile applications.

Compact MIMO which comprises of two identical suspended monopole antenna elements was investigated in [72]. Each antenna element was built with a Z-shaped capacitive coupled feed strip instead of a normal direct number feed structure in order to efficiently modify the antenna impedance matching and help in enhancing isolation between the two elements to 12 dB without employing any extra isolation enhancement approaches . The proposed structure operates over the LTE700MHz and considered as a good candidate for the 4G mobile handset.

Another single band antenna was proposed in [73], which is a type of two small printed monopole antennas each of which consists of a meandered line and an open-loop approach, and a modified T-shaped decoupling technique to mitigate the coupling between the antenna elements. The isolation between the antenna elements was effectively enhanced to around 17 dB.

In [74] a small 2 × 2 dual-band MIMO antenna was studied and analysed for use in WLAN applications. The proposed structure combines the horizontally and vertically polarised zigzag printed radiating elements. A partially stepped ground (PSG) approach was exploited to reduce the mutual coupling between radiating elements to be better than 21 dB. The proposed MIMO antenna covers both the 2400 and 5200 MHz WLAN bands.

The work in [75] proposed a 2 × 2 MIMO antenna. This MIMO antenna was made up of two monopole antenna based on PIFA configuration, with T-slots and two parasitic elements on a top plate. By exploiting such techniques, the proposed MIMO PIFA antenna was able to operate over the dual band of WLAN 2.4 GHz and WLAN 5.8 GHz, while the isolation between the two PIFA antennas was largely improved by introducing star-shaped slots over the ground plane. This antenna shows an improved isolation from −10 to −44 dB at WLAN 2.4 GHz and from −18.5 to −27 dB at WLAN 5.5 GHz, respectively.

In [76], an idea to propose a dual-band MIMO antenna for mobile handset was reported. This antenna structure lies in involving two symmetrical quarter wavelength-radiating strips and a slotted ground plane. The dual-band characteristic was achieved by cutting a slot with a T-shape at the bottom; this approach was reasonable for creating the lower band of LTE 700 MHz, while the other procedure of introducing two identical P-shaped slots at both sides of the PCB helped in accomplishing the upper resonant at 2.350 GHz. The mutual coupling was mitigated by placing a rectangular patch between the radiating strips. The added rectangular conductor creates an opposite current path, which enhances the isolation to be around −18 dBi at LTE 2300, WLAN 2.4 GHz and LTE 2500 band.

A triple band MIMO compact antenna was presented in [77]. This MIMO antenna was based on two identical folded printed monopole radiators placed on both top corners of the substrate. By carefully choosing the optimum dimensions and location of both folded printed arms, this proposed antenna was able to work over triple bands, namely, LTE 700 (698 ~ 862 MHz), LTE 2300 (2300 ~ 2400 MHz) and LTE 2500 (2500 ~ 2690 MHz). The isolation between the two antenna elements was improved to below −20 dB by placing a printed mushroom-type resonator on the ground plane exactly between the two closely spaced antennas. The results showed that the proposed antenna can be a good candidate for future 4G mobile applications.

A further approach to design a compact MIMO antenna with high isolation and able to operate both over the 3G (900/1800 GSM) and 4G (LTE 2600) standards was reported in [78]. The antenna element consists of three individual meander line-type inverted-L radiators; the highest frequency band radiator is fed by a transmission line, while the other two utilise the proximity-coupling feeding mechanism driven by the highest band radiator. The two-antenna element is closely located. Two approaches were exploited in order to reduce the mutual coupling between the two elements; these decoupling strategies include the T-shaped slot and the meandering microstrip line resonator. The T-shaped slot provided high isolation at the lower band (GSM, 900 MHz), while the meander line resonator was implemented to reduce the coupling at the higher band targeting LTE, 2600 MHz. Meanwhile, a negligible mutual coupling effect in the middle band (GSM, 1800 MHz) was accomplished by utilising a collinear-placed transverse meander line pair in the MIMO antenna.

Authors in [79] have come up with a compact printed monopole MIMO antenna, covering triple frequency bands, required for WLAN and WiMAX applications. The proposed MIMO antenna contains two identical printed modified C-shaped monopoles placed upon the same PCB. The triple frequency bands of 2.3–2.75 GHz, 3.4–3.75 GHz and 4.8–6 GHz were simply achieved by folding the two printed radiators to finally form the two modified C-shaped monopoles. The isolation between these two monopole elements was improved by etching a stepped slot ended together with an ellipse shape on the antenna PCB.

For wideband application, a new idea of modelling a wideband MIMO antenna was investigated in [80]. The suggested printed monopole MIMO configuration effectively constitutes two symmetrical radiators. Each radiator consists of four branches with different lengths that force the antenna to operate over a wide frequency range from 1.79 to 3.77 GHz. However, the isolation between these two antenna is above −10 dB. This means some current flows from one element to another, which leads to high mutual coupling between them. To this end, a T-shaped parasitic strip was printed on the common ground plane. This improved the isolation to below −10 dB. This MIMO antenna is said to be suitable for supporting most operational bands including LTE, WiMAX and WLAN standards.

A small wideband MIMO antenna with acceptable isolation was proposed in [81]. The achieved antenna comprises of identical two G-shaped elements printed over the top side of the substrate. This helped to broaden the bandwidth of the proposed design to cover 2300–7000 MHz. To reduce the mutual coupling between the two antennas within such a wide range, two inverted-L protrude branches and a T

slot were inserted over the shared ground plane. This showed an isolation value of around 22.5 dB over a wide range. This makes the proposed antenna to be a favourable applicant for mobile terminals covering LTE 2300/2600, WLAN 2.4/5.2/5.8-GHz and the lower UWB band (3.1–4.8 GHz).

A unique UWB MIMO antenna with good isolation was proposed in [82]. The proposed compact printed monopole antenna contains two modified coplanar waveguides that feed staircase-shaped radiating elements. This approach helped in accomplishing the UWB range from 2.3 to 12.5 GHz, while an additional technique consisting of two different fork-like stubs placed at the 45° axis was added in order to improve the isolation between the two elements to more than 20 dB. This enables the proposed design to operate on a wide frequency operating band (2.3–12.5 GHz), making it suitable for Bluetooth and UWB applications.

1.5 Balanced Antennas

Throughout the course of the previous sections within this chapter, we have developed the needs, requirements and challenges in antenna design for mobile and wireless applications, to come up with well-defined goals to steer the unbalanced antenna design strategy. However, these so-called unbalanced antennas reported in [1–82] have an unbalanced structure, in which the ground plane is part of the antenna. Although unbalanced structures have attracted much attention and report several advantages such as compact, low profile and low cost of manufacture, they still suffer from one acute weakness. While the device is being held by the users' hand, the current flows onto the human hand/body and leads towards depredating the antenna performance and creating losses [83].

To address these limitations, a balanced structure was announced as a smart alternative in order to avoid the degradation of antenna performance, which may take place in unbalanced antennas. The key benefit of the balanced structure lies within the current flow that is present only within the radiator while being cancelled on the ground plane. Consequently, when the mobile device is held by the user, no coupling exists between the antenna and the user's body, which in turn preserves the performance of the antenna. A balun is one key component used to mitigate the effects of unbalanced currents, which will enable compatibility between systems, and is used as a feeding mechanism for converting unbalanced circuit structures into balanced ones.

1.5.1 Balanced Antenna Concept, Requirements and Challenges

The concept of the balanced antenna design lies in modelling an antenna with a symmetrical structure that is fed with balanced current. The current of this antenna structure should have the same magnitude and 180° phase difference one with

another. These signals would only flow on the antenna, and will be cancelled out on the ground plane. This helps to improve the whole antenna performance, and also mitigate the coupling effects of the radiating element to the handset.

In this case, it is not feasible to feed the balanced structure with unbalanced feeding techniques such as a coaxial transmission, so as to keep zero potential outside the coaxial feeding line. However, there is a possibility to utilise the coaxial feeing line along with the balanced structure by employing some other approaches such as balun (balanced to unbalanced), whereby the unwanted flow current of the coaxial feeding may be tolerated.

Thus, the balun will bring some benefits over the inherent effect of using the coaxial cable within the unbalanced antennas. The balun is a known technique for balancing the area of conjunction between the feed line and the antenna input. By making this junction balanced, currents of equal amplitude but out of phase will still flow on the outside of the coaxial cable. However being out of phase, since it flows from both halves of the antenna, it cancels itself out and has very little if any measurable effect on the antenna radiation pattern.

This offers a promising improvement over unbalanced antennas. In the case of the unbalanced structure, currents may exist on the chassis that interact strongly with the unpredictable (response) characteristics of the body [84–86]. Furthermore, the SAR values of the balanced antennas have been in compliance with the FCC SAR limit when in proximity to the human head, compared with traditional counterpart of the unbalanced antennas [83].

Antennas for mobile devices are generally required to work over dual and/or group of frequency bands. The dimensions of a balanced antenna are almost inevitably larger than those of an unbalanced antenna (for the same impedance bandwidth), so although a balanced structure is entirely practicable for the upper bands (1710 MHz and above), unbalanced antenna such as PIFA and printed monopole for operating in the lower bands of GSM800/900 MHz is still widely used. However, recently there is a big effort and challenge for antenna designers and engineers to design a balanced antenna structure that covers the lower bands (800–900 MHz).

Therefore, suitable balanced antenna structures remain a significant design challenge, with further practical design considerations to include the overall weight of the package and the demand for multiple service bands. Numerous balanced designs along with novel approaches have been described [87–93], with desired objectives to include size reduction, while maintaining generally good electrical performance and maximising the number of possible service bands available to a single antenna.

For example in [87], a balanced dual folded inverted-F antenna integrated with a lumped LC balun to support the feeding network was studied and analysed. A type of L-slit shape was inserted over the antenna ground plane. The folded arms of the proposed antenna contributed towards a huge size reduction. In particular, the proposed lumped LC balun was not only an attractive solution to be used in mobile handset application due to its compact volume, but also allowed ease of integration with the proposed balanced antenna. The full assembly antenna (antenna with balun) operates at 2.45 GHz, making it suitable for practical WLAN applications in mobile handsets.

An approach to design a balanced antenna that operates in dual-band mode was proposed in [88]. It constitutes a printed meander line dipole that helps to reduce the antenna size as well as accomplish dual-band characteristics. A balun was exploited to verify the operation of the proposed balanced antenna structure. This antenna was able to cover the dual mode of 3.78 and 4.29 GHz, respectively.

A workable method to design a dual-band balanced antenna was reported in [89]. The principal configuration and structure of this design is based on the combination of a grated bow tie dipole, short dipole and a sectored arc; such a compact design was reached, after a comprehensive analysis of the main antenna elements. For practical reasons, a compact balun based on edges-even broadside couple strip-line (EEBCS) to coplanar waveguide (CPW) transition was also designed and integrated with the proposed antenna. This balun was positioned exactly between the radiating element and the circular ground plane. The proposed balanced antenna showed a dual-band frequency operation 1.54–3.24 and from 4.88 to 6.80 GHz, respectively.

Authors in [90] have obtained a balanced antenna mode, covering dual-band WLAN wireless communication. This antenna was constructed from a thin-strip planar dipole, with a folded structure and a dual-arm on each half of the dipole. Both resonant WLAN bands, namely, 2.4 and 5.5 GHz, were generated through two different respective approaches: first, two identical metal folded arms were created, one on each side. This step was an effective way to reduce the antenna size. The 2.4 GHzWLAN was produced by inserting symmetrical slots on each strip of the dipole conductor; the second resonant WLAN band (5.5 GHz) was created by introducing a novel technique of inserting a strip stub of appropriate length and width into each arm of the planar dipole with folded structure.

A study to design a balanced antenna for operation in a wide frequency range was carried out in [91]. The initial layout of this antenna is based on the planar open-end loop configuration that makes the antenna operate over the WLAN2.5GHz. The second step was to meet the objective of achieving a wide bandwidth. This was accomplished by adding a circular patch exactly in the centre of the balanced loops on each side. This approach helped in generating the wideband characteristics while not disturbing the key resonant frequency of the design, i.e. 2.5 GHz. This circular radiating patch was fed by extending the strip-line from the open end of the planar loops. The final layout proposes a compact balanced antenna that is capable to operate over a wide frequency range, covering several mobile services such as GPS1500MHz, GSM1800MHz, UMTS2100MHz, Bluetooth/WLANs 2400-2500 MHz and Wi-MAX3800MHz.

Different layout of the balanced antenna design was realised in [92]. This antenna is a type of Vivaldi antenna with balanced structure. The Vivaldi antenna is one of the best candidates for UWB applications. The antenna is made up of three layers: two external layers are connected to the feeding line ground planes and the central layer is connected to the signal conductor of the feeding line. Two substrates were exploited to support the copper layers. The proposed feeding method is a gradual transition from a strip-line to a tri-strip transmission line (TL). The proposed balanced Vivaldi antenna showed an extended bandwidth from 1 to 20 GHz that makes

the antenna a suitable candidate to cover some of the existing mobile services such as GPS, GSM, UTMS, WLAN and WiMAX, as well as at the same time operating in the whole range of UWB spectrum from 3.1 to 10.6 GHz.

Another attempt to design an UWB balanced Vivaldi antenna is based on the antipodal structure suggested in [93], where a new balun that operates in the same frequency range of the proposed antenna was proposed and integrated. The proposed balanced antipodal Vivaldi antenna integrating the new balun demonstrated a wide bandwidth from 3.1 to 11.5 GHz.

1.6 mm-wave Antenna

The previous sections have established different antenna design principles, challenges and technologies for low profile and space-efficient antennas, with suitable bandwidth for operation in single band, dual band, multi-band and wideband for 3G and 4G standard handsets and terminals. The major design challenges encountered in the open literature have been addressed where possible. The bandwidth and size constraints on several antennas have been addressed, and the various techniques used to improve this criterion have been applied, with particular reference to printed and suspended structures.

However, lately, mobile communication systems have become prevalent in various, if not even all, regions all over the global driven by a strong demand for ever-increasing high data rates, low latency and high-energy efficiency per service. Previous generations of wireless standards such as 3G and 4G have provided improvements in these areas by increasing the coding and modulation efficiency. However, mobile traffic is foreseen to increase exponentially over the next decade, driven by IoT (Internet of Things) technology and Smart City applications. This means the current cellular networks may need to deliver as much as a thousand times the capacity relative to current levels, and it is clear that legacy mobile systems will reach a saturation point providing the motivation for a new 5th Generation mobile network that can cater for this demand as well provide scale of economies. Moreover, with frequency spectrum becoming increasingly a valuable commodity due to shortage at the traditional microwave frequencies, 5G will look towards the mm-wave band, as a means to harness the large swathes of available spectrum raising new challenges in terms of handset, and in particular antenna design.

In 5G systems, the antennas are expected or/and entailed to have a high gain of at least 10 dBi and bandwidth greater than 1 GHz [94]. There are many works done on wireless communication, which utilise printed antenna technology for mm-wave bands [95–98]. Microstrip antenna is used for many applications due to its simple and low profile features. However, microstrip antenna suffers from narrow bandwidth typically 2–5% [99]. The metallic and surface wave loss of this type of antenna may reduce the antenna gain and efficiency considerably at mm-wave frequencies.

1.6.1 Millimetre-Wave Technology and Operation

Recently, the mm-wave technology has been a fascinating and remarkable area of research for both academia and industry. Several investigations and studies have considered the main characteristics of mm-wave channels and electronics and also try to find some avenues to fully get use of such characteristics and advantages in order to obtain better data rate. Moreover, standardisation bodies have allocated huge time and efforts to create a norm for mm-wave communication applications [100]. The conventional microwave frequency bands may be limited in terms of attainable gains to accomplish data rates exceeding 1 Gbps or even 10 Gbps. Consequently, it is not feasible to employ such relatively low frequency bands to meet the rapid increase of 5G traffic demands.

In spite of the endless employments of emerging mechanisms to improve spectrum efficiency, it remains challenging to obtain data rates exceeding 1 Gbps or even 10 Gbps. Thus, it has become unmanageable to come across the demands for 5G using the microwave spectrum. Moreover, interference becomes a limiting factor, especially in densely populated HetNets. Accordingly, millimetre-wave (mm-wave) technology ranging from 30 to 300 GHz has been announced as a practical and promising alternative to overcome the above-mentioned challenges. Figure 1.5 displays the whole spectrum of mm-wave frequency.

Despite these promising features, mm-wave bands until now have been considered unattractive for use in mobile communications. The key concern was targeting the physical barrier such as the potential high path loss as well as other losses, which place some restrictions on mm-wave applications to be only deployed within an indoor environment. However, thanks to the investigations done by a research group of New York University [101], that verified the possibility of using mm-wave transmission in the small cell of 4G communication under various urban environments at 28-GHz, 38-GHz and 73-GHz bands based on extensive measurement data. Moreover, a similar study in [102] was carried out over the 60 GHz band by both measurements and simulations, approving the potential use and deployment of mm-wave approach in an outdoor environment.

Operations at millimetre-wave spectrum have been suggested as the key answer to the constantly urging request for additional bandwidth and higher data rates.

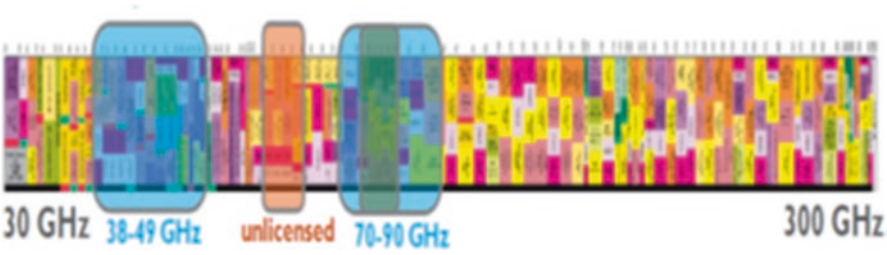

Fig. 1.5 The whole mm-wave spectrum

The traditional microwave frequency is no longer a feasible platform to deliver future services over smart mobile handset. This is due to the congestion and the constraints of the spectrum at these frequencies to meet the key demand for higher data rate, which required by mobile smartphone operators and users [103].

On the other hand, to satisfy this demand, the unused spectrum of millimetre-wave frequencies was introduced. Commonly, millimetre-wave frequency band refers to the range of frequency from 30 to 300 GHz, in which the corresponding wavelengths range from 1 to 10 mm. Moreover, even the frequency spectrum from 10 to 30 GHz is sometimes said to be deemed as millimetre-wave frequency, due to the fact that the transmitted signal has come up with more or less similar propagating features compared to its counterpart of millimetre-wave frequencies [104].

In spite of the significant features of the mm-wave frequency, there will be some challenges pertaining to deployment and operation of millimetre-wave frequency. The three raised challenges facing the propagation and operation of millimetre-wave frequencies are high free space path loss, absorption due to atmospheric gases and rainfall and non-line of sight propagation [103–105]. This forms the major challenge for millimetre-wave frequencies in 5G systems. To overcome this restriction, the antenna should have the ability to reconfigure its radiation pattern in order to avoid obstacles and maintain the link with other nodes in a network.

1.6.2 Millimetre-Wave Antenna Requirements, Challenges and Solutions as Potential Candidate for 5G-Enabled Applications

Over the last two decades, mobile and wireless communication networks (GSM, 2G, 2.5G, 3G) have witnessed remarkable progress and advancement. The multimedia applications for cellular system are restricted to frequency spectrum range from 0.7 to 2.6 GHz. The global spectrum bandwidth allocation for all the cellular networks does not exceed 780 MHz where each service provider has approximately 200 MHz across all of the different cellular bands of the available spectrum.

Due to a shortage of frequency spectrum below 6 GHz, bands at higher frequencies, e.g. the mm-wave frequency bands (30–300 GHz), have been suggested as the promising potential market candidate for 5G future cellular networks, since there are considerably larger bandwidths available that can be exploited towards increasing capacity and enabling users to experience several gigabits per second data rates. Figure 1.6 shows the available spectrum considered for mm-wave cellular.

This new market has created new requirements in speed and bandwidth that current technologies can hardly cover; the industry needs a way to increase channel capacity in wireless communications since legacy systems are too crowded to be useful. Take, for instance, the users of wireless local area network (WLAN) and wireless personal area network (WPAN) protocols, which share the same spectrum and, most of the time, collide and interfere with each other. Thus, many research

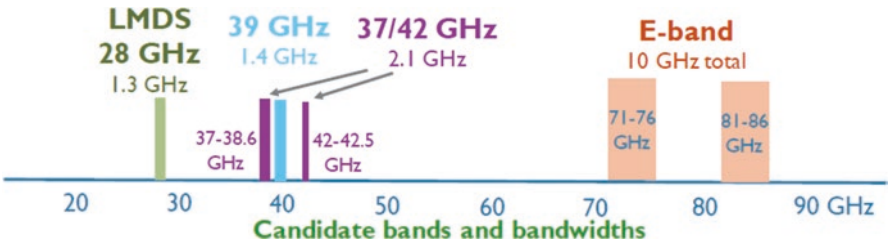

Fig. 1.6 Available spectrum considered for mm-wave cellular

groups are proposing the migration of wireless systems to millimetre-wave frequencies (30–300 GHz) as a feasible solution to these problems. Such problems in wave propagation are foreseen to be resolved by the helps of antenna design technologies.

There exist many challenges that mm-wave antenna designers may face. Firstly, for the same communication distance, the free-space path loss is increased by 3 dB with twice the transmission frequency. As a result, sophisticated antenna designs are required for mm-wave communication systems to overcome the severe attenuation and path loss between the transmitters and receivers. In addition, the extra attenuation experienced by mm-wave communications should also be taken into account. For instance, under conditions of heavy rainfall where the diameter of the raindrops could reach 3 mm that is the order of the mm-wave wavelength, scattering can occur that will severely impair the communication quality of mm-wave cellular networks.

Secondly, due to mechanical motions, for example, wind, the movement of antenna arrays is in the order of up to hundreds of mm-wave wavelengths, which will make mm-wave communications highly intermittent, especially when the antenna array has a very narrow beam pattern [106]. Finally, mm-wave communications between base stations (BSs) and access points (APs) are usually affected by various ground obstacles [107]. Since the wavelength of mm-wave bands is very short, effective communications generally require the transmitter and the corresponding receiver to be located in LOS range, so surrounding buildings and trees may impose a significant influence on the performance of mm-wave cellular networks, especially for mobile users. A number of mm-wave antennas with different approaches have been reported [108–113].

Authors in [108] have proposed a small monopole antenna with only one layer dielectric load. This proposed antenna based on PIFA configuration. The obtained antenna layout also has come up with two H-shaped slots in vertical and horizontal orientations. The presented antenna structure was proposed to operate over the resonant frequency of 28 GHz. The power gain of this antenna was improved by exploiting the advantages of high efficiency of the dielectric load. Again, this has promoted the present antenna to exhibit several benefits such as stable broadside radiation patterns, power high gain and improved efficiency, which in turn make it as a convenient candidate for 5G future handset devices.

In [109] a novel idea to present an antenna over wide mm-wave spectrum range was proposed. Two tiers/producers were carried out within this work. Initially, an investigation of designing low-cost wideband L-probe microstrip antenna which operates at millimetre-wave band was done. Such single element was modified by placing the horizontal portion of the L-probe at the same layer of the radiating patch. To excite this achieved single element, a novel coplanar waveguide (CPW) feed network has been proposed. This antenna covers a wide frequency range from 55 to 80 GHz, with power gain values fluctuating from 6.5 to 7.5 dBi over the aggregated wide bandwidth.

However, further modifications were made on the single element antenna in order to accomplish a high gain antenna structure. Thus, an array with 4×4 L-shaped probe microstrip patch antenna elements was modelled. Moreover, a four-way power divider was utilised in order to feed each subarray of 2×2 elements that are symmetrical to the antenna design. Elements in pairs are positioned opposite to each other with different spaces. This is because of the differential outputs provided by the feed network. By utilising the feeding approach of coplanar waveguide, four symmetrical 2×2 subarrays were seamlessly joined. The final layout of the array antenna has achieved a higher gain compared to the first single element antenna. The gain values of the array antenna varied from 14 to 16.5 dBi over the completely wideband.

A dual-band mm-wave antenna with simple structure was proposed in [110]. The topology of the selected antenna made of a monolayer structure with the bottom ground layer occupying the back side of substrate. An off-centred single microstrip line was used as a feeding technique within this study. The radiator part of the proposed antenna consists of the main copper patch and an L-slit shape was printed on this patch. This was considered as an efficient approach to accomplish the dual resonant frequencies. To be more explicit, the embedded L-slit in the optimum location over the patch resulted in adding booth capacitive and inductive effects which in turn led to introducing the multi-resonance operation. The obtained antenna design covers dual band of mm-wave spectrum, i.e. 28 and 38 GHz, and also it achieved circular polarisation. These features have enabled this antenna for use in future millimetre-wave mobile communication.

In [111], another idea to obtain a dual-band patch antenna for mm-wave frequency was presented. The main configuration of antenna design comprises of a radiating patch with a circular shape, which is located non-concentrically inside a circular slot etched off the ground plane. A proximity-feed technique was used to feed the structure. The proposed design was intended to operate over dual band of 28 and 38 for use in the future millimetre-wave mobile network communication.

A wideband mm-wave antenna with high gain characteristics was studied and analysed in [112]. The layout of the proposed contains a pair of radiators forming a bow tie. Each radiator is printed on the opposite side of the common dielectric substrate and fed through substrate integrated waveguide (SIW) feed line. The proposed antenna operates over a wide bandwidth range 57–64 GHz.

The power gain of the proposed layout was improved by arranging the bow tie radiators to cross each other symmetrically by tilting the feed lines by 30°. This also

helped in accomplishing the desired radiation patterns. Moreover, the issue of the back-lobe level was suppressed by loading a pair of double G-shaped resonators (DGRs) that were positioned in the area between radiators and SIW.

A new configuration of a compact mm-wave antenna that was printed over low-cost flexible PET substrate, which makes it suitable for future 5G wireless networks, was proposed [113]. This antenna layout comprises of a normal and simple rectangular patch structure having symmetrical arrangements of slots on both sides of the patch. The antenna was fed by means of a coplanar waveguide (CPW). By combing all the above-mentioned approaches as well as the good wideband features of CPW, the proposed antenna was able to cover a wide bandwidth from 22 to 40 GHz. Moreover, this antenna shows more or less high gain values varied from 4 to 8.2 dBi. Such an antenna with promising features was said to be a convenient for future 5G wireless networks with the flexibility to incorporate on planar surfaces like windows, doors, etc. or can be made a part of non-planar surfaces like uniform or casual clothing.

1.7 Summary

Antenna design has evolved and reflects the ever-increasing design requirements emanating from the mobile communication roadmap starting from 3rd Generation phones towards the latest release of LTE-A, and the future emerging 5G scenario.

This chapter provides a comprehensive discussion on the state-of-the-art technologies and challenges in antenna design for mobile communications. The chapter covers all the important aspects a research engineer may refer to when designing a new antenna, which includes how to design various antennas for different applications, how to introduce *different* approaches to achieve multi-band and wideband structures and how to sufficiently optimise such antennas and realise diverse experimental measurements.

This chapter has been divided into six sections, namely, multi-band antennas, wideband antennas, MIMO antennas, balanced antennas and, finally, mm-wave antennas, reflecting the new design requirements as we head towards 5G and beyond. Although there are several fragmented published work on the above-mentioned antennas for wireless and mobile applications, this chapter aims to harness these works to identify the very latest technologies and challenges where research efforts are still required. Thus, we evolve each antenna design driven by the concept, requirements, challenges and application and organised in this book according to the aforementioned sections.

The proposed antennas in this book are all miniature which enables ease of integration into future emerging mobile handsets or wireless devices.

Acknowledgements This work is carried out under the grant of the Fundacão para a Ciência e a Tecnologia (FCT - Portugal), with the reference number: SFRH / BPD / 95110 / 2013 and funded by national funds through FCT/MEC (PEst-OE/EEI/LA0008/2013 - UID/EEA/50008/2013).

References

1. V.-A. Nguyel, R.-A. Bhatti, S.-O. Park, A simple PIFA-based tunable internal antenna for personal communication handsets. IEEE Antennas Wireless Propag. Lett. **7**, 130–133 (2008)
2. N. Behbad, K. Sarabandi, Dual-band reconfigurable antenna with a very wide tenability range. IEEE Trans. Antennas Propag. **54**(2), 409–416 (2006)
3. G.F. Khodaei, J. Nourinia, C. Ghobadi, A practical miniaturized U-slot patch antenna with enhanced bandwidth. Prog. Electromagn. Res. B **3**, 47–62 (2008)
4. Y.F. Cao, S.W. Cheung, T.I. Yuk, A multiband slot antenna for GPS/WiMAX/WLAN systems. IEEE Trans. Antennas Propag. **63**(3), 952–958 (2015)
5. B. B. Chowdhury, R. De, M. Bhowmik. A novel design for circular patch fractal antenna for multiband applications. 2016 3rd international conference on signal processing and integrated networks (SPIN), Noida, India, 11–12 Feb 2016, pp. 1–5
6. K.-C. Lin, C.-H. Lin, Y.-C. Lin, Simple printed multiband antenna with novel parasitic-element design for multistandard mobile phone applications. IEEE Trans. Antennas Propag. **61**(1), 488–491 (2013)
7. R. Rajkumar, K.U. Kiran, A compact metamaterial multiband antenna for WLAN/WiMAX/ITUband applications. AEÜ Int J Electron Commun. **70**, 599–604 (2016)
8. L. Wakrim, S. Ibnyaich, M.M. Hassani, Multiband operation and performance enhancement of the PIFA antenna by using particle swarm optimization and overlapping method. Hindawi Publishing Corporation Applied Computational Intelligence and Software Computing **2017**, 3481709, 8 pages (2017)
9. A. Sharma, R.K. Gangwar, Triple-band dual-polarized hybrid cylindrical dielectric resonator antenna with hybrid modes excitation. Prog. Electromagn. Res. C **67**, 97–105 (2016)
10. B.K. Mehri, R. Pejman, S. Vahid, M.M. Fakharian, Small square reconfigurable antenna with switchable single/tri-band functions. Radioengineering **25**(1), 40–46 (2016)
11. N.M. Sahar, M.T. Islam, N. Misran, A reconfigurable multiband antenna for RFID and GPS applications. Elektronika Ir Elektrotechnika, ISSN 1392-1215 **21**(6), 44–50 (2015)
12. I.T.E. Elfergani, T. Sadeghpour, R.A. Abd-Alhameed, A.S. Hussaini, J.M. Noras, S.M.R. Jones, J. Rodriguez, Reconfigurable antenna design for mobile handsets including harmonic radiation measurements. IET Microwaves Antennas Propag. **6**(9), 990–999 (2012)
13. Y.S. Yu, D.H. Seo, S.G. Jeon, J.H. Cho, Design of an internal DTV antenna for portable multimedia player. Proceedings of Asia-Pacific Microwave Conference **2006**, 1601–1603 (2006)
14. H.K. Kan, R.B. Waterhouse, Shorted spiral-like printed antennas. IEEE Trans. Antennas Propag. **50**, 396–397 (2002)
15. M.C. Liang, K.C. Huang, M.L. Lo, A low frequency spiral C-patch antenna design for automotive application, in 2004 IEEE Antennas Propag. Soc. Int. Symp. Dig., vol. 1, pp. 1070–1073, Monterey, CA, USA
16. H. C. Tung, K.L. Wong, Dual-band inverted-L monopole antenna for GSM/DCS mobile phone, in 2002 IEEE Antennas Propag. Soc. Int. Symp. Dig., vol. 3, pp. 30–33, San Antonio, Texas, USA
17. F.S. Chang, K.L. Wong, Folded meandered-patch monopole antenna for low-profile GSM/DCS. Microw. Opt. Technol. Lett. **34**, 84–86 (2002)
18. N.P. Agrawall, G. Kumar, K.P. Ray, Wide-band planar monopole antennas. IEEE Trans. Antennas Propag. **46**, 294–295 (1998)
19. E. Lee, P.S. Hall, P. Gardner, Compact wideband planar monopole antenna. Electron. Lett. **50**, 2157–2158 (1999)
20. A.H. Kusuma, A.-F. Sheta, I.M. Elshafiey, Z. Siddiqui, M.A.S. Alkanhal, S. Aldosari, S.A. Alshebeili, A new low SAR antenna structure for wireless handset applications. Prog. Electromagn. Res. **112**, 23–40 (2011)
21. K.L. Wong, T.W. Kang, GSM850/900/1800/1900/UMTS printed monopole antenna for mobile phone application. Microw. Opt. Technol. Lett. **50**, 3192–3198 (2008)

22. D.B. Lin, I.T. Tang, M.Z. Hong, A compact quad-band PIFA by tuning the defected ground structure for mobile phones. Prog. Electromagn. Res. B **24**, 173–189 (2010)
23. C.H. Wu, K.L. Wong, Internal hybrid loop/monopole slot antenna for quad-band operation in the mobile phone. Microw. Opt. Technol. Lett. **50**, 795–801 (2008)
24. J.Y. Sze, Y.F. Wu, A compact planar hexa-band internal antenna for mobile phone. Prog. Electromagn. Res. **107**, 413–425 (2010)
25. W.J. Liao, S.H. Chang, L.K. Li, A compact planar multiband antenna for integrated mobile devices. Prog. Electromagn. Res. **109**, 1–16 (2010)
26. J.H. Chen, Y.L. Ban, H.M. Yuan, Y.J. Wu, Printed coupled-fed PIFA for seven-band GSM/UMTS/LTE WWAN mobile phone. J. Electromagnet. Wave. **26**(2–3), 390–401 (2012)
27. Y.-L. Ban, J.-H. Chen, L.-J. Ying, J.L.-W. Li, Y.-J. Wu, Ultrawideband antenna for LTE/GSM/UMTS wireless USB dongle applications. IEEE Antennas Wireless Propag. Lett. **11**, 403–406 (2012)
28. Z. Chen, Y.-L. Ban, J.-H. Chen, J.L.-W. Li, Y.-J. Wu, Bandwidth Enhancement of LTE/WWAN printed mobile phone antenna using slotted ground structure. Prog. Electromagn. Res. **129**, 469–483 (2012)
29. M. Naser-Moghadasi, Z. Mansouri, S. Sharma, F.B. Zarrabi, B.S. Virdee, Low SAR PIFA antenna for wideband applications. IETE J. Res. **62**(5), 564–570 (2016)
30. P.K. Bharti, H.S. Singh, G.K. Pandey, M.K. Meshram, Thin profile wideband printed monopole antenna for slim mobile handsets applications. Prog. Electromagn. Res. C **57**, 149–158 (2015)
31. C.-H. Wu, K.-L. Wong, Ultrawideband PIFA with a capacitive feed for penta-band folder-type mobile phone antenna. IEEE Trans. Antennas Propag. **57**(8), 2461–2464 (2009)
32. M. Kim, W. Lee, Y.J. Yoon, Wideband antenna for mobile terminals using a coupled feeding structure. IEEE International Symposium on Antennas and Propagation (APSURSI), 3–8 Jul 2011, pp. 1–4
33. Federal Communications Commission, FCC Report and Order on Ultra Wideband Technology, Federal Communications Commission, Washington, DC, USA, 2002
34. A.M. Abbosh, M.E. Bialkowski, Design of ultrawideband planar monopole antennas of circular and elliptical shape. IEEE Trans. Antennas Propag. **AP-56**(1), 17–23 (2008)
35. A.T. Mobashsher, A. Abbosh, Wideband unidirectional antenna for head imaging system, IEEE Antennas and Propagation Society International Symposium, Orlando, Florida, USA, 7–13 Jul 2013, pp. 674–675
36. N.C. Azenui, H.Y.D. Yang, A printed crescent patch antenna for ultrawideband applications. IEEE Antennas Wireless Propag. Lett. **6**, 113–116 (2007)
37. X.-L. Liang, S.-S. Zhong, W. Wang, Compact elliptical monopole antenna with impedance bandwidth in excess of 21:1. IEEE Trans. Antennas Propag. **55**(11), 3082–3085 (2007)
38. X.-R. Yan, S.-S. Zhong, G.-Y. Wang, Compact printed monopole antenna with 2 4: 1 impedance bandwidth. Electron. Lett. **44**(2), 73–74 (2008)
39. X.-L. Liang, S.-S. Zhong, W. Wang, Tapered CPW -fed printed monopole antenna. Microw. Opt. Technol. Lett. **48**(7), 1411–1413 (2006)
40. Z. Wang, Y. Yin, J. Wu, R. Lian, Printed monopole. IEEE Antennas Wireless Propag. Lett. **15**, 16–19 (2016)
41. Y. Wang, G. Fang, S. Hai, Y. Ji, S. Ye, X. Zhang, A novel UWB TEM horn antenna with a microstrip-type feed. Int. J. Antennas Propag. **2015**, 182140, 6 (2015)
42. A. Amini, H. Oraizi, M.A. Chaychizadeh, Miniaturized UWB log-periodic square fractal antenna. IEEE Antenna Wireless Propag. Lett. **14**, 1322–1325 (2015)
43. R.S. Brar, S. Singhal, A.K. Singh, Rotated quadrilateral dipole UWB antenna for wireless communication. Prog. Electromagn. Res. C **66**, 117–128 (2016)
44. M.M. Islam, M.R.I. Faruque, M.T. Islam, A compact disc-shaped printed antenna using parasitic element on ground plane for super wideband applications. ACES J. **31**(8), 960–969 (2016)
45. S.A. Naghdehforushha, H. Oraizi, F.H. Kashani, A.J. Deel, Design of a rectangular metallic monopole antenna with protruding normal plates for applications in UWB communication. Progr. Electromagn. Res. C **51**, 161–167 (2014)

46. K.-L. Wong, T.-C. Tseng, P.-L. Teng, Low-profile ultra-wideband antenna for mobile phone applications. Microw. Opt. Technol. Lett. **43**(1), 7–9 (2004)
47. S. Jegadeesan, Z. Mansouri, Ultra wideband PIFA antenna with supporting GSM and WiMAX for mobile phone applications, Fifth International Conference on Advanced Computing & Communication Technologies, 21–22 Feb 2015, pp. 1–6
48. R. Gomez-Villanueva, R. Linares-y-Miranda, J.A. Tirado-Mendez, H. Jardon-Aguilar, Ultra-wideband planar inverted-F antenna (PIFA) for mobile phone frequencies and ultra-wideband applications. Prog. Electromagn. Res. C **43**, 109–120 (2013)
49. N.G. do Serro UWB antenna for portable devices, IEEE Antennas and Propagation Society International Symposium, 5–11 Jul 2008, pp. 1–6
50. K.-L. Wong, S.-L. Chien, Wide-band cylindrical monopole antenna for mobile phone. IEEE Trans. Antennas Propag. **53**(8), 1–3 (2005)
51. Y.-T. Liu, S.-W. Su, An internal wideband monopole antenna for UMTS/WLAN dualmode mobile phone. Microw. Opt. Technol. Lett. **50**(7), 1741–1744 (2008)
52. C.H. See, R.A. Abd-Alhameed, F. Elmegri, D. Zhou, J.M. Noras, N.J. McEwan, S.M.R. Jones, P.S. Excell, Planar monopole antennas for new generation mobile and lower band ultra-wide band applications. IET Microw. Antennas Propag. **6**(11), 1207–1214 (2012)
53. W.-S. Chen, P.-Y. Chang, B.-Y. Lee, H.-T. Chen , and J.-S. Kuo, A compact microstrip-fed slot antenna with a dual-band notched function for WiMAX Operation, 2010 IEEE Antennas and Propagation Society International Symposium, 11–17 Jul 2010, pp. 1–4
54. W.-S. Chen, K.-Y. Ku, Band-rejected design of the printed open slot antenna for WLAN/WiMAX operation. IEEE Trans. Antennas Propag. **56**(4), 1163–1169 (2008)
55. Y. Xiao, Z.-Y. Wang, J. Li, Z.-L. Yuan, A.K. Qin, Two-step bevelled UWB printed monopole antenna with band notch. Int. J. Antennas Propag, 11 pages (2014, 173704, 2014)
56. T. Mandal, S. Das, Design of a microstrip fed printed monopole antenna for bluetooth and UWB applications with WLAN notch band characteristics. Int. J. RF Microw. C. E. **25**(1), 66–74 (2015)
57. J. Xu, D.-Y. Shen, G.-T. Wang, X.-H. Zhang, X.-P. Zhang, K. Wu, A small UWB antenna with dual band-notched characteristics. Int. J. Antennas Propag. **2012**, 656858, 7 pages (2012)
58. S.-F. Niu, G.-P. Gao, M. Li, Y.-S. Hu, B.-N. Li, Design of a novel elliptical monopole UWB antenna with dual band-notched function. Microw. Opt. Technol. Lett. **52**(6), 1306–1309 (2010)
59. Xu Chen, Feng Xu, and Xu Tan " Design of a compact UWB antenna with triple notched bands using nonuniform width slots" J. Sens. Volume 2017, 7673168, 9 pages2017
60. A. Abdollahvand, A. Pirhadi, M.R. Hosseinnezhad, H. Ebrahimian, A compact UWB printed monopole antenna with triple-band notched characteristics. ACES J. **30**(4), 374–380 (2015)
61. A. Paulraj, D. Gore, R. Nabar, H. Bölcskei, An overview of MIMO communications – a key to gigabit wireless. Proc. IEEE **92**, 198–218 (2004)
62. R.D. Murch, K.B. Letaief, Antenna systems for broadband wireless access. IEEE Commun. Mag. **40**(4), 76–83 (2002)
63. G. Foschini, Layered space-time architecture for wireless communication in a fading environment when using multi-element antennas. Bell. Labs. Tech. J. **1**(2), 41–59 (1996)
64. J. Wallace, M. Jensen, A. Swindlehurst, B. Jeffs, Experimental characterization of the MIMO wireless channel: Data acquisition and analysis. IEEE Trans. Wirel. Commun. **2**(2), 335–343 (2003)
65. G.J. Foschini, M.J. Gans, On limits of wireless communications in a fading environment when using multiple antennas. Wirel. Pers. Commun. **6**(3), 311–335 (1998)
66. Y. Gao, X. Chen, Z. Ying, C. Parini, Design and performance investigation of a dual-element PIFA array at 2.5 GHz for MIMO terminal. IEEE Trans. Antennas Propag. **55**(12), 3433–3441 (2007)
67. H. Chih-Chun, L. Ken-Huang, S. Hsin-Lung, L. Hung-Hsuan, and W. Chin-Yih, Design of MIMO antennas with strong isolation for portable applications, in Antennas and Propagation Society International Symposium, 2009. APSURSI '09. IEEE, 2009, pp. 1–4

68. T. Svantesson, On the capacity and correlation of multi antenna systems employing multiple polarizations. Proc. IEEE Antenn. Propag. Symp. **3**, 202205 (2002)
69. A.A. Abouda, S.G. Häggman, Effect of mutual coupling capacity of MIMO wireless channels in high SNR scenario, Progress In Electromagnetics Research, PIER 65, 2006, pp. 27–40
70. L. Zhao, L.K. Yeung, K.-L. Wu, A coupled resonator decoupling network for two-element compact antenna arrays in mobile terminals. IEEE Trans. Antennas Propag. **62**(5), 2767–2776 (2014)
71. W.-W. Lee, B. Jang, 2x2 Mimo antenna system with different antenna types for mobile terminals. Microw. Opt. Technol. Lett. **58**(6), 1337–1340 (2016)
72. X. Zhao, Y. Lee, J. Choi, Design of a compact MIMO antenna using coupled feed for LTE mobile applications. Int. J. Antenn. Propag. **2013**, 837643, 8 pages
73. S. Yoo, S. Kahng, S.-G. Mok, G. Jang Compact MIMO antenna of the open-loop and meandered-line 1-layer radiators with improved isolation**,** Proceedings of the IEEE International Symposium on Antennas and Propagation, 8–14 Jul 2012, pp. 1–2
74. L. Malviya, R.K. Panigrahi, M.V. Kartikeyan, A 2 × 2 Dual-band MIMO antenna with polarization diversity for wireless applications. Prog. Electromagn. Res. C **61**, 91–103 (2016)
75. M. ElHalaoui, A. Kaabal, H. Asselman, S. Ahyoub, A. Asselman Dual band PIFA for WLAN and WiMAX systems for mobile handsets, The 9th international conference interdisciplinary in Engineering, Tirgu-Mures, Romania. 8–9 Oct 2015, pp. 1–6
76. H.S. Wong, S. Kibria, M.T. Islam, J.S. Mandeep, N. Misran, Quad band handset antenna for LTE MIMO and WLAN application. Int. J. Antenn. Propag. **2014**, 341574, 7 pages (2014)
77. J.-H. Chou , H.-J. Li , D.-B. Lin, C.-Y. Wu, A Novel LTE MIMO antenna with decoupling element for mobile phone application, 2014 International Symposium on Electromagnetic Compatibility, Tokyo, 12–16 May 2014, pp. 1–4
78. J.-S. Sun, H.-S. Fang, P.-Y. Lin, C.-S. Chuang, Triple-band MIMO antenna for mobile wireless applications. IEEE Antennas Wireless Propag. Lett. **15**, 500–503 (2016)
79. Q. Fang, D. Mi, Y. Yin, A tri-band MIMO antenna for WLAN/WiMAX application. Prog. Electromagn. Res. Lett. **55**, 75–80 (2015)
80. A. Toktas, A. Akdagli, Wideband MIMO antenna with enhanced isolation for LTE, WiMAX and WLAN mobile handsets. Electron. Lett. **50**(10), 723–724 (2014)
81. X.-X. Xia, Q.-X. Chu, J.-F. Li, Design of a compact wideband MIMO antenna for mobile terminals. Prog. Electromagn. Res. C **41**, 163–174 (2013)
82. P. Gao, S. He, A compact UWB and bluetooth slot antenna for MIMO/diversity applications. ETRI J. **36**(2), 309–312 (2014)
83. R.A. Abd-Alhameed, P.S. Excell, R.A.K. Khalil, J. Mustafa, SAR and radiation performance of balanced and unbalanced mobile antennas using a hybrid computational electromagnetics formulation. IEE Proceedings-Science, Measurement and Technology special issue on Computational Electromagnetics **151**, 440–444 (2004)
84. S. Kingsley, Advances in handset antenna design, RF Design, May 2005
85. K. Ogawa, H. Iwai, Y. Koyanagi, Balance-fed planar built-in antenna. IEEE Electron. Lett. **37**, 476–478 (2001)
86. B. S. Collins, S. P. Kingsley, J. M. Ide, S. A. Saario, R. W. Schlub, and S. G. O'Keefe, A multi-band hybrid balanced antenna, IEEE International Workshop, Antenna Technology Small Antennas and Novel Metamaterials, 2006, pp. 100–103
87. W.-S. Lee, H.-S. Tae, O. Kyoung-Sub, J.-W. Yu, A balanced-fed dual inverted-F antenna with reduced human body effects. Int. J. Antennas Propag. **2013**, 814375, 5 pages (2013)
88. A. Iftikhar, M.M. Masud, M.S. Khan, Radiation performance and specific absorption rate (SAR) analysis of a compact dual band balanced antenna, The IEEE International Conference on Electro/Information Technology (EIT), 21–23 May 2015, pp. 1–4
89. W.-J. Lu, G.-M. Liu, K.F. Tong, H.-B. Zhu, Dual-band loop-dipole composite unidirectional antenna for broadband wireless communications. IEEE Trans. Antennas Propag. **62**(5), 2860–2865 (2014)
90. A.G. Alhaddad, R.A. Abd-Alhameed, D. Zhou, C.H. See, I.T.E. Elfergani, P.S. Excell, Low profile dual-band-balanced handset antenna with dual-arm structure for WLAN application. IET Microw. Antennas Propag. **5**(9), 1045–1053 (2011)

91. M. Ali Babar Abbasi, M. Rizwan, H. Zahra, S. Shahid, W.-H. Yeh Wideband balanced antenna with open-end loop for handset applications, Proceedings of ISAP 2014, Kaohsiung, Taiwan, 2–5 Dec 2014, pp. 1–2
92. A. R. Bayat, R. Mirzakhani, A parametric study and design of the Balanced Antipodal Vivaldi Antenna (BAVA), PIERS Proceedings, Moscow, Russia, 19–23 August 2012, pp. 1–5
93. S. Lin, J. Wang, Y. Deng, G. Zhang, A new compact ultra-wideband balun for printed balanced antennas. J. Electromagnet. Waves **29**(12), 1570–1579 (2015)
94. A.I. Sulyman, A.T. Nassar, M.K. Samimi, et al., Radio propagation path loss models for 5G cellular networks in the 28 GHz and 38 GHz millimeter-wave bands. IEEE Commun. Mag. **52**, 78–86 (2014)
95. Wong, H., K. B. Ng, C. H. Chan, K. M. Luk, Printed antennas for millimeter wave application, International Workshop on Antenna Tech. 2013, pp. 411–414
96. K.S. Chin, H.T. Chang, J.A. Liu, et al., 28-GHz patch antenna arrays with PCB and LTCC substrates. Cross Strait Quad-Regional Radio Science and Wireless Technology Conference **1**, 355–358 (2011)
97. K.F. Tong, K. Li, T. Matsui, Performance of millimeter-wave coplanar patch antennas on low-k materials. PIERS Online **1**(1), 46–47 (2005)
98. D. Wang, H. Wong, K. B. Ng, and C. H. Chan, Wideband shorted higher-order mode millimeter- wave patch antenna, IEEE Antennas and Propagation Society International Symposium, 5–6,2012
99. C.A. Balanis, *Antenna theory: Analysis and design* (Wiley-Interscience, New Jersey, 2005); 8. M. H. Jamaluddin, R. Gillard, R. Sauleau, et al., A dielectric resonator antenna (DRA) reecarray, Proc. European Microwave Conference, 25–28, 2009
100. S.-K. Yong, P. Xia, A. Valdes-Garcia, *60 GHz Technology for Gbps WLAN and WPAN: From Theory to Practice* (Wiley, Chichester, 2011)
101. S. Nie, G.R. MacCartney, S. Sun, T.S. Rappaport, 28 GHz and 73 GHz signal outage study for millimetre wave cellular and backhaul communications. In Proceedings of 2014 IEEE International Conference on Communications (ICC), Sydney, Australia, 10–14 June 2014, pp. 4856–4861
102. Y. Zhu, Z. Zhang, Z. Marzi, C. Nelson, U. Madhow, B.Y. Zhao, H. Zheng, Demystifying 60 GHz outdoor picocells. In Proceedings of the 20th Annual International Conference on Mobile Computing and Networking, Maui, HA, USA, 7–11 September 2014, pp. 5–16
103. T.S. Rappaport, R. Mayzus, Y. Azar, K. Wang, G.N. Wong, J.K. Schulz, M. Samimi, F. Gutierrez, Millimeter wave mobile communications for 5G cellular: It will work! IEEE Access **1**, 335–349 (2013)
104. P.A. Watson, Propagation factors in millimetre-wave radio-system design. Electron. Power **23**, 569 (1977)
105. Millimeter-Wave (MMW) radio transmission: Atmospheric propagation, link budget and system availability, Light Pointe White Paper Series, 2010
106. S. Hur et al., Millimeter wave beamforming for wireless backhaul and access in small cell networks. IEEE Trans. Commun. **61**(10), 4391–4403 (2013)
107. T. Bai, R. Vaze, R.W. Heath, Analysis of blockage effects on urban cellular networks. IEEE Trans. Wirel. Commun. **13**(9), 5070–5083 (2014)
108. K.M. Morshed, K.P. Esselle, M. Heimlich Dielectric loaded planar inverted-F antenna for millimeter-wave 5G hand held devices, 2016 10th European Conference on Antennas and Propagation (EuCAP), Davos, Switzerland, , 10–15 Apr 2016, pp. 1–3
109. M. Li, K.-M. Luk, Low-cost wideband microstrip antenna array for 60-GHz applications. IEEE Trans. Antennas Propag. **62**(6), 1–7 (2014)
110. H. Aliakbari, A. Abdipour, R. Mirzavand, A. Costanzo, P. Mousavi, A single feed dual-band circularly polarized millimeter-wave antenna for 5G communication, 2016 10th European Conference on Antennas and Propagation (EuCAP), Davos, Switzerland, 10–15 Apr 2016, pp. 1–5
111. N. Ashraf, O.M. Haraz, M.M. Mahmoud Ali, M.A. Ashraf, S.A.S. Alshebili, Optimized broadband and dual-band printed slot antennas for futuremillimeter wave mobile communication. Int. J. Electron. Commun. (AEÜ) **70**, 257–264 (2016)

112. A. Dadgarpour, B. Zarghooni, B.S. Virdee, T.A. Denidni, Millimeter-wave high-gain SIW end-fire bow-tie antenna. IEEE Trans. Antennas Propag. **63**(5), 2337–2342 (2015)
113. S.F. Jilani, A. Alomainy, Planar millimeter-wave antenna on low-cost flexible PET substrate for 5G applications, 2016 10th European Conference on Antennas and Propagation (EuCAP), Davos, Switzerland, 10–15 Apr 2016, pp. 1–3

Part II
Multi-Band Antennas

Chapter 2
Dual-Band Planar Inverted F-L Antenna Structure for Bluetooth and ZigBee Applications

Chan H. See, George A. Oguntala, Wafa Shuaieb, J.M. Noras, and Peter S. Excell

2.1 Introduction

Recently, due to the remarkable advancement of wireless communication technologies, the unprecedented demand of commercial market to have wireless devices was hugely catalysed. To meet this, an innovative antenna design along with effective approaches and technologies should be accordingly developed to meet the growing demand.

In order to maintain the profit margin when offering mobile services, mobile vendors are attempting to reduce the operational cost to attract more customers. Thus, competition has significantly increased in mobile service providers. One approach that facilitates this is the use of the licence-free ISM and UWB bands. Therefore, the ISM band has become more common and popular for use in a broad range of wireless electronic devices, while the UWB spectrum offers the potential for very significant expansion of this.

One of the most widely and widespread applications that uses the ISM bands is IEEE 802.11, wireless Internet (WLAN), namely, 2400 and 5200 MHz. The ISM band of IEEE 802.11b/g, i.e. 2400 MHz, is capable of operating over the range from 2400 to 2485 MHz, with data rates of up to 11, 54 Mbps. As for the ISM standard of 5200 MHz, it covers the frequency range from 5150 to 5350 MHz, along with data rate greater than 54 Mbps. Thus, to come up with an antenna that operates at

C.H. See (✉)
School of Engineering, University of Bolton, Deane Road, Bolton, UK, BL3 5AB
e-mail: C.See@bolton.ac.uk

G.A. Oguntala • W. Shuaieb • J.M. Noras
School of Electrical Engineering and Computer Science, University of Bradford, Richmond Road, Bradford, UK, BD7 1DP

P.S. Excell
Institute for Arts, Science and Technology, Glyndwr University, Wrexham, Wales, UK, LL11 2AW

I. Elfergani et al. (eds.), *Antenna Fundamentals for Legacy Mobile Applications and Beyond*, DOI 10.1007/978-3-319-63967-3_2

both bands of WLAN has become a huge challenge. Planar inverted F antennas (PIFAs) [1–3] are considered as a broadly candidate utilized within the WLAN application. This is due to their several advantages including low profile, dual and multi-frequency functions, high power gain and efficiency, low fabrication cost and most importantly mitigating the SAR values compared with other counterpart antennas.

Lately, a number of dual-band antennas along with single feeding point have been reported [1–6]. However, all these designs either have come up with poor radiation features or they are not suitable to be fitted or concealed into compact small portable devices due to space limitation within the chassis. Recently, several antennas with miniaturization approaches have been investigated; these methods include the employment of dielectric with high permittivity, modifying the antenna structures, using shorting wall and pins [7–9].

In recent times, employing the magnetic wall approach has been introduced as one of the effective antenna miniaturization techniques [10–12]. It was unsurprisingly noted that the whole performance of antenna with half-sized geometry with U-slot [10], E-shaped [11] and UWB patch structures [12] has come up with similar results in terms of antenna return loss, gain, far-field and huge size reduction compared to the antenna with full-size structures.

By further modifying the authors' published work in [13–15], the work within this chapter presents a small volume of dual-band planar inverted F-L antennas (PIFLAs) for WLAN applications. The full dimension of the proposed design is 30 mm × 15 mm × 8 mm. This type of suspended antenna was mounted over a metal ground plane with dimensions of 30 mm × 15 mm. This antenna has achieved 50% size reduction compared to previous published authors' design. All of the analysis was conducted using two commercial software packages [16, 17].

2.2 Antenna Design Structure and Procedures

The proposed geometry of the planar inverted F-L antenna (PIFLA) is depicted in Fig. 2.1. In fact this present antenna shares some similarities to previous authors' designs [13]; however, it has a great advantage of only half size of [13]. This huge size minimization was obtained due to the presence of magnetic wall on the antenna surface [10–12]. The key sensitive antenna geometry parameters, which may influence the whole performance, were as follows: L1 = 16.5 mm, L2 = 15 mm, h1 = 8 mm, h2 = 4.5 mm, d = 3.5 mm and w = 0 mm. It should be highlighted that the proposed antenna was from [13]; the only difference is the innovation of reducing the dimension into half while preseving its performance as full-size dimension. The antenna is made of copper with thickness of 0.5 mm.

To better comprehend the operating principle of this miniturised antenna, the current distribution of the antenna with both full F and L shapes proposed in [14] and the present half-size design are studied and analysed in Fig. 2.2. It should be noted that maximum currents were induced mainly at the edges of the antenna

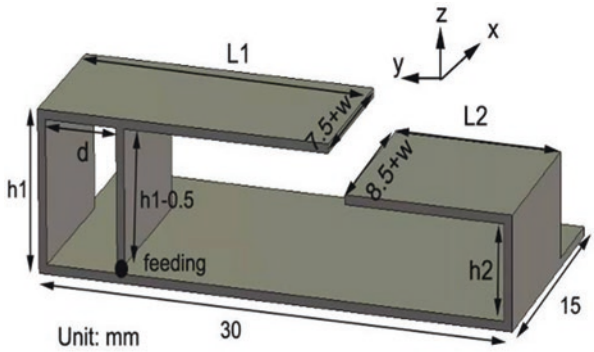

Fig. 2.1 Full geometry of the PIFLA antenna structure

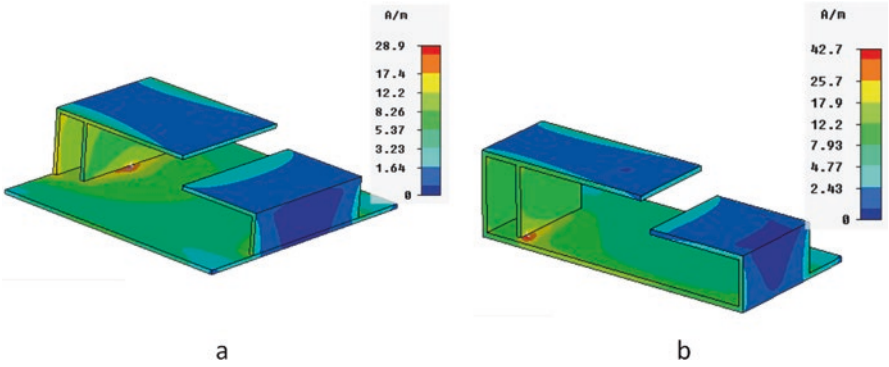

Fig. 2.2 Current distributions of (**a**) full size and (**b**) half cut PIFLA at 2450 MHz

design, while minimum currents were seen at the centre of the antenna. This is because of the presence of magnetic wall. As a result, by following and implementing the technical procedure of cutting half of this full-size structure, we can still assure that the present half-size F and L shapes will preserve the same surface current distributions, as illustrated in Fig. 2.2b.

To further verify the concept of miniaturization, the return losses of both full- and the half-size PIFLA are analysed. As shown in Fig. 2.3, the lower band still holds the same impedance bandwidth; however, the bandwidth for the upper band noticeably impairs to be around 12.2% (5–5.65 GHz) compared to work in [13] and roughly 3.8% (5.15–5.35 GHz) in comparison to the half structure. It concludes that the size and performance of the present half-size PIFLA antenna makes very suitable for concealing in the casings of portable devices.

The design mechanism and operation procedure of this antenna is further explained in order to offer some physical insight into its operation and the rationale for its geometry. The antenna procedure initially begins by joining the F-shaped radiator with both the L-shaped radiator and a rectangular plate feeding.

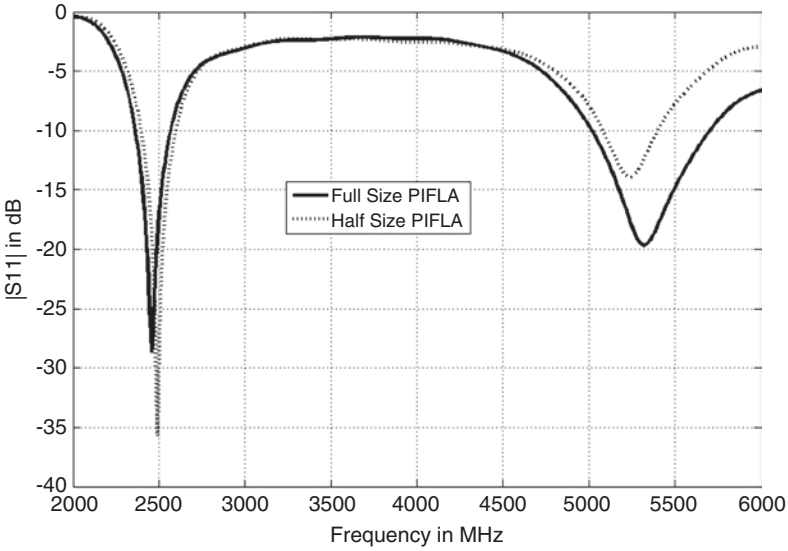

Fig. 2.3 Simulated refection coefficient of full and half size PIFLA design

The F-shaped radiator was mainly made in order to control the lower band of 2400 MHz, while the upper band of 5200 MHz was provided by introducing the L-shaped radiator. Generally, exciting the PIFA antenna with the conventional wiring feed normally leads to impedance bandwidth limitation between 4% and 12% [18, 19]. To this end, the feed plate was modified as in [18], in which the bandwidth considerably improved from 18% to 25%. Therefore, the rectangular feeding plate was selected and applied as the feeding method to enhance the bandwidth in this work.

2.3 Parametric Analysis

For further optimizations, a full parametric study was implemented in order to analyse the most sensitive and key antenna parameters against the variation of the antenna impedance bandwidth (defined at reflection coefficient S_{11} <−10 dB) at both the lower and upper bands. In this type of analysis, each simulation needs to be run only with one parameter varied, while other parameters keep constant. The changed and unchanged parameters are depicted in Fig. 2.1. The impedance bandwidth of present design profoundly depends on the isolation between the F- and L-shaped radiators. In fact, analytical methods are not feasible to be reached, and therefore, two EM software packages, namely, HFSS [16] and SEMCAD [17], have been exploited to carry out such investigation.

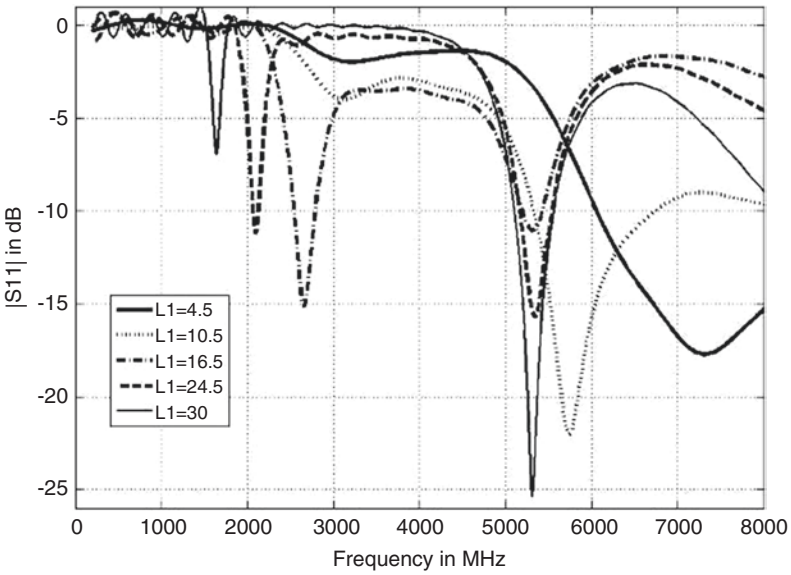

Fig. 2.4 The variation of the length of F-shaped radiator (*L1*) against the reflection coefficient

2.3.1 The Influence of the F-Shaped Radiator Length (L1)

The effects of changing the electrical length (L1) of the F-shaped antenna mainly appear on the lower band of 2400 MHz. The length of the F shape varied from 4.5 to 30 mm, with increment of 6 mm as indicated in Fig. 2.4. It should be noted that, in Fig. 2.4, the lower band fluctuates from 2650 to 1600 MHz, when the length of F radiator varied from 16.5 to 30 mm. On the other hand, the variation of L1 does not influence the upper band of 5200 MHz. In other words, the upper band seems to be independent of the variation of L1 length. Moreover, when the value of L1 was set at 16.5 mm, both bands of WLAN 2400 and 5200 MHz were, respectively, achieved with an excellent bandwidth impedance matching.

2.3.2 The Influence of the L-Shaped Radiator Length (L2)

As previously mentioned, the L-shaped arm is responsible of the high band operation. Thus, the effect of the L arm was comprehensively analysed as shown in Fig. 2.5. The L-shaped arm length varied from 2 to 24 mm. The variation length of such parameters was elaborated as follows: when the L2 length was set at 2 mm, only a single band at 2800 MHz was achieved, while two bands at 2600 and 5600 MHz were seen when the length of L2 was fixed at 8.5 mm; however, a

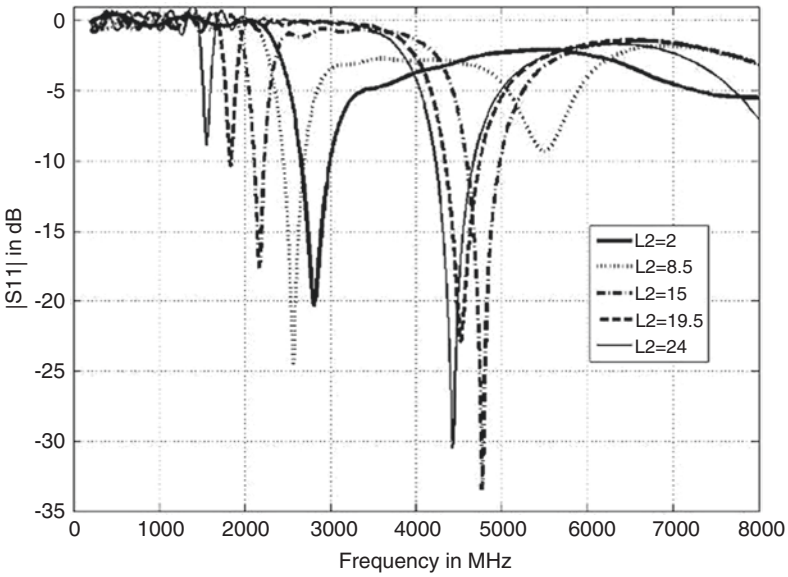

Fig. 2.5 The variation of the length of L-shaped radiator (*L2*) against the reflection coefficient

weak impedance matching was observed at the band of 5600 MHz. When the L2 length was increased to 19.5 and 24 mm, both desired bands of 2400 and 5200 MHz were not met. On the other hand, it is apparent that the targeted bands of WLAN allocated within this work were reached, when the length of L2 was set at 15 mm.

2.3.3 The Influence of the F-Shaped Radiator Height (h1)

The height of the F-structured radiator also mostly affects the upper band of 5200 MHz as clearly shown in Fig. 2.6. The height of F-shaped radiator serves the same role as L1 to control the fundamental resonant mode of the antenna, but it also contributes to the capacitive coupling with the ground plane. The height of this radiator shape was changed from 1 to 8 mm. One should note, when the height was set at 1 and 2.75 mm, the proposed design only operates over a single band around 4000 MHz, with impedance mismatching at 2.75 mm height. However, between the value of 4.5 and 8 mm, no obvious changes on dual-band bandwidth were seen. This has led to the conclusion that the F-shaped height (h1) may take any height between 4.5 and 8 mm to satisfy and meet the WLAN dual-band of 2400/5200 MHz.

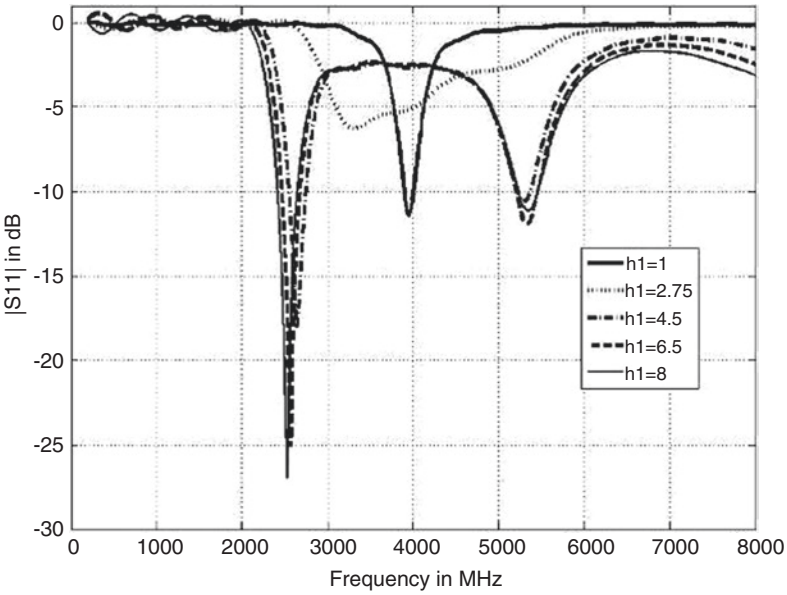

Fig. 2.6 The variation of the height of F-shaped radiator (*h1*) against the reflection coefficient

2.3.4 The Influence of the L-Shaped Radiator Height (h2)

The impacts of the height of the L-arm are depicted in Fig. 2.7. Both the desired lower and higher bands were seen greatly shifting downwards by varying the height of the L-shaped radiator from 1 to 8 mm. It is also noticeable the impedance mismatch occurs at the higher band when the height are set at the value of 1 and 2.75 mm. Moreover, when the value of h2 was fixed at 8 mm, the proposed antenna covers the band of 2200 and 5000 MHz, in which both bands are out of the interest of this work. However, when h2 was set at 4.5 mm, the lower band and upper band both perfectly matched, as well as with a great size reduction of the whole antenna volume.

2.4 Results and Discussion

Within the parametric analysis procedure, it was remarkably figuring out that, by carefully selecting the best and optimum values of the structure parameters, the presented antenna with F and L arms possibly to be modified and manipulated in order to make the antenna operating within the targeted dual-band of WLAN

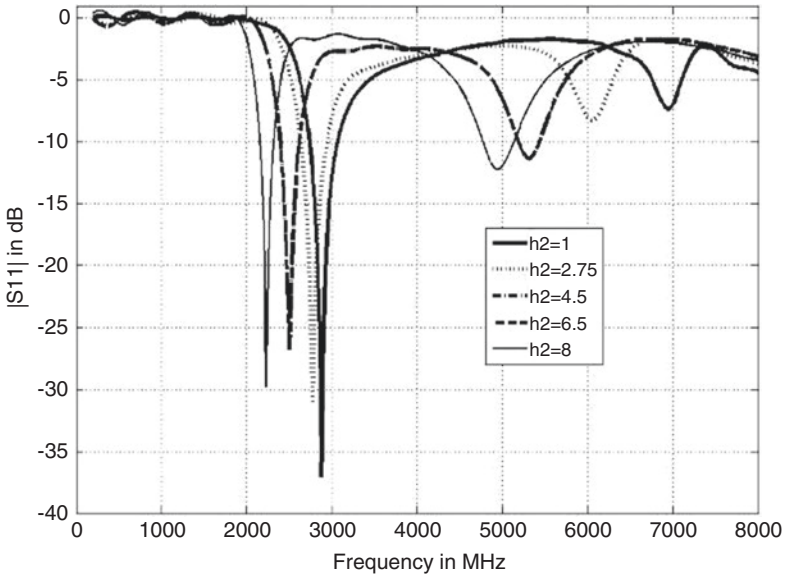

Fig. 2.7 The variation of the height of L-shaped radiator (*h2*) against the reflection coefficient

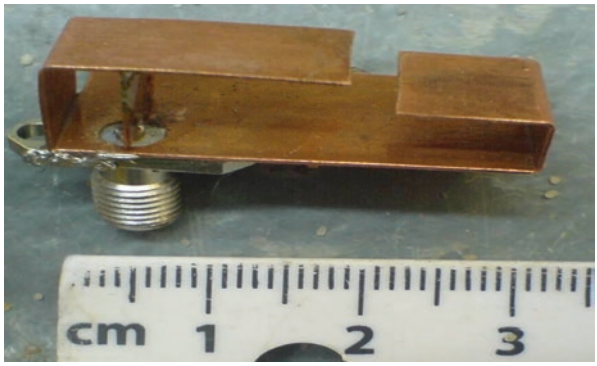

Fig. 2.8 Fabricated proposed antenna

standard allocated within this study. To prove the computed findings, the proposed antenna in Fig. 2.1 was prototyped and tested. The final fabricated antenna including the SMA feeding is shown in Fig. 2.8. The evaluations of the experimental antenna performances in terms of reflection coefficients $|S_{11}|$, radiation patterns, power gains and radiation efficiencies were carried out in a $3 \times 4.5 \times 5$ m^3 anechoic chamber. It should be noted that the return loss of the fabricated antenna was measured by using a vector network analyser (model: HP8510c), while the antenna radiation patterns and power gains were investigated inside the anechoic chamber by using gain comparison method.

For validation purposes, both the measured and calculated antenna reflection coefficient of the full-size and half-size PIFLAs is illustrated in Fig. 2.9. Dual reso-

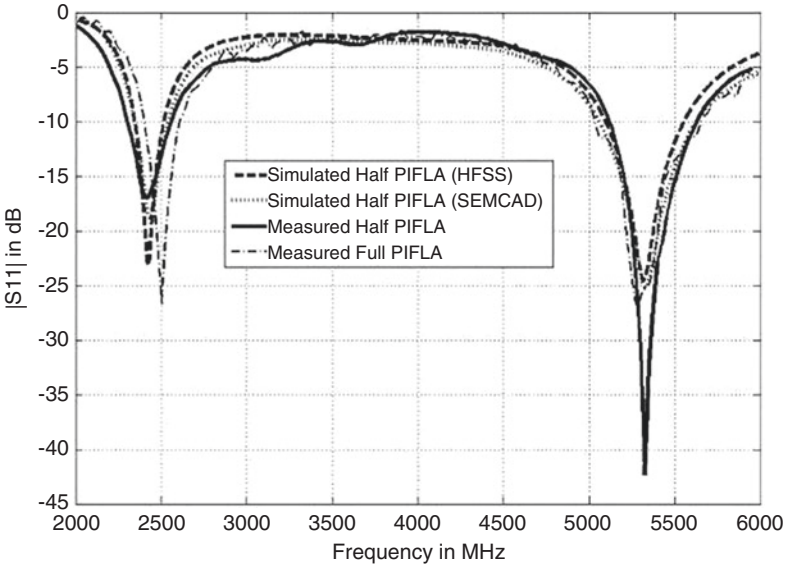

Fig. 2.9 Measured and simulated reflection coefficients $|S_{11}|$ for the dual-band PIFLA

nant frequencies in the range of reflection coefficient $|S_{11}| \leq -10$ dB are seen, i.e. 2450 and 5350 MHz. A relative bandwidth of around 12% was obtained at the lower band of 2400 MHz, while a bandwidth of 10.2% was provided at the higher band of 5200 MHz. This satisfies the allocated services of IEEE802.11b/g frequency band (2400–2485 MHz) and IEEE 802.11a (5150–5350 MHz) band, respectively. It is undoubtedly that the half-size proposed F-L antenna demonstrates same impedance bandwidth over the two WLAN bands, in which such feature has given this antenna an additional advantage of the full-size PIFLA structure as the size reduction is significantly accomplished while same bands are maintained.

Figure 2.10 explains the computed and practical power gains of the proposed structure over the frequency ranges from 2400 to 2480 MHz and 5000 to 5600 MHz, respectively. It should be noted that the power gain values at the lower band vary from 2.6 to 3.5 dBi, while values range 4.5–5.2 dBi may be seen at the upper band. Moreover, the power gains of the miniaturized design are in good agreement with the full-size design. This is again another benefit added to the proposed design, since it can propose similar power gain with a smaller antenna design compared to the full-size design.

The simulated and measured radiation efficiencies of both full and half sized antennas are indicted in Fig. 2.11. The simulated efficiency was produced with the help of previously mentioned software [16, 17], while the measured one was generated by suing the Wheeler Cap measurement method [20–22] (Fig. 2.5). The radiation efficiencies at the lower bands of both full- and half-size structure range from 0.96 to 0.98 and 0.93 to 0.94, respectively; values around 93.5% and 89% are obtained at the upper bands of both antenna versions.

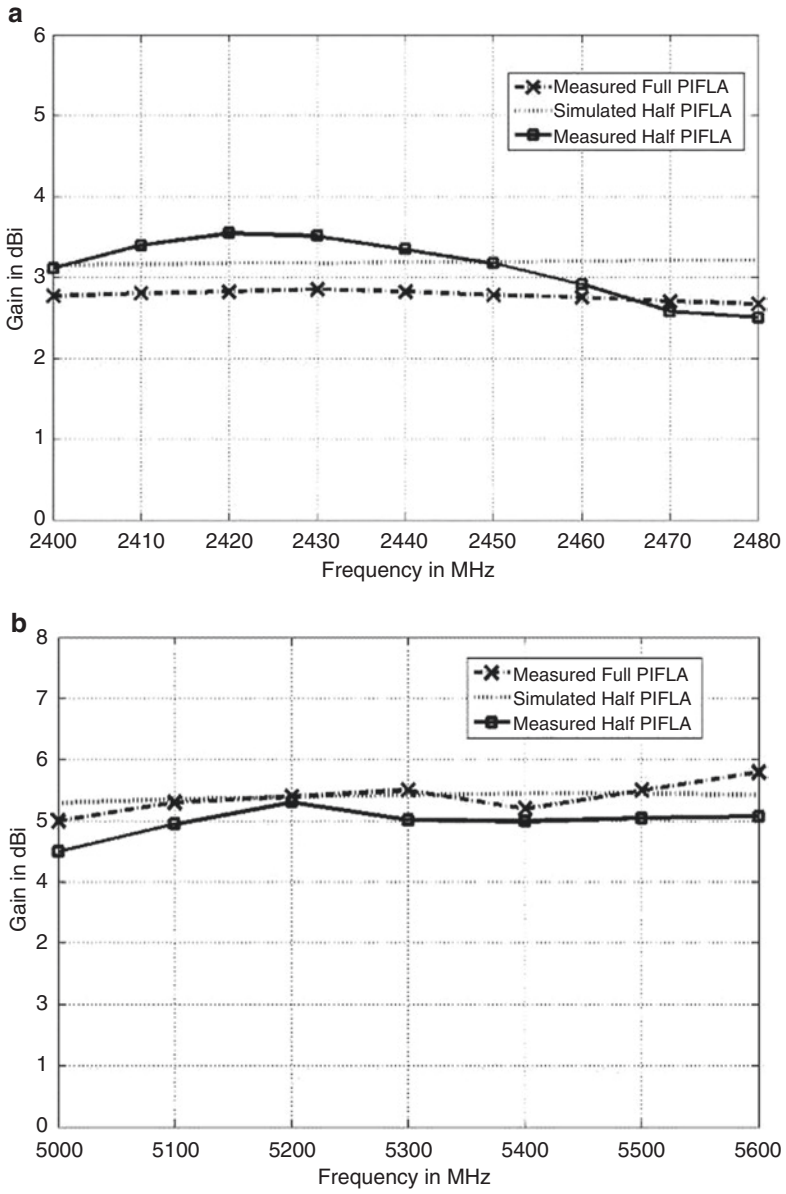

Fig. 2.10 Simulated and measured gains for the proposed design: (**a**) lower band and (**b**) higher band

The simulated and measured radiation patterns are depicted in Fig. 2.12. The computed far field data was generated by the EM simulators. However, the measurement setup with a calibrated broadband horn (EMCO type 3115), which was con-

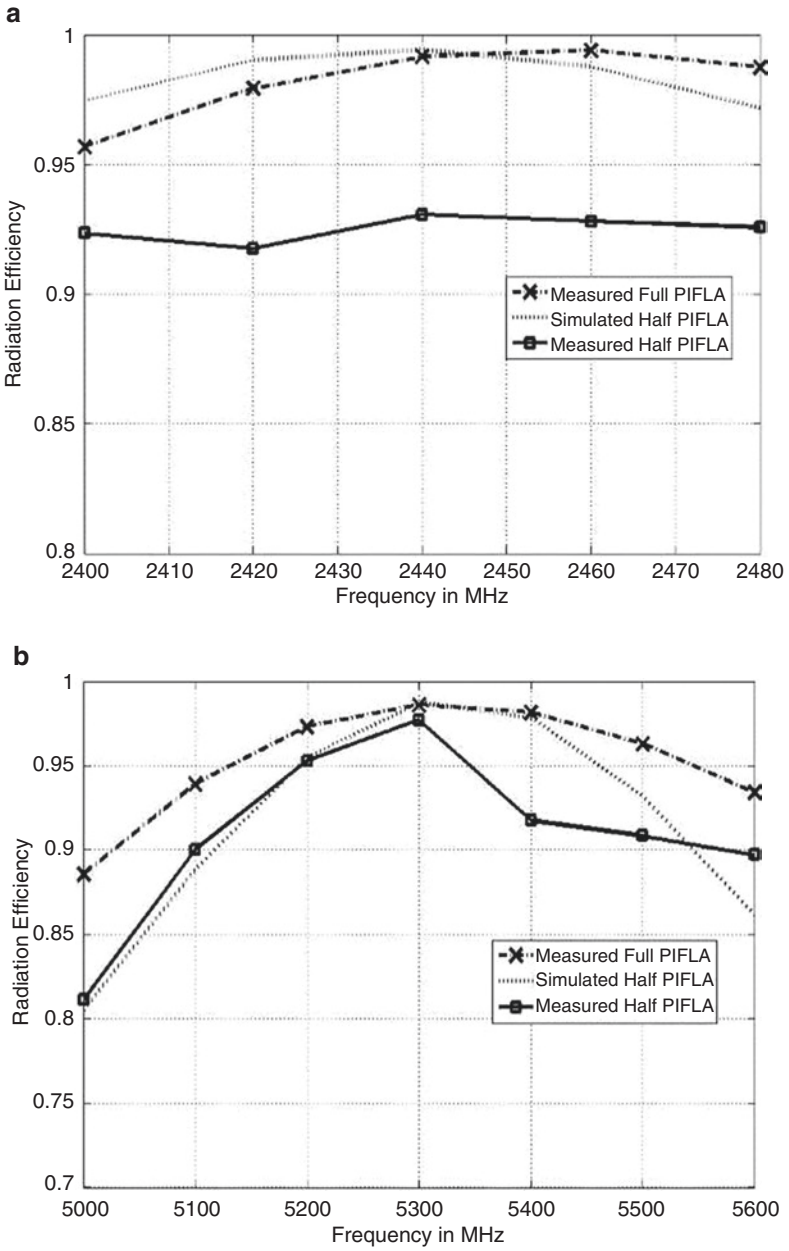

Fig. 2.11 Simulated and measured radiation efficiencies for proposed design at (**a**) lower band and (**b**) higher band

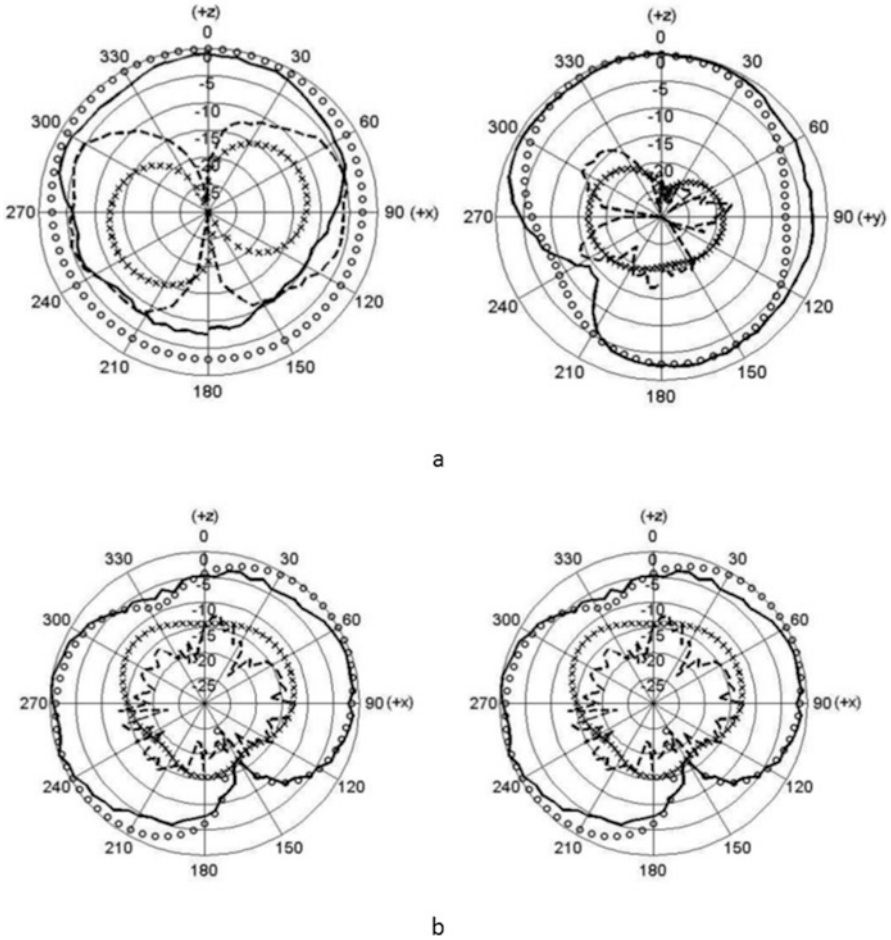

Fig. 2.12 Normalized simulated and measured radiation patterns of the proposed design for two planes (*x-z* plane, *y-z* plane) at (**a**) 2400 MHz and (**b**) 5200 MHz; 'xxxx' simulated cross-polarization, 'oooo' simulated co-polarization, '------' measured cross-polarization, '——' measured co-polarization

sidered as the reference antenna, also with a distance of 4 m with the proposed antenna (antenna under test), was used to test the antenna radiation patterns. Two pattern cuts (*x-z* and *y-z* planes) were selected for the both bands.

Figure 2.12 illustrates both the simulated and measured co-polar and cross-polar radiation patterns in the x-z and y-z planes at the targeted dual-band of 2400 and 5200 MHz for the miniaturized PIFLA. One can observe that both simulated and measured outcomes of the antenna radiation patterns are in reasonable matching. Moreover, in comparison with the radiation patterns for antenna with full F and L shaped in [14], it seems that both designs show indistinguishable radiation patterns. This proves that exploiting the size reduction approach within this study does not influence or impair the antenna radiation patterns.

2.5 Conclusion

A planar inverted F-L antenna (PIFLA), along with a size reduction approach with a simple geometry, has been modelled, investigated and measured. By applying an optimization analysis as well as miniaturization techniques, a novel PIFLA structure with almost 50% size reduction for use in WLAN applications has been accomplished. By compromising both the size and bandwidth limitations, the present design has come with a compact volume 30 mm × 15 mm × 8 mm, while covering the required operating frequency bands. The simulated model then has been fabricated and tested, in which its measured results were compared to the computed results obtained from the EM simulators. Both the experimental and calculated findings prove that the present antenna structure may be seen as a promising candidate for smart and future mobile applications.

References

1. L.O. Soo, B.P. Koh, P. Song, L. Lau, From a simple IFA to a dual band PIFA. International Workshop on on Antenna Technology, Chiba University, Japan, Mar 2008, pp. 386–389
2. Y.-B. Kwon, J.-I. Moon, S.-O. Park, An internal triple-band planar inverted-F antenna. IEEE Antennas Wireless Propag. Lett. **2**, 341–344 (2003)
3. C.-T. Lee, K.-L. Wong, Uniplanar printed coupled-fed PIFA with a band-notching slit for WLAN/WiMAX operation in the laptop computer. IEEE Trans. Antennas Propag. **57**, 1252–1258 (2009)
4. D. Liu, B. Gaucher, A new multiband antenna for WLAN/cellular applications, IEEE Vehicular Technology Society Conference, Milan, vol. 1, Sept 2004, pp. 243–246
5. H.-C. Tung, S.-T. Fang, K.-L. Wong, Printed dual-band monopole antenna for 2.4/5.2GHz WLAN access point. Microw. Opt. Technol. Lett. **35**(4), 286–288 (2002)
6. D.D. Krishna, M. Gopikrishna, C.K. Anandan, P. Mohanan, K. Vasudevan, CPW-fed Koch fractal slot antenna for WLAN/WiMAX applications. IEEE Antennas Wireless Propag. Lett. **7**, 389–392 (2008)
7. A.K. Skrivervik, J.-F. Zurcher, O. Staub, J.R. Mosig, PCS antenna design: The challenge of miniaturization. IEEE Antennas Propag. Mag. **43**, 12–27 (2001)
8. C.S. Lee, K.-H. Tseng, Size reduction of microstrip antennas. Electron. Lett. **37**, 1274–1275 (2001)
9. A.K. Shackelford, K.F. Lee, K.M. Luk, Design of small-size wide bandwidth microstrip-patch antennas. IEEE Antennas Propag. Mag. **45**(1), 75–83 (2003)
10. A.A. Deshmukh, G. Kumar, Half U-slot loaded rectangular microstrip antenna, in IEEE Antennas and Propagation Soc. Intl. Symp., Columbus, vol. 2, 2003, pp. 876–879
11. R. Chair, C.-L. Mak, K.-F. Lee, K.-M. Luk, A.A. Kishk, Miniature wide-band half U-slot and half E-shaped patch antennas. IEEE Trans. Antennas Propag. **53**(8), 2645–2651 (2008)
12. L. Guo, S. Wang, X. Chen, C. Parini, Miniaturised antennas for UWB communications, Proc. European Conf. on Antennas and Propagation, Berlin, Germany, Mar 2009, pp. 3774–3778
13. C.H. See, R.A. Abd-Alhameed, D. Zhou, P.S. Excell, Dual-frequency planar inverted F-L-antenna (PIFLA) for WLAN and short range communication systems. IEEE Trans. Antennas Propag. **56**, 3318–3320 (2008)
14. C.H. See, R.A.Abd-Alhameed, D. Zhou, E.A. Elkhazmi, M.M. Abusitta, K.N. Ramli, P.S. Excell, Miniature dual-frequency half planar inverted F-L-antenna for WLAN/cellular

applications, in the proceeding of Microwave Conference, 2009. APMC 2009, Asia Pacific, 7–10 Dec 2009, pp. 2802–2804
15. C.H. See, R.A. Abd-Alhameed, D. Zhou, P.S. Excell, A planar inverted F-L antenna (PIFLA) with a rectangular feeding plate for lower-band UWB applications. IEEE Antenna Wireless Propag. Lett. **9**, 149–151 (2010)
16. High Frequency Structure Simulator (HFSS), version 11, Ansoft LLC, Pittsburgh
17. SEMCAD X, version 14, Schmid & Partner Engineering AG, Zurich
18. R. Feick, H. Carrasco, M. Olmos, H.D. Hristov, PIFA input bandwidth enhancement by changing feed plate silhouette. Electron. Lett. **40**, 921–922 (2004)
19. H. Nakano, N. Ikeda, Y.-Y. Wu, R. Suzuki, H. Mimaka, J. Yamauchi, Realization of dual-frequency and wide-band VSWR performances using normal-mode helical and inverted-F antenna. IEEE Trans. Antennas Propag. **46**, 788–793 (1998)
20. R.W. Johnston, J.G. McRory, An improved small antenna radiation-efficiency measurement. IEEE Antenna Propag. Soc. Mag. **40**(5), 40–48 (1998)
21. H. Choo, R. Rogers, H. Ling, On the wheeler cap measurement of the efficiency of microstrip antennas. IEEE Trans. Antennas Propag. **53**(7), 2328–2332 (2005)
22. M.-C. Huynh, W. Stutzman, Ground plane effects on planar inverted-F antenna (PIFA) performance. IEE Proc.-Microw. Antennas Propag. **150**(4), 209–213 (2003)

Chapter 3
Double-Monopole Crescent-Shaped Antennas with High Isolation for WLAN and WIMAX Applications

Khalil H. Sayidmarie and Likaa S. Yahya

3.1 Introduction

In many applications, two or more antennas are needed to be closely placed. These antennas either operate in the same band as in the MIMO systems or in different bands depending on the application. When the antenna separation is electrically small, then some of the energy fed to one antenna will be coupled or radiated to the other one. As the antennas are reciprocal, the coupling is encountered in both transmission and reception modes and is called mutual coupling. The antenna proximity results in a mutual coupling problem that is exacerbated by the limited size allocated for the antennas as in portable devices. Closer antennas produce stronger coupling [1, 2]. It is also known that the mutual coupling between the antennas results in degraded performance of the MIMO system. Reduction of the mutual coupling leads to higher antenna efficiencies and lower envelope correlation coefficients [3]. In [4], it was shown that the separation between adjacent antenna elements should be at least half wavelength to obtain minimum coupling. Therefore, efficient mutual coupling reduction techniques are necessarily required in the design of closely placed antennas. The desirable properties of MIMO antennas in small devices are compact size, good radiation efficiency, proper radiation patterns, low envelope correlation, and minimum coupling between the antennas. The additional requirement of a multiband operation makes the design of such high-performance antennas a challenging task [5].

When two antennas are closely deployed as in MIMO systems, then the power supplied to antenna-1 is radiated by the antenna toward the receiver. Part of the

K.H. Sayidmarie (✉)
College of Electronic Engineering Ninevah University, Mosul, Iraq
e-mail: kh.sayidmarie@gmail.com

L.S. Yahya
Institute of Technology, Mosul, Iraq
e-mail: likaas.yahya@gmail.com

I. Elfergani et al. (eds.), *Antenna Fundamentals for Legacy Mobile Applications and Beyond*, DOI 10.1007/978-3-319-63967-3_3

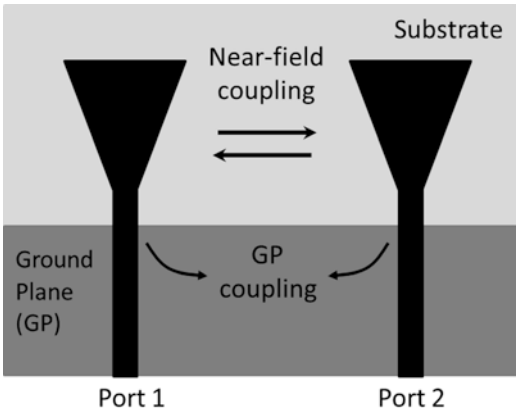

Fig. 3.1 The two paths of coupling between two closely spaced antennas

radiated power will be coupled or received by the other antenna (antenna-2) which is closely placed to antenna-1 as shown in Fig. 3.1. The path through which the power is coupled is usually very short, and the power transfer is a process of coupling rather than transmit/receive mechanism since the far-field distance of either antenna is in general much larger than the separation between the two antennas. If antenna-2 is not perfectly matched, then a fraction of the incident energy on antenna-2 is reflected and transmitted back to antenna-1. Optimum antenna matching was proposed as a solution to minimize the signal correlation in a two-port antenna diversity system [6]. The above situation makes the mathematical analysis of the coupling due to transmit/receive processes a difficult job.

Printed antennas have a conducting surface called the ground plane (GP) which is usually shared by the two closely spaced MIMO antennas. When an antenna is in transmission or reception mode, then there is a current flowing in the GP with certain density distribution (see Fig. 3.1). The shape of the distribution depends on the shape and size of the radiating element, shape of the GP, and the type of the feeding line, as well as the separation between the radiating element and GP. Due to the close placement of the MIMO antennas, the current distribution due to one antenna extends to that of the other antenna. This means another coupling mechanism is generated. Therefore, the two coupled signals (through radiation and GP coupling) will add constructively or destructively depending on the phase shift between them.

Various techniques have been proposed to minimize the mutual coupling between closely spaced antennas. These techniques try to minimize one or both of the coupling mechanisms described in the above paragraphs. In the following section, the various techniques that have been presented to reduce antenna coupling are summarized.

3.2 Techniques of Coupling Reduction

The various techniques that have been proposed to reduce the coupling between two closely spaced antennas can be categorized into the following.

3.2.1 Reduction of the Coupling Due to the Current in the Ground Plane

This approach has been implemented through one or more of the following designs:

1. Using slots or slits in the GP that modify the current distribution such that current due to one antenna is prevented from, or highly reduced before, reaching the vicinity of the other antenna. Examples of this approach can be found in [7–14]. A defected ground plane structure was also used in [15] for the coupling reduction.
2. Placing the two antennas at larger spacing so that the current density in the ground plane decays to adequately smaller value at the position of the other antenna [11]. This technique which will also reduce the coupling through radiation is eventually limited by either the limited available space as in the case of using two antennas in the mobile handset devices or the necessity to place array elements at about half wavelength to avoid the grating lobes.

3.2.2 Placing of Conducting Structures Between the Two Antennas

A variety of conducting structures have been placed between the two antennas in attempts to modify the current in the ground plane or reduce the radiation coupling. Placing a metamaterial strip between the two antennas has been found to reduce the coupling between the two antennas [16]. Placing of conducting strips or lines between the two antennas will modify the current distribution resulting in lower coupling [17, 18]. The ground plane has also been extended into the spacing between the two antennas [17].

3.2.3 Neutralization of the Coupled Signal

An innovative technique treats the combined signal due radiation coupling and current leakage as a composite signal in antenna-1 that should be eliminated by adding another signal. The added signal to achieve the required neutralization is derived from the other antenna by connecting the feed lines of the two antennas by a transmission line known as neutralization line. This line has to supply a signal of proper magnitude and phase that when added to the coupled signal in antenna-1 results in a minimal sum. The length of the neutralization line, its width as well as where it should be connected to the feed lines of the two antennas must be found to attain the required neutralization. The design is rather complex because many interdependent parameters have to be selected simultaneously to achieve the required goal. Therefore, an optimization technique has to be used to find the parameters of the

neutralization line [19–21]. The addition of the neutralization line may change the matching at the feed line where the neutralization line is connected. The matching can be fulfilled by adding lumped elements at both ends of the added line [22–24].

Another point of view considers the composite neutralization line and added lumped elements as a compensating circuit that works to reduce the coupling [22]. Parasitic elements between the two antennas were also added for reducing the coupling [25].

3.2.4 Using Combined Techniques

Various combinations of more than one of the foregoing approaches were implemented for the reduction of the coupling between the two antennas. A T-shaped line joining the two radiating patches, in addition to two slots on the ground plane, was used for the coupling reduction in [26]. Two meandered-line PIFA antennas were arranged in a MIMO configuration in [27] where a number of decoupling techniques were used to reduce the coupling between the two MIMO antennas working at the LTE (Band-Class-13) [27]. The fabricated prototype has a volume of $110 \times 65 \times 1.6$ mm^3, that is ($0.275 \times 0.1625 \times 0.004$) in wavelengths, and has achieved an isolation better than 12 dB [27].

A Tri-band MIMO antennae for Wi-Fi/WiMAX applications with separation distance between the two elements of 3 mm (0.024 wavelengths) has been recently proposed [28]. The coupling is reduced by inserting a neutralization line between the ground planes of the two antennas as well as using a beveled ground plane. The prototype MIMO antenna achieved isolations of nearly 25 dB at 5.5 GHz, 20 dB at 3.5 GHz and 18 dB at 2.4 GHz.

A low-profile double antenna was proposed in [29] where the first antenna is designed for the 2.45GHz WLAN while the second antenna is intended for the 3.5 GHz WIMAX. Each antenna consists of a crescent-shaped monopole following the design of [30]. A new technique was proposed to reduce the mutual coupling between the two antennas with a fractional wavelength spacing [29]. In the feed line of each antenna, an S-shaped slot is incorporated, and it is made to resonate at the frequency on which the other antenna is working. Adequate reduction of the coupling was obtained by using the slots in spite of the very small antenna separation of 9 mm (0.0735 wavelengths at 2.45 GHz frequency).

3.3 Antenna Design

The geometry of the proposed double-antenna configuration is shown in Fig. 3.2. The proposed antenna configuration consists of two monopole radiating elements having crescent shape of equal radii printed on the same ground plane. The used substrate is FR4 of 1.5 mm thickness, relative permittivity of 4.3, and dielectric loss

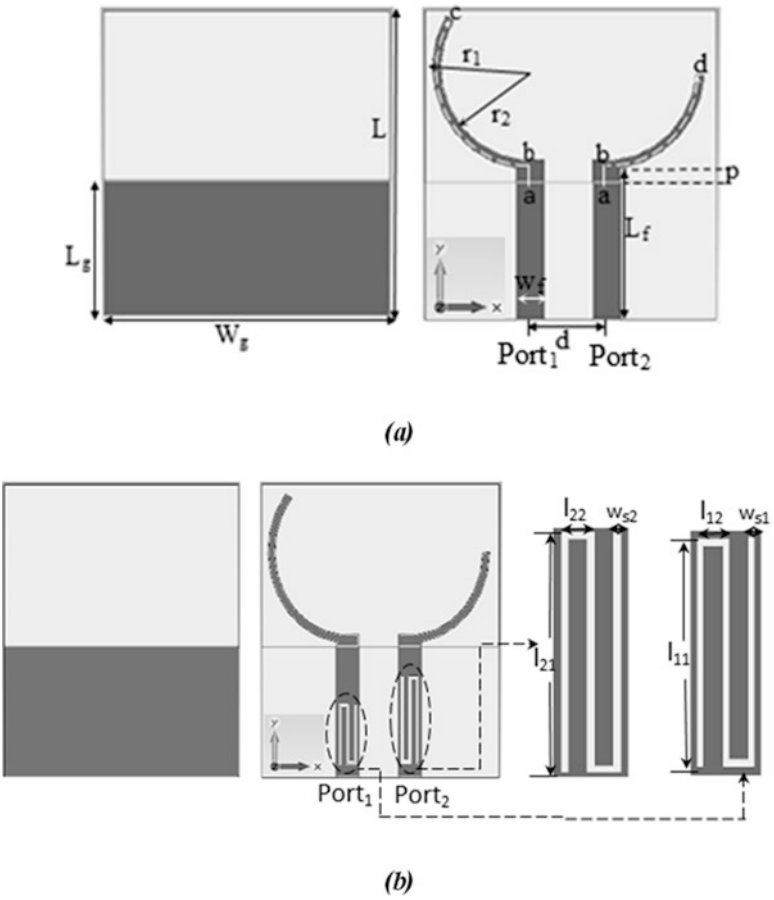

Fig. 3.2 Geometry of the proposed two-antenna configurations; (**a**) antenna-1 and (**b**) antenna-2 using S-slots at both feed lines [29]

tangent of 0.025. Each monopole is fed by an independent 50 Ω microstrip line. The two feed lines are separated by center-to-center distance of 9 mm (0.0735 free-space wavelengths at 2.45 GHz).

In the design process, the length of each monopole is set equal to a quarter of the effective wavelength (λ_e) at the operating frequency [29]. Initially, the lengths of the monopoles can be empirically predicted from the operating frequencies using the procedure described in [30]. Therefore, the long monopole should have a total length of 26 mm to excite the f_{r1} = 2.45 GHz frequency, and the short monopole must have a total length of 18.31 mm, in order to excite the upper band at f_{r2} = 3.5 GHz.

A technique is proposed here for the reduction of the mutual coupling arising from the closely spaced antennas without sacrificing their desirable performance. A slot with a length of half the guided wavelength (λ_g) at the frequency of the signal to

be isolated is introduced in the feed line of each antenna. Each slot is made to resonate at the operation frequency of the other antenna; thus, it can suppress the coupled signal at the other frequency. The narrow slot can be treated as a transmission line with short circuits at its two ends. Therefore, to set the slot in resonance at a certain frequency, the physical length of the slot L must be equal to $\lambda_g/2$. Thus, for an isolation frequency (f_n), the length of the slot is given by [30]:

$$L \cong \lambda_g / 2 \tag{3.1}$$

where

$$\lambda_g = \frac{c}{f_n \sqrt{\epsilon_e}} \tag{3.2}$$

$$\epsilon_e = \frac{(\epsilon_r + 1)}{2} + \frac{\epsilon_r - 1}{2}\left(\sqrt{1 + \frac{12h}{W}}\right)^{-1} \tag{3.3}$$

where L is the length of the slot, W is the width of the slot or the strip line, c is the speed of the light, ε_e is the effective dielectric constant, ε_r is the relative permittivity of the substrate, and h is the substrate thickness. To isolate the signal at the frequency (3.5 GHz) of the upper band, the total length of the slot line is calculated to be 21.47 mm, and this slot is placed in the feed line of the antenna operating at the 2.45 GHz frequency. The slot for the feed line of the other antenna, which is operating at 3.5GHz, has to be 30.67 mm long. Equations 3.1, 3.2 and 3.3 were found to give good estimates for the slot lengths. However, in the CST simulation, the length, width and positions of the slots can be carefully adjusted to get the desired frequencies and bandwidths to cover the bands which have to be isolated. The design parameters of the two proposed double antennas are listed in Table 3.1. In the following sections, the antennas are analyzed through various simulations using the CST Microwave Studio. The antenna parameters such as reflection coefficients S_{11} or S_{22} and couplings S_{12} and S_{21} are used to assess and optimize the performance of the proposed antenna configurations. The words isolation and coupling can refer to the same phenomenon, where reduced coupling means increased isolation.

3.3.1 Effects of Slots Parameters on the Performance

For further insight into the behavior of the added $\lambda_g/2$ slots, the antenna in Fig. 3.3b was analyzed using CST simulations. In order to comply with the limited size of the antenna, each slot is folded into the shape of the letter *S*, so that it can be engraved in the corresponding feed line as shown in Fig. 3.3b. Figure 3.3 demonstrates the effect of the slot position d_2 along the feed line for the short monopole (port2). The

Table 3.1 Parameters of the two proposed antennas

Antenna/ parameter	Antenna-1	Antenna-2
r_1	11.5	11.5
r_2	10.5	10.5
L_f	17.1	17.1
w_f	3.2	3.2
D	9	9
w_g	34	34
L_g	15.5	16.5
L	35	37
l_{11}		7.55
l_{12}		1.37
w_{s1}		0.25
l_{21}		11
l_{22}		1.4
w_{s2}		0.29

All dimensions are in millimeters

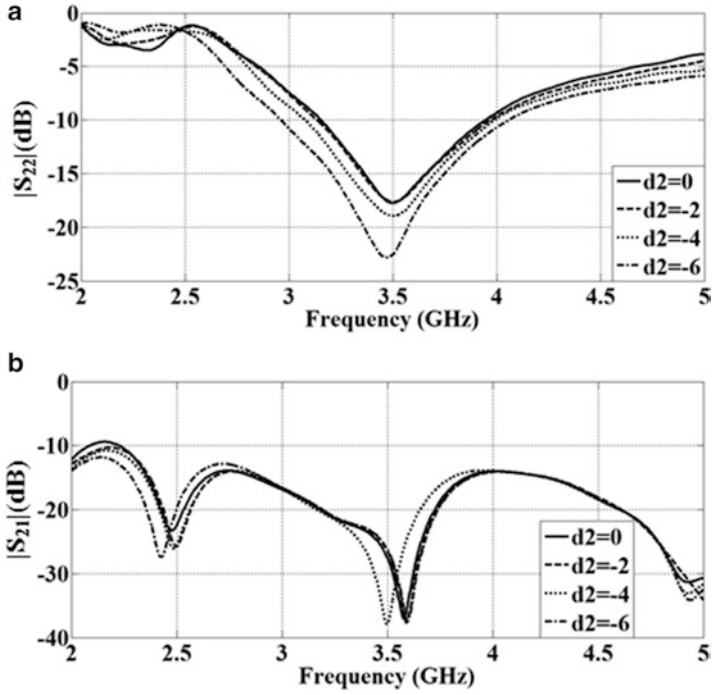

Fig. 3.3 Variation of the reflection coefficient S_{22} (**a**) and coupling (**b**) S_{21} in antenna-2 with frequency for various slot positions (d_2) [31]

results of the four investigated positions along the feed line are presented in Fig. 3.3a, while other parameters were kept constant. The impedance matching is improved as the slot is shifted toward the antenna port. The slot position has an obvious effect on the coupling parameter S_{21} at both of the frequency bands. The position (d_2 = 4 mm) was found to give a compromise between better matching at 3.5 GHz and lower coupling at both frequencies.

The effect of the slot width w_{s2} on the coupling between the two antennas is presented in Fig. 3.4, which shows a very little influence on S_{22} and little impact on S_{21} at upper frequency. However, at the lower band of the WLAN, the frequency at which maximum isolation is obtained changes as the slot width is varied. The simulations show that w_{s2} = 0.25 mm gives the best results (better matching at the upper band and lowest coupling at the lower 2.45 GHz band).

Figure 3.5 shows the influence of the slot length on the mutual coupling from port1 to port2 (S_{21}). As shown in Fig. 3.5a, variation of the slot length hardly affects the antenna matching which is a desired property. However, variation of the slot length l_{21} leads to varying the resonance frequency of the slot as can be concluded from Eq. 3.1. Minimum coupling at the 2.45 GHz band was obtained for $l_{21=}$11 mm. The parametric studies performed on the long arc antenna showed similar trends to those shown in Figs. 3.3, 3.4, and 3.5. The best results were obtained for $d_1 = -7$ mm, w_{s1} = 0.25 mm, and l_{11} = 7.5 mm.

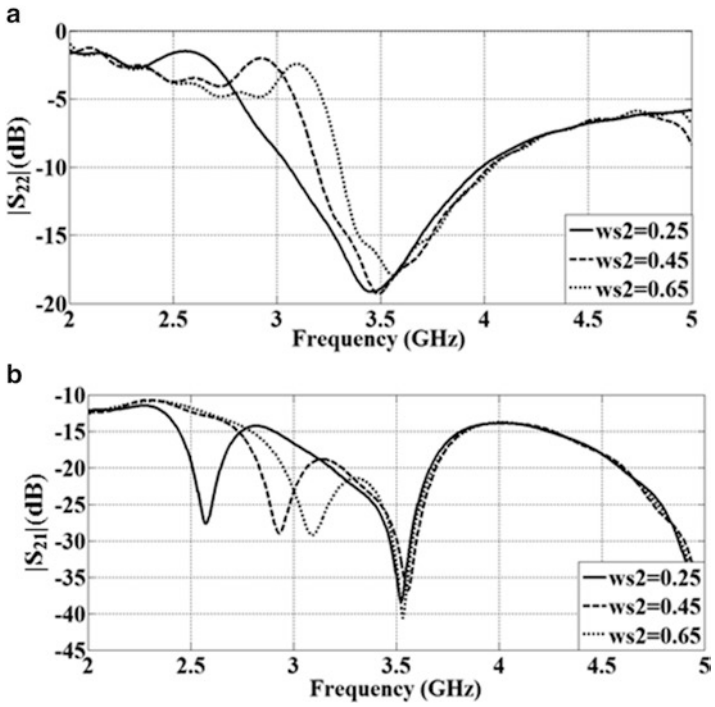

Fig. 3.4 Variation of the reflection coefficient S_{22} (**a**) and coupling (**b**) S_{21} in antenna-2 with frequency for various slot widths w_{s2} [31]

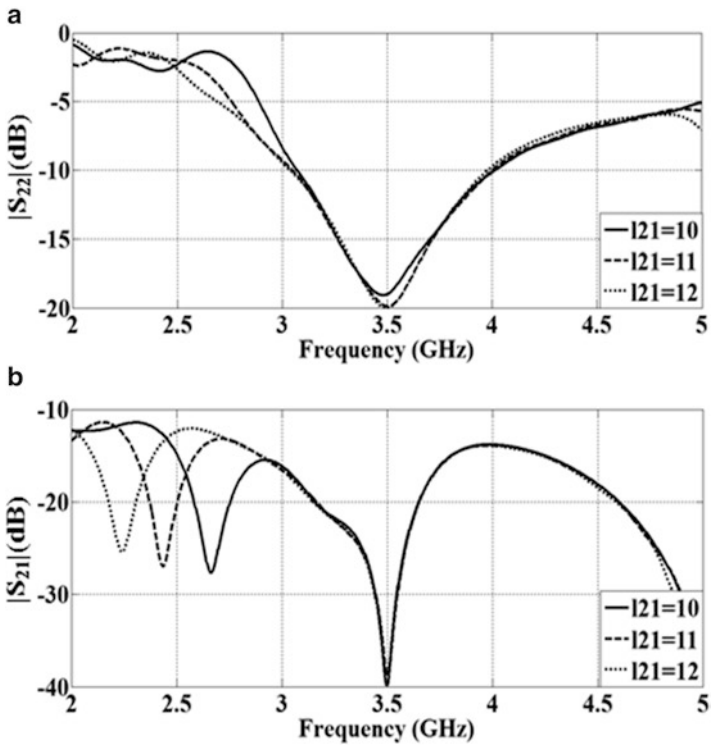

Fig. 3.5 Variation of the reflection coefficient S_{22} (**a**) and coupling (**b**) S_{21} in antenna-2 with frequency for various slot lengths l_{21} [31]

3.3.2 *Reflection Coefficient and Isolation*

The performances of the two proposed antenna configurations were investigated thoroughly using the commercial software CST Microwave Studio and the results are summarized in the following. The two antennas in Fig. 3.2 were simulated to obtain the performance of matching, coupling, and bandwidth. The two-port *S*-parameters of the antennas before and after deploying the two slots are shown in Fig. 3.6. Figure 3.6a displays variation of the S-parameters with frequency for the reference antenna-1. Each of the two antennas is properly matched across its operation band, while it shows high reflection coefficient at the other band. The –10 dB impedance relative bandwidth is found to be 18.22% at the lower band of 2.45 GHz center frequency and 24.48% at the upper band (3.5 GHz center frequency). The values of mutual couplings across the two bands are lower than −12.08 and −16.26 dB at the frequency of 2.45 and 3.5 GHz, respectively.

For comparison purposes, Fig. 3.6 b presents the S-parameters for the proposed antenna-2 having the two folded slots. The mutual coupling between the two antennas has been significantly reduced down to the level of −26.227 and –38.673 dB at 2.45 and 3.5 GHz, respectively. A minimum mutual coupling of −38.67 dB was achieved

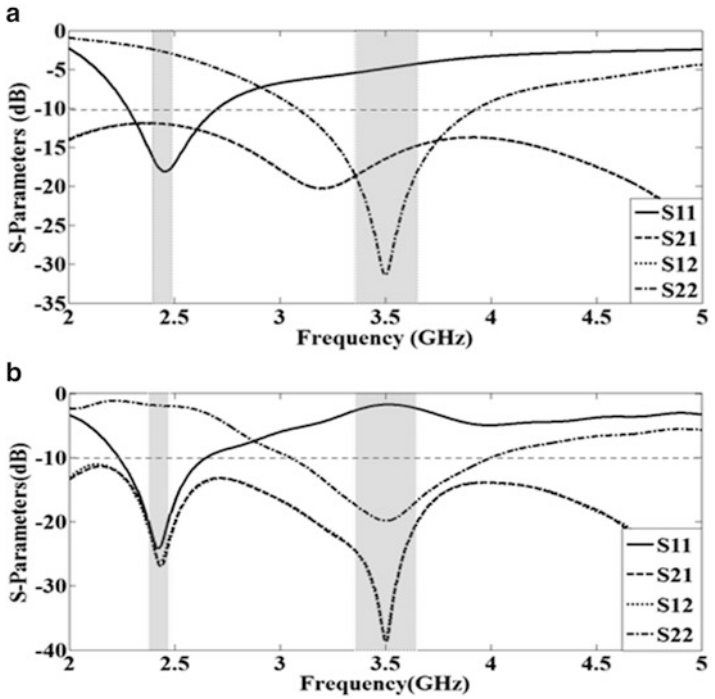

Fig. 3.6 Variation of the reflection coefficients and coupling of (**a**) antenna-1 and (**b**) antenna-2 with the frequency

Table 3.2 Comparison of the frequency response parameters of the proposed double-antenna configurations

Antenna/feature	Antenna-1	Antenna-2
Frequency range (GHz)		
1st band 2nd band	2.267–2.713 3.0835–3.94	2.235–2.648 3.05–3.997
BW (MHz) (%)		
1st band 2nd band	446.2 (18.22%) 856.8 (24.48%)	412.8 (16.8%) 944.4 (26.98%)
S_{11} & S_{12} (dB) for 1st band	−17.84 −12.087	−23.82 −26.22
S_{22} & S_{12} (dB) for 2nd band	−31.58 −16.25	−19.87 −38.673
Dimensions (mm)	34 × 36 × 1.5	34 × 37 × 1.5
Area (mm^2)	1224	1258

at 3.5 GHz, which represents an improvement of 22.42 dB compared to that of antennas (antennas-1), i.e., before using the slots. The obtained performances of the two proposed antennas are presented in Table 3.2. It is obvious that the addition of the two slots has highly improved the performance, especially the mutual coupling.

3.3.3 The Envelope Correlation Coefficients

The correlations between the signals received by the antennas in MIMO and diversity applications are figures of merit for evaluating the performance of the system. In general, the envelope correlation coefficients (ECC) can be calculated for the evaluation of some of the diversity capabilities of the system. Such diversity evaluations for a two-antenna system were presented in [32]. An alternative quick method consists of calculating the correlation coefficients using the scattering parameters of the tested antenna [33]. For example, the envelope correlation coefficient ρ_{12} for a double-antenna system is given by [34]:

$$\rho_{12} = \frac{\left|S_{11}^{*}S_{12} + S_{12}^{*}S_{22}\right|^{2}}{\left(1-\left|S_{11}\right|^{2}-\left|S_{21}\right|^{2}\right)\left(1-\left|S_{22}\right|^{2}-\left|S_{12}\right|^{2}\right)} \tag{3.4}$$

The above equation can be applied under the assumptions that the antenna system is lossless and operates in an environment having uniform scattering. Figure 3.7 presents the variations of the envelope correlation coefficients with frequency, which are calculated for the two proposed double-antenna configurations. It is obvious that the introduction of the two slots has significantly reduced the values of the ECC at the two operation bands. Table 3.3 shows a comparison between the obtained values of the correlation coefficients for the two investigated antennas. It can be concluded from Table 3.3 and Fig. 3.7 that with the introduction of the slots, the envelope correlation coefficient ρ_{12} has been reduced by 35-fold at the 2.45 GHz and by 21-fold at the 3.5 GHz.

3.3.4 Current Distribution at the Antennas

The operation of the added slots in the feed lines of the two antennas can be explained by observing the surface current distributions across the antenna structure. Figure 3.8 shows the current distributions with and without slots when a 2.45 GHz signal is applied at port-1, while port-2 is terminated by a 50 Ω load. The left antenna is thus in transmission mode while the right antenna is receiving. Before adding the slots, the right antenna has certain current distribution due to coupled and leaked signal from the other antenna which is fed by the 2.45 GHz signal. After addition of the slots, the current density at the short arc shows a lower density as well as the current at the ground plane between the two feed lines. Moreover, the

Table 3.3 Comparison of the obtained correlation coefficients of the proposed antennas

ECC at	Antenna-1	Antenna-2	ECC1/ECC2
2.45 GHz	0.1233	0.00345	35.8
3.5 GHz	0.009024	0.0004138	21.8

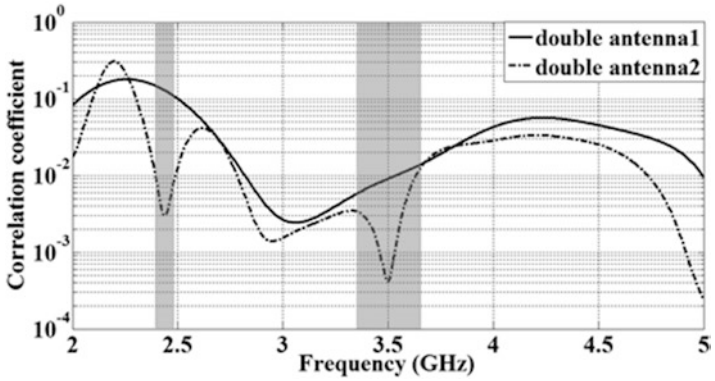

Fig. 3.7 Variation of the envelope correlation coefficient with frequency for the two double-antenna configurations

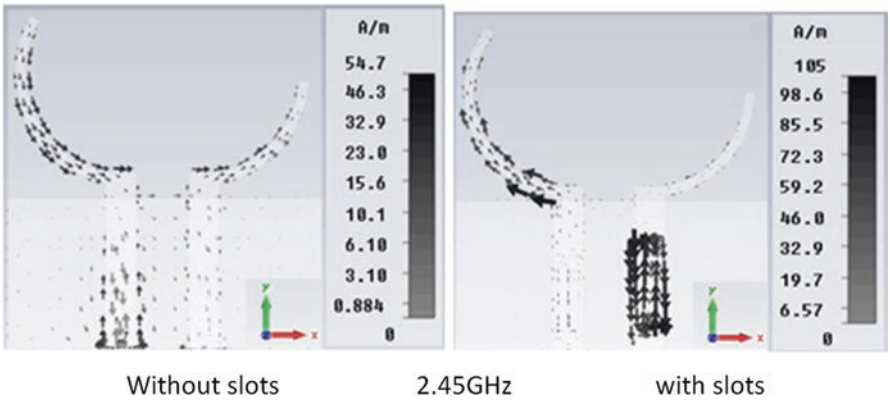

Fig. 3.8 Current distributions at the surface of antenna-2 when a 2.45 GHz signal is applied to port-1 (long arc) while port-2 (short arc) is connected to a 50 Ohm load

resonating slot at the feed line of the short arc has trapped the 2.45 GHz signal from reaching the output (port-2). The resonance in the slot at the feed line of the right antenna has resulted in high current density along the slot.

Figure 3.9 demonstrates a similar trend where a signal of 3.5 GHz frequency is applied at port-2, while port-1 is terminated by a 50 Ω load. The short arc is thus in a transmission mode, while the long arc is in a receiving mode. Before adding the slots, the antenna at left has certain current distribution due to coupled and leaked signal from the operating antenna at the right. After addition of the slots, the current at the left antenna has been reduced, while the resonating slot at its feedline has trapped the 3.5 GHz signal from reaching the output (port-1) of the long arc. The resonance in this slot has produced the high current density observed along the slot. When a signal of the proper frequency is applied to one port, then the slot at the other antenna will prevent the coupled signal from reaching the other port. Each of

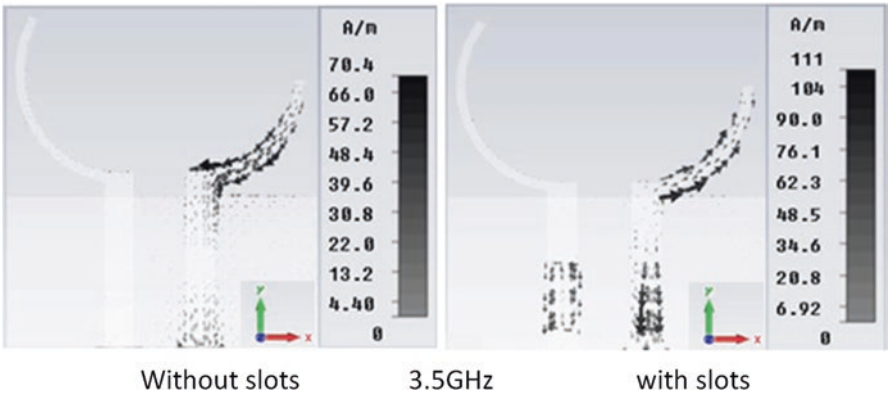

Fig. 3.9 Current distributions at the surface of antenna-2 when a 3.5 GHz signal is applied to port-2 (short arc) while port-1 (long arc) is connected to a 50 Ohm load

the used slots can be considered as a series filter that prevents the signal to be isolated from reaching the port in operation. The filters need no extra size since they are implemented in the feed lines.

3.4 Comparison with Published Works

The performances of the proposed antennas are compared with those of the antennas reported in [6, 7, 10, 11, 14, 16, 17, 19, 25, 26, 28, 33, 35]. Table 3.4 shows the parameters of frequency range, separating distance, maximum isolation at resonance frequency, as well as antenna dimension and volume that are considered in the comparison. The results in the table show a reasonably superior band isolation performance of the proposed technique (antenna-2) as compared to those of most of the reported antennas.

3.5 Experimental Validations

Based on the results listed in Table 3.1, two prototypes representing antenna-1 and antenna-2 were fabricated and experimentally investigated [31]. Measurements of the S-parameters of the antennas were performed using a vector network analyzer (VNA). The measurement results of the proposed double antenna-1 and antenna-2 are presented in Fig. 3.10. Figure 3.10a shows the measured reflection coefficient and coupling of the double antenna-1. The measured –10 dB bandwidth extends across the range from 2.136 to 2.55 GHz (i.e. 17.1%), and the isolation is better than 5.885 dB for the lower band. The upper band extends from 3.3 to 3.859 GHz (i.e. 15.97%) at an isolation of 11.9 dB. As shown in Fig. 3.2b, the two S-slots were

Table 3.4 Performance comparison of the proposed antennas with previous published work found in the literature

Reference	Frequency range (GHz)	Center to center separation (mm)	Frequency (GHz) /isolation (dB)	Dimensions (mm)	Volume (mm3)
[6]	5–6	28	5.2/33.3 5.8/21.1	48 × 25.5 × 1	1224
[7]	2.26–2.5 5.41–5.79	10	2.4/27 5.6/40	30 × 65 × 1.5	2925
[10]	1.5–2.8 4.7–8.5	14	1.5–2.8/15 4.7–8.5/20	50 × 63 × 0.8	2520
[11]	1.7–2.9		2.45/30	55 × 99 × 1.6	8712
[14]	2.4–2.48 5.15–5.725	12	2.4–2.48/35 5.15–5.72/24	17.3 × 22 × 7.7	2931
[16]	5.22–5.38	34	5.36/20	36 × 68 × 1.6	3917
[17]	2.39–3.75 5.03–7	21	3.07/20 6/25	40 × 30 × 1	1200
[19]	2.4–4.2	26.8	3.3/17	40 × 90 × 0.8	2880
[25]	2.4–2.5 5.15–5.825	8	2.45/18 5.5/36	28 × 22 × 1.6	986
[26]	2.34–2.55 5.13–5.85	16	2.45/27 5.8/30	38 × 43 × 1.6	2614
[28]	2.4–2.6 3.33–4.4 4.8–6	25	2.5/18 3.86/20 5.4/25	47 × 36 × 1.6	2707
[34]	2.23–2.535 3.34–3.8 5.49–7.176	10	2.4, 3.5, 5.8/22	40 × 75 × 1.6	4800
[35]	5–6.5	10.4	5.7/20	35 × 61 × 0.76	1627
Antenna-1	2.267–2.713 3.0835–3.94	9	2.45/12.09 3.5/16.25	34.4 × 42 × 1.5	2167
Antenna-2	2.235–2.648 3.05–3.997	9	2.45/26.22 3.5/38.673	30.4 × 42 × 1.5	1915

added in antenna-2 to reduce the coupling between the two antennas. The measured S-parameters for antenna-2 are presented in Fig. 3.10b. The isolation becomes 16.8 and 28.2 dB at 2.45 and 3.5 GHz, respectively. This shows more than 10 dB increase in the isolation for the lower band and an 11 dB increase in the isolation for the upper band when the slots were deployed. The –10 dB impedance bandwidth covers each of the bands of WLAN and WIMAX. The isolation at 2.45 GHz is 15.1 dB and increases to 26.63 dB at 3.5 GHz. As shown in Fig. 3.10a, b, there is a general shift to higher frequencies in the responses of S_{12} and S_{21}. The shift is 0.05 GHz (2.05%) for the first band and 0.15 GHz (4.29%) for the second band. This difference is attributed to the fabrication errors.

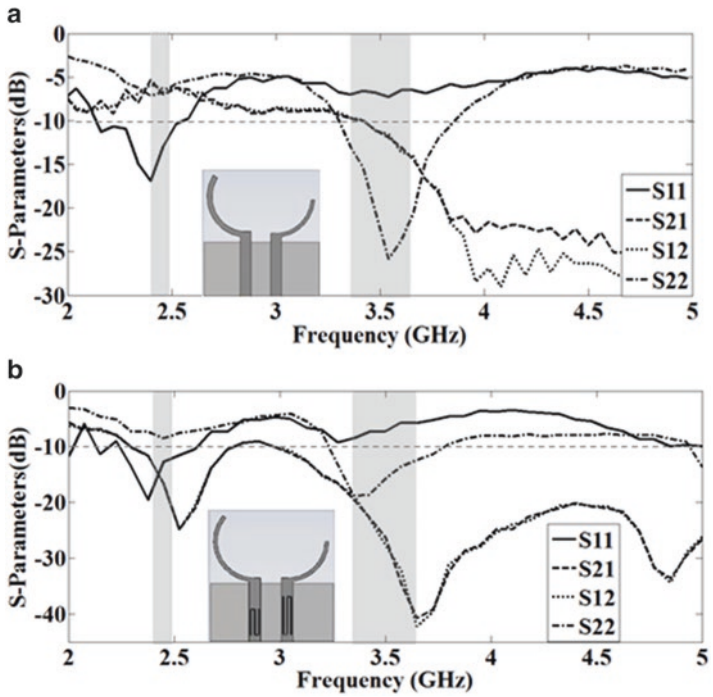

Fig. 3.10 Variation of the measured S-parameters with frequency for: (**a**) double antenna-1 and (**b**) double antenna-2

Figure 3.11 shows the calculated correlation coefficients from the measured S-parameters with and without using the slots. It can be observed that, when adding the slots, the correlation coefficient is improved from 0.2581 to 0.004125 at 2.45 GHz and from 0.4284 to 0.0002031 at 3.5 GHz.

3.6 Conclusions

Two low-profile dual-port antenna configurations for WLAN and WIMAX applications have been presented. In each configuration, the two antennas were found to be capable of supporting two separate frequency bands at their two ports. The proposed two S-slots in the feed lines proved to achieve higher isolation. The parametric study was applied to tune the position, length, and width of the inserted slots for the control of the position of the notched bands and obtain lower mutual coupling. The simulated results showed that the double antenna with S-slots provides low mutual coupling of less than –26 dB at 2.45 GHz and –38 dB at 3.5 GHz. These results also enhanced the envelope correlation coefficients values to 0.00345 at 2.45 GHz and 0.0004138 at 3.5 GHz. This is a 35-fold reduction at the 2.45 GHz

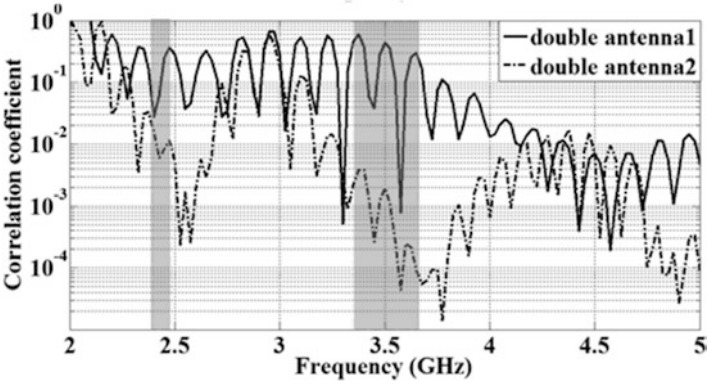

Fig. 3.11 The calculated envelope correlation coefficients from the measured S-parameters for the two double-antenna configurations

and 21-fold at the 3.5 GHz frequency in comparison with the case before using the two slots. The measured results showed quite reasonable agreement with the simulation results.

References

1. S.R. Saunders, A.A. Zavala, *Antennas and Propagation for Wireless Communication Systems*, 2nd edn. (Wiley, Chichester, 2007)
2. J. Leivo, Improving the performance of strongly coupled antennas using a compensating transmission line network, MSc Thesis, Gothenburg, Chalmers University of Technology, 2009
3. S. Zhang, Investigating and enhancing performance of multiple antenna systems in compact MIMO/diversity terminals, PhD Thesis , KTH Royal Institute of Technology, Stockholm, 2013
4. R.J. Vaughan, J.B. Anderson, Antenna diversity in mobile communications. IEEE Trans. Veh. Technol. **36**(4), 149–172 (1987)
5. Y.-T. Wu, Q.-X. Chu, Dual-band multiple input multiple output antenna with slitted ground. IET Microwaves Antennas Propag. **8**(13), 1007–1013 (2014)
6. S. Dossche, S. Blanch, J. Romeu, Optimum antenna matching to minimize signal correlation on a two-port antenna diversity system. Electron. Lett. **40**(19), 1164–1165 (2004)
7. S.-L. Zuo, Y.-Z. Yin, W.-J. Wu, Z.-Y. Zhang, J. Ma, Investigations of reduction of mutual coupling between two planar monopoles using two λ/4 slots. Prog. Electromagn. Res. Lett. **19**, 10–18 (2010)
8. S. Cui, Y. Liu, W. Jiang, S.X. Gong, Compact dual-band monopole antennas with high port isolation. Electron. Lett. **47**(10), 579–580 (2011)
9. J. OuYang, F. Yang, Z.M. Wang, Reducing mutual coupling of closely spaced microstrip MIMO antennas for WLAN application. IEEE Antenna Wirel. Propag. Lett. **10**, 310–313 (2011)
10. X. Zhou, X. Quan, R. Li, A dual-broadband MIMO antenna system for GSM/UMTS/LTE and WLAN handsets. IEEE Antennas Wirel. Propag. Lett. **11**, 551–554 (2012)
11. D. Shen, T. Guo, F. Kuang, X. Zhang, K. Wu, A novel wideband printed diversity antenna for mobile handsets, IEEE Vehicular Technology Conference (VTC), San Diego, 6–9 May 2012, pp. 1–5

12. S.H. Lee, C.Y. Yang, W.G. Yang, High isolation MIMO antenna design by using ground slits for mobile handset, Progress In Electro magnetics Research Symposium Proceedings, Moscow, 19–23 Aug 2012, pp. 589–592
13. Q. Rao, D. Wang, A compact, high isolation and wide bandwidth antenna array for long term evolution wireless devices. IEEE Trans. Antennas Propag. **60**(10), 4960–4963 (2012)
14. R. Addaci, K. Haneda, P.L. Thuc, C. Luxey, R. Staraj, P. Vainikainen, Dual-Band WLAN multi antenna system and diversity/MIMO performance evaluation. IEEE Trans. Antennas Propag. **62**(3), 1409–1415 (2014)
15. K.M. Prasanna, S.K. Behera, A hexagonal MIMO antenna system with defected ground structure to enhance bandwidth and isolation, IEEE International Conference on Communication & Signal Processing, ICCSP, Melmaruvathur, TamilNadu, 3–5 Apr 2013
16. M. Naser-Moghadasi, R. Ahmadian, Z. Mansouri, F.B. Zarrabi, M. Rahimi, Compact EBG structures for reduction of mutual coupling in patch antenna MIMO arrays. Prog. Electromagn. Res. C **53**, 145–154 (2014)
17. L. Xiong, P. Gao, Compact dual-band printed diversity antenna for WIMAX/WLAN applications. Prog. Electromagn. Res. C **32**, 152–165 (2012)
18. C.H. See, R.A. Abd-Alhameed, N.J. Mcewan, P.S. Excell, Design of a printed MIMO/diversity monopole antenna for future generation handheld devices. Int. J. RF Microwave Comput. Aided Eng. **24**(3), 348–359 (2014)
19. H. See, R.A. Abd-Alhameed, Z.Z. Abidin, N.J. McEwan, P.S. Excell, Wideband printed MIMO/diversity monopole antenna for Wi Fi/WiMAX applications. IEEE Trans. Antennas Propag. **60**(4), 2028–2035 (2012)
20. A. Diallo, C. Luxey, P. Le Thuc, R. Staraj, G. Kossiavas, Enhanced two-antenna structures for universal mobile telecommunications system diversity terminals. IET Microwaves Antennas Propag. **2**(1), 93–101 (2008)
21. Q. Luo, H.M. Salgado, J.R. Pereira, Compact printed monopole antenna array for dual-band WLAN application, IEEE International Conference on Computer as a Tool (EUROCON), Lisbon, 27–29 Apr 2011, pp. 1–4
22. M.A. Moharram, A.A. Kishk, General decoupling network design between two coupled antennas for MIMO applications. Prog. Electromagn. Res. Lett. **37**, 134–142 (2013)
23. H. Sato, Y. Koyanagi, K. Ogawa, M. Takahashi, A method of dual-frequency decoupling for two-element MIMO antenna, Progress In Electromagnetics Research Symposium Proceedings, Stockholm, pp. 1853–1857, 12–15 Aug 2013
24. S.-C. Chen, Y.-S. Wang, S.-J. Chung, A decoupling technique for increasing the port isolation between two strongly coupled antennas. IEEE Trans. Antennas Propag. **56**(12), 3650–3658 (2008)
25. R. Addaci, A. Diallo, C. Luxey, P.L. Thuc, R. Staraj, Dual-band WLAN diversity antenna system with high port-to-port isolation. IEEE Antennas Wirel. Propag. Lett. **11**, 244–247 (2012)
26. H. Qin, Y.-F. Liu, Compact dual-band MIMO antenna with high port isolation for WLAN applications. Prog. Electromagn. Res. C **49**, 97–104 (2014)
27. A.A. Naser, K.H. Sayidmarie, J.S. Aziz, Compact High Isolation Meandered-Line PIFA Antenna for LTE (Band-Class-13) Handset Applications. Prog. Electromagn. Res. C **67**, 153–164 (2016)
28. A.M. Saleh, K.H. Sayidmarie, R.A. Abd-Alhameed, S. M. Jones, J.M. Noras, P.S. Excell, Compact tri-band MIMO antenna with high port isolation for WLAN and WiMAX applications, Antennas & Propagation Conference (LAPC), Loughborough, 14–15 Nov 2016
29. L.S.Yahya, K.H. Sayidmarie, F. Elmegri, R.A. Abd-Alhameed, Crescent- shaped double-monopole antennas with reduced coupling for WLAN and WIMAX applications, IEEE Internet Technologies and Applications (ITA), Sept 2015, pp. 393–398
30. K.H. Sayidmarie, L.S. Yahya, Design and analysis of dual band crescent shape monopole antenna for WLAN applications. Int. J. Electromagn. Appl. **3**(4), 96–102 (2013)
31. L.S. Yahya, Analysis, modeling and design of multiband antennas for communicationsystems, Ph.D. Thesis, College of Engineering, University of Mosul, Iraq, Dec 2015

32. S.C.K. Ko, D. Murch, Compact integrated diversity antenna for wireless communications. IEEE Trans. Antennas Propag. **9**(6), 954–960 (2001)
33. S. Blanch, J. Romeu, I. Corbella, Exact representation of antenna system diversity performance from input parameter description. IET Electron. Lett. **39**(9), 705–707 (2003)
34. H.U. Iddi, R. Kamarudin, T.A. Rahman, A.Y. Abdurahman, R. Dewan, A.S. Azini, Triple band planar monopole antenna for MIMO application, Progress In Electromagnetics Research Symposium Proceedings, Stockholm, Sweden, 12–15 Aug 2013, pp. 1421–1424
35. K. Wang, L. Li, T.F. Eibert, A decoupling technique based on partially extended ground plane for compact two-port printed monopole antenna arrays, 8th German Microwave Conference, Aachen, 10–12 Mar 2014

Chapter 4
Electrically Small Planar Antennas Based on Metamaterial

Mohamed Lashab, Naeem Ahmad Jan, Fatiha Benbdelaziz, and Chems Eddine Zebiri

4.1 Introduction

Many research works have focused on planar antennas for terrestrial digital video broadcasting or, more recently, mobile networks, which need high performances such as low cross-polarization, an omnidirectional beam, an ultrawide band, and low side lobes of the radiation pattern. Electrically small antennas (ESAs) can offer most of these performances [1–4]. ESAs are widely used in electromagnetic scattering for their interesting applications, especially when loaded with different types of dielectric materials [5–9], ferrite, chiral materials, or artificial materials to enhance the bandwidth and the radiation pattern [10]. Metamaterial is one of the most used artificial materials, known for absorption of undesirable wave effects in antenna design and also used for antenna miniaturization purposes [11–13]. Some applications already employing this technology can be listed as NFC (near field communication) systems, including RFID (radiofrequency identification), UWB (ultrawideband), and wireless broadband systems such as WLANs (wireless local area networks) and WiMAX (Worldwide Interoperability for Microwave Access) [14].

M. Lashab (✉)
Larbi Ben M'hidi University, O.E.Bouaghi Algeria
e-mail: lashabmoh@yahoo.fr

N.A. Jan
School of Engineering and Informatics, University of Bradford, Bradford, UK

F. Benbdelaziz
Constantine University, Algeria
e-mail: benabdelaziz2003@yahoo.frl

C.E. Zebiri
Sétif university, Algeria
e-mail:Zebiri@ymail.com

I. Elfergani et al. (eds.), *Antenna Fundamentals for Legacy Mobile Applications and Beyond*, DOI 10.1007/978-3-319-63967-3_4

Metamaterial is known as an artificial material. In the literature, it is defined as left handed. Antennas of high absorption are usually based on metamaterial; also, antennas loaded with metamaterial can exhibit miniaturization effects. Many research studies have been carried out recently on metamaterial and have attracted great interest, both for theoretical development [15] and for experimental works [16, 17]. For more than a decade, many research workers have studied the effects of dielectric, chiral, or ferrite items inside planar antennas or even aperture antennas such as horn antennas in the taper (efficeint part of the horn antenna just beyond the feed) many research work have been investigated on horn antenna loaded with artificial dielectrics [18–20]. In this chapter, we are interested in the latest development concerning planar antennas loaded with metamaterials. We are looking for advantages, applications, and limitations in broadband and terrestrial applications.

4.2 Small Antenna Limitations

An electrically small antenna can be defined as an antenna with physically small dimensions relative to its wavelength. Another definition is an antenna with a very low resonant frequency relative to its physical dimensions. Many definitions have been given for ESAs, but probably the most suitable one was given by King [21], who defined small antennas as antennas with dimensions bounded by the relation of ($k.a \leq 0.5$), where a is the radius of a sphere circumscribing the maximum dimensions of the antenna, and ($k = 2\pi/\lambda$), where λ is the wavelength of the antenna [22].

Limitations of ESAs have been discussed by many researchers [23]. They could have almost the same performance as an ordinary antenna. The problem is that the smaller the antenna is, the antenna it is to get impedance matching. Usually ESAs have a narrow bandwidth and high Q compared to ordinary antenna. Some practical solutions could improve the bandwidth and the Q [24]; this could be done, for instance, just by insertion of network circuits as was proposed in reference [25], or by adding a non-Foster circuit based on negative differential resistance [26]. That is why many researchers have confirmed that there are no limitations of ESAs; it is just a matter of finding better adaptations of the antenna to the environment by adding some techniques, as listed above.

4.3 Fundamentals of Metamaterials

4.3.1 Physical Properties

For more than a decade, many researchers have carried out work looking for more than ordinary materials, starting from anisotropic to bianisotropic and chiral structures, where the electric and magnetic constitutive parameters of the material are configured differently in the optical axis [27]. In addition to the difficulties or complicated fabrication of these materials, they are actually very limited in their application in the

very narrow frequency band where these materials can exhibit their artificial properties. Actually, photonic and electromagnetic band gap (EBG) materials [28] are much easier to fabricate and can yield more interesting antenna designs. Unfortunately EBG structures lose their interesting properties for antenna design when the wavelength is much smaller than its intrinsic period [29]. Nevertheless, these structures can find applications in many antenna designs simply for their basic configurations.

Nowadays there is a new type of artificial material that can go beyond some of the previous limitations. The so-called electromagnetic metamaterials (MTMs) are generally defined as efficiently homogeneous electromagnetic structures with unusual properties and peculiar behavior not available in nature [30]. An efficient homogeneous structure is one whose structural average size of the unit cell p (p is the size of the cell) is much smaller than the guided wavelength; $p \ll \lambda$ (λ is the wavelength) [31]. Once this condition is satisfied, the relationship that relates the effective parameters—the effective relative electric permittivity ε_{eff} and the effective magnetic permeability μ_{eff}—to the index of refraction n is given by:

$$n = \pm\sqrt{\varepsilon_{\text{eff}}\,\mu_{\text{eff}}} \tag{4.1}$$

The value of the constitutive parameters, i.e., permittivity and permeability, depend on the geometric shape of the unit cell (inclusion) or on the mutual space between cells. Thus, one can choose the cells' shape or spacing to obtain desired constitutive parameters; the cells could be implemented on a planar substrate in a 2D or 3D configuration [32]. Metamaterials can be classified or categorized by the graph in Fig. 4.1, where the permeability and the permittivity are both negative. With regard

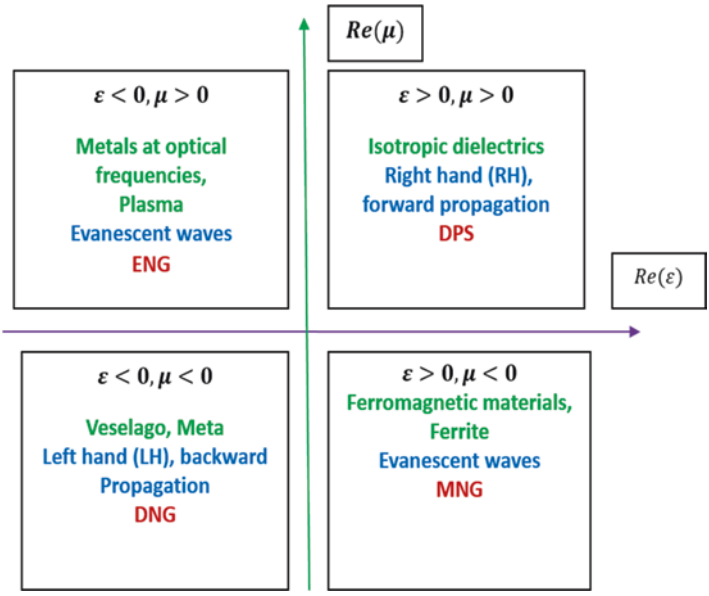

Fig. 4.1 Materials classification

to double negative parameters (DNG), this type of material has interested many researchers. In 1968, Veselago started working on media with double negative permeability and obtained remarkable results. Other regions considered as metamaterial ones are the regions near the zero axes, ENZ (ε near zero) and MNZ (μ near zero); both regions lead to ZIM (zero index metamaterial) [32].

Double positive (DPS) permittivity and permeability are isotropic dielectrics known as right hand propagation of electromagnetic waves in the forward sense. The ENG (ε negative) region is also a metamaterial region, realized with parallel plate or wire inclusion, and a great variety of shapes can be suggested. The last region, MNG (μ negative), is for ferromagnetic and ferrite materials.

4.3.2 Theoretical Aspects

A metamaterial is an artificial material whose permittivity and permeability are not known and vary with respect to the operating frequency. The extraction of the constitutive parameters needs experimental tests or analytical models. The Drude–Lorentz model [33, 35], known as the dispersion model, is a very accurate analytical method used to extract the constitutive parameters for unknown structures, for the split ring resonator (SRR), or for the complementary SRR (CSRR), as shown in Fig. 4.2. Using the Drude–Lorentz model, the magnetic permeability and electric permittivity are described below:

$$\mu_r = \mu_o \left(1 + \frac{F_u f^2}{f^2 - f_{ou}^2 + j\gamma f} \right) \tag{4.2}$$

and:

$$\varepsilon_r = \varepsilon_o \left(1 + \frac{F_e f^2}{f^2 - f_{oe}^2 + j\gamma f} \right) \tag{4.3}$$

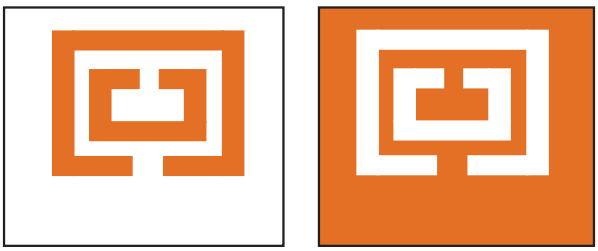

Fig. 4.2 Metamaterial structures: (**a**) SRR; (**b**) CSRR

where μ_o and μ_o are the background permeability and the background permittivity, respectively; $F_u$and F_e are the magnetic resonant intensity and the electric resonant intensity, respectively; f_{ou} is the magnetic resonant frequency and f_{oe} is the electric resonant frequency; and γ is the damping factor of the resonance. All of these parameters have to be found analytically for several frequencies, and appropriate codes or programs have to be used [34].

Another much easier method of constitutive parameter extraction is known as the standard retrieval procedure [35, 36]. In this method, the effective permittivity and effective permeability are extracted from the transmission and reflection coefficients, provided by commercial software or experimental results, although the microscopic and macroscopic delivered values of the constrictive parameters are not in good agreement [37].

4.3.3 CRLH-TL Resonator

The transmission line (TL) structure is essential to realize a resonant planar antenna with no dependence on its physical dimensions. This structure supports an infinite wavelength at its fundamental mode which is denoted by ZOR [38]. A practical realization of an LH-TL, which includes the essential part as described above for RH effects, is known as a CRLH-TL; this technology can produce an infinite wavelength ($\beta=0, with\ \omega\neq 0$). By this fact, and based on the advantage of this resonator, this was used to realize the proposed antenna [39]. The electric equivalent circuit of the homogeneous resonator CRLH-TL unit cell is presented in Fig. 4.3, as a "T" shape. The resonance condition of such an open-ended resonator is given by the dispersion relation [40]:

$$\beta = \frac{n\pi}{l}\left(0,,,\pm 1,,,,.,.,,\pm\left(N-1\right)\right) \tag{4.4}$$

Regarding Eq. 4.4, we denote by l the physical length of the resonator; n is the mode number, and N is the number of unit cells, for n equal to zero, the fundamental mode of the compensated right/left hand (CRLH-TL) resonator is obtained.

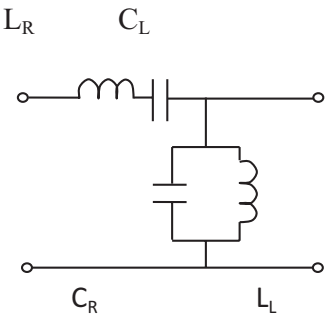

Fig. 4.3 CRLH-TL resonator, electric circuit

The impedance Z and the admittance Y given below can be electrically implemented on the antenna, so as to obtain a compensated effect of the right hand and left hand:

$$Z = j\left(\omega L_R - \frac{1}{\omega C_L}\right) \tag{4.5}$$

$$Y = j\left(\omega C_R - \frac{1}{\omega L_L}\right) \tag{4.6}$$

The unit cell of zero order resonators (ZORs) is inserted into the proposed antenna. Thus, the size of the antenna can be compact. In the case of open boundary conditions, the infinite wavelength resonance depends on the shunt parameters of the unit cell, L_L and $C_R$and the resonant frequencies are given by:

$$\omega_{\text{sh}} = \frac{1}{\sqrt{L_L C_R}} \text{ And } \omega_{\text{se}} = \frac{1}{\sqrt{L_R C_L}} \tag{4.7}$$

where ω_{sh} is the shunt resonant frequency and ω_{se} is the serial resonant frequency [32]. A different combination of zero order can be designed, more complicated than that given in Fig. 4.3, like a "pi" shape for instance, where the input and output have symmetrically the same components as in references [41–43], or a combined "T" shape and "pi" shape such as in references [44–46], where more than two resonant frequencies are obtained.

A dispersion diagram of the CRLH structure is given in Fig. 4.4. In contrast to ordinary materials where the constant of propagation is positive $\beta > 0$, the composite

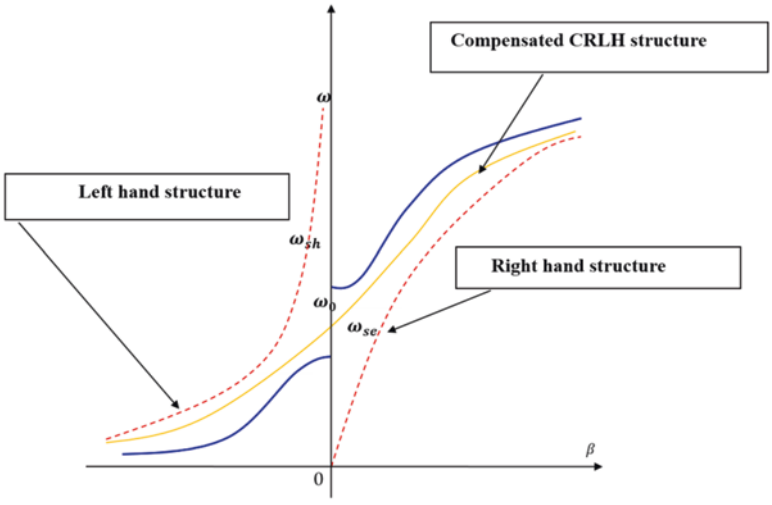

Fig. 4.4 Dispersion diagram of the CRLH structure

CRLH structure can have a constant of propagation that is null $\beta=0$, or even negative $\beta<0$. The CRLH structure is generally called compensated left hand/right hand when there is only one frequency ω_o for which $\beta=0$.

4.4 Monopole Antenna Loaded with SRR

4.4.1 Introduction

For a two band antenna realized by a monopole bowtie type, this is loaded with one unit cell SRR as a metamaterial at the bottom of the antenna; this is designed similarly to reference [39]. The aim of this work is to exhibit the improvement of the gain and the notched bandwidth by metamaterial inclusion. The proposed antenna has geometric dimensions of 60 mm × 40 mm.

The obtained results from the HFSS simulation dealing with the constitutive parameters of the SRR show that there is an ENG (permittivity negative) caused by the unit cell. In this work, the operating bandwidth of the proposed antenna is in the range of 0.75–0.95 GHz as the DVB-T band, and 1.18–3.5 GHz as Wi-Fi, WLAN, and WiMAX applications. Here in this work, the inserted unit cell of the SRR has a significant effect in the second band of the antenna [39].

4.4.2 Unit Cell Design

The unit cell is fabricated on FR4 epoxy substrate; it is composed of four split rings, and the metamaterial unit cell has dimensions of 30 mm × 30 mm. Here in this work, the inclusion of one unit cell of SRR is considered in this design in order to show the benefit of the effect of metamaterial placement on the bottom side of the antenna. The antenna is simulated with and without metamaterial just to exhibit the antenna's performance. The unit cell is realized using the well-developed printed circuit board (PCB) technology. Figure 4.5 presents the geometric dimensions of the unit cell SRR metamaterial.

The SRR dimensions are given as follows: the first square is 30 mm × 30 mm, the second one is 25 mm × 25 mm, the third one is 19 mm × 19 mm, the fourth one is 13 mm × 13 mm, the gap between the squares is given as 2 mm, the thickness of all of the square rings is 2 mm, and the spacing between rings is 1 mm. In this design, the substrate is the epoxy FR4 with relative permittivity $\varepsilon_r = 4.4$ and a dielectric loss tangent $\delta = 0.02$; the thickness of the chosen substrate is 1.6 mm. The unit cell is designed by HFSS, and the "S" parameters are explored for eventual extraction of the constitutive parameters.

The transmission and reflection coefficients of the unit cell of the SRR as a metamaterial are presented in Fig. 4.6a, where four resonant frequencies are observed.

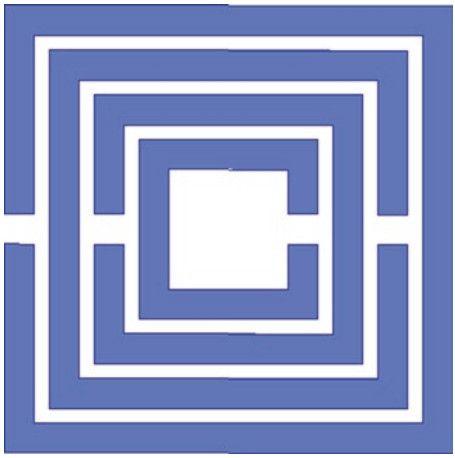

Fig. 4.5 SRR metamaterial unit cell

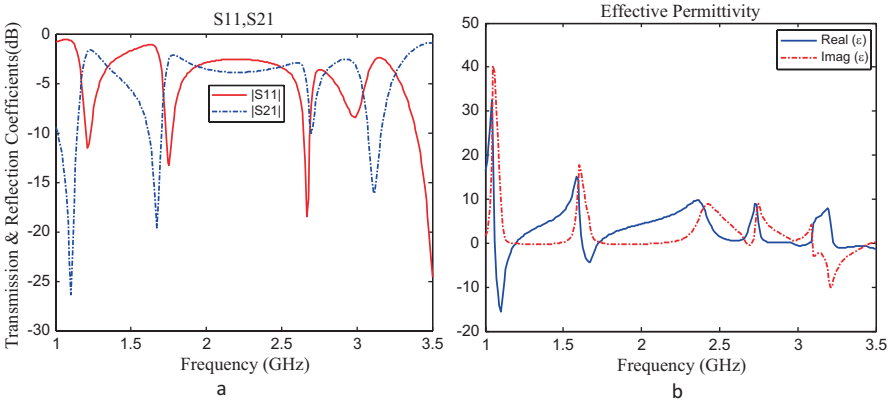

Fig. 4.6 (**a**) Transmission and reflection coefficient; (**b**) effective permittivity

The first one is at 1.25 GHz, the second one is at 1.75 GHz, the third one is at 2.75 GHz, and the last one is at 3.5 GHz. The simulated unit cell on HFSS has shown very interesting results. Figs. 4.6b and 4.7a present the imaginary and real parts of the permittivity and the permeability, respectively.

As can be seen from Figs. 4.6b there are negative values of the permittivity (ENG), from 1.07 to 1.18 GHz in the DVB-T band, and from 1.62 GHz to 1.75 GHz. In figure 4.7a, it can be observed negative values of the permeability (MNG), starting from 3.0 GHz to 3.15 GHz and from 3.4 GHz to 3.5 GHz. Figure 4.7b shows the index of refraction with respect to the frequency, zero index metamaterial (ZIM) is observed at 1.25 GHz and 1.75 GHz. All of these metamaterial behaviors cover the following applications: Wi-Fi, WLAN, and WiMAX.

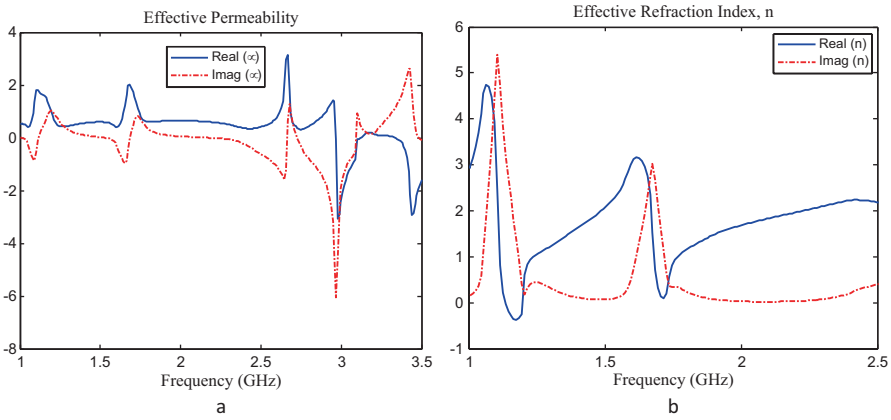

Fig. 4.7 (**a**) Effective permeability; (**b**) effective index of refraction

4.5 Antenna Design

The monopole bowtie type antenna used in this work is constituted by a set of two triangular shaped patches related together by a thin wire of 0.5 mm thickness and 6 mm in length. The two patches are fed by a monopole slot of 2 mm thickness and 23 mm in length, as shown in Fig. 4.8a. The SRR metamaterial cell is placed on the ground plane on the bottom side of the antenna, as shown in Fig. 4.8b. The total gain shown in Fig. 4.9 is recorded for three frequencies—2.5 GHz, 3.0 GHz, and 3.5 GHz—considered the main frequencies contained in both antenna bandwidths (with and without SRR).

Figure 4.9a presents the gain in the radiation pattern in the case of an antenna without SRR in the yoz plane for three frequencies: 3.5 GHz, 3.0 GHz, and 2.5 GHz. The maximum value of the radiation pattern is obtained at 3.0 GHz as −4.35 dBi. Figure 4.9b presents the case of an antenna without SRR in the xoz plane; almost all of the frequencies present the same maximum value as −6.68 dBi.

The radiation pattern in Fig. 4.10 is recorded also for three frequencies, given as 2.5 GHz, 3.0 GHz, and 3.5 GHz. This is the case of the monopole antenna loaded with one unit cell previously presented in Fig. 4.8. Figure 4.10a is concerned with the yoz plane; the maximum gain is obtained at the frequency of 3.0 GHz, which is precisely −0.95 dBi. Compared to the case of the antenna without SRR, there is an increase of 47%. Concerning the radiation pattern in the xoz plane presented in Fig. 4.10b, the maximum gain value is observed at the frequency of 2.5 GHz, which is −1.25 dBi; compared to the case of the antenna without SRR, there is an increase of 86.9%, which is really very important. The results obtained by simulation concerning the unit cell justify the gain enhancement in the frequency range from 2 to 3.5 GHz.

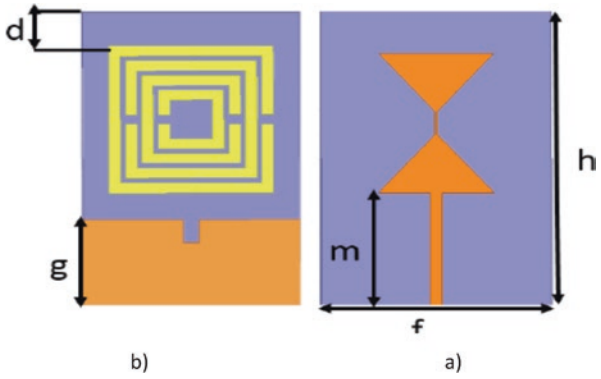

Fig. 4.8 (**a**) Top view of the bowtie monopole antenna; (**b**) bottom view of the bowtie monopole antenna; $m = 23$ mm, $g = 17.5$ mm, $f = 40$ mm, $d = 7$ mm, $h = 60$ mm

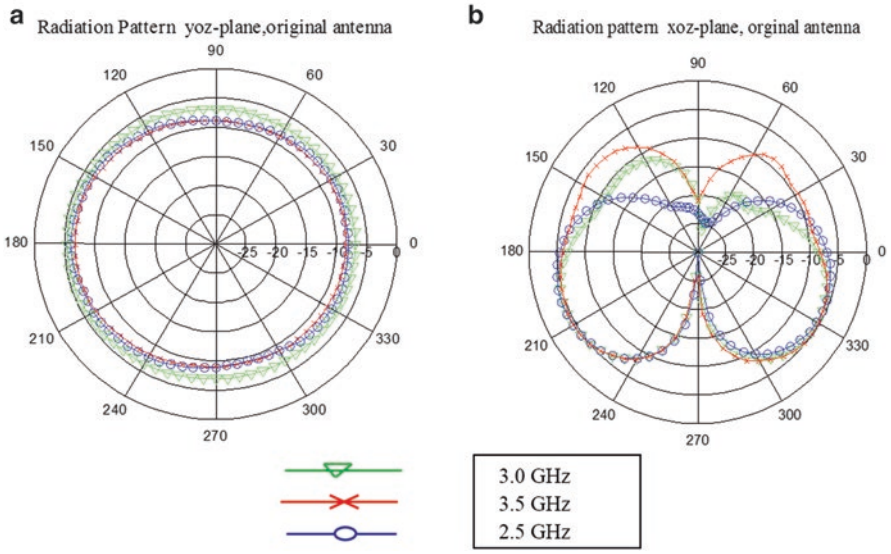

Fig. 4.9 Total gain in the radiation pattern without SRR for three frequencies: (**a**) *yoz plane*; (**b**) *xoz plane*

In summary, Fig. 4.11 shows the total gain of the antenna with and without SRR. A brief comparison between the two antennas gives a clear idea about the effect of the metamaterial unit cell. The SRR unit cell exhibits its phenomena starting from 2 to 4 GHz, but the great effect is observed in the frequency range from 2.5 to 3.5 GHz.

Figure 4.12 shows the coefficient of reflection with and without SRR. Although the bandwidth is reduced about 10%, two important things are shown in this figure: first, the return loss at 1.5 GHz is very small; second, a new resonant frequency

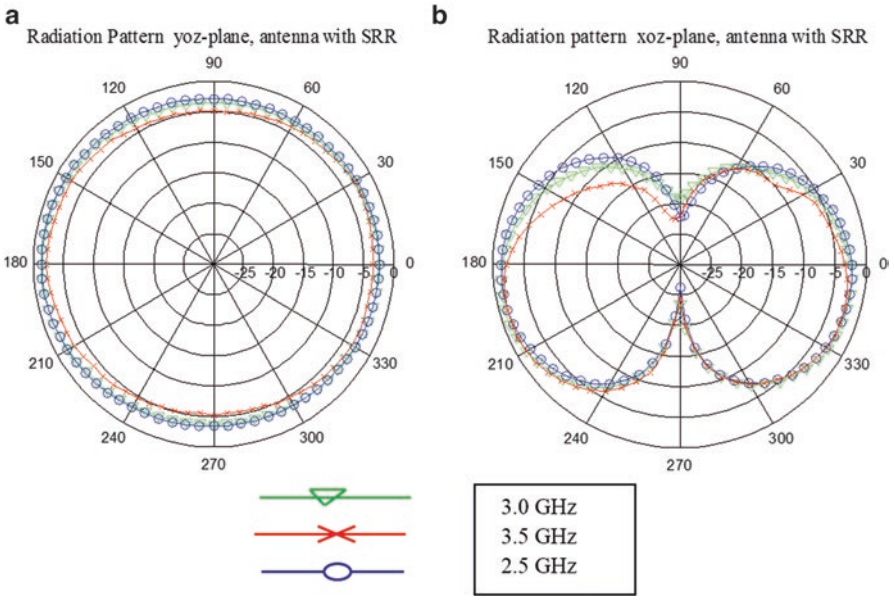

Fig. 4.10 Total gain in the radiation pattern in the antenna with SRR for three frequencies: (**a**) yoz plane; (**b**) xoz plane

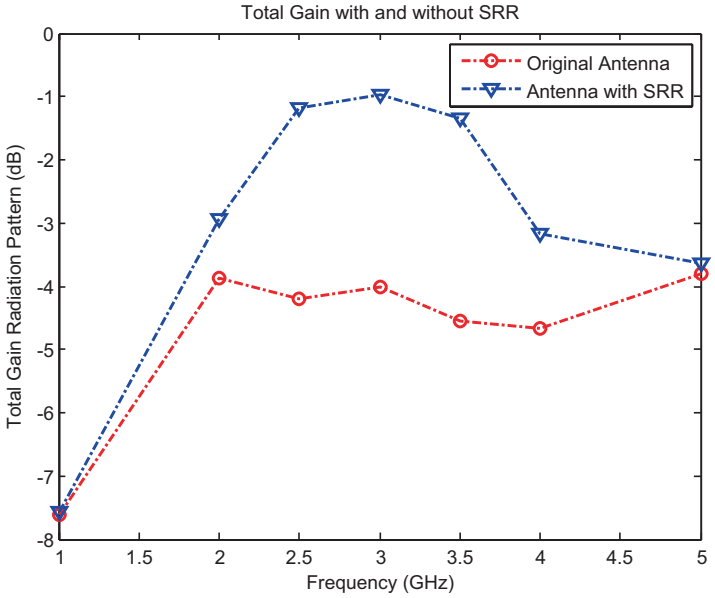

Fig. 4.11 Gain comparison with and without SRR

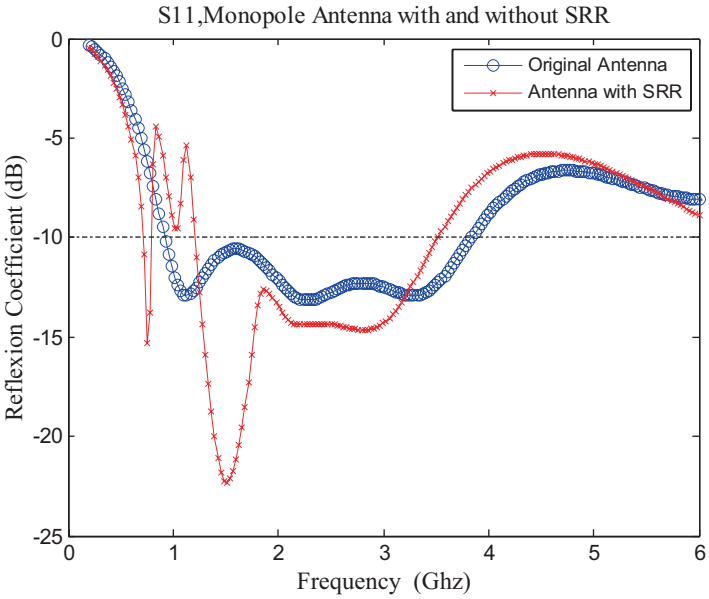

Fig. 4.12 Return loss with and without SRR metamaterial

appears at 0.85 GHz. The inclusion of SRR metamaterial has produced two important behaviors that mainly characterize the metamaterials, especially the appearance of lower frequencies. This can suggest the idea of miniaturization.

4.6 Metamaterial-Inspired Antenna

In this work, an electrically small planar metamaterial-inspired coplanar fed waveguide (CPW-Fed) antenna is applied for WLAN and ultrawideband applications [40]. The antenna is based on a simple slot (very thin) loaded onto a rectangular patch and a zigzag shaped metamaterial-inspired unit cell. The idea behind the proposed antenna is to enable a miniaturization effect. The proposed antenna can provide a multipurpose dual band application. The first one is a Wi-Fi band at a frequency of 2.45 GHz with an impedance bandwidth of 150 MHz; the second one is an ultrawide band extending from 4.2 GHz to 6.5 GHz. Two antennas are designed and fabricated with and without metamaterial-inspired loading. The simulated and measured results regarding the return loss (S11), gain, and radiation pattern are discussed. The metamaterial-inspired antenna seems to have better performance.

4.6.1 Antenna Design

In this design, a novel coplanar waveguide MTM-inspired antenna is designed, fabricated, and tested [40]. The lower Wi-Fi frequency at 2.45 GHz is the result of the zigzag E-shaped MTM loading. The second resonant frequency is obtained because of the CPW-Fed antenna, which is from 4.2 GHz to 6.5 GHz, an ultrawide band with the help of a small rectangular patch of 4 mm × 3.25 mm, and a gap to help maintain this band steady throughout at S11 <= -10 dB. The geometric configuration of the metamaterial-inspired antenna is shown in Fig. 4.13, and the photographic prototype of the antenna is shown in Fig. 4.14. The antenna is simulated in HFSS using an FEM technique. The substrate is the epoxy FR4 with relative permittivity of 4.4, tangential loss of 0.02, and thickness of 1.6 mm. The strip antenna is loaded at the top edge on the right side with a zigzag E-shaped metamaterial unit cell. This small metamaterial-inspired structure gives rise to the left handed media characteristic, and it resonates at a frequency of 2.45 GHz. The antenna is fed by a CPW of a 50 ohm transmission line with a width of 3 mm.

The overall size of the antenna is 28 × 24 × 1.6 mm^3. The upper ground is 12 × 10 mm^2 with a gap of 0.5 mm between the transmission line and the ground on each side. The dimensions of the strip antenna are 10.75 × 7 mm^2, which appears as

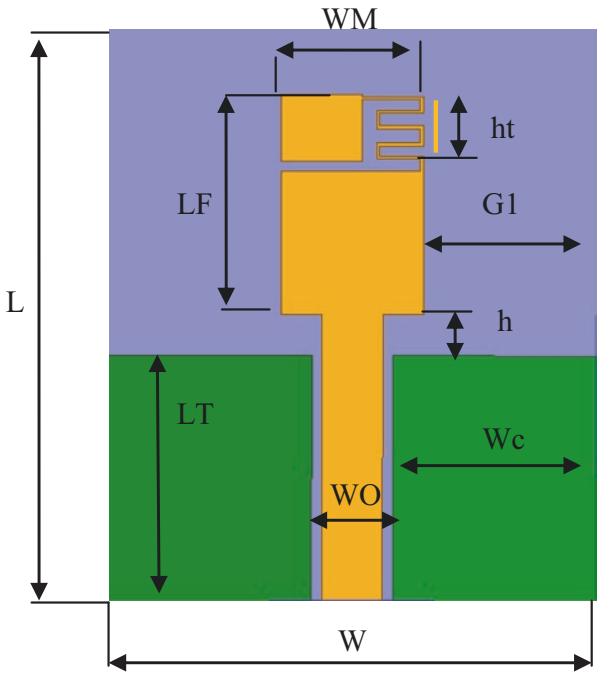

Fig. 4.13 Geometry of proposed metamaterial-inspired antenna. L = 28, w = 24, LF = 10.75, WM = 7, ht = 4, $T2$ = 12, Wc = 10, WO = 3, h = 2, $G1$ = 5

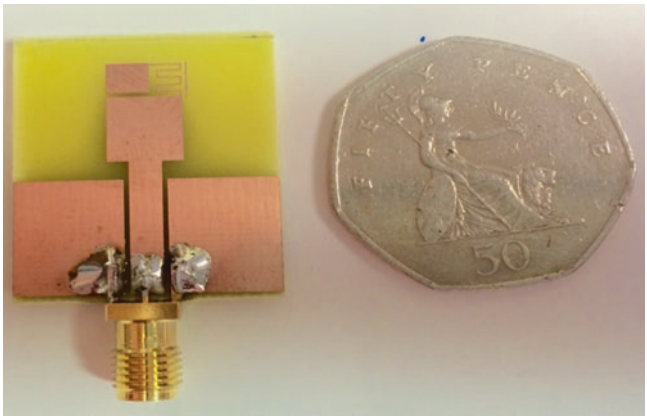

Fig. 4.14 Photograph of the proposed antenna

two patches connected by a small loading on the top right side. There is a small metallic wire 4×0.15 mm^2 in size placed in the vicinity of the zigzag unit cell. The width of the metamaterial unit cell is taken as 0.15 mm, and the gap between the metallic wire and the unit cell is 0.35 mm. The gap between the antenna and the ground is taken as 2 mm. The gap on each side of the antenna is 8.5 mm. The antenna is a single layer type and it is also compact and easy to fabricate.

4.6.2 Results and Discussion

The experimental results were interesting. Figure 4.15 shows the comparison of the simulated return loss (S11) of the conventional coplanar waveguide and metamaterial-inspired coplanar antenna. The graph clearly indicates a negative order resonance (NOR) at 2.45 GHz for the metamaterial-inspired antenna; that is because of the negative characteristics (permittivity and permeability) produced by the zigzag E-shaped metamaterial-inspired unit cell. There is a clear shift in the first order resonance for the lower frequency band from 4 to 2.45 GHz, and the second order resonance for the metamaterial-inspired antenna is a UWB from 4.2 to 6.5 GHz without any discontinuity. Regarding the effect of the wire width, Fig. 4.16 shows the parametric study of the metamaterial-inspired antenna for different n sizes, where n is the width of the zigzag unit cell on the top right side of the coplanar waveguide. The best result is obtained for the wire width $n = 0.15$ mm.

In Fig. 4.17a, b, the radiation pattern and the gain of the metamaterial-inspired antenna are given, respectively, in the yoz plane and xoz plane, which are 0.85 dBi, 2.6 dBi, and 2.77 dBi at 2.45 GHz, 5.2 GHz, and 5.8 GHz, respectively. When the small wire in front of the zigzag unit cell is removed, the gain is enhanced from 0.85 dBi to 0.91 dBi, but the resonant frequency is also moved from 2.4 to 2.2 GHz.

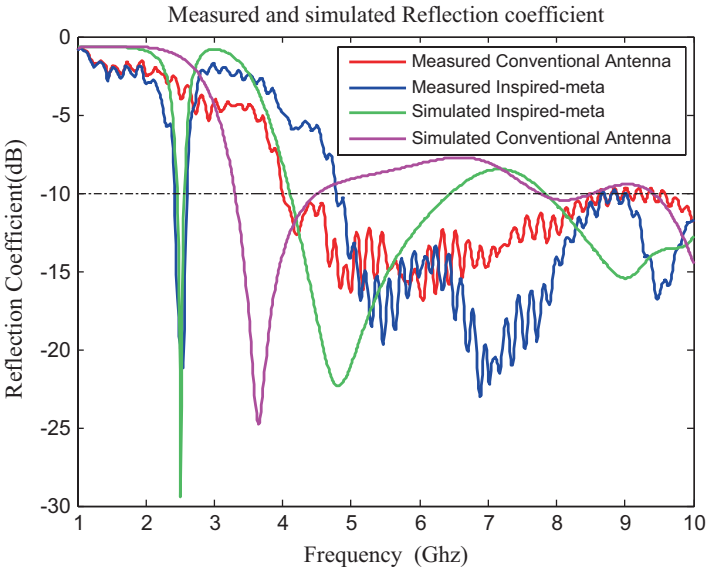

Fig. 4.15 Reflection coefficient of conventional and metamaterial-inspired antenna: simulated and measured results

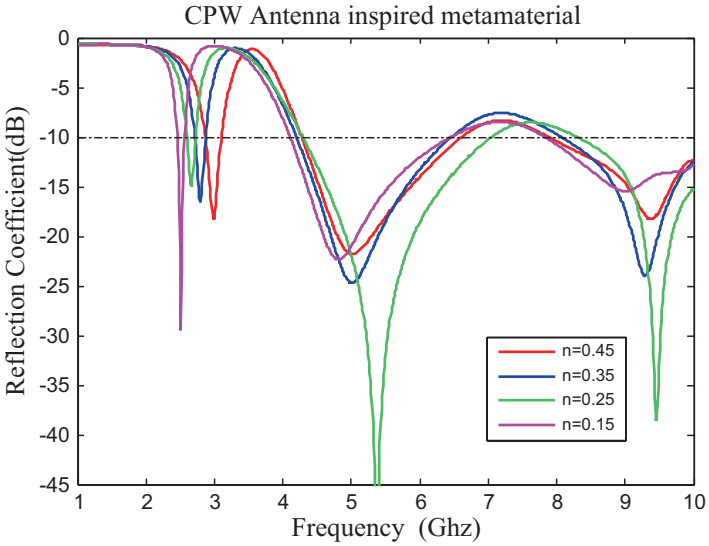

Fig. 4.16 Reflection coefficient of metamaterial-inspired antenna, for different thickness of *n*

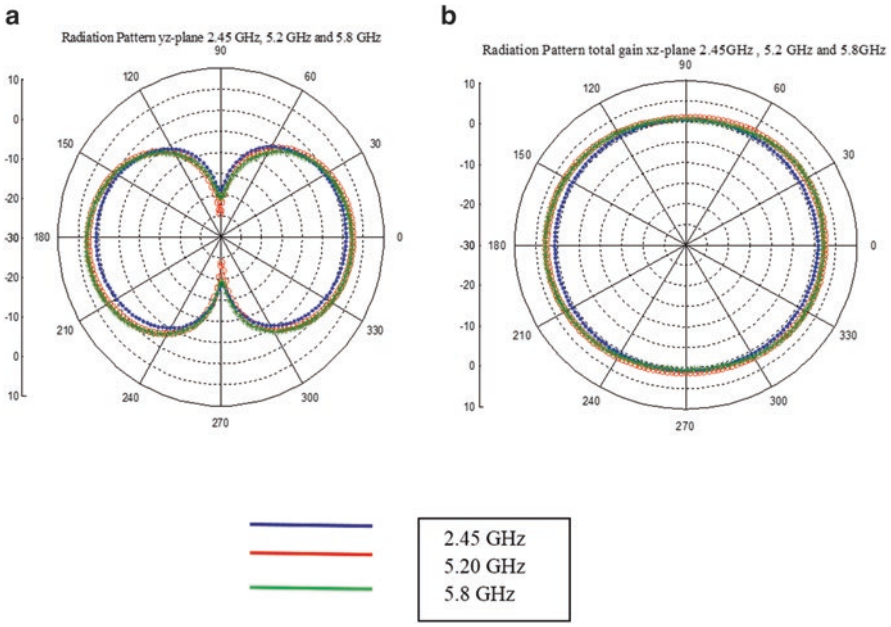

Fig. 4.17 Simulated yoz plane (**a**) and xoz plane (**b**) at 2.4 GHz, 5.2 GHz, and 5.8 GHz

The metamaterial-inspired antenna can be improved by choosing a suitable size for the wire in the zigzag shape or by choosing the shape of a zigzag.

4.7 Antenna Loaded with CRLH

In this work, a CRLH-TL resonator and EBG are implemented in a coplanar waveguide fed antenna for multiband, gain improvement, and a miniaturization effect. All of these can find many applications in industry and in daily life.

The antenna is built up with a monopole antenna with two grounded plates on the top side. The CRLH is loaded with a TL set, as inductors and capacitors, and this work is presented similarly to that in reference [47]. The plan of this work is to provide the miniaturization of the antenna and to exhibit the gain improvement. The antenna dimensions are 25 mm × 30 mm. When loaded with a CRLH resonator, it presents the first resonant frequency at 1.5 GHz. The results obtained by simulation from HFSS give a clear idea about the antenna operating frequencies, with a triband frequency: from 2.65 to 2.75 GHz as the LTE band; from 3.35 to 3.55 GHz as WiMAX; and from 4.35 to 5.45 GHz as WLAN. The maximum gain in the radiation pattern is recorded as 4.4 dBi at 6 GHz; this is achieved in the last band as WLAN.

4.7.1 Antenna Design

In this design of a coplanar waveguide antenna, based on a CLRH-TL resonator with EBG squares implemented in the antenna, the objective is to produce a multi-band frequency. Lower band frequencies can find great applications, and this antenna is simulated by HFSS. The obtained results show that a lower resonant frequency can be generated independently of the antenna size. In addition, the gain can be improved considerably, particularly by the inclusion of EBG squares, as shown in Fig. 4.18. A photograph of the proposed antenna is given in Fig. 4.19.

In order to observe the advantage of EBG inclusion or CRLH insertion, three types of antenna are designed by HFSS. The obtained results are explored and compared in order to see the advantage of each inclusion separately. Figure 4.19 shows these three antennas, presented as the original antenna in Fig. 4.20a, the antenna loaded with a CRLH resonator in Fig. 4.20b, and the antenna loaded with both the CRLH resonator and EBG squares in Fig. 4.20c.

The three antennas are simulated and their reflection coefficients are presented in Fig. 4.21. The first antenna, as the original one, shows one resonant frequency at 5.15 GHz with a bandwidth range from 4.45 to 6.35 GHz. The antenna loaded with CRLH provides three resonant frequencies: the first one is located at 2.75 GHz, corresponding to the zero mode ($n = 0$), with a frequency bandwidth range from 2.65 to

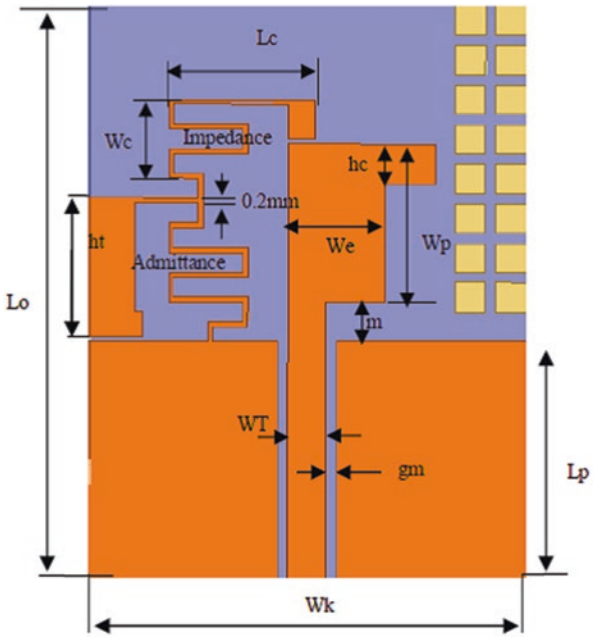

Fig. 4.18 Proposed antenna dimensions in mm: $Lo = 30$, $Wk = 25$, $Lp = 12$, $Wp = 8$, $We = 5$, $ht = 7$, $Lc = 8$, $Wc = 5$, $WT = 2$, $m = 2$, $hc = 2$, $gm = 0.5$

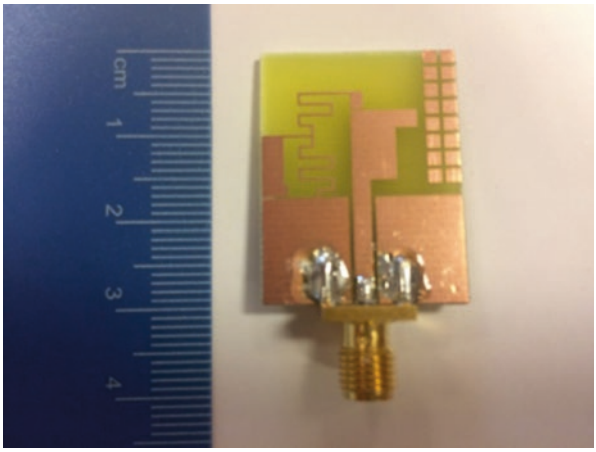

Fig. 4.19 Photograph of the proposed antenna

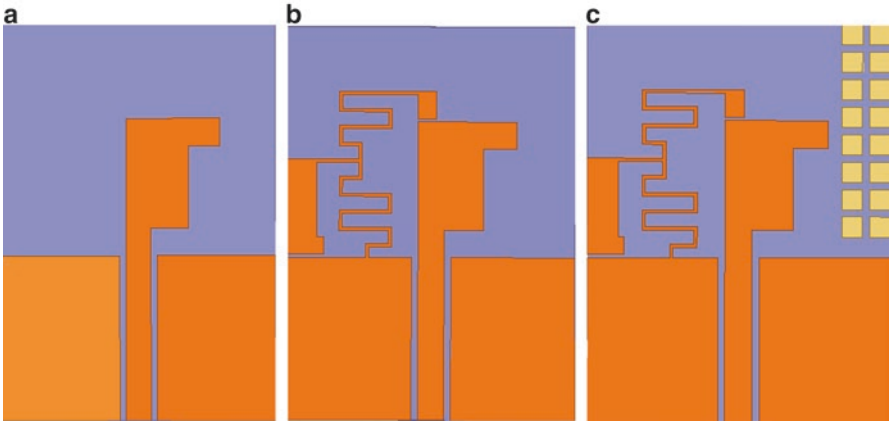

Fig. 4.20 Three types of antenna: (**a**) original; (**b**) CRLH; (**c**) CRLH + EBG

2.75 GHz; the second resonant frequency is located at 3.4 GHz, which is related to the first mode ($n = 1$), with a frequency bandwidth range from 3.25 to 3.55 GHz; the third resonant frequency is located at 5.15 GHz, with a frequency bandwidth range from 4.25 to 5.5 GHz.

The antenna is equipped with 16 EBG squares simply presented as small patches of 1.5 mm on each side. The spacing is set to 0.5 mm between squares; this value is optimized in order to improve the radiation pattern, as the dimensions of these squares can provide the frequency leading to an optimized radiation pattern.

Figure 4.22a presents the radiation pattern in the yoz plane. This figure shows that the original antenna has a total gain greater than the antenna loaded with a CRLH resonator and the combined case of the antenna loaded with CRLH plus EBG, at the frequency of 6 GHz; the maximum gain reached by the original antenna

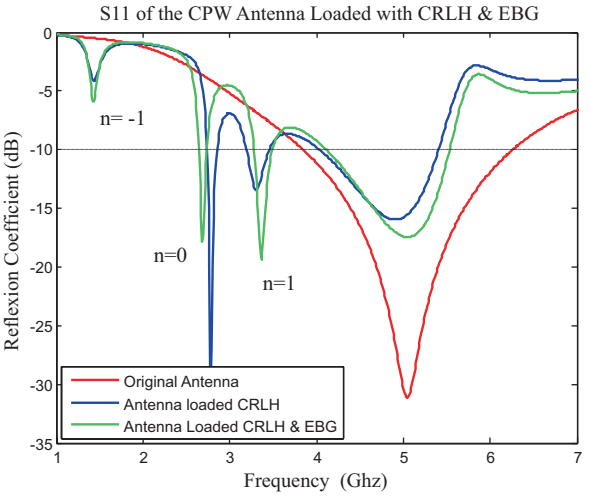

Fig. 4.21 Reflection coefficients for the three types of antenna

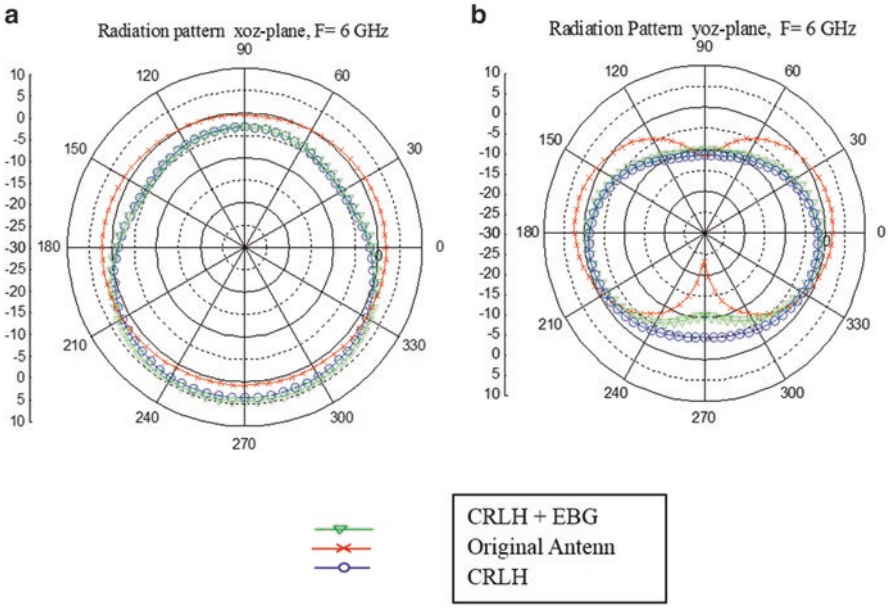

Fig. 4.22 Total gains in radiation patterns: (**a**) xoz plane; (**b**) yoz plane. $F = 6$ GHz

is 2.34 dBi. The radiation pattern in the xoz plane of the three antenna types is given in Fig. 4.22b. The very important improvement in the gain at the frequency of 6 GHz is remarkable, particularly for the combined case of the antenna loaded with a CRLH resonator plus EBG squares. In this figure, the gain has reached 4.45 dBi, whereas the case of the CRLH has reached a gain of 3.65 dBi.

In summary, the radiation pattern in the xoz plane has obtained an improvement of 26% for the combined case antenna with CRLH plus EBG and an improvement of 17% for the case of the antenna loaded with a CRLH resonator, but in the yoz plane the radiation pattern has decreased for both antennas (CRLH and CRLH plus EBG) by 15%. Also, it can be seen that the antenna loaded with CRLH plus EBG has improved the bandwidth of the three bands compared to the CRLH antenna by almost 12%.

The evolution of the total gain versus the frequency is presented in Fig. 4.23. This figure presents a comparison of the total gain provided by the three antennas. The figure shows that the gain of the CRLH antenna is much better than the original antenna—from 2.5 to 7.5 GHz—and the antenna loaded with CRLH plus EBG has enhanced the gain, starting from 4.5 to 7.5 GHz. Unfortunately the bandwidth of this antenna ends at 5.6 GHz. In future work, one could choose CRLH plus EBG to operate at a lower frequency.

In the literature regarding similar work, antennas loaded with ZORs [48, 49] and other research work based on EBG [50] could also have remarkable effects on the miniaturization of antennas. When combining the two structures, the effect is more explicit and more important.

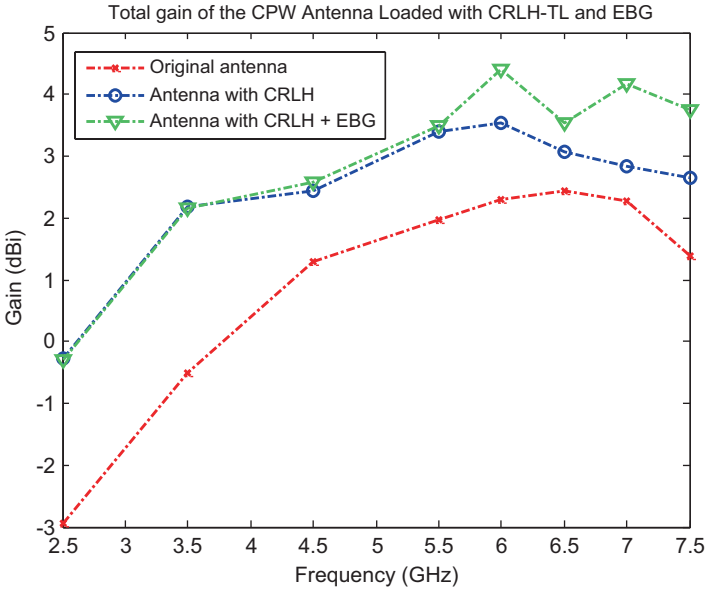

Fig. 4.23 Total gain comparison of the three antennas

4.8 Moon Shaped Antenna with Defected Ground and EBG

In this work, the designed antenna is a coplanar waveguide fed type, in which the ground is defected on the top, by cutting a triangular piece from each ground plate. The antenna is supplied with an EBG, configured as a grid, with three vertical slots and five horizontal slots. The insertion of EBG enhances the bandwidth by 31%, and the gain is improved by 29%. The designed antenna contains two bandwidths: the first one operates in the frequency range of 3.34 to 4.82 GHz, and the second one operates at 5.6 to 6.1 GHz. The maximum gain in the radiation pattern obtained is 2.95 dBi, obtained at the frequency of 4.5 GHz. The applications of this antenna are mainly WiMAX and WLAN. In the literature, similar work can be found concerning the inclusion of EBG in antennas [51–54].

4.8.1 Antenna Design

The coplanar waveguide antenna, loaded with an EBG grid, is based on small squares implemented in the antenna. The aim of this work is to enhance the bandwidth and make improvements in the gain in radiation. This antenna is simulated by HFSS. The obtained results show that the bandwidth has increased considerably and the gain has improved, especially in the frequency range from 3.0 to 4.5 GHz. The EBG squares' dimensions are optimized to 1.25 mm on each side. These squares are placed on the top side of the antenna on the left hand side of the moon shape, as shown in Fig. 4.24.

In order to observe the effect of the defected ground (DG), regarding the proposed antenna, three types of antenna are simulated by HFSS. Fig. 4.25 shows the three types of antenna.

The first antenna is without defection, as the original antenna Fig. 4.25a, the second antenna with a small defection Fig. 4.25b, and the third antenna with a big defection in Fig. 4.25c. The aim of making different types of defection is to look for better reflection coefficients with enhanced bandwidth. The reflection coefficients of these three antennas are presented in Fig. 4.26. The original antenna without ground defection has only one resonant frequency at at 2.8 GHz, with bandwidth of 0.9 GHz. The second simulated antenna has a small ground defection. This antenna has two resonant frequencies: the first one is at 2.4 GHz with very narrow band width, ideally suitable for Wi-Fi applications, the second resonant frequency at 3.9 GHz with bandwidth of 1.01 GHz.This antenna is ideally applied for WiMAX and WLAN.

The third simulated antenna has a big ground defection. This antenna has also two resonant frequencies: the first one is at 3.0 GHz with a bandwidth of 0.8 GHz; the second one is at 5.7 GHz with a bandwidth of 0.31 GHz. This antenna can find applications in LTE and WiMAX.

The antenna with a small ground defection is chosen as ideal for the given application. The inclusion of the EBG grid on the top side of the antenna has produced two resonant frequencies different from the previous antenna: the first resonant frequency is at 4.05 GHz with a bandwidth of 1.48 GHz; the second resonant frequency is at 5.8 GHz with a bandwidth of 0.41 GHz. This is observed in Fig. 4.27, which presents

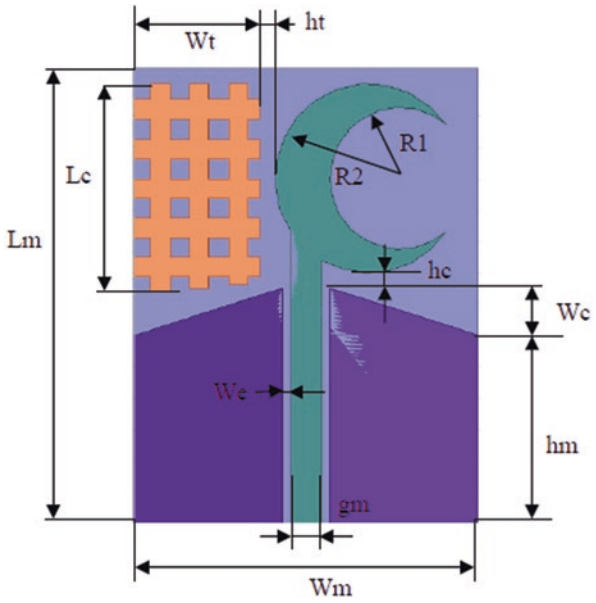

Fig. 4.24 Proposed antenna dimensions in mm: *Lm* = 29, *Wm* = 22, *Lc* = 14, *R1* = 4.5, *ht* = 1, *hm* = 12, *Wc* = 8, *R2* = 6, *hc* = 1, *gm* = 2

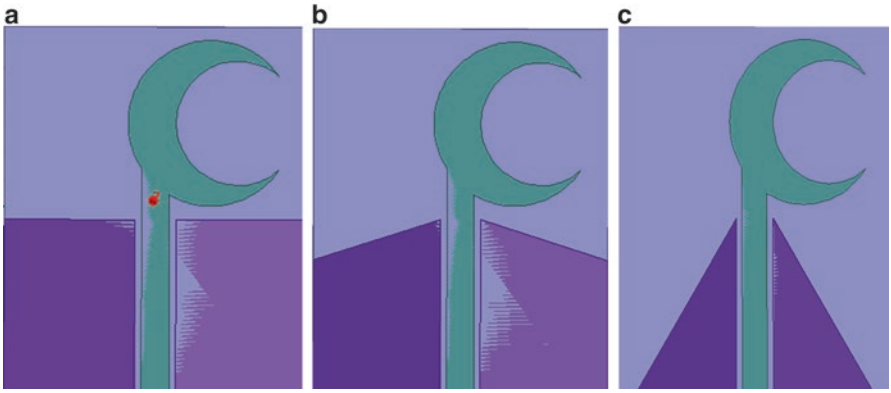

Fig. 4.25 Three types of antenna: (**a**) without defection; (**b**) with a small defection; (**c**) with a big defection

the reflection coefficients of the two antennas with and without EBG. It shows clearly that the bandwidth has improved from 0.9 to 1.48 GHz, considered as a 31% increase in the bandwidth of the antenna. Figure 4.28a presents the radiation pattern in the yoz plane. The figure shows the case of the moon shaped antenna without the EBG grid. Three frequencies are recorded, given as 3.0 GHz, 3.8 GHz, and 4.5 GHz. It seems that the maximum value of the gain is recorded at 4.5 GHz, which is 2.25 dBi.

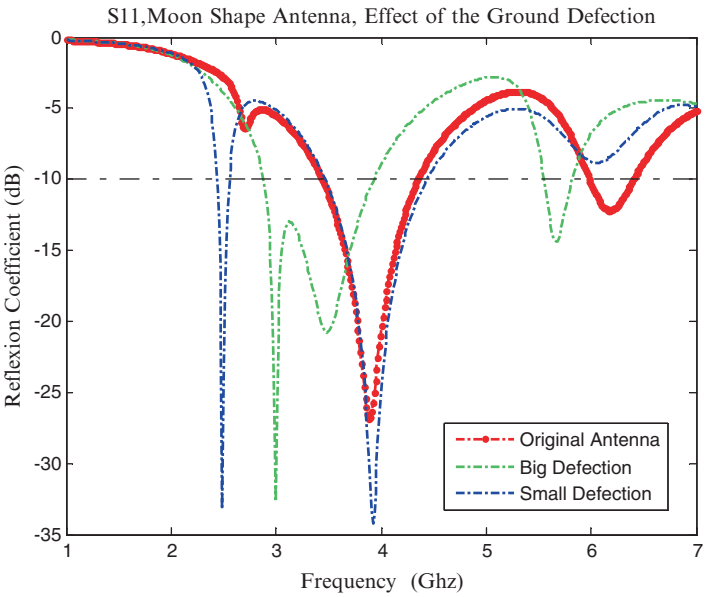

Fig. 4.26 Reflection coefficients and the effect of the defected ground

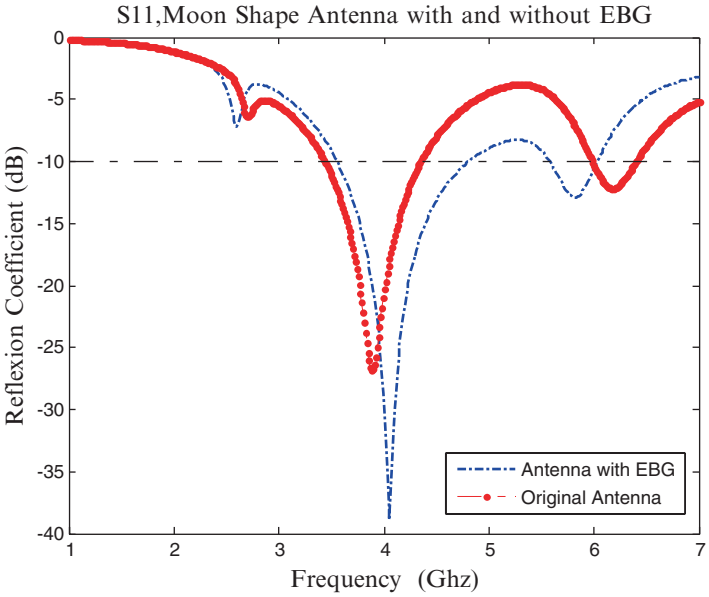

Fig. 4.27 Reflection coefficients of the moon shaped antenna with and without EBG

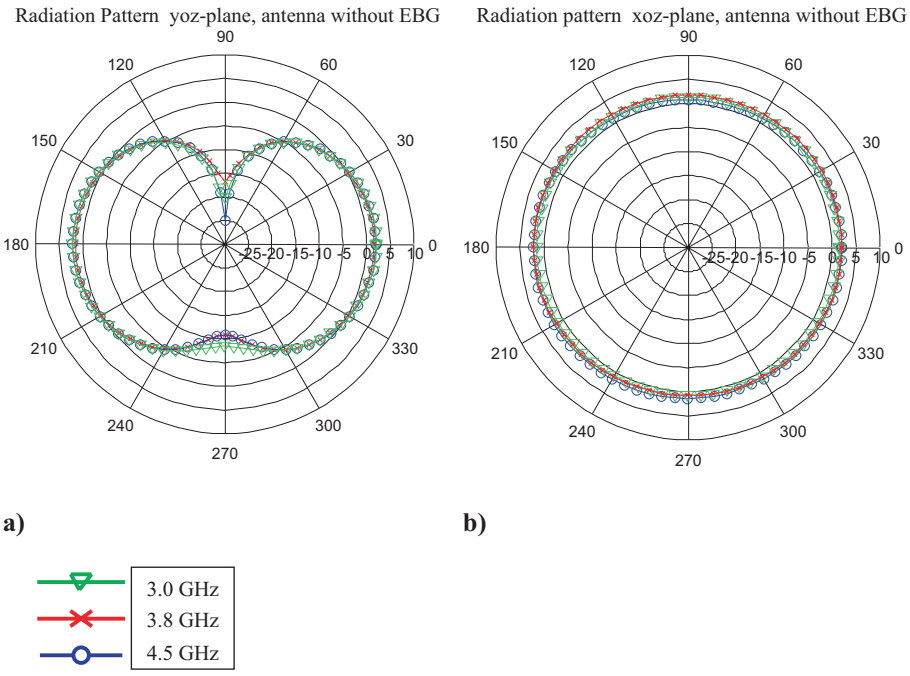

Fig. 4.28 Total gain in the radiation pattern in the antenna without EBG, for three frequencies: (**a**) yoz plane; (**b**) xoz plane

Figure 4.28b presents the gain in the radiation pattern in the xoz plane in the case of the antenna without EBG, recorded for three frequencies—3.0 GHz, 3.8 GHz, and 4.5 GHz—and again the maximum value of the radiation pattern is obtained at 4.5 GHz as 2.35 dBi.

Figure 4.29a presents the case of the moon shaped antenna with EBG in the yoz plane, recorded for the same three frequencies as given above. The maximum gain in the radiation pattern is obtained at the frequency of 4.5 GHz as 2.40 dBi. The radiation pattern in Fig. 4.29b is recorded also for three frequencies given as 3.0 GHz, 3.8 GHz, and 4.5 GHz in the case of the antenna loaded with EBG. Here, also, the maximum gain in the radiation pattern is obtained at the frequency of 4.5 GHz as 2.75 dBi.

In order to observe the effect of the EBG inclusion, a comparison of the total gain of the moon shaped monopole antenna, with and without the EBG grid, is given in Fig. 4.30. The figure presents the total gain versus the frequency. It is very clear that that the effect of the EBG grid starts from 2.5 GHz and ends beyond 6 GHz; the remarkable effect is between 4 and 5 GHz. At exactly 4.5 GHz, the maximum total gain is 3.0 dBi for the loaded antenna with the EBG grid, alongside 2.2 dBi for the antenna without EBG.

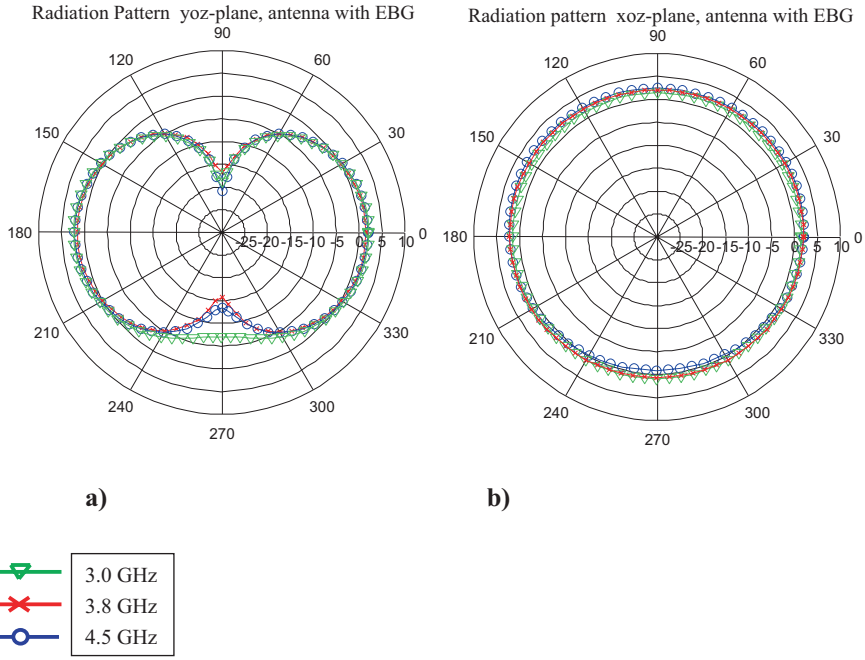

Fig. 4.29 Total gain in the radiation pattern in the antenna with EBG, for three frequencies: (**a**) yoz plane; (**b**) xoz plane

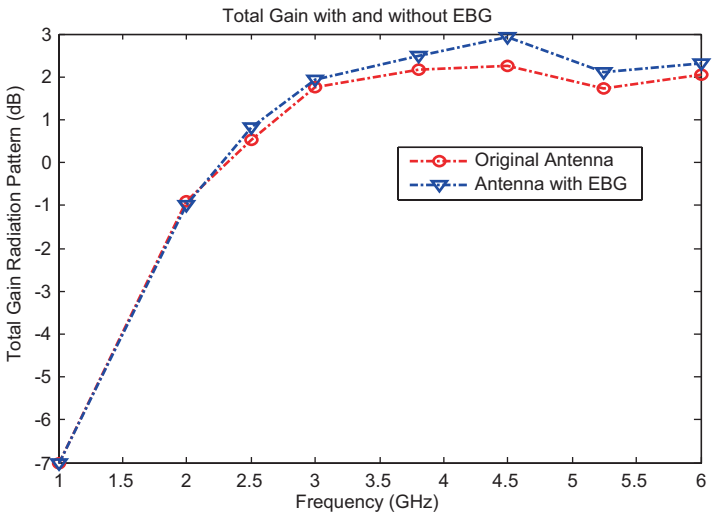

Fig. 4.30 The antenna total gain comparison

4.9 Summary

In this chapter, the applications and limitations of electrically small antennas (ESAs) have been presented, and the fundamentals and different aspects of metamaterial have been clearly discussed. An emphasis on zero order resonators or so-called compensated right/left handedness (CRLH) based on transmission line theory (TL) is presented, showing how zero order can be obtained and how the metamaterial parts can affect the performance of the antenna.

Three types of electrically small antenna have been presented and studied in this chapter, in the scope of metamaterial applications. The antennas had different forms of metamaterial, with inclusion of SRRs, metamaterial-inspired, and finally a zero order resonator. All of these types of antenna have shown that the presence of metamaterial and EBG in the antenna can produce a miniaturization effect from 10% to 25%, and can produce a gain in radiation pattern enhancement from 47% to 68.9% (in the case of SRR inclusion). The last design concerning the moon shaped antenna loaded with EBG shows first that the defected ground can greatly modify the bandwidth of the antenna; a lower resonant frequency can be obtained, which enables a miniaturization effect. Also, the inclusion of EBG has produced an improvement in the gains in the radiation pattern and the bandwidth. An electrically small antenna can be realized also by other structures that are not mentioned in this chapter but are available in the literature, such as defected ground, fractal structures and a high impedance surface (HIS), and also a surface integrated waveguide (SIW). This can be studied and discussed with real applications in future work.

References

1. M.A. Christou, A.C. Polycarpou, Far-field scattering from an electrically small circular aperture in a conducting screen. IEEE Trans. Electromagn. Compat. **59**(2), 404–410 (2017)
2. T. Jang, Z. Cheng, H. Youn, J. Zhou, L. Jay Guo, Semi-transparent and flexible mechanically reconfigurable electrically small antennas based on tortuous metallic micromesh. IEEE Trans. Antennas Propag. **65**(1), 150–158 (2017)
3. M. Ignatenko, D.S. Filipovic, On the design of vehicular electrically small antennas for NVIS communications. IEEE Trans. Antennas Propag. **64**(6), 2136–2145 (2016)
4. M. Manteghi, A wideband electrically small transient state antenna. IEEE Trans. Antennas Propag. **64**(4), 1201–1208 (2016)
5. V.G. Daniele, R.D. Graglia, G. Lombardi, P.L.E. Uslenghi, Size-independent cylindrical resonator half-filled with DNG metamaterial and excited by a line source. IEEE Antennas Wireless Propag. Lett. **12**, 785–788 (2013)
6. C. Caloz, T. Itoh, Transmission line approach of left-handed (LH) materials and microstrip implementation of an artificial LH transmission line. IEEE Trans. Antennas Propag. **52**(5), 1159–1166 (2004)
7. P. Turalchuk, I. Munina, M. Derkach, O. Vendik, I. Vendik, Electrically small loop antennas for RFID applications. IEEE Antennas Wireless Propag. Lett. **14**, 1786–1789 (2015)
8. K. Li, Z. Cheng, Design of electrically small metamaterial antenna with ELC and EBG loading. IEEE Antennas Wireless Propag. Lett. **12**, 678–681 (2013)
9. N. Zhu, R.W. Ziolkowski, Active metamaterial-inspired broad-bandwidth, efficient, electrically small antennas. IEEE Antennas Wireless Propag. Lett. **10**, 1582–1585 (2011)

10. R.W. Ziolkowski, Metamaterial-based efficient electrically small antennas. IEEE Trans. Antennas Propag. **54**(7), 2113–2130 (2006)
11. E.E. Altshuler, T.H. O'Donnell, An electrically small multi-frequency genetic antenna immersed in a dielectric powder. IEEE Antennas Propag. Mag. **53**(5), 33–40 (2011)
12. T. Simpson, Electrically small spheroidal loops wound on hollow ferrite cores. IEEE Propag. Mag. **50**(3), 88–94 (2008)
13. F. Paredes, G. Zamora, F. Martin, J. Bonache, Miniaturization of RFID Tag by Means of an Electrically Small Resonator. 2010 IEEE International Conference on Wireless Information Technology and Systems
14. S. Zuffanelli, G. Zamora, P. Aguilà, F. Paredes, F. Martin, J. Bonache, Passive UHF-RFID Tag Based On Electrically Small Square-Shaped Split Ring Resonator (SRR) Antenna. 2016 IEEE International Symposium On Antennas And Propagation (Apsursi)
15. K.B. Alici, E. Ozbay, Theoretical study and experimental realization of a low-loss metamaterial operating at the millimeter-wave regime: Demonstrations of flat- and prism-shaped samples. IEEE J. Sel. Topics Quantum Electron. **16**(2), 386–393 (2010)
16. G. Lubkowski, R. Schuhmann, T. Weiland, Extraction of effective metamaterial parameters by parameter fitting of dispersive models. Microw. Opt. Technol. Lett. **49**(2), 285–288 (2007)
17. R.W. Ziolkowski, P. Jin, J.A. Nielsen, M.H. Tanielian, C.L. Holloway, Experimental verification of Z antennas at UHF frequencies. IEEE Antennas Wireless Propag. Lett. **8**, 1329–1333 (2009)
18. E. Lier, Review of soft and hard horn antennas, including metamaterial-based hybrid-mode horns. IEEE Antennas Propag. Mag. **52**(2), 31–39 (2010)
19. F. Bilotti, L. Di Palma, D. Ramaccia, A. Toscano, Self-filtering low-noise horn antenna for satellite applications. IEEE Antennas Wireless Propag. Lett. **11**, 354–357 (2012)
20. Guo Qing Luo, Wei Hong, , Hong Jun Tang, Ji Xin Chen, Xiao Xin Yin, Zhen Qi Kuai, Ke Wu, "Filtenna consisting of horn antenna and substrate integrated waveguide cavity FSS", IEEE Trans. Antennas Propag., 55, 1. 92–98, 2007
21. R.W.P. King, *The Theory of Linear Antennas* (Harvard University Press, Cambridge, 1956), p. 184
22. K. Fujimoto, H. Morishita, *Modern Small Antennas* (Cambridge University Press, Cambridge, 2013)
23. H.A. Wheeler, Fundamental limitations of small antennas. Proc. IRE **35**, 1479–1484 (1947)
24. Y. Zheng, J. Wang, Y. Luo, Extremely broad bandwidth input/output coupling structure design for a Q band sheet-beam traveling-wave tube. IEEE Antennas Propag. Mag. **42**(10), 3339–3343 (2014)
25. G.S. Moschytz, High high-q factor insensitive active RC network, similar to the Tarmy-Ghausi circuit but using single-ended operational amplifiers. Electron. Lett. **08**(18), 458–459 (1972)
26. D.S. Nagarkoti, Y. H., K.Z. Rajab, Q-bandwidth enhancement of an antenna using non-Foster circuit based on negative differential resistance devices. 2016 10th European Conference on Antennas and Propagation (EuCAP)
27. C. Zebiri, M. Lashab, F. Benabdelaziz, Rectangular microstrip antenna with uniaxial bi-anisotropic chiral substrate-superstrate. IET Microw. Antennas Propag. **05**(01), 17–29 (2011)
28. J. Zhang, G. Ci, Y. Cao, N. Wang, H. Tian, A wide bandgap slot fractal UC-EBG based on Moore space-filling geometry for microwave application. IEEE Antennas Wireless Propag. Lett. **16**, 33–37 (2016)
29. R.M. Hashmi, B.A. Zeband, K.P. Esselle, Wideband high-gain EBG resonator antennas with small footprints and all-dielectric superstructures. IEEE Trans. Antennas Propag. **62**(6), 2970–2977 (2014)
30. B. Zong, G. Wang, C. Zhou, Y. Wang, Compact low-profile dual-band patch antenna using novel TL-MTM structures. IEEE Antennas Wireless Propag. Lett. **14**, 567–570 (2015)
31. Y. Li, M.F. Iskander, Z. Zhang, A new low cost leaky wave coplanar waveguide continuous transverse stub antenna array using metamaterial-based phase shifters for beam steering. IEEE Trans. Antennas Propag. **61**(7), 3511–3518 (2013)
32. T.J. Cui, D.R. Smith, R. Liu, *Metamaterial, Theory, Design and Applications* (Springer, New York/Dordrecht/Heidelberg/London, 2010)
33. C. Sabah, S. Uckun, Multilayer system of Lorentz-Drude type metamaterials with dielectric slabs and its application to electromagnetic filters. Prog. Electromagn. Res. **91**, 349–364 (2009)

34. D.R. Smith, S. Shultz, P. Markos, C.M. Soukoulis, Determination of effective permittivity and permeability of metamaterials from reflection and transmission coefficients. Phys. Rev. B **65**, 195104 (2002)
35. X. Chen, T.M. Grzegorczyk, B.I. Wu, J. Pacheco, J.A. Kong, Robust method to retrieve the constitutive effective parameters of metamaterials. Phys. Rev. E **70**, 016608-016601–016608-016607 (2004)
36. M. Rahm, D. Schurig, D.A. Roberts, S.A. Cummer, D.R. Smith, J.B. Pendry, Design of electromagnetic cloaks and concentrators using form-invariant coordinate transformations of Maxwell's equations. Phot. Nanostr. Fund. Appl. **6**, 8795 (2008)
37. Z. Ruan, M. Yan, C.W. Neff, M. Qiu, Ideal cylindrical cloak: Perfect but sensitive to tiny perturbations. Phys. Rev. Lett. **99**, 113903 (2007)
38. M. Lashab, N.A. Jan, C. Zebiri, The I Shape Antenna Loaded With ZOR For WLAN and WiMAX Application. LAPC'15 Loughborough, 2015
39. M. Lashab, C. Zebiri, N.A. Jan, F. Benabdelaziz, R.A. Abd-Alhameed, M. Child, CPW-Fed Antenna Based on Metamaterial For Broadband Application. LAPC'14, Loughborough, 2014, UK
40. N.A. Jan, F. Elmegri, M. Bin-Melha, R.A. Abd-Alhameed, M. Lashab, C.H. See, Compact size uni-planer small metamaterial-inspired antenna for UWB applications. 2015 Internet Technologies and Applications (ITA)
41. Y.-J. Chi, F.-C. Chencompact, CPW-based zeroth-order resonant antenna with interleaving CRLHD unit cells. Prog. Electromagn. Res. C **40**, 119–130 (2013)
42. S.K. Sharma, A. Gupta, R.K. Chaudhary, Epsilon negative CPW-FED zeroth-order resonating antenna with backed ground plane for extended bandwidth and miniaturization. IEEE Trans. Antennas Propag. **36**(11), 5197–5203 (2015)
43. L. Li, Z. Jia, F. Huo, W. Han, A novel compact multiband antenna employing dual-band CRLH-TL for smart mobile phone application. IEEE Antennas Wireless Propag. Lett. **12**, 1688–1691 (2013)
44. H.-p. Li, G.-m. Wang, X.-j. Gao, L. Zhu, CPW-FED multiband monopole antenna loaded with DCRLH unit cell. IEEE Antennas Wireless Propag. Lett. **14**, 1243–1246 (2015)
45. S.R. Best, The significance of composite right/left-handed (CRLH) transmission-line theory and reactive loading in the design of small antennas. IEEE Antennas Propag. Mag. **56**(4), 15–33 (2014)
46. N. Amani, M. Kamyab, A. Jafargholi, A. Hosseinbeig, J.S. Meiguni, Compact tri-band metamaterial-inspired antenna based on CRLH resonant structures. Electron. Lett. **50**(12), 847–848 (2014)
47. N.A. Jan, M. Lashab, C.E. Zebiri, D. Linda, R.A. Abd-Alhameed, F. Benabdelaziz, Compact CPW antenna loaded with CRLH-TL and EBG for multi-band and gain enhancement. 2016 Loughborough Antennas & Propagation Conference (LAPC)
48. H. Lee, D.-J. Woo, S. Nam, Compact and bandwidth-enhanced asymmetric coplanar waveguide (ACPW) antenna using CRLH-TL and modified ground plane. IEEE Antennas Wireless Propag. Lett. **15**, 810–813 (2016)
49. T. Jang, J. Choi, S. Lim, Compact coplanar waveguide (CPW)-fed zeroth-order resonant antennas with extended bandwidth and high efficiency on vialess single layer. IEEE Trans. Antennas Propag. **59**(2), 363–372 (2011)
50. S.-G. Mao, C.-M. Chen, D.-C. Chang, Modeling of slow-wave EBG structure for printed-bowtie antenna array. IEEE Antennas Wireless Propag. Lett. **1**, 124–127 (2002)
51. Y. Li, K.P. Esselle, Small EBG resonator high-gain antenna using in-phase highly-reflecting surface. Electron. Lett. **45**(21), 1058–1060 (2009)
52. K.-H. Chan, R. Ikeuchi, A. Hirata, Effects of phase difference in dipole phased-array antenna above EBG substrates on SAR. IEEE Antennas Wireless Propag. Lett. **12**, 579–582 (2013)
53. G. Expósito-Domínguez, J.-M. Fernandez-Gonzalez, P. Padilla, M. Sierra-Castaner, Mutual coupling reduction using EBG in steering antennas. IEEE Antennas Wireless Propag. Lett. **11**, 1265–1268 (2013)
54. L. Leger, T. Monediere, B. Jecko, Enhancement of gain and radiation bandwidth for a planar 1-D EBG antenna. IEEE Microw. Wireless Compon. Lett. **15**(9), 573–575 (2005)

Part III
Wide-Band Antennas

Chapter 5
Impact of Microstrip-Line Defected Ground Plane on Aperture-Coupled Asymmetric DRA for Ultra-Wideband Applications

Chemseddine Zebiri, Djamel Sayad, Fatiha Benabelaziz, Mohamed Lashab, and Ammar Ali

5.1 Introduction

Although it was mainly used for military and radar applications since the early 1960s, ultra-wideband (UWB) technology has received tremendous attention from academia and industry. It has been widely utilized in recent years for the proliferation of short-range high-throughput wireless communications, medical imaging, ad hoc networking, and other wireless sensing and monitoring applications [1]. The widespread use of UWB technology is due to its prime advantages, such as high-resolution reliable data, low transmission-power consumption, high immunity to multipath interferences, high channel capacity, and high security measures [2, 3].

By definition, a UWB signal should have more than 25% fractional bandwidth or occupy a bandwidth greater than 500 MHz [4]. The Federal Communication Commission allowed a frequency band from 3.1 to 10.6GHz for low-power UWB communications. Other bands of operation are also defined in lower frequencies for some other pertinent UWB applications [5].

C. Zebiri (✉)
Department of Electronics, University of Ferhat Abbas, Setif -1-, 19000 Setif, Algeria
e-mail: czebiri@univ-setif.dz; zebiri@ymail.com

D. Sayad
Department of Electrical Engineering, 20 Aout 1955 University, 21000 Skikda, Algeria

F. Benabelaziz
Department of Electronics, University Mentouri of Constantine -1-,
25000 Constantine, Algeria

M. Lashab
Department of Electronics, University of Larbi Ben M'Hidi, Oum El bouaghi 4000, Algeria

A. Ali
School of Engineering and Informatics, University of Bradford, Bradford BD7 1DP, UK

I. Elfergani et al. (eds.), *Antenna Fundamentals for Legacy Mobile Applications and Beyond*, DOI 10.1007/978-3-319-63967-3_5

Wideband and broadband characteristics can be obtained by considering different configurations: slotted apertures and defected ground structures (DGS) [6–10] and DRA structures [11–13].

The defected ground plane has taken much attention in the microwave field and millimeter wave applications where the defected ground is realized by etching the ground plane with a certain lattice shape that disturbs the current distribution of the antenna. There exist different shapes of DGS in literature, such as concentric ring, circle, spiral, dumbbell, elliptical, and U and V slots [14].

DGS configurations are used in [15, 16] to achieve a desired band-notched circuit performance, whereas in our study they are used to enhance the impedance bandwidth of the patch antennas [17, 18]. Furthermore, this technique can reduce the structure size and give rise to excitation of additional resonance bands [19], where with a simple compact structure with defected ground plane [20], we have a multifrequency microstrip antenna with a single feed [21]. Moreover, large slots and defected grounds can excite other modes such as in [12, 13] and [22, 23].

5.2 History of Dielectric Resonator Antenna

Dielectric resonator antenna applications were first proposed in the early 1980s (rectangular or cylindrical form) [24, 25]. The first experimental research for wideband DRA was carried out in 1989 by Kishk et al. Since then, dielectric resonators are used to realize the miniaturization of active and passive microwave components, such as oscillators and filters [26, 27]. When a dielectric resonator is not entirely enclosed by a conductive boundary, it can radiate and form an antenna. Full DRA was successfully built and described in [28].

DRAs exhibit a relatively large bandwidth (~10% for εr ~10), whereas in their basic form, patch antennas have a typical bandwidth of only 1–3%. Systematic experimental investigations on dielectric resonator antennas were first carried out by Long et al. in 1983 [28–30].

Many studies have concentrated on the cylindrical DRA structures [31], for which the TM and quasi-TM modes may be excited by having the dielectric disk situated on a ground plane [32]. In [33], a brief discussion is given for some characteristics of the DRAs related to the HEM11δ and the HEM12δ modes compared to the more commonly studied TM01δ mode and TE01δ mode.

DRAs of diverse shapes have also been widely investigated. Long et al. brought forward and investigated the cylindrical [12, 13, 22, 25], rectangular [34], and an equivalent rectangular DRA to two cylindrical DRAs have been studied in [13], and hemispheric DRA in [30], which has provided a good foundation for the development of the DRA structures. Other configurations including triangular, cylindrical-ring DRAs [35] were studied as well.

Subsequent to the cylindrical DRA, Long and his research group investigated the rectangular [36] and hemispherical [30] DRAs. This work created the foundation for future investigations of the DRA. Kishk et al. studied the radiation characteristics

of cylindrical DRA with new applications [37]. Many other shapes such as triangular [38], spherical-cap [39], cylindrical ring [40, 41], conical [42], and tetrahedron [43] were also studied. Section-spherical [44], flipped staired pyramid [45], stepped [46], stacked double annular ring [47], elliptical [48], two-layer hemispherical [49], and Sierpinski carpet fractal patterned cylindrical [50] were also used recently for the enhancement of various antenna properties. The basic principles and mode nomenclatures of the DRA were discussed in detail in the review paper [51]. In [52], the input impedance of stacked cylindrical dielectric resonator antennas is investigated experimentally and the dielectric resonators are made up of different materials and bandwidth of 25% has been achieved [52].

The quarter volume of cylindrical DRA (QVCDRA) was first designed and proposed in [53]. QVCDRA can work stably at HEM11-like mode by proper settings of boundaries and exciting mechanism.

The inner field distribution of the dielectric resonator antenna (DRA) depends on the boundary conditions [35] and the dimensions and dielectric constant of the DRA are the main factors that influence the antenna performance [53]. Professor Long brought forward, in [25], the magnetic wall model to validate that the resonance frequency decreases with the increase of the antenna volume. In [53], three QVCDRAs are placed on a circular floor and arranged together around *Z*-axis to form a novel three-port DRA centered at 5.2GHz.

Two rectangle DRAs have been integrated to implement reconfigurable pattern on three frequency bands in [54]. A slot-fed DRA is studied in [55], where it is stated that by varying the slot length, the frequency of the DRA can be controlled, which in turn could help achieve reconfigurable radiation patterns.

Recently, many investigations have been reported on dielectric resonator antennas (DRAs) with dual-frequency or wideband operation using various approaches, such as two mode excitation, or two stacking DRAs [56, 57]. When a single-shaped DRA operates in a fundamental mode, its bandwidth is typically below 10%. Kishk et al. in 1989 [58] stacked two different DRAs on top of one another to obtain a dual-resonance operation. Since then, other wideband DRAs using stacking methods have been utilized [57, 59–61].

Over the last decades, several studies have been reported on DRAs for bandwidth enhancement techniques in multiband frequency and wideband operations using various approaches, such as different coupling Schemes [62, 63], hybrid structures [64], external matching networks and combining multiple DRs with and without segment [65–67], choice of the position of DRA [66, 67], modified DR structures [43, 68], compact circular/annular sector [69], stacking two or more dielectric resonators (DRs) [58] with different permittivity materials and its aspect ratios and DRA with air gap, and the multilayer multipermittivity DRA [65, 70].

In [71], a two-segment rectangular dielectric resonator antenna (DRA) for broadening the impedance bandwidth is discussed. In this study [71], two rectangular dielectrics with different sizes and permittivities separated by a perfect *E* plate section are used [71, 72]. With this configuration, it is possible to excite two adjacent resonant frequencies, and can use the frequency band 3.32–7.46GHz.

Formerly, the overlap multi-segment DRA was developed to enhance coupling from the microstrip lines [73, 74]. By using an extra metallic plate in a conventional DRA, which acts as an electric wall, the size of the DRA has been reduced approximately by one half [75].

The main objective of the study in [66] is to improve the bandwidth of the DRA using three-element multilayer cylindrical dielectric resonator antenna (MCDRA) array above the ground plane. MCDRA is easy to design and excite with HE11δ mode excited in each MCDRA by a centrally placed dielectric resonator in which TM01δ mode is excited. The effect of design parameters such as probe height, arrangement of dielectric layers, and permittivity of materials are studied, and the excited modes (i.e., TM01δ and HE11δ) are also confirmed by simulations.

The proposed multilayer cylindrical dielectric resonator antenna (MCDRA) can offer an impedance bandwidth of ~47% for a –10 dB return loss where frequency range is from 4.5 to 6.8 GHz and resonance frequency is 4.91 GHz [66].

The bandwidth enhancement in DRA has been introduced by Guha et al., by employing three-element cylindrical dielectric resonator array as a wideband low-profile monopole-like antenna [67]. Using this approach, nearly 29% impedance bandwidth (S11 < −10 dB) with uniform monopole-like radiation pattern over the entire band is achieved. The multilayer multipermittivity approach has been studied for higher mode separation in dielectric resonator in microwave integrated circuit (MIC) environment [70].

In [76], multiband cylindrical DRAs having a permittivity variation in φ-direction (required to have a definite position) fed by coaxial probe are analyzed, fabricated, and measured. A dual-band response is obtained by the combination of two half-split cylindrical DRs of different permittivities, whereas triple-band is also obtained by considering three equal sectors of split DRs. A hybrid DRA with radiating slot for dual-band operation is proposed in [64], and the objective in [76] was to design a new, low-profile and compact-size hybrid structure antenna that can operate at two different frequencies with stable radiation characteristics. On the other hand, axial and radial directions do not influence a lot the mode profile in the working frequency band, hence they provide wideband performance in CDRA [76–78].

5.3 Proposed Antenna Geometry and Summarized Results

The proposed asymmetric UWB antenna is designed and simulated using Ansoft HFSS V.14 software. The final antenna configuration with an FR4 substrate of thickness 0.8 mm is shown in Fig. 5.1. A microstrip feed is utilized for the proper impedance matching and other important features [13], with two modifications (l_f = 20.5 mm in [13], l_f, d_s in this case). The proposed asymmetric slot with seven DRAs ultra-wideband antenna with a defected ground plane was designed and simulated using Ansoft HFSS [79] based on finite element method.

The prototype was fabricated on an FR4 substrate with a relative permittivity of ε_{rs} = 4.4, a loss tangent of 0.017, and a thickness t = 0.8 mm. The microstrip feed line was placed symmetrically with respect to the coupling aperture [11–13].

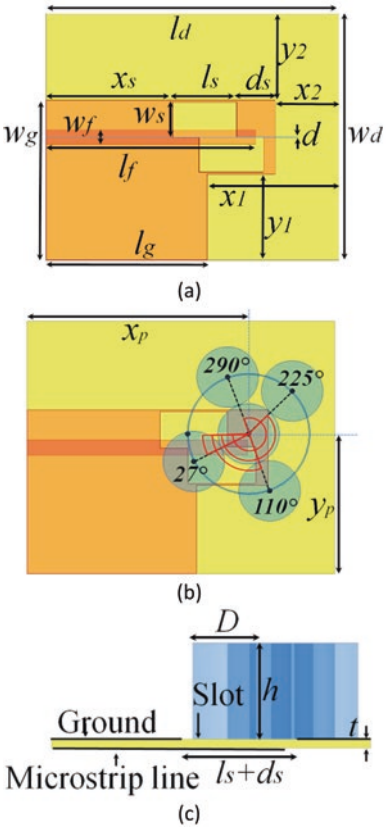

Fig. 5.1 Aperture-coupled asymmetric five DRAs, (**a**) without DRAs top view, (**b**) with DRAs top view, and (**c**) side view

The microstrip line dimensions were calculated using empirical formulas given in [11–13, 80], resulting in length 20.5 mm, and in this work the length is $l_f = 21.5$ mm and the width is $w_f = 1.5$ mm. Two rectangular apertures (large slots) of length l_s and width w_s were etched on the ground plane, shifted from the center of the feed line by a distance d. The values of all the parameters in the final antenna configuration of Fig. 5.1 are: $w_g = 16.25$ mm, $l_g = 16.5$ mm, $w_d = 25$ mm, $l_d = 30$ mm, $w_f = 1.5$ mm, $l_f = 21.5$ mm, $x_s = 12.95$ mm, $w_s = 3.5$ mm, $l_s = 6.6$ mm, $d_s = 3.95$ mm, $d = 0.05$ mm, $x_1 = 13.5$ mm, $y_1 = 8.75$ mm, $x_2 = 6.5$ mm, and $y_2 = 8.75$ mm. The five-DRA structure consists of a central DRA located at $x_p = 13.85$ mm, $y_p = 21.6$ mm and surrounded by four DRAs.

Building on previous works [11–13, 80], the originality of this work resides in the creation of a defected ground plane to excite more modes [11] and the use of five DRAs to enhance both the bandwidth and gain. The steps established in our model are shown in Fig. 5.3. This original antenna presents an enhancement of S_{11}, as illustrated in Fig. 5.2. All antennas, (ii–v), have a bandwidth greater than that for case (i). The modeled antenna with defected ground technology, large slot, and five DRAs results in a bandwidth of 2.92–11.97GHz; we can note that this technique has a more important effect on the frequencies below 7GHz.

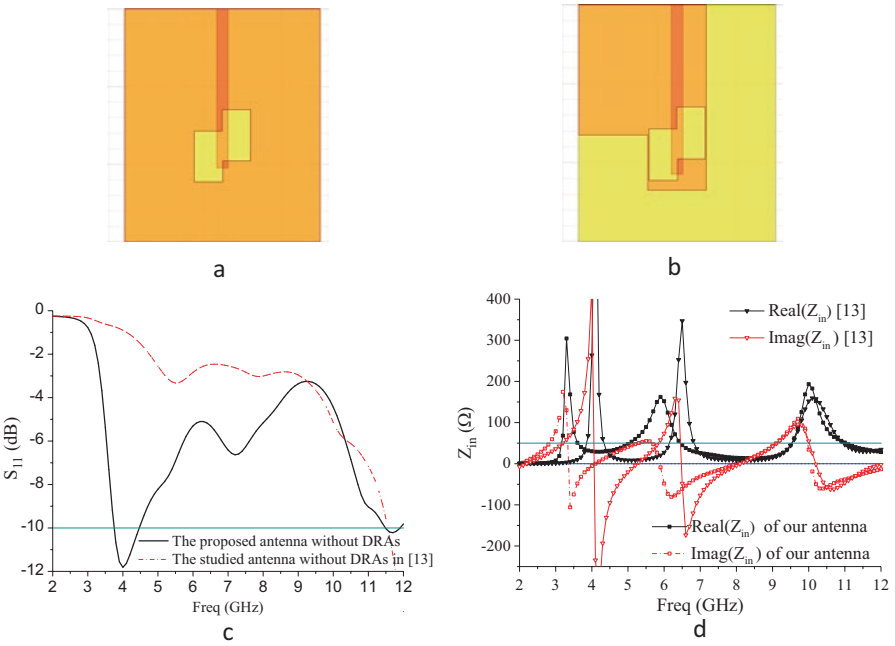

Fig. 5.2 (**a**) Realized antenna without DRA published in [13]. (**b**) Present work antenna without DRA. (**c**) Compared S_{11} of our proposed antenna without DRA with the realized antenna in [13]. (**d**) Compared Z_{in} of our proposed antenna without DRA with the realized antenna in [13]

5.3.1 Antenna Without the DRAs

We notice that the set of components of the antenna (the defected ground plane and the microstrip line) has as effect the excitation of three modes at 3.35GHz, 5.85GHz, and 10.05GHz.

In [13], a rectangular slot of length L_s, which is short-circuited at both ends, can have a first mode resonance when the slot length is equal to half the guided wavelength λg:

$$L_s = 0.5\ \lambda_g \tag{5.1}$$

The guided wavelength is given by

$$\lambda_g = \frac{\lambda_0}{\sqrt{\varepsilon_{re}}} = \frac{c}{f\sqrt{\varepsilon_{re}}} \tag{5.2}$$

where f_r is the resonance frequency, and ε_{re} is the effective dielectric constant for the wave inside the slot given by

$$\varepsilon_{re} = \frac{\varepsilon_{rs} + 1}{2} \tag{5.3}$$

where ε_{rs} is the dielectric constant of the substrate material. Combining Eqs. 5.4, 5.5, and 5.6, we get

$$f_r = \frac{c}{L_s \sqrt{2(\varepsilon_{rs} + 1)}} \tag{5.4}$$

For the used slot length, L_s = 6.6 mm, the obtained f_r is 13.7 GHz. This frequency value is very near (within 7%) to the resonance frequency of 12.7 GHz that is seen in the presented results. The shift in the estimated frequency can be attributed to the following: Eq. 5.6 assumes an average dielectric constant that is the mean of air and the substrate values, but when the DR is placed adjacently to the slot, the average value ε_{rs} will be higher, leading to a lower value of the frequency as compared to that given by Eq. 5.4.

In this study, a rectangular slot configuration is assumed. With the use of two adjacent rectangular slots, one can assume the existence of two cases of resonance as explained, where the electric field of the resonating modes is indicated by arrows. The first case assumes two independent slots each of length L_s resonating at the frequency given by Eq. 5.6. The second case is represented by an equivalent slot comprising the two merged slots. This longer slot has an equivalent length value between L_s and $2L_s$, depending on the overlap of the two slots. In the built prototype, the slot length is about 6.6 mm, and the combined slots have 9.6 mm. This equivalent length leads to a resonance frequency of 9.4 GHz. Of course, this value will be affected by the proximity of the DR leading to a slightly lower frequency value.

The lower band of frequencies results from the combined effects of the slot, single DR, or two DRs. The other element that may be considered in resonance calculations is the microstrip feed line. This line is connected between the 50 Ω input impedance connector and a combination of open-end, slots, and two DRs. In the lower frequency band, the feed line can be considered to work as a 1/4 wavelength transformer. Thus, a dip in the input reflection coefficient is noticed when the line length is equal to 1/4 or 3/4 of the guided wavelength. For the used substrate, the thickness h = 0.8 mm and line width w = 1.5 mm, so that the effective dielectric constant is given by [25]

$$\varepsilon_e = \frac{\varepsilon_r + 1}{2} + \frac{\varepsilon_r - 1}{2}\left(1 + 12\frac{h}{w}\right) \tag{5.5}$$

and found to be 3.393. For a feed line length of 21 mm, the resonance frequencies are 1.94 GHz for the 1/4 wave length case, and 5.82 GHz for the 3/4 wave length case. The second frequency value is very near to the lower band frequencies (Fig. 5.2), thus verifying the existence of the lower band [13]. We can notice that the defected ground enhances S_{11} and increases the input impedance as well.

5.3.2 Antenna with Two DRAs

Building on the previous work [11–13, 80], the originality of the current work resides in the creation of two adjacent large slots combined with two, three, four, and five cylindrical DRA to excite further modes.

An alumina material, alumina-96pct, with $\varepsilon_{rd} = 9.4$, diameter $D = 6$ mm, and height $h = 9$ mm, was used for the DR structure (Fig. 5.1). The resonant frequency in gigahertz of a single segment CDRA excited in $HEM_{11\delta}$ mode can be derived from [11–13, 80]:

$$f_r\left(GHz\right) = \frac{c}{2\pi a\sqrt{\varepsilon_r}}\left(1.71 + \frac{a}{h} + 0.1578\left(\frac{a}{2h}\right)^2\right) \tag{5.6}$$

where $a = D/2$ (in cm), c is the velocity of light, with the other values given earlier. For these dimensions and with the DRA properties, the calculated resonance frequency is 10.63 GHz [11, 80].

In this section, different shapes of the aperture with different number of DRA elements are examined in order to observe their effect on the reflection coefficient and bandwidth. Figure 5.2 presents five configurations of the aperture starting from the very basic one, the rectangular shape shown in Fig. 5.2a. This figure shows that the slot length has the most important effect on the reflection coefficient and the resonant frequency; however, it also affects, to some extent, the impedance bandwidth of the antenna [80].

Our research orientation, which allows us to publish several works, is based on the same structure presented in [80]. The difference is articulated around the techniques of the antenna properties improvement by the creation of a slot in the microstrip line [11], which is also combined with a reduced ground plane [12]. As such, we could improve the bandwidth by enlarging the slot, which has never been treated before, by a 100% ratio. In our recent work, the ground plane is cut out [13]. The slot coupled with DRAs in [13] is very large compared to those studied in the literature, so we are interested in structure 4 simulated in [13], and we have changed the DRA pair position in order to shift the operating frequency to about 3.1 GHz.

The objective of the first step is to find the best position and thus the best coupling of the two DRAs with such a large slot. Several displacements are made until achieving the frequency band 3.25–12 GHz. These movements of the two DRAs are shown in Figs. 5.3a and 5.4 and the related S_{11} are shown in Fig. 5.3b and Fig. 5.4b, respectively. These positions allowed us to move the bandwidth from 5.9 GHz for antenna (i) to 3.67 GHz for antenna (ii), to reach 3.45 GHz for the antenna (iii), and 3.25–12 GHz for the last position of the two DRAs in antenna (iv).

The positioning of the two DRAs of the last antenna (iv) was carried out according to the following figures (Fig. 5.4a, b), which indicate the important effects of the positions of the DRAs with such a large slot and defective ground plane.

In Fig. 5.4a, b, it can be seen that such a structure (the broad slot and the defected ground plane) contributes perfectly to the DRAs. According to [13], these DRAs can excite the frequencies of TEδ11, TE1δ1, and TE11δ and are: 7.1926, 10.2248,

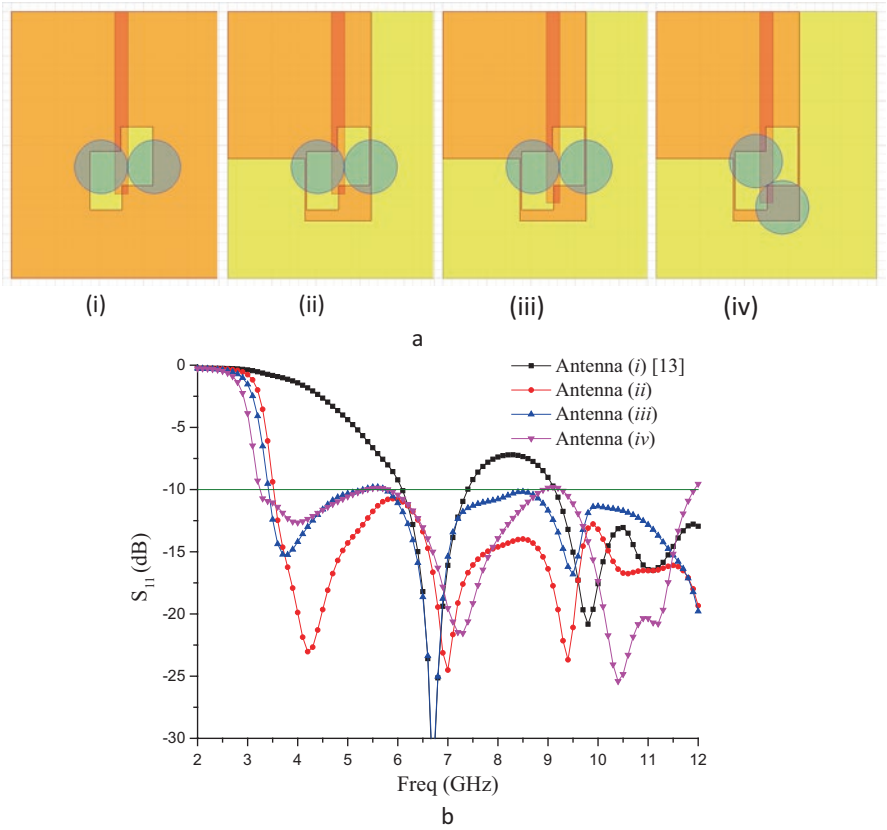

Fig. 5.3 (**a**) Aperture-coupled asymmetric DRA with defected ground plane top view with steps of the designed antenna with different positions of the two DRAs. (i) Antenna published in [13], (ii) (l_f = 20.5 mm), (iii) proposed antenna with l_f = 21.5 mm, and (iv) our first proposed antenna (l_f = 21.5 mm). (**b**) Simulated reflection coefficient of the antenna with the four positions of the two DRAs shown in Fig. 5.3a

and 10.5091 GHz, respectively. We may conclude that both DRAs can generate and excite other modes less than 10.5 GHz (as in a single DRA). In addition, the presence of defected ground could reach a bandwidth of 3.25–12 GHz. In this case, the resonant mode generated by the defected ground at 5.85 GHz (Fig. 5.2b) reacted completely with these DRAs and slightly with the first mode at 3.35 GHz.

5.4 Antenna with Various (3, 4, and 5) DRAs

This section consists in adding DRAs and varying their positions around the two DRAs. The results show an improvement of S_{11}. According to Fig. 5.5a, we notice that the effect of the third DRA is considerable in the bands 3.07–4.5 GHz and 7–12 GHz,

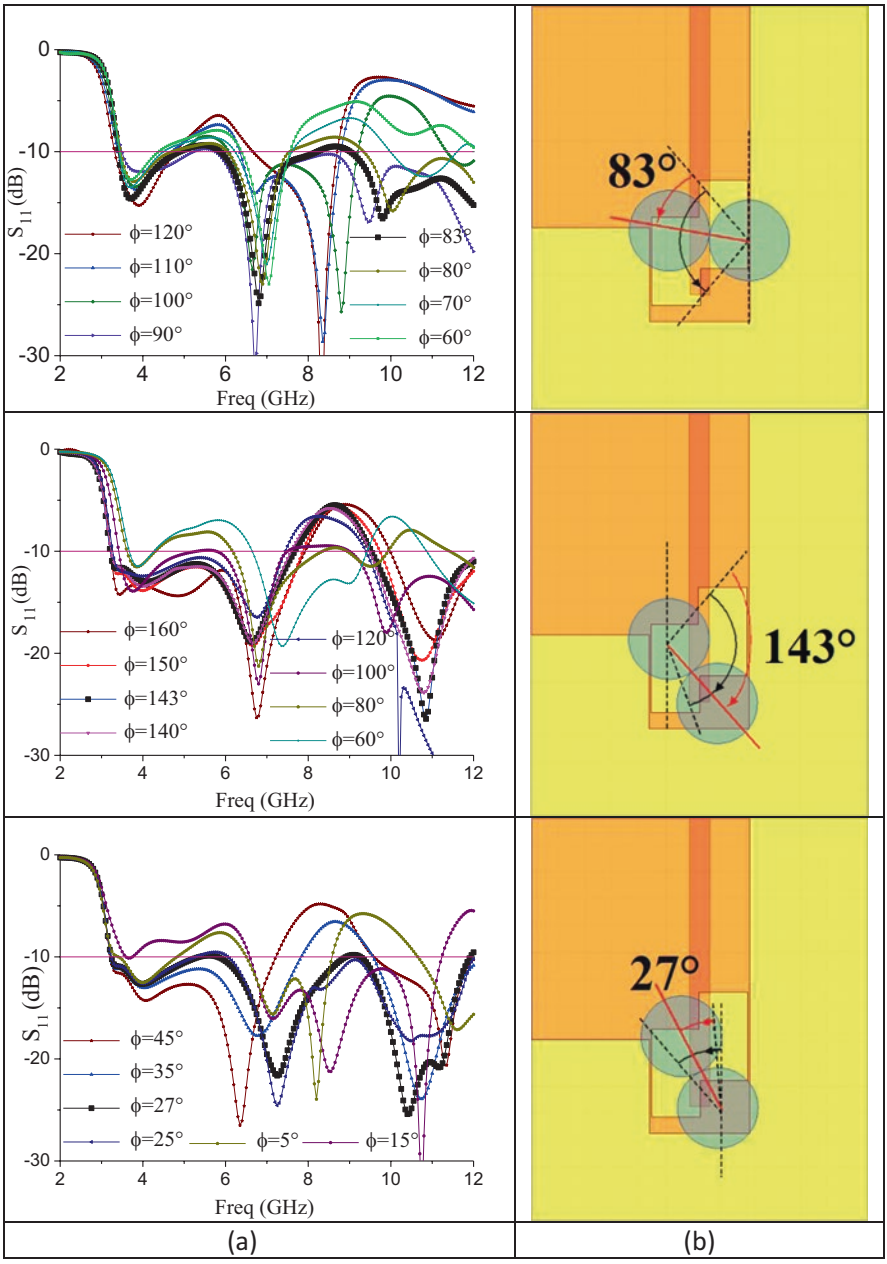

Fig. 5.4 (**a**) Aperture-coupled asymmetric two DRAs with defected ground plane top view with steps of the designed antenna. (i–iii) Design steps of the proposed antenna. (**b**) Simulated reflection coefficient of the antenna with the three different positions of the asymmetric DRAs with defected ground plane top view with steps of the designed antenna. (i–iii) Steps of the proposed antenna

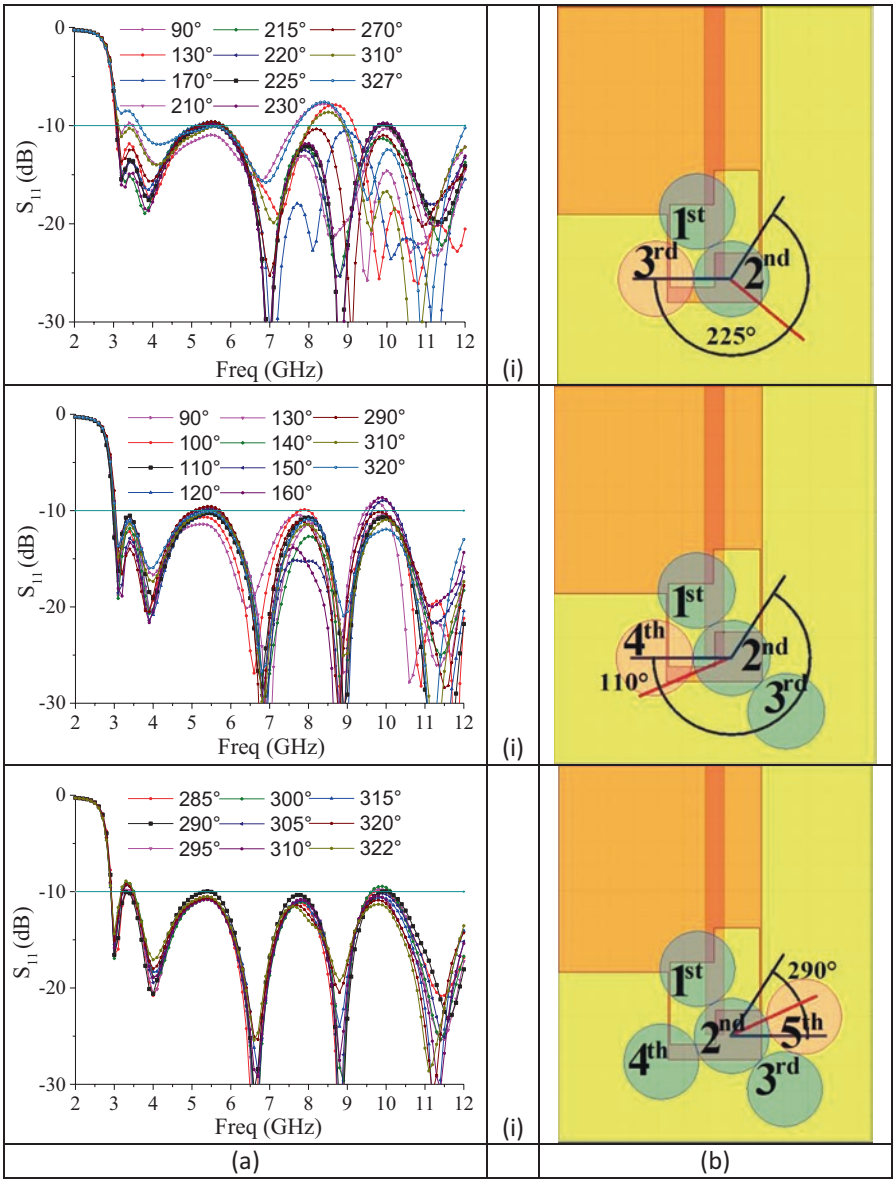

Fig. 5.5 S_{11} of aperture-coupled asymmetric DRA with defected ground plane top view with steps of the designed antenna. (i) Antenna proposed with three DRAs, (ii) antenna proposed with four DRAs, and (iii) antenna proposed with five DRAs

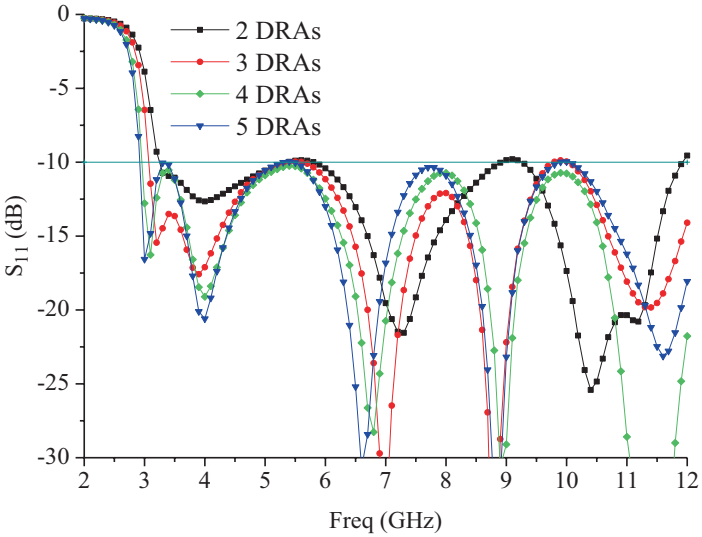

Fig. 5.6 Effect of the DRAs' number on S_{11}

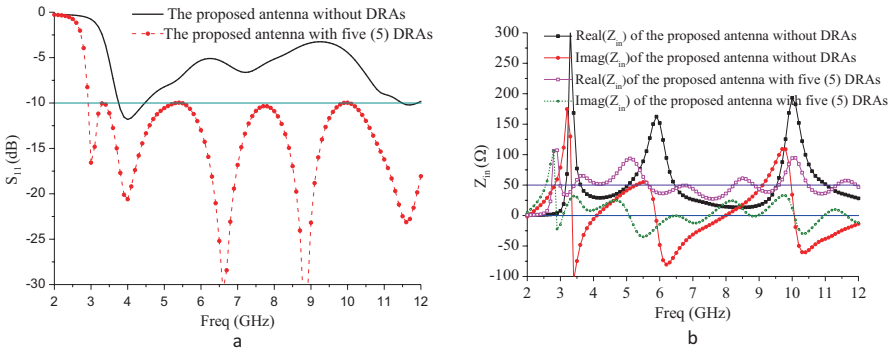

Fig. 5.7 (**a**) Compared S_{11} of the proposed antenna without and with five DRAs. (**b**) Input impedance of the proposed antenna without and with five DRAs

and that the other mode is generated by all the three DRAs, as explained in [13]. In this case, the achieved bandwidth is from 3.07 to 12 GHz. Now, we add the fourth and the fifth DRAs, respectively, and we try to vary the position around the DRAs to find the best position. Thus, according to Fig. 5.5b, c, the effect of the fourth and fifth DRAs leads to a slight improvement in S_{11} and bandwidth. With four DRAs, the bandwidth reaches 2.96 GHz and with five DRAs we have 2.92–12 GHz.

The obtained results of the different steps are recapitulated in Fig. 5.6, and the comparison of the S_{11} is illustrated in Fig. 5.7a, where it is clearly seen that the effect of the DRAs, in terms of number or position, is very important in the coupling of the large slot and defected ground.

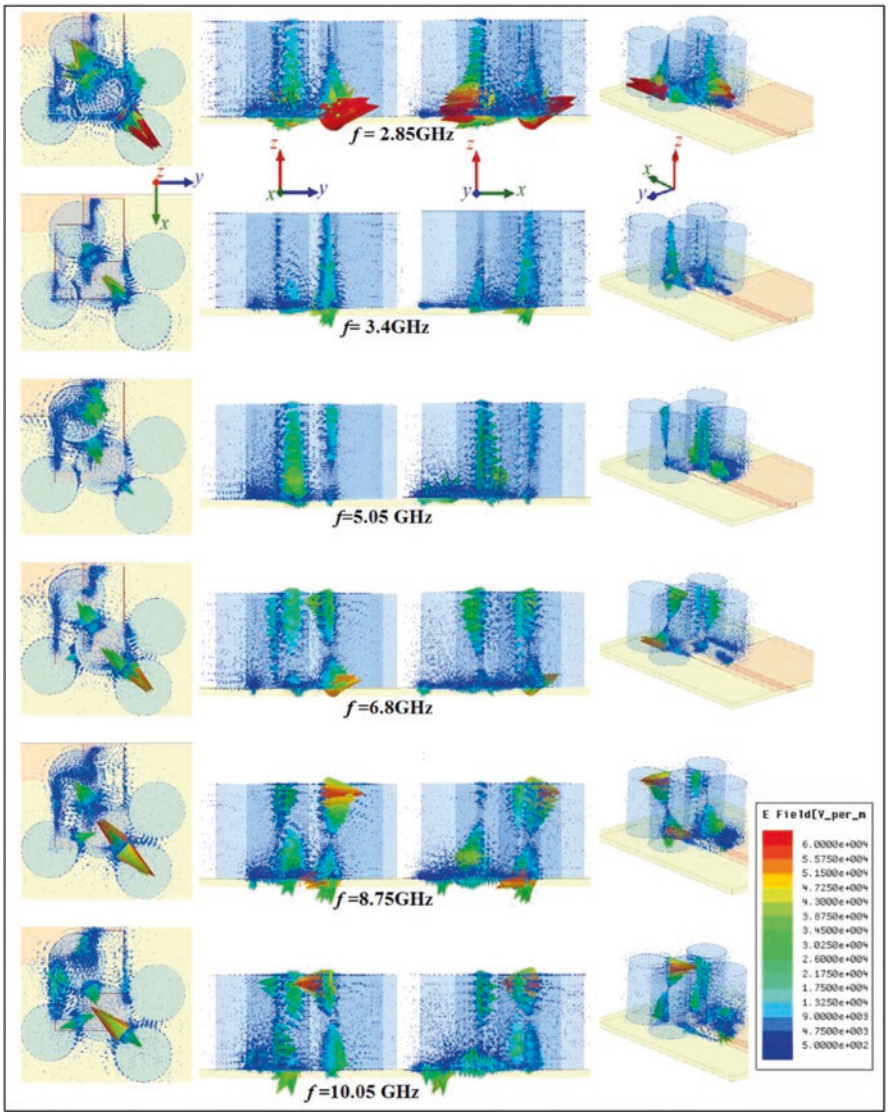

Fig. 5.8 Simulated radiation patterns at frequencies of 3.1, 6.5, and 10.6 GHz

According to the input impedance shown in Fig. 5.7b and the magnitude of the electric field shown in Fig. 5.8, we find that the DRAs first shift the resonant mode of the slot with the defective ground plane and we notice the appearance of three resonator modes in addition to the DRAs, which makes a total of six frequencies, which are: 2.85, 3.4, 5.05, 6.8, 8.75, and 10.05 GHz.

This shows that the antenna has a wide radiation pattern with maximum radiation along the normal to the substrate covering half-space, and in xy-plane (due to the

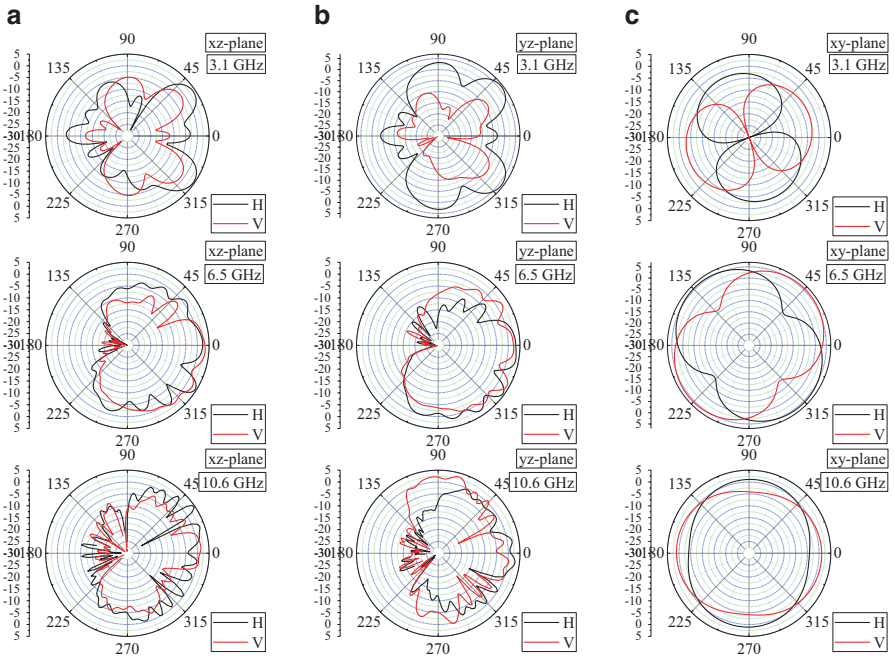

Fig. 5.9 Simulated radiation patterns: (**a**) *xz*-plane, (**b**) *yz*-plane, and (**c**) *xy*-plane

cross-polarization) an almost omnidirectional radiation pattern is obtained, as shown in Fig. 5.9. This depends, of course, on the shape and the dimensions of the slot.

The simulated gain values are shown in Fig. 5.10. This figure reveals that the shape of the defected ground plane makes a difference in the gain bandwidth performance (especially with the increase in number of DRs, a significant increase around 2.8 GHz and a decrease of more than 8 GHz). Note that the defected ground technique can actually improve the gain and bandwidth of the antenna. In our case, there are three proposed structures (case of 3, 4, and 5 DRAs) that all show an increase in gain and an improvement in bandwidth (>3.1–10.6 GHz).

5.5 Conclusion

A five-element compact dielectric resonator antenna with a defected ground plane microstrip line feeding for wideband applications has been analyzed. The proposed design is a result of a comprehensive parametric simulation study using HFSS 2014. The investigations showed the effect of various DRA parameters, positions and numbers, of the microstrip fed antenna on the resulting performance. Simulation results show that the proposed DRA has a -10 dB impedance bandwidth of 121.2%, covering the frequency range from 2.92 to 12 GHz, and a maximum gain of 9.1dBi.

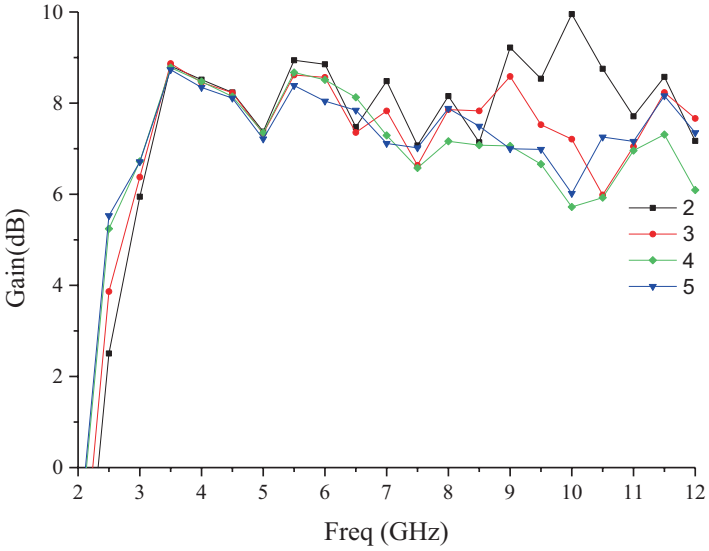

Fig. 5.10 Simulated antenna gain of the proposed antenna versus the number of DRAs

References

1. Z. Jinyun, P.V. Orlik, Z. Sahinoglu, A.F. Molisch, P. Kinney, UWB systems for wireless sensor networks. Proc. IEEE **97**(2), 313–331 (2009)
2. A.F. Molisch, Ultra-wide-band propagation channels. Proc. IEEE **97**(2), 353–371 (2009)
3. C. Chia-Chin, F. Watanabe, H. Inamura, Potential of UWB technology for the next generation wireless communications. IEEE Ninth international symposium on spread spectrum techniques and applications, Manaus-Amazon, 28–31 August, 2006, pp. 422–429
4. H. Schantz, *The Art and Science of Ultrawideband Antennas* (Artech House, Boston, 2005)
5. F. C. Commission, Revision of part 15 of the commission's rules regarding ultra-wideband transmission systems, Technology Report, ET-Docket 98–153, FCC02–48, April 2002
6. S. Fu, Broadband circularly polarized slot antenna array fed by asymmetric CPW for L-band application. IEEE Antennas. Wireless Propag. Lett. **8**, 1014–1016 (2009)
7. K.L. Wong, *Compact and Broadband Microstrip Antennas* (John Wiley & Sons Inc, New York, 2002)
8. J.Y. Sze, Axial-ratio bandwidth enhancement of asymmetric-CPWfed circularly-polarized square slot antenna. Electron. Lett. **44**(18), 1048–1049 (2008)
9. T.N. Chang, Circular polarized antenna for 2.3-2.7GHz Wi-MAX band. Microw. Opt. Technol. Lett. **51**(12), 2921–2923 (2009)
10. B.T.P. Madhav, Substrate permittivity effects on the performance of slotted aperture stacked patch antenna. Int. J. Appl. Eng. Res. **8**(8), 909–916 (2013)
11. C. Zebiri, F. Benabelaziz, M. lashab, D. Sayad, F. Elmegri, I.T.E. Elfergani, N.T. Ali, A.S. Hussaini, R.A. Abd-Alhameed, J. Rodriguez, Aperture-coupled asymmetric dielectric resonator antenna with slotted microstrip line for enhanced ultrawideband, EUCAP International conference, 2016
12. C. Zebiri, D. Sayad, NT Ali, M. Lashab, F. Benabelaziz, R.A. Abd-Alhameed I.T.E. Elfergani, J. Rodriguez, Reduced ground plane aperture-coupled DRA fed by slotted microstrip for

ultra-wideband application, 2017 11th European Conference on Antennas and Propagation (EUCAP), pp 965–969, 2017
13. C.E. Zebiri, M. Lashab, D. Sayad, I.T.E. Elfergani, K.H. Sayidmarie, F. Benabdelaziz, R.A. Abd-Alhameed, J. Rodriguez, J.M. Noras Offset aperture-coupled double-cylinder dielectric resonator antenna with extended-wideband, Accepted IEEE AP (2017)
14. L.H. Weng, Y.C. Guo, X.W. Shi, X.Q. Chen, An overview on defected ground structure. Prog. Electromagn. Res. B **7**, 173–189 (2008)
15. K. Yin, J.P. Xu, Compact ultra-wideband antenna with dual bandstop characteristic. Electron. Lett. **44**, 453–454 (2008)
16. D.-H. Bi, Z.Y. Mo Yu, S. Guo, X.C. Yin, Two new ultra-wideband antennas with 3.4/5.5GHz dual band-notched characteristics. Microw. Opt. Tech. Nol. Lett. **51**, 2942–2945 (2009)
17. M.A. Antoniades, G.V. Eleftheriades, A compact multiband monopole antenna with a defected ground plane. IEEE Antennas and Wireless Propagation Letters **7**, 652–655 (2008)
18. K.H. Chiang, K.W. Tam, Microstrip monopole antenna with enhanced bandwidth using defected ground structure. IEEE antennas and wireless propagation letters **7**, 532–535 (2008)
19. W.-C. Liu, C.-M. Wu, Y. Dai, Design of triple-frequency microstrip-fed monopole antenna using defected ground structure. IEEE Trans. Antennas Propag. **59**(7), 2457–2463 (2011)
20. W. Hu, Y.-Z. Yin, P. Fei, X. Yang, Compact triband square-slot antenna with symmetrical L-strips for WLAN/WiMAX applications. IEEE Antennas Wireless Propag. Lett. **11**, 462–465 (2010)
21. A.K. Gautam, A. Bisht, B.K. Kanaujia, A wideband antenna with defected ground plane for WLAN/WiMAX applications. AEU Int. J. Electron. Commun. **70**(3), 354–358 (2016)
22. J. Pei, A.G. Wang, S. Gao, W. Leng, Miniaturized triple-band antenna with a defected ground plane for WLAN/WiMAX applications. IEEE Antennas and Wireless Propagation Letters **10**, 298–301 (2011)
23. R.K. Gangwar, A. Sharma, M. Gupta, S. Chaudhary, Hybrid cylindrical dielectric resonator antenna with HE11δ and HE12δ mode excitation for wireless applications. Int. J. RF Microw. Comput. Aided Eng. **26**(9), 812–818 (2016)
24. M.W. McAllister, S.A. Long, G.L. Conway, The rectangular dielectric resonator antenna. Paper presented at the IEEE international AP-S symposium, University of Houston, Houston, Texas, May 1983
25. S.A. Long, M.W. McAllister, L.C. Shen, The resonant cylindrical dielectric cavity antenna. IEEE Trans. Antennas Propag. **31**(3), 406–412 (1983)
26. J.K. Plourde, C.L. Ren, Application of dielectric resonators in microwave components. IEEE Trans. Microw. Theory Techn. **MTT-29**(8), 754–770 (1981)
27. D. Kajfez, P. Guillon (eds.), *Dielectric Resonators* (Artech House, Norwood, 1986)
28. S.A. Long, M. McAllister, L.C. Shen, The resonant cylindrical dielectric cavity antenna. IEEE Trans. Antennas Propag **AP-31**, 406–412 (1983)
29. M. McAllister, S.A. Long, G.L. Conway, Rectangular dielectric resonator antenna. Electron. Lett. **19**, 219–220 (1983)
30. M. McAllister, S.A. Long, Resonant hemispherical dielectric antenna. Electron. Lett. **20**, 657–659 (1984)
31. A.A. Kishk, M.R. Zunoubi, D. Kajfez, A numerical study of a dielectric disk antenna above a grounded dielectric substrate. IEEE Trans. Antennas Propag. **AP-41**, 813–821 (1993)
32. G.P. Junker, A.A. Kishk, A.W. Glisson, Input impedance of aperture coupled dielectric resonator antenna. IEEE Trans. Antennas Propag. **AP-44**(5), 600–607 (1996)
33. S.K.K. Dash, T. Khan, A. De, Dielectric resonator antennas: an application oriented survey. Int. J. RF Microwave Comput. Aided Eng. (2016)
34. M.W. McAllister, S.A. Long, G.L. Conway, Rectangular dielectric resonator antenna. Electron. Lett. **19**(6), 218–219 (1983)
35. K.M. Luk, K.W. Leung, *Dielectric Resonator Antennas* (Research Studies Press, Baldock, 2002)
36. F. Elmegri, C.H. See, R.A. Abd-Alhameed, C. Zebiri, P.S. Excell, Dielectric resonator antenna design for UWB applications. In antennas and propagation conference (LAPC), 2013 Loughborough (pp. 539–542). IEEE (2013)

37. A.A. Kishk, H.A. Auda, B.C. Ahn, Radiation characteristics of cylindrical dielectric resonator antennas with new applications. IEEE Antennas Propag. Soc. Newsletter **31**, 587–589 (1989)
38. A. Ittipiboon, R.K. Mongia, Y.M.M. Antar, P. Bhartia, M. Cuhaci, Aperture fed rectangular and triangular dielectric resonators for use as magnetic dipole antennas. Electron. Lett. **29**, 2001–2002 (1993)
39. K.W. Leung, K.M. Luk, E.K.N. Yung, Spherical cap dielectric resonator antenna using aperture coupling. Electron. Lett. **30**, 1366–1367 (1994)
40. R.K. Mongia, A. Ittipiboon, P. Bhartia, M. Cuhaci, Electric monopole antenna using dielectric ring resonator. Electron. Lett. **29**, 1530–1531 (1993)
41. K.W. Leung, K.Y. Chow, K.M. Luk, E.K.N. Yung, Excitation of dielectric resonator antenna using a soldered through probe. Electron. Lett. **33**, 349–350 (1997)
42. A.A. Kishk, Y. Yin, A.W. Glisson, Conical dielectric resonator antenna for wideband applications. IEEE Trans. Antennas Propag. **50**, 469–474 (2002)
43. A.A. Kishk, Wideband truncated tetrahedron dielectric resonator antenna excited by a coaxial probe. IEEE Trans. Antennas Propag. **51**, 2913–2917 (2003)
44. H.-T. Chen, Y.-T. Cheng, S.-Y. Ke, Probe-fed sectionspherical dielectric resonator antennas. Microw. Conf. (1999 Asia Pacific) (2), 359–362 (1999)
45. R. Chair, A.A. Kishk, K.F. Lee, C.E. Smith, Wideband flipped staired pyramid dielectric resonator antennas. Electron. Lett. **40**(10), 581–582 (2004)
46. K. Pliakostathis, D. Mirshekar-Syahkal, Stepped dielectric resonator antennas for wideband applications. IEEE Antennas Propag. So. Int. Symp. **2**, 1367–1370 (2004)
47. Y.-X. Guo, Y.-F. Ruan, X.-Q. Shi, Wide-band stacked double annular-ring dielectric resonator antenna at the end-fire mode operation. IEEE Trans. Antennas Propag. **53**(10), 3394–3397 (2005)
48. S.-l.S. Yang, R. Chair, A.A. Kishk, K.-F. Lee, K.-M. Luk, Study on sequential feeding networks for subarrays of circularly polarized elliptical dielectric resonator antenna. IEEE Trans. Antennas Propag. **55**(2), 321–333 (2007)
49. K.W. Leung, K.K. So, Theory and experiment of the wideband two-layer hemispherical dielectric resonator antenna. IEEE Trans. Antennas Propag. **57**(4, part 2), 1280–1284 (2009)
50. Karmakar D.P., Soren D., Ghatak R., Poddar D.R., Mishra R.K., A wideband Sierpinski carpet fractal cylindrical dielectric resonator antenna for X-Band application, Applied Electromagnetics Conference (AEMC), pp. 1–3, 2009
51. R.K. Mongia, P. Bhartia, Dielectric resonator antennas – A review and general design relations for resonant frequency and bandwidth. Int. J. Microw. Millimeter Wave Comput. Aided Eng. **4**, 230–247 (1994)
52. A.A. Kishk, B. Ahn, D. Kajfez, Broadband stacked dielectric resonator antennas. IET Electron Lett. **25**, 1232–1233 (1989)
53. Y. Liu, M. Wei, H. Liu, S.X. Gong, A novel compact three-port dielectric resonator antenna with reconfigurable pattern for WLAN systems. Progress In Electromagnetics Research C **47**, 37–45 (2014)
54. L. Huitema, M. Koubeissi, M. Mouhamadou, Compact and multiband dielectric resonator antenna with pattern diversity for multistandard mobile handheld devices. IEEE Trans. Antennas Propag. **59**(11), 4201–4208 (Nov. 2011)
55. M.G. Nabi Alsath, B. Sridhar, K. Malathi, A dual band frequency and pattern reconfigurable dielectric resonator antenna. Prog. Electromagn. Res. C **27**, 115–128 (2012)
56. R. Chair, A.A. Kishk, K.F. Lee, Wideband simple cylindrical dielectric resonator antennas. IEEE Microw. Wireless Comp. Lett. **15**(4), 241–243 (2005)
57. A.A. Kishk, X. Zhang, A.W. Glisson, D. Kajfez, Numerical analysis of stacked dielectric resonantor antennas excited by a coaxial probe for wideband applications. IEEE Trans. Antennas Propag. **51**(8), 1996–2006 (2003)
58. A.A. Kishk, B. Ahn, D. Kajfez, Broadband stacked dielectric resonator antennas. Electron. Lett. **25**, 1232–1233 (1989)
59. S.M. Shum, K.M. Luk, Stacked annular-ring dielectric resonator antenna excited by axisymmetric coaxial probe. IEEE Trans. Antennas Propag. **43**(8), 889–892 (1995)

60. K.W. Leung, K.M. Luk, K.Y. Chow, E.K.N. Yung, Bandwidth enhancement of dielectric resonator antenna by loading a low-profile dielectric disk of very high permittivity. Electron. Lett. **33**, 725–726 (1997)
61. A. Sangiovanni, J.Y. Dauvignac, C. Pichot, Stacked dielectric resonator antenna for multifrequency operation. Microw. Opt. Technol. Lett. **18**, 303–306 (1998)
62. A. Buerkle, K. Sarabandi, H. Mosallaei, Compact slot and dielectric resonator antenna with dual-resonance, broadband characteristics. IEEE Trans. Antennas Propag. **53**(3), 1020–1027 (2005)
63. Y. Coulibaly, T.A. Denidni, H. Boutayeb, Broadband microstrip fed dielectric resonator antenna for X-band applications. IEEE Antennas Wireless Propag. Lett. **7**, 341–345 (2008)
64. T.A. Denidni, Q. Rao, Hybrid dielectric resonator antennas with radiating slot for dualfrequency operation. IEEE Antennas Wireless Propag. Lett. **3**, 321–323 (2004)
65. K.M. Luk, K.W. Leung, *Dielectric Resonator Antennas* (Research Studies Press LTD., London, 2003)
66. R.K. Chaudhary., K.V. Srivastava, A. Biswas, in *An investigation on three element multilayer cylindrical dielectric resonator antenna excited by a coaxial probe for wideband applications*. Applied Electromagnetics (APACE), 2010 IEEE Asia-Pacific Conference on pp. 1-5. (IEEE., 2010)
67. D. Guha, Y.M.M. Antar, Four-element cylindrical dielectric resonator antenna for wideband monopole-like radiation. IEEE Trans. Antennas Propag. **54**, 2657–2662 (2006)
68. L.Z. Thamae, Z. Wu, Broadband bowtie dielectric resonator antenna. IEEE Trans. Antennas Propag. **58**, 3707–3710 (2010)
69. M.T.K. Tam, R.D. Murch, Compact circular sector and annular sector dielectric resonator antennas. IEEE Trans. Antennas Propag. **47**, 837–842 (1999)
70. R.K. Chaudhary, V.V. Mishra, K.V. Srivastava, A. Biswas, Multi-layer multi-permittivity dielectric resonator: a new approach for improved spurious free window, in Proceedings of EuMC-2010, Paris, France, Oct. 2010
71. P. Rezaei, M. Hakkak, K. Forooraghi, Design of wide-band dielectric resonator antenna with a two-segment structure. Progress In Electromagnetics Research **66**, 111–124 (2006)
72. P. Rezaei, M. Hakkak, K. Forooraghi, Dielectric resonator antenna for wireless LAN applications. IEEE Antennas Propag. Soc. Int. Symp. **2**, 1005–1008 (2006)
73. A. Petosa, N. Simons, R. Siushansian, A. Ittipiboon, M. Cuhaci, Design and analysis of multisegment dielectric resonator antennas. IEEE Trans. Antennas Propag **48**(5), 738–742 (2000)
74. A. Rashidian, K. Forooraghi, M. Tayfeh-Aligodarz, Investigations on two-segment dielectric resonator antennas. Microw. Opt. Technol. Lett. **45**(6), 533–537 (2005)
75. M.T.K. Tam, R.D. Murch, Half volume dielectric resonator antenna designs. Electron. Lett. **33**(23), 1914–1916 (1997)
76. R.K. Chaudhary, K.V. Srivastava, A. Biswas, Multi-band cylindrical dielectric resonator antenna using permittivity variation in azimuth direction. Prog. Electromagn. Res. C **59**, 11–20 (2015)
77. R.K. Chaudhary, K.V. Srivastava, A. Biswas, A practical approach: design of wideband cylindrical dielectric resonator antenna with permittivity variation in axial directio and its fabrication using microwave laminates. Microw. Opt. Technol. Lett. **55**, 2282–2288 (2013)
78. Chaudhary, R. K., K. V. Srivastava, and A. Biswas, A concentric three-layer half-split cylindrical dielectric resonator antenna for wideband applications, In *URSI International Symposium on Electromagnetic Theory (EMTS)*, 664–667, Hiroshima, Japan, 2013
79. Ansoft High Frequency Structure Simulation (HFSS). Ansoft Corporation, 2012, Ver. 14
80. A.H. Majeed, A.S. Abdallah, F. Elmegri, K.H. Sayidmarie, R.A. Abd-Alhameed, J.M. Noras, Aperture-coupled asymmetric dielectric resonator antenna for wideband applications. IEEE Antennas Wireless Propag. Lett. **13**, 927–930 (2014)

Chapter 6
Simple and Compact Planar Ultra-Wideband Antenna with Band-Notched Characteristics

Issa Elfergani, Pedro Lopes, Jonathan Rodriguez, and Dominique Lo Hine Tong

6.1 Introduction

Ultra-wideband (UWB) is a radio technology, which has seen an increase in popularity in the past years due to its appealing properties. This technology finds applications such as medical imaging [1], indoor position systems [2] and communications systems. With the allocation of a band, from 3.1 to 10.6 GHz, for unlicensed UWB communications systems by the FCC in 2002 [3], there has been a special interest by the research community in those systems since then, as it allows for high data transmission rates. However, in order not to interfere with other systems within the allocated band, they are limited in power transmission, finding its use for short-range communications.

For UWB communications to be feasible, antennas with attractive characteristics over the working bandwidth are necessary. Printed monopole UWB antennas come as a solution, as they provide attractive features such as low cost, small size and ease of fabrication. This type of antennas simply consists of a planar radiator and a ground plane printed over the same plane of a substrate or on opposite planes. Printed monopole antennas are quite popular in the research community. Several printed monopole UWB designs have been reported in the literature [4–6].

I. Elfergani (✉)
Instituto de Telecomunicações, Campus Universitário de Santiago, Aveiro, Portugal
e-mail: i.t.e.elfergani@av.it.pt

P. Lopes
Universidade de Aveiro, Aveiro, Portugal

J. Rodriguez
Instituto de Telecomunicações, Campus Universitário de Santiago, Aveiro, Portugal

University of South Wales, Pontypridd, UK

D. Lo Hine Tong
Technicolor Connected Home, Rennes, France

I. Elfergani et al. (eds.), *Antenna Fundamentals for Legacy Mobile Applications and Beyond*, DOI 10.1007/978-3-319-63967-3_6

Some of the most used feeding techniques for printed monopole antennas are coplanar waveguide (CPW) and microstrip line. In the CPW feeding technique, the conductor and the ground plane are place on the same plane of the substrate. There is a variant of this technique known as conductor-backed coplanar waveguide (CBCPW), where another ground plane is added at the opposite side of the substrate. This technique has good broadband performance, low dispersion and cheap fabrication costs, since it only needs to be printed on one side of the substrate. Numerous antennas using this kind of feeding technique have been studied. Some of those include printed monopole antennas as in [7] where their usable bandwidth covers the 2.44–2.58 and 3.5–9.85 GHz bands, or with UWB characteristic as in [8–11]. On the other hand, in the microstrip feeding technique, the conductor strip line is located on the top side, while the ground plane is on the opposite of the substrate. One variation of this technique is inset feeding, which gives the possibility to control the impedance of the antenna. Microstrip feeding is very popular due to its simplicity. An example of a normal microstrip and inset microstrip lines was seen in [12, 13]. Other examples of UWB antennas with microstrip feeding can easily be found in the literature [14–16].

Since the UWB has to coexist with other systems that operate in the frequency bands within its bandwidth, the ability to filter those interferences is quite desirable. One common example is the interference by the wireless local area network (WLAN) communication system, which operates from 5.15 to 5.35 GHz and 5.725 to 5.825 GHz. Printed monopole antennas designing with effective techniques to filter these unwanted frequency bands have been developed [17–24]. These notch creating techniques make the use of filters dispensable, decreasing the fabrication cost and size of the whole system. Two popular techniques for notch creation make use of slots and stubs. In the first technique, either a strip from the patch, feeding line or ground plane is taken off to create a resonance at a desired frequency. An example in [25] can explain how a dual notch is achieved by doing a slot in the patch and feeding line. In the stub technique, an extra strip if the conductor is added to either the patch, feeding line or ground plane. By doing this, it's possible to produce a resonance at a certain frequency, and therefore as seen in [26], a notch is generated by adding a stub to the ground plane.

A printed monopole UWB antenna with dual band-notch characteristics is presented in this chapter. The antenna configuration employs a combination of hexagonal-shaped structure together with approaches of defected ground structure (DFG) and a stub added in the feeding strip to achieve a larger bandwidth. The technique of embedded a half and full hexagonal slots was applied to accomplish both a single and dual rejected bands, respectively.

To prove the concept, three versions were designed. The first version operates in the UWB frequency range from 3.2 to 14 GHz, while in the second design, a half hexagonal slot was embedded on the radiator to present a UWB antenna including a single band notch at WLAN 5.2 GHz. Finally, a full hexagonal slot was introduced on the same antenna structure; however, dual-band notches were simultaneously achieved, i.e. at the lower WLAN 5.2 and 10 GHz.

6.2 First Version: Main UWB Antenna Design and Concept

The full configuration of the initial version of the antenna is illustrated in Fig. 6.1. The design for the printed monopole UWB antenna consists of a hexagonal patch structure with a small stub along the feeding strip and a truncated ground plane, as shown in Fig. 6.1. The antenna is printed over a FR-4 (Loss-free) substrate with a 0.8 mm thickness and relative permittivity $\varepsilon = 4.3$. The proposed antenna occupies a compact volume of $30 \times 30 \times 0.8$ mm^3. A 50-Ohm microstrip line is used as feeding method within this work. The antenna associated ground plane with an appropriate length is printed on the other side of the substrate. The ground plane is virtually shared by both the radiator and its feed line.

The full dimensions of the radiator together with its feeding line and the trapezoidal DGS are stated in Table 6.1.

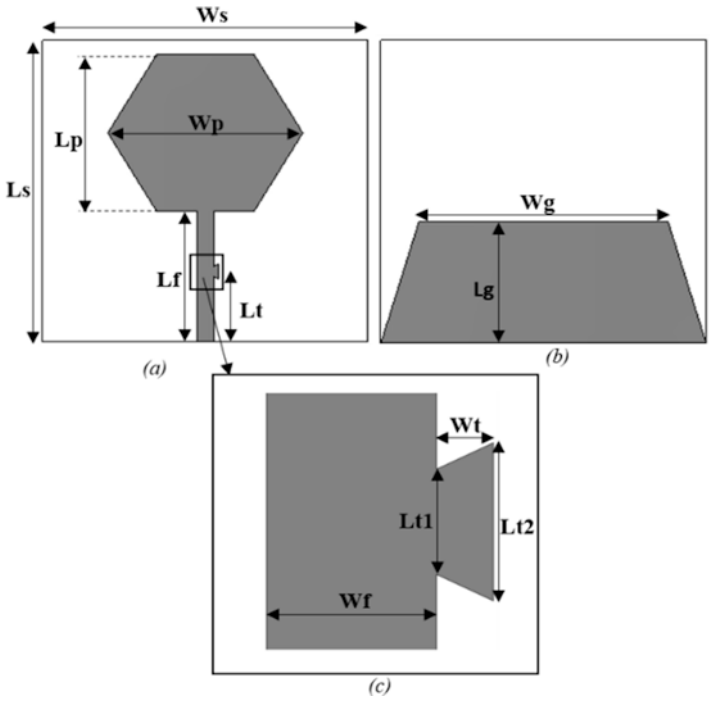

Fig. 6.1 Design of the first version of the proposed antenna. (**a**) Front view, (**b**) bottom view, (**c**) stub close-up

Table 6.1 Physical dimensions of the antenna

Parameter	Value (mm)
Ws	30
Ls	30
Wp	18
Lp	15.6
Wf	1.5
Lf	13
Wg	23
Lg	12
Wt	0.5
Lt	7
Lt1	1
Lt2	1.5

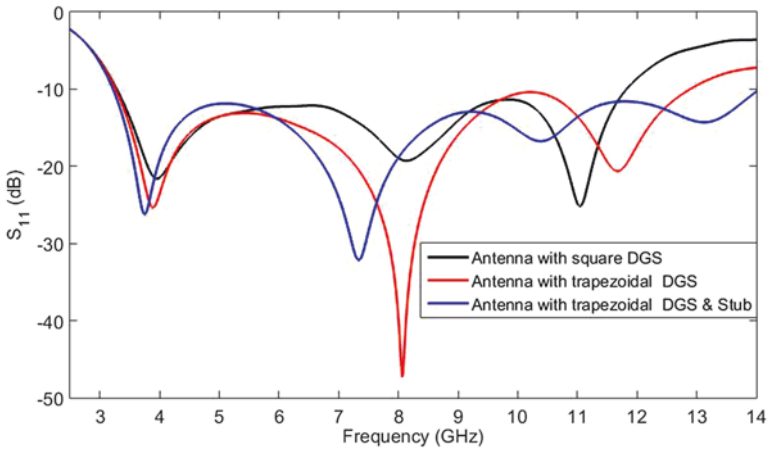

Fig. 6.2 The S11 variations of the antenna with square DGS, with trapezoidal DGS and joining both trapezoidal DGS with the stub in the feeding line

6.2.1 The Approaches of Improved Bandwidth

To realise the effectiveness of both truncated ground plane and the stub in improving the bandwidth, the S11 of the antenna with square DGD, with trapezoidal DGS and joining the trapezoidal DGS together with the stub in the feeding line, was demonstrated in Fig. 6.2. It should be noted that the proposed antenna with square defected ground plane is capable of covering the whole range of UWB spectrum, .i.e. 3.3–11.75 GHz. However, by truncating the defected ground plane to form a trapezoidal shape, this has shown a significant effect on the higher mode and also slightly influenced the lower band of UWB spectrum. This improvement made this antenna version operating from 3.2 to 13 GHz. The final approach of joining both

the trapezoidal ground and stub over the strip line further improved the antenna operational from 3.2 to 14 GHz as indicated in Fig. 6.2.

6.2.2 *The Analysis of Ground Plan*

Prior to obtaining the final and optimal UWB antenna design, a parametric analysis of the defected ground structure length was carried out to ensure that the antenna has a stable performance and an improved bandwidth, which makes it seamlessly incorporated into today's portable wireless devices. The size of the defected ground plane length was studied and investigated. This investigation and optimisation study was generated with help of CST simulator [27].

The outcomes of the variation length of ground plane size on the reflection coefficient $|S_{11}|$ are shown in Fig. 6.3. The length of ground plane varies from 11 to 13 mm. When the length (Lg) set at 11 and 11.5 mm, the antenna accomplishes dual-band features of the band of 3.85 and 11.8 GHz. On the other hand, when Lg fixed at 12.5 mm, a wide band from 3.3 to 10.3 GHz and another relatively narrow band from 12.5 to 14 GHz were obtained. Another dual band at 4 and 14 GHz feature was met, while the Lg set at 13 mm. All the above achievements do not satisfy the goal of this work to obtain an extreme UWB range. Surprisingly, the impedance matching for the entire desired UWB frequency range of the antenna improved as the ground plane length was set at 12 mm. Therefore, the length dimension of 12 mm was selected to meet this target.

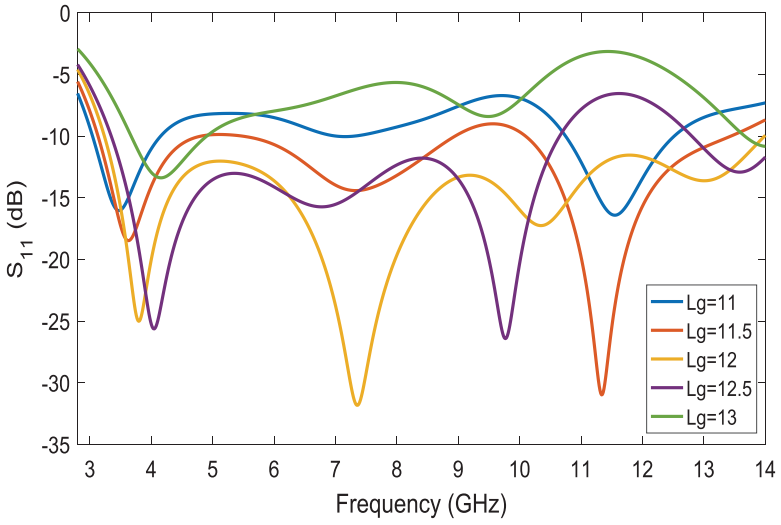

Fig. 6.3 Simulated return loss (S_{11}) for different heights of the ground plane on the first version of the proposed antenna

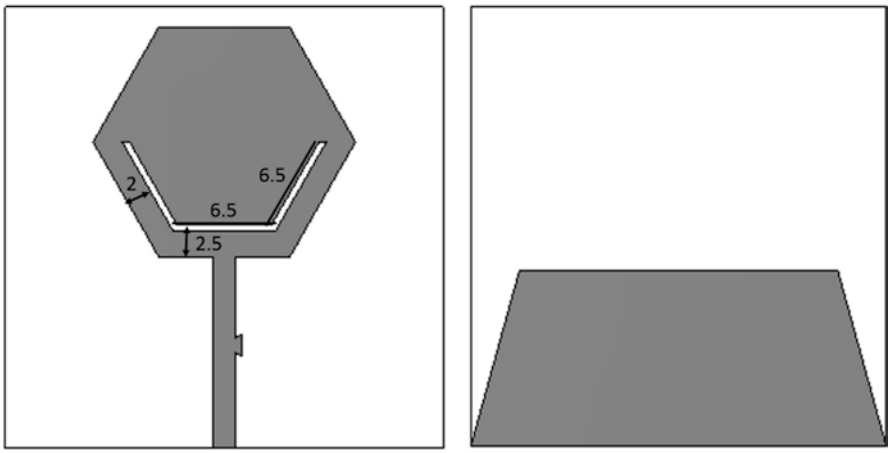

Fig. 6.4 Design of the second version of the proposed antenna with half hexagonal slot. (**a**) Front view and (**b**) bottom view

6.3 Second Version: UWB Antenna Design with Single Notched Band

The proposed printed monopole UWB antenna with a half hexagonal slot is illustrated in Fig. 6.4. This antenna still maintains exactly same geometry size and structures with the antenna presented in Fig. 6.1, but a half hexagonal slit was embedded over the hexagonal radiating shape. The given dimensions and specification of the slot was shown in Fig. 6.4. This has same UWB spectrum range achieved by the antenna in Fig. 6.2, except at the resonant frequency around 5.2 GHz, in which the band-notched was created. Thanks to the etched slot, it was very sufficient to create the first rejected band. The dimensions and position of the embedded slot were wisely selected and optimised to meet the first desired rejected band at higher band of WLAN 5.2GHz.

6.3.1 Results Analysis for Single Band-Notched Design

The S11 of the proposed UWB antenna with and without including the half hexagonal slot is depicted in Fig. 6.5. From Fig. 6.5, one can realise that the proposed structure without adding any slot operates over a wide frequency range from 3.2 to 14 GHz. However, this proposed UWB antenna share part of its frequency spectrum with several services such as WLAN, Hyperlan/2 and WiMax systems. This will make this antenna to most likely cause interferences with those existing services. Thus, to address this, a slot of half hexagonal shape was generated over the proper

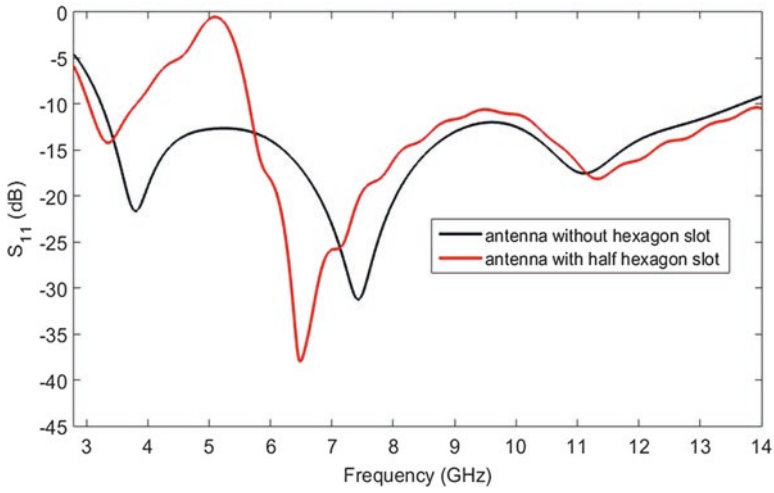

Fig. 6.5 The S11 of the proposed antenna with a half hexagonal slot

location over the antenna surface as indicated in Fig. 6.4. This simple and effective approach has led to suppressing the unwanted frequency band at WLAN 5.2 GHz, where the rejected band is created. As shown in Fig. 6.5, the proposed design with the embedded slot covers the UWB spectrum from 3.2 to 14 GHz with return loss of less than −10 dB, with filtering frequency at 5.2 GHz. Having such type of antenna functioning, as a radiator and stop-band filter at the same time and within one structure, will lead to a huge reduction in terms of the weight and complexity, and the economical factor should be taken into consideration since the need of filter is neglected.

To further understand the operation of the proposed antenna with and without slot, the input impedance of both versions is investigated and analysed. Figure 6.6 represents the real and imaginary parts of both versions of the antenna. As expected, the reactance of the antenna without slot maintains around 3 ohm over the entire UWB range, while the resistance varies from 46 to 51 Ω. This response satisfies the good impedance matching condition to a 50-Ω load. On the other hand, the reactance of the antenna with the incorporated slot keeps more or less same response compared to the first antenna; however, there is tremendous decrease of the reactance value at the band of 5.2 GHz, where the notched band is produced, while the resistance curve of the slotted design shows a smooth response around 50 Ω from 3.2 to 4.8 GHz, then faced a significant increase up to 800 Ω at 5.2 GHz, and then dropped again to be around 50 Ω from 5.5 GHz up to 14 GHz. This is a typical anti-resonance behaviour and it occurs at around 5.2 GHz resulting in a high input resistance value of around 800 Ω. This response exhibits a typical band suppression characteristic.

The current surfaces of antennas 1 and 2 are illustrated in Fig. 6.7. Three resonant frequencies were selected for the aggregated bandwidth, i.e. 3.5, 5.2 and

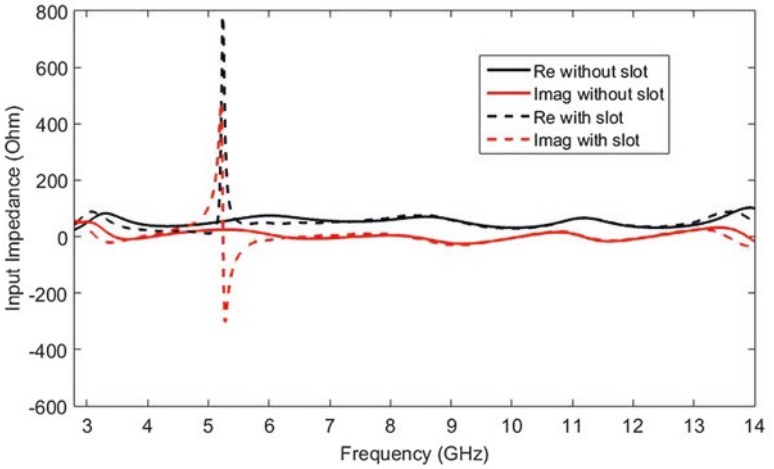

Fig. 6.6 The input impedance of the second antenna version with hexagonal slot

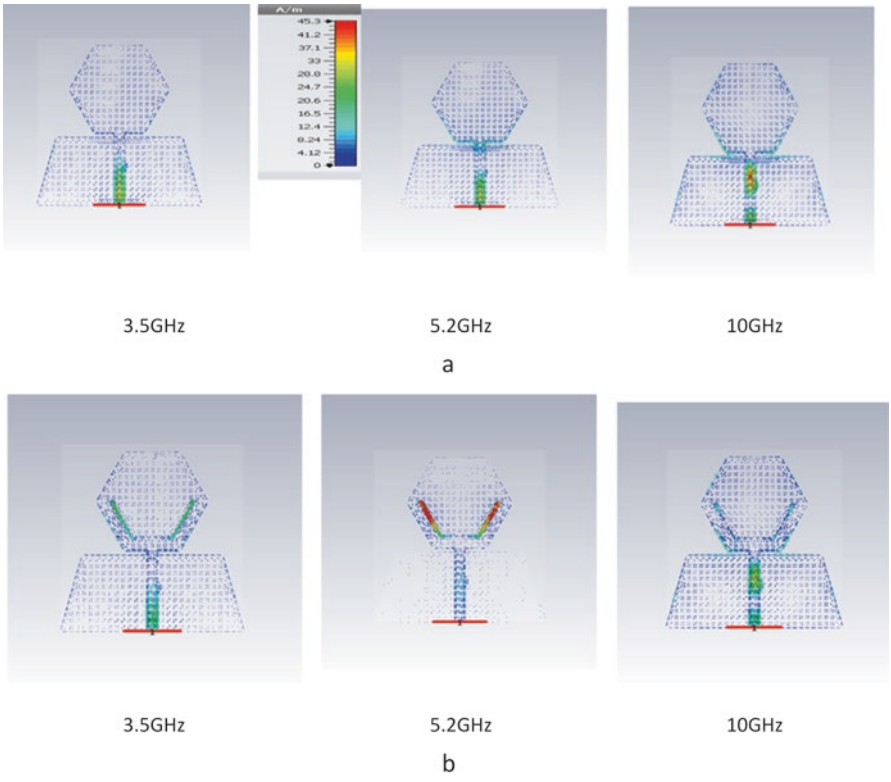

Fig. 6.7 Current surface for: (**a**) the un-slotted antenna and (**b**) half hexagonal slot antenna at 3.5, 5.2 and 10 GHz

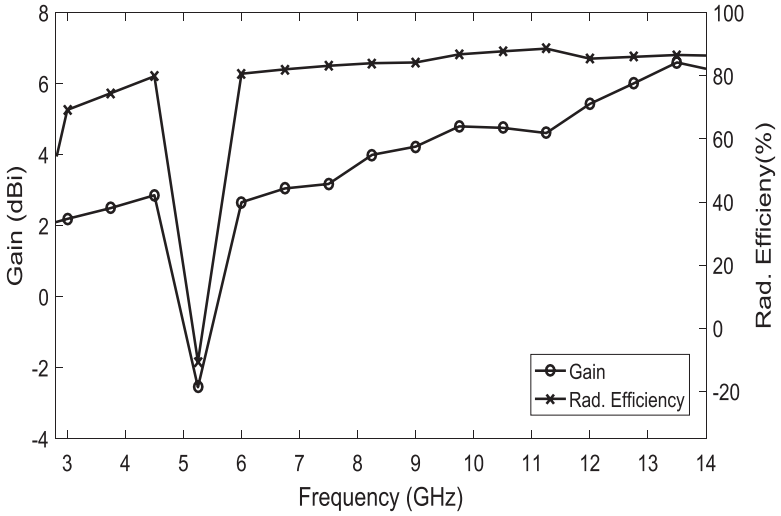

Fig. 6.8 The power gains and efficiencies of the half hexagonal slot design

10 GHz. Looking at the currents of the UWB antenna design in Fig. 6.7a, one can conclude that most of the currents exist mainly on the feeding line at the three bands, while they gradually taper as we head further towards the radiator and ground plane. However, by examining the current distributions for the second design (antenna with a single notched band), it is undoubtedly seen that the currents at the band of 3.1 GHz are induced over the strip lines, with a small value which flowed of the patch due to the embedded slot. Also, the proposed design at 10 GHz shows most of its currents represent mainly on the feeding line as shown in Fig. 6.7b. However, at 5.1 GHz, as can easily be discerned in Fig. 6.6b, strong electric currents are concentrated in the half hexagonal slot and marginally over the feeding strip of the radiator, in comparison to those realised at 3.5 GHz and 10 GHz. This is due to the fact that the proposed antenna with half hexagonal slot is being considered as a stop-band filter to suppress the undesirable frequency at WLAN 5.2 GHz. This proves the claim in the previous section for the antenna to simultaneously function as a radiator and stop-band filter within a single system device.

From the above investigation, the present antenna with an embedded slot does not operate at the upper band of WLAN 5.2 GHz. To verify this finding, both the gain and efficiency of slotted antenna were studied. Figure 6.8 displays the power again and efficiencies of the single notch UWB antenna. It should be noted that the achieved band suppression design (with slot) shows a gradual improved gain starting from 2.2 dBi at the frequency of 3.5 GHz up to around 6 dBi at 14 GHz, except at the created notch, when the gain was extremely dropped to −1.8 dBi at the 5.2 GHz as indicated in Fig. 6.8. The antenna efficiencies also as expected agreed with the obtained gain. To be more explicit, the proposed slotted design exhibited good radiation efficiencies varied from 78% to 86% over the completely desired

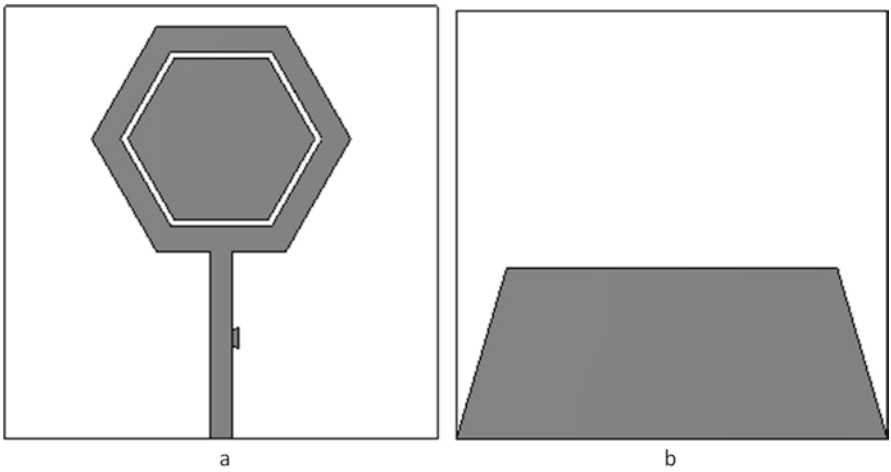

Fig. 6.9 Design of the third version of the proposed antenna with full hexagonal slot (**a**) Front view and (**b**) bottom view

frequency range, except at the suppressed band at 5.2 GHz, when the antenna efficiency was hugely decreased to reach a low level of 23% as depicted in Fig. 6.8.

6.4 Third Version: UWB Antenna Design with Dual Band-Notched

Although the filtering feature at the upper WLAN of 5.2 GHz was successfully accomplished, the useable spectrum from 5.5 to 14 GHz, in which the proposed antenna operates, is still very wide and may coexist with other systems that operate within the same frequency range, in which interferences are foreseen. Thus, another filtering is required to avoid other common interferences. To this end, another half hexagonal slot was also printed and combined with the previous half hexagonal slot on the antenna surface. This has finally made a shape of full hexagonal slot as indicated in Fig. 6.9. This dual band-notched design can be realised as follow-on to the foregoing single notched band antenna structure by providing an additional half hexagonal slot. The position of the second slot is placed at the top side of the radiator and then was easily joint with the down slot as depicted in Fig. 6.9. This newly added slot can work independently to achieve another notched band.

In this study, the dimensions and positions of both hexagonal slots should be adjusted in correspondence to the central frequency of lower WLAN at 5.2 GHz and the 10 GHz. Figure 6.9 presents the final layout of the UWB antenna with dual rejected band's features. One can note that the geometry of the radiator remains the same after adding the second slot. In fact, these two hexagonal slots act as two resonators that can be controlled independently for the desired notched frequency.

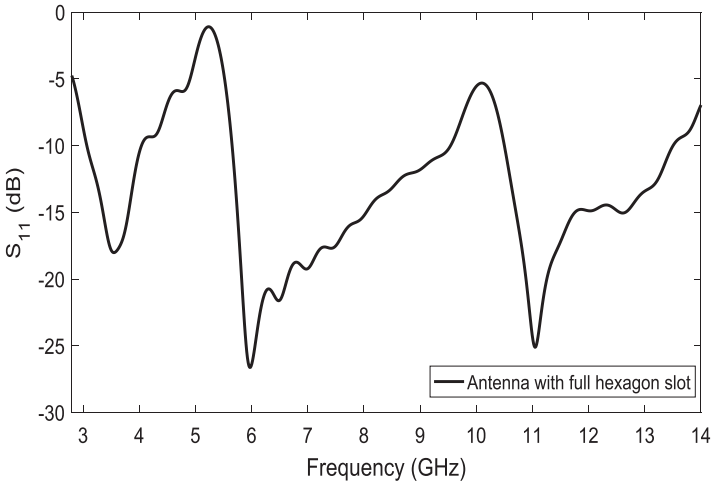

Fig. 6.10 The S11 of the proposed antenna with full hexagonal slot

6.4.1 Analysis of Dual Band-Notched Design

Performance of the dual band-notched design is predicted and analysed using CST simulator. Figure 6.10 presented the S11 of the proposed antenna. The antenna design with a full hexagonal slot shape exhibits two individual band-notcheds at the expected notched frequencies with excellent band-notch phenomenon. The effect on the rejection level of the proposed designs, including dual band-notched, is illustrated in Fig. 6.10. It is clearly seen that the rejection level of the first notched band design at 5.2 GHz outperforms the single notched band level at 10 GHz in terms of antenna S11. This antenna has come up with the advantage of having two filtering notches within the same antenna structure and size compared to previous design with single rejected band. This leads to not implement another filter to suppress the resonant frequencies and may accordingly result in less complexity, low cost and seamless circuit integration.

The input impedance of the proposed antenna with the inclusion of full hexagonal slot can be seen in Fig. 6.11. The antenna shows a resistance that oscillates to be around 50 Ω, except at the dual created rejected bands at 5.2 and 10 GHz, with resistance value at 800 and 150 Ω, respectively, and the reactance value that fluctuates from −3 to 2 Ω over the entire bandwidth, with the exception of the two filtering bands, whereby the values of −354 and 75 Ω correspondingly occurred. This again verifies the exploitation of the embedded slots as effective filtering approach.

To prove the usage of the embedded slot as an operational filtering method, the surface current distribution of the full hexagonal slot antenna at each notch frequency (5.2 GHz and 10 GHz) is analysed in Fig. 6.12. The surface currents mainly concentrate at the surrounding area of the corresponding slot at the each notch frequency in both cases. This implies that the neighbouring slit has little mutual

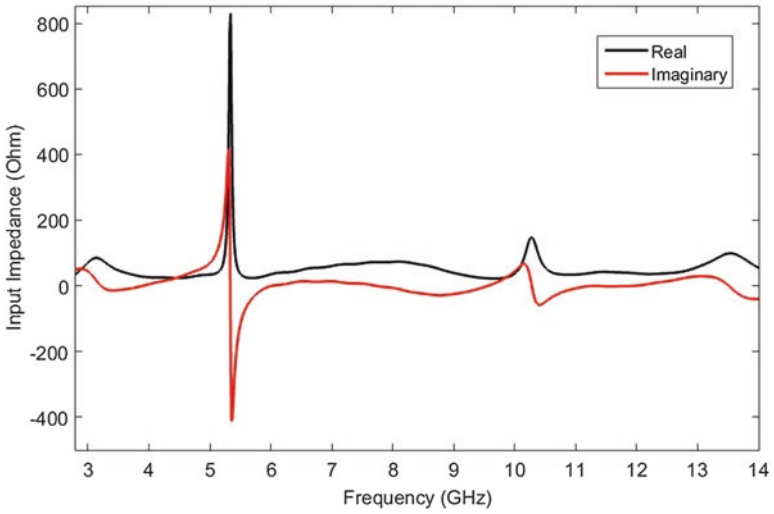

Fig. 6.11 The input impedance of the third antenna version with full hexagonal slot

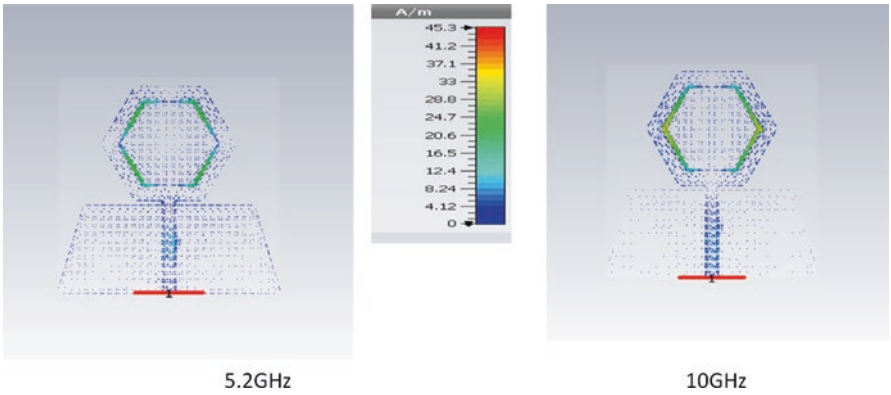

Fig. 6.12 Current surface for the full hexagonal slot antenna at 5.2 and 10 GHz

effect to the other in band-notch performance, which also confirms the corresponding behaviour of the other performances such as the S11 and input impedance in Fig. 6.12.

Figure 6.13 demonstrates the antenna gain and radiation efficiency. It can be noted that the gain increases gradually from 2.1 dBi to more than 5.6 dBi within the pass band, with a significant drop of −3.8 dBi and −2.4 dBi at the notch frequencies of 5.2 GHz and 10 GHz, respectively. The radiation efficient can also be seen falling down at the notch frequencies to be around 10% and 17%, while the antenna achieves a good efficiency ranges from 78% to 90% at the pass band as indicated in Fig. 6.13.

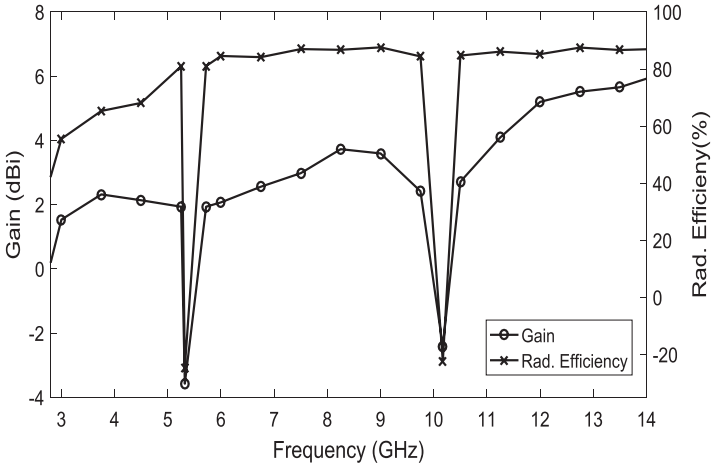

Fig. 6.13 The power gains and efficiencies of the full hexagonal slot design

The radiation pattern performances of dual notched antenna are shown in Fig. 6.14. The radiation patterns were produced at three bands, i.e. 3.5, 7.5 and 13 GHz, in which all the aggregated UWB spectrum ranges would be covered. Figure 6.14 displays the far-field radiation patterns in the two principal-plane pattern cuts, .i.e. E plane (*xz* plane) and H plane (*yz* plane) for the above-mentioned three bands. It should be noted that the proposed antenna accomplishes a relatively omnidirectional radiation in both *xz* and *yz* planes at these frequencies.

6.5 Conclusion

A new compact printed monopole antenna with a frequency band-notched function for UWB systems has been studied and investigated. Three antenna designs have been designed and analysed: firstly, a monopole antenna design with hexagon radiating shape with defected trapezoidal ground and stub on the feeding line was proposed to cover the UWB range from 3.2 to 14 GHz. Secondly, an etched half hexagonal slot was printed on the down side of the radiator, in which its main objective was to create a single rejected band at the upper WLAN of 5.2 GHz; thirdly, another half hexagonal slot was introduced at the top of the radiator to be joined together with the down slot and finally form a full hexagonal slot. This final antenna design with the full hexagonal slot was able to keep the same frequency range from 3.2 to 14 GHz, while dual band-notched at 5.2 and 10 GHz were sufficiently made. The three versions of the proposed antennas have demonstrated good performance and results in terms of S11, input impedance, current distribution, radiation pattern, gain and efficiency. The measured results agreed well with the simulation results. The proposed designs are shown to be able to achieve desired band-notched characteristics, making the design an attractive candidate for the UWB system applications.

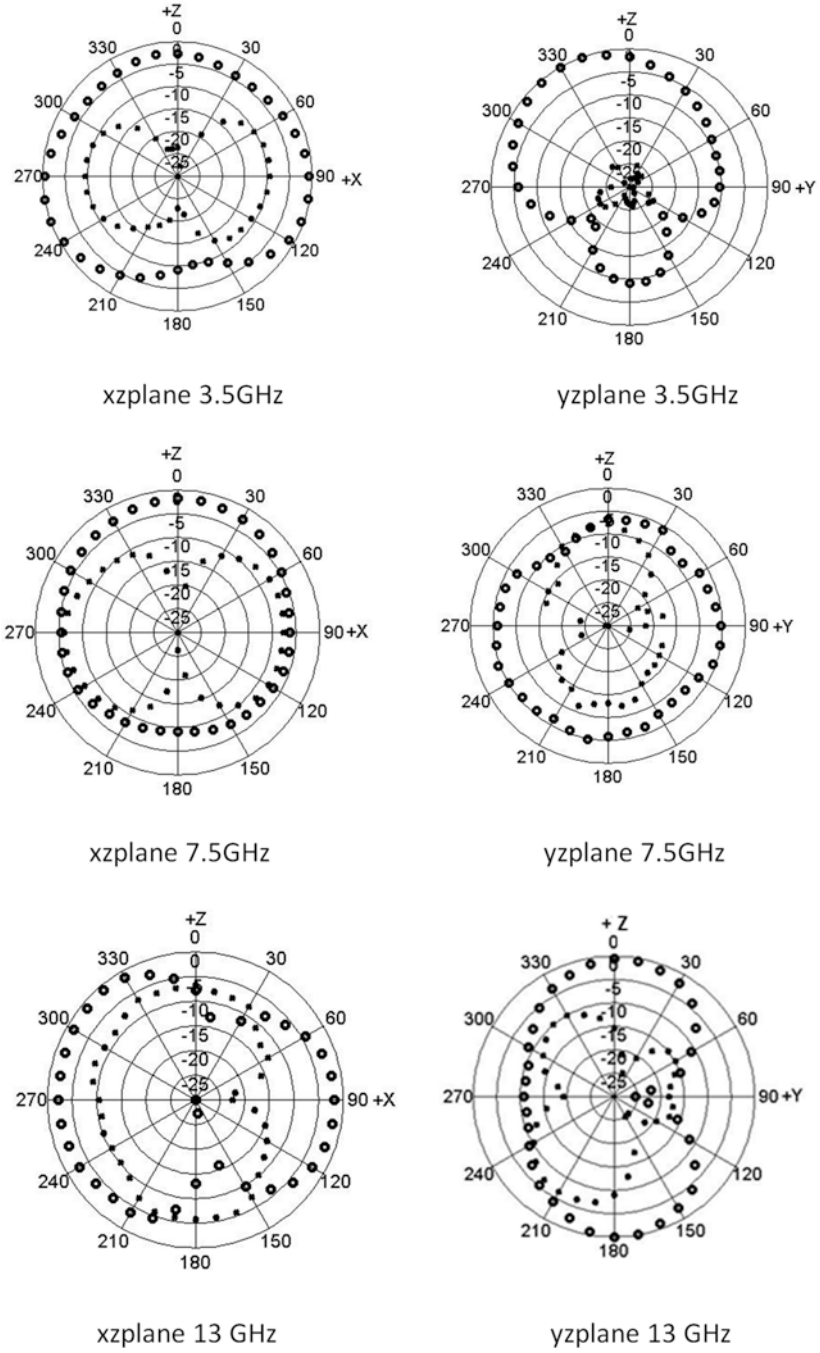

Fig. 6.14 Normalised antenna radiation patterns for two planes (*left*, *x*–*z* plane; *right*, *y*–*z* plane) at 3.5, 7.5, and 13 GHz. "ooooo" co-polarisation; "xxxxxx" cross-polarisation

Acknowledgements This work is carried out under the grant of the Fundacão para a Ciência e a Tecnologia (FCT – Portugal), with the reference number: SFRH/BPD/95110/2013.

References

1. I. Balasingham, R. Chávez-Santiago, J. Bergsland, T. A. Ramstad, E. Fosse, Ultra wideband wireless body area network for medical applications, in *International Symposium on Use of Advanced Technologies and New Procedures in Medical Field Operations – North Atlantic Treaty Organization*, Essen, 2010, pp. 1–24
2. A. Alarifi et al., Ultra wideband indoor positioning technologies: Analysis and recent advances. Sensors **16**(5), 707 (2016)
3. F. C. Commission, *Revision of Part 15 of the Commission's Rules Regarding Ultra-Wideband Transmission Systems*, no. FCC02–48. 2002, pp. 1–118
4. A. Locatelli et al., Highly directional planar ultra wide band antenna for radar applications, in *Proceedings of the 37th European Microwave Conference, EUMC*, No. October, 2007, pp. 1421–1424
5. B. Hammache, A. Messai, I. Messaoudene, M. A. Meriche, Reconfigurable triple notched-band ultra wideband antenna, in *International Conference on Innovations in Information Technology (IIT)*, 2016, pp. 8–12
6. C.-C. Lin, H.-R. Chuang, A 3-12 Ghz Uwb planar triangular monopole antenna with ridged ground-plane. Prog. Electromagn. Res. **83**, 307–321 (2008)
7. A. Singh, S. Singh, A novel CPW-fed wideband printed monopole antenna with DGS. AEU – Int. J. Electron. Commun. **69**(1), 299–306 (2015)
8. P.V. Naidu, R. Kumar, Design of CPW-fed dual-band printed monopole antennas for LTE/WIMAX/WLAN and UWB applications. Prog. Electromagn. Res. C **54**, 103–116 (2014)
9. S.K. Ghosh, R.K. Badhai, Printed monopole antenna for UWB and SWB with directional radiation characteristics and high F / B ratio, 2016, pp. 1590–1594
10. O.A. Safia, A. Omar, M. Nedil, CPW-fed UWB antenna based on packing congruent circles in a circular patch, no. 1, 2016) p. 3–5
11. M. Karamanoglu, M. Abbak, S. Simsek, A simple and compact CPW-fed UWB printed monopole antenna with defected ground structures, in *Electrical and Electronics Engineering (ELECO), 2013 8th International Conference on*, Bursa, 2013, pp 443–447
12. E. Sarbazi, M. H. Mirmozafari, A. Ghobadi, R. Shayanfar, B. Yousefi Darani, Planar ultra-wideband monopole antenna with band-notch performance, in *2011 IEEE International RF & Microwave Conference*, no., Seremban, 12–14 Dec 2011, pp. 282–284
13. R. Kshetrimayum, Printed monopole antennas for multiband applications. Int. J. Microw. Opt. Technol. **3**(4), 474–480 (2008)
14. K.P. Ray, S.S. Thakur, Printed annular ring with circular patch monopole UWB antenna, *Proceedings of 2012 International Conference Advances in Computing and Communications. ICACC 2012*, 2012, pp. 270–273
15. J.C. Jihak Jung, W. Choi, A small wideband microstrip-fed monopole antenna. IEEE Microw. Wirel. COMPONENTS Lett. **15**(10), 703–705 (2005)
16. X.J. Yang, L. Liu, S.W. Cheung, Y.Y. Sun, A simple UWB monopole antenna using half-elliptical radiator. 2013 Int. Work. Antenna Technol. iWAT **2013**, 145–149 (2013)
17. F.B. Zarrabi, Z. Mansouri, N.P. Gandji, H. Kuhestani, Triple-notch UWB monopole antenna with fractal Koch and T-shaped stub. AEU – Int. J. Electron. Commun. **70**(1), 64–69 (2016)
18. J. Acharjee, K. Mandal, S.K. Mandal, P.P. Sarkar, A compact printed monopole antenna with enhanced bandwidth and variable dual band notch for UWB applications. J. Electromagn. Waves Appl. **30**(15), 1980–1992 (2016)
19. R. George, A. Kaladharan, "A wideband bluetooth-UWB antenna with triband notched characteristics, in *2016 International Conference on Emerging Technological Trends [ICETT]*, 2016

20. C.T. Chuang, T.J. Lin, S.J. Chung, A band-notched UWB monopole antenna with high notch-band-edge selectivity. IEEE Trans. Antennas Propag. **60**(10), 4492–4499 (2012)
21. S.Y. Chen, Q.X. Chu, A reconfigurable notched-band UWB antenna, in *2016 IEEE Antennas Propagation Society International Symposium (APSURSI) 2016 – Proceedings*, 2016, pp. 1513–1514
22. Y. Shu, B. Yang, H. Qian, X. Luo, Compact UWB antenna with quad-notched bands. 2016 IEEE Antennas Propag. Soc. Int. Symp. APSURSI 2016 – Proc **81**, 1791–1792 (2016)
23. P. Moeikham, N. Chudpooti, and P. Akkaraekthalin, Printed Ulta-wideband antenna with 3.5/5.5 GHz band notching, in *2016 13th International Conference on Electrical Engineering/ Electronics, Computer, Telecommunications and Information Technology, ECTI-CON 2016*, 2016, **1**(1), 1–6
24. S. Koziel, A. Bekasiewicz, Fast geometry scaling of UWB band-notch antennas, *2016 21st International Conference on Microwaves, Radar and Wireless Communications MIKON 2016*, pp. 5–8, 2016
25. T. Pechrkool, T. Hongnara, S. Chaimool, P. Akkaraekthalin, K. Chung, A dual band-notched UWB monopole antenna with C-shaped slot and hairpin slot. IEEE 2013 Tencon – Spring, TENCONSpring 2013 – Conf. Proc **1**, 43–46 (2013)
26. N. Takemura, D. Kaneko, J. Suzuki, T. Takeda, T. Hiraguri, Design of UWB printed monopole antenna with short stub, *Proceedings 2016 International Symposium on Electromagnetic Compatibility – EMC Europe 2016, Wroclaw, Poland, 5–9 Sept 2016*, pp 566–569
27. CST-Computer Simulation Technology AG (2014)

Chapter 7
Miniaturized Monopole Wideband Antenna with Tunable Notch for WLAN/WiMAX Applications

Issa Elfergani, Abubakar Sadiq Hussaini, Jonathan Rodriguez, Abdelgader Abdalla, Ifiok Otung, Charles Nche, Mathias Fonkam, and Babagana M. Mustapha

7.1 Introduction

The rapid evolution in advanced multimedia communications has created the need for wideband or multiband antennas. These antennas would need to have a low profile, be compact, and be wideband in nature in order to be aligned with the requirements of new handsets and devices. Although wideband antenna technologies have undergone many significant developments, there are still a lot of challenges to solve in terms of practical design.

The structure of a planar monopole antenna is a promising applicant for wireless communication services due to several benefits such as compact volume, simplicity

I. Elfergani (✉) • A. Abdalla
Instituto de Telecomunicações, Aveiro, Portugal
e-mail: i.t.e.elfergani@av.it.pt

A.S. Hussaini
Instituto de Telecomunicações, Aveiro, Portugal

School of Information Technology & Computing, American University of Nigeria, Yola, Adamawa, Nigeria

J. Rodriguez
Instituto de Telecomunicações, Aveiro, Portugal

University of South Wales, Pontypridd, UK

I. Otung
University of South Wales, Pontypridd, UK

C. Nche • M. Fonkam
School of Information Technology & Computing, American University of Nigeria, Yola, Adamawa, Nigeria

B.M. Mustapha
Department of Electrical & Electronics Engineering, University of Maiduguri, Nigeria

I. Elfergani et al. (eds.), *Antenna Fundamentals for Legacy Mobile Applications and Beyond*, DOI 10.1007/978-3-319-63967-3_7

during the design/fabrication process, a broad frequency range, and an omnidirectional radiation pattern [1]. The printed monopole antenna is regarded as a special case of the microstrip antenna configuration, but with an infinite ground plane.

A printed monopole antenna (PMA) is basically produced by replacing the radiator above the ground plane with a planar sheet. Numerous different shapes and geometries of planar monopoles have been recently reported for use in many applications. To be more explicit, PMAs have been developed with significant features such as a broad bandwidth along with great ability to control the envisaged impaired radiation pattern and power gain [2, 3]. Moreover, the feature of low group delay deviation obtained with PMAs may make them an appropriate choice for use in pulse-based systems such as ultrawideband (UWB), which has recently received great attention from both academia and industry.

7.1.1 Techniques to Enhance the Monopole Antenna Bandwidth

Owing to the above-mentioned advantages of printed antennas, several interesting designs of printed monopoles with a wide bandwidth have been recently demonstrated [4–20]. Numerous procedures have been proposed to improve the bandwidth of planar monopole antennas, which include embedding slots [7–11]; a truncated ground plane approach [12]; a monopole antenna with a T-shape [5, 13]; employing a defected ground structure (DGS) [14, 15]; exploiting PGK and CPGK fractal shapes [16] with a notched ground plane and a new arc-shaped strip [17]; and employing a radiator of different shapes such as rectangles, circles, triangles, squares, annual rings, ellipses (both horizontal and vertical), pentagons, and hexagons [18]. The bandwidth may improve by introducing tapered transitions and an inset feed [19], with addition of a chordal strip to the outer crescent shape [20].

7.1.2 Techniques to Mitigate Interference in UWB Systems

In spite of the fact that the above-mentioned PMA designs accomplish a broader bandwidth, the defined frequency band for UWB) systems [1–20] may still cause interference with the existing narrow wireless communication systems, such as the wireless local area network (WLAN) IEEE802.11b/g and IEEE802.11a standards (2.4–2.485 GHz), the Worldwide Interoperability for Microwave Access (WiMAX) IEEE802.16 bands (2.5–2.69 GHz, 3.3–3.7 GHz), the IEEE 802.11j WLAN band operating at 4.9–5.0 GHz and 5.03–5.091 GHz, and the IEEE 802.11a WLAN band operating at 5.15–5.35 GHz and 5.47–5.725 GHz.

To solve this problem, several designs of printed monopole UWB antennas incorporating rejected frequency bands have been proposed and designed [11, 21–35]. Numerous approaches were used to mitigate such interference within the spectrum of UWB systems—for example, inserting various shapes of slots into the

radiating elements [11, 21–24], generating slots in the ground plane [25, 26], embedding slots into the feeding strip [27], parasitic elements, electromagnetic band gap (EBG) structures [28], using a DGS [29, 30], employing the EBG and DGS techniques simultaneously [31, 32] and adopting frequency selective surfaces (FSS) [33]. Another popular method) is to use various types of resonators on the other side of the substrate [34, 35].

7.1.3 Tuning the Created Reject Bands

The antenna designs in references [11, 21–35] have dealt with the issue of interference within the UWB spectrum, caused by coexisting WLAN, WiMAX, and Long-Term Evolution (LTE) systems. Moreover, such antenna designs, along with the created band notches, have contributed significantly to the market share of the legacy antenna devices and will continue to play a role as we head toward 5G and beyond, which will require antenna characteristics that are low in power and support high data rate communications.

However, these antennas [11, 21–35] have fixed rejected frequency bands, which in turn will not allow their geometry structures to be modified once fabricated. Thus, one way to overcome this issue is to tune/reconfigure the created notches, while keeping the frequency range as well as the antenna geometry without changing/modifying it.

Recently, there has been a significant drive toward designing a UWB antenna with tunable/reconfigurable rejected frequency bands. The most common method to tune the antenna is discrete tuning by using a PIN diode [36–38] and/or continuous tuning by employing varactor diode [39–41] techniques.

This has allowed the antenna to adaptively switch to the notched band of the precise resonant frequency whenever interference from other systems takes place. Regardless of the issue of interference within the UWB antenna performance, the filtering feature will be initiated. Thus, the functionally of the UWB antenna with a created notch will be enhanced when the possibility of a tuning mechanism is exploited.

7.2 Comparison with Previous Work

Surveying the previous published work on relevant antenna designs in references [2, 4, 5, 7–10, 12, 13, 15], it was concluded that these were engineered for the universal mobile telecommunications system (UMTS) band (1.92–2.17 GHz), IEEE 802.11 a/b/g (2.4–2.485 GHz, 5.15–5.35 GHz), and lower band UWB (3.1–4.8 GHz). In this work, a compact monopole antenna is presented, where the impedance bandwidth can be improved to cover frequency bands from 1.5 to 5.5 GHz. This gives the proposed antenna a significant advantage over the previously mentioned work [2, 5, 7–10, 12, 13, 15], with the capability to operate over additional wireless standards such as GPS/L1 (1.565–1.585 GHz), the Iridium satellite band (1.616–1.6265 GHz), the personal communications service (PCS) band (1.85–1.99 GHz), the digital cellular service

(DCS) band (1.71–1.88 GHz), the UMTS band (1.92–2.17 GHz), IEEE 802.11 a/b/g (2.4–2.485 GHz, 5.15–5.35 GHz), and lower band UWB (3.1–4.8 GHz).

Moreover, the antenna designs in references [11, 17–35] cannot concurrently cover mobile and UWB applications; in fact, the results in references [7–20] are only capable of operating in UWB applications. Thus, the proposed antenna design has the additional benefit of covering both mobile and UWB applications, unlike the work described in references [7–20].

On the other hand, the work described in references [11, 21–35] shows several UWB antenna designs with rejected frequency bands either in the WiMAX IEEE802.16 bands (2.5–2.69 GHz, 3.3–3.7 GHz), the IEEE 802.11j WLAN band operating at 4.9–5.0 GHz and 5.03–5.091 GHz, or the IEEE 802.11a WLAN band operating at 5.15–5.35 GHz and 5.47–5.725 GHz. For instance, references [11, 22] show UWB antenna structures including the rejected frequency bands in the WiMAX spectrum (2.5–2.69 GHz, 3.3–3.7 GHz), while references [23, 26, 28, 29, 32–34] demonstrate UWB antenna designs with frequency notches in the WLAN band operating at 5.15–5.35 GHz and 5.47–5.725 GHz and/or joining both the WiMAX IEEE802.16 bands (2.5–2.69 GHz, 3.3–3.7 GHz) and the IEEE 802.11a WLAN band operating at 5.15–5.35 GHz and 5.47–5.725 GHz, as in references [21, 25, 27, 30, 31, 35].

However, one can note that none of the antenna designs in references [11, 21–35] can mitigate the interference that may take place at the (2.4–2.485 GHz) WLAN standard. To this end, this chapter documents a compact reconfigurable rejected band monopole antenna that accomplishes size miniaturization as well as having the capability to operate over the mobile part of the UWB spectrum at the same time, except in the 2.4–2.485 GHz band of WLAN and the 3.3–3.7 MHz band of WiMAX.

From the tuning perspective, unlike the results reported in references [36–41], the present antenna design has the additional feature of covering mobile and UWB applications with a wider continued rejected band tuning range compared to references [36–40] and operating in other existing wireless bands such as GPS/L1 (1.565–1.585 GHz), the Iridium satellite band (1.616–1.6265 GHz), the PCS band (1.85–1.99 GHz), and the DCS band (1.71–1.88 GHz), in contrast to references [36, 41].

To sum up, designing a compact antenna that is capable of covering both mobile and UWB applications with the targeted and desired notch is the preferred engineering design aligned with market interests. However, in viewing the work described in references [4–41], it should be noted that none of those antenna designs have met these criteria, as they can only offer either mobile or UWB spectrum bandwidth. To this end, a compact monopole antenna with a tunable notch is studied and investigated in this chapter. This work is the improved version of the design proposed in references [11, 15]. In contrast to reference [11], the idea of electronically switching the created rejected band has been realized. This has been implemented by simply allocating a varactor device in the optimum location exactly between the two chorded crescent shapes. By means of altering the capacitance value of the varactor from 0.25 to 10.5 pF, the rejected band can be shifted

downward over a broad frequency range from 3.5 to 2.4 GHz to cover the WLAN IEEE802.11b/g and IEEE802.11a standards (2.4–2.485 GHz) and the WiMAX IEEE802.16 bands (3.3–3.7 MHz).

7.3 Antenna Design Structure and Procedure

The configuration and geometry of the proposed antenna is depicted in Fig. 7.1. It consists of two chorded crescent shapes, and it has some similarities to our previous work [11, 15]. Both shapes are directly printed over an FR4 dielectric substrate with relative permittivity of ε_r = 4.4 and a loss tangent of 0.017, with no ground plane directly underneath it. The substrate thickness is 0.8 mm. A microstrip line with

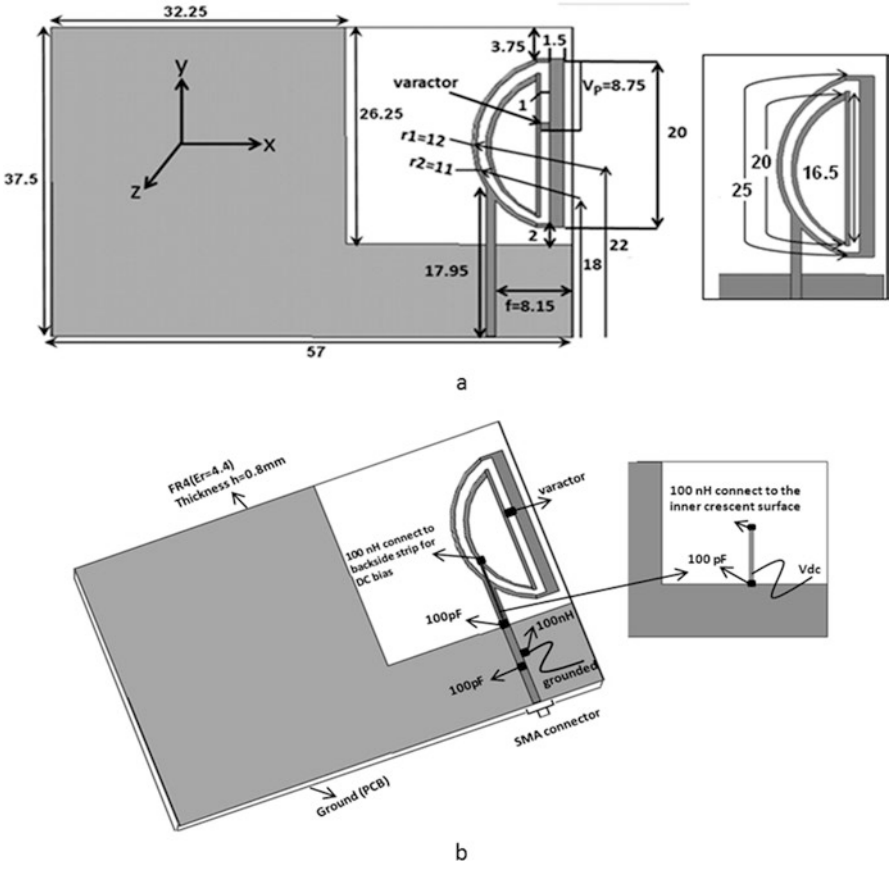

Fig. 7.1 Basic antenna structure: (**a**) top view; (**b**) bottom view [42]

dimensions of 17.95 × 1 mm was utilized to feed the printed patch. It should be noted that the defected area size of 24.75 mm × 26.25 mm located on the top of the ground plane was introduced for improving impedance matching at the input port of the antenna.

7.3.1 *Methods to Improve the Bandwidth of the Proposed Monopole Antenna*

In order to enhance the bandwidth of the proposed antenna, several techniques were exploited in this study. Initially, the ground plane of the proposed antenna with only crescent shapes was cut, as shown in Fig. 7.2. The technique of the defected ground plane effectively contributed to improving impedance matching across the operating frequency band from 1.7 to 3.1 GHz, as shown in Fig. 7.2. Secondly, introducing a chordal strip to the crescent shape to form the full outer chorded shape also helped in enhancing the antenna bandwidth, which, in turn, makes the proposed band operate over a broad bandwidth range from 1.5 to 5.5 GHz, as depicted in Fig. 7.2.

The full dimensions of the present antenna are 57 mm × 37.5 mm, which are ideal for applications in mobile devices. As can be seen from Fig. 7.2, the broad impedance bandwidth features of the proposed structure were accomplished by two procedures: firstly by cutting a square part of the antenna PCB exactly underneath the radiator, and secondly by introducing a chordal strip to the outer crescent shape.

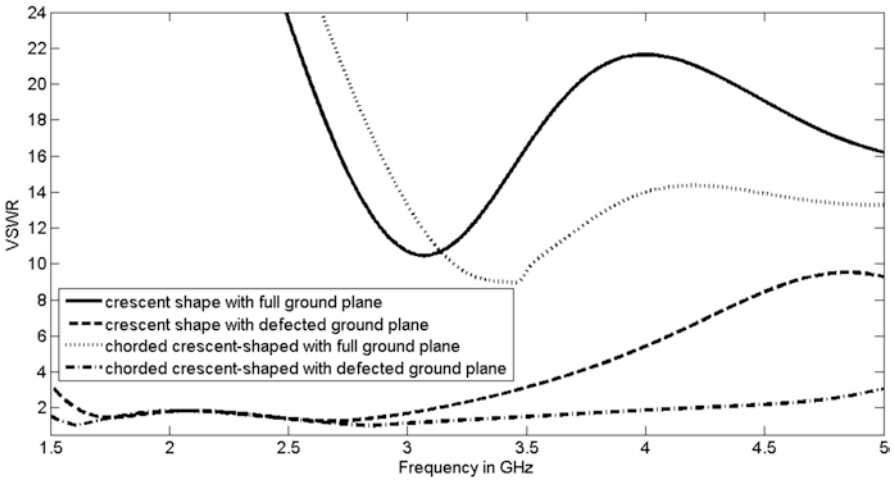

Fig. 7.2 Simulated VSWR of the crescent and chorded crescent-shaped proposed antenna with and without a defected ground plane

7.3.2 *Avenue to Create the Rejected Band of the Proposed Monopole Antenna*

The notched band was generated by printing an inner chorded crescent shape together with an outer chorded crescent shape over the RF4 substrate, as indicted in Fig. 7.3. To conclude this, the printed parasitic inner chorded crescent shape had a length of 36.5 mm, which is equivalent to half a wavelength at 4.25 GHz. Consequently, this design structure performs as a band stop filter to reject the resonant frequency around 4.25 GHz, as indicated in Fig. 7.3. Figure 7.3 demonstrates the simulated VSWR for the proposed antenna with only the outer chorded crescent shape as a stand-alone and also with both inner and outer shapes together. It can be clearly seen that the proposed antenna is capable of operating over a wide frequency range from 1.5 to 5 GHz, while rejecting the frequency at 4.25 GHz. This enables the antenna to work over several mobile services such as GPS, DCS, PCS, UMTS, WLAN, LTE, and WiMAX.

7.4 Current Surface of the Unloaded Printed Monopole Antenna

To suggest the best possible location for the varactor, the surface currents of the unloaded antenna with only the outer chorded crescent shape, and with both the outer and inner chorded crescent shapes, were studied and verified, as depicted in Fig. 7.4. Three particular operating frequencies—namely 1.6, 2.7, and 4.25 GHz, covering the aggregate bandwidth—were selected.

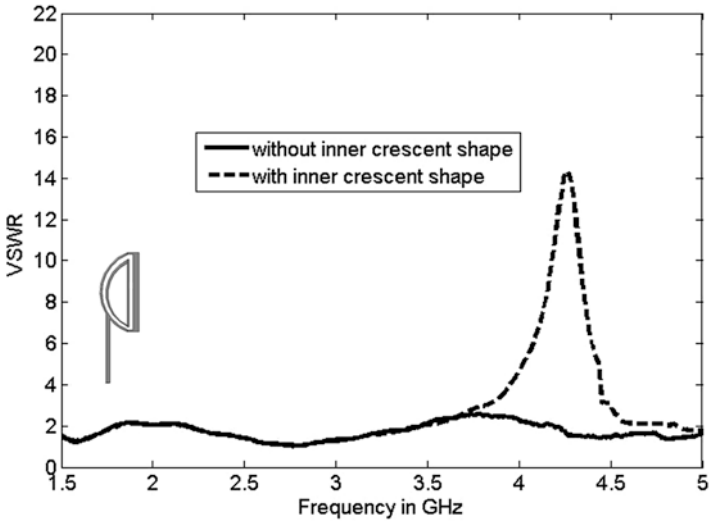

Fig. 7.3 Simulated VSWR with the inner and outer chorded crescent shapes

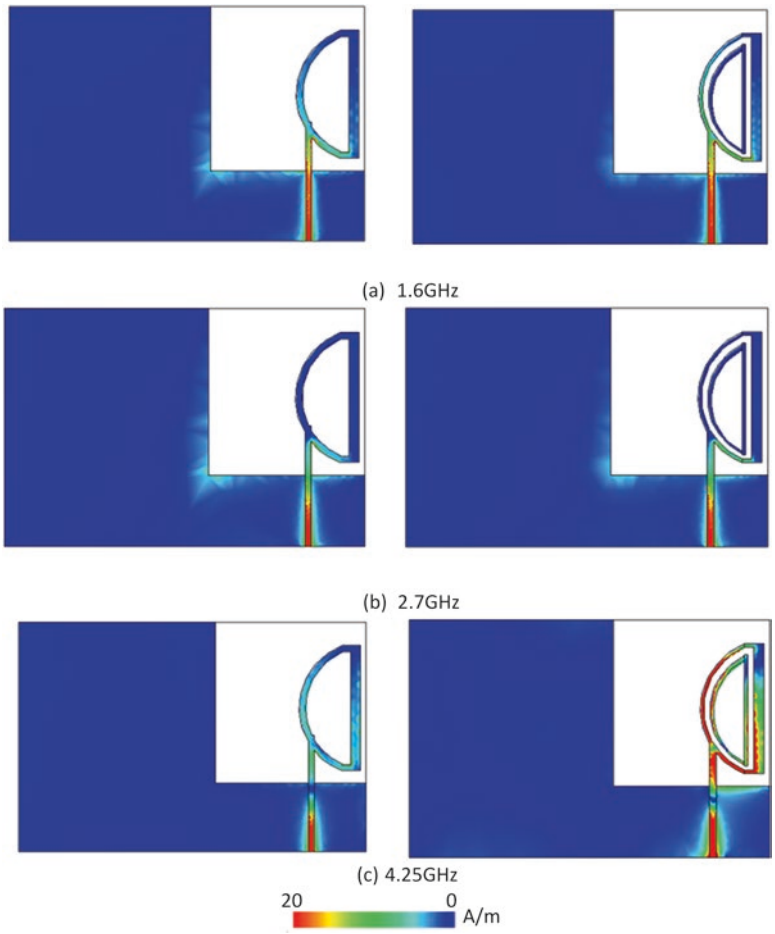

Fig. 7.4 Current surface for the outer chorded crescent shape and both chorded crescent shapes at (**a**) 1.6 GHz; (**b**) 2.7 GHz; and (**c**) 4.25 GHz

As can be clearly realized, the currents for the designated resonant frequencies of 1.6, 2.7, and 4.25 GHz for the outer chorded crescent-shaped proposed antenna are predominantly induced in the feed strip and almost negligible over the PCB. This agrees well with the investigation of the antenna ground plane size in the previous section. In addition, this is an indication to prove that extending the ground plane size does not affect impedance matching. By doing the current surface examination of the antenna with the inner and outer chorded crescent shapes together, it was observed that the inducing currents are almost the same at 1.6 and 2.7, which indicates that both proposed antennas maintain the same performance, as depicted in Fig. 7.4a, b. It was certainly noted that the maximum currents take place mainly near the antenna feed line.

However, at 4.25 GHz, as presented in Fig. 7.4c, the second version of the present antenna displays strong electric currents concentrated in the inner and outer chorded crescent shapes and feed line areas of the radiator compared with those seen at other operating frequencies; this again verifies the finding of adding the inner chorded crescent shape to create the rejected band. Moreover, it is recommended that the varactor be positioned in the part where less current is induced. This will help in not impairing the antenna performance in the desired operating frequency band.

7.5 Tuning Methods for the Rejected Bands

Reconfigurable rejected bands exhibit various advantages over their conventional counterparts of fixed rejected bands. The antenna with the tuned notched frequencies can be used to mitigate interference over multiple frequency bands. This will significantly contribute to size reduction and minimizing the cost of the hardware. The needs for reconfigurable notched band antennas are becoming ever more widespread to match the increasing demand for channel interference mitigation approaches over a wide frequency range spectrum. In recent years, novel communication architectures have been developed (software defined radio, MIMO, and cognitive radio) that will alleviate the stress on the wireless networks and open up new opportunities for drastic improvements in the bandwidth and efficiency of the wireless network. Thus, in order for such architectures to be implemented, antennas capable of wideband operation are required. However, the defined frequency band for UWB systems may cause interference with the existing narrow wireless communication systems, as mentioned in previous sections. Therefore, wideband antennas with a fixed rejected band can be tuned to operate over a larger range of frequencies while reconfiguring the notched band over a desired range, thus effectively enhancing the antenna performance. Generally, frequency reconfigurability of antenna can be achieved using the following techniques.

7.6 Continuous Tuning

In this kind of tuning, the antenna is capable of achieving a wide frequency range of operation. In order to achieve continuous tuning, a frequency reconfigurable antenna usually employs structural changes, material changes, or reactive loading. The switching mechanism most commonly used to achieve reactive loading is a varactor diode. Since varactors are voltage devices, they have very low power consumption, but they sometimes require relatively high DC voltages.

Varactor Diode: This diode operates with a reverse bias that corresponds to the capacitance variation. With a change in bias, the capacitance induced at the radiating edge is changed, resulting in a change in the effective electrical length of the

patch. This allows for continuous tuning of the operating frequency. On the other hand, increasing the reverse bias voltage decreases the resultant capacitance and shifts the frequency band.

7.6.1 Discrete Tuning

By utilizing this type of reconfigurability, the antenna is capable of a finite number of states or operating bands. With the purpose of achieving discrete tuning, a frequency reconfigurable antenna typically employs some sort of switching mechanism. The switching mechanism most commonly used to accomplish discrete tuning is a PIN diode.

PIN Diode Switching: A PIN diode is situated on the appropriate place over the patch to alter the current paths on the patch. When the diode is OFF, currents travel around the slot and the antenna operates at a lower frequency, whereas when the diode is ON, the effective length of the patch is shorter and the antenna operates in a higher frequency band.

The varactor diode was chosen to be used as a tuning device to tune the created rejected bands in this study. Note that the tunability of the antenna is achieved in the simulation by tuning the diode. By checking the current surface of the present design, the location of the varactor is optimally chosen in order to accomplish maximum reconfigurability with less perturbation of the antenna matching. The junction capacitance of the varactor varies against the reverse bias voltage applied, and these different capacitive loadings correspond to different electrical lengths and thus different resonant frequencies.

In the simulation model, the varactor diode was modeled with an RLC boundary sheet with varying capacitance values over the desired range. Tellingly, the varactor diode has a variable capacitance. Depending on the capacitance range of the practical diode, the diode can be simulated with these values.

7.7 Parametric Studies

Prior to the fabrication process—and to obtain a sufficient and ideal antenna size, and to maintain good impedance matching over the desired wide frequency range defined within this study, including the targeted rejected bands—a comprehensive parametric analysis was carried out. Three parameters were selected for this study: the ground plane size, the strip feed position, and the varactor location between the two chorded crescent shapes. These parameters are deemed the most sensitive parameters in determining the targeted frequency bands along with the desired notches. Each simulation was run with only one parameter varied, while the other parameters stayed unchanged. Both fixed and variable parameters are shown in Fig. 7.1.

7.8 Influence of the Ground Plane Size

The effect of the ground plane was examined by checking the variations in the VSWR against the size of the ground plane for the selected capacitance values (0.5 and 10 pF). Figure 7.5 shows the effect of a ground plane with four selected sizes together with the mentioned capacitance values: 21 × 37.5 mm^2 ($0.25\lambda_0 \times 0.385\lambda_0$), 42 × 42 mm^2 ($0.5\lambda_0 \times .5\lambda_0$), 57 × 37.5 mm^2 ($0.68\lambda_0 \times 0.385\lambda_0$), and 84 × 84 mm^2 ($\lambda_0 \times \lambda_0$). As can be noted in Fig. 7.5, the target frequency range and notched band cannot be achieved when the ground plane is set to 21 × 37.5 mm^2 and 42 × 42 mm^2 for these capacitance values. On the other hand, the entire frequency range with a target notched band is obtained when the ground plane is set at 57 × 37.5 mm^2 and 84 × 84 mm^2. Even when the ground plane is 84 × 84 mm^2, the desired frequency range with tunable notches can be accomplished for both capacitance values (0.5, 10.5 pF), but this is at the cost of the antenna size. It should be noted that the DGS plays a significant role in improving impedance matching across the desired operating bands, but the actual ground plane dimensions are minimized as far as possible to fit the space available inside a transceiver casing. Therefore, the 57 × 37.5 mm^2 ($0.68\lambda_0 \times 0.385\lambda_0$) ground plane size was selected as optimal, since it satisfies the entire tuned frequency range with the required rejection bands of WLAN (2.4–2.485 GHz) and WiMAX (3.2–3.6 GHz) for all capacitance values.

7.8.1 Effect of the Feed Line Position

The influences of the feeding position are depicted in Fig. 7.6. In this study, the feeding position is initially set to the edge of the antenna structure, which corresponds to 5.15 mm, then it is moved in steps of 1 mm closer to the center of the crescent structure, which is at 9.15 mm. As can be seen for the lower resonant mode (1.5–3.5 GHz), the impedance bandwidth remains essentially the same for 0.5 and 10.5 pF. At the higher resonant mode (3.5–5 GHz), an unacceptable mismatch will occur when the feeding position is set closer to the edge, which is below 8.75 mm. Therefore, this feeding position at 8.75 mm can be taken as the best value for both capacitance ranges (0.5 and 10.5 pF) to obtain the desired frequency range with the targeted notch.

7.9 Effect of the Varactor Location Between the Two Shapes

The varactor position is one of the most sensitive parameters in this study. Its variation can significantly impair impedance matching over the desired operating frequency band with a tunable notch for both 0.5 and 10 pF, as illustrated in

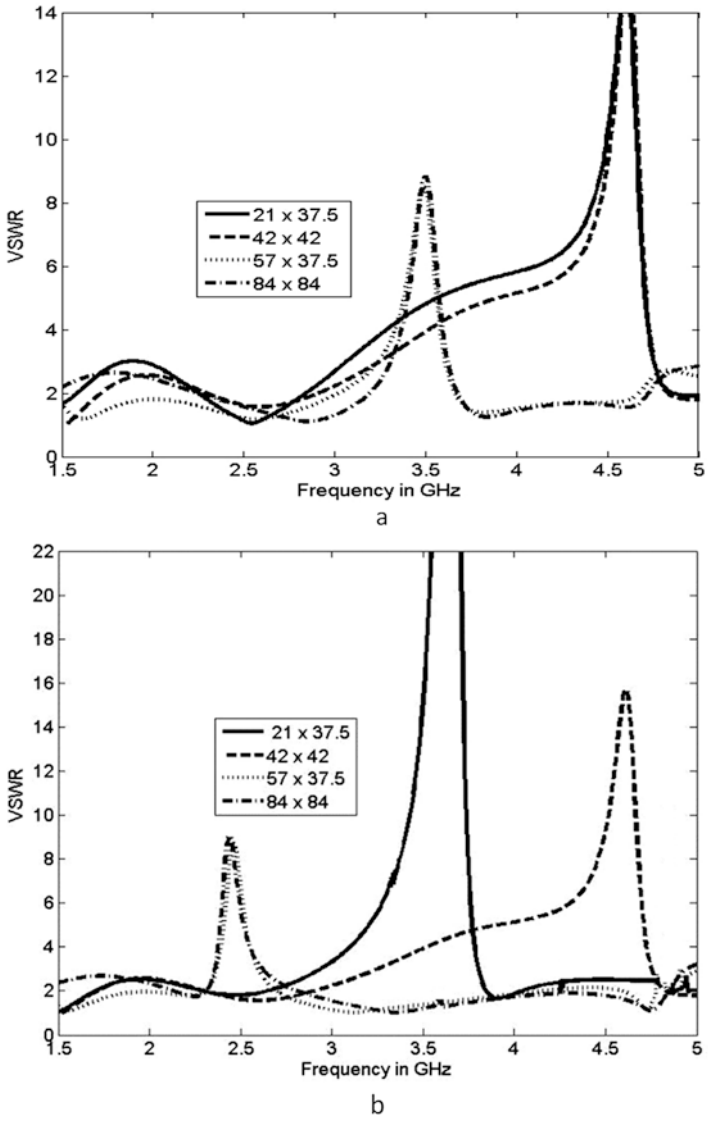

Fig. 7.5 Simulated VSWR corresponding to the variation parameters of the ground plane with a loaded capacitor: (**a**) 0.5 pF; (**b**) 10.5 pF

Fig. 7.7. This parameter is investigated by starting from 6.75 mm and increasing to 11.75 mm in 1 mm increments. It is clear that when it is at 9.75, 10.75, and 11.75 mm, the antenna does not satisfy the frequency band with the notch of interest. As it is decreased further (vp = 8.75 mm), good impedance matching can be achieved over the band at VSWR $\leq$2 for both capacitance values (0.5 and

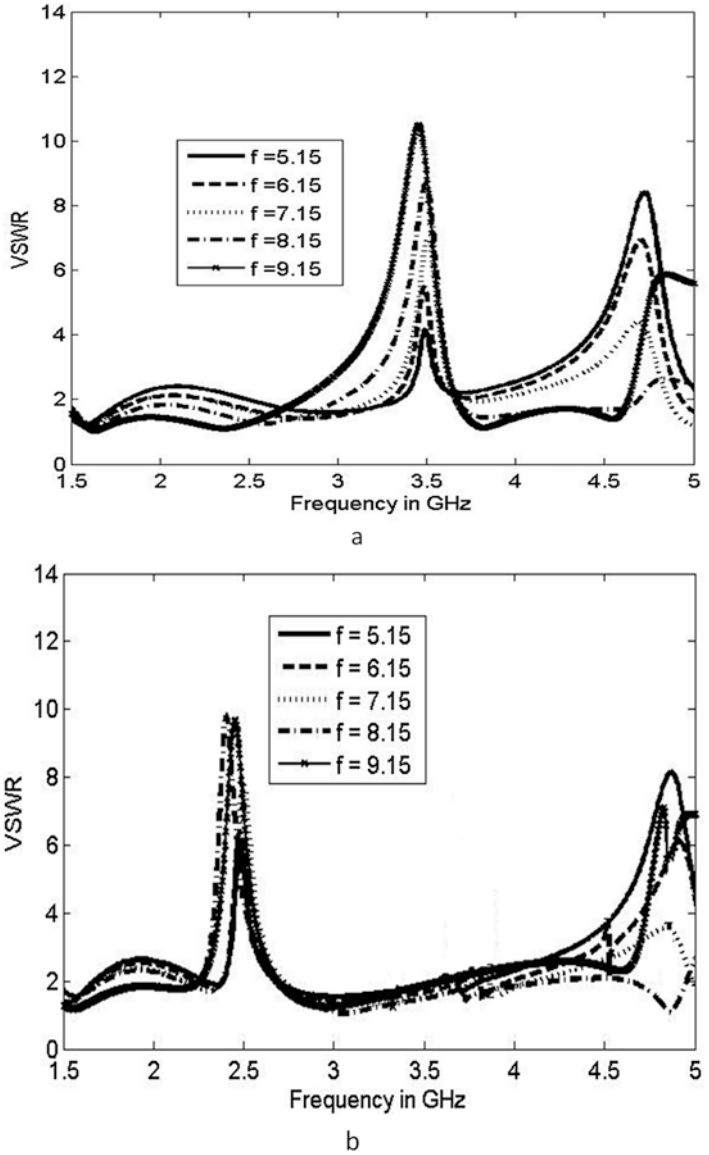

Fig. 7.6 Simulated VSWR corresponding to the variation parameters of the feeding position with a loaded capacitor: (**a**) 0.5 pF; (**b**) 10.5 pF

10.5 pF). By further decreasing it to 7.75 and 6.75 mm, an impedance mismatch will occur in the upper frequency resonance mode. This leads to the conclusion that for the best impedance matching, the varactor position should be kept at 8.75 mm.

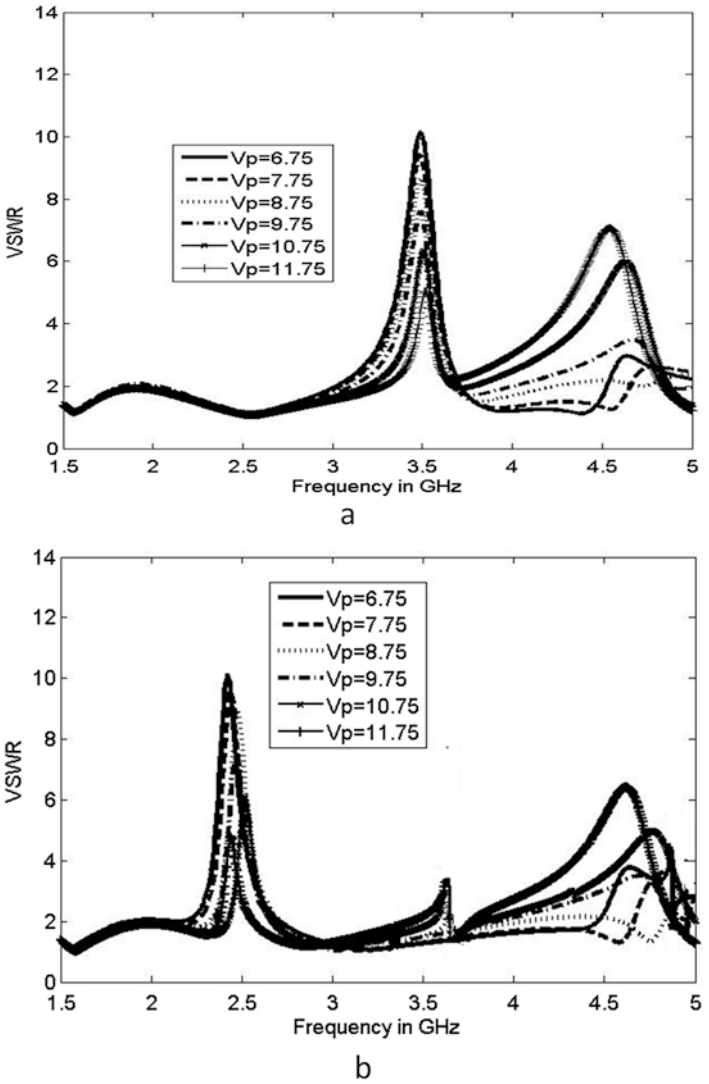

Fig. 7.7 Simulated VSWR corresponding to the variation parameters of the varactor location with a loaded capacitor: (**a**) 0.5 pF; (**b**) 10.5 pF

7.10 Simulation and Measurement Results

As previously mentioned in Sect. 2.2, by adding a parasitic inner chorded crescent shape with a length of 36.5 mm (equivalent to half the wavelength of 4.25 GHz), this enables the structure to perform as a resonator to reject the frequencies around the 4.25 GHz band. However, the rejected frequencies do not meet the objective of this study; as a result, a varactor is needed to shift the created notch downward to meet the goal of this work. With the proposed geometry, as shown in Fig. 7.1, the

outer and inner shapes are completely separated and no short circuit point exists in order to generate a DC potential difference across the varactor diode for tuning purposes. This also helps to accommodate the varactor at a fixed location between the two chorded crescent shapes for tuning the created rejection band at 4.25 GHz.

Figure 7.8 illustrates the simulated VSWR for the full assembly of the proposed antenna (*inner and outer shapes*). It is worth observing that when the capacitance value of the attached capacitor was varied from 0.25 to 10.5 pF, this made the rejected band shift down from 3.87 GHz to 2.38 GHz. All of the simulations described were performed using Ansoft HFSS [43]. For more explanation, Fig. 7.8 clearly displays a notched band from 3.28 to 3.65 GHz when the antenna is loaded with 0.5 pF, and from 2.42 to 2.55 GHz when it is loaded with 10 pF. This is effective to omit undesirable signals from WLAN standards employing the band of 2.4–2.485 GHz and WiMAX standards in the band of 3.3–3.7 GHz.

For validation purposes, the created rejection band was tuned by using a varactor diode with a suitable DC bias circuit. The tuning circuit utilizes the varactor diode BBY52–02 W, with a wide tuning capacitance from 0.25 to 10.5 pF over a 0–15 V reverse bias voltage range. It should be noted that the DC bias components are fitted on the back side of the ground plane, as indicated in Fig. 7.9. A 100 nH radiofrequency choke (RFC) was utilized to isolate the DC voltage from the RF signal. This kind of inductor has some promising features such as a high Q (>40) at high frequency, a tolerance of ±5%, and chip inductors featuring a monolithic body made of low loss ceramic, wound with wire to achieve an optimal high frequency performance. Two chip capacitors with a value of 100 pF were also used in order to provide DC blocking in the microstrip feed line and DC isolation of the short-circuited back strip, as shown in Fig. 7.9. These capacitors also have several good properties, including being small in size and multilayer, with a high Q (>40), a tolerance of ± 0.25%, and an ultralow ESR. The fabricated antenna model, along with the varactor diode and other passive components, is depicted in Fig. 7.9.

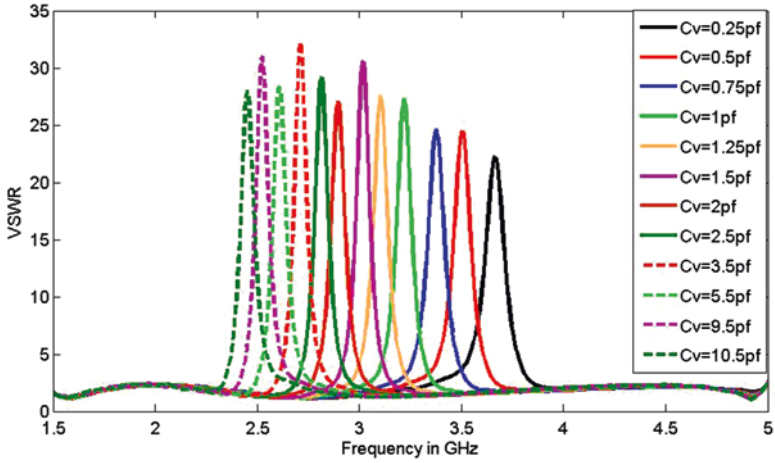

Fig. 7.8 Simulated VSWR with variable capacitor (from 0.25 to 10.5 pF) loading

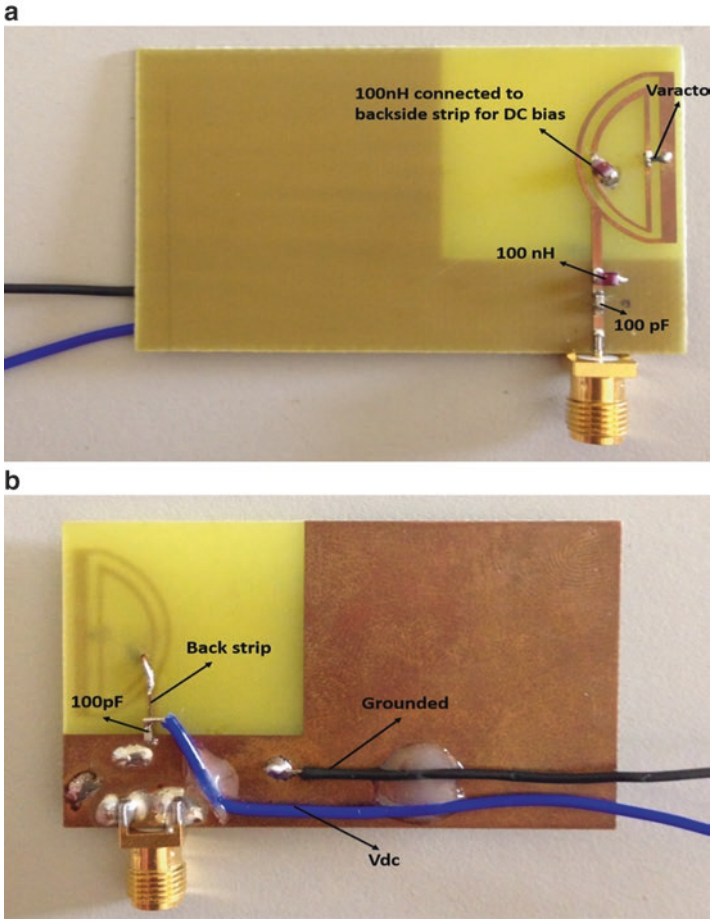

Fig. 7.9 Antenna prototype with a DC bias circuit: (**a**) top view; (**b**) bottom view

One can note that by changing the DC bias of the exploited varactor over the values of 5 V and 11 V, the rejected frequency band is reconfigured to suppress the bands of WLAN (2.4–2.485 GHz) and WiMAX (3.3–3.7 MHz), as presented in Fig. 7.10. A satisfactory continuously tunable rejected band occurs at all intermediate bias voltages.

The measured power gains in both scenarios of the proposed design (with and without the varactor) are illustrated in Fig. 7.11. From Fig. 7.11, it is noticeable that in the case of the loaded varactor, the notches are shifted downward when the DC values are varied from 5 and 11 V, while the power gain does not alter substantially. The antenna without inclusion of the varactor demonstrates a power gain of 2.8 dBi at the notch band center frequency of 3.5 GHz and 1.9 dBi at 2.48 GHz. On the other hand, when the antenna is loaded with a varactor, the peak antenna gain at 5 V DC excitation is reduced to −9 dBi and to −7.5 dBi at 11 V. This indicates that there is approxi-

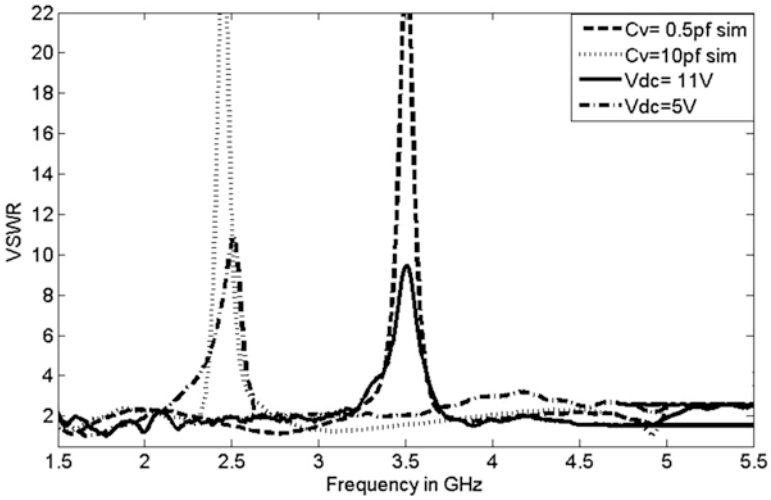

Fig. 7.10 Simulated and measured VSWR for the proposed loaded varactor antenna

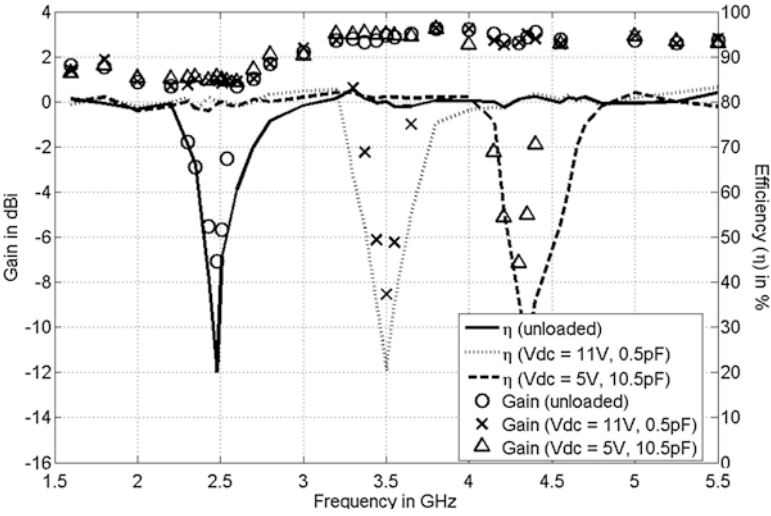

Fig. 7.11 Measured peak gain and radiation efficiency of the proposed antenna

mately 11.8 and 9.4 dB of gain suppression for the DC of 5 V and 11 V, corresponding to equivalent fixed lumped element capacitors of 0.5 and 10 pF, respectively.

The radiation efficiency of the proposed antenna is shown in Fig. 7.11. The Wheeler cap method is exploited here to investigate the antenna radiation efficiency. This method is considered the most common method to measure efficiency in practice [44–46]. From Fig. 7.11, it can be seen that the proposed antenna has achieved acceptable efficiency values, which are more or less around 80% over the aggregated bandwidth, namely from 1.5 to 5 GHz, except in the notch bands at 4.25 GHz

in the case of the unloaded antenna and 3.5 GHz/2.4 GHz in the loaded antenna paradigm, where the efficiencies dropped to below 22%.

Figure 7.12 shows the simulated and measured far-field radiation patterns. The simulated radiation patterns were generated with the aid of HFSS software, while the measured ones were carried out in a far-field anechoic chamber. In the measure-

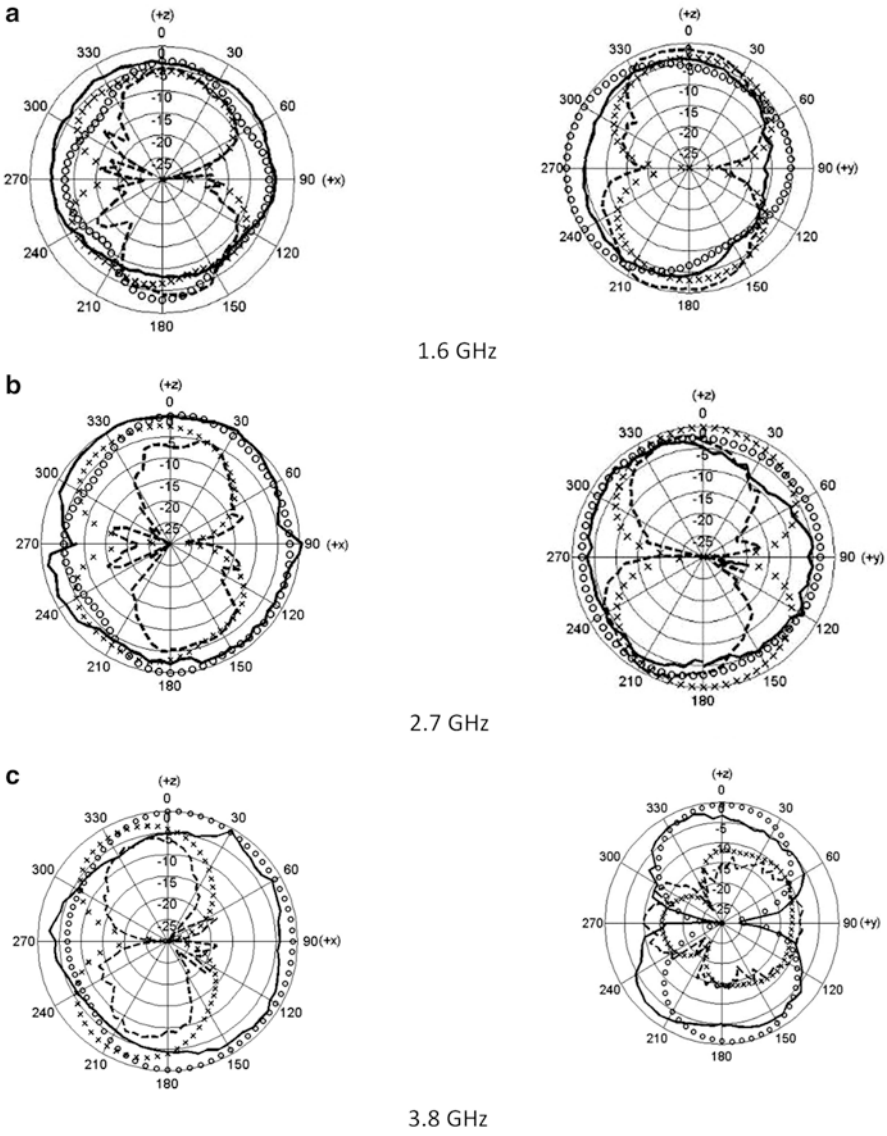

Fig. 7.12 Simulated against measured normalized antenna radiation patterns for two planes (*left*: *x–z* plane, *right*: *y–z* plane) at (**a**) 1.6; (**b**) 2.7; and (**c**) 3.8 GHz. "– – –" simulated co-polarization, "+++++" simulated cross-polarization, "——" measured co-polarization, "ooooo" measured cross-polarization

ment scenario, the reference antenna was a broadband horn (EMCO type 3115) positioned at 4 m from the antenna under test. Two pattern cuts (i.e. the *x*–*z* and *y*–*z* planes) were selected at three selected operating frequencies, namely 1.6, 2.7, and 3.8 GHz. The radiation patterns of the prototype antenna at 1.6, 2.7, and 3.8 GHz when the varactor diode was excited by 5 and 11 V were measured, and the corresponding results were cross-validated with the simulation data, as shown in Fig. 7.12. Both computed and measured radiation patterns display nearly omnidirectionally, with distorted short-dipole characteristics, and are said to be in close agreement one with the another.

7.11 Conclusion

A printed crescent-shaped monopole antenna geometry with reconfigurable band rejection characteristics has been modeled, designed, and implemented. The proposed antenna occupies a compact envelope with dimensions of $57 \times 37.5 \times 0.8$ mm^3 while covering the required wide band with a sufficiently tunable rejection frequency band ranging from WLAN (2.4–2.485 GHz) to WiMAX (3.3–3.7 GHz). The notch center frequency shift was quite stable and consistent over the selected spectrum without a serious change in the notch bandwidth. The proposed antenna structure is optimized for best results through simulation. The computed results are in good agreement with the measured results. The antenna can satisfy typical requirements of bandwidth and interference reduction arising from current market trends in legacy and future emerging wireless communications.

Acknowledgments This work was carried out under a grant from the Fundação para a Ciência e a Tecnologia (FCT - Portugal), with the reference number SFRH / BPD / 95110 / 2013. The research leading to these results received funding from the Fundação para a Ciência e Tecnologia and the ENIAC JU (THINGS2DO–GA n. 621221).

References

1. R. Singh, G. Kumar, Broadband planar monopole antennas, M.Tech credit seminar report, Electronics System Group, EE Dept, IIT Bombay, 2003
2. M. Ammann, Control of the impedance bandwidth of wideband planar monopole antennas using a beveling technique. Microw. Opt. Technol. Lett. **30**(4), 229–232 (2001)
3. N.P. Agrawall, G. Kumar, K. Ray, Wide-band planar monopole antennas. IEEE Trans. Antennas Propag. **46**(2), 294–295 (1998)
4. J.-Y. Jan, J.-W. Su, Bandwidth enhancement of a printed wide-slot antenna with a rotated slot. IEEE Trans. Antennas Propag. **53**(6), 2111–2114 (2005)
5. S.-W. Su, K.-L. Wong, H.-T. Chen, Broadband low-profile printed T-shaped monopole antenna for 5-GHz WLAN operations. Microw. Opt. Technol. Lett. **42**, 243–244 (2004)
6. Z.N. Chen, Broadband planar monopole antenna. IEE Proc Microwave Antennas Propagat **147**, 526–528 (2000)

7. A. Duhan, B. Singh, M. Zayed, H. Rana, G. Tiwari, S. Yadav, Compact monopole wideband antenna for WiMAX/WLAN/BLUETOOTH/IEEE 802.11y services. The Eighth International Conference on Contemporary Computing (IC3).20–22, 2015, Noida, India.p. 1–4
8. R. Zhu, X. Wang, G. Yang, A wideband monopole antenna using parasitic elements. Applied Mechanics and Materials, Trans. Tech. Publications, Switzerland **52–54**, 1515–1519 (2011)
9. C.F. Tseng, C.L. Huang, C.H. Hsu, Microstrip-fed monopole antenna with a shorted parasitic element for wideband application. Progress In Electromagnetics Research Letters **7**, 115–125 (2009)
10. A.T. Mobashsher, B. Bais, N. Misran, M.T. Islam, Compact wideband microstrip antenna for universal 5 GHz WLAN applications. Aust. J. Basic Appl. Sci. **4**(8), 3411–3417 (2010)
11. C.H. See, R.A. Abd-Alhameed, F. Elmegri, D. Zhou, J.M. Noras, N.J. McEwan, S.M.R. Jones, P.S. Excell, Planar monopole antennas for new generation mobile and lower band ultra-wide band applications. IET Microwave Antennas Propag **6**, 1207–1214 (2012)
12. M.N. Suma, P.C. Bybi, P. Mohanan, A wideband printed monopole antenna for 2.4-GHz WLAN applications. Microw. Opt. Technol. Lett. **48**(5), 871–873 (2006)
13. S. Saou-Wen, K.-L. Wong, H.-T. Chen, Broadband low-profile printed T-shaped monopole antenna for 5-Ghz WLAN operation. Microw. Opt. Technol. Lett. **42**(3), 234–245 (2004)
14. A. Singh, S. Singh, A novel CPW-fed wideband printed monopole antenna with DGS. Int. J. Electron. Commun. **69**(1), 299–306 (2015)
15. H.I. Hraga, C.H. See, R.A. Abd-Alhameed, D.Zhou, S. Adnan, I.T.E. Elfergani, P. S. Excell, Small wideband antenna for GSM and WLAN applications. In proceedings of the European Conference on Antennas and Propagation: EuCAP, 2010, Barcelona, Spain
16. M. Naghshvarian-Jahromi, N. Komjani, Novel fractal monopole wideband antenna. J Electromagn. Waves and Appl. **22**, 195–205 (2008)
17. M.N. Shakib, M. Moghavvemi, W.N.L. Mahadi Optimization of planar monopole wideband antenna for wireless communication system, 1–15, (2016). doi:10.1371/journal.pone.0168013
18. Y.Y. Sun, S.W. Cheung, T.I. Yuk, Planar monopole ultra-wideband antennas with different radiator shapes for body-centric wireless networks. Progress In Electromagn Res Symp Proc, KL, MALAYSIA **27–30**, 839–843 (2012)
19. G. Bozdag, A. Kustepeli, Wideband printed planar monopole antenna for PCS, UWB and X-band applications. Progress In Electromagnetics Research C **60**, 95–103 (2015)
20. Y. Lu, Y. Huang, Senior Member, IEEE, Hassan Tariq Chattha, and Ping Cao "reducing ground-plane effects on UWB monopole antennas". IEEE Antennas Wirel Propag Lett **10**, 147–150 (2011)
21. W.S. Chen, P.Y. Chang, B.Y. Lee, H.T. Chen, J.-S. Kuo, *A compact microstrip-fed slot antenna with a dual-band notched function for WiMAX Operation Antennas and Propagation Society International Symposium (APSURSI)* (Ontario, Canada, Toronto, 2010), pp. 1–4
22. W.S. Lee, D.Z. Kim, J.W. Yu, Wideband crossed planar monopole antenna with the band-notched characteristic. Microw. Opt. Technol. Lett. **48**(3), 543–545 (2006)
23. J.-B. Jiang, Z.-H. Yan, C. Wang, A novel compact UWB notchfilter antenna with a dual-Y-shaped slot. Progr. Electromagn. Res. Lett. **14**, 165–170 (2010)
24. Y.K. Manish Sharma, H.S. Awasthi, R. Kumar, S. Kumari, Compact printed high rejection triple band-notch UWB antenna with multiple wireless applications. Eng Sci Technol Int J **19**, 1626–1634 (2016)
25. E. Pancera, D. Modotto, A. Locatelli, F.M. Pigozzo, C. De Angelis, Novel design of UWB antenna with band-notch capability, in *Proc. Eur. Conf. on Wireless Technologies*, 2007, p. 48–50
26. Y.F. Weng, W.J. Lu, S.W. Cheung, T.I. Yuk, UWB antenna with single or dual band-notched characteristic for WLAN band using meandered ground stubs, in *Proc. Loughborough Antennas and Propagation Conf. (LAPC)*, 2009, p. 757–760
27. C.M. Li, L.H. Ye, Improved dual band-notched UWB slot antenna with controllable notched bandwidths. Prog. Electromagn. Res. **115**, 477–493 (2011)
28. P. Lin, R. Cheng-Li, UWB band-notched monopole antenna design using electromagnetic-bandgap structures. IEEE Trans. Microw. Theory Tech. **59**, 1074–1081 (2011)
29. Y.-B. Yang, F.-S. Zhang, F. Zhang, L. Zhang, Y.-C. Jiao, Design of novel wideband monopole antenna with a tunable notched-band for 2.4 GHz WLAN and UWB applications. Prog Electromagn Res Lett **13**, 93–102 (2010)

30. W.-M. Li, T. Ni, S.-M. Zhang, J. Huang, Y.-C. Jiao, UWB printed slot antenna with dual band-notched characteristic. Prog Electromagn Res Lett **25**, 143–151 (2011)
31. J.-Q. Sun, X.-M. Zhang, Y.-B. Yang, R. Guan, L. Jin, Dual band-notched ultra-wideband planar monopole antenna with M- and W-slots. Prog Electromagn Res Lett **19**, 1–8 (2010)
32. S.K. Mishra, R. Gupta, A. Vaidya, J. Mukherjee, Printed fork shaped dual band monopole antenna for bluetooth and UWB applications with 5.5 ghz wlan band notched characteristics. Prog Electromagn Res C **22**, 195–210 (2011)
33. J. Yeo, R. Mittra, A novel wideband antenna package design with a compact spatial-notch filter for wireless applications. Microw. Opt. Technol. Lett. **35**, 455–460 (2002)
34. L. Wen-jun, C. Chong-hu, Z. Hong-bo, Improved frequency notched ultrawideband slot antenna using square ring resonator. IEEE Trans. Antennas Propag. **55**, 2445–2450 (2007)
35. C. Tang, N. Yang, A novel compact UWB antenna with triple notched bands using square ring short stub loaded resonator. Prog Electromagn Res Lett **58**, 17–22 (2016)
36. W. Wu, Y.B. Li, R.Y. Wu, C.B. Shi, T.J. Cui, Band-notched UWB antenna with switchable and tunable performance. Int J Antennas Propag. Article ID 9612987, 1–6, 2016
37. S.A. Aghdam, J. Bagby, Resonator type for the creation of a potentially reconfigurable filtering band in a UWB antenna. Prog Electromag Res Lett **52**, 17–21 (2015)
38. V. Sharbati, P. Rezaei, M.M. Fakharian, E. Beiranvand, A switchable band-notched UWB antenna for cognitive radio applications. IETE J Res **61**(4), 423–428 (2015)
39. T. Li, H. Zhai, L. Li, C. Liang, Y. Han, Compact UWB antenna with tunable band-notched characteristic based on microstrip open-loop resonator. IEEE Antennas Wirel Propag Lett **11**, 1584–1587 (2012)
40. J. Malik, P.K. Velalam, M.V. Kartikeyan, Continuously tunable bandnotched ultrawideband antenna. Microw. Opt. Technol. Lett. **57**(4), 924–928 (2015)
41. H.A. Mohamed, A.S. Mohra, Controllable band-notched UWB printed monopole antenna. Int J Eng Res **5**(2), 110–114 (2016)
42. I.T.E. Elfergani, A.S. Hussaini, P. Marques, R.A. Abd-Alhameed, C.H. See, J. Rodriguez, A miniaturized monopole wideband antenna with reconfigurable band rejection for WLAN/WiMAX, CST Int Conf. Wireless Int – WICON, Lisbon, Portugal. 146, 1–6, 2014
43. Ansoft high frequency structure simulator v10 user guide (CA, USA) (n.d.)
44. R.W. Johnston, J.G. McRory, An improved small antenna radiation-efficiency measurement. IEEE Antenna Propagat. Soc. Mag. **40**, 40–48 (1998)
45. D. Agahi and W. Domino, Efficiency measurements of portable handset antennas using the wheeler cap, Appl Microwave Wireless. **12**, 32–34 (2000)
46. H.Choo, R. Rogher, H. Ling, On the Wheeler cap measurement of the efficiency of microstrip, IEEE Transactions on Antennas and Propagation, **53**(7), (2005), 2328–2332

Part IV
MIMO Antennas

Chapter 8
Miniature EBG Two U-Shaped Slot PIFA MIMO Antennas for WLAN Applications

Z.Z. Abidin, S.M. Shah, and Y. Ma

8.1 Introduction

At present, electromagnetic band gap (EBG) materials are rapidly advancing in electromagnetic (EM) research area. The EBG structures are broadly categorized as metamaterials with attractive properties that unavailable in nature. The materials have attracted much consideration and are widely used for improving the electromagnetic performance. EBG materials belong to the unique class of artificially fabricated structures that have the ability to control and manipulate the propagation of EM waves to produce forbidden frequency gaps where the propagation is prohibited [1, 2], hence resulting in improving the gain and reducing mutual coupling of antennas in an array configuration. The EBG structures are typically realized by a periodic arrangement of dielectric materials and metallic conductors either in one-, two-, or three-dimensional manners which can be characterized by stop band and pass band.

EBG structure can be considered as the perfect magnetic conductor (PMC), which means that the distance between the antenna and the EBG can be less than $\lambda/4$ (Fig. 8.1) which makes it possible to be implemented on the low profile antenna [3]. Compared to the antennas with the perfect electric conductor (PEC), the separation between it should be greater than $\lambda/4$ (Fig. 8.2) for the antenna to radiate efficiently. This is due to the fact that the EBG surface reflects all power just like a PEC, but it reflects in-phase, rather than out-of-phase and thus, allowing the radiating element to be directly adjacent to the surface.

Z.Z. Abidin (✉) • S.M. Shah
Research Center of Applied Electromagnetic, Universiti Tun Hussein Onn Malaysia Parit Raja, Batu Pahat, Johor, Malaysia
e-mail: zuhairia@uthm.edu.my

Y. Ma
National Astronomical Observatories (NAOC), Chinese Academy of Sciences, Chaoyang, China

I. Elfergani et al. (eds.), *Antenna Fundamentals for Legacy Mobile Applications and Beyond*, DOI 10.1007/978-3-319-63967-3_8

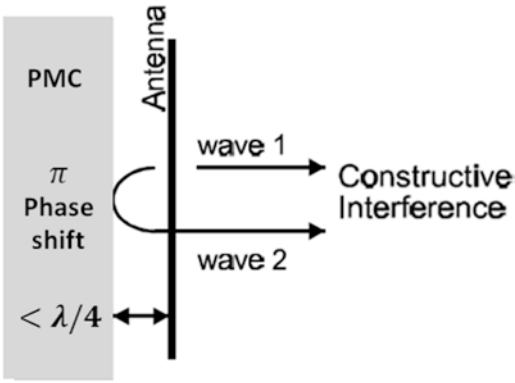

Fig. 8.1 A perfect magnetic conductor (PMC) as a ground plane [3]

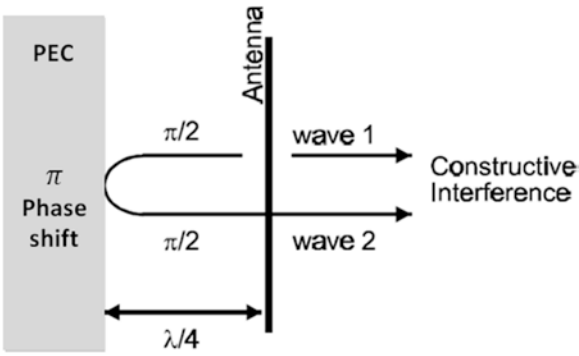

Fig. 8.2 A perfect electric conductor (PEC) as a ground plane [3]

8.2 Uniplanar Compact Electromagnetic Band Gap (UC-EBG)

In this work, we focus on the uniplanar compact EBG (UC-EBG) structure which is one type of the EBG planar surfaces. The development of a planar EBG structure is via-less and further reduces the complexities in the fabrication process. By observing the current trends, there is a requirement to design low-cost and compact size planar EBG structures that operate below the 6 GHz to meet the demands of several applications, such as mobile phone, WLAN, WiMAX, etc., as reported in [4–10].

In this chapter, the properties of the proposed UC-EBG structure are examined and tested, with a smaller unit cell of 9.7×9.7 mm^2, operating at 2.4 GHz on a relatively low dielectric constant material. In addition, to corroborate the performances of the UC-EBG, a compact dual U-shaped slot Planar Inverted-F Antenna (PIFA) antenna integrated with the proposed EBG structures is also presented. A comparison between the simulated and measured scattering parameters for proposed antenna with and without EBG structures is analysed. In addition, an assessment and analysis on few MIMO antenna parameters has also been conducted.

8.3 Design Concept Based on Sievenpiper's Equations

The geometrical parameters and dimensions of the proposed EBG are summarized in Fig. 8.3 and Table 8.1, respectively. The centre frequency of a band gap is based on the approximation by the surface equivalent capacitance C and inductance L as follows:

$$\omega_o = \frac{1}{\sqrt{LC}} \tag{8.1}$$

The corresponding relative bandwidth of the band gap is given by:

$$\mathrm{BW} = \frac{\Delta\omega}{\omega} = \frac{1}{\eta}\sqrt{\frac{L}{C}} \tag{8.2}$$

where η is the free space wave impedance.

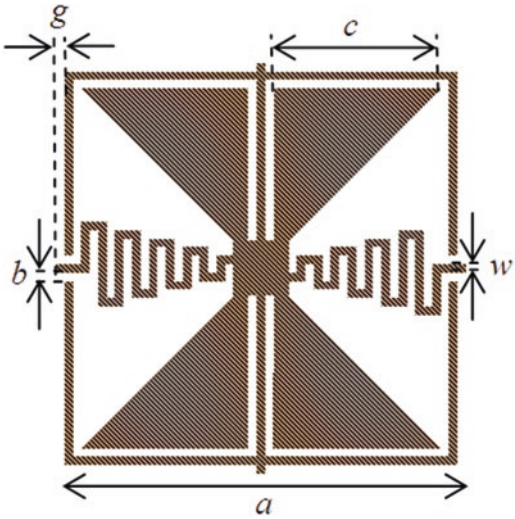

Fig. 8.3 Proposed UC-EBG [11]

Table 8.1 Parameters of the proposed UC-EBG [11]

Parameters	Dimensions (mm)
a	9.7
b	0.2
c	4.0
g	0.2
w	0.2

Based on Eq. (8.1), it is necessary to increase the value of inductance, *L*, and capacitance, *C*, per unit cell in order to produce a more compact EBG structure with a lower frequency band gap. Hence, in this design, we could summarize that the triangular metal plates and meander line elements will produce the necessary equivalent inductance, and the additional conductor edges are used adequately to increase the fringe capacitance. In addition, these elements contribute in enhancing the value of inductance and capacitance of the unit cell with a smaller unit cell EBG is realized.

8.4 EBG Characterization Results

There are two outstanding EBG characteristics that can be realized in this proposed design. The first characteristic is to prevent the propagation of the electromagnetic fields within a band gap. The second is based on a high impedance surface (HIS) within a specifically limited frequency range which is generally known as in-phase reflection band. Therefore, to get these two characteristics, two techniques are presented in this chapter: (a) reflection phase and (b) suspended microstrip line technique [12].

8.4.1 Reflection Phase

Generally, reflection phase can be defined as the phase of the reflected electric field which is normalized to the phase of the incident electric field at the reflecting surface. It can be identified as in-phase reflection or out-of-phase reflection. The EBG structures demonstrate a frequency-dependent reflection phase which is fluctuating between $+180^{o}$ and -180^{o} compared to 0° for the perfect magnetic conductor (PMC), which does not exist in nature, and 180^{o} for the perfect electric conductor (PEC) for a normally incident plane wave. Based on Finite Integration Technique (FIT) in CST Microwave Studio® [13], the proposed EBG structure for reflection phase technique is analysed. The model configuration for the reflection phase response of the proposed EBG structures is presented in Fig. 8.4. The boundaries of a single unit cell model are defined as a pair of PEC and PMC walls and a de-embedded waveguide port is placed on the top to evaluate the reflection phase data directly at the EBG surface.

8.4.2 Suspended Microstrip Line

In order to comprehend the design process and to get the target performances, the EBG structure is realized from 3×9 periodic array. The periodic EBG arrays are constructed on a low dielectric material with a relative permittivity of 4.5, and a

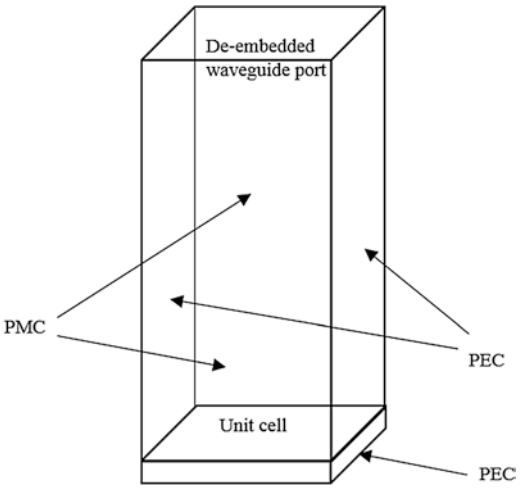

Fig. 8.4 Reflection phase configuration for compact EBG unit cell in CST

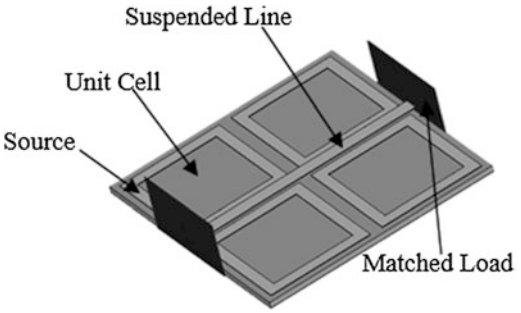

Fig. 8.5 Example of suspended line technique

50-Ω microstrip line with dielectric thickness of 1.6 mm is directly placed above the EBG. Figure 8.5 illustrates the example of the suspended line technique models.

Figure 8.6 depicts the simulated results for both techniques. It can be observed that from the reflection phase technique, the proposed EBG structures can reflect normally incident electromagnetic wave with a zero phase shift at a frequency of 2.4 GHz (red colour), while based on the suspended line technique, it is examined that a band gap in the range of 2.0 GHz–2.6 GHz (blue colour) is achieved as showed in Fig. 8.6.

8.5 MIMO Antenna Parameters

Multiple-Input Multiple-Output (MIMO) technology is revolutionary in communication system design. MIMO exploits space dimensions to improve wireless systems capacity, range and reliability. A few MIMO antenna parameters need to be considered to improve the performance of the MIMO antenna. In this section, empirical equations related to the performances of the MIMO antennas are discussed.

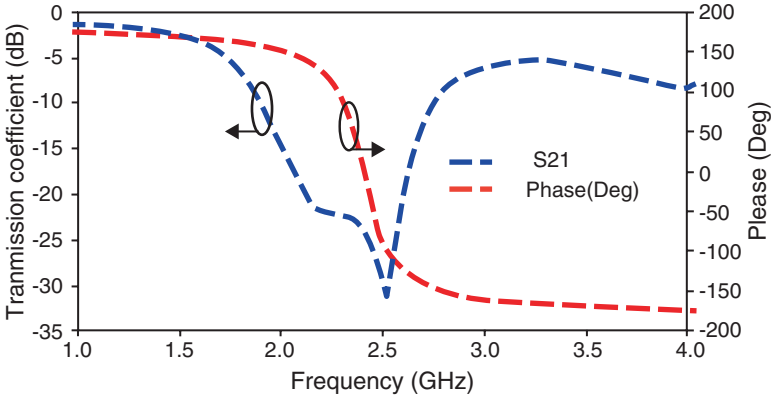

Fig. 8.6 Simulated S_{21} and reflection phase parameters of the EBG

8.5.1 *Total Active Reflection Coefficient (TARC)*

M. Manteghi et al. in [14] defined that TARC (Γ) is 'the ratio of the square root of total reflected power divided by the square root of the total incident power':

$$\Gamma_a^t = \sqrt{\sum_N^{i=1} |b_i|^2} \Big/ \sqrt{\sum_N^{i=1} |a_i|^2} \tag{8.3}$$

where a_i is incident signal and b_i is reflected signal.

By assuming the antenna is lossless, the TARC for the $N \times N$ port antennas can be calculated using a scattering matrix defined as follows:

$$\begin{bmatrix} b_1 \\ \vdots \\ b_N \end{bmatrix} = \begin{bmatrix} S_{1,1} & \cdots & S_{N,1} \\ \vdots & \ddots & \vdots \\ S_{N,1} & \cdots & S_{N,N} \end{bmatrix} \cdot \begin{bmatrix} a_1 \\ \vdots \\ a_N \end{bmatrix} \tag{8.4}$$

8.5.2 *Correlation Coefficient*

The correlation coefficient, ρ, of an antenna array demonstrates the influence of different propagation paths of the radio frequency (RF) signals that reach the antenna elements. It can be calculated in two different ways either by using a far-field radiation pattern (3D) [15] or by scattering parameters (S-parameters) obtained at the antenna terminals [16]. Due to the complexity of the 3D far-field measurement and

calculation, the S-parameter method of computing the correlation coefficient of the two antennas is used based on a simple closed-form equation that relates the S-parameters of the elements in an array configuration. The correlation coefficient, ρ, of an $N \times N$ antenna system represented by the S-parameters can be determined as follows [17]:

$$\rho(i,j,N) = \frac{\left| \sum_{N}^{n=1} S^{*}i,nS_{n,j} \right|^{2}}{\Pi_{k=i,j}\left[1 - \sum_{N}^{n=1} S^{*}k,nS_{n,k} \right]} \tag{8.5}$$

8.5.3 Capacity Loss

Theoretically, the channel capacity of the MIMO system can be improved by increasing the number of antennas. However, the existence of uncorrelated Rayleigh-fading MIMO channels will induce the loss of channel capacity. The loss can be calculated from the correlation matrices given in [18–20]. In the case of high signal-to-noise ratio (SNR), the capacity loss is given by [19]:

$$C_{\text{loss}} = -\log_2 \det\left(\psi^{\text{R}}\right) \tag{8.6}$$

where ψ^{R} is the receiving antenna correlation matrix.

$$\psi^{R} = \begin{pmatrix} \rho_{1,1} & \cdots & \rho_{1,N} \\ \vdots & \ddots & \vdots \\ \rho_{N,1} & \cdots & \rho_{N,N} \end{pmatrix} \tag{8.7}$$

8.5.4 Channel Capacity

Channel capacity is related to the information handling capacity of a given channel. Based on the channel transfer matrix, H, the Shannon capacity, C, for the MIMO system channel with an assumption that the received signals obey the Gaussian distribution independently, is given by [21]:

$$c = \log_2\left(\det\left(I + \frac{SNR}{M} HH^{\dagger} \right) \right) \tag{8.8}$$

where $H^{\dagger}$ is the Hermitian matrix and H with the '†' is the conjugate transpose operation. M is the number of receivers, SNR is the estimated channel signal-to-noise ratio, I is the identity and det is the determinant.

8.6 Antenna Design and Consideration

To validate the performances of the EBG, a compact dual U-shaped slot PIFA antenna operating at 2.4 GHz is integrated with the proposed EBG structures. As demonstrated in [22], the existence of the U-shaped slot can improve the impedance bandwidth of the antenna. The antenna is mounted on a 45 × 85 mm^2 ground plane. The antenna is assembled from a 0.5 mm thick metal plate, with a dimension of 15 × 15 mm^2, and shorted to the ground plane by a metallic strip and fed by a standard 50 Ω SubMiniature version A (SMA) connector. The shorting plate is added in order to minimize the size of the PIFA. The width of the plate is carefully optimized to obtain the required operating frequency. The antenna is fabricated on the same substrate type as EBG structures with the distance (centre-to-centre) between the antenna elements is kept at 30 mm. The geometries and dimensions of the PIFAs alone and PIFAs with EBG are shown in Fig. 8.7. The photo of the proposed designs can be viewed in Fig. 8.8 [23].

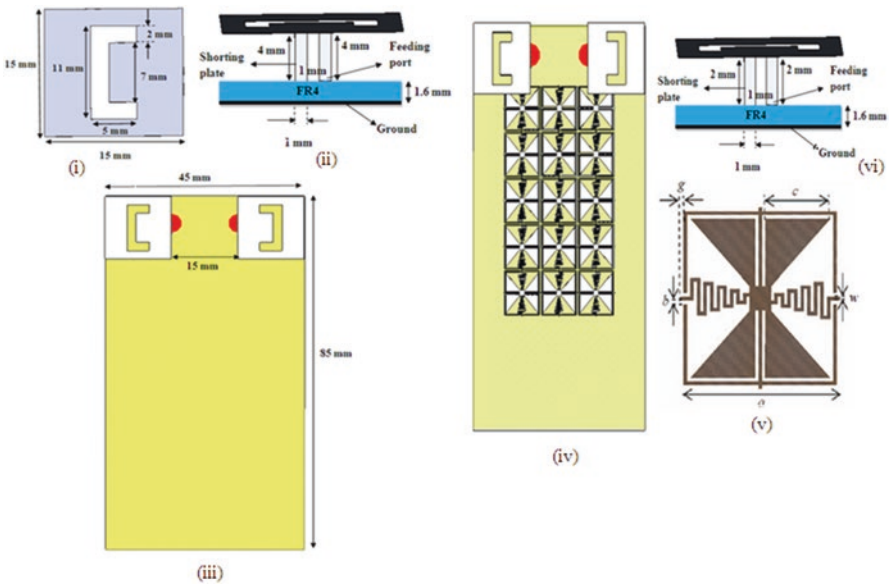

Fig. 8.7 Geometry and dimensions: U-shaped PIFA (i) top view, (ii) side view, (iii) 2-D schematic; U-shaped PIFAs with EBG, (iv) 2-D schematic, (v) EBG unit cell [11], (vi) side view

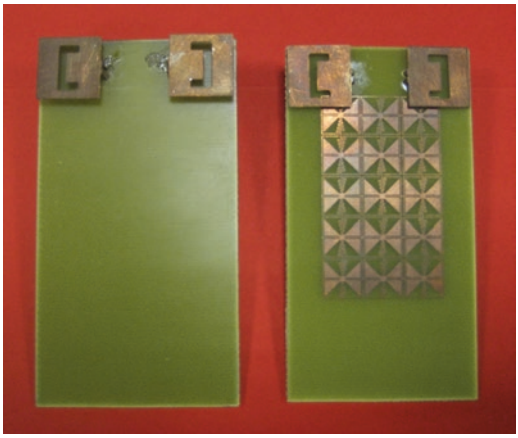

Fig. 8.8 Antenna prototype: PIFAs alone (*left*) and PIFAs with EBG (*right*)

Table 8.2 S-parameters and gain for different heights of antenna [24]

PIFAs	Return loss (dB)	Mutual coupling (dB)	Antenna gain (dB)
Alone (as reference)	−16.23	−16.28	3.78
With EBG (h = 4 mm)	−19.09	−20.92	4.10
With EBG (h = 3 mm)	−17.86	−21.90	4.15
With EBG (h = 2 mm)	−18.02	−23.30	4.42

8.6.1 Results and Discussions

As stated earlier, the height of the antenna between the ground planes could be reduced due to the existence of the EBG as a ground plane. Therefore, the parametric studies on the performance of the PIFAs with EBG for three different heights of the antenna are presented in Table 8.2 as the PIFAs alone act as a reference antenna. It is discovered that the optimum height of 2.0 mm gave a better improvement in the S-parameters and gain. As mentioned in [16], it is worth noting that, at optimum height, the proposed PIFAs with the EBG material are shown to alleviate the effects of mutual coupling, and thus improves the antenna efficiency. The prototype of the proposed PIFAs with EBG is then fabricated for measure purposes, with the height of the antenna from the EBG surface at 2 mm.

Figures 8.9 and 8.10 display the simulated and measured S-parameters of the PIFAs alone and PIFAs with EBG structures, respectively. From the measured results, it can be seen that for both PIFAs, the S-parameters are reasonably agreed with the simulated, with the obtainable impedance bandwidth of 11.2% for both designs. The inconsistencies are assumed to be due to the minor irregularities in prototyping. From Fig. 8.11, it is observed that the mutual coupling, S_{21}, of the

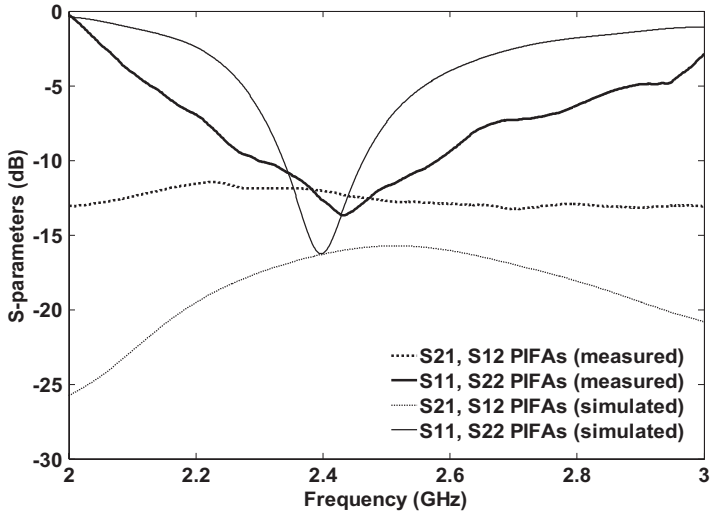

Fig. 8.9 Simulated and measured S-parameters of PIFAs alone

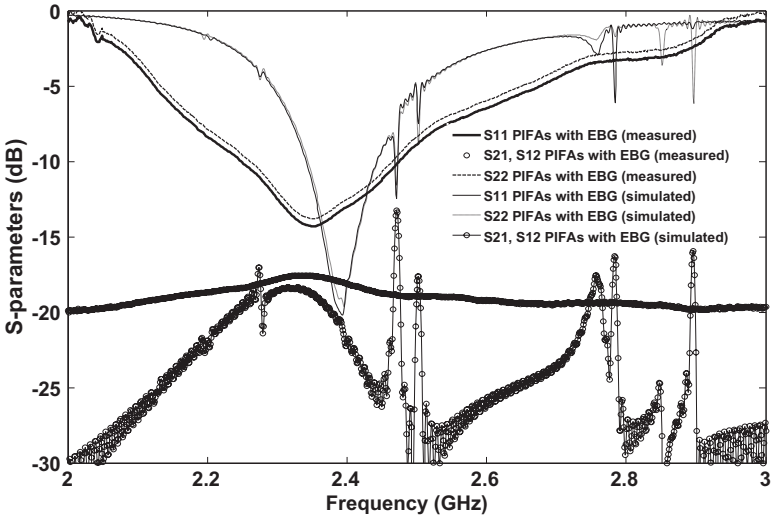

Fig. 8.10 Simulated and measured S-parameters of PIFAs with EBG

PIFAs alone is −16.28 dB as compared to PIFAs with EBG with the value of −23.3 dB and an isolation enhancement of 7.02 dB. Further, the existence of the EBG structures caused the resonant frequency of the PIFAs with EBG to be shifted down to 2.35 GHz, with an effective operating range of 2.25 GHz–2.43 GHz. In that case, to prevent any frequency shifting, the dimensions of the antenna have to be optimized. However, the dimensions of the antenna in this chapter remain the same.

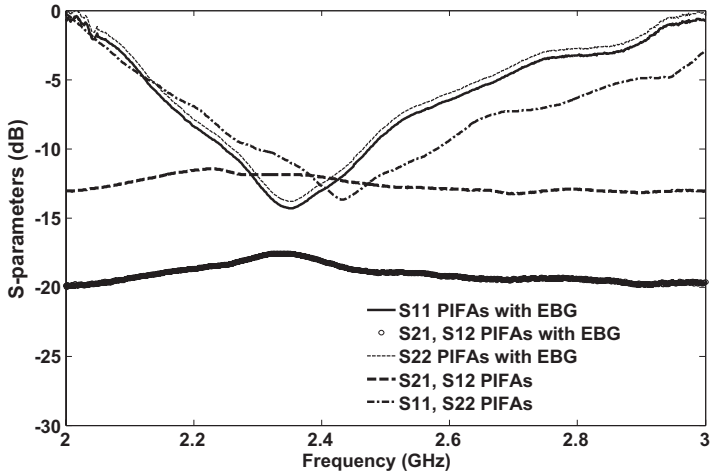

Fig. 8.11 Measured S-parameters of PIFAs with and without EBG

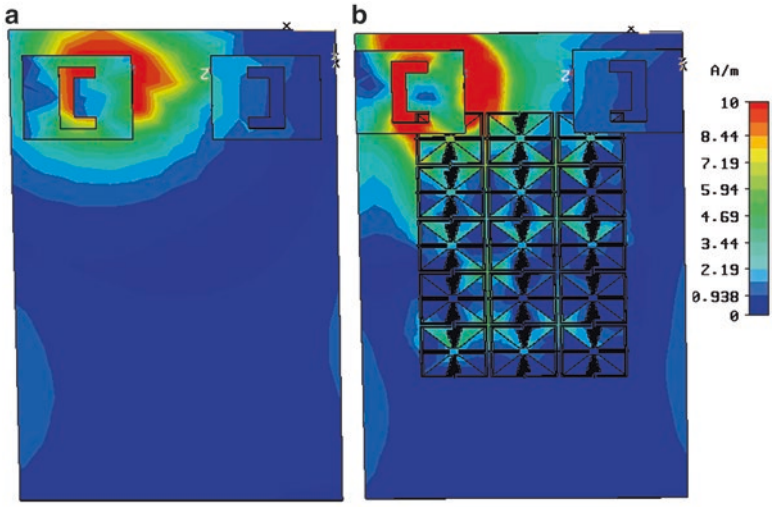

Fig. 8.12 Contour plot surface current distributions for (**a**) PIFAs alone and (**b**) PIFAs with EBG. Port 1 (*left*) is excited and port (2) is terminated with 50 Ω loads

Figure 8.12 depicts the simulated surface currents generated from the CST Microwave Studio®. It can be seen from the figure that, when port 1 is excited and port 2 is terminated with 50-Ω load, the electric field in the conventional PIFAs is not as intense as the PIFAs with EBG structures. The electric field is mostly engaged closer to the PIFAs when the EBG structure is employed. The effect of the surface wave suppression shown appears to be a promising method to suppress the mutual coupling in the antenna arrays.

The measured radiation patterns of PIFAs alone and PIFAs with EBG at E-plane and H-plane are shown in Fig. 8.13. The measurement has been performed in full-anechoic chamber. It is noticeable that PIFAs with EBG reduce the back radiation by at least 20 dB. It proved that the proposed EBG could be able to reduce the front-back ratio of the antenna.

The improvement in the performance of the MIMO antenna is influenced by the correlation between the signals at the antenna terminals. Table 8.3 presents a measured outcome of the diversity performance of the PIFAs alone and PIFAs with the EBG. The results show that the PIFAs with EBG material realized a better performance compared to PIFAs alone with an improvement on correlation coefficient, TARC and capacity loss. The channel capacity of PIFAs alone and PIFAs with EBG is 5.62 bits/s/Hz and 5.64 bits/s/Hz, respectively, at 2.4 GHz as can be viewed in Fig. 8.14. From the results, it can be summarized that good impedance and isolation lead to low correlation coefficient which decreases the capacity loss and improves the TARC performance. All the results for the MIMO parameters are determined by using empirical equations (8.3), (8.4), (8.5), (8.6), (8.7), (8.8).

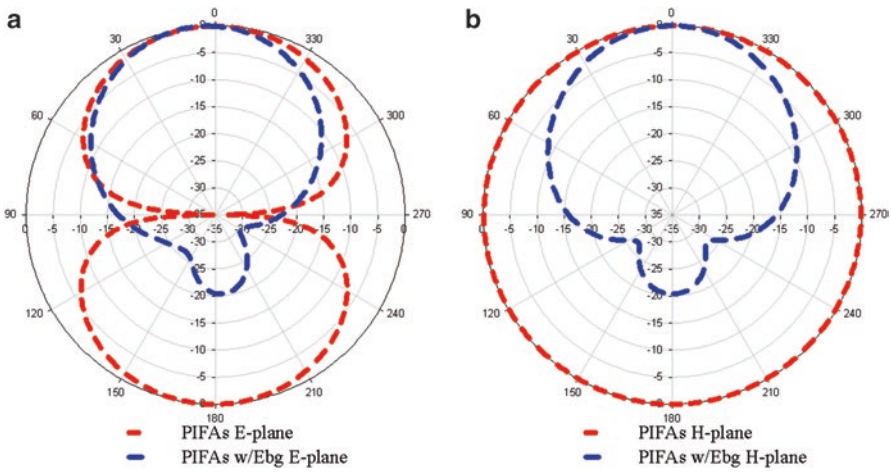

Fig. 8.13 Measured radiation pattern for PIFAs alone and with EBG at (**a**) E-plane; (**b**) H-plane

Table 8.3 Measured results for correlation coefficient, TARC and capacity loss

	PIFAs alone	PIFAs with EBG	Improvement between PIFAs alone and PIFAs with EBG
Correlation coefficient (dB)	−43.99	−50.23	6.24
TARC (dB)	−5.74	−8.53	2.79
Capacity loss (bits/s/Hz)	0.55	0.39	0.16

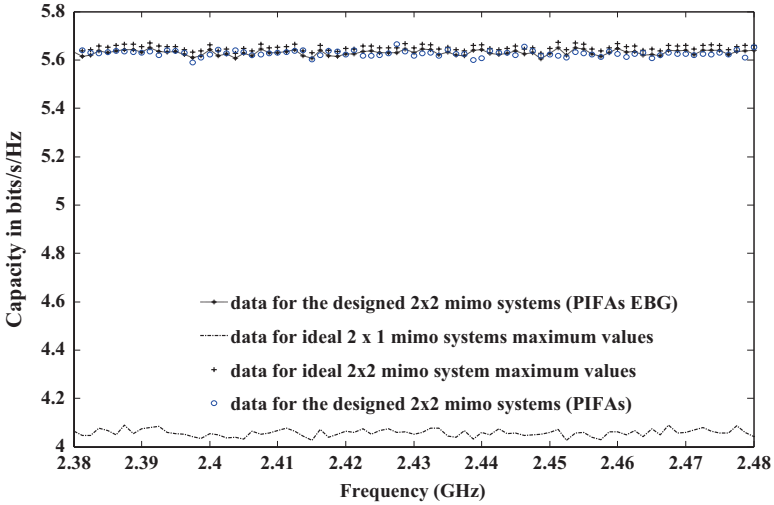

Fig. 8.14 Channel capacity of both PIFAs with and without EBG

8.7 Conclusion

A compact dual U-shaped PIFA antenna with miniaturized EBG structure is successfully designed, simulated and measured. The EBG structure acts as PMC is used to reduce the separation between the antenna and the ground plane. In addition, the presence of the EBG structure resulting an improvement of the performances of the MIMO antennas. Thus, it can be concluded that the proposed antenna with EBG structure can be a good candidate for mobile handset applications.

References

1. C.M. Soukoulis, Photonic crystals and light localization in the 21st century. NATO ASI Series C **563**, 475–487 (2001)
2. S. Sundhakaran, Negative refraction from electromagnetic periodic structures and its applications, Ph.D. Dissertation, Department of Electronic Engineering, Queen Mary, University of London, 2006
3. D. Sievenpiper, L. Zhang, R.F.J. Broas, N.G. Alexopolus, E. Yablonovitch, High-impedance electromagnetic surfaces with a forbidden frequency band. IEEE Trans. Microwave. Theory. Tech **47**, 2059–2074 (1999)
4. S.D. Assimonis, T.V. Yioultsis, C.S. Antonopoulos, Design and optimization of uniplanar EBG structures for low profile antenna applications and mutual coupling reduction. IEEE Trans. Antennas Propag. **60**, 4944–4949 (2012)
5. L. Kurra, M.P. Abegaonkar, A. Basu, S.K. Koul, FSS properties of a uniplanar EBG and its application in directivity enhancement of a microstrip antenna. IEEE Antennas Wireless Propag Lett **15**, 1606–1609 (2015)

6. A.M. Soliman, D.M. Elsheakh, E.A. Abdallah, H. El-Hennawy, Design of planar inverted-F antenna over uniplanar EBG structure for laptop MIMO applications. Microw. Opt. Technol. Lett. **57**, 277–285 (2015)
7. M. Luberto, W. G. Fano, in *Microstrip antenna design using EBG (Electromagnetic Band Gap) structures at 2.4GHz*, XVI Workshop on Information Processing and Control (RPIC), (Argentina, 2015), pp. 1–7
8. M.F. Abedin, M.Z. Azad, M. Ali, Wideband smaller unit-cell planar EBG structures and their application. IEEE Trans. Antennas Propag. **56**, 903–908 (2008)
9. B.-Q. Lin, X.-Y. Ye, X.-Y. Cao, F. Li, Uniplanar EBG structure with improved compact and wideband characteristics. Electron. Lett. **44**, 1362–1363 (2008)
10. W. Wang, X.-y. Cao, W.-y. Zhou, T. Liu, A novel compact uni-planar electromagnetic band-gap (UC-EBG) structure. Int. Conf. Microwave Millimeter Wave Technol **4**, 1634–1636 (2008)
11. Z. Z. Abidin, R.A.Abd-Alhameed, N. J. McEwan, S. M. R. Jones, K. N. Ramli, and A. G. Alhaddad, in *"Design and Analysis of UC-EBG on Mutual Coupling Reduction",* Antennas & Propagation Conference, (LAPC 2009), (Loughborough, 2009), pp. 693–696
12. A. Aminian, F. Yang, Y. Rahmat-Samii, In-phase reflection and EM wave suppression characteristics of electromagnetic band gap ground planes. Antennas Propag Soc. Int. Symp. IEEE **4**, 430–433 (2003)
13. CST Microwave Studio [Online]. Available: http/www.cst.com
14. M. Manteghi, Y. Rahmat-Samii, Multiport characteristics of a wide-band cavity backed annular patch antenna for multipolarization operations. IEEE Trans. Antennas Propag. **53**, 466–474 (2005)
15. R.G. Vaughan, J.B. Andersen, Antenna diversity in mobile communication. IEEE Trans. Veh. Technol. **36**, 149–172 (1987)
16. S. Blanch, J. Romeu, I. Corbella, Exact representation of antenna system diversity performance from input parameter description. Electron. Lett. **39**, 705–707 (2003)
17. J. Thaysen, K.B. Jakobsen, Envelope correlation in (N, N) MIMO antenna array from scattering parameters. Microw. Opt. Technol. Lett. **48**, 832–834 (2006)
18. S.H. Chae, S.-k. Oh, S.-O. Park, Analysis of mutual coupling, correlations, and TARC in WIBro MIMO array antenna. IEEE Antennas Wireless. Propag. Lett. **6**, 122–125 (2007)
19. H. Shin, J.H. Lee, Capacity of multiple-antenna fading channels: spatial fading correlation, double scattering, and keyhole. IEEE Trans. Inform. Theory **49**, 2636–2647 (2003)
20. D. Valderas, P. Crespo, C. Ling, UWB portable printed monopole array design for MIMO communications. Mirowave. Opt. Technol. Lett **52**, 889–895 (2010)
21. G.J. Foschini, M.J. Gans, On limits of wireless communications in a fading environment when using multiple antennas. Wirel. Pers. Commun. **6**, 311–335 (1998)
22. H.-T. Hu, F.-C. Chen, Q.-X. Chu, A wideband U-shaped slot antenna and its application in MIMO terminals. IEEE Antennas Wirel. Propag. Lett **15**, 508–511 (2016)
23. Z. Z. Abidin, Y. Ma, R. A. Abd-Alhameed, K. N. Ramli, D. Zhou, M. S. Bin-Melha, J. M. Noras, R. Halliwell, in *Design of 2 × 2 U-shape MIMO slot antennas with EBG material for mobile handset applications*, Progress In Electromagnetics Research Symposium Proceedings, (Marrakesh, Morocco, 2011), pp. 1275–1278
24. Z. Z. Abidin, Design, modeling, and implementation of antennas using electromagnetic band-gap material and defected ground planes, Ph.D. Thesis, University of Bradford (2011)

Chapter 9
Compact MIMO Antenna Array Design for Wireless Applications

O. Arabi, N.T. Ali, B. Liu, R.A. Abd-Alhameed, and P.S. Excell

9.1 Introduction

Since the launch of the digital mobile phone system in the early 1990s (GSM or '2G'), the rate of growth in mobile bandwidth per terminal has been faster than the rate of growth in number of gates on an integrated circuit chip, as predicted by Moore's Law (Fig. 9.1). In the nature of the progression of digital businesses, both customers and investors will come to expect this trend to continue and hence great ingenuity will be needed to find ways of providing more and more bandwidth as time advances. One way of achieving this is simply to embrace higher frequencies, such as millimetre-wave bands, where large amounts of unused bandwidth exist. Unfortunately, there are various problems in utilising these bands, not least the difficulties of propagation through walls and around obstacles. As an alternative strategy, ways are being found to exploit the existing bands at lower frequencies more

O. Arabi
Wrexham Glyndwr University, Wrexham, UK

Khalifa University of Science and Technology, Abu Dhabi, UAE

N.T. Ali
Khalifa University of Science and Technology, Abu Dhabi, UAE

B. Liu
Wrexham Glyndwr University, Wrexham, UK

R.A. Abd-Alhameed
Wrexham Glyndwr University, Wrexham, UK

University of Bradford, Bradford, UK

P.S. Excell (✉)
Wrexham Glyndwr University, Wrexham, UK

University of Bradford, Bradford, UK
e-mail: p.excell@glyndwr.ac.uk

I. Elfergani et al. (eds.), *Antenna Fundamentals for Legacy Mobile Applications and Beyond*, DOI 10.1007/978-3-319-63967-3_9

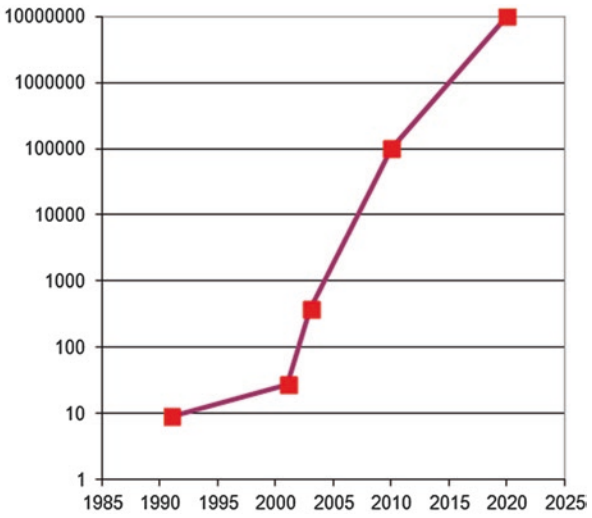

Fig. 9.1 Theoretical maximum data bandwidths (kilobits per second) for successive generations of digital mobile phone technology (2G–2.5G–3G–4G–5G: 5G target is still aspirational)

and more efficiently. A key initiative that has moved from exotic research into mainstream applications has been the exploitation of the ideas of multiple-input multiple-output (MIMO) to get multiple data channels in the same frequency spectrum allocation, by discriminating between the angle of arrival of scattered waves. This has now been widely exploited in later versions of the IEEE 802.11 wireless data standard.

Another innovation that has progressed from government applications into an offering in the commercial marketplace has been ultrawideband (UWB), which enables wireless signals to be overlaid on traditional, relatively narrowband, signals by conveying information in a form that appears simply to be underlying noise. Attempts to crystallise this in a commercial standard were made under the aegis of IEEE 802.15.3a, although work on this is currently stalled due to irreconcilable differences between key proponents [1]. Nonetheless, the radical technical opportunities that this technology offers suggest that it cannot remain forever dormant.

MIMO systems were originally conceived to exploit spatial discrimination of the angle of arrival of direct and scattered signal paths, but this requires the use of array antennas that can become physically rather large in the context of the requirements of a mobile handset, since the elements must be spaced a significant fraction of a wavelength apart. An alternative approach is to exploit polarisation discrimination, as was first propounded in a landmark paper in the journal *Nature* [2]: this enables the antennas on the receiving array to be effectively co-located at a single point, only differing in their relative orientations. Such an array is substantially smaller than one using spatial discrimination and hence more amenable to incorporation into a handset.

Recently, ultrawideband (UWB) systems have attracted more attention because they allow signal transmission over a large bandwidth with a low energy level [3–6]. In practical applications, planar antennas, such as microstrip patch antennas, are good candidates for integration in compact electronic devices. However, they are inherently narrowband in their basic form and hence advanced design techniques are required to make them capable of meeting the demands of UWB operation. However, in order to further increase data throughput and exploit multipath propagation, MIMO has also been considered for UWB systems [7].

In this chapter, a UWB array antenna is presented, which consists of two elements, each with four electromagnetically coupled parasitic elements with a driven patch, placed back to back in a stacked structure. The patch shape, feeding structure, substrate properties and the antenna configuration are chosen to achieve the desired performance in the UWB frequency band. The design achieves a bandwidth of 3.7 GHz while maintaining a satisfactory isolation between the channels.

9.2 Antenna Configuration, Underlying Mechanism and Feeding Structure

9.2.1 Antenna Geometry and Configuration

The proposed stacked UWB MIMO antenna array had the dimensions 30 mm × 30 mm × 10 mm, with two feeding ports, as illustrated in Fig. 9.2, and with design parameters as shown in Table 9.1: the precise design parameters shown in the third column of this table are those that were found after use of the optimisation procedure discussed later in this chapter.

In order to widen the impedance bandwidth, four parasitic elements were used and stacked on top of the driven element, placed on the dielectric layer of Rogers Corp. RO4003C laminate, having dielectric constant $\varepsilon_r = 3.38 \pm 0.05$, dissipation factor tan $\delta = 0.0027$ and thickness of 3.048 mm (two laminates of 1.524 mm thickness bonded together). The four top patches with size 8.4 mm × 8.4 mm (nearly $\lambda/4$) are separated by the same gap, $d3 = 0.036\lambda$, in both x and y directions and electromagnetically coupled to a driven patch (10 mm × 10 mm) etched on the second

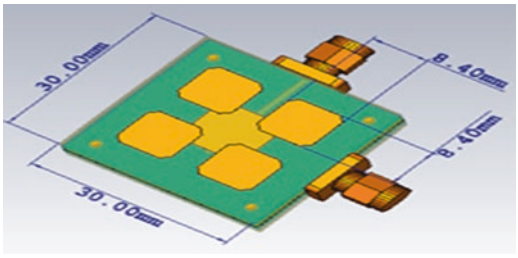

Fig. 9.2 Antenna structure

Table 9.1 Antenna design parameters

Parameters	Specifications	Dimensions (mm)
Antenna width	*Ly*	30
Antenna length	*Lx*	30
Parasitic patch width	*L*3	8.4
Parasitic patch length	*w*3	8.4
Main patch width	*L*2	10
Main patch length	*w*2	10
Separation b/w parasitics	*d*3	1.68
Feeding strip length	*x*_port	20.45
1st layer thickness	*h*3	3.048
2nd layer thickness	*h*2	1.905
3rd layer thickness	*h*1	0.813
Ports width control	*w*1	1.1
Via wrt. main patch ctr.	*x*_via	3.5

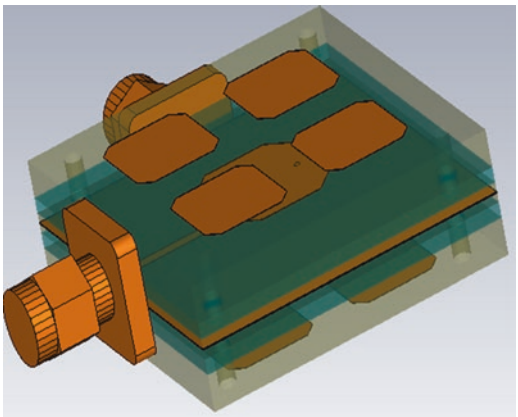

Fig. 9.3 The UWB MIMO antenna with the feeding structure

dielectric layer. The second layer is Rogers Corp. RT/duroid 6006 laminate, with dielectric constant $\varepsilon_r = 6.15 \pm 0.15$, dissipation factor tan $\delta = 0.0027$ and thickness 1.90 mm.

The feeding structure is a stripline of approximately $\lambda/2$ in length and placed on the 4003C layer, having the same characteristics as given earlier but with a reduced thickness of 0.813 mm, under the radiating patch on the dielectric layer. Both the stripline and the main patch are connected by means of vias on the RT/duroid 6006 layer, as shown in Fig. 9.3. This arrangement is placed in a back-to-back structure in which a replicated version is placed on the opposing side. To achieve additional polarisations, an orthogonal configuration can also be created, as shown in Fig. 9.4. The antenna geometries can be efficiently optimised by adjusting the size of the top patches, the separation of the patches on the top layer and the spacing between the two dielectric substrates. However, the latter is restricted by the availability of laminate thicknesses.

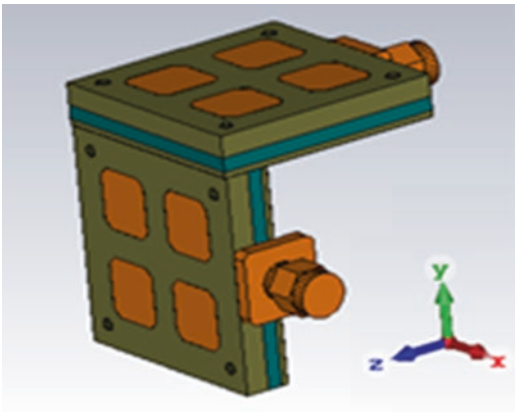

Fig. 9.4 UWB MIMO antenna with orthogonal structure

9.2.2 Antenna Feeding Considerations

An exploded view of the feeding structure is shown in Fig. 9.5. In order to increase the operational bandwidth of the patch antenna with the standard feeding technique (edge-fed), the thickness of the radiating element must be increased. However, a considerable increase in the size of the feeding line would occur, resulting in the radiation pattern of the antenna being significantly affected [8, 9]. Using a thick substrate is not an efficient alternative since it would be considerably more expensive than standard versions and it would support the excitation of the surface wave, leading to radiation losses and diffraction effects, resulting in antenna radiation pattern perturbation [8, 9].

To eliminate these drawbacks, a practical solution is to use a via-coupled microstrip patch with the stripline in which the patch substrate layer can be modified without affecting the feed layer. In this arrangement, a substrate of RT/duroid 6006 with thickness 1.90 mm is used for the patch layer, and a substrate of 4003C with thickness 0.813 mm is applied for the feed layer. Thus, this arrangement provides structural rigidity and minimises the effects of air gaps [10].

Figure 9.6 shows the general structure of the basic corporate feed for operation with a 50 Ω transmission line. The feeding stripline with length of 0.44λ (20.45 mm) and width of 0.024λ (1.1 mm) is connected to the radiating patch by means of a stud on a via in the layer between the main patch and the feeding line.

By precisely adjusting the location of the feeding point, impedance matching between the microstrip line and the radiating patch will be achieved. The antenna excited by this feeding structure usually features a wider impedance bandwidth and high polarisation purity, although it has higher fabrication complexity and cost than single-layered structures. Hence, feed structure design plays a substantial factor in widening the impedance bandwidth and enhancing radiation performance.

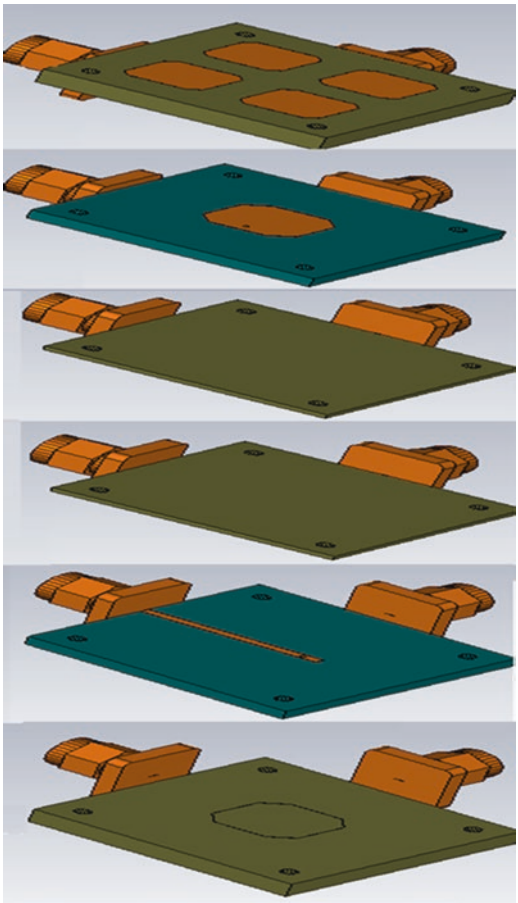

Fig. 9.5 The UWB MIMO antenna feeding structure

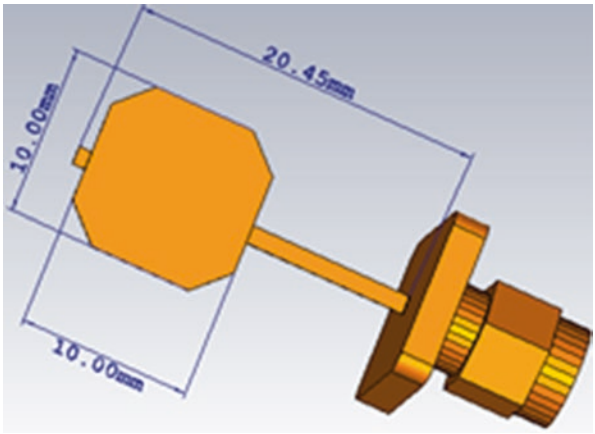

Fig. 9.6 Feeding structure

9.2.3 *Antenna Design and Bandwidth Requirements*

It is well known that basic microstrip patch antennas suffer from narrow bandwidth due to the strongly resonant nature of the simple patch. Therefore, such an antenna can be considered as a high-Q circuit; so, in order to alleviate the narrow bandwidth, an approach is to decrease the Q. While the enhancement of the bandwidth is relatively limited, different methods and techniques have been explored to reduce the Q, such as choosing an appropriate radiator shape, increasing the losses, thickening the substrate and lowering the dielectric constant [11–13]. On the other hand, using impedance matching and introducing multiple resonances has been proved to make significant enhancements to the microstrip bandwidth.

The four parasitic radiating patches are excited by the means of electromagnetic coupling between them and the driven patch below: the parasitic patches are stacked above the radiating patch with a slight offset from the centre and this small gap allows the elements to be strongly coupled with the radiating patch. In this arrangement, the combination of the coplanar and stacked structures achieves a low-profile design with an ultrawide bandwidth and high gain. This allows the impedance bandwidth to be significantly enlarged: typically, the bandwidth is in the order of 62–82%, with a voltage standing-wave ratio (VSWR) of less than two over the operational frequency.

For the examination of the impedance matching and the radiation performance of the antenna, the main key parameters of the design must be considered: the size of the top four patches, the separation between the patches, the spacing between the two dielectric substrate layers and the location of the via with respect to the radiating patch and the feeding stripline. By using the technique of "parameter, sweep" available in the CST simulation software [14], it is possible to vary the patch and stripline geometries so that the output S-parameters can be assessed, as will be explained in the following paragraphs.

By initially considering the length and the width of the top patches $w3$ and $L3$ respectively, these are varied from 5 mm to 10 mm simultaneously, with $d3 = 1.68$ mm, $h3 = 3.048$ mm and $x\_via = -3.5$ (see Table 9.1). As seen in Fig. 9.7, increasing the parasitic patch size results in excitation of the upper resonance at

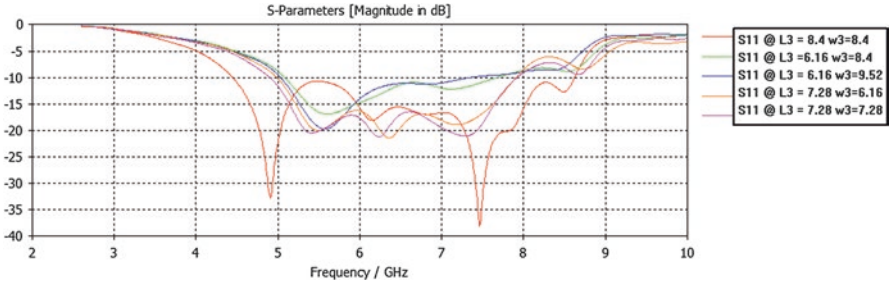

Fig. 9.7 Predicted S-parameters with varying parasitic patch size

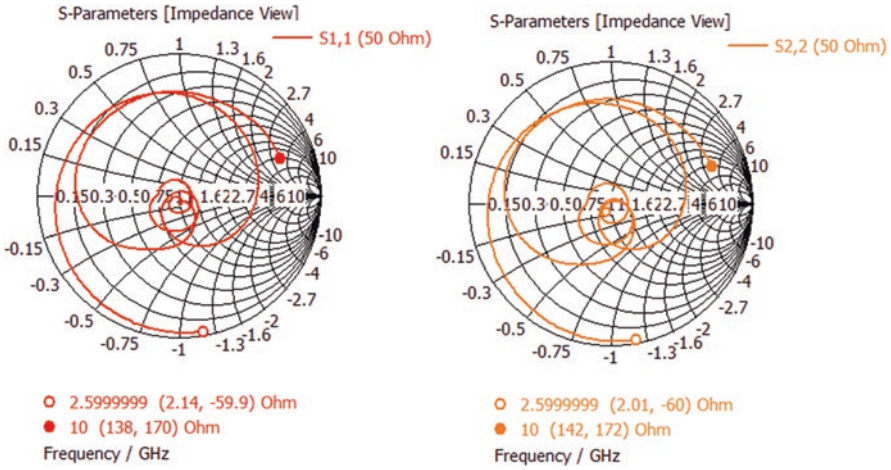

Fig. 9.8 Simulated S_{11} and S_{22} Smith charts for optimised UWB MIMO antenna

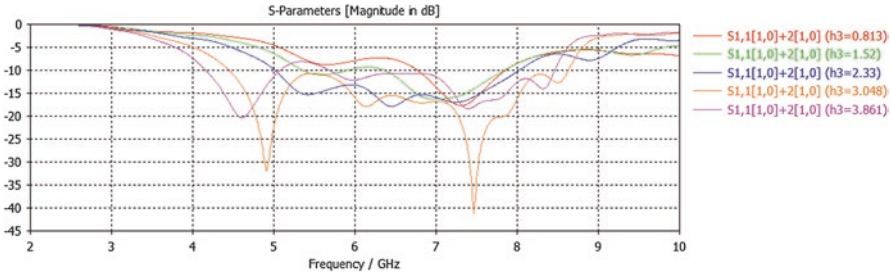

Fig. 9.9 S-parameters with varying substrate height $h3$

frequencies higher than 8.48 GHz. Further increases in the size lead to the disappearance of the lower resonance at around 4.45 GHz. Also, the S-parameter results show that, in terms of S_{11} less than −10 dB, the two resonances are well excited when the size of $L3$ and $w3$ is equal to 8.4 mm. This is demonstrated in Fig. 9.8, showing that the minor loops encompass the centre of the Smith chart with the size of the patches being 8.4 mm × 8.4 mm; hence, optimal impedance matching is accomplished.

Further, the effect of variation of the separation distance $h3$ between the top layer (4003C) and the middle layer (RT6006) was investigated. As mentioned earlier, this parameter is restricted by the thicknesses of the standard dielectric laminates that are commercially available, to avoid the considerable rises in cost and complexity of the design if non-standard thicknesses were to be chosen. Thus, different standard thicknesses of Rogers Corp. RO4003C laminate were considered: 0.813 mm, 1.52 mm, 2.33 mm (two laminates of 1.52 mm and 0.813 mm bonded together) and 3.048 mm (two laminates of 1.52 mm bonded together). The S-parameter results are shown in Fig. 9.9: it is noticeable that when $h3$ is around 0.813 mm, the resonances

almost disappear, but with the increase in the height of the substrate the resonances start to be manifested, until $h3$ reaches 3.048 mm, at which height a well-matched bandwidth is achieved. From the graph, it is clear that any further increase in the spacing $h3$ will result in degradation of the bandwidth as the lower resonance fades.

In Fig. 9.10, the effects of varying the separation $d3$ between the parasitic elements are illustrated. The separation distance is varied from 1.49 mm to 2.8 mm with other parameters set at the best design values. It can be seen that, with increase of the separation $d3$, the bandwidth starts to broaden until it reaches UWB performance at $d3 = 1.68$ mm, after which the frequencies corresponding to the lower and upper edges of the bandwidth are gradually shortened. As $d3$ increases, the upper resonance disappears, leading to a considerable degradation in the bandwidth.

Finally, a crucial factor in the design is the location of the via, x_via, connecting the radiating patch to the stripline through the layer RT6006. The variation in the via location affects the stripline length (which is nearly $\lambda/2$), as well as the excitation of the driven patch. For the geometry sweep, we consider the measured distance for the via location with respect to the centre of the main patch: this distance was varied arbitrarily with respect to the centre and the coordinates of the radiating patch, the designated points for the sweep being −4.5 mm, −3.5 mm, 0 mm, 3.5 mm and 4.5 mm.

From Fig. 9.11, showing S_{11} for the varying via locations, it is observed that, as the via moves away from the centre, the stripline length will increase and the antenna

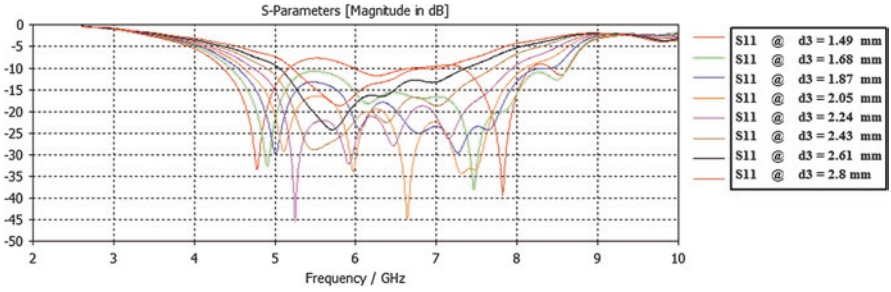

Fig. 9.10. S-parameters with varying patch spacing distance $d3$

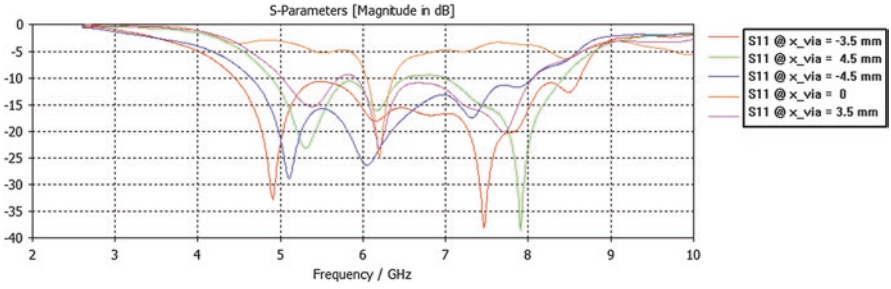

Fig. 9.11 S-parameters with varying via locations x_via

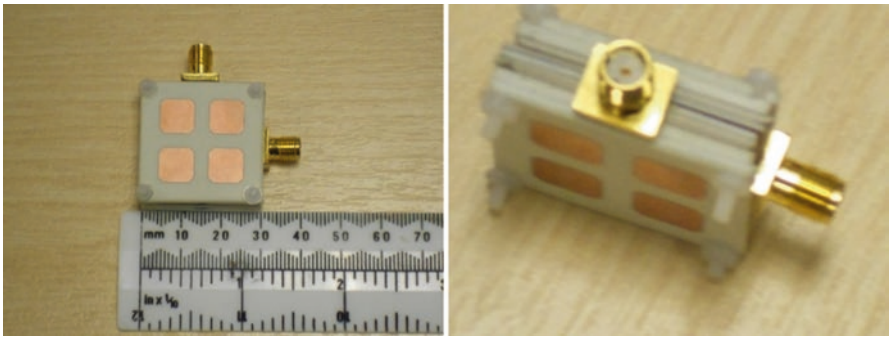

Fig. 9.12 The UWB MIMO antenna prototype

bandwidth increases until it is distorted at 4.5 mm. The optimum result was achieved when the via was located at −3.5 mm with respect to the radiating patch centre and in the specified direction.

From the results achieved and reviewed above, it is clear that, for an efficient and effective design, an optimisation tool must be employed to select the best geometry parameter values since there could be significant interactions between the parameters that have been varied. However, the current optimisation tools have several drawbacks that might not lead to accurate results within an acceptable time frame, and for this problem a new technique was developed, based on the method presented in [15], in which the multi-fidelity framework is proposed, with the design objective of minimising maximum S_{11} over the entire operational frequency band. However, as mentioned earlier, this design has constraints that must be satisfied in order to preserve the structure functionality. The results obtained from the multi-fidelity framework have been used for the design of the antenna presented in the rest of this chapter: the obtained best design parameters are shown in Table 9.1.

9.3 Tests of Physical Implementation

The optimised design of the compact UWB MIMO antenna was fabricated, as shown in Fig. 9.12. However, the following issues arose during the design and fabrication. Firstly, the material duroid/RT6006 was not available with the required size from the Rogers Corporation, and so it was replaced by Rogers 3006 with the dielectric constant $\varepsilon_r = 6.15 \pm 0.15$, dissipation factor tan $\delta = 0.0020$ and thickness 1.28 mm. This thickness is less than the optimum simulated design thickness of 1.92 mm, and so obviously the bandwidth will be reduced, as demonstrated by the parameter sweep for varying $h3$.

Secondly, due to unavailability of the 4003C laminate with a thickness of 3.048 mm, the parasitic element layer of this material has been made of two laminates of thickness 1.52 mm bonded at the sides by screws. Finally, other fabrication tolerance issues should be noted, such as the losses due to the soldering and soldering

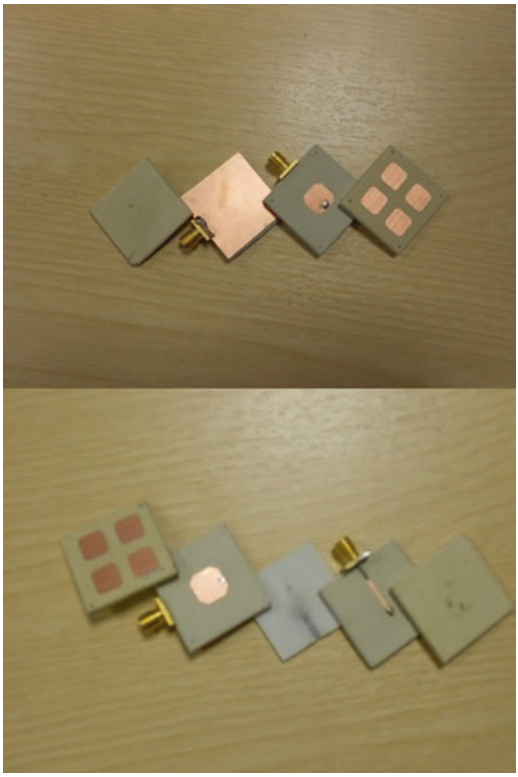

Fig. 9.13 The layers of the physical implementation of the antenna

gaps, laminate cutting, cabling and the test chamber calibration tolerances. The components of the measured antenna and the feeding structure are illustrated in Fig. 9.13.

9.3.1 Return Loss and Impedance Bandwidth

In this section, the simulated and measured S-parameters of the prototype antenna are presented. The simulation results were obtained using the time-domain solver of CST Microwave Studio [14]. The bandwidth performance was measured with an Agilent E3333B vector network analyser. Figure 9.14 compares the measured and simulated results of S_{11}. From the simulation result, it is observed that the antenna exhibits UWB behaviour, with the lower frequency band limit at 4.45 GHz and the upper limit at 8.48 GHz, giving an overall bandwidth of 4.03 GHz. Moreover, it is seen that both feeding ports have the same impedance bandwidth (determined from −10 dB return loss), which is about 82% referenced to the resonant frequency at 4.9 GHz. On the other hand, the measured result exhibits a bandwidth of 3.66 GHz (4.53–8.19 GHz), which is lower than the simulated one. As stated earlier, h3 is one

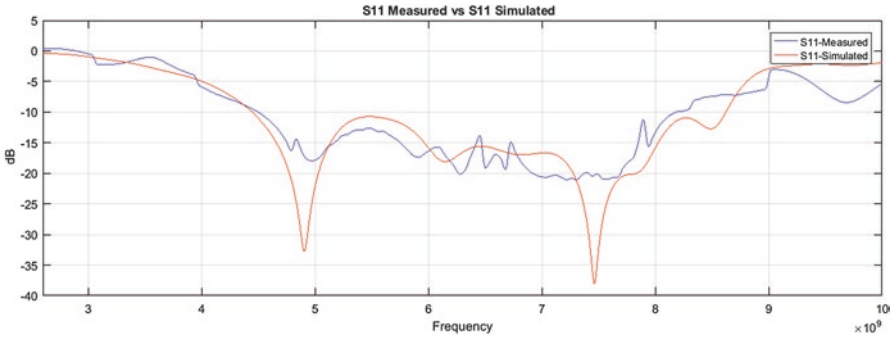

Fig. 9.14 Measured and simulated S_{11}

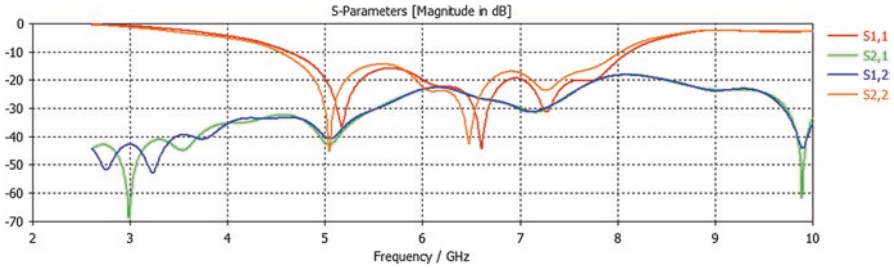

Fig. 9.15 Full set of simulated S-parameters

of the critical parameters of the design, and the $h3$ variance between the simulated and measured designs is 0.64 mm, which is sufficient to affect the impedance bandwidth negatively.

Figure 9.15 shows the full set of simulated S-parameters, and Fig. 9.16 shows the measured S_{12} and S_{21}. Generally speaking, the measured and simulated S-parameters are in reasonably good agreement, with tolerable discrepancies. It is noteworthy that, across the entire required bandwidth, the simulated mutual coupling (S_{21}) is below −18 dB, while the measured results show mutual coupling below −30 dB. Hence, the antenna satisfies the impedance matching requirement for the entire UWB frequency band, as specified by the United States federal communications commission (FCC) as well as mutual coupling of less than −15 dB that is sufficient for UWB applications [16].

9.3.2 Orthogonal Configuration of Elements

For polarisation diversity, the orthogonal arrangement shown in Fig. 9.4 is needed. The results are closely similar to the back-to-back configuration with some deviations. The S-parameters are shown in Fig. 9.17: over a bandwidth of 3.7 GHz (4.78 GHz–8.4 GHz), S_{11} and S_{22} are better than −10 dB except for a small region at

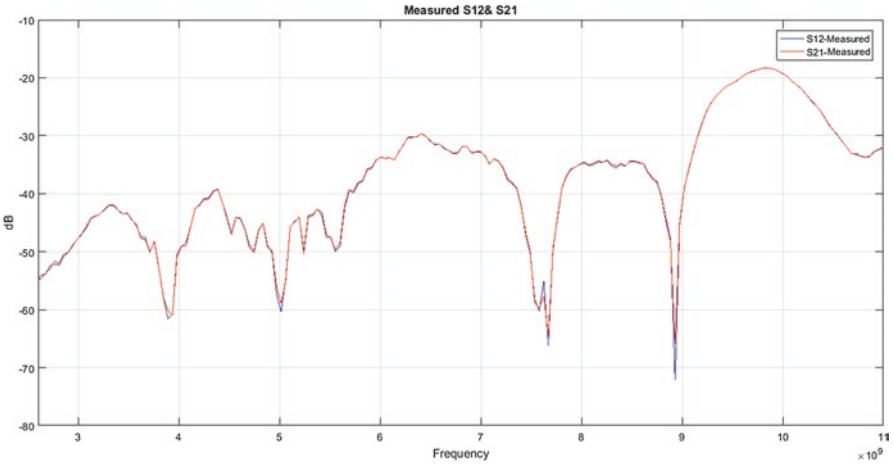

Fig. 9.16 Measured S_{12} and S_{21}

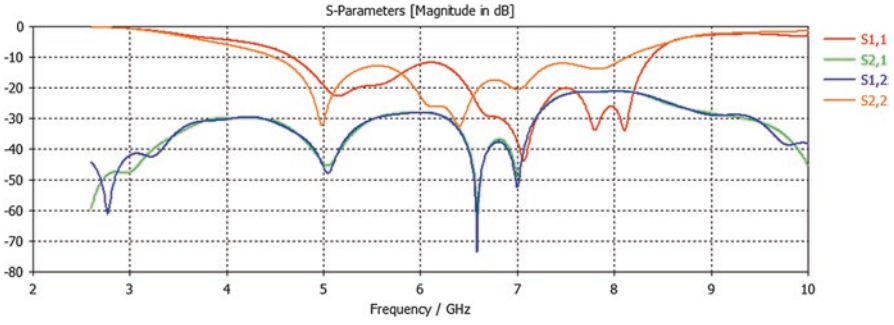

Fig. 9.17 S-parameters for antenna in orthogonal configuration

the top end of the band for S_{22} (it is certain that this could be cured with some minor tuning); the mutual coupling is better than −21 dB over the operational band, which is more than adequate for UWB applications.

9.3.3 Radiation Patterns

Representative simulated and measured radiation patterns for the non-orthogonal antenna are shown in Figs. 9.18 and 9.19. The simulation results were produced using the CST simulation software. The radiation patterns of the antennas were measured in an anechoic chamber. The measured patterns show reasonably good agreement with the simulated ones. The discrepancies in the measured results are caused by gain error of the standard antenna, mounting position of the test antenna, and the mast of the positioner.

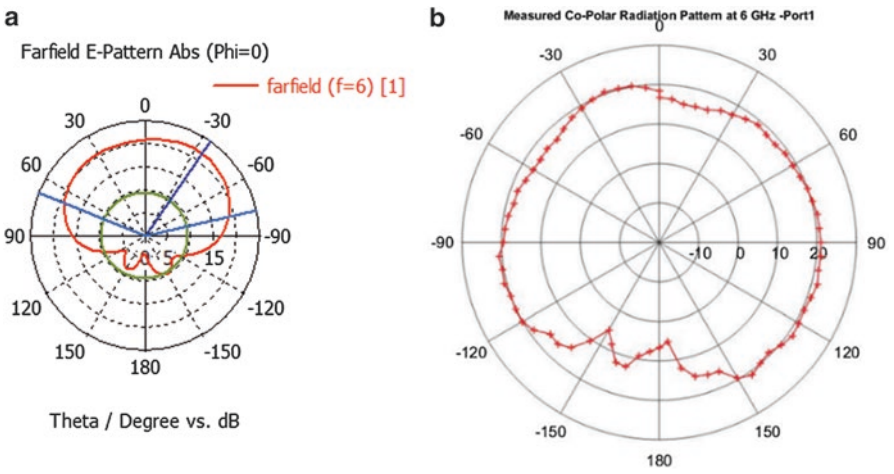

Fig. 9.18 (**a**) Simulated and (**b**) measured co-polar radiation patterns at 6 GHz for port 1

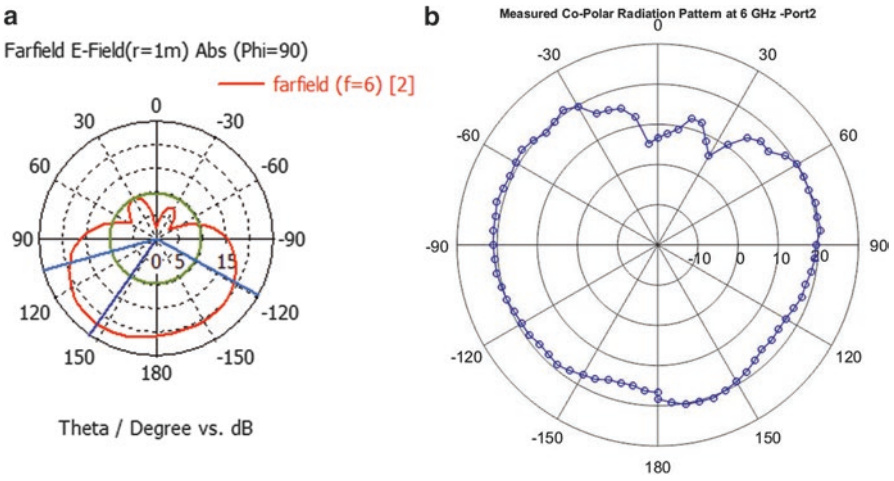

Fig. 9.19 (**a**) Simulated and (**b**) measured co-polar radiation patterns at 6 GHz for port 2

However, the simulated and measured results for cross-polar components (Figs. 9.20 and 9.21) show values less than 15 dB lower than the co-polar components. Cross-polar radiation is undesirable in many cases because it causes crosstalk in polarisation diversity systems and hence it has to be suppressed; however, 15 dB suppression is sufficient for most applications.

Simultaneous excitation of ports 1 and 2 demonstrated an approximately omni-directional behaviour, as shown in Fig. 9.22.

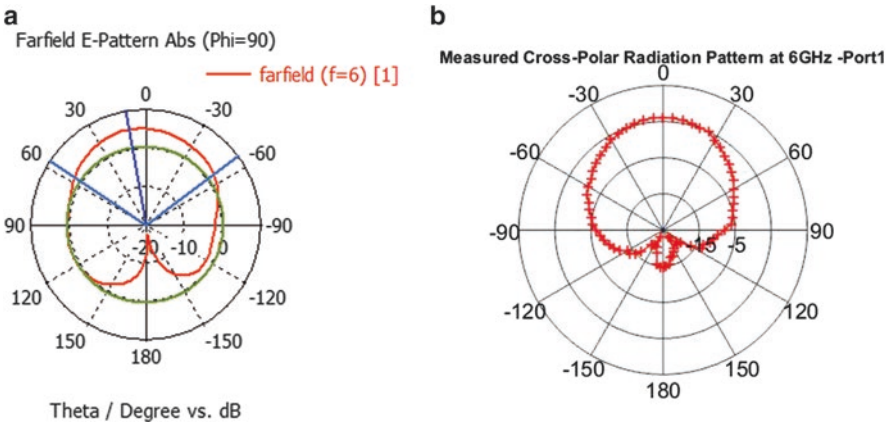

Fig. 9.20 (**a**) Simulated and (**b**) measured cross-polar radiation pattern at 6 GHz for port 1

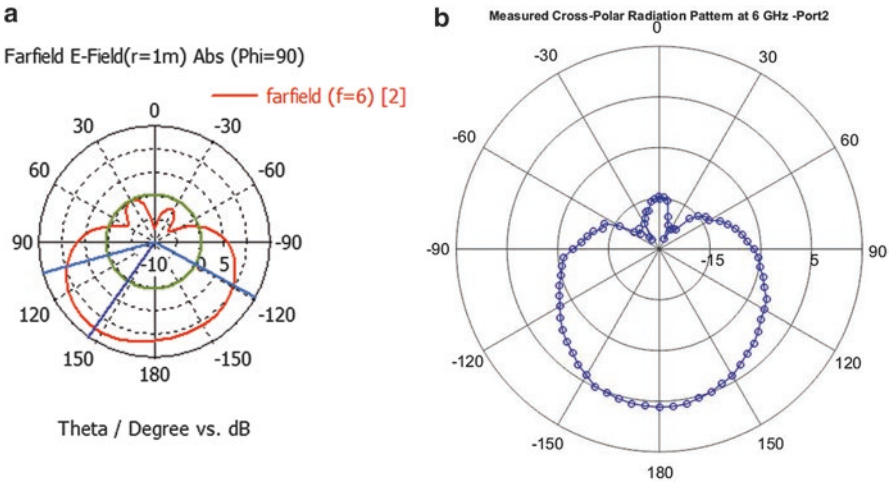

Fig. 9.21 (**a**) Simulated and (**b**) measured cross-polar radiation pattern at 6 GHz for port 2

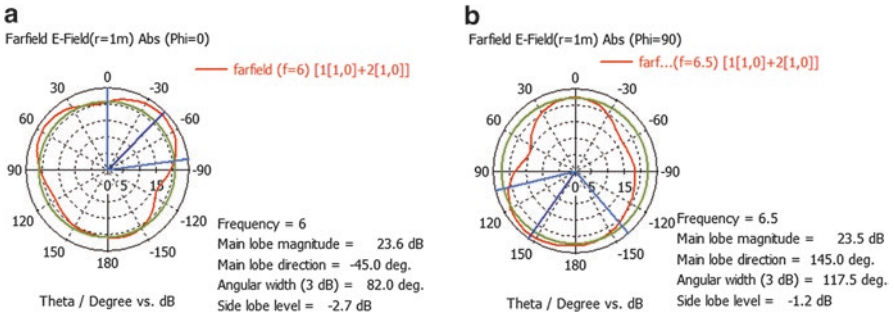

Fig. 9.22 Simulated radiation patterns at 6 and 6.5 GHz for simultaneous excitation of ports 1 and 2

9.3.4 Current Distributions

The simulated current distributions on the UWB MIMO antenna at a frequency of 6.5 GHz are presented in Fig. 9.23, as a typical example. On the parasitic patches, the current is mainly distributed along the edges of the slots. The current patterns indicate the existence of different resonance modes, confirming that the antenna is capable of supporting multiple resonant modes, and the overlapping of these multiple modes leads to the UWB characteristic.

9.3.5 MIMO Diversity and Correlation Coefficient

Fading is one of the main reasons for signal degradation with single channels in scattering-rich environments, due to multipath propagation. One way to overcome this is to use diversity reception, so that weakness in one path can be compensated by strength in another. The two feeds in the prototype antenna can be used in this way. In order to confirm the diversity feature of the antenna, the diversity gain was computed from the radiation pattern, as shown in Fig. 9.24. It can be noticed that the diversity gain is on the average around 8.5 dB and reaches a maximum in the desired band of 8.7 dB at 7 GHz, having adequate values over the entire operational frequency band.

Another important factor for MIMO operation is the envelope correlation coefficient. In order to obtain good diversity, the correlation between the antenna elements must be low. Antenna envelope correlation can be caused by small antenna spacing but, as shown in Fig. 9.25, the coupling between the antenna elements has been minimised, causing the envelope correlation coefficient to be almost zero over the entire desired operational band. From the low correlation coefficient and high diversity gain, it can be confirmed that the antenna is suitable for MIMO applications.

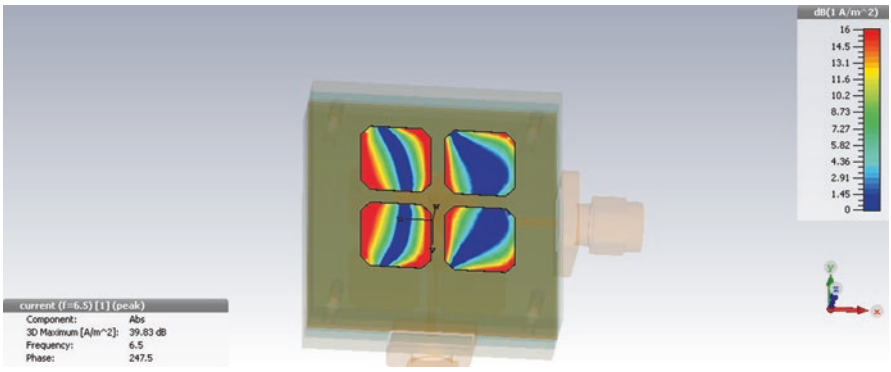

Fig. 9.23 Simulated current distribution at 6.5 GHz

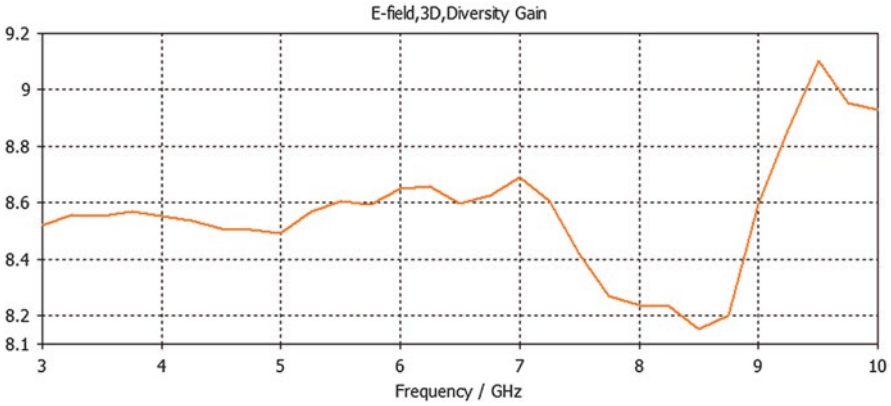

Fig. 9.24 Simulated diversity gain from E-field for antenna

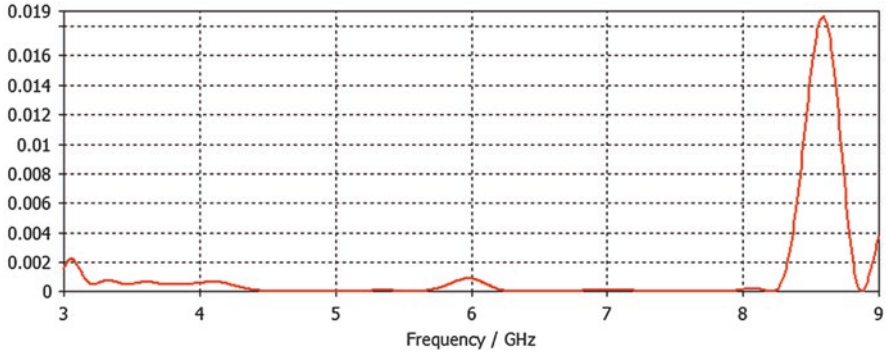

Fig. 9.25 Simulated envelope correlation coefficient from radiation pattern for antenna

9.4 Conclusions

The design of a compact ultrawideband two-element array antenna has been presented. The two elements are orthogonally polarised, giving excellent isolation between them despite their close proximity. This permits them to form the basis of a multiple-input multiple-output (MIMO) array exploiting the principle of multi-polarisation MIMO, which permits much more compact antennas than for the more widely known spatial discrimination approach. The antenna exploits a novel stacked structure and special feeding mechanism, which enables it to operate over a very wide bandwidth, corresponding to the UWB regime. From the parameter sweep exercise, it was observed that, in order to achieve a high-quality design, an optimisation mechanism must be employed to achieve the desired output results efficiently: an advanced approach based on evolutionary algorithms was applied to achieve this.

Experimental tests of a physical realisation confirmed the UWB characteristics of the proposed antenna. Nearly omnidirectional radiation properties of each element into its own half-space over the majority of the bandwidth were demonstrated. The isolation between the two element ports was better than −18 dB, confirming the predicted decoupling required for MIMO. Ideally, at least three elements are needed for full-scale multi-polarisation MIMO, but the third element can be constructed on the same principles. Alternatively the two-element array can be used for diversity reception, with a simpler receiver. The design is considered to be the basis of an attractive candidate for future UWB MIMO applications.

References

1. S. Jogi, M. Choudhary, *Ultra Wideband Demystified: Technologies, Applications, and System Design Considerations.* River Publishers, Gistrup DK. (2009)
2. M.R. Andrews, P.P. Mitra, R. deCarvalho, Tripling the capacity of wireless communications using electromagnetic polarization. Nature **409**, 316–318 (2001). doi:10.1038/35053015
3. L. Wang, B. Huang, Design of ultra-wideband MIMO antenna for breast tumor detection. Int. J. Antennas Propag. **2012**, 1–7 (2012)
4. S. Mohammad, A. Nezhad, H.R. Hassani, A. Foudazi, A dual-band WLAN/ UWB printed wide slot antenna for MIMO/diversity applications. Microw. Optical Technol. Lett. **55**(3), 461–465 (2013)
5. M. Jusoh, M.F. Jamlos, M.R. Kamarudin, F. Malek, M.H. Mat, M.A. Jamlos, A novel compact tree-design antenna (NCTA) with high gain enhancement for UWB application. J. Electromagn. Waves Appl. **25**(17–18), 2474–2486 (2011)
6. S. Zhang, Z. Ying, J. Xiong, S. He, Ultrawideband MIMO/diversity antennas with a tree-like structure to enhance wideband isolation. IEEE Antennas Wireless Propag. Lett. **8**, 1279–1282 (2009)
7. A. Toktas, A. Akdagli, Compact multiple-input multiple-output antenna with low correlation for ultra-wide-band applications. IET Microw. Antennas Propag. **9**, 822–829 (2015)
8. P.S. Hall, C.M. Hall, Coplanar corporate feed effects in microstrip patch array design. Proc. IEE, Part H, **135**, 180–186 (1988)
9. J. Huang, The finite ground plane effect on the microstrip antenna radiation pattern. IEEE Trans. Antennas Propag. **AP-31**(4), 649–653 (1983)
10. J.F. Zurches, The SSFIP: a global concept for high performance broadband planar antennas. Electron. Lett. **24**(23), 1433–1435 (1988)
11. D. M. Pozar, D. H. Schaubert (eds.), *Microstrip Antennas: Analysis and Design.* Wiley, New York. (1995)
12. K.F. Lee, K.M. Luk, K.F. Tong, S.M. Shum, T. Huynh, R.Q. Lee, Experimental and simulation studies of the coaxially fed U-slot rectangular patch antenna. IEE Proc Microw. Antennas Propag. **144**(5), 354–358 (1997)
13. R. Garg, P. Bhartia, I. Bahl, A. Ittipiboon, *Microstrip Antenna Design Handbook.* Artech House, Boston, MA. (2001)
14. CST Software Author Team, Studio-workflow and solver overview. Darmstadt: CST-Computer Simulation Technology AG. (2016)
15. B. Liu, S. Koziel, Q. Zhang, A Multi-fidelity surrogate-model-assisted evolutionary algorithm for computationally expensive optimization problems. J Comput. Sci **12**, 28–37 (2016)
16. L. Liu, S.W. Cheung, T.I. Yuk, Compact MIMO antenna for portable devices in UWB applications. IEEE Trans. Antennas Propag. **61**(8), 4257–4264 (2013)

Chapter 10
Compact Wideband Printed MIMO/Diversity Monopole Antenna for GSM/UMTS and LTE Applications

Chan H. See, Adham Saleh, Ali A. Alabdullah, Khalid Hameed, Raed A. Abd-Alhameed, S.M.R. Jones, and Asmaa H. Majeed

10.1 Introduction

With unprecedented use of the portable devices such as mobiles and tablets, the existing capacity and bandwidth of current wireless communication systems have become insufficient, in particular for the future mobile generations. Thus, new systems along with sufficient and adequate data rates have been recently come into the market. These new systems include HSPA (3.5G), LTE (4G), WiFi, WiMAX and UWB [1–3]. In addition, the new mobile handsets are foreseen not only to have seamless inter-operation with the present systems such as second and third generations but also to be easily adopted to those new standards.

The technology of the multiple-input-multiple-output (MIMO), which uses multiple antennas at both sides of the transmitter and receiver, is expected to offer high data rates and low latency communication system, without the need to have an additional or extra power and other requirements in the rich scattering environments [2, 4, 5].

However, antenna designers are still facing a prominent and recurring problem when implementing the MIMO paradigm application. This problem is related to strong coupling between the antenna elements and this results leakage current when MIMO needs to be deployed in a limited space, such as mobile handsets. In this

C.H. See (✉)
School of Engineering, University of Bolton, Deane Road, Bolton BL3 5AB, UK
e-mail: C.See@bolton.ac.uk

A. Saleh • A.A. Alabdullah • K. Hameed • R.A. Abd-Alhameed • S.M.R. Jones
School of Electrical Engineering and Computer Science, University of Bradford, Richmond Road, Bradford BD7 1DP, UK

A.H. Majeed
College of Engineering, University of Al-Nahrain, Baghdad, Iraq

I. Elfergani et al. (eds.), *Antenna Fundamentals for Legacy Mobile Applications and Beyond*, DOI 10.1007/978-3-319-63967-3_10

context, the correlation coefficients between MIMO antenna elements are very high leading to a drastic drop in the antenna efficiency. Moreover, another challenge is the tremendous demand to design an MIMO antenna, which operates in existing services together with the new standards such as the Long Term Evolution (LTE), the term that is given to 4G in mobile communication networks. For more clarifications, contemporary MIMO antennas should cope and meet whole the characteristics and performances of a single-element antenna, emphasizing to have a low mutual coupling between the antenna elements.

Over the last decade, several significant and novel approaches to improve the isolation between the MIMO antenna elements have been reported [6–25]. These techniques and solutions were applied to several antenna design with different band classifications such as narrow band [6–17], wideband [18–21] and dual/triple band [22–26].

10.1.1 Narrow Band MIMO Antennas with Reduced Mutual Coupling

A remarkable effort and solution have been invested to design narrow band MIMO antennas. The narrow band MIMO antennas comprise of several standards starting from the existing generations up to the new and expected services. For example, in [6] MIMO antenna design for the operation in the LTE700 MHz was proposed, GSM800 MHz MIMO antenna was studied and investigated in [7, 8], a UTMS MIMO antenna was studied in [9] and another MIMO antenna covering the lower and upper WLAN, namely, 2400 MHz and 5200 MHz, was presented in [10–14].

Moreover, several approaches in order to improve the mutual coupling were applied to those MIMO antennas. A ferrite material was used to improve the isolation between the MIMO antenna element as in [6]; a method called magneto-dielectric substrates was employed to antenna in [7], which hugely minimize the mutual coupling, and the idea of introducing some parasitic elements exactly between the two antennas was proposed in [8, 9], the aid of using resonators was also seen as an effective avenue to improve the isolation between the antenna elements as in [10], a novel approach of reducing the coupling was seen through the implementation of neutralization line [11] and generating a sort of slits over the PCB could also be a way to stop the current flow from one element to another [12], introducing the lumped elements [13, 14], ground plane with heavily slots [15], orthogonal arrangement of the antenna elements [16] and a reconfigurable mechanism by using a varactor diode [17].

As can be noted in Table 10.1, all these techniques have accomplished good mutual coupling which ranges from 10 dB to 40 dB for reasonable inter-element distances from 0.03 λ_0 to 0.17 λ_0.

Table 10.1 Previous work of narrow band MIMO antennas

Reference	Size (mm^3)	Bandwidth (GHz)	Separation distance	Isolation/return loss (dB)
[6]	110 × 50 × 3.8	0.677–0.765	0.1 λ_0	16.4/6.0
[7]	100 × 50 × 4.2	0.746–0.823	0.15 λ_0	15.0/6.0
[8]	50 × 40 × 1.6	0.760–0.886	0.03 λ_0	12.0/10.0
[9]	95 × 60 × 0.8	1.92–2.17	0.17 λ_0	20.0/10.0
[10]	50 × 50 × 6	2.3–2.4	0.09 λ_0	25.0/10.0
[11]	65 × 30 × 0.8	2.4–2.5	0.112 λ_0	15.0/10.0
[12]	75 × 50 × 2.6	2.4–2.5	0.08 λ_0	25.0/10.0
[13]	67.5 × 22 × 0.8	2.4–2.5	0.04 λ_0	20.0/10.0
[14]	34.6 × 34.6 × 1	5.2–5.3	0.1 λ_0	20.0/10.0
[15]	32 × 27.8 × 0.8	5.75–5.85	0.031 λ_0	40.0/10.0
[16]	38 × 15 × 3.2	5.75–5.83	0.14 λ_0	20.0/10.0
[17]	50 × 40 × 0.8	1.4–1.65	0.05 λ_0	10.0/10.0

10.1.2 Wide Band MIMO Antennas with Reduced Mutual Coupling

The key challenge here is to compromise between the operating frequency bandwidth, isolation level as well the limited space between the MIMO antenna elements. In other words, it is not desirable to achieve one of the above features at the cost of another one. For example, it is not practical to come up with a wideband MIMO design, while the isolation is significantly high. In addition, having a much larger MIMO antenna with longer distance between the elements will help in reducing the coupling; however, it is not practical to be incorporated within today's smart devices.

To meet this challenge, some methods to enable wideband operation, while the isolation is being improved, were reported in [18–21]. In [18], an isolation as high as −11 dB at 0.25 λ_0 spacing for a broadband range from 1.65 to 2.5 GHz has been achieved. An improved mutual coupling is observed within the very limited spacing distance by orthogonal arrangement of the antenna elements [19], introducing inverted L-parasitic monopoles [20], placing the approach of neutralization lines between the antenna elements [21]. Table 10.2 summaries the above-mentioned MIMO antenna design along with their operational bandwidth and mutual coupling improvement approaches.

10.1.3 Dual-/Triple-Band MIMO Antennas with Reduced Mutual Coupling

Several dual- and triple-band MIMO antennas that demonstrate improved mutual coupling techniques have been proposed in [22–26]. It is considerably seen that an improved isolation may be obtained by employing techniques within only a single

Table 10.2 Previous work of wideband MIMO antennas

Reference	Size (mm^3)	Bandwidth (GHz)	Separation distance	Isolation/return loss (dB)
[18]	67 × 50 × 0.254	1.65–2.5	0.25 λ_0	11.0/10.0
[19]	86 × 86 × 1.52	1.63–2.05	0.1 λ_0	20.0/10.0
[20]	95 × 60 × 0.8	1.85–2.17	0.063 λ_0	14.8/10.0
[21]	90 × 40 × 0.8	2.4–4.2	0.19 λ_0	17.0 /10.0

Table 10.3 Previous work of dual- or triple-band antennas

Reference	Size (mm^3)	Bandwidth (GHz)	Separation distance	Isolation/return loss (dB)
[22]	95 × 60 × 0.8	1.92–2.17 2.4–2.5	0.038 λ_0	13.0,18.0/10.0, 10.0
[23]	100 × 40 × 6	2.4–2.5 3.4–3.6	0.0088 λ_0	19.2, 22.8/10.0, 10.0
[24]	150 × 100 × 0.8	2.4–2.5 5.15–5.825	0.06 λ_0	15.0, 22.0/10.0, 6.0
[25]	63 × 50 × 0.8	1.5–2.8 4.7–8.5	0.13 λ_0	15.0, 17.0/10.0,10.0
[26]	105 × 55 × 7.5	868–915 1.7–2.3 2.4–3.5	0.05 λ_0	10.0, 10.0, 10.0/6.0, 10.0, 10.0

band or by combing more other bands. For instance, in [22] an approach of etching two-inverted L-shaped line together with T-shaped branch over the ground plane shows reduced mutual coupling at the standards of UMTS and WLAN 2.4 GHz bands.

To simultaneously design a MIMO antenna capable of operating over the lower WLAN 2.4 GHz and WiMAX 3.5 GHz service, along with an improved isolation, authors in [23] achieve this by introducing a folded L-slot in the antenna surface at the same time inserting a T-shaped slot over the antenna PCB. A MIMO antenna operates over a wide frequency range of WLAN spectrum from WLAN 2400 MHz to 5800 MHz, while achieving low mutual coupling was proposed in [24], the mutual coupling was improved by wisely modifying the lengths of parasitic elements.

A promising broadband MIMO antenna was investigated in [25]. It was suggested that a U-shaped slot was placed over the defected ground plane to perform as an effective decoupling method. On the other hand, an antenna design in [26] utilizes three-dimensionally folded monopole elements in order to accomplish triple resonant modes together with an improved mutual coupling over the three allocated bands. The details of dual- and triple-band MIMO antennas were stated in Table 10.3.

To sum up, it is remarkably released that most of the above-mentioned MIMO designs are able to operate over single-mode [6–17], broadband frequency range as in [18–21] or dual-mode [22–25]. These structures are not capable of operating over the whole bands of existing mobile services, with the exception of work in [25, 26]. Thus, within this chapter we present a MIMO antenna to overcome this constraint. The present MIMO design is based on printed monopole configuration. It is found

to be capable to cover the full mobile services from 3G to 4G, namely, GSM1800/1900, UMTS2000, LTE2300, LTE2600, WiFi and WiMAX. The high isolation of 14 dB between the proposed antenna elements is accomplished by simply introducing an I-shaped branch over a slotted ground plane.

10.2 Antenna Design Concept and Structure

The full geometry of the printed monopole MIMO antenna depicts in Fig. 10.1. The proposed antenna comprises of two crescent-shaped radiators which are printed over the top of substrate surface, where the bottom part is the ground plane with defected area exactly underneath the both radiators [27]. The Duroid 5870 dielectric material with a 0.79 mm height, dielectric constant (ε_r) of 2.33 and a loss tangent of 0.0012 was used throughout this work. The single antenna of this design has some similarities with previous work in [21, 28].

The only difference is that, the proposed antenna has come up with straight extensions at its crescent shape's end. As can be seen from Fig. 10.1, each radiator was excited by a microstrip line with a dimension of 18 × 1 mm. This strip has two sections: the lower one has a length of 11.25 mm, while the upper one comes with a 6.75 mm height. The ground plane of the proposed antenna occupies dimensions of 71.5 × 50 mm^2 with a defected part of 26.8 × 12 mm^2 underneath the radiators. The main objective of this defected area is to enhance the antenna impedance bandwidth. The presented MIMO structure has finally come with a compact size of 90 × 50 × 0.8 mm, which is said to be fitted for the future application of mobile

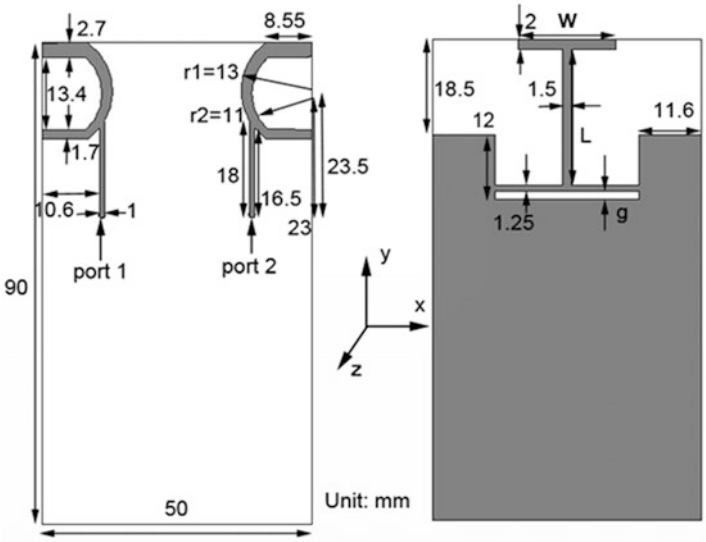

Fig. 10.1 Geometry of the proposed antenna

device. It is believed that, this design demonstrates a size reduction with comparison to work in [21, 26].

Prior to the final and optimum proposed design of wideband MIMO antenna, three different processes were carried out. Initially, we started with optimizing only a single crescent-shaped element over one of the corners of a 50 × 90 mm^2 ground plane. Basically, by modifying and controlling the geometries of $r1$ and $r2$ parameters (see Fig. 10.1), both the lower and higher modes may be tuned, in which the form of wideband frequency range may take place [21].

For improving the bandwidth, two tiers were applied: first tier, the length of both ends of crescent-shaped radiator (d) was adjusted and further modified till the best length is achieved; second tier, optimizing the defected area to obtain a dimension of 26.8 × 11.25 mm^2 helped hugely in enhancing the antenna bandwidth. Secondly, as soon as the desired operation of the single element antenna was accomplished, another identical version was symmetrically copied and placed on the other corner of the substrate surface to form the present MIMO antenna design. For better isolation, a distance of 24 mm was made between the two identical.

Thirdly, a slot together with T-shaped stub was added on the ground plane, in which an I-shaped strip was finally formed on the ground plane of the antenna. The dimensions and positions of this I-structure were then to be studied and analysed to meet the best performance in terms of both antenna return loss and isolation.

10.2.1 The Optimization of I-Shaped Decoupling Network

To assure the best effectiveness and efficiency of I-shaped decoupling approach on both reflection coefficient $|S_{11}|$ and mutual coupling $|S_{21}|$, an optimization parametric analysis was carried out and conducted. The main objective of this analysis was to obtain an antenna design which operates from 1.6 to 2.8 GHz; at the same time, an improved isolation of at least <−14 dB should be also achieved. Three parameters were deemed to be the key and most sensitive ones that affect the antenna performance. These parameters as shown in Fig. 10.1 are the top horizontal section width (w), the vertical section length (L) and the gap spacing (g) of the slot.

One can obviously observe that, by increasing the width (w) from 16 mm to 22 mm by 2 mm step each time, this will only influence the lower frequencies as they shifted downwards from 1.63 GHz to 1.45 GHz, while no significant effect was seen on the upper bands as depicted in Fig. 10.2. On the other hand, as the w is augmented, both $|S_{11}|$, $|S_{21}|$ get gradually impaired. Thus, for compromising purposes, the width value should be kept between 19 mm and 21 mm. This will ensure the best performance of both $|S_{11}|$ and $|S_{21}|$.

The vertical section length of the I-strip (L) over the ground plane is mainly responsible for the lower resonant frequency. The length (L) was varied from 21 mm to 27 mm, with an increment of 2 mm. The $|S_{11}|$ and $|S_{21}|$ are depicted in Fig. 10.3. It is interestingly noticed that, when the L was set at the lower value of 21 mm and the higher value of 27 mm, both the $|S_{11}|$ and $|S_{21}|$ have not met the desired frequency

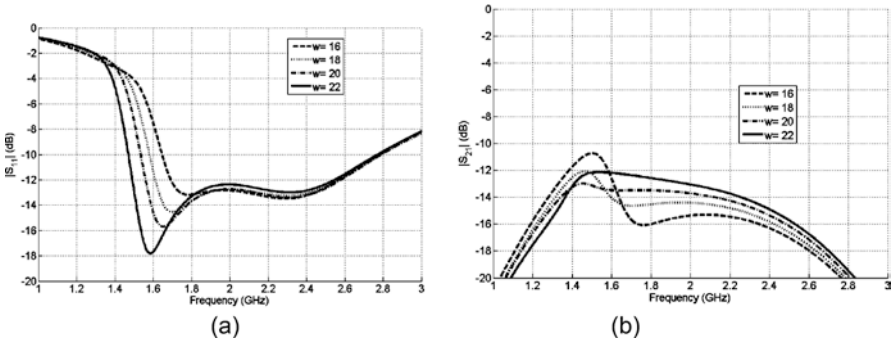

Fig. 10.2 S-parameters with variation of the top horizontal section width of I-shaped decoupling network (*w*)

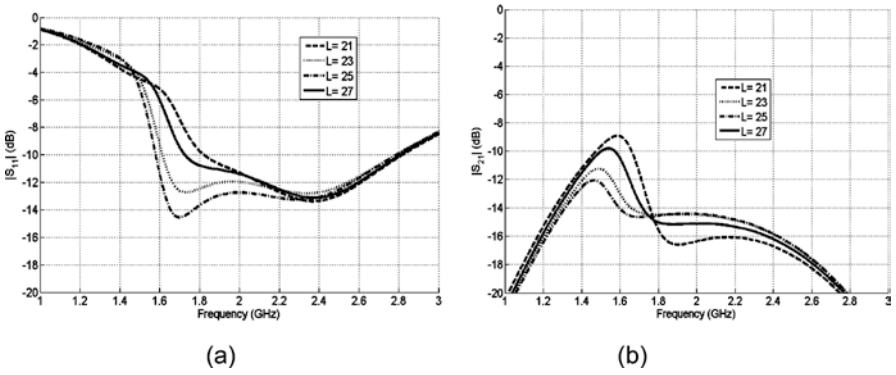

Fig. 10.3 S-parameters with variation of the vertical section length of I-shaped decoupling network (*L*)

range within this study. On the other hand, when the length *L* was fixed between the value of 24 mm and 26 mm, the targeted bandwidth from 1.6 GHz to 2.8 MHz was easily achieved, along with high isolation over the whole bandwidth.

The width of the slot (*g*) printed on the ground plane was carefully studied and analysed as shown in Fig. 10.4. The width of the gap was changed from 0 mm to 3 mm, with 1 mm step for each time. As can be seen from the plot of the $|S_{11}|$ and $|S_{21}|$ in Fig. 10.4, that the performance of the proposed antenna without etched slot (i.e. $g = 0$ mm) at the lower bands has shown sort of degradation. However, when the gap (*g*) was set at 1 mm up to 3 mm, the present antenna demonstrates same performance, in which the $|S_{11}|$ shows the wide range of frequency from 1.6 to 2.8 GHz, with value remains below −10 dB. Also, the $|S_{21}|$ stayed exactly same without any remarkable changes, when the (*g*) width varied from 1 to 3 mm.

After the optimization and validation of the I-shaped strip position and dimensions, the S-parameters of the present MIMO design with and without the high isolation approach of the I-shaped branch are depicted in Fig. 10.5. Looking at the

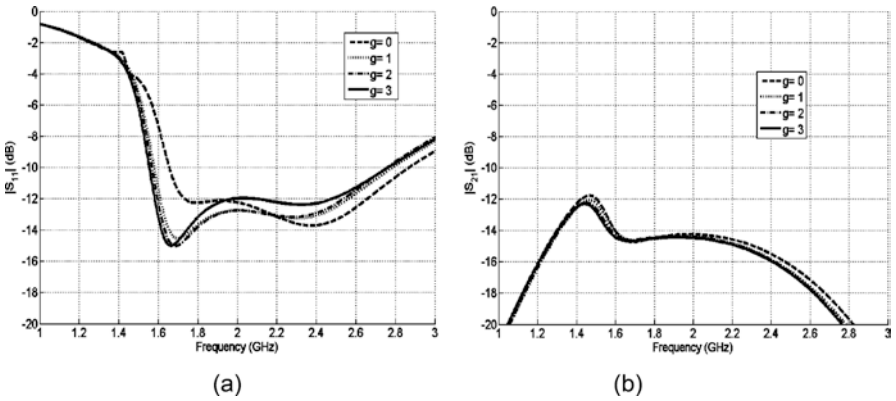

Fig. 10.4 S-parameters with variation of the slot width over the ground plane (g)

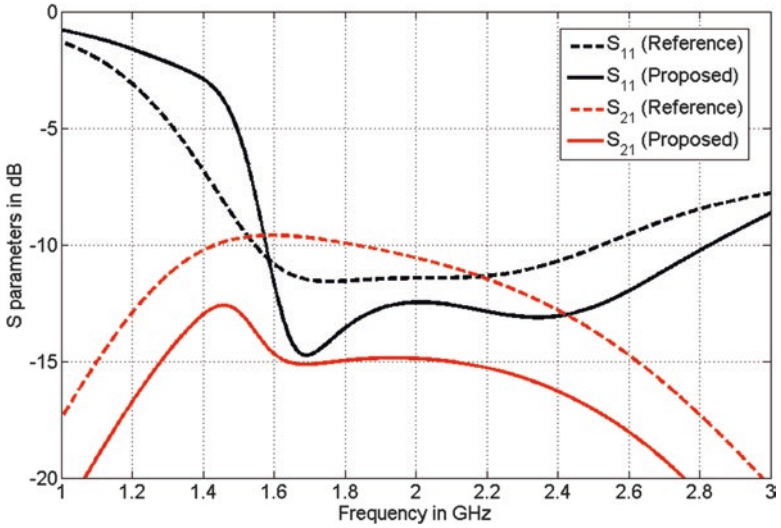

Fig. 10.5 S-parameters of the proposed MIMO antenna with and without I-shaped strip

performance of the antenna without the added strip in terms of $|S_{11}|$, it is clearly observed that the antenna displays frequency range from 1.5 to 2.5 GHz, which does not meet the allocated bandwidth within this work. Nevertheless, when the I-strip was introduced, the broadband features of spectrum from 1.6 to 2.8 GHz were accomplished. Moreover, checking the $|S_{21}|$ results, the isolation between the antenna elements was interestingly improved by around −5 dB from −9 to −14 dB over the aggregated bandwidth, in comparison with the performance of the antenna without the I-shaped strip. Therefore, this proves the function of the I-shaped as an impedance bandwidth improvement as well as decoupling approach.

To further prove the effectiveness of the I-shaped approach in improving the antenna bandwidth, the surface current distribution plots of the present design in both scenarios, i.e. with and without decoupling networking technique, are examined and analysed as in Fig. 10.6. Three resonant frequencies, namely, 1.7, 2.1 and

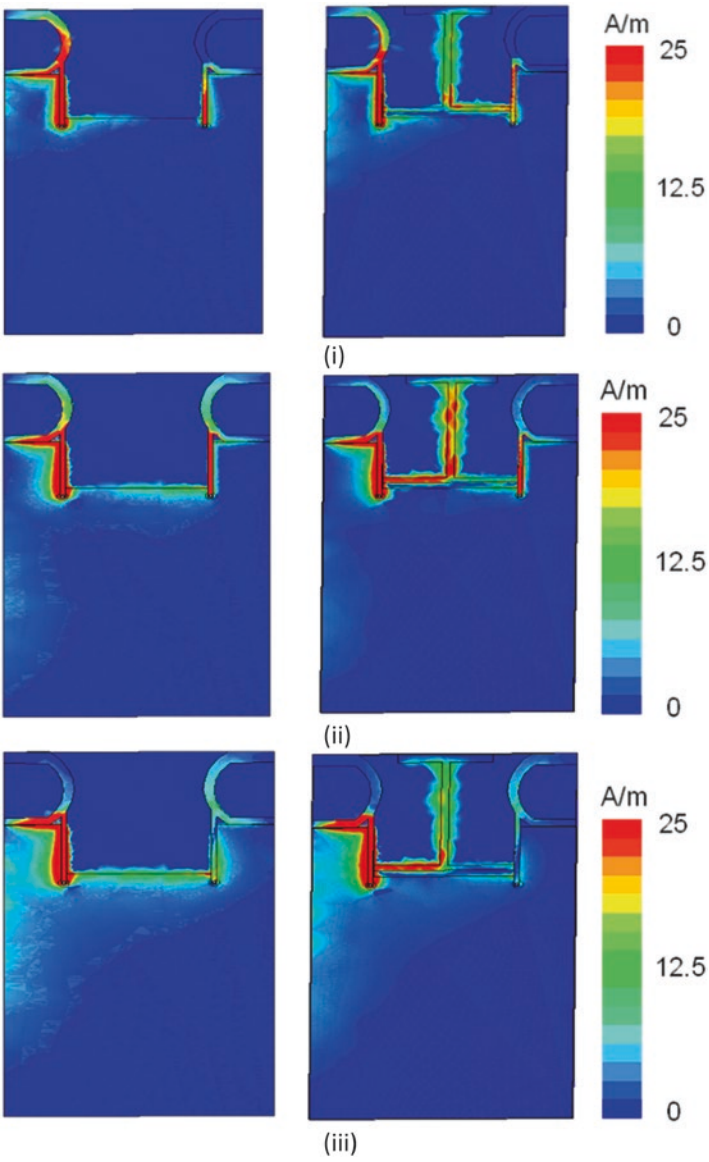

Fig. 10.6 Surface currents of antenna with and without the I-shape at (i) 1.7 GHz, (ii) 2.1 GHz and (iii) 2.5 GHz. Port 1 (*left*) is excited and port 2 is terminated in 50 Ω

2.5 GHz, were chosen to cover the entire desired range. It should be noted that when port 1 of the antenna without the inclusion of I-shaped strip is excited and port 2 is terminated in 50 Ω, a strong current flows from the port 1 to the port 2 antenna element. This is basically due to two factors, firstly the incidence of a near field coupling current and secondly sharing common ground plane. On the other hand, once the I-strip is etching over the common ground plane, it is noticed that the I-strip prevents the current passing from port 1 to port 2 of the antenna elements. In other words, the current is trapped on this decoupling structure, rather than flowing toward nearby port of the antenna. This concludes that the I-shaped strip can be considered as an effective method to decouple the currents on the antenna port 2 and, therefore, improve the whole antenna performance.

10.3 Validation of Measured and Simulation Results

For proof of concept, the final configuration of the proposed antenna in Fig. 10.1 was prototyped as indicated in Fig. 10.7. This prototyped design was tested to verify and confirm the outcomes of the theoretical model, which generated by utilizing the HFSS software package [29]. Both calculated and measured S-parameters of the present MIMO design are illustrated in Fig. 10.8. From Fig. 10.8, it is found that, both the simulated and fabricated designs have demonstrated a broad bandwidth of around 1.2 GHz covering the range from 1.6 to 2.8 GHz, with S_{11} value of less than −10 dB.

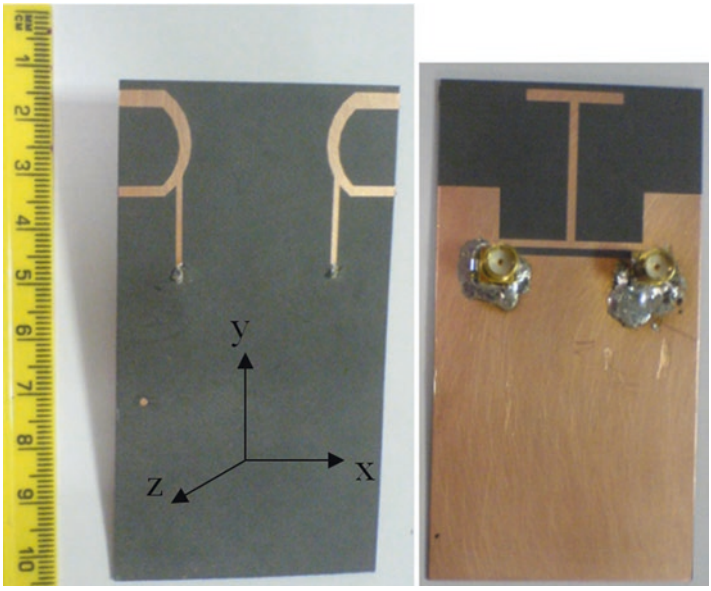

Fig. 10.7 Prototype photo of the proposed MIMO design

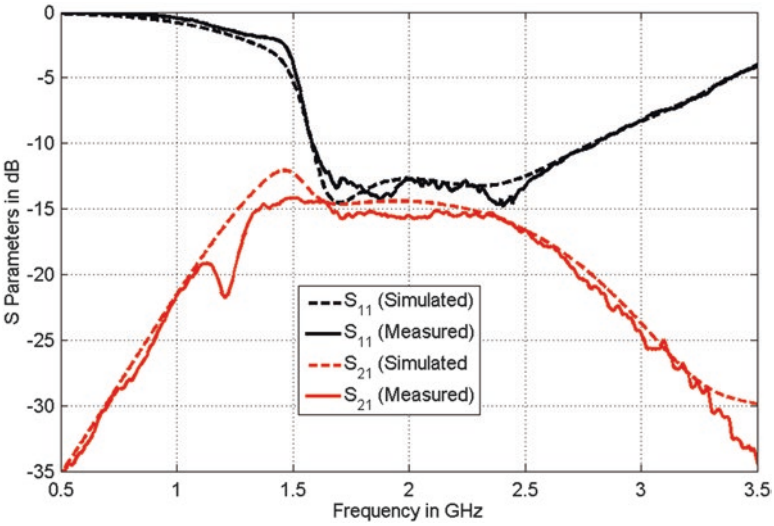

Fig. 10.8 Simulated and measured S-parameters of the proposed antenna

Achieving such a wide frequency range makes the proposed structure to be capable of covering the existing mobile services of GSM1800/1900, UMTS2000, WiFi and WiMAX as well as together operating over the newly released standards of LET2300 and LT2600. The isolation between the antenna element $|S_{21}|$ plots is also studied, which indicate a good isolation of −14 dB over the aggregated bandwidth has been attained.

To prove the performance of the presented MIMO design, two paramount features should be taken into consideration, i.e. envelope correlation coefficient (ECC) and channel capacity loss. Generally, the ECC may be obtained by exploitation of 3D far-field data as in [4–5] or from S-parameter procedures [30]. However, due to the fact that the measurement of far-field radiation patterns is time consuming and expensive. Thus, the second approach of using S-parameters technique is favoured. The ECC ρ_e of a two antennas system can be calculated from the following equation [30]:

$$\rho_e = \frac{\left|S_{11}^* S_{12} + S_{21}^* S_{22}\right|^2}{\left(1-\left|S_{11}\right|^2-\left|S_{21}\right|^2\right)\left(1-\left|S_{22}\right|^2-\left|S_{12}\right|^2\right)} \tag{10.1}$$

The computed and measured ECC plots of the present MIMO design structure are depicted in Fig. 10.9a. One can note that, both results are agreed well with each other. The values of ECC are said to be less than 0.008 over the entire bandwidth. These values are in good comparison with previous published data in [11, 21, 25]. The second important feature of the channel capacity loss of a 2 × 2 MIMO system can be calculated from the following expression as in [11, 21]:

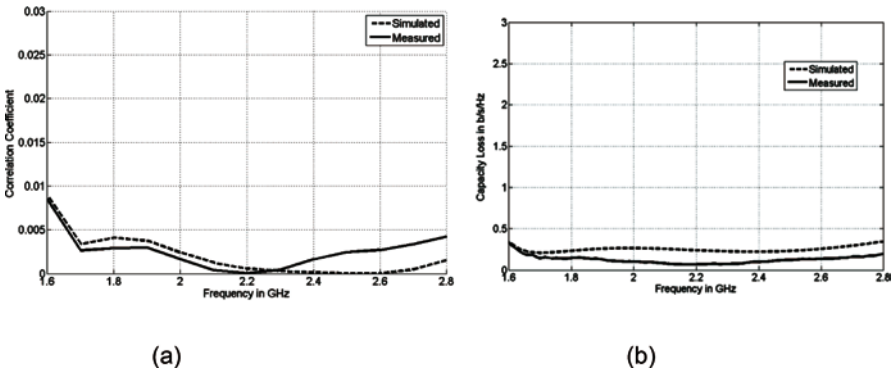

Fig. 10.9 Simulated and measured MIMO characteristics of the proposed antenna, (**a**) envelope correlation coefficient, (**b**) capacity loss

$$C_{\text{loss}} = -\log_2 \det\left(\psi^R\right) \tag{10.2}$$

where ψ^R is the receiving antenna correlation matrix: $\psi^R = \begin{bmatrix} \rho_{11} & \rho_{12} \\ \rho_{21} & \rho_{22} \end{bmatrix}$,

with $\rho_{ii} = (1 - (|S_{ii}|^2 + |S_{ij}|^2))$ and $\rho_{ij} = -\left(S_{ii}^* S_{ij} + S_{ji}^* S_{jj}\right)$, for i or $j = 1$ or 2.

The computed and practical results of the channel capacity loss of the proposed antenna were evaluated from the above equation as indicated in Fig. 10.9b. It should be noted that the channel capacity loss is found to be less than 0.3 b/s/Hz; this is said to be acceptable for practical MIMO systems [11, 25]. The slight differences between the curves may be due to the mistakes and errors during the fabrication process.

The simulated and measured power gain and efficiencies of the present MIMO design are illustrated in Fig. 10.10. The values of power gains varied from 1.7 to 2.7 dBi for the fabricated model, while they ranged from 1.2 to 2.3 dBi for the simulated design as seen from Fig. 10.10. It is clearly seen that about 0.5 dBi disagreement was found in particular at the lower band of around 1.6 GHz. By investigating the antenna efficiencies, one can note that, both calculated and measured data are in the range of 70–90% over the entire bandwidth, and are seen to be in good agreement.

The far-field patterns of both fabricated and simulated models are described in Fig. 10.11. During the measurement of the radiation patterns, three pattern cuts (i.e. *x*-*z*, *y*-*z* and *x*-*y* planes) were used at two resonant frequencies, covering the desired bandwidth, explicitly the 1.8 and 2.4 GHz. From Fig. 10.11, it is noted that the patterns at the above-mentioned bands are in consistency; also both simulated and measured plots are found in acceptable agreement.

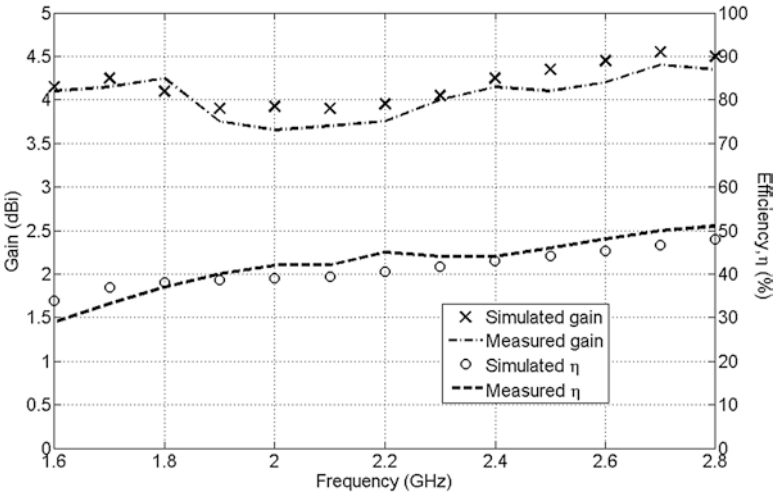

Fig. 10.10 Measured and simulated peak gains and radiation efficiencies of the proposed antenna

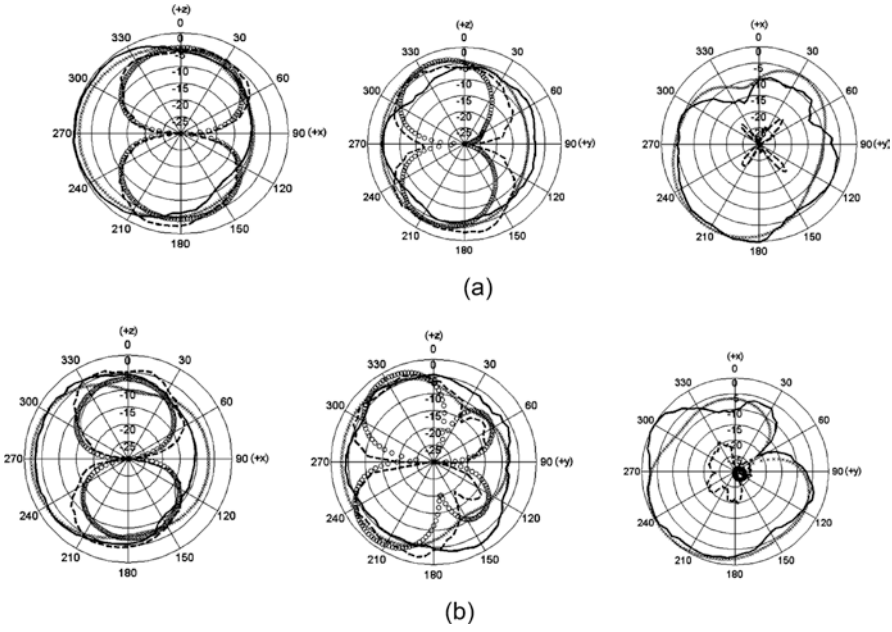

Fig. 10.11 Simulated and measured normalized radiation patterns of the proposed antenna for three planes (*left*, *x-z* plane; *centre*, *y-z* plane; *right*, *x-y* plane) at (**a**) 1.8 GHz and (**b**) 2.4 GHz, where port 1 is excited and port 2 is terminated to 50 Ω. 'xxxx' simulated co-polarization, 'oooo' simulated cross-polarization, '——' measured co-polarization, '------' measured cross-polarization

10.4 The Performance of the Proposed Antenna with the Hand and Head Models

The coupling between the antenna model within the handheld casing and both the head and hand models are examined and investigated within this subsection. The same parameters, which have been studied in previous section such as reflection coefficient, mutual coupling, power gains, far-field and efficiency, will be checked again with the presence of hand and head scenarios. Figure 10.12 displays the simulated hand and head

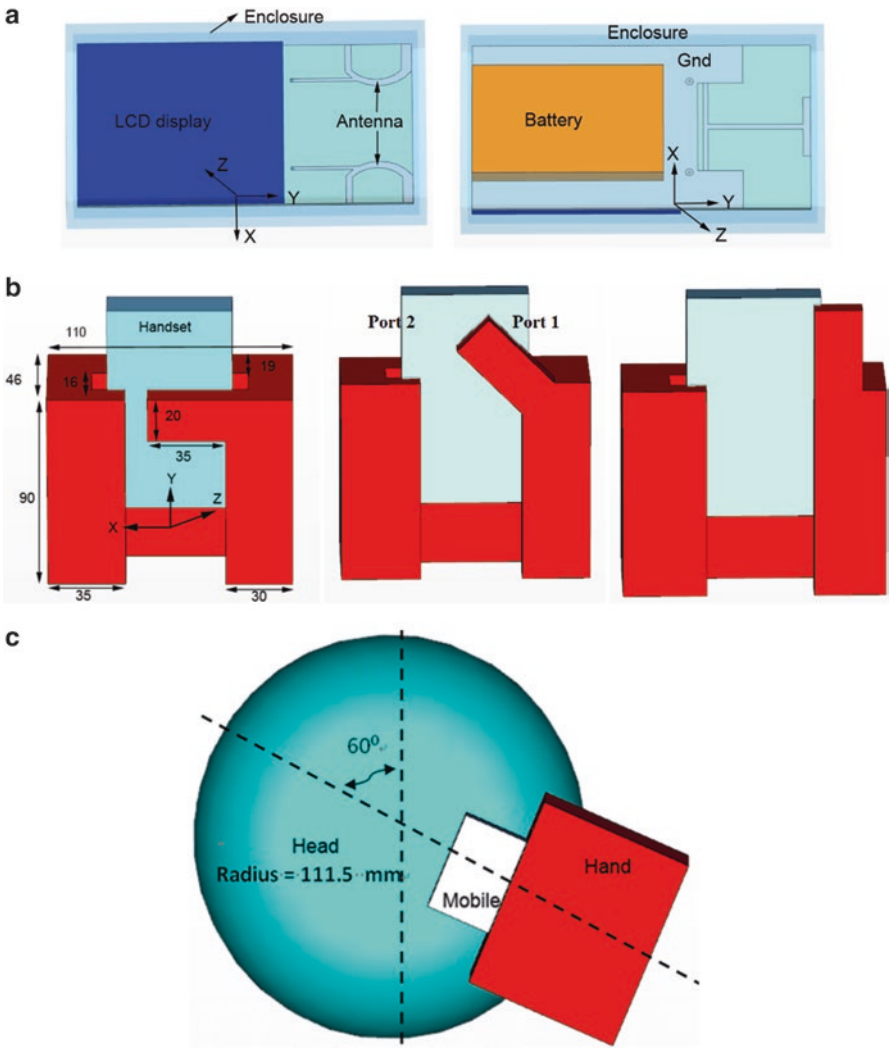

Fig. 10.12 The proposed antennas within three scenario models: (**a**) antenna with handheld casing, (**b**) antenna with hand models, (**c**) antenna with hand and head models

models as well as the present antenna within the handset casing with the common talking positions.

To fully understand the near-field coupling effects of every physical part of the models, i.e. handset enclosure, battery, circuit board, LCD, battery, human hand and head, that may influence the antenna performance, four scenarios, i.e. the antenna as stand-alone model, the antenna within the handset casing, the antenna in handheld paradigm and finally the antenna with both hand and head models, have been studied in Fig. 10.12.

As can be observed from Fig. 10.12, the first model presents the antenna within the handset casing. This model consists of the presented antenna with a volume of $52 \times 60 \times 2$ mm^3, a $33 \times 50.5 \times 4.5$ mm^3 battery, a $52 \times 60 \times 2$ mm^3 LCD as well as a plastic housing with a thickness of 2 mm. The battery and LCD were modeled as copper, while a dielectric of ABS plastic (DK=3.0) was used as the material of the handset housing.

The second model demonstrates the common cases of using the handset with three finger positions of the hand, namely, 0° (left), 45° (middle) and 90° (right). The hand model is proposed to be as a single layer of muscle tissue with a relative permittivity of 54 and a conductivity of 1.45 S/m [31]. As can be found in [30], the antenna performance may significantly impair when the antenna is being used at finger moves to 90° comparing to finger at 0° and 45°.

Due to the above reason, the third model is established to show the worst scenario where the finger at 90° position with the presence of a simplified head model, as depicted in Fig. 10.12c. In this case, the handset is located within the hand and then attached to the spherical head [32, 33]. The head phantom includes the following: dual layers, namely, the glass shell ($\varepsilon_r = 4.6$, $\sigma = 0$) and tissue equivalent material ($\varepsilon_r = 42.9$, $\sigma = 0.9$). To demonstrate the most common human talking mode, the device mobile chassis is being positioned at an angle of 60° along with the vertical axis of the human head; the distance between them is kept to be around 5 mm.

The examination of the S-parameters of the proposed antenna within the three mentioned paradigms was depicted in Fig. 10.13. As indicated in Fig. 10.13a, the level of reflection coefficient within the desired operating bandwidth remains below −10 dB. The mutual coupling of the antenna within the above three models is found to be around −12.5 dB, in which 1.5 dB is found to be worse than the reference proposed antenna as illustrated in Fig. 10.13b.

The power gains and radiation efficiencies of the antenna against the desired operating band are shown in Fig. 10.14. It is apparently seen that the power gains of the antenna together with the analysed models were relatively decreased from 0 to 0.5 dBi at the higher band (2.5–2.8GHz) compared to the power gains of the proposed referenced MIMO antenna.

On the other hand, the power gain of the antenna with the hand and head/hand cases at port 1 indicates a gradual decrement with a difference of 0.2–1.7 dBi in the

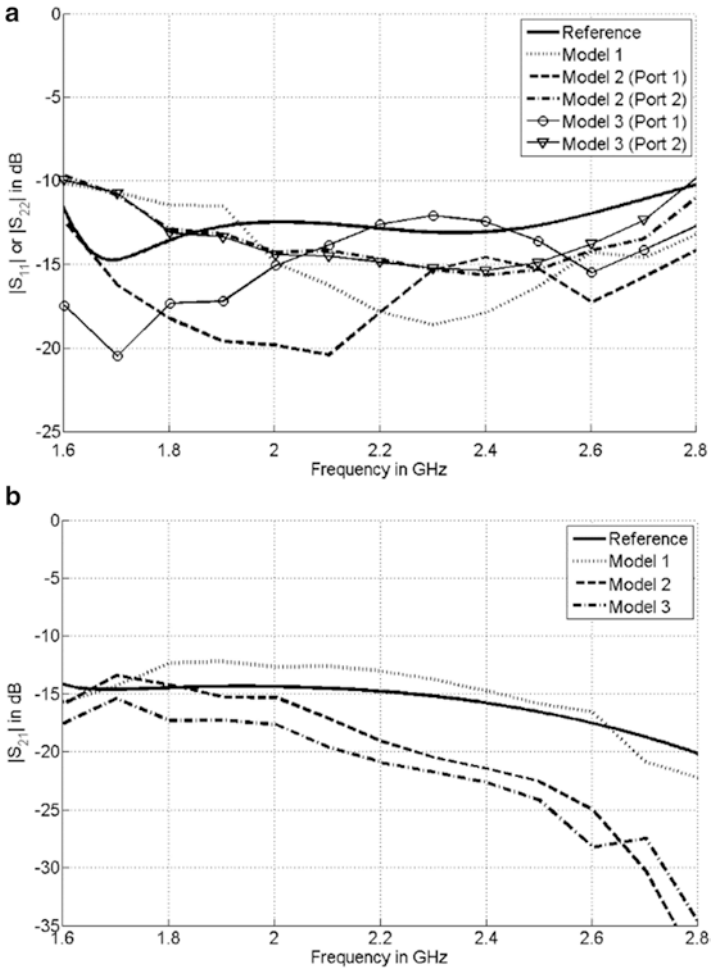

Fig. 10.13 Comparison of antenna S-parameters in the scenarios of free space, hand and head/hand model

hand model scenarios and drop from 0.3 to 1.9 dBi in the hand/head paradigm compared to the reference antenna model.

The plots of the radiation efficiency agree with the variation of the gain plots. From Fig. 10.14, the antenna efficiency is mostly degraded in the case of hand/head model. The efficiencies of antenna within the hand model alone and also within the hand/head models together at port 1 fluctuates from 20% to 35% for the hand model and 15% to 28% in the case of hand/head models. A reduction of 60% occurred in contrast to the reference model at the band of 2 GHz. This is deemed as the worst efficiency drop.

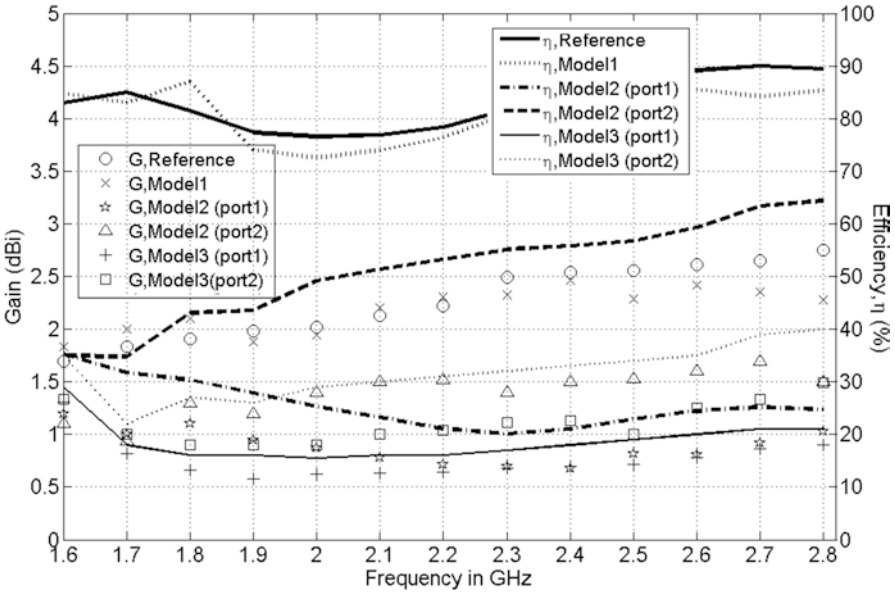

Fig. 10.14 The variation of the antenna peak gain and radiation efficiency in the presence of the hand and head model

10.5 Conclusion

A printed monopole antenna operates in a wide bandwidth characteristics from 1.6 to 3.8 GHz has been modelled and examined. The isolation of the proposed antenna was improved to 14 dB, by means of using an I-shaped strip approach printed over the ground plane. The proposed MIMO antenna has been analysed in different scenarios such as free space, within the handset casing, presence of hand model and cases of both hand/head models. It demonstrates good performance in all mentioned cases which makes it suitable for commercial mobile/wireless handheld devices. The obtained simulated model then fabricated and tested to prove its practical usability. This MIMO antenna, with a compact volume of $50 \times 90 \times 0.8$ mm^3, exhibits sufficient impedance bandwidth, reasonable far-field characteristics, acceptable power gains, low-level correlation coefficient and minimum channel capacity loss. These features confirmed that it is a good candidate to combat the multipath propagation issues.

References

1. L. Hanzo, H. Haas, S. Imre, D. O'Brien, M. Rupp, L. Gyongyosi, Wireless myths, realities, and futures: from 3G/4G to optical and quantum wireless. Proc. IEEE **100**, 1853–1888 (2012)

2. L. Hanzo, M. El-Hajjar, O. Alamri, Near-capacity wireless transceivers and cooperative communications in the MIMO era: evolution of standards, waveform design, and future perspectives. Proc. IEEE **99**(8), 1343–1385 (2011)
3. Z. Ying, Antennas in cellular phones for mobile communications. Proc. IEEE **100**(7), 2286–2296 (2012)
4. H. Shin, J.H. Lee, Capacity of multiple-antenna fading channels: spatial fading correlation, double scattering, and keyhole. IEEE Trans. Inf. Theory **49**, 2636–2647 (2003)
5. J. Wallace, M. Jensen, A. Swindlehurst, B. Jeffs, Experimental characterization of the MIMO wireless channel: data acquisition and analysis. IEEE Trans. Wirel. Commun. **2**(2), 335–343 (2003)
6. J. Lee, Y.-K. Hong, S. Bae, G.S. Abo, W.-M. Seong, G.-H. Kim, Miniature long-term evolution (LTE) MIMO ferrite antenna. IEEE Antennas Wirel. Propag. Lett. **10**, 2364–2367 (2011)
7. Y.S. Shin, S.O. Park, A monopole antenna with a magneto-dielectric material and its MIMO applications for 700MHz LTE-band. Microw. Opt. Technol. Lett. **52**, 603–606 (2010)
8. M.S. Sharawi, S.S. Iqbal, Y.S. Faouri, An 800 MHz 2 X 1 compact MIMO antenna system for LTE handsets. IEEE Trans. Antennas Propag. **59**(8), 3128–3131 (2011)
9. Z. Li, Z. Du, M. Takahashi, K. Saito, K. Ito, Reducing mutual coupling of MIMO antennas with parasitic elements for mobile terminals. IEEE Trans. Antennas Propag. **60**(4), 473–481 (2012)
10. L. Minz, R. Garg, Reduction of mutual coupling between closely spaced PIFAs. Electron. Lett. **46**(6), 392–394 (2010)
11. S.-W. Su, C.-T. Lee, F.-S. Chang, Printed MIMO-antenna system using neutralization-line technique for wireless USB-dongle applications. IEEE Trans. Antennas Propag. **60**(2), 456–463 (2012)
12. H. Li, J. Xiong, S. He, A compact planar MIMO antenna system of four elements with similar radiation characteristic and isolation structure. IEEE Antennas Wirel. Propag. Lett. **8**, 1107–1110 (2009)
13. S.-C. Chen, Y.-S. Wang, S.-J. Chung, A decoupling technique for increasing the port isolation between two strongly coupled antennas. IEEE Trans. Antennas Propag. **56**(12), 3650–3658 (2008)
14. M. Krairiksh, P. Keowsawat, C. Phongcharoenpanich, Two-probe excited circular ring antenna for MIMO application. Prog. Electromagn. Res. **97**, 417–431 (2009)
15. J. OuYang, F. Yang, Z.M. Wang, Reducing mutual coupling of closely spaced microstrip MIMO antennas for WLAN application. IEEE Antennas Wirel. Propag. Lett. **10**, 310–313 (2011)
16. A.R. Mallahzadeh, S. Es'haghi, A. Alipour, Design of an E Shaped MIMO antenna using IWO algorithm for wireless application at 5.8 GHz. Prog. Electromagn. Res. **97**, 417–431 (2009)
17. X. Tang, K. Mouthaan, J.C. Coetzee, Tunable decoupling and matching network for diversity enhancement of closely spaced antennas. IEEE Antennas Wirel. Propag. Lett. **11**, 268–271 (2012)
18. X. Zhou, R. Li, G. Jin, M.M. Tentzeris, A compact broadband MIMO antenna for mobile handset applications. Microw. Opt. Technol. Lett. **53**(12), 2773–2776 (2011)
19. S. Zhang, P. Zetterberg, S. He, Printed MIMO antenna system of four closely-spaced elements with large bandwidth and high isolation. Electron. Lett. **46**(15), 1052–1053 (2010)
20. G. Kang, Z. Du, K. Gong, Compact broadband printed slot-monopole-hybrid diversity antenna for mobile terminal. IEEE Antennas Wirel. Propag. Lett. **10**, 159–162 (2011)
21. C.H. See, R.A. Abd-Alhameed, Z.Z. Abidin, N.J. McEwan, P.S. Excell, Wideband printed MIMO/diversity monopole antenna for WiFi/WiMAX applications. IEEE Trans. Antennas Propag. **60**(4), 2028–2035 (2012)
22. Y. Ding, Z. Du, K. Gong, Z. Feng, A novel dual-band printed diversity antenna for mobile terminals. IEEE Trans. Antenna Propag. **55**, 2088–2096 (2007)
23. S. Zhang, B.K. Lau, Y. Tan, Z. Ying, S. He, Mutual coupling reduction of two PIFA with a T-shape slot impedance transformer for MIMO mobile terminals. IEEE Trans. Antennas Propag. **60**(3), 1521–1531 (2012)
24. R. Addaci, A. Diallo, C. Luxey, P.L. Thuc, R. Staraj, Dual-band WLAN diversity antenna-system with high port-to-port isolation. IEEE Antennas Wirel. Propag. Lett. **11**, 244–247 (2012)
25. X. Zhou, X. Quan, R. Li, A dual-broadband MIMO antenna system for GSM/UMTS/LTE and WLAN handsets. IEEE Antennas Wirel. Propag. Lett. **11**, 551–514 (2012)

26. Q. Rao, K. Wilson, Design, modeling, and evaluation of a multiband MIMO/diversity antenna system for small wireless mobile terminals. IEEE Trans. Compon. Packag. Manuf. Technol. **1**(3), 410–419 (2011)
27. C.H. See, R.A. Abd-Alhameed, N.J. McEwan, S.M.R. Jones, R. Asif, P.S. Excell, Design of a Printed MIMO/diversity monopole antenna for future generation handheld devices. Int. J. RF Microwave Comput Aided Eng. **24**(3), 349–359 (2014)
28. C.H. See, R.A. Abd-Alhameed, D. Zhou, T.H. Lee, P.S. Excell, A crescent-shaped multiband planar monopole antenna for mobile wireless applications. IEEE Antenna Wirel. Propag. Lett. **9**, 152–155 (2010)
29. HFSS version 14, High frequency structure simulator web site, 2013 [Online]. Available: http://www.ansys.com/
30. S. Blance, J. Romeu, I. Corbella, Exact representation of antenna system diversity performance from input parameter description. Electron. Lett. **39**(9), 705–707 (2003)
31. D. Zhou, R.A. Abd-Alhameed, C.H. See, A.G. Alhaddad, P.S. Excell, A compact wideband balanced antenna for mobile handsets. IET Microwaves Antennas Propag. **4**, 600–608 (2010)
32. IEEE, *Std 1528TM-2003, IEEE Recommended Practice for Determining the Peak Spatial Average Specific Absorption Rate (SAR) in the Human Head from Wireless Communications Devices Measurement Techniques* (IEEE, New York, 2003)
33. M.A. Ebrahimi-Ganjeh, Interaction of dual band helical and PIFA handset antennas with human head and hand. Prog. Electromagn. Res. **77**, 225–242 (2007)

Part V
Balanced Antennas

Chapter 11
Compact Wideband Balanced Antenna Structure for 3G Mobile Handsets

D. Zhou, N.J. McEwan, and P.S. Excell

11.1 Introduction on Balanced Antennas for Mobile Handsets

Conventionally for mobile handsets, unbalanced type of internal antennas has been widely used. For this type, the antenna radiator and its associated ground plane both played a part in the antenna design and radiation mechanism. The unbalanced designs usually result in very small antennas to achieve sufficient antenna radiation efficiency and bandwidth, e.g. many planar inverted F antenna (PIFA) designs and inverted F antenna (IFA) designs [1]. As the antenna ground plane is also part of the antenna radiation, which leads to the fact that radiating currents are induced on both the antenna element itself and the ground plane in free space. However, the performance of these antennas varies considerably when held by users. This is mainly because the current induced on the phone ground plane is disturbed by the users' hand and head, which causes performance degradation of the antenna's radiation properties and introduces losses and antenna impedance mismatching.

A good alternative candidate is a balanced type of antenna [2, 3]. This type of antenna concept requires an antenna with symmetrical structure, which is fed with balanced currents to make it electrically symmetrical. *With this type of antenna, the key advantage is that unlike unbalanced type the balanced currents only flow on the antenna element itself, thus* dramatically reducing the effect of current flow on the ground plane. *The radiation mechanism of this type of antenna design possesses* weak coupling of the antenna with the handset case in order to achieve an impedance match that is both good and stable in the presence of a human body. *As a result,*

D. Zhou (✉)
Huawei Device Limited, Beijing, China
e-mail: daweizhou@hotmail.com

N.J. McEwan • P.S. Excell
North East Wales Institute of Higher Education, Wrexham LL11 2AW, UK

I. Elfergani et al. (eds.), *Antenna Fundamentals for Legacy Mobile Applications and Beyond*, DOI 10.1007/978-3-319-63967-3_11

balanced antennas maintain their performance in both free space and handheld scenarios [4–6].

The effect of a balanced antenna design on the current distribution on the ground plane can also be observed from the radiation pattern. Morishita et al. [2, 5, 6] studied the radiation patterns for both balanced and unbalanced antennas with and without the presence of the human body. The patterns produced by the balanced antenna system were relatively regular in free space; while the patterns produced by the unbalanced antenna system were irregular, and thus more nulls appeared. Clearly, the patterns of the balanced antenna are to be preferred in practice to those of the unbalanced antenna. Thus, in simulation and experiment, when a head and/or hand model is present next to an antenna, the effect of the human tissue on the antenna performance is relatively small in the balanced system, whereas degradation is substantial in the unbalanced system.

From the current distribution of the two antenna systems, a small change in the input impedance is expected in the balanced antenna system when the handset is placed in the vicinity of a human head or hand, but a larger change is expected in the unbalanced case. From the results of computed input impedance for balanced and unbalanced antennas, the small change in impedance of the balanced antenna with respect to the unbalanced antenna indicates that it has lower mutual coupling with the head [7].

In addition, in the context of health concerns, it is expected that low absorbed power in a mobile phone user's head can be realised by making the mobile antenna deliver low intensity in the near field [8, 9]. *Moreover, if such an antenna is well designed, then the maximum specific absorption rate (SAR) value is likely to be reduced when the phone is placed beside the head due to the relatively weak coupling of the antenna to the body of the handset. A detailed study by Abd-Alhameed* et al. [7] *has confirmed that the balanced antenna offers significant advantages over the unbalanced antenna. Owing to the well-balanced structure, the antenna isolates current flows on the metallic structure of the handset, which in turn also results in low SAR values in the ear and cheeks of the user.*

Besides the desirably stable performance in free space and handheld cases, there are also some limitations to balanced type of antennas, such as narrow bandwidth. This limitation is mainly due to only the antenna element itself being as a radiator. For commercial exploitation, in addition to the traditional design objectives of small size and low cost, it is now essential to address the need to develop novel techniques to improve balanced antenna bandwidth to achieve wide or multiple band operation and compliance with international safety guidelines on SAR [8, 9].

In this chapter, several design techniques are demonstrated to address the bandwidth limitation issue with the balanced type of antenna designs. In order to achieve compact design, folded structures of symmetrical balanced-fed loop and dipole design are exploited for mobile handset applications. To feed wide bandwidth balanced antennas, the corresponding wide bandwidth balun is also required and equivalently important for balanced antenna designs. The design of wide bandwidth balun is also designed and its performance for wideband operation is validated in this chapter.

11.2 Folded Loop Antenna with a Single-Band Operation

In this section, a simple folded loop antenna (FLA) with a balanced type of antenna concept for mobile handsets is presented. This design is for the purpose of realising with relatively wideband impedance to cover a single 2G or 3G band, respectively. The folded loop antenna structure is designed and optimised using genetic algorithms (GA) [10]. The geometry of proposed FLA, shown in Fig. 11.1, was adopted from the Morishta's work [6]. Parameters, used to define this antenna structure, were optimised and evaluated using GA with the aid of NEC-2 source code [11, 12]. Hardware was fabricated and a wideband balun was also designed for the measurement validation.

11.2.1 Folded Loop Antenna Design and Optimisation Using Genetic Algorithm

Configuration of FLA antennas and important antenna design parameters with associated ground plane size are shown in Fig. 11.1. The intended antenna was designed for a single-band application, covering 2G GSM1800 (1710–1860 MHz) and 3GUMTS applications (1920–2170 MHz), respectively.

Important parameters shown in Fig. 11.1 of the FLA antenna structure were optimised with GA using real-valued chromosomes. Performance of the generated antenna samples by GA method was then computed using NEC-2 source code, and a desired fitness of the GA was then evaluated using a predefined cost function, as shown in Eq. 11.1:

$$F = \sum_{n=1}^{3} W_n \cdot \left(1 / VSWR\right)_{\text{fn}} \tag{11.1}$$

where W_n (n = 1,…,3) are the predefined weight coefficients for the cost function and are all set to be 1 here. The principle of GA optimisation and procedure of GA

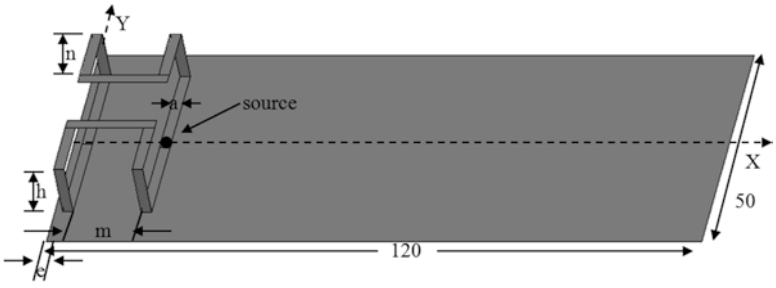

Fig. 11.1 Geometry of the folded loop antenna with ground plane

Table 11.1 Summary of design parameters, optimisation range and optimal design using GA

	FLA for UMTS		FLA for GSM1800	
GA parameters	Parameters (m)	Optimal (m)	Parameters (m)	Optimal (m)
Number of population size = 6	Wire radius (a) (0.0004–0.0008)	0.0007905	Wire radius (a) (0.0004–0.0008)	0.00074
Number of parameters = 7	FLA length (b) (0.03–0.04)	0.03690	FLA length (b) (0.03–0.04)	0.03978
Probability of mutation = 0.02	FLA height (h) (0.003–0.012)	0.01179	FLA height (h) (0.003–0.012)	0.01173
Maximum generation = 500	FLA arm length (n) (0.002–0.015)	0.009881	FLA arm length (n) (0.002–0.015)	0.008785
Number of possibilities = 32,768	Parallel wires distance (m) (0.005–0.015)	0.013599	Parallel wires distance (m) (0.005–0.015)	0.01489
Ground plane size (120 × 50 mm)	FLA distance to GP edge (e) (0.0–0.002)	0.001137	FLA distance to GP edge (e) (0.0–0.002)	0.0008643
Distance between FLA and GP (h_0) (not shown in Fig. 11.1) (0.001–0.003)		0.001146	h_0 (0.001–0.003)	0.001112

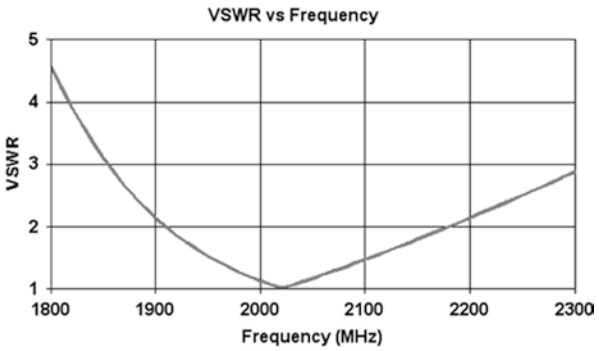

Fig. 11.2 VSWR against frequency for a single-band operation at 3G UMTS

applied to optimised antennas in cooperation with NEC-2 were described in authors' previous work [13, 14].

Table 11.1 summarises the design parameters, optimisation range of each parameter and optimal design after GA optimisation converged to meeting GA design target for 2G GSM1800 and 3G UMTS bands, respectively. The excellent antenna impedance matching in terms of VSWR for the optimal design configuration is presented in Figs. 11.2 and 11.3. It should be noted that GA has been approved as an efficient design and optimisation tool, and it has potential in the other types of antenna designs and optimisation work.

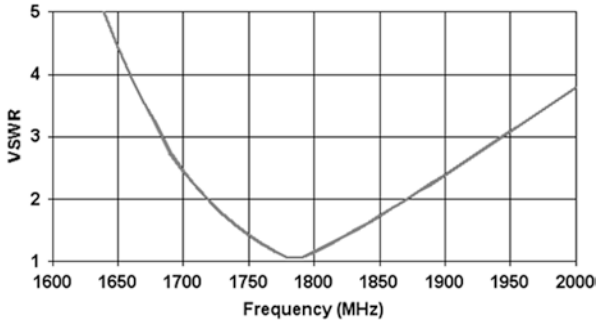

Fig. 11.3 VSWR against frequency for a single-band operation at 2G at GSM1800

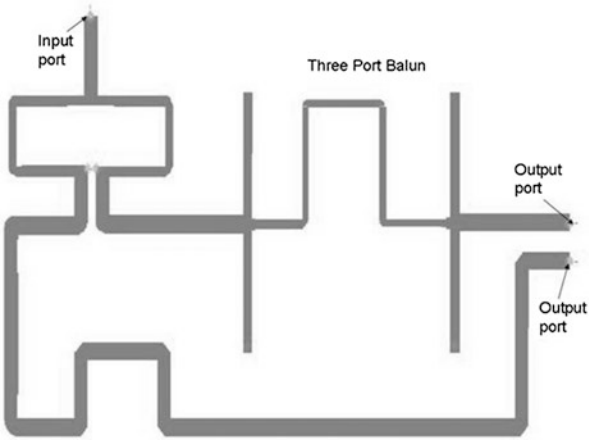

Fig. 11.4 Simulation layout of the wideband balun design to be used testing the balanced antennas

11.2.2 Wide Bandwidth Planar Balun Design and Validation

To test balanced antenna, a balun is needed. A balun is a feeding network to provide a pair of balanced feed (a pair of signals with same amplitude but 180° out of phase) from an unbalanced source. In this chapter, the balanced antennas are designed to cover wide bandwidth from 1.7 to 2.5 GHz at mobile communication bands of GSM, UMTS and 2.4 GHz; thus, a relatively wideband balun is necessary.

In this section, a planar wideband balun is designed and presented. Its original structure was adopted from a published work in [15] due to its wide bandwidth feature (1.7–3.3 GHz) (see Fig. 11.4) [15], and design modification was subsequently applied to make sure that the two balanced ports are well located at the feeding points of the proposed balanced antenna designs. The design was firstly

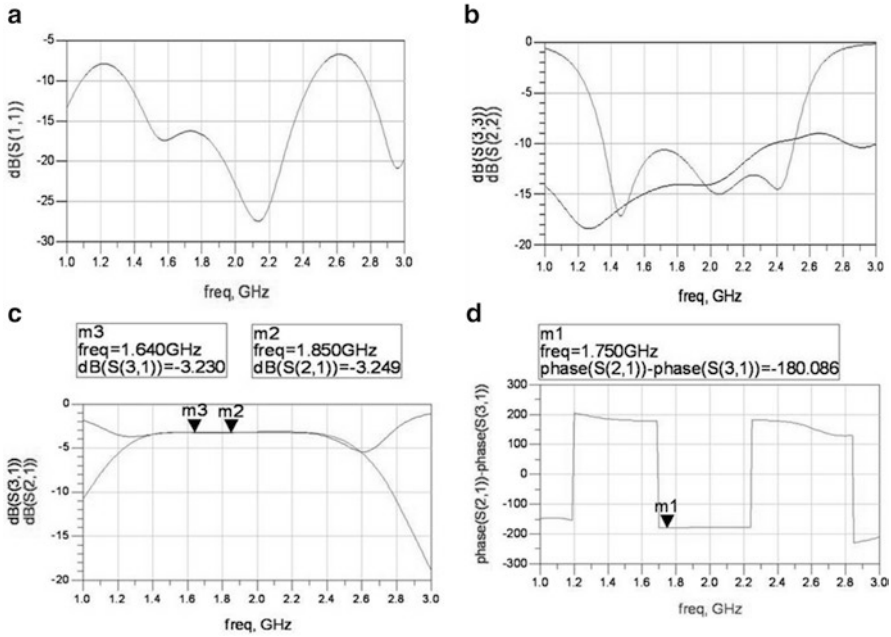

Fig. 11.5 Simulated wideband balun performance. (**a**) Impedance matching at input unbalanced port; (**b**) impedance matching at output balanced port; (**c**) amplitude imbalance between the two output balanced ports; (**d**) phase difference between two balanced output ports

simulated using circuit simulator Agilent ADS software [16] and then the layout was optimised again using Momentum package. In simulation the planar balun substrate used was on Duriod substrate with material property as followed, Er = 3.48, $h = 0.8$ mm, and $\tan\delta = 0.0019$.

To characterise good performance of a wideband balun, three important aspects should be evaluated properly: (1) the input impedance matching at the unbalanced port and two balanced ports should be less than −10 dB, (2) very little amplitude imbalance between the two balanced output ports and (3) 180° phase difference between the two balanced output ports. Figure 11.5 demonstrates the wideband balun performance in prediction. As can be seen, excellent wideband balun performance can be observed. It should be noted that the exact frequency range of this designed balun can be optimised depending on the balanced antenna operation frequency bands.

To validate the simulated wideband balun performance, a back-to-back wideband planar balun was built up, as shown in Fig. 11.6. It was used to characterise the amplitude imbalance between the two output ports as well as the insertion loss of the balun. Phase difference between the two balanced output ports was also measured. The measured amplitude imbalance and phase difference of the two balanced

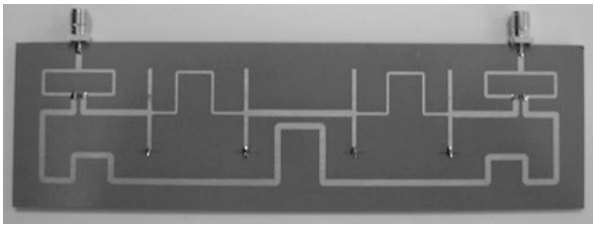

Fig. 11.6 Photograph of a back-to-back planar balun

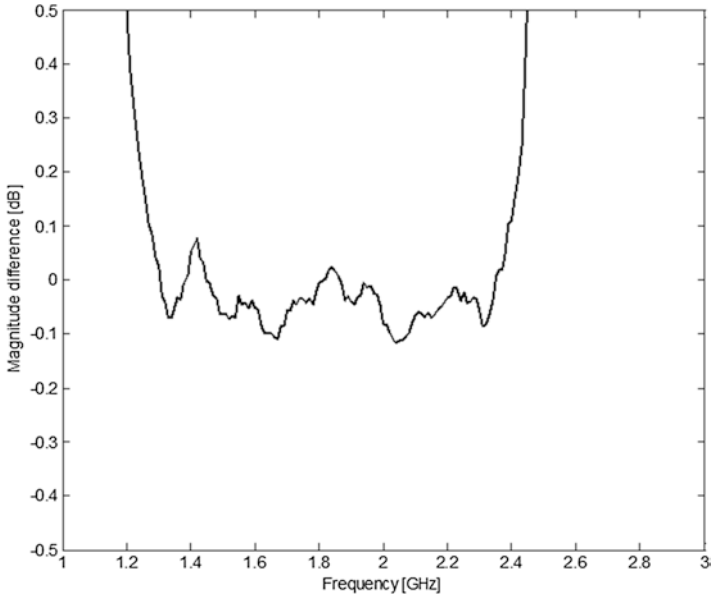

Fig. 11.7 Measured amplitude difference of two balanced ports

ports using a single balun are shown in Figs. 11.7 and 11.8, respectively. As can be seen, an excellent wideband balance in magnitude and phase between the two balanced ports was found, as summarised in Table 11.2.

Figures 11.9 and 11.10 present the fabricated balun prior to artwork [15] and present work.

11.2.3 Measurement Validation

A prototype (see Fig. 11.11) of this folded loop antenna was fabricated and tested using the presented balun in previous section in the measurement. Copper thickness of 0.15 and 0.5 mm was used for fabricating the antenna element and the ground plane.

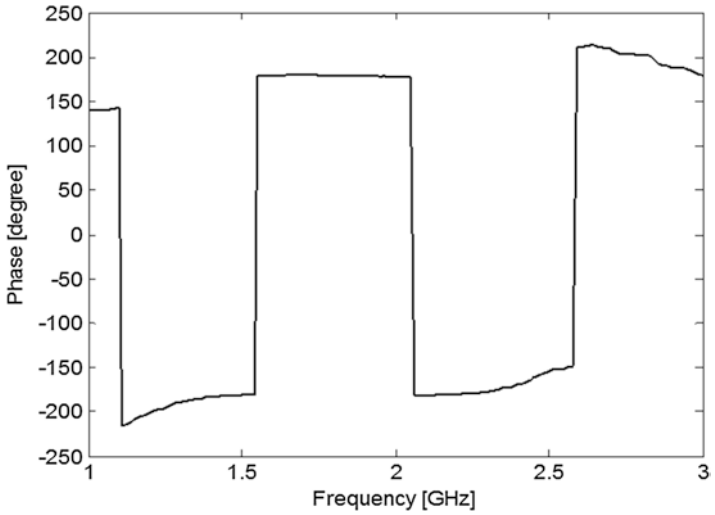

Fig. 11.8 Measured phase difference of two balanced ports

Table 11.2 Summary of the present balun performance prior to artwork

Item	Operating frequency (GHz)	Insertion loss (back-to-back) (dB)	Balanced difference: amplitude (dB), phase (°)	Return loss (dB)
Zhang et al.'s balun [15]	1.7–3.3	–	Within 0.3, ± 5°	−10
Present balun	1.4–2.4	1.65	Within 0.1, ± 2°	−10

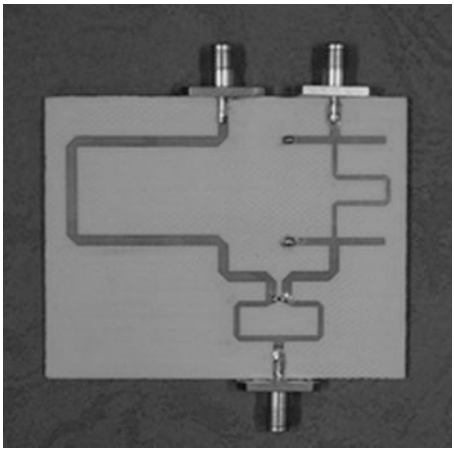

Fig. 11.9 Photograph of the fabricated balun in [15]

Figure 11.12 presents the simulated VSWR of the GA-optimised antenna configuration and prototype results with integrated wideband balun as the feed network. As can be seen, a reasonable agreement can be observed between the simulation and measurement. These comparable results also confirm the effectiveness of the GA as an efficiency tool for the antenna design and optimisation.

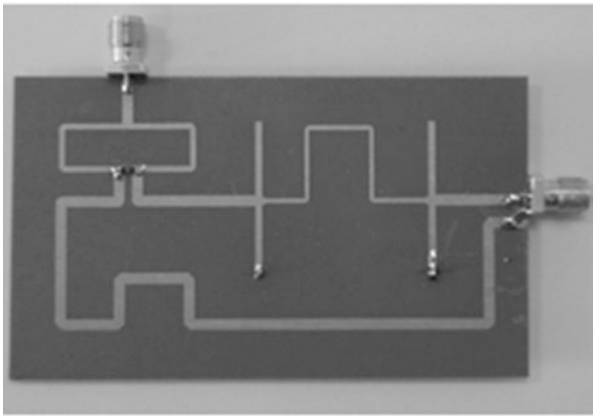

Fig. 11.10 Photograph of wideband balun adopted and modified in [15]

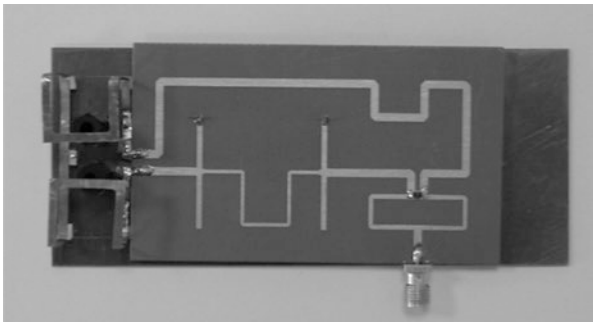

Fig. 11.11 Photograph of prototype of FLA design

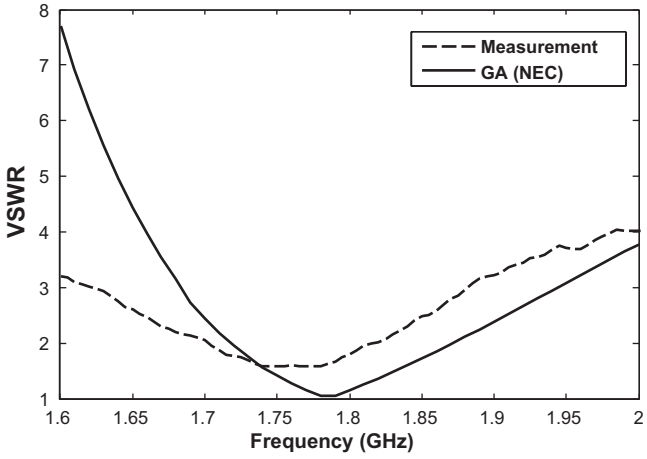

Fig. 11.12 The simulated and measured VSWR against operating frequency

11.3 Wideband Balanced-Fed Folded Arm Dipole Antenna Designs

In the previous section, a balanced folded loop type of antenna has been demonstrated for a single-band design. Wideband design with balanced-fed folded dipole antenna structures is presented in this section. The design is intended to cover GSM1800/GSM1900/UMTS bands, as well as 2.4 GHz band.

11.3.1 Folded Dipole for Wideband Design

A balanced-fed dipole antenna with folded arm structure for achieving a low profile for internal designs has been reported in [17]. The proposed antenna structure is presented in Fig. 11.13, where a simple technique is used by inserting a pair of slots in each of the dipole arm closing the ground plane area (1 mm away). These introduced slots have the effect of mitigating the ground plane impact on the folded dipole antennas, and at the same time without major degrading the antenna performance. In addition, trimmed triangles with a symmetrical structure at the feeding point area have been employed in order to improve the antenna impedance matching [18].

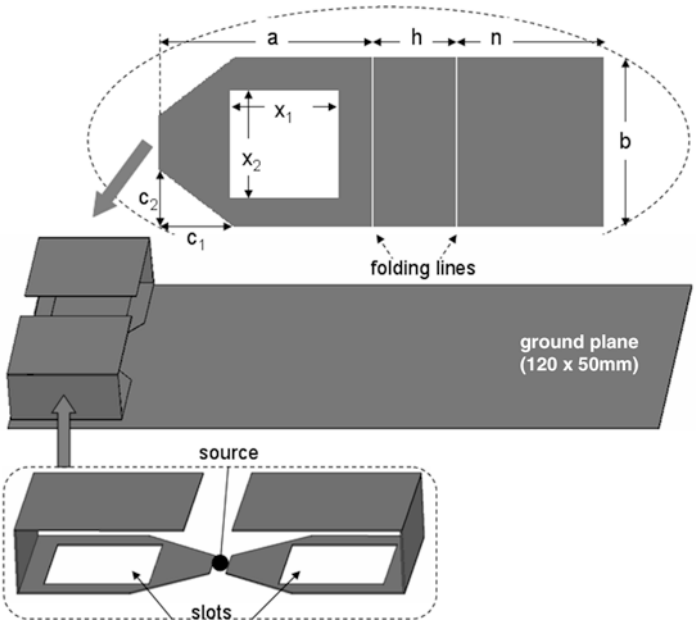

Fig. 11.13 Antenna configuration studied in [17]

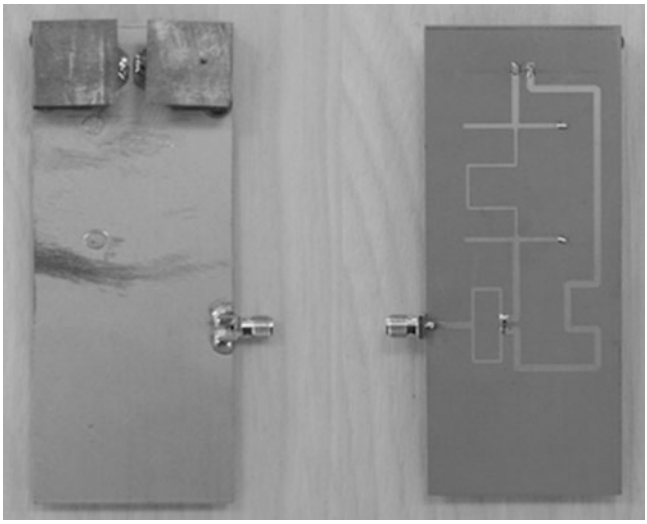

Fig. 11.14 Photograph of the fabricated board for the modified balun

The measurement methods of this wideband folded dipole antennas is worth mentioning. Two measurement methods were considered and used in this work. The first one is to measure the antenna impedance using the previously design wideband balun network, and this method is called 'two port method'. A prototype of such method is shown in Fig. 11.14. As can be seen that the balun well designed and placed the beneath the antenna feeding area on the opposite side for an integrated solution as a single antenna balun system. The other measurement method was adopted from reference [19], where a copper plate with size of 500 mm × 500 mm was used as the finite ground in the measurement, as shown in Fig. 11.15. This measurement method here is called 'monopole method'. Figure 11.16 presents the comparative results of the two different methods against the simulated one. It can be seen that a fairly good agreement can be observed. This result also confirms the effectiveness of the monopole-type measurement method, which in comparison has the advantage of not requiring a well-designed wideband balun as a feeding network.

11.3.2 Folded Dipole with Wideband Dual-Arm Design

Folded arm dipole antenna design concept presented Sect. 11.3.1 is continued to improve its bandwidth. A new technique to further enhance the antenna impedance bandwidth has been reported in [20], in which a pair of thin-strip arm was inserted for each dipole arm in order to achieve an additional band to cover 2.4 GHz WLAN

Fig. 11.15 Photograph of one-port measurement method

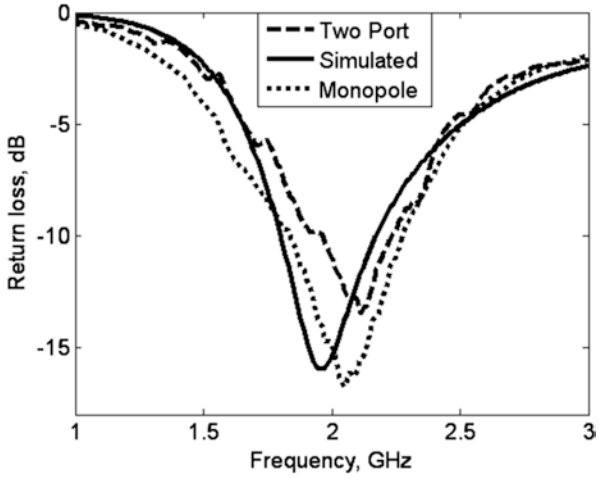

Fig. 11.16 Comparative results among the simulation and two different measurement methods

for multiband applications. The proposed antenna structure in [20] is illustrated in Fig. 11.17 . It should be noted that a step feed structure was adopted in this work. The reason for this is that it was found the antenna impedance matching could be relatively improved with this configuration arrangement.

The optimal antenna configuration was then fabricated for hardware validation. Figure 11.18 presents the measured and simulated return loss. It can be seen that a multiband operations has been achieved with such a technique.

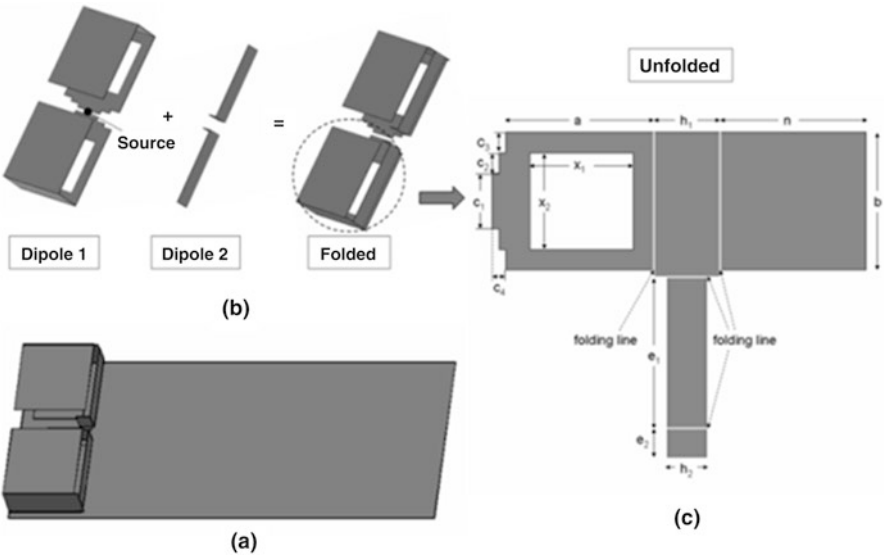

Fig. 11.17 Antenna configuration studied. (**a**) Balanced folded dipole antenna with conducting plate; (**b**) front view of the antenna design; (**c**) unfolded structure of the proposed antenna

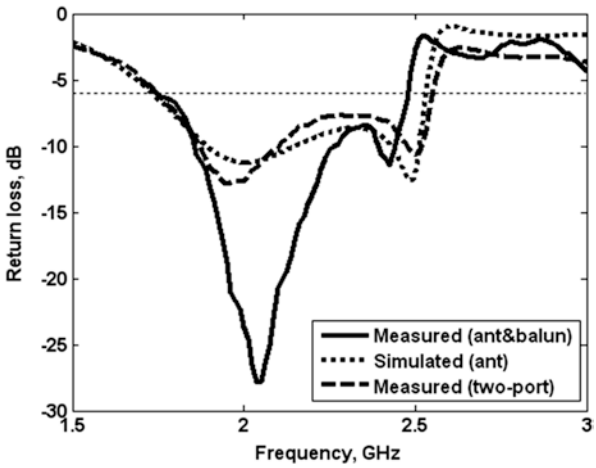

Fig. 11.18 The simulated and measured return loss against operating frequency

11.3.3 Compact Folded Arm Dipole Antenna with Wideband Dual-Arm Design

In this design reported in [21], the dual-arm folded dipole structure was continuously investigated; the purpose of this design example was use the same technique for multiband operation, but to realise a compact design in size.

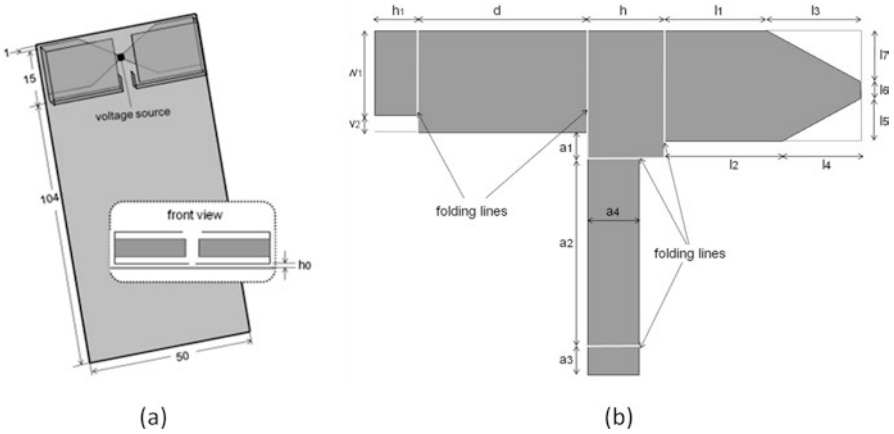

Fig. 11.19 Antenna configuration studied. (**a**) Balanced antenna with conducting plate; (**b**) important parameters of the proposed antenna

To achieve, the folded dipole width is reduced in order to mitigate the coupling between the balanced antenna element and the closely placed antenna ground plane (1 mm away). Previously, inserting a slot was introduced on the folded arm. In this design, the slot was not necessary to be applied here. As the width of the folded arm was reduced, it was equivalently to reduce the ground plane impact on the folded dipole antenna design. In addition, a triangle-shaped feeding structure was adopted here with design optimisation. Figure 11.19 presents the proposed antenna structure and important antenna parameters in [21]. As can be seen that the antenna volume is considerably reduced, comparing the design reported in [20] and Fig. 11.17.

Figure 11.20 presents the measured return loss of the prototype antenna against the computed one. It should be noted that two measurement methods were also used to cross validate the measurement results, one was adopted in work [19] and the other one was measured with integrated wideband balun network. As can be seen, similar bandwidth was observed with this compact design structure.

The normalised measured and simulated SAR values are shown in Fig. 11.21. A reasonable agreement in SAR distribution between the measured and computed results can be easily noted from Fig. 11.19. The maximum unaveraged measured and computed SAR values for 1 W input power are 3.2 W/kg and 3.02 W/kg, respectively. These results are much lower than those reported in [22, 23] for a GSM 1800 terrestrial handset, for which the peak SAR in the head was between 10 and 21 W/kg for a head-handset separation of 7.5 mm.

11.4 Summary

Several novel designs of balanced antennas for mobile handsets have been presented and analysed. Firstly, a folded loop antenna has been designed and optimised using GA for 2G and 3G operation, respectively. Then, a design example has achieved

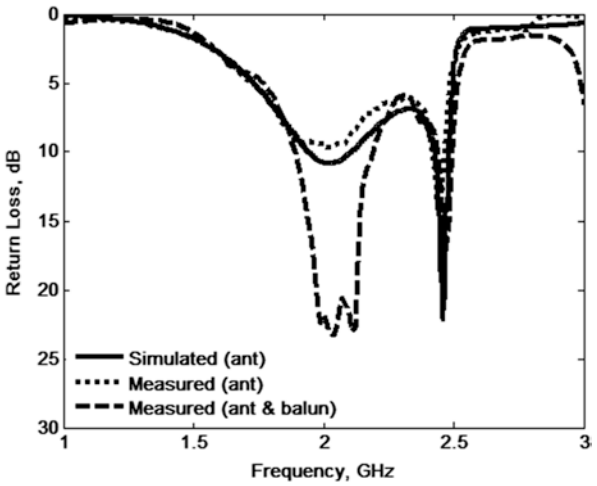

Fig. 11.20 The simulated and measured return loss versus the operating frequency

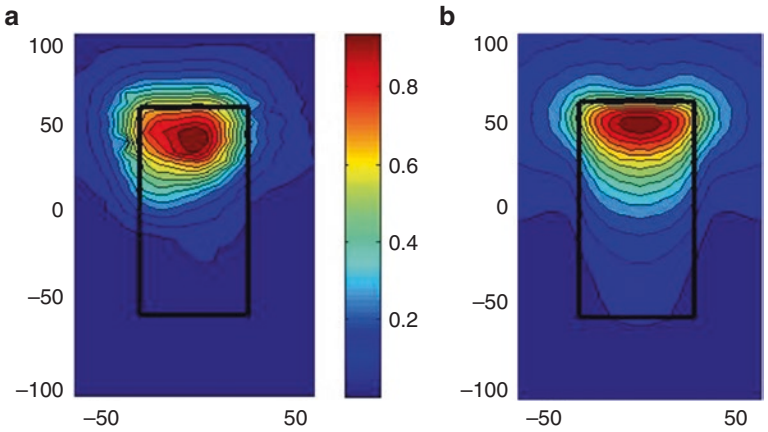

Fig. 11.21 The normalised SAR distribution at 1.8 GHz: (**a**) measured SAR, (**b**) computed SAR

wideband operation covering DCS, PCS and UMTS bands. Furthermore, a dual-arm technique has been demonstrated to realise an additional band in order to further enhance the balanced antenna impedance bandwidth to support 2.4 GHz band.

With achieved wideband balanced antenna designs, designing an equivalently wideband balun as feeding network in the measurement is also important. Efforts have been in this chapter to demonstrate how to design and characterise a wideband balun. Moreover, an integrated measurement technique in the measurement was also addressed to form a single system, which integrating the planar balun and the

antenna ground plane mounting on either side of one substrate. In addition, another method was also adopted to cross validate the wideband balanced antennas. It was found that both measurement methods were effective and their measured results have shown reasonable agreement.

The presented designs with the balanced antenna concept for mobile handsets have proved wideband impedance matching can be achieved. These results demonstrate the attractiveness of such design concept for practical application in mobile phones. Besides, the current design has some practical limitations since it does not cover the operation of the frequency bands below 1 GHz, e.g. GSM850/900 frequency band, which is still in demand at present; moreover, with the newly allocated Long Term Evolution (LTE) bands at 700 MHz, it seems that an unbalanced type of design is more suitable for bands below 1 GHz; with the aid of RF switching, these bands can be easily tuned to the desired bands with an acceptable loss caused by the RF switch itself. At mobile frequency bands above 1 GHz starting 1710 MHz, a balanced type of antenna is a good candidate for mobile handset, as this type of antenna can offer stable antenna performance in FS and handheld cases. However, the demand to drive antenna engineers to come up with even more compact design is still needed. For the future work, further development of balanced antennas will address this issue of developing new techniques for multiband realisation.

References

1. F.R. Hsiao, H.T. Chen, G.Y. Lee, T.W. Chiou, K.L. Wong, A dual-band planar inverted-F patch antenna with a branch-line slit. Microw. Opt. Technol. Lett. **32**, 310–312 (2002)
2. H. Morishita, H. Furuuchi, H. Ide, Z. Tanaka, K. Fujimoto, A balance-fed loop antenna system for handset. IEICE Trans. Fundam. **E82-A**(7), 1138 (1999)
3. H. Morishita, Y. Kim, H. Furuuchi, K. Sugita, Z. Tanaka, K. Fujimoto, Small balance-fed helical antenna system for handset. Proc. IEEE Veh. Technol. Conf. **2**, 1377–1380 (2000)
4. Y. Kim, H. Morishita, Y. Koyanagi, K. Fujimoto, A folded loop antenna system for handsets developed and based on the advanced design concept. IEICE Trans. Commun. **E84-B**(9), 2468–2475.200
5. H. Morishita, Y. Kim, K. Fujimoto, Analysis of handset antennas in the vicinity of the human body by the electromagnetic simulator. IEICE Trans. Electron. **E84-C**(7), 937 (2001)
6. H. Morishita, H. Furuuchi, K. Fujimoto, Performance of balanced-fed antenna system for handsets in the vicinity of a human head and hand. IEE Proc. Microw. Antennas Propag. **149**(2), 85–91 (2002)
7. R.A. Abd-Alhameed, P.S. Excell, K. Khalil, R. Alias, SAR and radiation performance of balanced and unbalanced mobile antennas using a hybrid formulation, Fifth international conference on computation in electromagnetics (CEM 2004), Stratford-upon-Avon, Apr 2004, pp. 25–26
8. FCC, Evaluating compliance with FCC guidelines for human exposure to radio frequency electromagnetic fields, Federal communication Commission, Washington, DC, OET Bulletin 65, Aug 1997
9. I.C.N.I.R.P. Guidelines, Guidelines for limiting exposure to time-varying electric, magnetic, and electromagnetic fields (up to 300 GHz). Health Phys. **74**(4), 494–522 (1998)
10. D.E. Goldberg, *Genetic Algorithms in Search, Optimization and Machine Learning* (Addison-Wesley, Reading, 1989)

11. D.L. Carroll, FORTRAN Genetic Algorithm Driver, Version 1.7, Download from: http://www.staff.uiuc.edu/~carroll/ga.html, 12/11/98
12. G.L. Burke, A.J. Poggio, *Numerical Electromagnetics Code (NEC)-Method of Moments* (Lawrence Livermore Laboratory, Livermore, 1981)
13. D. Zhou, R.A. Abd-Alhameed, C.H. See, P.S. Excell, E.A. Amushan, Design of quadrifilar helical and spiral antennas in the presence of mobile handsets using genetic algorithms, in *Proceeding of the First European Conference on Antennas and Propagation (EuCAP 2006)*, (Nice, 2006)
14. D. Zhou, R.A. Abd-Alhameed, P.S. Excell, Bandwidth enhancement of balanced folded loop antenna design for mobile handsets using genetic algorithms, in *Proceeding of IEEE International Antenna and Propagation Symposium*, (Hawaii, 2007), pp. 3568–3571
15. Z.Y. Zhang, Y.X. Guo, L.C. Ong, A new wideband planar balun on a single-layer PCB. IEEE MicrowaveWireless Compon. Lett. **15**(6), 416–418 (2005)
16. Agilent Technologies, Advanced Design System, ADS2005A
17. D. Zhou, R.A. Abd-Alhameed, C.H. See, P.S. Excell, Design of wideband balanced folded-arms dipole antenna for mobile handsets. Electromagnetics **29**(8), 641–651 (2009)
18. M.J. Ammann, Z.N. Chen, Wideband monopole antennas for multi-band wireless systems. IEEE Antennas Propag. Mag. **45**(2), 146–150 (2003)
19. R. Meys, F. Janssens, Measuring the impedance of balanced antennas by an S-parameter method. IEEE Antennas Propag. Mag. **40**(6), 62–65 (1998)
20. D. Zhou, R.A. Abd-Alhameed, C.H. See, P.S. Excell, Wideband balanced folded dipole antenna with a dual-arm monopole structure for mobile handsets. IET Microwaves Antennas Propag. **4**(2), 240–246 (2010)
21. D. Zhou, R.A. Abd-Alhameed, C.H. See, A.G. Alhaddadand, P.S. Excell, Compact wideband balanced antenna for mobile handsets IET Microwaves Antennas Propag. (Spec. issue). **45**, 600–608 (2010)
22. D. Zhou, R.A. Abd-Alhameed, C.H. See, A.G. Alhaddad, P.S. Excell, New mobile balanced mobile antenna with wide bandwidth performance. in *Proceeding of the European Conference on Antennas and Propagation*, (Berlin, 2009), pp. 549–552
23. J. Mustafa, PhD thesis, "Mobile communication handset antennas with reduced user coupling: design of array and balanced antennas for 1.8 GHz personal communication handset to reduce specific absorption rate", Submitted to Bradford University, July 2005

Chapter 12
Coplanar-Fed Miniaturized Folded Loop Balanced Antenna for WLAN Applications

A.G. Alhaddad, R.A. Abd-Alhameed, and Embarak M. Ibrahim

12.1 Introduction

With the continuous progress and growth in personal communications along with the non-stop demand of the customer hope and ambition, the compact antennas that operate in wide bandwidth features with the emphasizing of outstanding radiation, high power gain and better efficiencies have been given more considerations. Recently, balanced antennas for use in mobile applications have drawn the attention to the antenna designers in both industry and academia. This is because of several advantages such as compact volume, acceptable gain, better efficiency and interestingly the stable performance of the balanced antenna when it is held in vicinity to the human body by the user of mobile device [1].

Usually, to support the feed networks of balanced structures, a balun circuit needs to be applied. This may affect the antenna bandwidth, but will compromise the intended performance such as radiation patterns and gain [2]. The efficiency performance of the used balun will obviously contribute in defining the symmetry radiation pattern of the balanced structures, in which suboptimal pattern shaping may be achieved [3]. This has put some constraints on the degree of potentiality to exploit the balanced design layout in some handset applications.

To address this limitation, an appropriate solution is to employ the coplanar configurations. The type of coplanar transmission line antenna structures have become of a great interest for antenna researchers owing to their simple structure, seamlessly integration with both passive and active devices within the same layer [4]. The layout of the coplanar lies in printing both the radiator and ground plane

A.G. Alhaddad • R.A. Abd-Alhameed (✉)
Faculty of Engineering & Informatics, University of Bradford, Bradford, UK
e-mail: R.A.A.Abd@bradford.ac.uk

E.M. Ibrahim
College of Electronic Technology, Bani Walid, Libya

I. Elfergani et al. (eds.), *Antenna Fundamentals for Legacy Mobile Applications and Beyond*, DOI 10.1007/978-3-319-63967-3_12

conductors in the same plane, which is the top surface of the dielectric material [5]. The term of coplanar structure as a transmission line has been recently heavily studied and become as rigorous area of study. The coplanar transmission line has remarkable features, which make it very suitable to accomplish a board frequency range as well as with simple manufacturing procedure [6, 7]. Another benefit of the antenna structures with coplanar feeding approach shows stable and constant gain values over a wide bandwidth features [7–10].

12.2 Theory of the Shielded Balanced Loop

The conventional balanced shielded loop configuration consists of coaxial line with a thin gap in the outer shield. The main antenna with loop layout is adjusted and improved to be fed with an unbalanced coaxial cable. This can be done by integrating the loop antenna with a balun [11]. The inner line of the coaxial, which is considered as coplanar transmission structure is ended on the outer conductor or the grounded sheath (this is also equivalent to the coplanar ground plane) of the opposite half loop at the gap. Power will still be transmitted to the load Z_L [12]. The coplanar structure integrating with a balun transformer is shown in Fig. 12.1.

12.3 Microstrip Patch Antenna

Microstrip patch antennas are a popular printed antenna for narrowband microwave wireless links that require semi-hemispherical coverage. Microstrip patch antennas have considered as one of the most widespread antennas used in small portable wireless communication equipment [13].

A patch antenna usually derives its name from its shape/structure. Figure 12.2 shows a patch antenna, which has a rectangular top layer and thus names appropriately. Atypical patch antenna consists of two metal planes, the bottom layer being

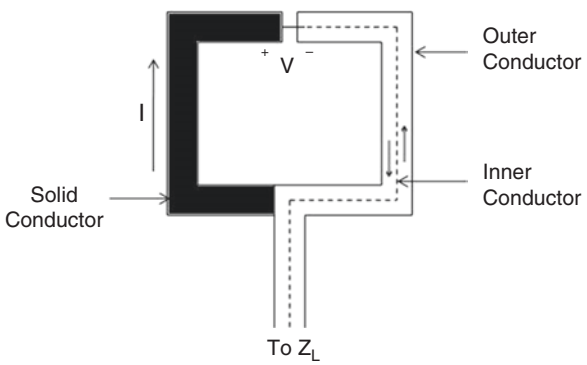

Fig. 12.1 The structure of the balanced antenna along with integrated balun

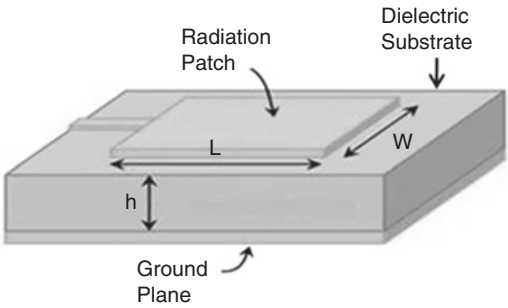

Fig. 12.2 Microstrip patch antenna

the ground plane and the top layer is the radiating patch and a dielectric material between them. The shape dimensions of the patch antenna usually determine the frequency of operation and thus these antennas are categorized as resonant antennas. Microstrip antennas have been classified into four basic groups: microstrip patch antennas, printed slot antennas, microstrip travelling wave antennas and finally microstrip dipole antennas [14].

Microstrip antennas have come up with several advantages such as easy integration with both passive and active components over the PCB of the portable devices [15]. However, the key concern with the microstrip patch structure is regarding its size. This is because to make this type of antenna operate over the low microwave frequency spectrum, it occupies a large volume, in which it becomes very complicated and even not feasible to be concealed within a handset device. Such antenna structures work as a result of the fringing field that takes place between the patch edges and the Printed Circuit Board (PCB) [15].

To come up with a high and efficient performance of the microstrip antenna, three key losses should be taken into account, namely, the conducting losses, losses of dielectric substrate and surface wave losses. To obtain satisfactory efficiency, bandwidth enhancement and antenna size reduction, both the dielectric constant and height of the used substrate need to be as minimum as possible [14].

12.4 Coplanar Waveguide (CPW) Antennas

Above, we mentioned the use and/or the employment of the microstrip technology to the type of planar antennas. However, it is obvious that microstrip antennas should consist of radiating patch on the top of the substrate and also ground plane underneath the substrate material to support the feeding microstrip line. Actually, the ground plane underneath the substrate material is required to allow the electromagnetic waves to travel along the feed line. Thus, it is obvious that manufacturing on both sides of the substrate is an obligatory task with the microstrip approach.

On the other hand, when using the approach of the coplanar waveguide (CPW) feed network, both radiating conductor and PCB will be printed on the same side of the top surface of the substrate. This in turn will lead to the conclusion that the

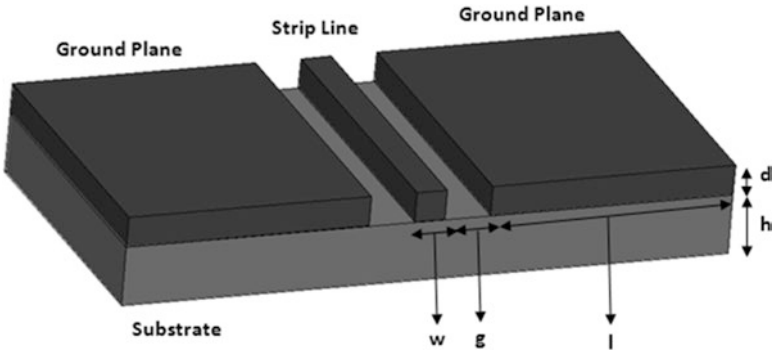

Fig. 12.3 The basic structure of coplanar waveguide

electromagnetic wave flows in the slots on the surface of the substrate, and therefore, less energy will be within the substrate. This one feature promotes the coplanar antenna structure to be considered as suitable candidate for wide bandwidth wireless applications [4]. A coplanar waveguide method was initially recommended by Wen [5]; it is made of a centre conductor with two sides of ground plane placed on both sides as depicted in Fig. 12.3.

Coplanar waveguide procedures were categorized as conventional CPW, conductor CPW and micro machined CPW. The key features and benefits of CPW along with its applications were reported in [16–18].

12.5 Antenna Structure

The proposed CPW antenna consists of three main rectangular conducting parts, namely, the central strip line and two identical conducting arms one on each side, which are viewed as the ground plane as illustrated in Fig. 12.4a.

The accomplished design was modelled and optimized to cover the dual band of WLAN at 2.4 GHz and 5.2 GHz. Within this work, the CPW is utilized as an antenna by prolonging the transmission lines together with the conducting strip of the ground planes. The exploited transmission line has taken a 'P' shape, while the open circuit may be observed from the top. With the aim of having a balanced configuration, the structure is reproduced, and then inverted to be coupled with the main figure via the inner with the minimum gap. The width of the central part of the present antenna is = 0.7 mm, while both outer strips have come with dimension width of 5.45 mm. The central strip and the two conductors presented on each side were separated by a small gap *m* with width of 0.2 mm. The full dimensions of the antenna configuration are stated in Table 12.1.

With the target to accomplish antenna size miniaturization, the present design is bent from both ends with an optimum height of 3 mm. This finally makes the antenna for being formed as a folded dipole [19]. The optimum configuration of this antenna is depicted in Fig. 12.4b.

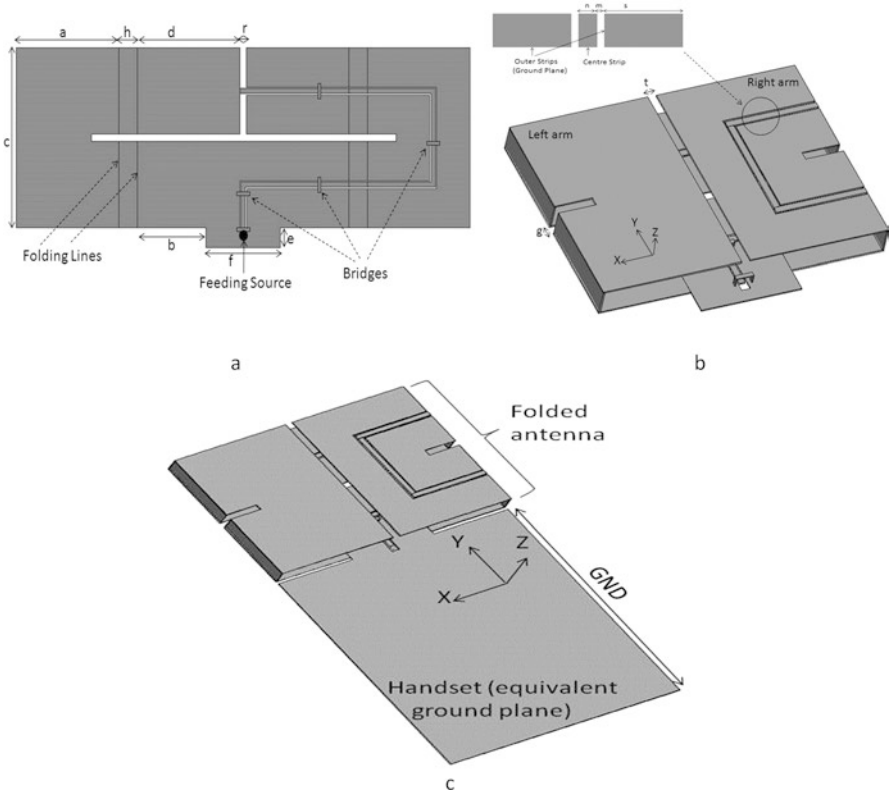

Fig. 12.4 The basic antenna configuration, (**a**) the unfolded coplanar antenna, (**b**) the optimum folded antenna, (**c**) equivalent ground plane

Table 12.1 The full dimensions of the coplanar antenna

Parameter	Value (mm)
a	16.5
b	11
c	25
d	16.5
h	3
g	1
r	1
s	5.45
f	12
t	1
n	0.7
m	0.2
e	2.75

12.6 Effect of Variation of Parameters on Return Loss

Within this analysis, the key sensitive parameters, which can influence the return loss characteristic of the proposed antenna, have been given more attention and consideration. This study and analysis will efficiently contribute in obtaining the optimum and desired design needed to meet the goal allocated within this chapter. Four parameters were selected to be the most effective ones on the return loss of the antenna. These are: the height of the design, length of antenna, distance between the folded ends of the antenna and the size of ground plan. This investigation was implemented with the aid of CST design suite [20].

12.6.1 Variation of the Antenna Height h

The influences of height of the structure against the return loss are given in Fig. 12.5. The height was varied from 1 mm to 6 mm with an increment of 1 mm. It is obviously noted that the resonant frequencies kept shifting downwards when the height of the structure increased. This concludes that the height of the structure plays an important role in controlling the resonant frequency as well as the whole structure size.

12.6.2 Variation of the Length of the Antenna b

Figure 12.6 displays the effect of the antenna length, which may occur on the performance of the return loss. The antenna length (*b*) was changed from 9 mm to 13 mm, with 1 mm step each time. Again, both bands of WLAN at 2.4 GHz and

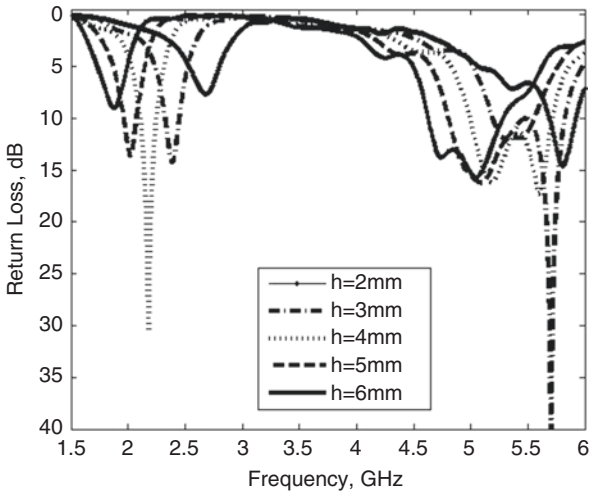

Fig. 12.5 The variation of the antenna height against the return loss

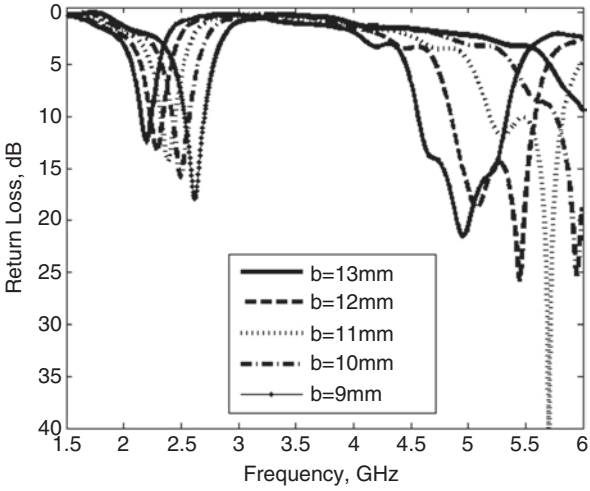

Fig. 12.6 The variation of the antenna length on the return loss

5.2 GHz were seen to be swept down as long as the length of the antenna keeps increasing. As one can note, the best value to achieve both desired bands of WLAN within this work was 11 mm.

12.6.3 Variation of the Gap Between the Folded Ends of the Antenna t

The investigation of gap between both bent ends is indicated in Fig. 12.7. The spacing between both ends varied from 1 mm to 3 mm with an increment of 0.5 mm. One should note that both resonant frequencies are very sensitive to the variation of the gap between both bends. This also proves the earlier say to keep the gap as small as possible between both ends. This is because when the spacing was set at 1 mm, both WLAN bands were accomplished, with a perfect impedance matching.

12.6.4 The Effect of the Ground Plane Size

The effect of handset size (equivalent ground plane) was also checked against the antenna return loss. For more clarifications, the current study was only done on the length of the ground plane, while the width was considered to take exactly same width as the antenna. The length of the PCB was varied over a wide range from 20 mm to 80 mm, with 20 mm step each time. From Fig. 12.8, it is obvious that there is no much effect of the ground plane length on the antenna return loss. From this finding, we can again prove that the balanced antenna is a ground plane independent structure, in which its performance will not be degraded when it's being held by the mobile users.

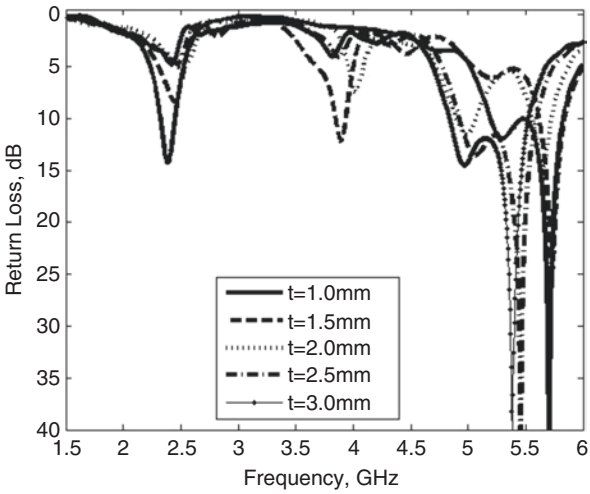

Fig. 12.7 The variation of the gap between the two ends on the return loss

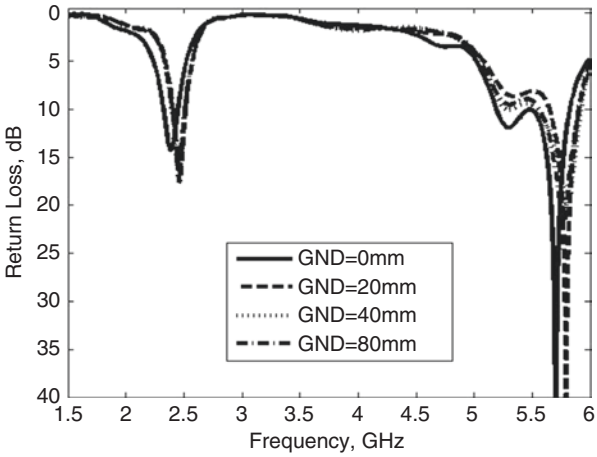

Fig. 12.8 The variation of the ground plane size on the return loss

12.7 Antenna Prototype and Measured Results

The simulated antenna with coplanar feeding proposed in Fig. 12.4 was fabricated on special substrate of foam with height of 2.5 mm and relative permittivity of 1.1. Printing the antenna over this type of flexible material has facilitated the folding process to be in the shape this antenna was [preferred to be]. This also was effectively helped in the size reduction. The final fabricated antenna with feeding approach is depicted in Fig. 12.9.

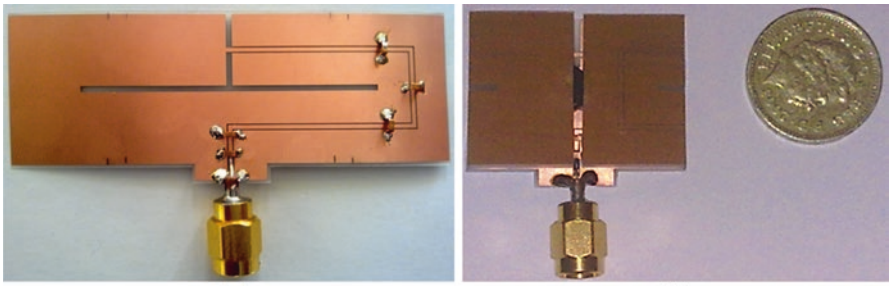

Fig. 12.9 Fabricated proposed folded balanced antenna with coplanar feeding, (**a**) unfolded structure, (**b**) folded antenna structure

During the fabrication process, it was a challenge to detach the foam from the antenna to be harmonized with the same process made during the simulation procedure and also to come up with the same results, which were already obtained from the theory.

As can be noted, the present antenna design is made of a CPW line that displays one dominant CPW mode. In fact, between the two slots, the CPW mode shows an electric field that has an opposite polarity. Thus, as shown in Fig. 12.9a, air bridges are located over CPW in order to keep the PCBs at the same potential. This was contributed in eliminating the influence of the slot line mode over the CPW line. Later, the response of the proposed antenna is analysed to accomplish balanced features. Furthermore, a dielectric material was introduced between the top and bottom of the antenna. This is done in order to support and also to keep the arms exactly at the same height, and maintain the same surface structure.

The current surfaces of the proposed the antenna with and without the inclusion of employed air bridges are indicated in Fig. 12.10. It should be noted that a stronger induced current is taken place, as long as the air bridges are placed between the outer strips (ground plane).

The simulated return loss of the proposed balanced antenna is illustrated in Fig. 12.11. CST EM simulator was initially used to achieve the computed return loss, and then another EM software package, namely, HFSS [21], was also exploited to check the simulated return loss. As can be clearly seen, the results of both packages show more or less similar response at the dual band of WLAN 2400 MHz and 5500 MHz, respectively. For proof of concept, the measured return loss of the fabricated model was also studied and analysed. In Fig. 12.11, it is apparently noticed that the measured data agrees very well with the computed ones from CST and HFSS. The slightly differences may be attributed to complexity and difficulties of folded arms, placing air bridges and feeding soldering during the fabrication process.

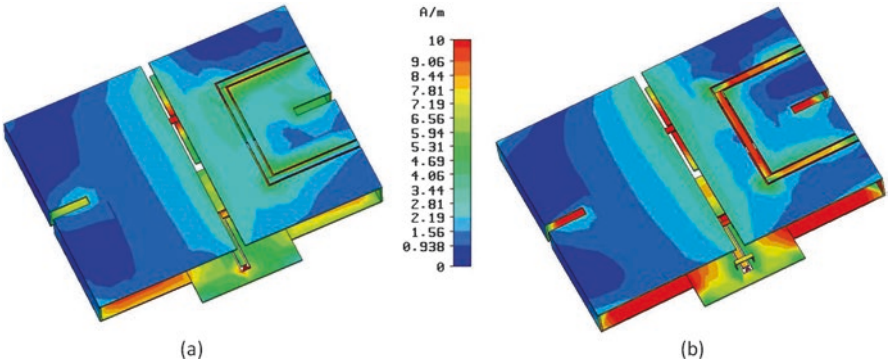

Fig. 12.10 The current surface of the proposed folded balanced, (**a**) without bridges, (**b**) with bridges

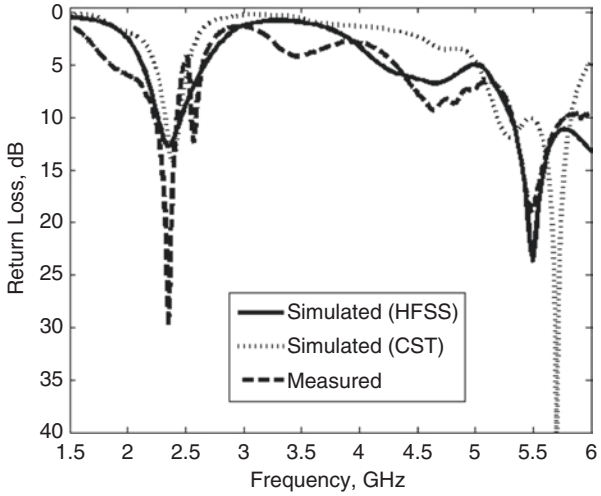

Fig. 12.11 The simulated and measured return loss of the proposed antenna

12.8 The Radiation Pattern and Power Gain of the Antenna

The measured far-field outcomes of the manufactured antenna were generated inside the anechoic chamber. Three plane cuts, namely, *xz*, *yz* and *xy* planes, were selected for the three bands (2.4 GHz, 2.45 GHz and 5.2 GHz) that cover the entire targeted WLAN operational bandwidth in this chapter. The practical results of the far-filed patterns were normalized and indicated in Fig. 12.12. From Fig. 12.12, it is said that both findings of simulation and measurement analyses show satisfactory agreement and said to be nearly omnidirectional.

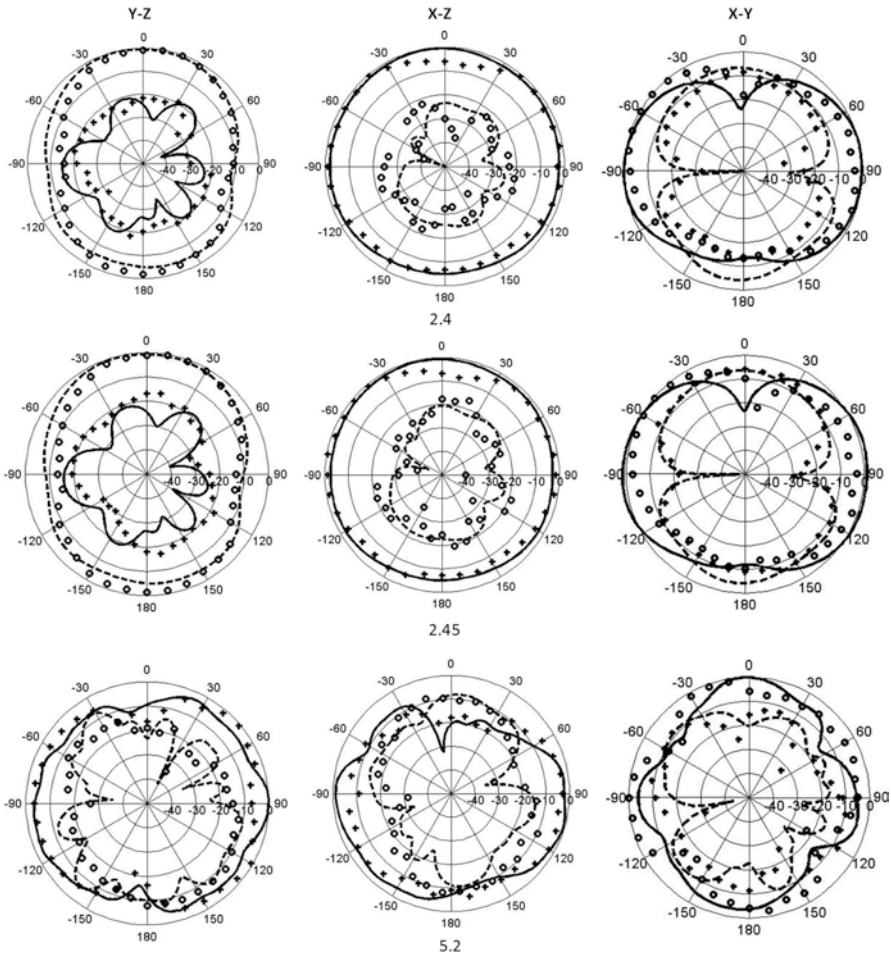

Fig. 12.12 Radiation patterns of the proposed antenna at 2.4, 2.45 and 5.2 GHz for *yz*, *xz* and *xy* planes. 'ooo' measured E_θ,'----' simulated E_θ,'xxx' measured E_ϕ '——' simulated E_ϕ

Figure 12.13 demonstrates the measured power gains of the proposed antenna for the two frequencies of 2.4 GHz and 5 GHz bands. It is noticeably seen that from Fig. 12.13, the measured antenna power gain values fluctuated from 1.5 dBi to 1.9 dBi within the lower band of 2.4 GHz, while values varied from 1.4 dBi to 2.4 dBi at the higher band of 5.2 GHz.

The measured radiation efficiency of the proposed antenna at both WLAN bands was shown in Fig. 12.14. A Wheeler cap method was selected and applied to measure the radiation efficiency [22, 23]. The Wheeler cap was chosen, as it is the most popular and convenient approach for measuring the antenna efficiency.

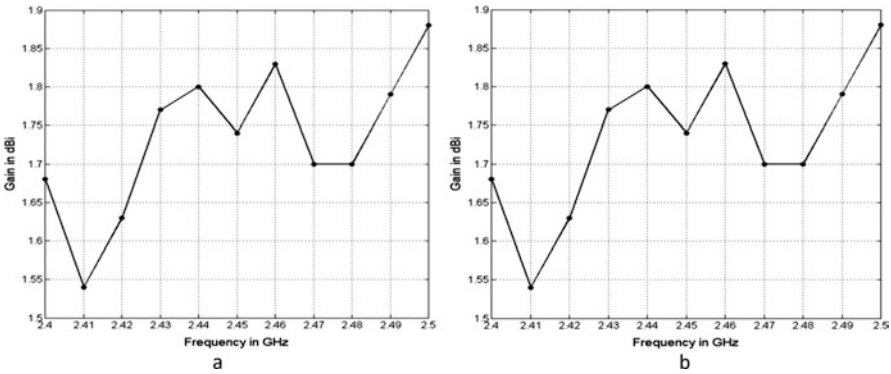

Fig. 12.13 Measured antenna power gain at (**a**) 2.4 GHz band, (**b**) 5.2 GHz band

The calculated and practical radiation efficiencies of the proposed CWP balanced antenna for the WLAN lower band, which ranges from 2400 MHz to 2460 MHz, and the WLAN higher band, which varies from 5200 MHz to 5800 MHz, are investigated in Fig. 12.14. In the lower WLAN band (see Fig. 12.14a), the discrepancies of radiation efficiency are fluctuated from 0.92 to 0.87 which correspond to average of 90% over the bands of interest. On the other hand, at the higher band of WLAN (see Fig. 12.14b), the values of the radiation efficiency are varied from 0.84 to 0.90, demonstrating that an efficiency of 87% is accomplished. Both computed and measured data of the radiation efficiencies are in close agreement.

12.9 Conclusions

A novel design of dual-band CPW balanced antenna for use in WLAN applications has been proposed and analysed in this chapter.

One advantage of the proposed design was the elimination of the balanced feed network. With several attempts and a comprehensive parametric analysis of the key effective parameters, the proposed antenna was able to cover both bands of WLAN, namely, 2400 MHz and 5500 MHz. The simulated model then was fabricated, and its results were validated with the simulated outcomes in terms of return loss, radiation pattern, power gains and radiation efficiency.

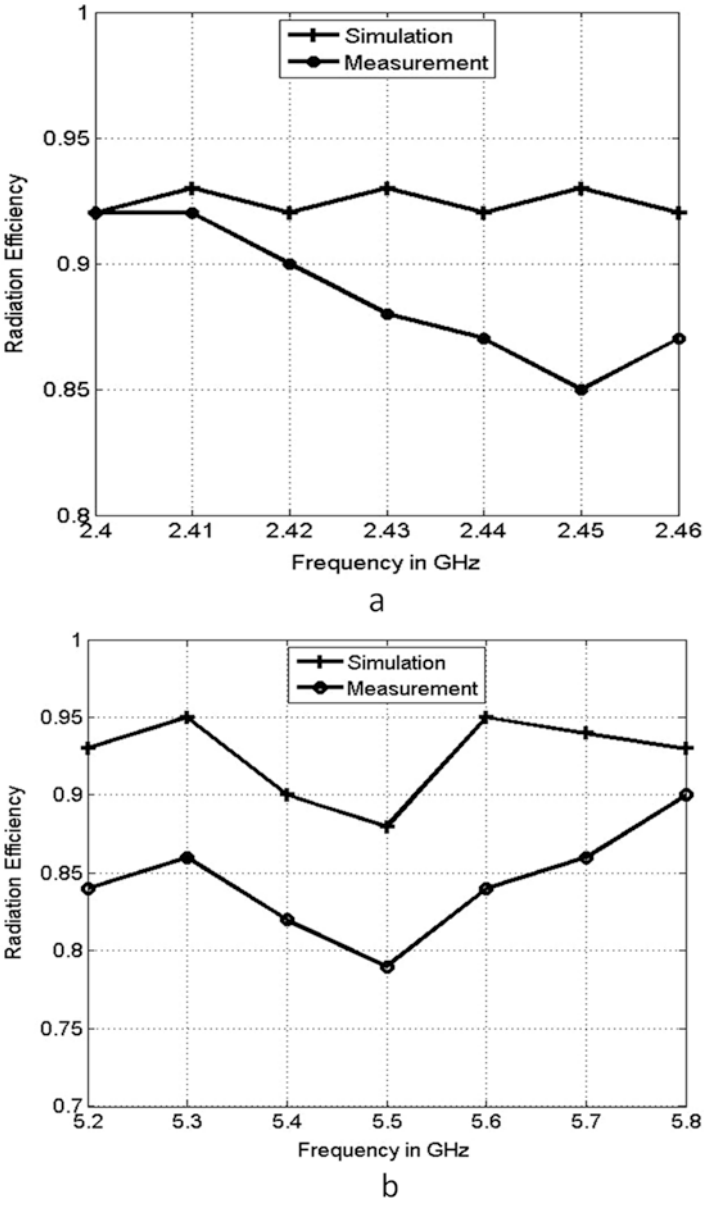

Fig. 12.14 Measured and simulated radiation efficiency of the proposed folded balanced coplanar antenna at (**a**) lower band, (**b**) upper band

References

1. H. Morishita, H. Furuuchi, K. Fujimoto, Performance of balance-fed antenna system for handsets in the vicinity off a human head or hand. IEE Proc. Microwave Antennas Propag. **149**, 85–91 (2002)
2. D. Zhou, R.A. Abd-Alhameed, C.H. See, A.G. Alhaddad, P.S. Excell, Compact wideband balanced antenna for mobile handsets. IET Microwaves Antennas Propag. **4**, 600–608 (2010)
3. J.S. McLean, Balancing networks for symmetric antennas: Part I: Classification and fundamental operation. IEEE Trans. Electromagn. Compat. **44**, 503–514 (2002)
4. G. Ghione, C.U. Naldi, Coplanar waveguides for MMIC applications: Effect of upper shielding, conductor backing, finite-extent ground planes, and line-to-line coupling. IEEE Trans. Microwave Theory Tech **35**, 260–267 (1987)
5. C.P. Wen, Coplanar waveguide: A surface strip transmission line suitable for nonreciprocal gyromagnetic device applications. IEEE Trans. Microwave Theory Tech **MTT-17**, 1087–1090 (1969)
6. R.L. Smith, J.T. Williams, Coplanar waveguide feed for microstrip patch antennas. Electron. Lett. **28**, 2272 (1992)
7. S.-M. Deng, M.-D. Wu, P. Hsu, Analysis of coplanar waveguide-fed microstrip antennas. IEEE Trans. Antennas Propag. **43**, 734–737 (1995)
8. R.K. Raj, M. Joseph, C.K. Aanandan, K. Vasudevan, P. Mohanan, A new compact printed antenna with coplanar configuration. Antennas Propag. Soc. Int. Symp. IEEE **2A**, 442–445 (2005)
9. K. Tilley, X.-D. Wu, K. Chang, Dual frequency coplanar strip dipole antenna. Antennas Propag. Soc. Int. Symp. IEEE **2**, 928–931 (1994)
10. Y. Jee, Y.-M. Seo, Triple-band CPW-fed compact monopole antennas for GSM/PCS/DCS/WCDMA applications. Electron. Lett. **45**, 446–448 (2009)
11. M.N. Z.Abidin, Measurement of current distribution on wire antennas, Master of Science Dissertation in Radio Frequency and Microwave Engineering, University of Bradford, September 1993
12. L.L. Libby, Special aspects of balanced shielded loops. Proc. IRE **34**, 641–646 (1946)
13. K.-L. Wong, *Compact and Broadband Microstrip Antennas* (John Wiley & Sons, Inc., New York, 2002)
14. R. Garg, P. Bhartia, I. Bahl, A. Ittipihoon, *Microstrip Antenna Design Handbook* (Artech House, Inc., Boston, 2001)
15. G. Kumar, K.P. Ray, *Broadband Microstrip Antenna* (Artech House, Inc., Boston, 2003)
16. R.N. Simons, *Coplanar Waveguide Circuits, Components, and Systems* (John Wiley & sons, New York, 2001)
17. A. Z. Jakal, New coplanar printed antennas: a family of broadband uniplanar printed antennas in endfire, broadside and omnidirectional forms, and suitable for integration with coplanar waveguide, vol. Ph.D: Bradford, 1997
18. W. Menzel, W. Grabherr, A microstrip patch antenna with coplanar line feed. IEEE Microwave Guid. Wave Lett. **1**, 340–342 (1991)
19. A.G. Alhaddad, R.A. Abd-Alhameed, D. Zhou, C.H. See, P.S. Excell, S.M.R. Jones, Folded loop balanced coplanar antenna for WLAN applications. IEEE Trans. Antennas Propag. **60**(10), 4916–4920 (2012)
20. Computer Simulation Technology Corporation, CST Microwave Studio, Version 5.0, Germany
21. High Frequency Structure Simulator, Version 11, Ansoft Corporation, USA
22. R.W. Johnston, J.G. McRory, An improved small antenna radiation-efficiency measurement. IEEE Antenna Propag. Soc. Mag. **40**, 40–48 (1998)
23. H. Choo, R. Rogers, H. Ling, On the wheeler cap measurement of the efficiency of microstrip antennas. IEEE Trans. Antennas Propag. **53**, 2328–2332 (2005)

Chapter 13
Performance of Dual-Band Balanced Antenna Structure for LTE Applications

Issa Elfergani, Abubakar Sadiq Hussaini, and Jonathan Rodriguez

13.1 Introduction

The ever-increasing market requirements in the mobile industry have reflected the more stringent engineering design requirements for mobile handsets, particularly in the antenna design. There are many challenges facing the antenna design for mobile phone applications, such as an ease of integration into portable handset devices, use of conducting materials in the cover, and moreover must have additional attributes such being thin, lightweight, small and have low energy requirement. There are several antenna types adopted for the internal antenna design targeting mobile handset applications, such as the printed monopole antennas [1–4], planar PIFA antennas [5–7] and printed microstrip patch antennas [8, 9].

Several practical techniques such as in [10] focus on modifications of the main radiator to reduce size and improve impedance matching. Another strategy aims to elongate the main radiator's physical length to achieve multiple resonant modes [11]. However, creating several radiating branches may occupy more space, hence making the antenna physically larger than the preferred volume.

Moreover, the requirement to extend the bandwidth of such antennas in mobile handheld devices is becoming increasingly important, driven by the market need

I. Elfergani (✉)
Instituto de Telecomunicações, Campus Universitário de Santiago, Aveiro, Portugal
e-mail: i.t.e.elfergani@av.it.pt

A.S. Hussaini
Instituto de Telecomunicações, Campus Universitário de Santiago, Aveiro, Portugal

School of Information Technology & Computing, American University of Nigeria, Yola, Adamawa, Nigeria

J. Rodriguez
Instituto de Telecomunicações, Campus Universitário de Santiago, Aveiro, Portugal

University of South Wales, Pontypridd, UK

I. Elfergani et al. (eds.), *Antenna Fundamentals for Legacy Mobile Applications and Beyond*, DOI 10.1007/978-3-319-63967-3_13

to support ever-growing data rates and feasibility thanks to additional spectrum availability. Also, a prominent figure of merit is the degree of antenna coupling with the human head and hand, and thus advanced designs that can mitigate this effect (reduced SAR – Specific Observation Rate) would indeed capture the interest of the mobile market. Conventionally, the unbalanced PIFA antennas [1–4] are the foremost popular candidates for closely packed inbuilt mobile handset antennas. Those unbalanced antennas utilize the bottom plane as the radiation ground, which allows such compact antenna to realize adequate gain and bandwidth.

However, in all the above-mentioned unbalanced structures [1–11], the radiator element only forms part of the radiation mechanism, whilst the ground plane also plays a pivotal role. If the ground plane size is changed, or other components were to be moved around within the ground plane surface, the antenna detunes and needs to be reengineered. Moreover, the surface current of the unbalanced antennas may be induced on the radiator as well as on the ground plane system, which will impair the antenna performance when it is being handheld. In addition, if such unbalanced antennas were to be integrated with other RF components within an integrated RF module, the cost of customization would be even greater. Therefore, the unbalanced antenna architecture has been perceived as a major stumbling block towards the full radio and antenna integration within handsets.

An alternative strategy may be a balanced antenna [12–18] containing a regular structure that can be fed with balanced currents. Recently, it has been revealed that a balanced handset antenna is an effective candidate for reducing the currents on the ground plane [12, 13].

The leading and commonly encountered balanced antennas are dipoles and loops [12–18]. In these balanced structures, the currents merely flow on the antenna element, thus severely decreasing the current flow effect on the ground plane. As an outcome, balanced antennas potentially have good efficiency and significantly sustain their performance when used side by side with the human body. Balanced antennas may, nonetheless, offer a few impediments, among which antenna size, especially in low-frequency bands (e.g. LTE700) for mobile phones application. Some novel strategies are anticipated for enhancing the impedance bandwidth, for example, a genetic algorithm strategy has been proposed to improve the impedance bandwidth [18]; and a parametric study has been linked to the length and width of strip lines to acquire a more extensive bandwidth for the folded loop antenna framework [15].

In contrast, due to the increased demand for higher data rate and larger bandwidth, a new technology has arisen, namely, fourth-generation Long Term Evolution (LTE). However, none of these balanced antenna designs in [12–18] have the capability to operate in the range of LTE bands and, in particular, the lower band of 700 MHz; expect the authors' previous work in [12, 13]. However, the proposed antenna in this chapter accomplishes a smaller size, better efficiency as well as a higher power gain.

In this chapter, the attributes of the compact balanced antenna with slotted folded arm dipole structure targeted for 4G mobile handsets is designed and examined. The antenna is designed to support the LTE dual-band operation, i.e. 698–748 MHz and 2500–2690 MHz.

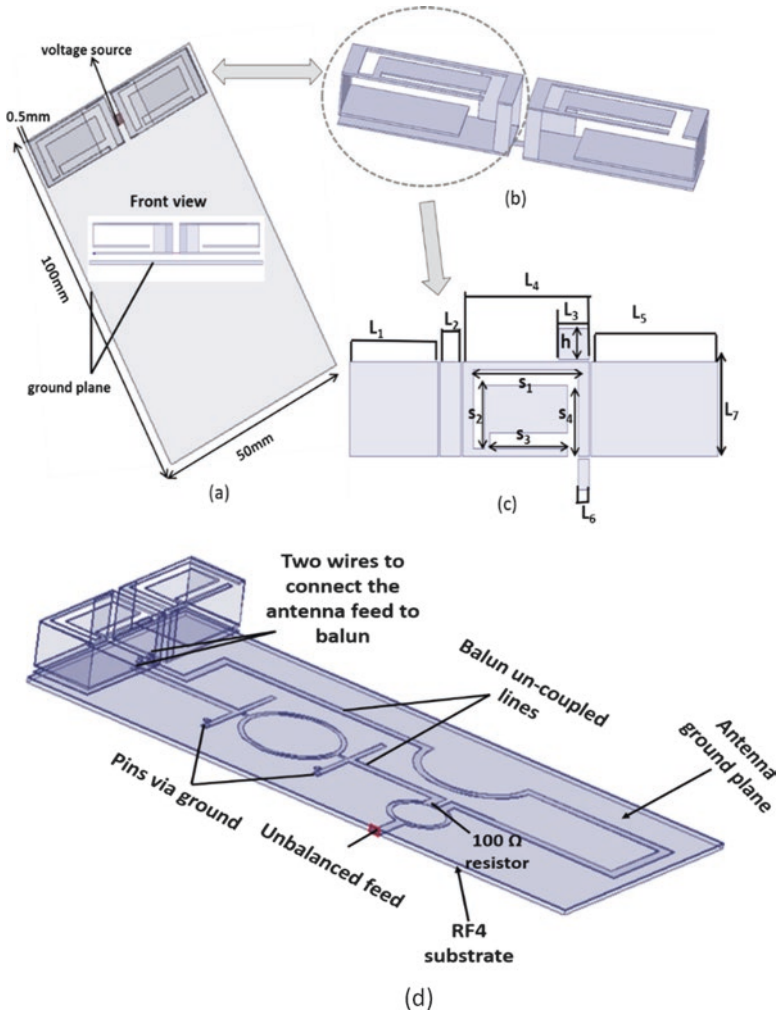

Fig. 13.1 Basic antenna structure; (**a**) 3D view of antenna without balun, (**b**) folded slotted arms, (**c**) unfolded slotted arm, (**d**) antenna with integrated balun

13.2 Antenna Design and Concept

The proposed balanced antenna was modelled to generate the dual-band operation of 700 and 2600 MHz LTE bands. The configuration of the proposed balanced antenna is based on the printed folded arms technique that supports size miniaturization. Figure 13.1 shows the geometry of the balanced antenna for a mobile phone. The top radiator was initially designed and mounted with a height of 4 mm over the ground plane system, with size of 50 × 100 mm^2. This ground plane was used as a circuit board that acts as the mobile handset chassis, as seen in Fig. 13.1. The top radiators were slotted with a uniform width of 2 mm as depicted in Fig. 13.1b.

Table 13.1 Detailed dimensions of folded arm radiators

Parameter	Value (mm)	Parameter	Value (mm)
L_1	16	L_7	12
L_2	3.2	S_1	19
L_3	5	S_2	8
L_4	23	S_3	14
L_5	23	S_4	9
L_6	2	h	4

The aim of employing such patterned slots was to effectively shrink the antenna size in synergy with the folded arm paradigm, as well as to drag the resonant frequencies downwards to meet the dual band of the LTE 700/2600 MHz, the frequency range considered in this chapter. The full dimensions of the folded arm dipoles are stated in Table 13.1 and are fairly aligned with practical handset sizes. These folded arm dipoles were assembled from a copper sheet with a thickness of 0.15 mm. Firstly, the proposed balanced antenna was fed by two wires with 180° out-of-phase as depicted in Fig. 13.1a. The dual-coax cables were used for antenna characterization purpose only. However, a balun which meets both the targeted dual-band frequencies is required instead of the two coaxial cables. Thus, a wide band planar balun covering the both desired bands of 700/2600 MHz was integrated together with the proposed antenna as depicted in Fig. 13.1d.

13.2.1 The Effect of the Slot Over the Folded Arms

To further understand the key contribution of embedded slot technique over the copper folded arms in antenna size miniaturization, two procedures were carried out. Firstly, starting with the folded dipole arms and without the slot patterned surface as illustrated in Fig. 13.2. One can note that the unslotted folded arm structure works over the dual band of 1200/5800 MHz as depicted in Fig. 13.2.

Yet, as the aim of this work was to come up with a balanced antenna design that can cover the dual band of LTE700/2600MHZ, the head-on approach was to embed a set of slots over the surface of both symmetric folded arms as shown in Fig. 13.1b. After several simulation attempts, the final optimum slots were formed/shaped as shown in Fig. 13.1b. The effective contribution in antenna size shrinking as well as meeting the desired dual band was initially seen through the computed reflection coefficient generated by the HFSS simulator [19]. From Fig. 13.2, it is clear that the idea of embedded slot is to downshift both aforementioned frequencies obtained from the unslotted antenna. The loaded slot reduces the resonance frequency and thus the electrical antenna dimensions drastically. Therefore, fundamentally, the objective of the slot was to tune the radiator structure to resonate at our targeted bands of LTE 700/2600 MHz. This again was achieved through multiple simulated attempts, by conducting several modifications of the antennas in [20, 21] to move

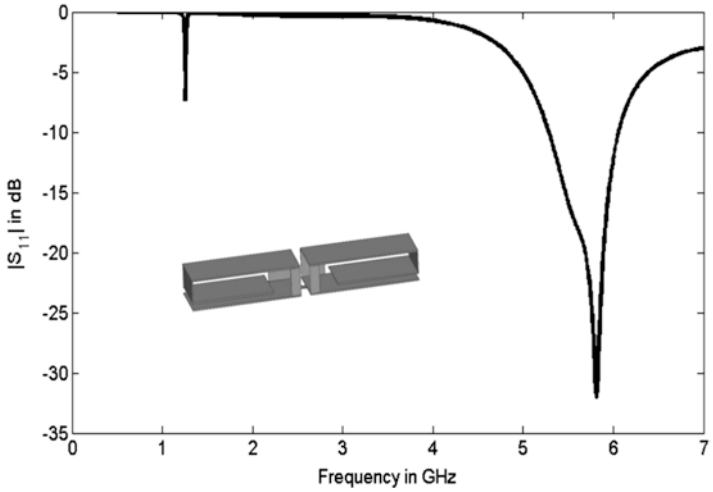

Fig. 13.2 The S_{11} of the unslotted folded arm proposed antenna

towards the desired outcome of developing highly compact and dual-band antenna for use in LTE applications. It is clear that the S_{11} of proposed slotted folded arm antenna without the balun generated by the HFSS shows a smooth result over the dual band of LTE700/2600 MHz as shown in Fig. 13.2.

13.3 Antenna Simulated Results

13.3.1 Simulated Reflection Coefficient of the Proposed Antenna

To support the feeding network of the proposed balanced antenna, a printed balun with a bandwidth that meets the frequency range of the proposed antenna should be designed and integrated with the proposed antenna as depicted in Fig. 13.1d. The added balun [22] was realized by a microstrip structure for solidarity and continuity of the ground plane. The balun was designed based on the concept of the non-coupled lines and the Wilkinson power divider. The balun was printed and fabricated on a single-layer printed circuit board with a size of 100 × 50 mm^2, FR4 material with a thickness of 0.8 mm, a relative permittivity of 4.4 and a loss tangent of 0.017. The size of the PCB of the balun has exactly same dimensions with the antenna PCB proposed in Fig. 13.1a, in which both devices can be easily integrated within the same PCB, to be used as a single-layer system as shown in Fig. 13.1d.

The simulated S_{11} of the presented balun show a broadband performance of the reflection coefficient (S_{11}) less than −10 dB over the 700–3200 MHz frequency

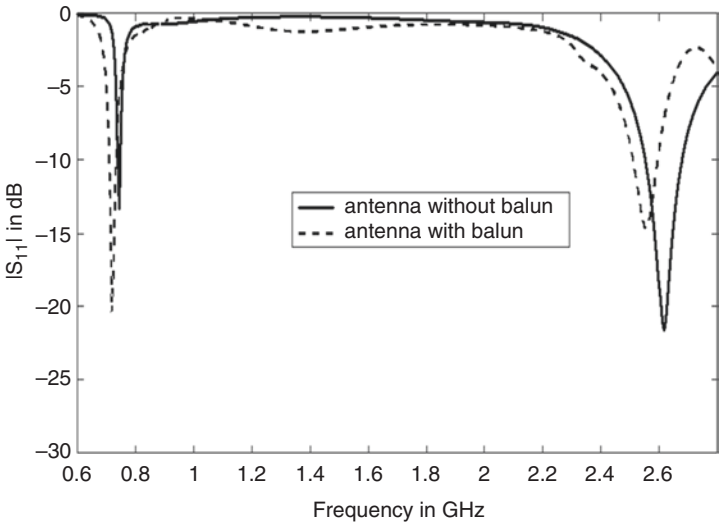

Fig. 13.3 The simulated S_{11} of the proposed slotted folded arms antenna with and without balun

range indicating that the device is perfectly matched. The transmission parameters (S_{21} and S_{31}) have an average value around −3.1 dB over the aggregated bandwidth. S_{21} varies from −2.99 to −3.1 dB, whilst S_{31} changes from −2.95 to −3.15 dB. This makes the proposed balun a good candidate to be printed exactly underneath the ground plane of the proposed balanced antenna within this chapter, which in turn may not affect the whole system performance.

One can notice that the ground plane of the antenna was placed on one side of the FR4 dielectric with a thickness of 0.8 mm, a permittivity of 4.4, and a tangent loss of 0.025, whilst the planar balun was located on the opposite side as depicted in Fig. 13.1d. The location of the two balanced ports of the balun was wisely designated to be exactly in direct position underneath the antenna feeding point on the upper sheet of the substrate. Dual thin cables were exploited in order to join the wideband balun to the antenna feeding point via holes. In this manner, the integration of both the antenna and its balanced feeding system was successfully accomplished. The proposed balun operates over a wide frequency range from 700 to 3200 MHz in which the targeted frequency bands of 700 and 2600 MHz proposed in this work can be easily met.

Figure 13.3 shows the computed S_{11} of the proposed antenna with and without the integration of the balun. It should be seen that the S_{11} performance of both versions of the antenna, those being with and without balun, is in good agreement over the dual band of LTE 700/2600 MHz and shows a return loss of better than −10 dB at both bands.

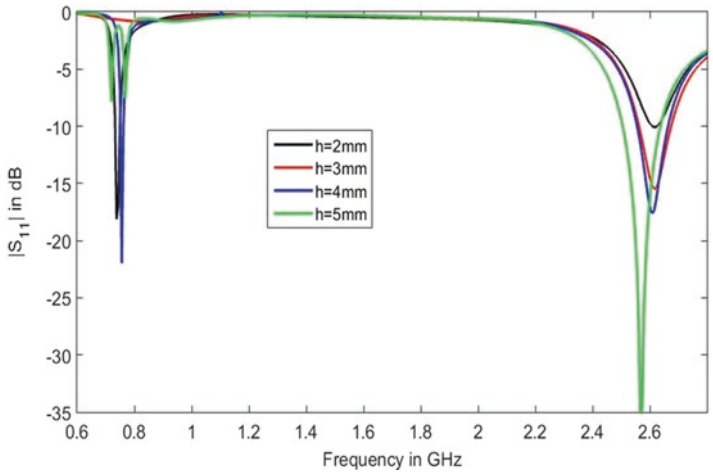

Fig. 13.4 The antenna height variations against the S_{11}

13.3.2 Parametric Analysis of the Proposed Antenna

In recent times, smaller and slimmer smart mobile devices are in a big demand by both vendors and customers; however, this should not be made at the cost of mobile performance, where the antenna design plays a very pivotal role concerning mobile functionality and performance. Therefore, to come out with a compact antenna structure that can fit todays' smart mobile devices, a broad analysis of the paramount antenna parameters should be implemented. In this chapter, it was concluded that the antenna height over the mobile PCB and the length of the top radiator were considered as the most effective parameters that could affect the antenna performance. Thus, it is believed that analysing such paramount parameters may hugely contribute in achieving the optimum performance and volume that is being used in most of today's smart mobile phones.

The influence of antenna height over the ground plane was performed and depicted as in Fig. 13.4. The antenna was mounted over the PCB with different heights starting from 2 mm up to 5 mm with an increment of 1 mm as indicated in Fig. 13.4. It was noted that when the radiator height is set at 2 mm, the lower band of 700 MHz was attained, whilst the higher band of 2600 MHz was not accomplished to match the return loss power of −10 dB. On the other hand, when the height was set at 3 mm, the higher band of 2600 MHz was easily achieved and the impedance of the antenna at 700 MHz was completely mismatching. Moreover, at a 5 mm height, the proposed antenna could not meet the desired dual-band target investigated in this chapter, in particular at a higher band of 2600 MHz. However, the LTE dual band of 700/2600 MHz was perfectly developed and showed a − 10 dB of return loss at both bands when the antenna height is set at 4 mm as shown in Fig. 13.4. This proves that the proposed balanced antenna design may be easily concealed in today's smart phone devices whilst maintaining a good performance.

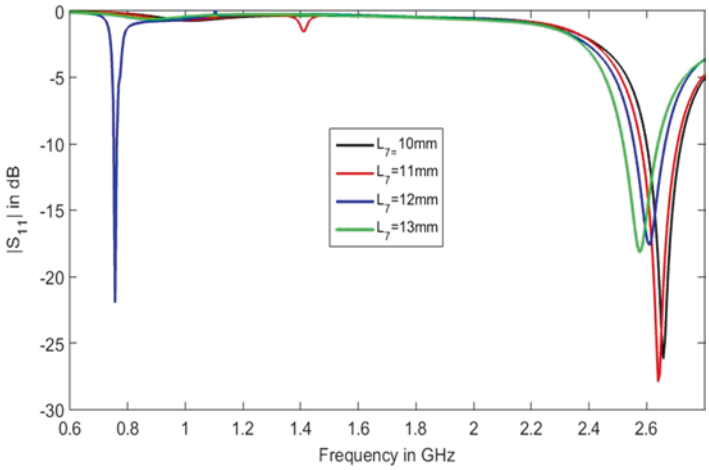

Fig. 13.5 The antenna length variations against the S_{11}

The second sensitive parameter is the antenna length. Studying such parameter is of high importance to achieve compact and miniaturized antenna volume. Therefore, the length of the antenna was examined and analysed within this work. The antenna length was varied from 10 to 13 mm with an increment of 1 mm as shown in Fig. 13.5. One can undoubtedly note that when the length is set at 10 mm, 11 mm and 13 mm, the antenna was not able to reach the impedance matching at the lower band of 700 MHz in all cases. However, when the length is set at 12 mm, the targeted dual bands were met with a good return loss of −10 dB. Thus, the optimum length of the proposed antenna was fixed at 12 mm throughout this chapter.

13.3.3 The Effect of the Handheld on the Simulated Proposed Antenna

For more clarification, the simulated S_{11} of the proposed antenna was investigated in free space and in human hand scenarios. The full size of the hand model used within this analysis is depicted in Fig. 13.6. For simplification, the proposed hand model is deemed a muscle tissue having simply one layer with a relative permittivity material of 54 and a conductivity of 1.45 S m^{-1} [21, 22].

The simulated paradigm of hand model was shown in Fig. 13.6 with the arrangement of three common talk positions of holding the mobile device along with finger position, namely, 0° (left), 45° (middle) and 90° (right).

Figure 13.7 indicates the calculated S_{11} of the proposed antenna in the handheld case. It is clear that the results of S_{11} in the presence of hand model with three finger positions, i.e. 0°, 45° and 90°, are more or less similar to the ones in the free space scenario as shown in Fig. 13.7. From these findings, it is demonstrated that the

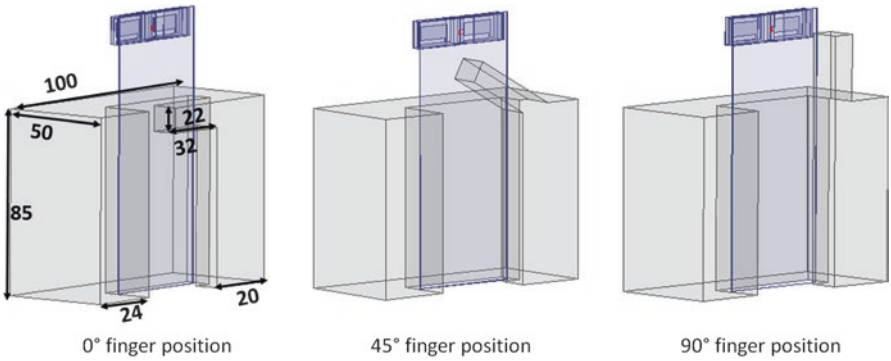

Fig. 13.6 Simulated hand model with different finger positions

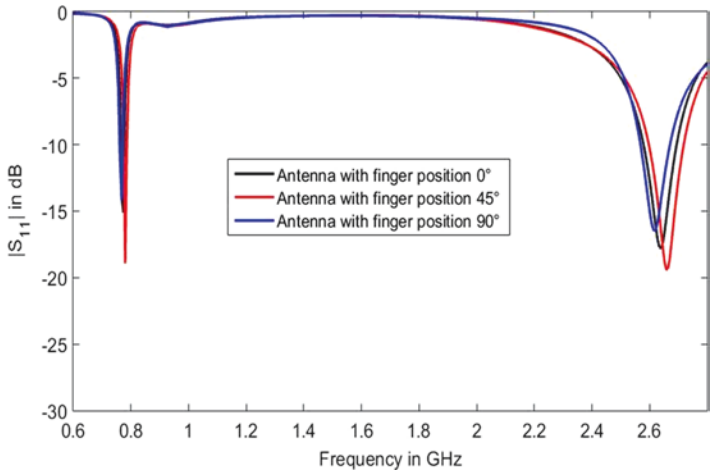

Fig. 13.7 The simulated reflection coefficients $|S_{11}|$ of proposed antennas with the handheld effect

proposed balanced antenna is said to be insensitive to the human hand. This in turn shows a very low detuning/effect on the S_{11} over the three finger positions, especially at the higher band of the 2600 MHz. This again is one advantage of the balanced structure over its counterpart (unbalanced) that makes it such a promising choice for use in today's mobile handset applications.

To confirm the fact that the balanced antenna is a ground plane independent structure, the current surface in the ground plane of the proposed antenna for the free space and handheld scenarios were checked and examined as shown in Fig. 13.8. It should be seen that in the case of free space, the current on the ground plane flows only in the area underneath, and more precisely close to the feeding source, whilst currents are almost vanished as we move away of this point in the rest of the ground

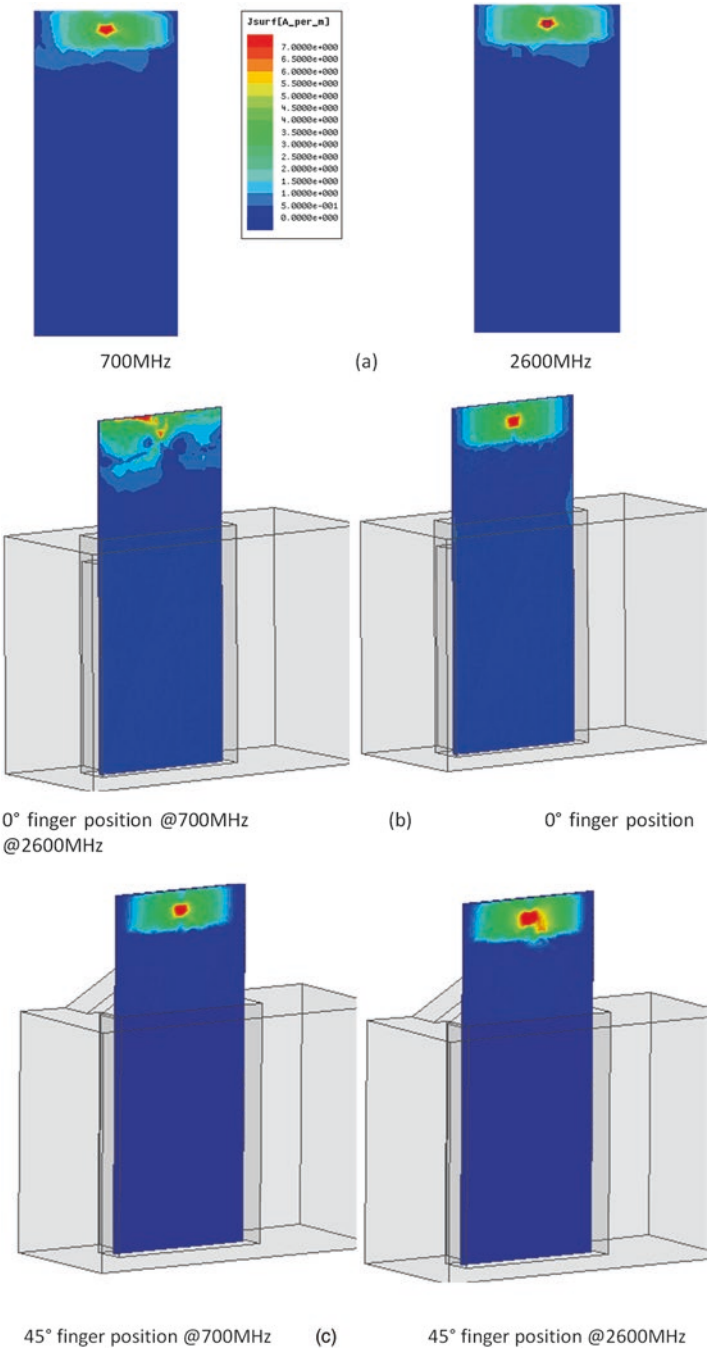

Fig. 13.8 The proposed antenna current surface, in free space (**a**), with finger position 0° (**b**), with finger position 45° (**c**), with finger position 90° (**d**)

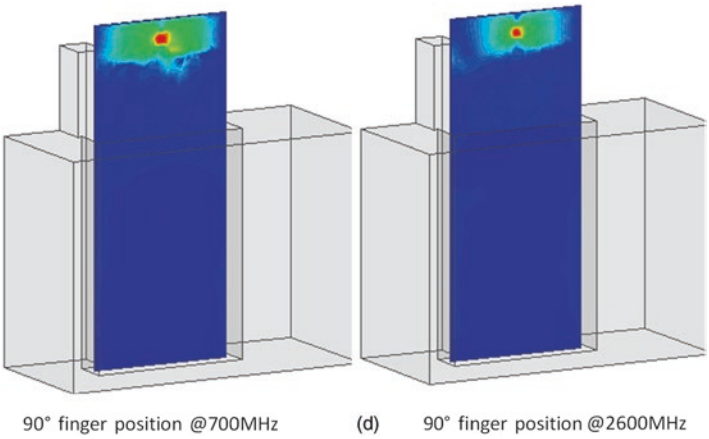

Fig. 13.8 continued

plane for both dual band of the 700/2600 MHz as shown in Fig. 13.8a. It is said that the current induced on the ground plane of the present antenna is in good comparison to the work done in [23]; moreover, it has come up with the benefit of less induced current compared to antenna design in [24].

On the other hand, in the hand model paradigm for the three above-mentioned finger positions as shown in Fig. 13.8b, c, d, the proposed antenna again showed a high magnitude surface current as indicated at the proximity of the feeding point and becomes almost zero far away from it over the both bands of interest as depicted in Fig. 13.8b, c, d.

This proves the fact that, the weak surface current on the ground plane ensures better antenna performance by amount of radiated towards the human body when the antenna is being in proximity to users head.

13.4 Measured Results of the Proposed Antenna

13.4.1 The Methods to Measure the Input Impedance of Balanced Antenna

Generally speaking, there are two different methods to measure the reflection coefficient, S_{11}, of the balanced antenna. These methods are the *S*-parameter method and the balun method. During the measurement of the S_{11} of the proposed antenna, the two above techniques were used. In the *S*-parameter, we basically dealt with the proposed balanced antenna in the absence of a balun, as a two-port device as depicted in Fig. 13.9a. In this case, the *S*-parameters of the present design can be directly measured and accomplished using a well-calibrated network analyser.

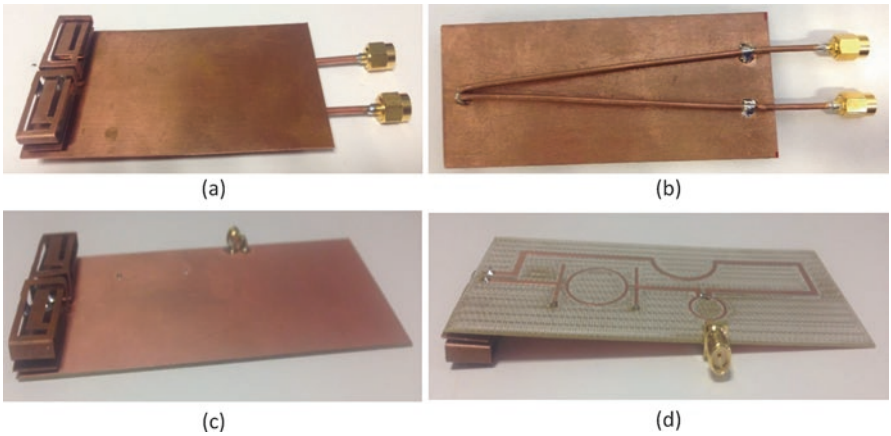

Fig. 13.9 The antenna prototypes, (**a**) *top view* antenna without balun, (**b**) *bottom view* antenna without balun, (**c**) *top view* antenna with balun, (**d**) *bottom view* antenna with balun

In the second method, a balun is usually required as a feeding network that takes the form of a balanced antenna structure such as dipole. This is to provide a balanced feed from an unbalanced source. Moreover, the balun brings system stability when the radiation pattern of the antenna is being measured. Therefore, the simulated planar balun in Fig. 13.1c was fabricated and subsequently integrated with the antenna exactly in the same simulated scenario shown in Fig. 13.9c, d. The fully fabricated antenna assembly (antenna with balun) is shown in Fig. 13.9c, d. As one can notice, the balun was printed underneath the antenna ground plane, to appear as one single layer as well as to effectively reduce the complexity of the whole system.

Proof of concept: the proposed antenna with and without balun was fabricated and tested. The measured reflection coefficient S_{11} of the fabricated balanced antenna with and without balun was shown in Fig. 13.10. Both measured results of the *S*-parameters and balun methods show fair agreement, and both achieved at least a −10 dB return loss at the targeted dual band of LTE700/2600 MHz for 4G mobile handset applications.

13.4.2 The Effect of the Handheld on the Fabricated Proposed Antenna

To prove the simulated findings of the hand effect on the antenna reflection coefficient indicated in Fig. 13.7, the same scenarios of the three finger positions were used to check the effect of the human hand with the prototyped version of the antenna. As we can see from Fig. 13.11, the measured S_{11} of the three cases of the hand model along with the finger positions shows roughly a stable performance compared with the same simulated paradigm of Fig. 13.7.

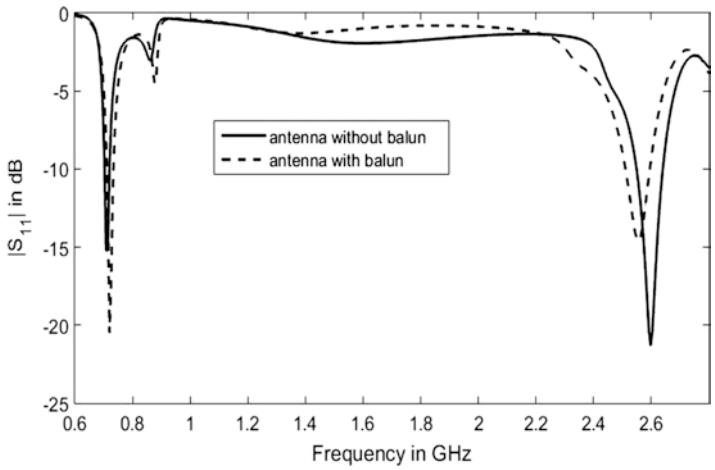

Fig. 13.10 The measured S_{11} of the proposed slotted folded arm antenna with and without balun

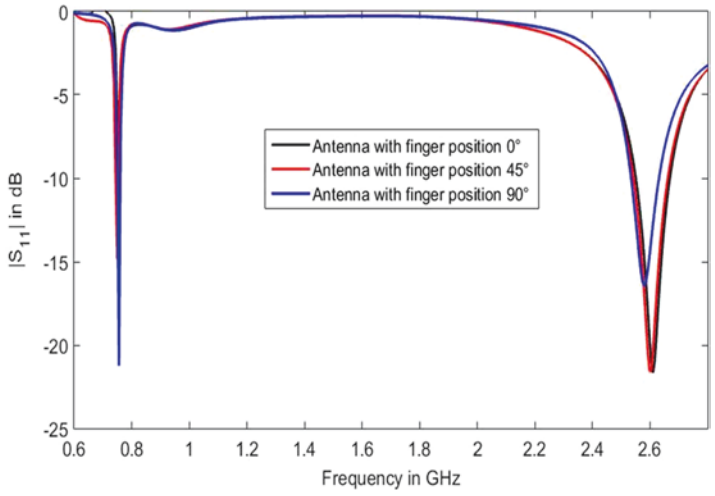

Fig. 13.11 The measured reflection coefficients $|S_{11}|$ of proposed antennas with the handheld effect

Moreover, the influence of human hand does not show a significant difference on the S_{11} in comparison to the free space cases shown in Fig. 13.10. This again demonstrates that the proposed balanced antenna has a so-called independent ground plane, and since the current flows on the ground plane is limited. This will mitigate the coupling between the antenna PCB and human hand, which in turn may not impair the antenna performance.

13.4.3 Measured Power Gain and Efficiency in Free Space and Handheld Scenarios

Figure 13.12a shows the computed and measured power gain of the full assembly antenna in free space and handheld situations. The simulated and measured gain of the proposed antenna at both bands agrees with the free space cases as shown in Fig. 13.12; an acceptable difference may be attributed to the tolerance of the

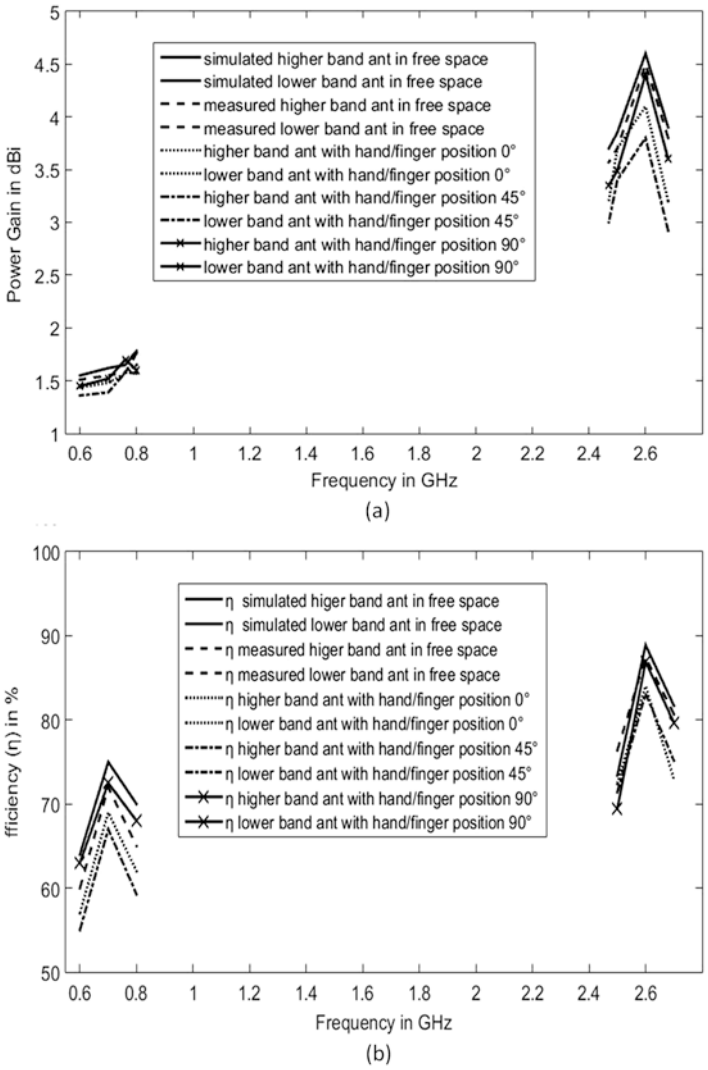

Fig. 13.12 Simulated and measured power gain of the proposed antenna (**a**), simulated and measured radiation efficiency of the proposed antenna (**b**)

fabrication process in particular the integration of the balun as well as the positioning of the feeding point. On the other hand, the antenna power gain in the handheld scenarios varies from one finger position to another as indicated in Fig. 13.12. For example, in the case of 0° finger position, the gain at the lower band varied from 1.41 to 1.56 dBi, whilst at the higher band, it ranged from 3.48 to 4.38 dBi. When the antenna is placed within the hand model with a finger position of 45°, power gains varying from 1.39 to 1.51 dBi at the lower band of 700 MHz and from 2.95 to 3.7 dBi at the higher band of 2600 MHz were accomplished. Lastly, when the proposed antenna is positioned inside the 90° of the hand model, power gains fluctuating from 1.42 to 1.52 dBi over the lower band and from 3.4 to 4.3 dBi were observed. The results concluded that the proposed antenna in both paradigms demonstrated acceptable power gains over the dual band of LTE 700/2600 MHz as illustrated in Fig. 13.12a.

The calculated and measured antenna efficiency were implemented and indicated in Fig. 13.12b. Again, the proposed antenna efficiency was examined in both scenarios of free space and handheld. In the free space scenario, the simulated efficiency over the range of 600 MHz, 700 MHz and 800 MHz varied from 64% to 75%, whilst ranges from 73% to 87% over the bands of 2500 MHz, 2600 MHz and 2700 MH were detected. On the other hand, the measured efficiency at the bands of 600 MHz, 700 MHz and 800 MHz fluctuated from 61% to 73% and from 74% to 86% at the bandwidths 2500 MHz, 2600 MHz and 2700 MHz.

In the case of handheld, the same hand model with three finger positions (0°, 45° and 90°) has been used to check the efficiency of the proposed antenna. At the 0° finger position, the efficiency over the range from 600, 700 and 800 MHz was measured to be from 58% to 68%, whilst it was varying from 70% to 78% over the frequency range 2500 MHz, 2600 MHz and 2700 MHz. In the second scenario of 45° finger position, the efficiency values show various ranges from 60% to 73% at the lower bands of 600 MHz, 700 MHz and 800 MHz and from 75% to 83% at the higher bands of 2500 MHz, 2600 MHz and 2700 MHz, respectively. When the proposed antenna was placed within the hand model of 90° finger position, the efficiency varies from 63% to 73% over the frequencies 600 MHz, 700 MHz and 800 MHz and from 69% to 85% over the frequencies 2500 MHz, 2600 MHz and 2700 MHz.

13.4.4 Measured and Simulated Far Fields of the Proposed Antenna

The simulated and measured radiation patterns of the full assembly proposed antenna at the dual band of 700/2600 MHz are shown in Fig. 13.13. The *xz* and *yz* planes were the two cut planes that were selected within this process. The computed radiation patterns at both desired bands were generated with the aid of HFSS software, whilst the measured far fields of the full assembly antenna prototype were carried out inside the anechoic chamber in which the reference fixed antenna was a

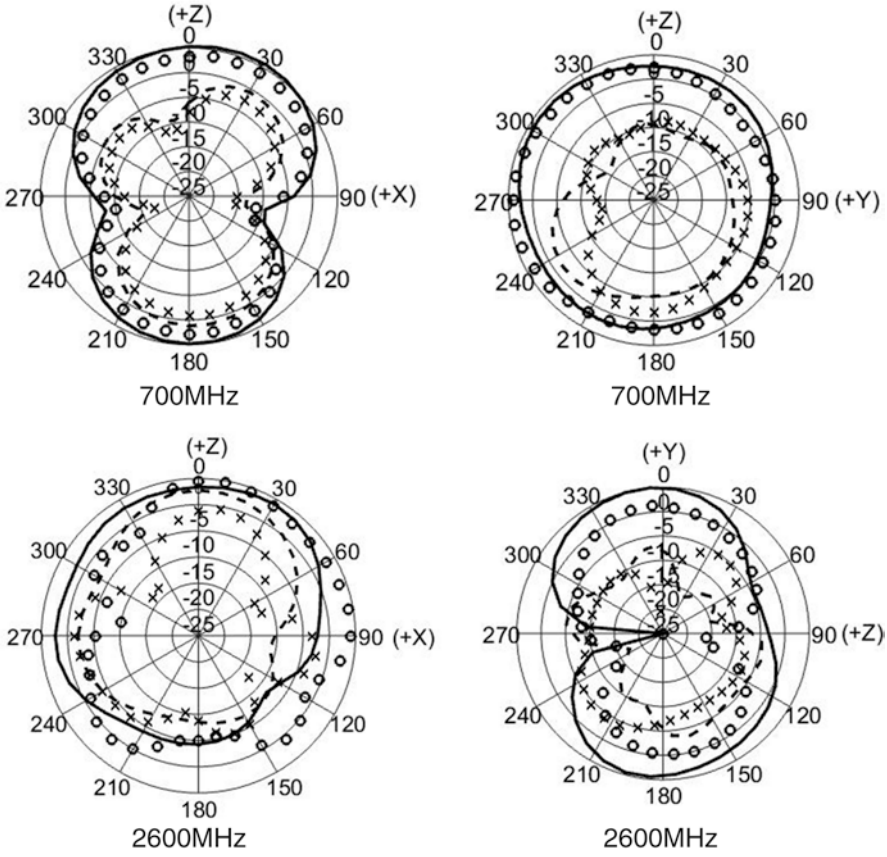

Fig. 13.13 Normalized antenna radiation patterns for *xz* and *yz* planes at 700 MHz, 2600 MHz, '____' measured co-polarization, '000000' simulated co-polarization, '------' measured cross-polarization, 'xxxxx' simulated cross-polarization

broadband horn (EMCO type 3115) positioned at 4 m from the antenna under test. Both the simulated and measured outcomes at the two dual bands of the 700/2600 MHz show near-omnidirectional radiation patterns as indicated in Fig. 13.13.

13.5 Conclusion

Within this chapter, a compact volume of balanced antenna structure with the capability to serve the dual bands of the LTE standards 698–748 MHz and 2500–2690 MHz has been modelled, fabricated and tested. The results of the S_{11} of both antenna versions (with and without balun) exhibited sufficient impedance matching

of $S_{11} \leq -10$ dB in the cases of free space and handheld scenarios. Moreover, to verify the statement of the balanced model being ground plane independent, the surface current analysis of the proposed antenna in free space and handheld scenarios was checked, and proved that the currents are reduced over the entire ground plane, except underneath the feeding point, which showed improved immunity to the handheld effect. The power gains and efficiencies of the proposed antenna over the targeted dual band showed acceptable ranges. The antenna demonstrated near-omnidirectional radiation over the two operating bands. In context of such findings, it is concluded that the present balanced antenna has the potential to be a promising candidate for practical LTE applications in mobile phones.

Acknowledgements This work is carried out under the grant of the Fundacão para a Ciência e a Tecnologia (FCT – Portugal), with the reference number SFRH/BPD/95110/2013, and funded by national funds through FCT/MEC (PEst-OE/EEI/LA0008/2013 – UID/EEA/50008/2013).

References

1. I.T.E. Elfergani, T. Sadeghpour, R.A. Abd-Alhameed, A.S. Hussaini, J.M. Noras, S.M.R. Jones, J. Rodriguez, Reconfigurable antenna design for mobile handsets including harmonic radiation measurements. IET Microwaves Antennas Propag. **6**(9), 990–999 (2012)
2. I.T.E. Elfergani, R.A. Abd-Alhameed, C.H. See, T. Sadeghpour, J.M. Noras, S.M.R. Jones, Small size Tuneable printed F-slot antenna for mobile handset applications. Microw. Opt. Technol. Lett. **54**(3), 794–802 (2012)
3. F.-R. Hsiao, H.-T. Chen, T.-W. Chiou, G.-Y. Lee, K.-L. Wong, A dual-band planar inverted-f patch antenna with a branch-line slit. Microw. Opt. Technol. Lett. **32**(4), 310–312 (2002)
4. K.L. Wong, S.C. Chen, Printed single-strip monopole using a chip inductor for Penta-band WWAN operation in the mobile phone. IEEE Trans. Antennas Propag. **58**(3), 1011–1014 (2010)
5. C.H. See, R.A. Abd-Alhameed, H.I. Hraga, M.M. Abusitta, I.T.E. Elfergani, S. Adnan, Design of a PIFA with parasitic F-element miniaturised antenna assembly for lower band ultra-wide-band and IEEE 802.11a applications. Microw. Opt. Technol. Lett **53**(9), 1970–1074 (2011)
6. A. Cabedo, J. Anguera, C. Picher, M. Ribo, C. Puente, Multi-band handset antenna combining PIFA, slots, and ground plane modes. IEEE Trans. Antennas Propag. **57**(9), 2526–2533 (2009)
7. I. Elfergani, R. Abd-Alhameed, M.S. Bin-Melha, C. See, D.-W. Zhou, M. Child, P. Excell, A frequency tunable PIFA design for handset applications." MOBIMEDIA 2010, LNICST. Lect. Notes Comput. Sci **77**, 688–693 (2012)
8. T. Gandara, C. Peixeiro, Compact double U-slotted microstrip patch antenna element for GSM1800, UMTS and HIPERLAN2. IEEE antennas and propagation society international symposium, Monterey, 20–25 June 2004, pp. 1459–1462
9. J. Brissos, C. Peixeiro, Triple-band microstrip patch antenna element for GSM1800, UMTS and HiperLAN2. Proc. 2003 IEEE Int. Antennas and Prop. Symp, Columbus, 22–27 June 2003, pp. 130–133
10. K. Gosalia, G. Lazzi, Reduced size, dual-polarized microstrip patch antenna for wireless communications. IEEE Trans. Antennas Propag. **51**(9), 2182–2186 (2003)
11. S.T. Fang, S.H. Yeh, K.L. Wong, Inverted-F antennas for GSM/DCS mobile phones and dual ISM-band applications, IEEE Antenna Propag. Society Int. Symp. Vol. 4, 2002 Microw, pp. 524–527

12. I.T.E. Elfergani, A.S. Hussaini, J. Rodriguez, R.A. Abd-Alhameed, Dual-band printed folded dipole balanced antenna for 700/2600MHz LTE Bands. The 10th European conference on antennas and propagation (EuCAP2016), Davos, 10–15 April 2016, pp 1–5
13. I.T.E. Elfergani, A.S. Hussaini, J. Rodriguez, R.A. Abd-Alhameed, Miniaturized dual-band balanced antenna for LTE using meander lines. The 13th international conference on synthesis, modelling, analysis and simulation methods and applications to circuit design (SMACD), Lisbon, 27–30 June 2016, pp. 1–4
14. H. Morishita, H. Furuuchi, K. Fujimoto, Performance of balanced-fed antenna system for handsets in the vicinity of a human head or hand. IEE Proc.—Microw. Antennas Propag **149**, 85–91 (2002)
15. Shogo Hayashida, Hisashi Morishita, Yoshio Koyanagi, and Kyohei Fujimoto. Wideband folded loop antenna for handsets. in *Antennas and Propagation Society International Symposium*, San Antonio,Texas vol. 3, p. 2, (2002)
16. S. Kingsley, Advances in handset antenna design. RF Des., 16–22 (2005)
17. BS Collins, SP Kingsley, JM Ide, SA Saario, RW Schlub, and Steven Gregory OKeefe. A multi-band hybrid balanced antenna. in *IEEE 2006 International Workshop on Antenna Technology: Small Antennas; Metamaterials*, New York, USA, pp. 100–103, (2006)
18. D. Zhou, R.A. Abd-Alhameed, P.S. Excell, Bandwidth enhancement of balanced folded loop antenna design for mobile handsets using genetic algorithms. PIERS ONLINE **4**(1), 136–139 (2008)
19. Ansoft High Frequency Structure Simulator v10 Uses Guide, CA, USA
20. A.G. Alhaddad, R.A. Abd-Alhameed, D. Zhou, I.T.E. Elfergani, C.H. See, P.S. Excell, M.S. Bin-Melha, Low profile balanced handset antenna with dual-arm structure for WLAN application. IET Microwaves Antennas Propag. **5**, 1045–1053 (2011)
21. D. Zhou, R.A. Abd-Alhameed, C.H. See, A.G. Alhaddad, P.S. Excell, Compact wideband balanced antenna for mobile handsets. IET Microwaves, Antennas Propag. **4**, 600–608 (2010)
22. D. Zhou, R.A. Abd-Alhameed, C.H. SEE, P.S. Excell, Design of Wideband Balanced Folded-Arms Dipole Antenna for mobile handsets. Electromagnetics **29**, 641–651 (2009)
23. J.J. Arenas, J. Anguera, C. Puente, Balanced and single-ended handset antennas: Free space and human loading comparison. Microw. Opt. Technol. Lett. **51**(9), 2248–2254 (2009)
24. Y.-W. Chi, K.-L. Wong, Very-small-size printed loop antenna for GSM/DCS/PCS/UMTS operation in the mobile phone. Microw. Opt. Technol. Lett. **51**(1), 184–192 (2009)

Part VI
mmWave Antennas for 5G

Chapter 14
Millimeter-Wave Pattern Reconfigurable Antenna

Muhammad Kamran Saleem and Majeed A.S. Alkanhal

14.1 Introduction

Antennas are considered to be one of the most essential and significant elements of any wireless communication system. The commonly used antennas in a wireless communications system are monopoles, dipoles, loop antenna, horn antenna, and microstrip antenna. Each type of antenna possesses its own advantages and disadvantages that make it suitable for particular application. The initial design properties of these antennas such as bandwidth, frequency of operation, radiation characteristics, etc. are fixed and cannot be changed. The modern transmitting and receiving systems demand increased functionality such as direction finding, radars, beam steering, and command and control within a confined area. The reconfigurable antennas are a solution to tackle these challenges. The reconfigurability in an antenna is achieved by intentionally changing its frequency of operation, polarization, or radiation characteristics. This change is accomplished by various techniques that reallocate the antenna currents and thus changes electromagnetic fields of the antenna's effective aperture. Figure 14.1 describes the reconfiguration techniques that are mostly based on the integration of switches such as radio frequency microelectromechanical systems (RF-MEMS), PIN diodes, varactors, and photoconductive elements. Furthermore, the application of smart materials such as ferrites and liquid crystals can also be utilized for physical alteration of the antenna radiating structure, to achieve required reconfigurability in antenna operation.

M.K. Saleem (✉)
Electrical Engineering Department, University of Central Punjab, Lahore, Pakistan
e-mail: mksa05@gmail.com

M.A.S. Alkanhal
Electrical Engineering Department, King Saud University, Riyadh, Saudi Arabia

I. Elfergani et al. (eds.), *Antenna Fundamentals for Legacy Mobile Applications and Beyond*, DOI 10.1007/978-3-319-63967-3_14

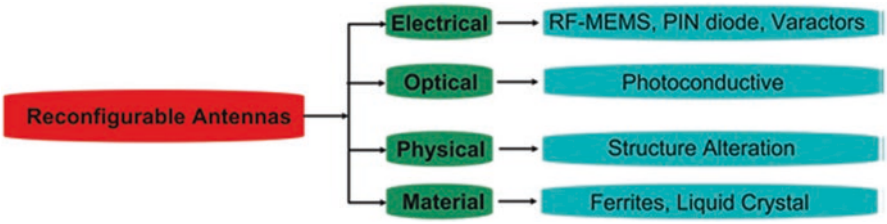

Fig. 14.1 Techniques adopted to achieve reconfigurable antennas

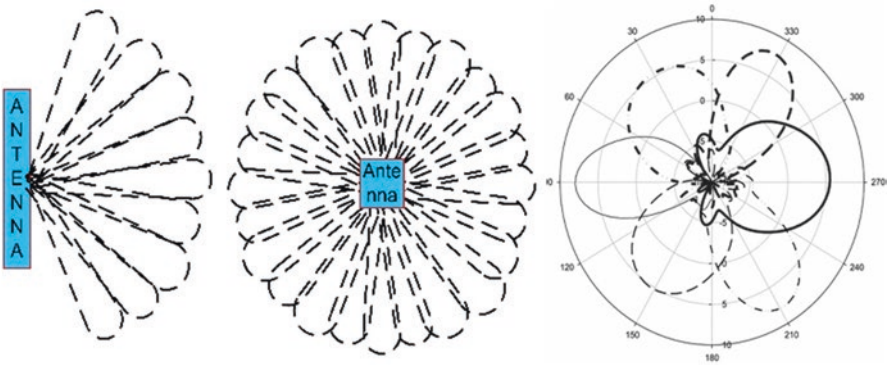

Fig. 14.2 Antenna with reconfigurable radiation patterns

The term reconfigurable antenna is broad and extends to antennas that can change their parameters such as impedance bandwidth, frequency of operation, polarization, and radiation pattern [1–3]. In this chapter the focus will be on the class of reconfigurable antennas with the capability of altering their radiation patterns in the far field; the presented work is an extension to research work published previously in [4]. This reconfiguration of antenna radiation pattern can be utilized efficiently for power/energy by directing signals only toward the intended directions, avoiding noisy sources, improving system gain and security, etc. The antenna radiation pattern reconfigurability is illustrated in Fig. 14.2, where a single element antenna or an antenna array can have more than one radiation patterns associated with it. The design and development of these radiation pattern reconfigurable antennas poses many challenges, not only in obtaining the desired levels of antenna functionality but also in the implementation of the antenna itself. However, in most of the ILAs the degradation of gain, beamwidth, and side lobe level of antenna radiation beams particularly due to interelement coupling and shadow effect at the two extreme edges of scanning range is inevitable [5–8].

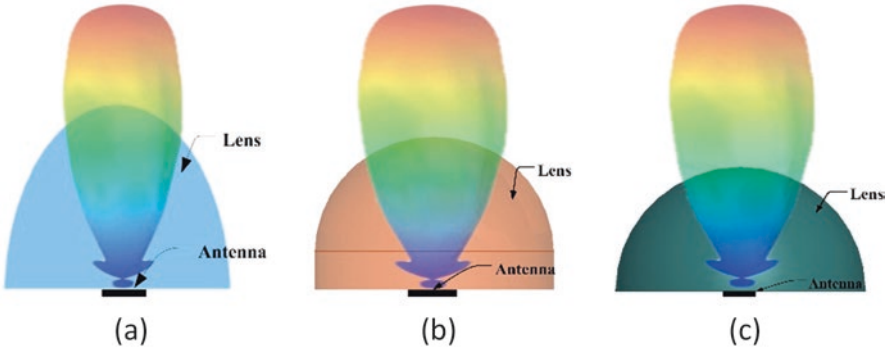

Fig. 14.3 Dielectric lenses. (**a**) Hemispherical lens, (**b**) extended hemispherical lens, (**c**) elliptical lens

14.2 Dielectric Lens for Millimeter-Wave Applications

The commonly used dielectric lenses are found in shape of hemispherical or extended hemispherical [3], elliptical, or cylindrical as shown in Fig. 14.3. The dielectric lenses can be made up of various materials with low or high dielectric permittivity such as Teflon and Rexolite. The hemispherical, extended hemispherical, and elliptical lenses are usually utilized to enhance antenna gain in broadside direction and are very promising candidates for millimeter-wave antennas with beam steering applications. The extended hemispherical lens as shown in Fig. 14.3b is preferred over elliptical and hemispherical lenses since it is easy to manufacture. Furthermore, the antenna feed is placed at the bottom of the lens, providing a broadside radiation pattern.

14.3 Microstrip Patch Antenna for 60 GHz Applications

The configuration of a simple microstrip patch antenna (MPA) is shown in Fig. 14.4. The MPA is placed over Rogers RT/duroid 5880 substrate ($\varepsilon_r = 2.2$) having thickness of 0.254 mm. The bottom side of substrate is fully copper plated (th = 0.018 mm) and acts as antenna ground plane. The important design parameters of MPA are shown in Fig. 14.4b. The initial dimensions for MPA are calculated by conventional set of equations given in [9]. The MPA structure having a tapered feed is optimized, utilizing the 3D EM solver ANSYS HFSS [10] to achieve required bandwidth and gain. The optimum dimensions are found to be: $T_1 = T_2 = T_3 = 1.07$ mm, $L_m = 11.96$ mm, $L_1 = 0.5$ mm, $Lp = 1.56$ mm, $Wp = 2.08$ mm, $L = 21.73$ mm, $W = 13$ mm.

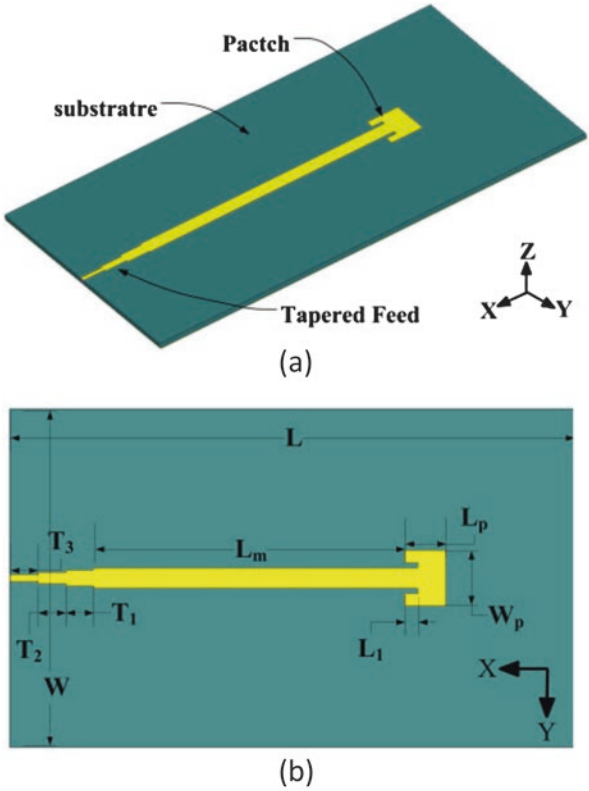

Fig. 14.4 MPA structure for 60 GHz applications. (**a**) 3D configuration, (**b**) top view

The structure of MPA is optimized and the impedance bandwidth is found to be 4.5 GHz (58–62.5 GHz) as shown in Fig. 14.5. The antenna 3 dB beamwidth for the two radiation patterns in two orthogonal plans, i.e., in *YZ*-plane and *XZ*-plane, is found to be 64° and 102°, respectively, as shown in the 2D normalized radiation pattern in Fig. 14.6. The realized gain is found to be above 6 dB in most of the frequency band of operation as shown in Fig. 14.7. It can also be observed that the maximum gain if found to be 7.5 dB at 61.5 GHz.

14.3.1 Dielectric Lens Integration with MPA

The integration of an extended hemispherical (Teflon) have ε_r of 2.1 lens is made to the MPA structure presented previously. The structure of MPA with extended hemispherical Teflon lens is shown in Fig. 14.8. The alignment markers are utilized to place the dielectric lens at specified location.

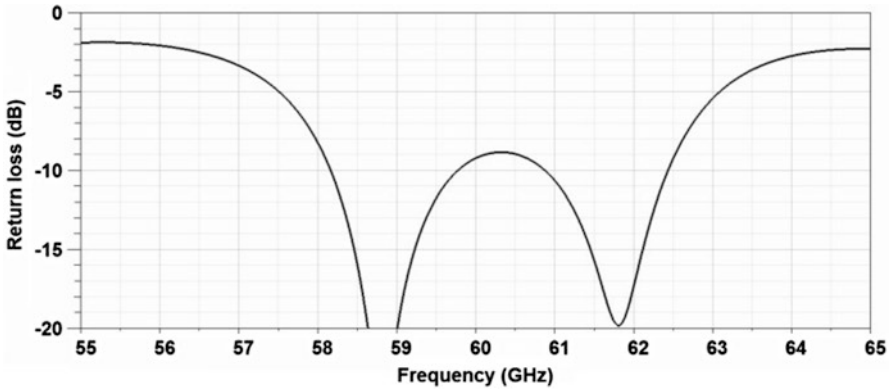

Fig. 14.5 Simulated return loss of MPA

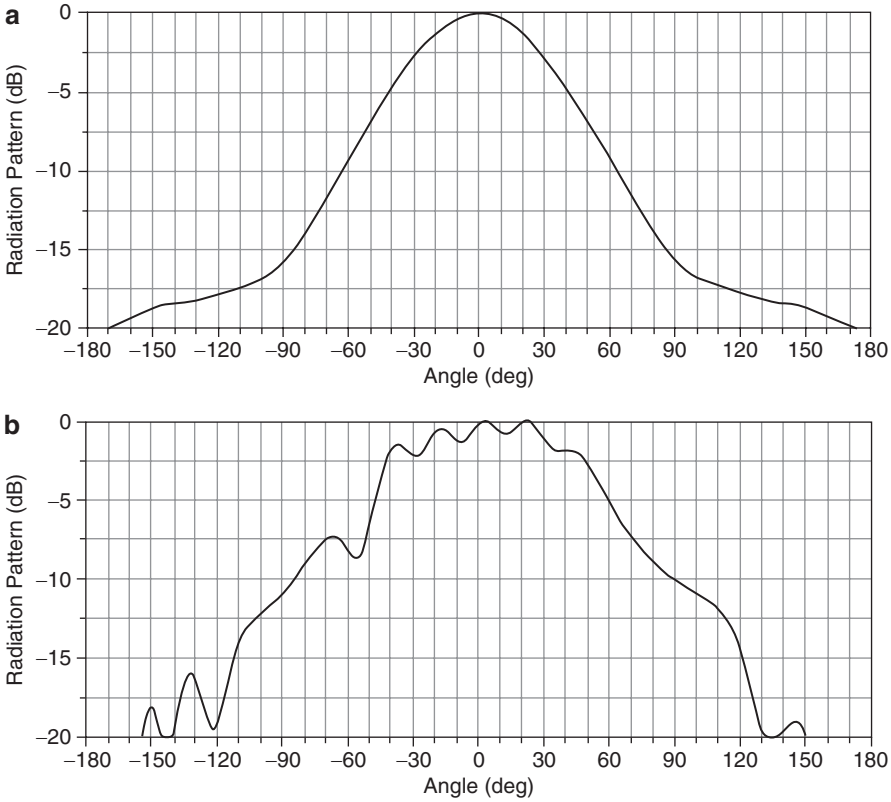

Fig. 14.6 MPA simulated radiation patterns. (**a**) *YZ*-plane, (**b**) *XZ*-plane

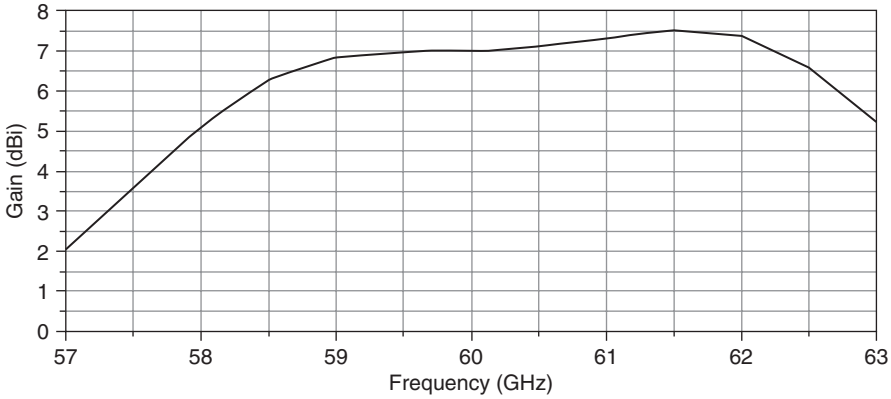

Fig. 14.7 MPA simulated gain

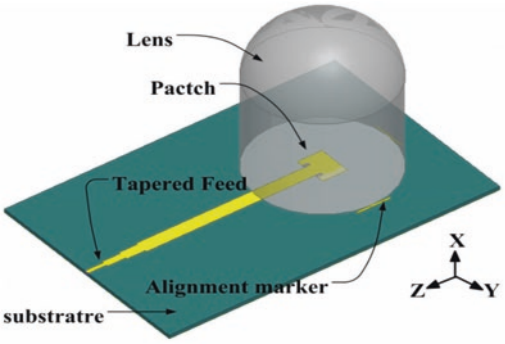

Fig. 14.8 Structure of MPA with extended hemispherical Teflon lens

The extended hemispherical lens is placed over the MPA. The side and top view of MPA structure integrated with extended hemispherical dielectric lens is shown in Fig. 14.9. The extended hemispherical dielectric lens consists of a Teflon cylinder ($\varepsilon_r = 2.1$) with a Teflon half sphere on top. The height and diameter of the cylinder are referred to as H and D, respectively, whereas the radius of the top half sphere is referred to as R. The procedure given in [11] is employed to design the extended hemispherical lens. The initial radius of top hemispherical part was chosen to be λg (where λg is guided wavelength in Teflon), resulting in cylindrical extension height $H_1 = 8.8$ mm. The center of MPA and center of lens are aligned. A tedious optimization is carried out over the structure of the MPA with extended hemispherical lens to achieve maximum impedance bandwidth, gain, and radiation beamwidth of 24°. The inset of MPA (g) is optimized keeping in mind the available manufacturing tolerances. However, a special attention is given to widths of tapered feed (W_3) so that a V-band connector can easily be connected to the feed point. The optimum dimensions for the MPA with extended hemispherical lens are found to be: $D = 8$ mm, $H_1 = 7$ mm, $H_2 = R = 4$ mm, $T_1 = T_2 = T_3 = 1.1$ mm, $W_1 = 0.62$ mm,

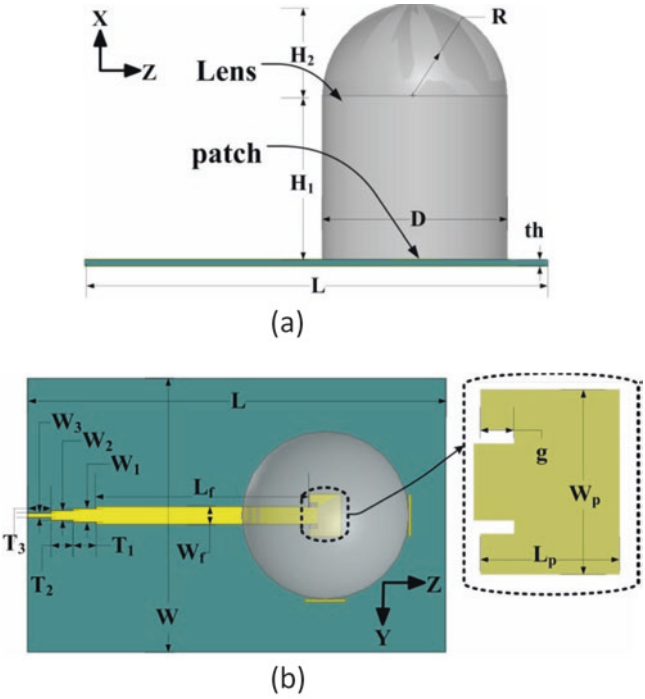

Fig. 14.9 Structure of MPA with Teflon lens with important design parameters. (**a**) Side view, (**b**) top view

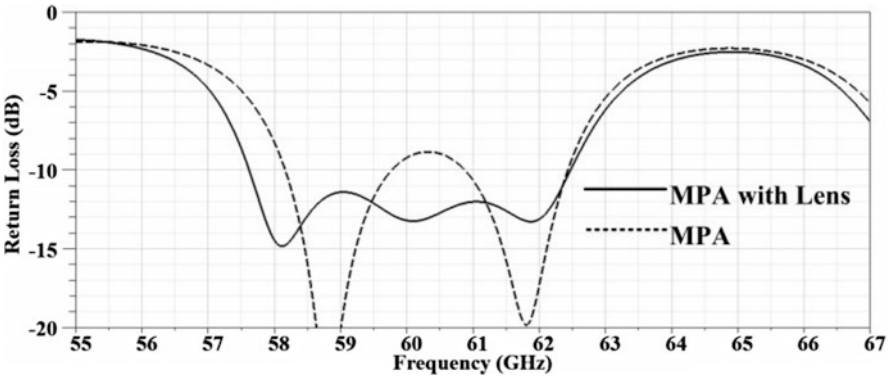

Fig. 14.10 Comparison between simulated return loss of MPA and MPA integrated with dielectric lens

W_2 = 0.43 mm, W_3 = 0.23 mm, L_f = 10.2 mm, W_f = 0.824 mm, g = 0.35 mm, L_p = 1.5 mm, W_p = 2.02 mm, L = 20 mm, W = 13 mm.

The simulated return loss of the optimized MPA and MPA with dielectric lens is compared in Fig. 14.10. The simulated return loss bandwidth of both antennas,

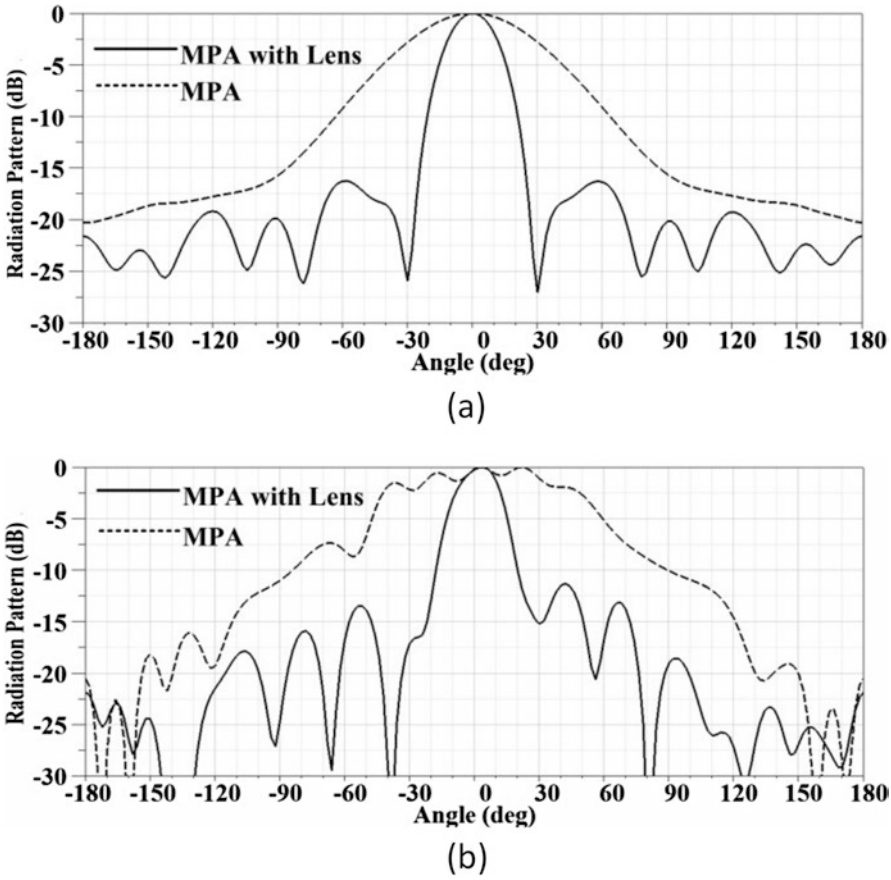

Fig. 14.11 Simulated normalized radiation pattern of MPA and MPA integrated with lens. (**a**) *XZ*-plane, (**b**) *XY*-plane

i.e., MPA and MPA with dielectric lens, is found to be approximately 5 GHz (57.5–62.5 GHz).

In Fig. 14.11 the comparison between the simulated radiation pattern of MPA and MPA with extended hemispherical dielectric lens in two orthogonal planes at 60 GHz is shown. As illustrated in Fig. 14.11a the 3 dB beamwidth in *XZ*-plane is found to be 64° and 24° for MPA and MPA with lens, respectively, whereas in Fig. 14.11b the 3 dB beamwidth in *XY*-plane is found to be 102° and 24° for MPA and MPA with lens, respectively. It is important to mention that the side lobe level in case of MPA with lens is below 16 dB and 12 dB in both *XZ*-plane and *XY*-plane. For a better understanding of radiation pattern characteristics the 3D radiation patterns of MPA and MPA with lens are shown in Fig. 14.12. It can be easily observed that when utilizing an extended hemispherical dielectric lens, the radiation pattern of the simple MPA is varied and a uniform beamwidth in both orthogonal planes is achieved. As seen in Fig. 14.12b the 3 dB beamwidth in *XZ*-plane and *XY*-plane is found to be very similar, i.e., approximately 24° as shown in Fig. 14.11. This gives

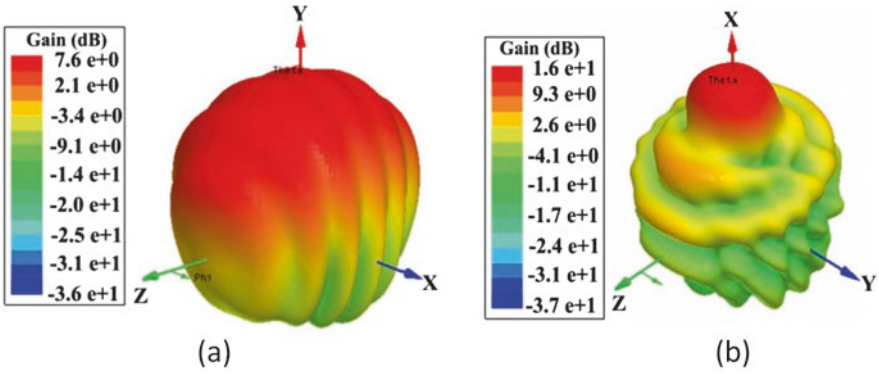

Fig. 14.12 3D radiation patterns. (**a**) MPA, (**b**) MPA integrated with lens

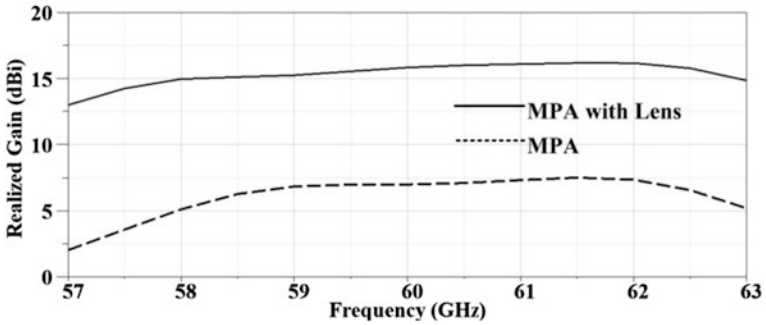

Fig. 14.13 Simulated realized gain of MPA and MPA integrated with lens

the proposed antenna structure an added advantage especially for applications involving the beam switching techniques.

Furthermore, as expected the gain of conventional MPA is enhanced by 9 dB by integration of the extended hemispherical dielectric lens as shown in Fig. 14.13. The maximum gain of MPA with lens is found to be 16.25 dBi at 61.5 GHz, whereas it remains above 15 dBi in most of the frequency bands of operation, i.e., from 58.5 to 62.5 GHz.

A prototype is fabricated to verify the simulation results of MPA integrated with extended hemispherical dielectric lens. The photograph of the fabricated prototype of MPA integrated with Teflon lens and V-band connector is shown in Fig. 14.14. The MPA was manufactured utilizing the LPKF (Laser). However, the dielectric lens (Teflon) is glued over the MPA utilizing a very thin layer of 3 M glue film (50 μm). Furthermore, the V-band removable connector is connected to the tapered feed for test and measurement purpose.

The comparisons between the simulated and measured results of MPA with extended hemispherical dielectric lens are shown in Fig. 14.15, which are found to be in good agreement. The return loss measurement of developed prototype is

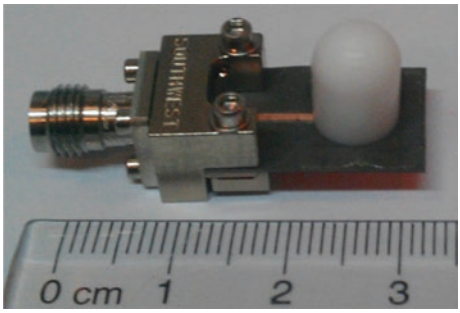

Fig. 14.14 Fabricated MPA with extended hemispherical dielectric lens, MPA and V-band connector

performed by utilizing Anritsu vector network analyzer. The impedance bandwidth of 5 GHz (57.5–62.5 GHz) is achieved as shown in Fig. 14.15a. The antenna radiation pattern is obtained by utilizing a custom base system consisting of V-band horn, VNA, V-band cables and contactors, and AUT (antenna under test). As shown in Fig. 14.15b, c, the 3 dB beamwidth is found to be 24° in both *XZ*-plane and *XY*-plane, whereas the side lobe level is found to be below 16 dB and 12 dB in both *XZ*-plane and *XY*-plane, respectively, at 60 GHz. The small variation observed between the simulated and measured results is probably due to 3 M glue film (50 μm) used to fix the lens and the presence of V-band connector.

14.3.2 Element MPA Array with Extended Hemispherical Teflon Lenses

In this section the simulation and measured results of 15-element microstrip patch antenna (MPA) array with hemispherical dielectric (Teflon) lenses operating in 60 GHz band are presented. The MPA with extended hemispherical dielectric lens described in previous section is utilized to form a circular array as shown in Fig. 14.16. The dimensions of dielectric lens (Teflon) and MPA are kept the same as mentioned before. The array is designed to cover a wide scan angle of full 360° in azimuth plane ($\theta = 90°$) with impedance bandwidth of 5 GHz (57.5–62.5 GHz) and gain higher than 16 dB and 3 dB crossover. The array support is made of acrylonitrile butadiene styrene (ABS), since it is a low-cost plastic, easy to machine, ideal material for structural applications, and easy to glue with other materials. The ABS support is necessary part for the antenna development and measurements since all single element MPAs with Teflon lens are glued over this support to develop a prototype for test and measurements. The dielectric constant of ABS material varies in range of 2–3.5. The simulations are carried out with various different dielectric constants and no abnormality in results is observed.

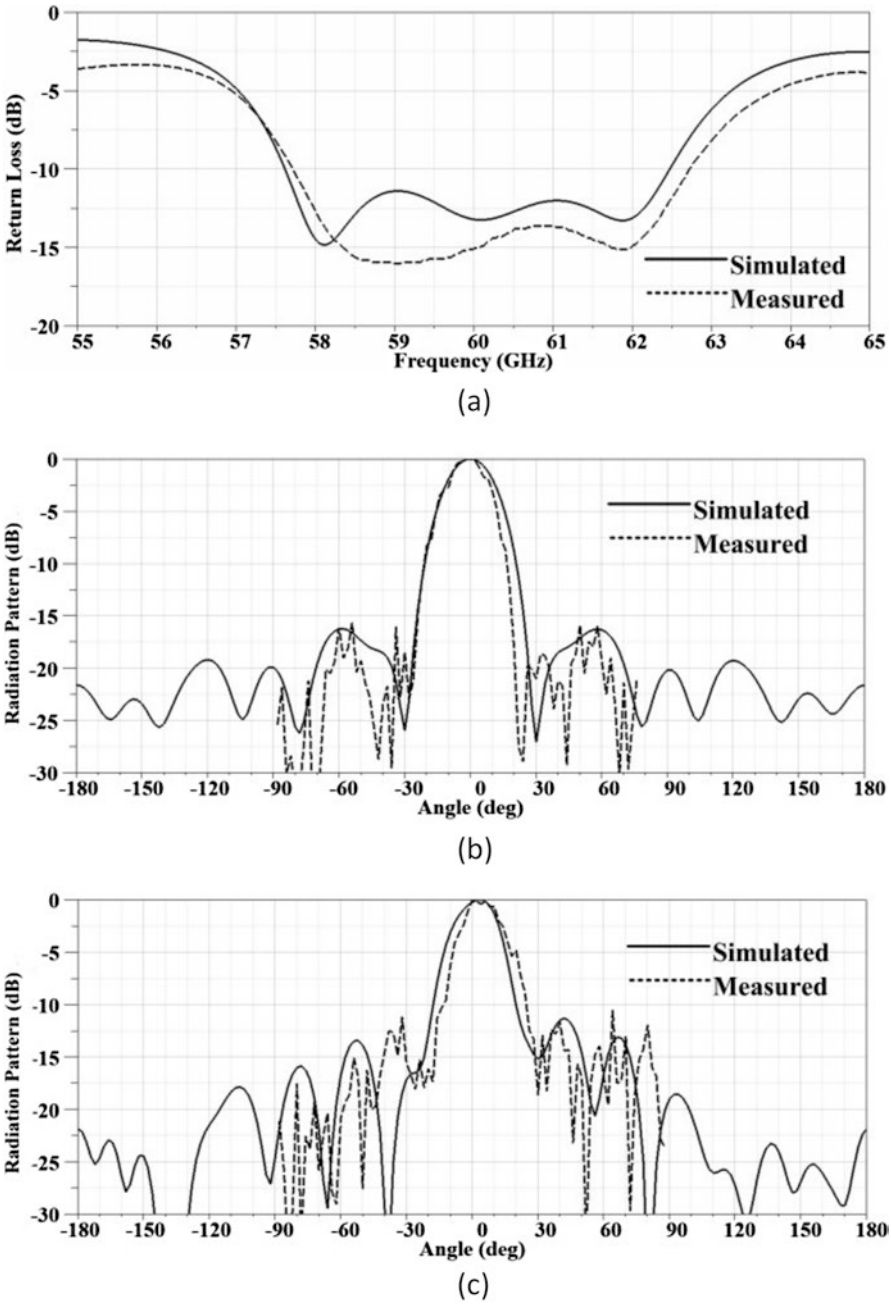

Fig. 14.15 Comparison between simulated and measured results of MPA with lens. (**a**) Return loss, (**b**) *XZ*-plane normalized radiation pattern at 60 GHz, (**c**) *XY*-plane normalized radiation pattern at 60 GHz

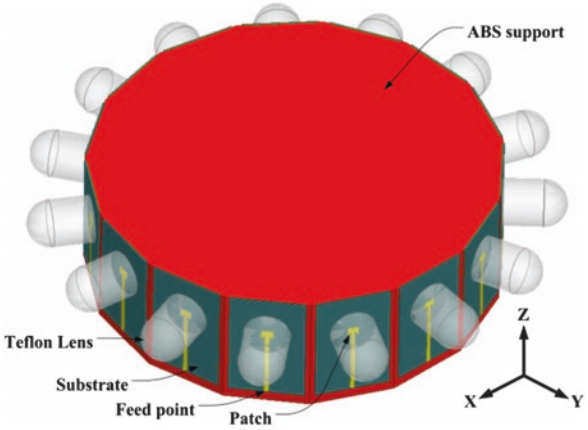

Fig. 14.16 15-element circular microstrip patch antenna array with dielectric lenses (3D view)

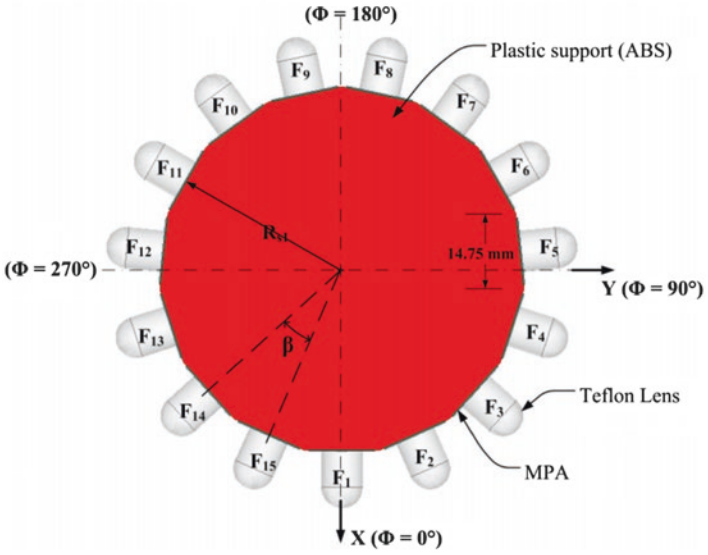

Fig. 14.17 15-element circular patch antenna array with integrated lenses (top view)

The top view of the 15-element circular array is shown in Fig. 14.17. As shown the ABS support consists of 15 edges each having length of 14.75 mm. The angular distance between the adjacent elements is set to be $\beta = 24°$ to achieve full 360° coverage in azimuthal plane and 3 dB crossover. By activating each array element one by one while all others are terminated by 50 Ω termination, the antenna beam is scanned over the whole 360° in azimuth plane with 3 dB crossover. Some important

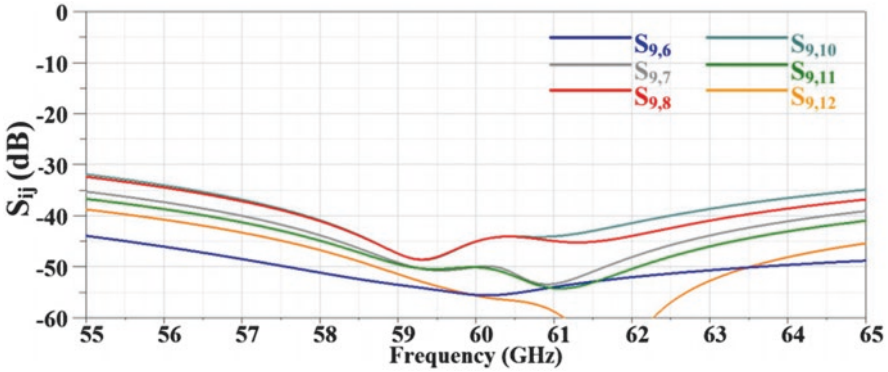

Fig. 14.18 Mutual coupling between array elements

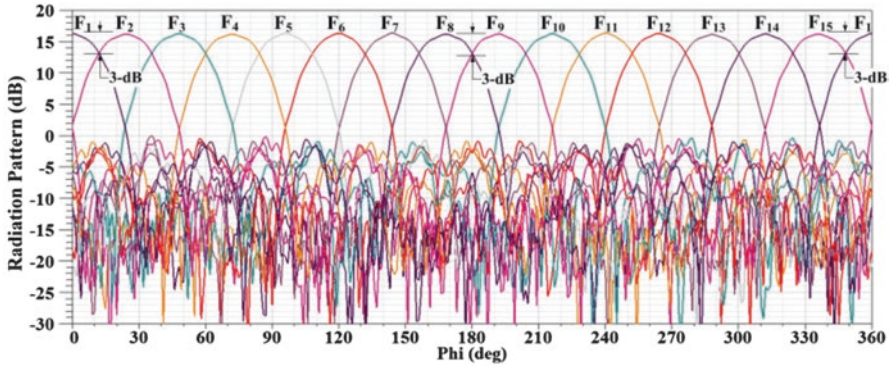

Fig. 14.19 Simulated 2D radiation pattern in azimuth plane ($\theta = 90°$) of 15-element circular patch antenna array with integrated lenses (zoomed)

array parameters as mentioned in Fig. 14.17 are $R_a = 35.01$ mm, $S = 14.55$ mm, and $\beta = 24°$, where R_a and β are optimized to achieve 3 dB crossover between the neighboring radiation patterns.

The mutual coupling between the array elements is one of the important parameters, especially in antennas with reconfigurable radiation patterns. With the proposed antenna array structure the mutual coupling between the array elements is found to be below −35 dB in required frequency band of operation as shown in Fig. 14.18.

The 2D radiation pattern in azimuth plane ($\theta = 90°$) of the 15-element MPA array with Teflon lenses is shown in Fig. 14.19. The simulations are carried out by exciting each feed (MPA integrated with Teflon lens) one by one while all other feeds are terminated by a matched load. The 3 dB crossover between the adjacent MPA feeds is achieved. The 3 dB beamwidth is found to be approximately 24° having side lobe level below −18 dB, and constant gain is achieved in whole scan range for radiation pattern from each feed (i.e., F_1, F_2, F_3,...,F_{15}).

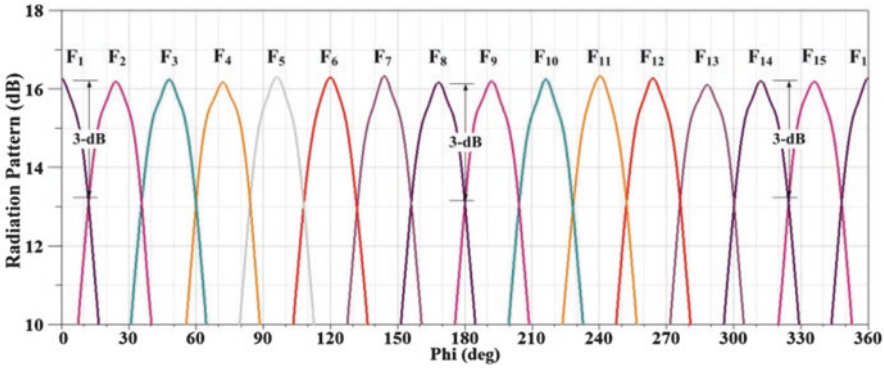

Fig. 14.20 Simulated 2D radiation pattern in azimuth plane ($\theta = 90°$) of 15-element circular patch antenna array with integrated lenses (zoomed)

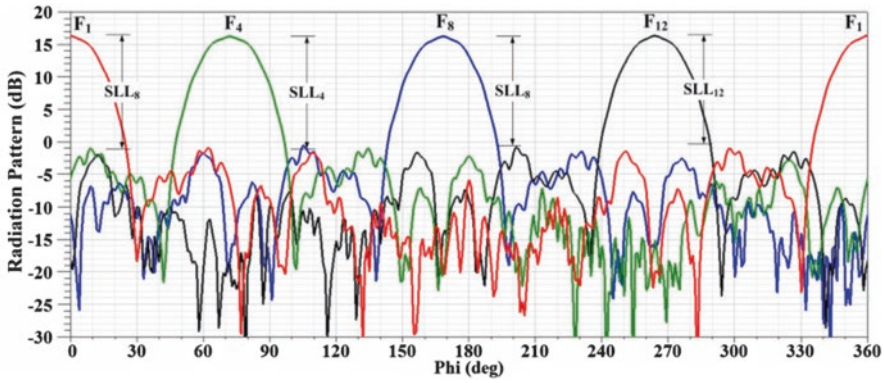

Fig. 14.21 Simulated 2D radiation pattern in azimuth plane ($\theta = 90°$) from 15-element circular patch antenna array with integrated lenses (radiation patterns from feed 1, feed 4, feed 8, and feed 12 are shown for clarity)

The 2D radiation pattern in azimuth plane ($\theta = 90°$) of the 15-element MPA array integrated with Teflon lenses is zoomed and shown in Fig. 14.20. The antenna array covers full 360° in azimuth plane. The gain in azimuth is found to be above 16 dB for each feed. It is clearly evident that the array covers the scan range of, i.e., $\phi = 0°$–$360°$ with 3 dB crossover.

For a better understanding of the side lobe level (SLL), the 2D radiation patterns in azimuth plane ($\theta = 90°$) from the four feeds, i.e., F_1, F_4, F_8, and F_{12}, are shown in Fig. 14.21. It is clearly evident that the side lobe level is almost similar for all beams SLL 1 = SLL 4 = SLL 8 = SLL 12 = −17 dB. Similarly, the beamwidth of all beams generated by activating each array element one by one while all others are termi-

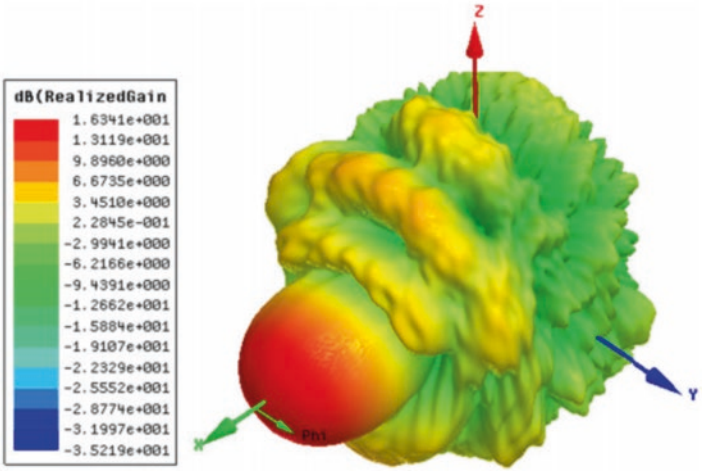

Fig. 14.22 Simulated 3D radiation pattern from 15-element circular patch antenna array with integrated lenses (feed 1 is active)

nated with 50Ω load are found to be 24°. The 3D radiation pattern achieved by activating a single array element is shown in Fig. 14.22 for a better understanding of antenna radiation properties.

The 2D radiation pattern in elevation plane (ϕ = constant) of MPA feed 1, feed 7, and feed 13 is shown in Fig. 14.23. The 3 dB beamwidth is approximately 22.5° for all feeds with SLL of approximately 12 dB. As a conclusion the antenna is suitable for wide scan angle of ±180° (i.e., from ϕ = 0°–360°) with a gain better than 16 dB and 3 dB crossover.

To validate the proposed design, a 5-element array is developed as shown in Fig. 14.24. The five elements are referred to as F_7, F_8, F_9, F_{10}, and F_{11}. The comparison between the simulated and measured return loss is shown in Fig. 14.25, which is found to be in good agreement. However, the variation between the simulated and measured results can be attributed to manual work such as placing the Teflon lens on the patch antenna, placing and connecting the removable V-band connector to the antenna printed circuit board (PCB), and gluing of array elements on ABS support.

The comparison between simulated and measured radiation pattern at 60 GHz in azimuth plane for the five elements is shown in Fig. 14.26, which are found to be in good agreement. It can be easily seen that the crossover between the adjacent array elements is at approximately 3 dB, and maximum side lobe level is found to be approximately 15 dB. The beamwidth, gain, and side lobe level of each of the beams from the array remain constant throughout the whole scan range. This gives the proposed design an advantage over the beam scanning ILAs found in literature.

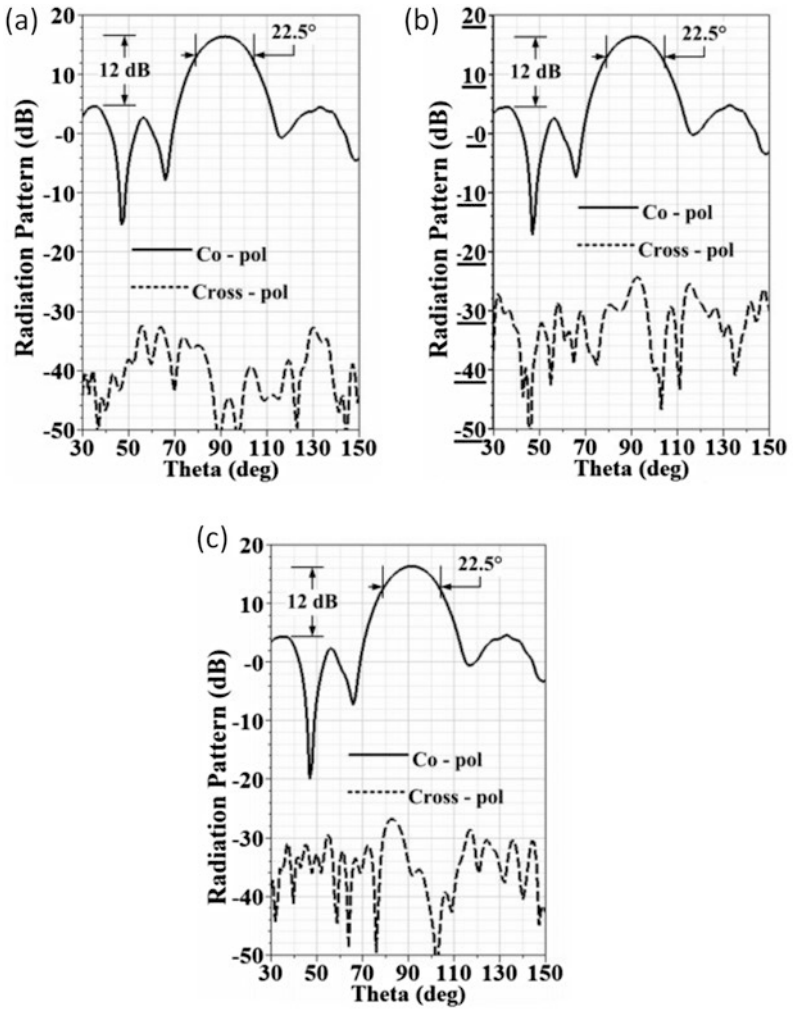

Fig. 14.23 2D radiation pattern in elevation plane (ϕ = constant) of 15-element circular patch antenna array with lenses. (**a**) Feed 1, (**b**) feed 7, (**c**) feed 13

14.4 Conclusion

A 15-element antenna array operating at 60 GHz with beam switching capability in azimuth plane is proposed. The array covers a wide impedance bandwidth of 5 GHz (57.5–62.5 GHz) with gain higher than 15 dBi in frequency band of operation. The matching and the radiation characteristics of the presented switched beam antenna array are validated by measurements performed on a 5-element corresponding array prototype. A very good agreement between the measured and simulated results is

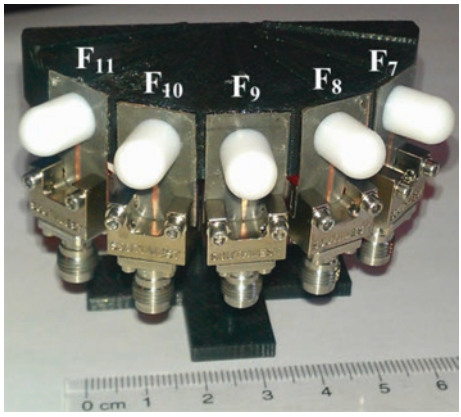

Fig. 14.24 Developed prototype of 5-element antenna array for test and measurements

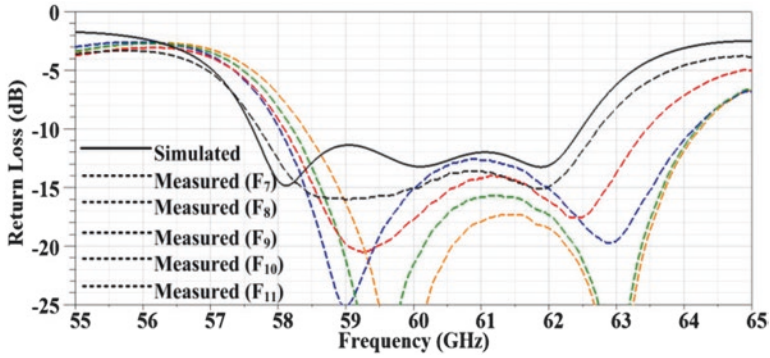

Fig. 14.25 Comparison between the simulated and measured return loss

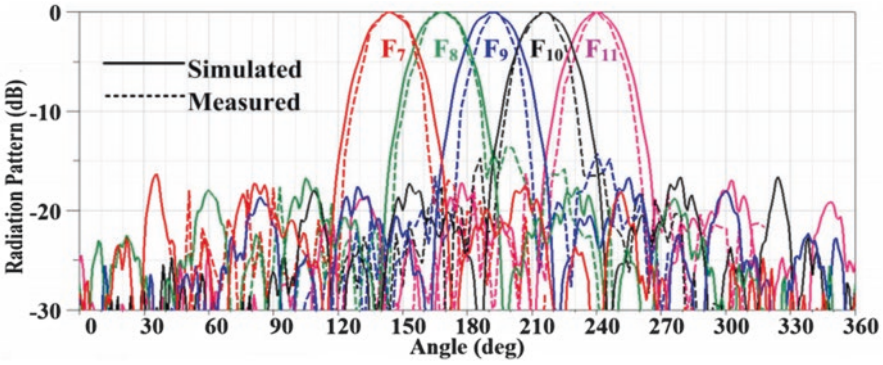

Fig. 14.26 Comparison between the simulated and measured radiation pattern

observed. The beamwidth, gain, and side lobe level of each of the beams from the array remain constant throughout the whole scan range of 360° in azimuth plane. This gives the proposed design an advantage over the beam scanning ILAs found in literature.

References

1. M.T. Jusoh, O. Lafond, F. Colombel, M. Himdi, Performance of a reconfigurable reflector antenna with scanning capability using low cost plasma elements. Microw. Opt. Technol. Lett. **55**, 2869–2874 (2013)
2. A. Artemenko, A. Mozharovskiy, A. Maltsev, R. Maslennikov, A. Sevastyanov, V. Ssorin, Experimental characterization of e-band two-dimensional electronically beam-steerable integrated lens antennas. IEEE Antennas Wirel. Propag. Lett. **12**, 1188–1191 (2013)
3. B. Schoenlinner, X. Wu, J.P. Ebling, G.V. Elefheriades, G.M. Rebeiz, Wide-scan spherical-lens antennas for automotive radars. IEEE Trans. Microwave Theory Tech. **50**, 2166–2175 (2002)
4. Y.J. Cheng, Y. Fan, Millimeter-wave miniaturized substrate integrated multibeam antenna. IEEE Trans. Antennas Propag. **59**, 4840–4844 (2011)
5. X. Ding, B.-Z. Wang, G.-Q. He, Research on a millimeter-wave phased array with wide-angle scanning performance. IEEE Trans. Antennas Propag. **61**, 5319–5324 (2013)
6. Y.J. Cheng, W. Hong, K. Wu, Millimeter-wave substrate integrated waveguide multibeam antenna based on the parabolic reflector principle. IEEE Trans. Antennas Propag. **56**, 3055–3058 (2008)
7. O. Lafond, M. Himdi, H. Merlet, P. Lebars, An active reconfigurable antenna at 60 GHz based on plate inhomogeneous lens and feeders. IEEE Trans. Antennas Propag. **61**, 1672–1678 (2013)
8. M. Kamran Saleem, M.A.S. Alkanhal, A. Fattah Sheta, M. Abdel Rahman, M. Himdi, Integrated lens antenna Array with full azimuth plane beam scanning capability at 60 GHz. Microw. Opt. Technol. Lett. **59**(1), 116 –120 (2017)
9. C.A. Balanis, *Antenna Theory: Analysis and Design* (John Wiley & Sons, New York, 2012)
10. Ansys, Hfss, v14, ANSYS Corporation Software (Pittsburgh, U.S.A., 2014)
11. C.A. Fernandes, E.B. Lima, J.R. Costa, *Dielectric Lens Antennas: Handbook of Antenna Technologies,* pp 1001–1064 (Springer Singapore, 2016)

Chapter 15
Wide-Angle Beam Scanning Antenna at 79 GHz for Short-Range Automotive Radar Applications

Muhammad Kamran Saleem, Majeed A.S. Alkanhal, and Hamsakutty Vettikaladi

15.1 Introduction

Radars are found to be the most promising technology due to their robust performance in the face of environmental influences such as bad light, weather conditions, and extreme temperatures [1, 2]. This chapter focuses on automotive radars, which are classified into three main categories based on range, distance, and field of view: Short-Range Radar (SRR), Medium-Range Radar (MRR), and Long-Range Radar (LRR). In recent years, automotive radars operating at millimeter-wave range have been widely investigated [3–5]. The frequency band of 77–81 GHz has been allocated for automotive MRR and SRR applications, such as blind spot detection, precrash vehicle preparation, and collision warning [6, 7]. For many MRR and SRR applications, it is favorable to have an antenna with a narrow beam in horizontal plane [8, 9]. A promising technique to achieve wide-angle beam scanning with narrow beam widths and high gain is to integrate a set of planar antenna array with dielectric lens. Such an antenna with beam-switching capability is a better alternative to conventional phased array antenna, due to high metallic and phase shifter losses, especially at millimeter-wave frequency band.

This chapter focuses on antenna array integrated with cylindrical Luneburg lens operating at 79 GHz. The element in antenna array consists of planar log periodic dipole antenna (PLPDA) implemented on quartz substrate. The gain of PLPDA is enhanced by integrating it with inhomogeneous cylindrical dielectric lens (Luneburg lens) and beam switching is achieved by activating each array element in antenna array one by one, resulting in a unique predefined radiation pattern associated with

M.K. Saleem (✉)
Electrical Engineering Department, University of Central Punjab, Lahore, Pakistan
e-mail: mksa05@gmail.com

M.A.S. Alkanhal • H. Vettikaladi
Electrical Engineering Department, King Saud University, Riyadh, Saudi Arabia

I. Elfergani et al. (eds.), *Antenna Fundamentals for Legacy Mobile Applications and Beyond*, DOI 10.1007/978-3-319-63967-3_15

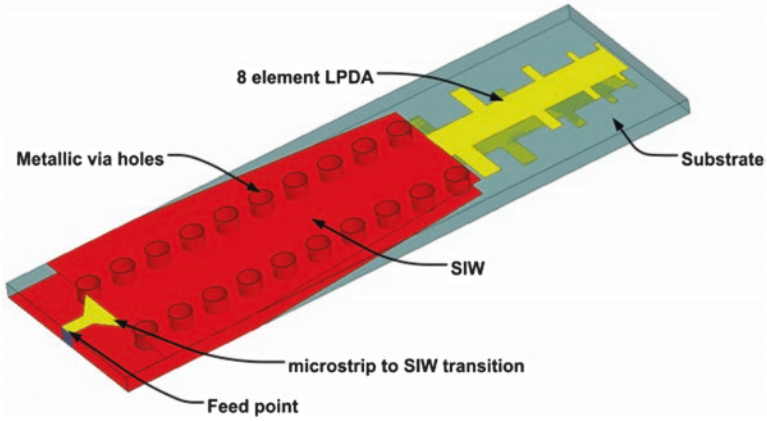

Fig. 15.1 PLPDA configuration including LPDA, SIW, triangular transition, and microstrip feed

each antenna element in array [10, 11]. The array covers 4 GHz (77 –81 GHz) bandwidth with similar radiation pattern characteristics. The 3 dB beam width of each array element is found to be 10° with gain higher than 15 dB. By activating each array element one by one while all other are terminated by 50 Ω matched load, the antenna beam can be switched, resulting in beam-scanning capability of full 170° in azimuth plane ($\theta = 90°$). The design is validated by developing and testing a prototype. The comparison between the simulation and the measured results is presented, which are found to be in good agreement.

15.2 PLPDA Configuration for 79 GHz Operation

The proposed Printed Log Periodic Antenna (PLPDA) operating at 79 GHz for development of 17-element array to cover 170° in azimuth plane ($\theta = 90°$) is presented in this section. The PLPDA is integrated with substrate integrated waveguide (SIW) to reduce metallic losses that are inherent at proposed millimeter wave band. The design equations presented in [12–14] are utilized to find the initial dimensions for the proposed PLPDA configuration. As per design requirements for the short-range automotive radar applications, the antenna directivity is selected to be 9 dB resulting in initial values of scale factor (τ) and spacing factor (σ) to be 0.915 and 0.17, respectively, for a log periodic dipole antenna. The maximum frequency (f_{max}) and minimum frequency (f_{min}) are chosen to be 85 GHz and 75 GHz, respectively. The quartz substrate ($\varepsilon_r = 3.75$, th = 0.2 mm, $\tan\delta = 0.0004$) is chosen as antenna substrate. The proposed antenna configuration consisting of PLPDA with SIW transition and microstrip feed is shown in Fig. 15.1. The PLPDA is fed by a microstrip

Table 15.1 Optimized dimensions for SIW integrated PLPDA

$a_1 = 0.250$	$a_2 = 0.198$	$a_3 = 0.158$	$a_4 = 0.126$	$a_5 = 0.099$
$a_6 = 0.079$	$a_7 = 0.063$	$a_8 = 0.050$	$L_1 = 8.133$	$W_1 = 2.629$
$b_1 = 0.651$	$b_2 = 0.518$	$b_3 = 0.411$	$b_4 = 0.327$	$b_5 = 0.260$
$b_6 = 0.207$	$b_7 = 0.164$	$b_8 = 0.131$	$L_2 = 5.383$	$L_3 = 3.500$
$s_0 = 0.180$	$s_1 = 0.609$	$s_2 = 0.484$	$s_3 = 0.385$	$s_4 = 0.306$
$s_5 = 0.243$	$s_6 = 0.193$	$s_7 = 0.154$	$M_1 = 0.217$	$M_2 = 0.321$
$W_{siw} = 1.263$	$T_1 = 0.910$	$T_2 = 0.262$	$g = 0.200$	$D = 0.300$
$T_W = 0.577$	$W_3 = 0.383$			

All dimensions in mm

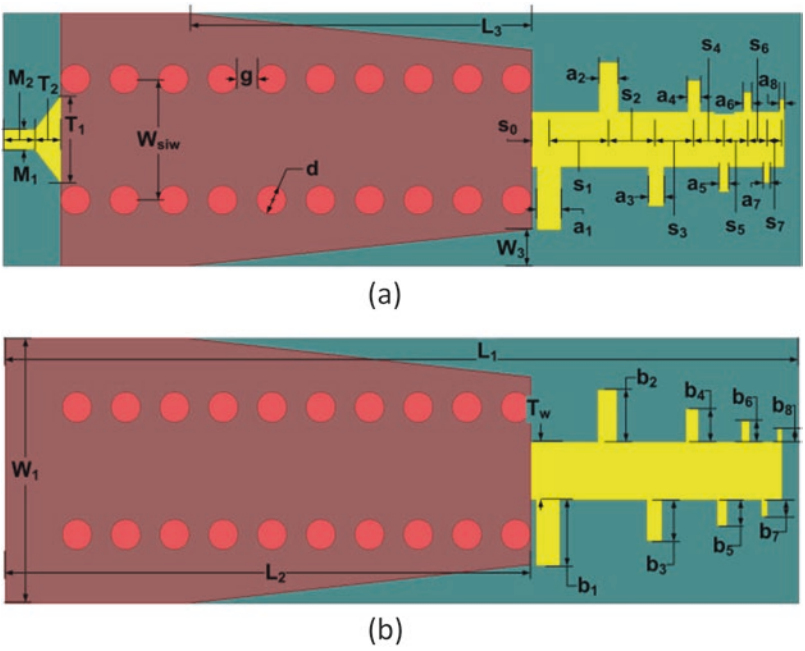

Fig. 15.2 Proposed PLPDA design parameters. (**a**) Top view. (**b**) Bottom view

line integrated with a triangular transition and SIW. The proposed antenna design is optimized utilizing ANSYS HFSS [15] to achieve required performance such as impedance bandwidth of 4 GHz (77–81 GHz) and gain higher than 7 dB.

The top and bottom view of the SIW integrated PLPDA along with important design parameters are shown in Fig. 15.2, where, total antenna length and width are L_1 and W_1, respectively. The final optimized dimensions are given in Table 15.1.

The simulated return loss of proposed antenna is shown in Fig. 15.3. The antenna impedance bandwidth is found to be 9 GHz (74 –83 GHz) covering the required frequency band of operation (77–81 GHz) with gain higher than 7 dB.

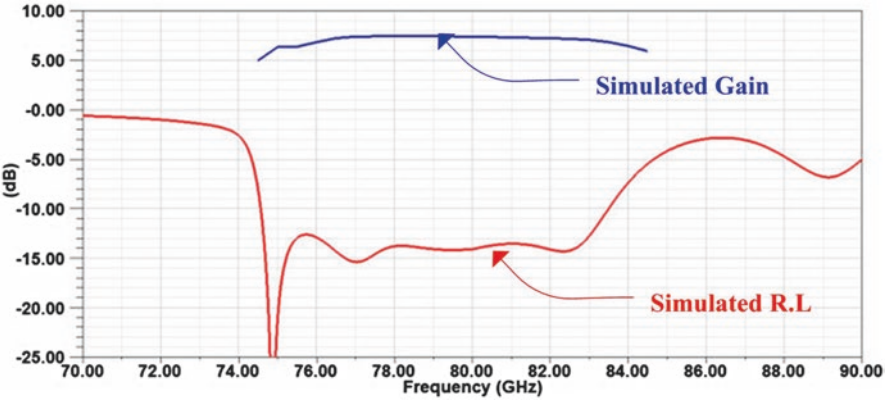

Fig. 15.3 Simulated return loss and gain of proposed PLPDA configuration

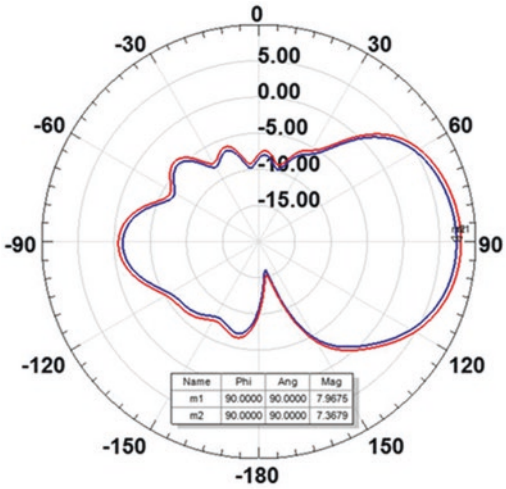

Fig. 15.4 Simulated 2D radiation pattern in azimuth of the proposed PLPDA configuration

The two-dimensional (2D) radiation pattern in azimuth ($\theta = 90°$) at center frequency of 79 GHz is shown in Fig. 15.4, where the maximum directivity and gain are found to be 7.9 dB and 7.3 dB, respectively. The 3 dB beam width is found to be approximately 50°.

15.3 PLPDA Integration with Luneburg Lens

To achieve a wide scan angle antenna performance, the integration of proposed PLPDA with inhomogeneous dielectric lens (Luneburg Lens) is discussed in this section. The inhomogeneous Luneburg lens is referred to as a gradient index lens

Table 15.2 Permittivity and radius of each layer in Luneburg lens having outer diameter of $6\lambda_0$

Area/layers	Permittivity	Radius
1	1.92	4.65
2	1.77	6.60
3	1.62	8.06
4	1.46	9.31
5	1.31	10.4
6	1.15	11.4

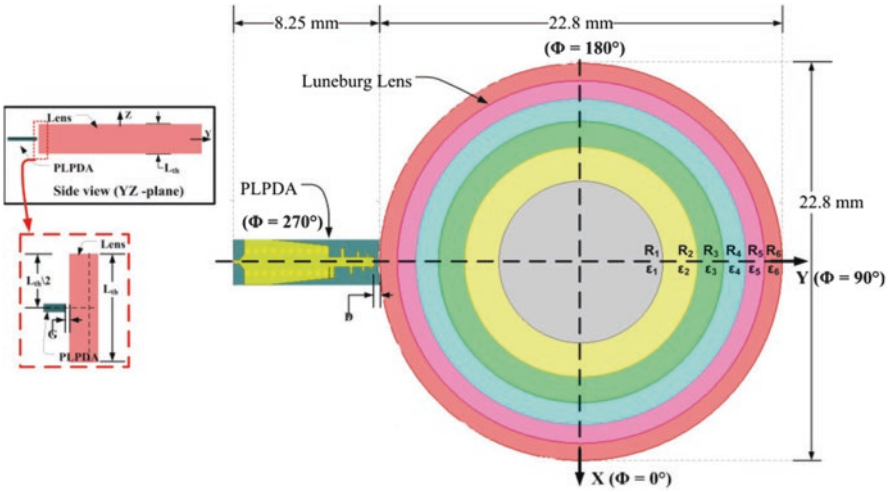

Fig. 15.5 Simulation model of PLPDA integrated with cylindrical Luneburg lens (top view)

whose relative permittivity varies radially [16]. A detailed description of integrated Luneburg lens can be found in [16, 17]. The optimum dimensions for integrated six-layer Luneburg lens are described in Table 15.2.

The planar end-fire PLPDA on quartz substrate described previously is integrated with six-layer Luneburg lens as shown in Fig. 15.5. The PLPDA feed is placed at $\phi = 270°$. As shown in the inset, the center of PLPDA feed is aligned with center of Luneburg lens. The diameter of outer shell of Luneburg lens is chosen to be $6\lambda_0$ (22.8 mm), where λ_0 is the free space wavelength at 79 GHz and thickness of Luneburg lens is chosen to be $L_{th} = 3$ mm. The gap between the quartz PCB consisting of PLPDA and Luneburg lens is kept to be 0.1 mm. Furthermore, the PLPDA feed is placed very close to Luneburg lens, that is, $D = 0.05$ mm. The corresponding values of dielectric constant and radius of each cylindrical layer in Luneburg lens (outer diameter $6\lambda_0$) are kept the same as tabulated in Table 15.2. In the structure of PLPDA array integrated with Luneburg lens, the lens radius (R), lens thickness L_{th} and lens to PLPDA feed distance (D) are optimized to achieve maximum gain and required impedance bandwidth with acceptable side lobe level (SLL) in azimuth

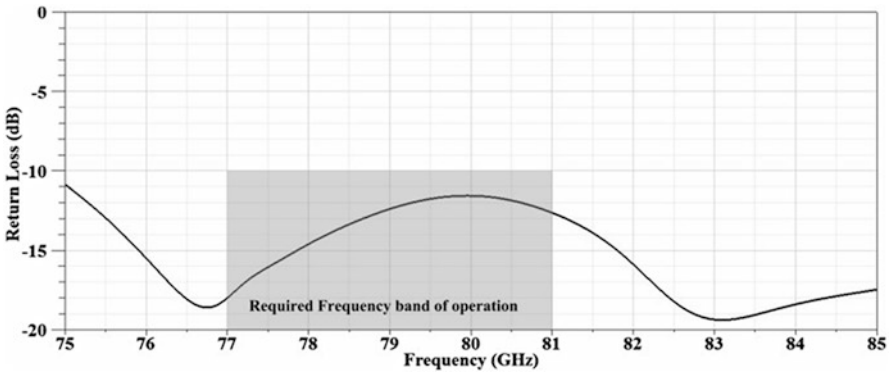

Fig. 15.6 Simulated return loss of PLPDA with six-layer Luneburg lens

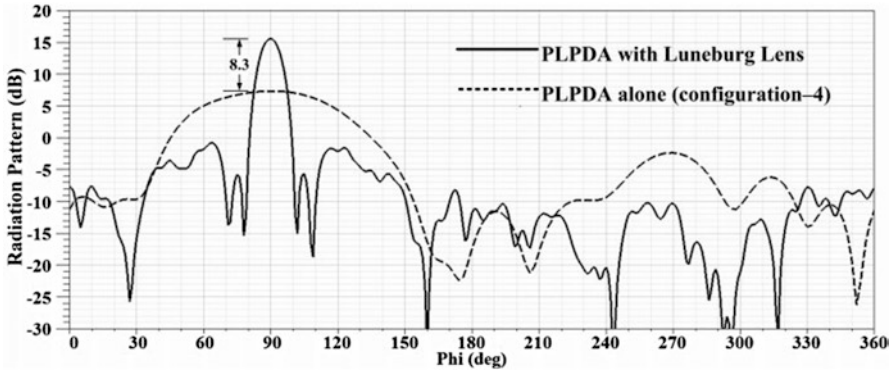

Fig. 15.7 Comparison between simulated 2D radiation patterns of PLPDA alone and PLPDA integrated with Luneburg lens at 79 GHz

and elevation plane. The optimum parameters are found to be R = 11.4 mm, L_{th} = 3.5 mm, and D = 0.3 mm, respectively.

The simulated return loss of PLPDA integrated with Luneburg lens is shown in Fig. 15.6, where the reflection coefficient is found to be below −10 dB in required frequency band (77–81 GHz) as highlighted. The planar end-fire PLPDA as shown in Fig. 15.5 is placed at ϕ = 270°. With proposed configuration of PLPDA feed with Luneburg lens, the maximum radiation is expected to be at ϕ = 90°. The radiation characteristics of single PLPDA feed alone and PLPDA feed integrated with Luneburg lens are studied. The 2D radiation patterns in azimuth plane (θ = 90°) at 79 GHz are compared in Fig. 15.7. The gain enhancement is clearly evident, that is, from 7.2 dB (PLPDA alone) to 15.5 dB (PLPDA integrated with Luneburg lens).

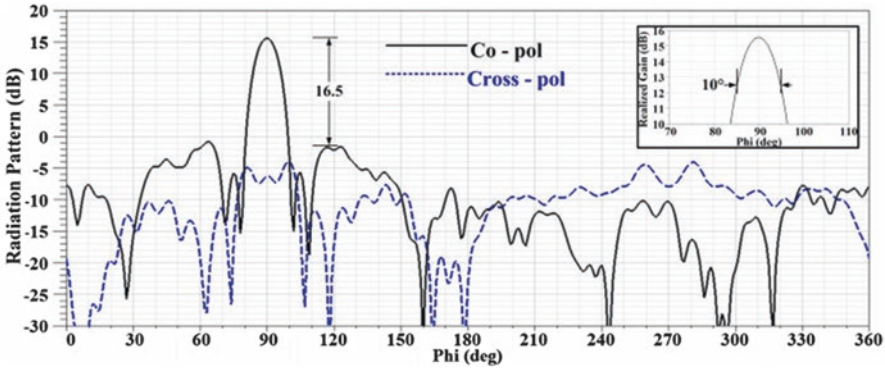

Fig. 15.8 Simulated 2D radiation pattern in azimuth plane ($\theta = 90°$) of PLPDA integrated with Luneburg lens

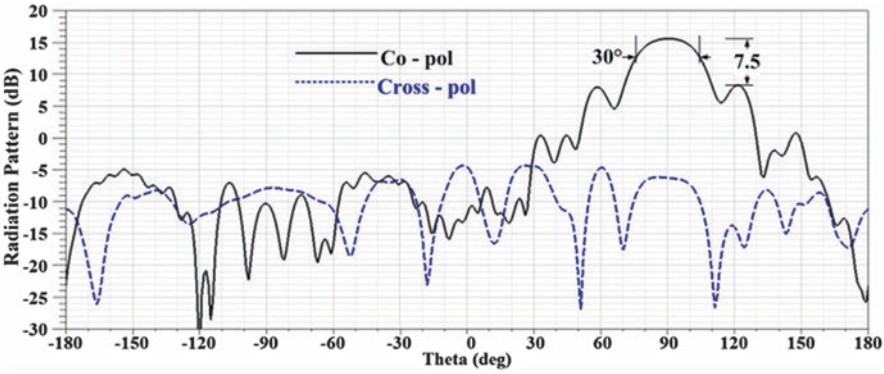

Fig. 15.9 Simulated 2D radiation pattern in elevation plane ($\phi = 90°$) of PLPDA integrated with Luneburg lens

The 2D radiation patterns of PLPDA feed integrated with Lsuneburg lens in azimuth plane ($\theta = 90°$) is shown in Fig. 15.8. The maximum gain is found at $\theta = 90°$ with 3 dB beam width of 10°. The Side Lobe Level (SLL) is found to be better than 16.5 dB. The cross-polarization is below −5 dB, as clearly evident in Fig. 15.8. Furthermore, the 2D radiation pattern in elevation plane ($\phi = 90°$) is shown in Fig. 15.9 and maximum gain is found to be at $\theta = 90°$ with 3 dB beam width of 30°. The SLL is found to be 7.5 dB with cross-polarization level below −5 dB.

For a better understanding of proposed antenna radiation characteristics, the three-dimensional (3D) radiation pattern of PLPDA feed integrated with Luneburg lens is shown in Fig. 15.10. It is clearly evident that the antenna radiation in end-fire direction and 3 dB beam width is narrower in azimuth plane with respect to beam width in elevation plane.

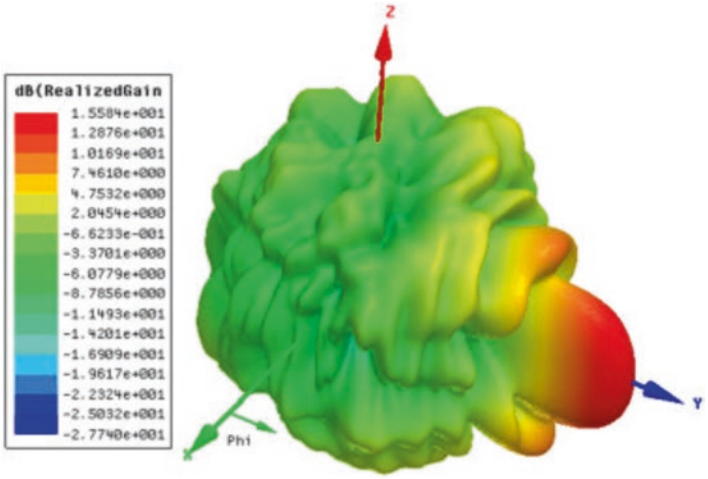

Fig. 15.10 3D radiation pattern of PLPDA integrated with LL

15.4 Integration of Three PLPDA Feeds with Luneburg Lens

The structure of single PLPDA feed with Luneburg lens is extended to three PLPDA feeds with Luneburg lens, as shown in Fig. 15.11. The crossover requirements between the adjacent PLPDA feeds as well as to validate the feasibility of antenna development are studied. The optimum angular distance (β) between the three feeds (i.e., F_1, F_2, and F_3) is found to be 10.25° to achieve 3 dB crossover between the radiation patterns of the two adjacent feeds. It is important to mention that the ground cuts introduced in PLPDA design play an important role. Utilization of these cuts results in some extra freedom in bringing the two adjacent feeds closer to each other. As shown in Fig. 15.11, the three PLPDA feeds (F_1, F_2, F_3) are placed at $\phi = 270°$, $\phi = 280.25°$, and $\phi = 260.25°$, respectively with $\beta = 10.25°$. The three beams resulting from switching between the PLPDA feeds are expected to be at $\phi = 90°$, 100°, and 80°. The inner and outer radius of semicircular quartz substrate is set to $R_{s1} = 11.5$ mm and $R_{s2} = 19.65$ mm, respectively.

The simulations are carried out by exciting each PLPDA feed one at a time and terminating other feeds with matched loads. The simulated return loss for the three feeds is shown in Fig. 15.12; it is clearly evident that the three feeds fulfill the requirement of impedance bandwidth of 4 GHz (77–81 GHz) with return loss better than 10 dB.

The 2D radiation pattern in azimuth plane ($\theta = 90°$) of three PLPDA feeds integrated with Luneburg lens is shown in Fig. 15.13. The maximum in radiation pattern

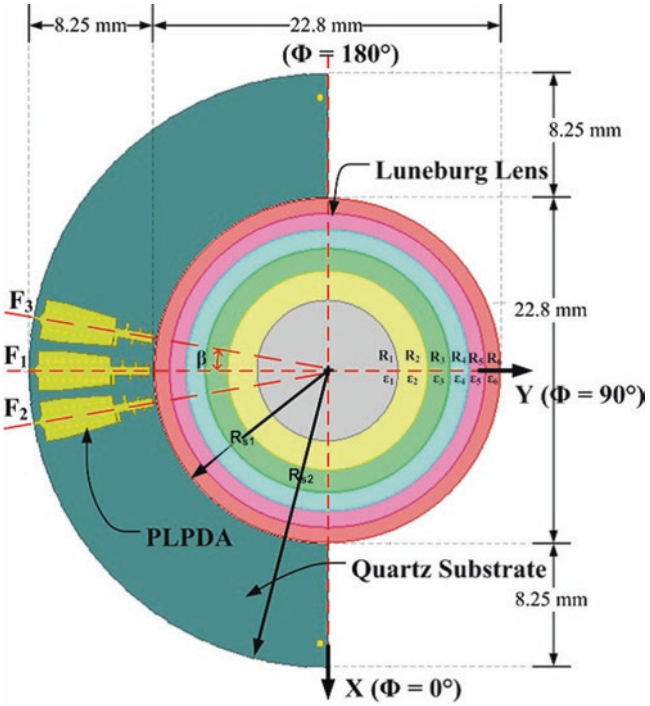

Fig. 15.11 Three PLPDA feeds integrated with Luneburg lens (top view)

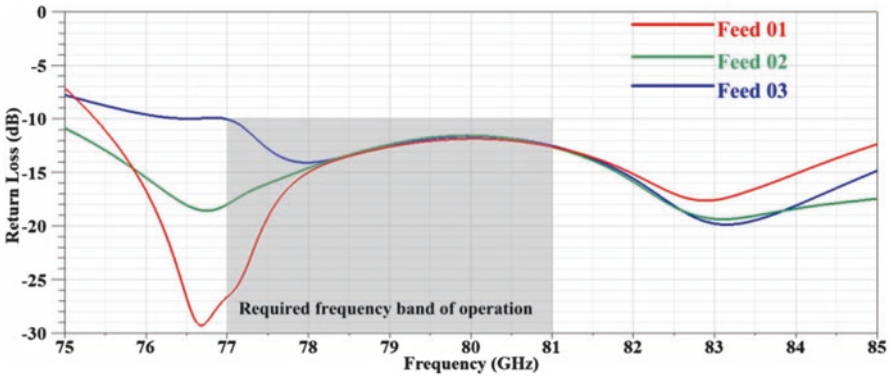

Fig. 15.12 Simulated return loss of Luneburg lens with three PLPDA feeds

is found to be at $\phi = 80°$, 90°, and 100° from each PLPDA feed (i.e., F_3, F_1, F_2). The SLL is better than 16 dB for all feeds and the crossover point is found to be 3.5 dB as shown in the inset of Fig. 15.13. It is important to mention that the crossover can be adjusted as per requirements by changing the angular distance β between the two adjacent feeds.

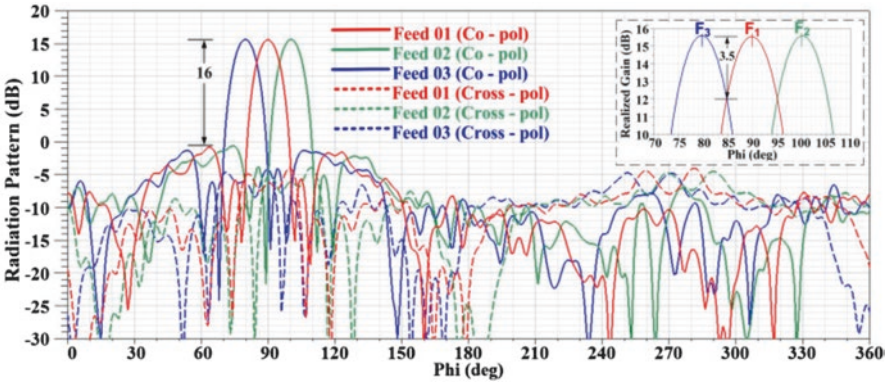

Fig. 15.13 Simulated 2D radiation pattern in azimuth plane ($\theta = 90°$) of three PLPDA feeds integrated with Luneburg lens (one PLPDA feed is excited with other two terminated with the matched loads)

15.5 Integration of 17-Element PLPDA Array with Luneburg Lens

Once the crossover point is adjusted as per requirement (i.e., 3.5 dB) the structure of three PLPDA feeds with Luneburg lens is extended to 17 PLPDA feeds with Luneburg lens as shown in Fig. 15.14. This 17 element PLPDA array integrated with Luneburg lens can provide a wide-scan angle 170° coverage in azimuth plane (θ = 90°). The inner and outer radius of antenna PCB is kept the same, that is, R_{s1} = 11.5 mm and R_{s2} = 19.65 mm, respectively. Each PLPDA feed is represented by $F_1, F_2, F_3, \ldots, F_{17}$, having angular displacement between adjacent feeds $\beta = 10.25°$.

In Fig. 15.15, the simulated return loss of 17 PLPDA feeds integrated with Luneburg lens is shown. The overall impedance bandwidth is found to be 7.5 GHz (77–84.5 GHz) covering the required impedance bandwidth, that is 77 –81 GHz with return loss better than 10 dB. The mutual coupling between antenna elements is shown in Fig. 15.16, which is found to be below −20 dB for the neighboring feeds and decays to −40 dB for the furthest feed.

The 2D radiation patterns in azimuth plane (θ = 90°) for the 17 PLPDA feeds integrated with Luneburg lens are shown in Fig. 15.17. The crossover between adjacent PLPDA feeds varies in the range of 3.5–3 dB, whereas the 3 dB beam width is found to be approximately 10° for radiation pattern from each PLPDA feed (i.e., F_1, $F_2, F_3, \ldots, F_{17}$).

The 2D radiation pattern is zoomed in for better understanding, as shown in Fig. 15.18. It is clearly evident that with 17 PLPDA feeds, the array covers 170° in azimuth plane (i.e., ϕ = 5°–175°). The maximum gain is found to be 15.55 dB at ϕ = 90° from the feed at the center (i.e., F_9 placed at ϕ = 270°). The minimum gain of 12.85 dB at ϕ = 8° is found to be for the feeds at the edge (i.e., F_{17}) placed at ϕ = 188°. Whereas for the other edge (i.e., F_1 placed at ϕ = 352°), the gain is found to be 13 dB at ϕ = 172°.

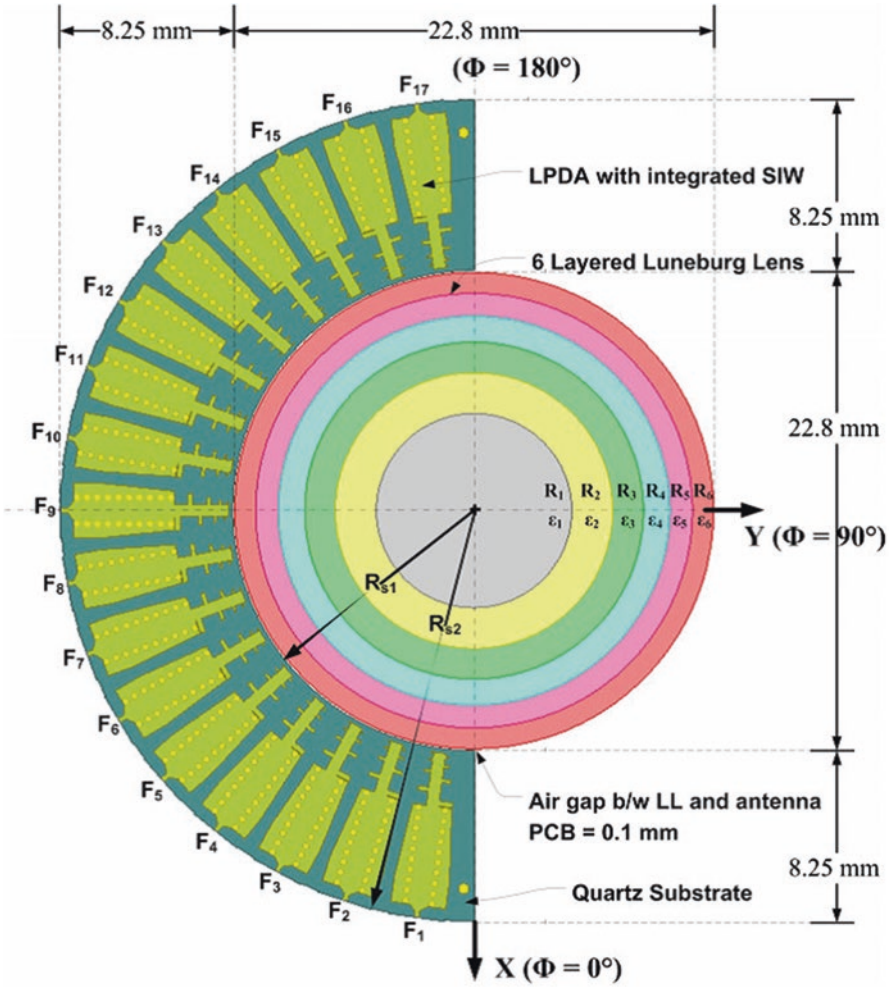

Fig. 15.14 The 17 PLPDA feeds integrated with six layer cylindrical Luneburg lens (top view)

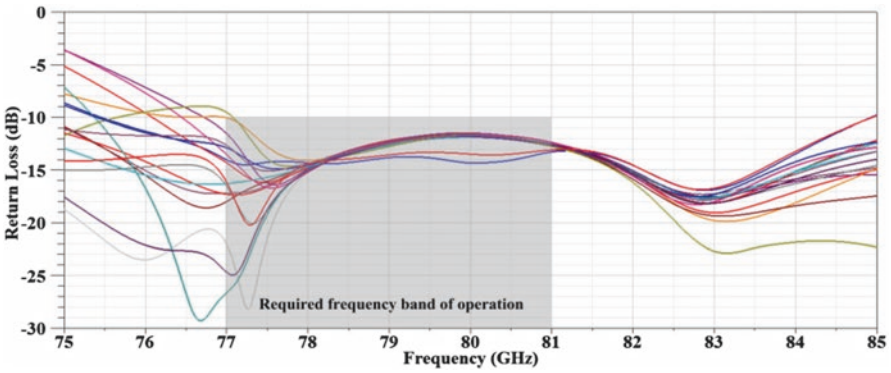

Fig. 15.15 Simulated return loss of 17 PLPDA feeds integrated with Luneburg lens

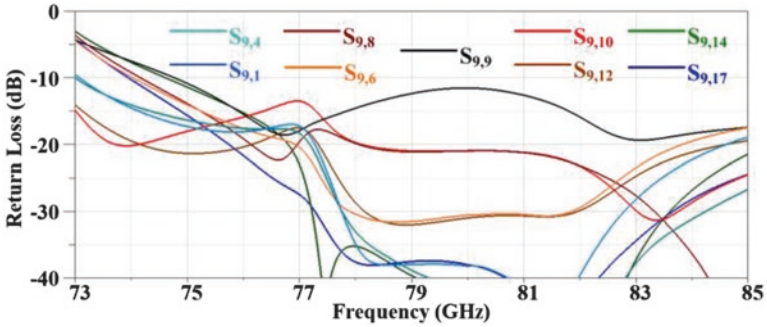

Fig. 15.16 Mutual coupling between antenna feeds

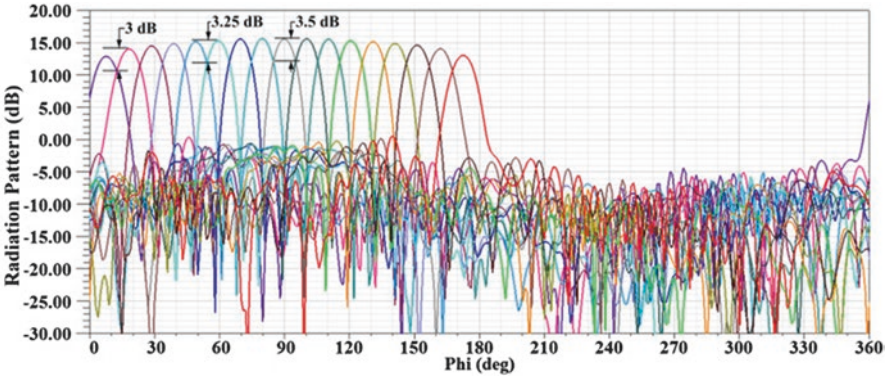

Fig. 15.17 Simulated 2D radiation pattern in azimuth plane ($\theta = 90°$) of 17 PLPDA feeds integrated with Luneburg lens

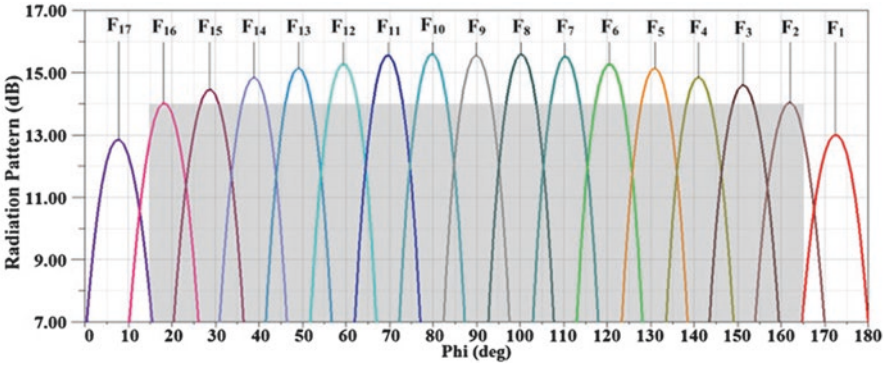

Fig. 15.18 Simulated 2D radiation pattern in azimuth plane ($\theta = 90°$) of 17 PLPDA feeds integrated with Luneburg lens (zoomed)

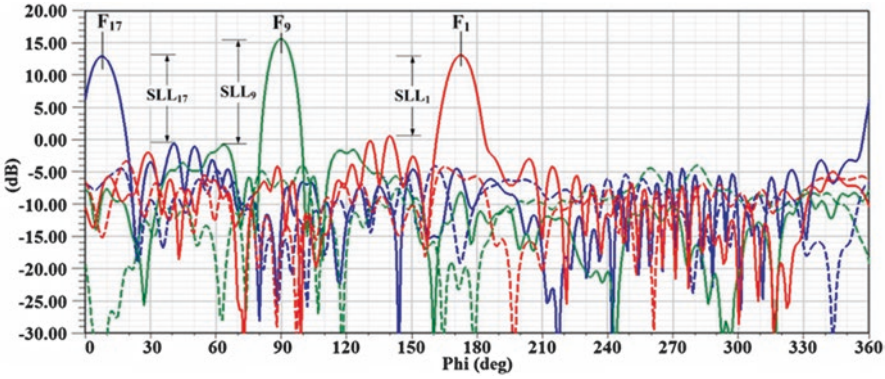

Fig. 15.19 Simulated 2D radiation pattern in azimuth plane ($\theta = 90°$) from 17 PLPDA feeds integrated with Luneburg Lens

The 2D radiation patterns from the three feeds, that is, center feed (F_9) and two feeds at the edges (F_1 and F_{17}) are shown in Fig. 15.19 for better understanding. The side lobe level (SLL) for the three feeds is found to be SLL_9 = 16.5 dB, SLL_1 = 13.6 dB, and SLL_{17} = 13.45 dB. The gain drop of approximately 2.5 dB at the edges is observed, which is attributed to scattering caused by the power radiated from F_1 passing through lens and facing F_{17}. This can also be observed in Fig. 15.20, where it can be seen that when the center PLPDA feed F_9 is active, the wave propagation is smooth through the lens. However, when the feeds at the edges (i.e., F_1 or F_2) are active, the wave propagation is not smooth and it experiences scattering from the presence of the PLPDA feeds at opposite end.

The simulated co- and cross-polarization radiation patterns in elevation plane (ϕ = constant) for feeds 1, 5, 9, 13, and 17 are shown in Fig. 15.21. The 3 dB beam width is approximately 30° for all cases. The SLL from PLPDA feeds at the edges (i.e., F_1 and F_{17}) is 4 dB, whereas for the middle feed (F_9), the SLL is found to be 7.75 dB.

The simulated maximum realized gain of the center feed (i.e., feed 9) and two feeds at the edges (i.e., feed 1 and feed 17) in required frequency band of operation (77–81 GHz) is shown in Fig. 15.22. The gain is maximum (>15 dB) from the center PLPDA feed (F_9) and decays when moving toward the feeds at the edges (i.e., F_1 and F_{17}) to a minimum value of approximately 13 dB.

Furthermore, it is important to mention that with the proposed design, by activating multiple feeds at the same time, a wider 3 dB beam width can be achieved. This is illustrated in Fig. 15.23. It can be easily seen that when one feed (F_9) is active, the 3 dB beam width is 10°. By activating more elements at the same time, the 3 dB beam width is widened to 28° (F_8, F_9, F_{10}) and 45° (F_7, F_8, F_9, F_{10}, F_{11}), respectively.

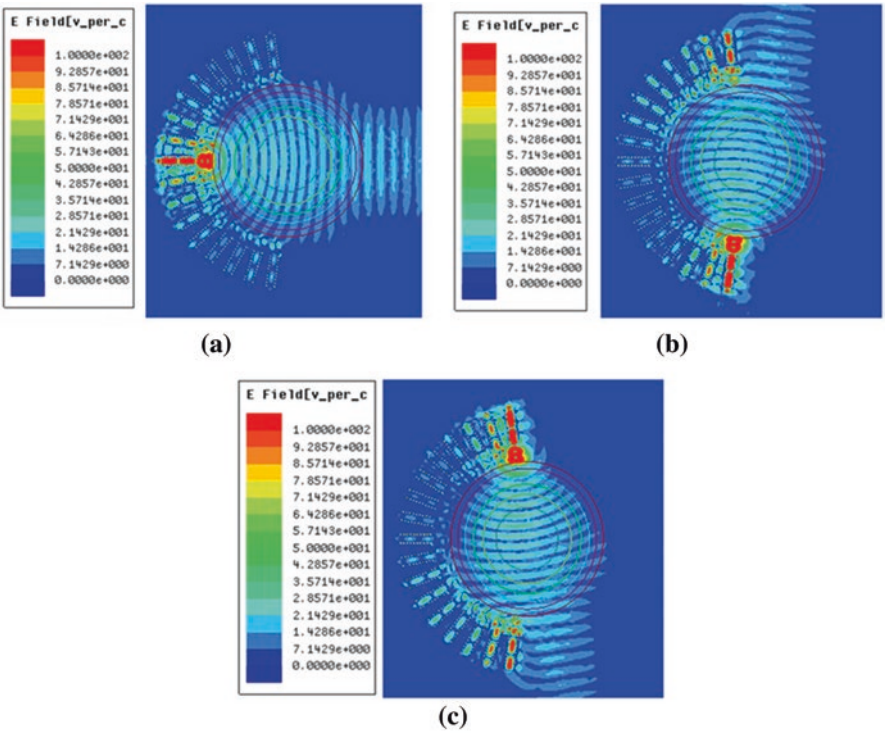

Fig. 15.20 E-field distribution in *XY* plane of 17 PLPDA feeds integrated with Luneburg lens. (**a**) Feed 9 is active, (**b**) feed 1 is active, (**c**) feed 17 is active

15.6 Antenna Fabrication and Measurements

The prototype fabrication is carried out in three steps:

- Fabrication of 6-layer Luneburg lens
- Fabrication of 17 elements PLPDA PCB on quartz substrate
- Integration of Luneburg lens and Quartz PCB along with W-band connector for measurements

The six-layer Luneburg lens is developed by following the approach given in [17], that is, pressing a basic foam material such as airex R82 (ε_r = 1.12) in controlled manner to obtain different permittivity values in required area to have a 3.5 mm final thickness. The air bubbles are removed from the materials by pressing it at 90 °C. So it becomes possible to control the dielectric constant of pressed foam by approximately choosing the right area density ratio $\xi = H_i/H_f$, where H_i is the initial foam thickness pressed to final thickness H_f. An initial foam cylinder-shaped slab is drilled with 2D mechanical processes to obtain the different areas with different thicknesses (Fig. 15.24), as reported in Table 15.3. Dielectric constant and

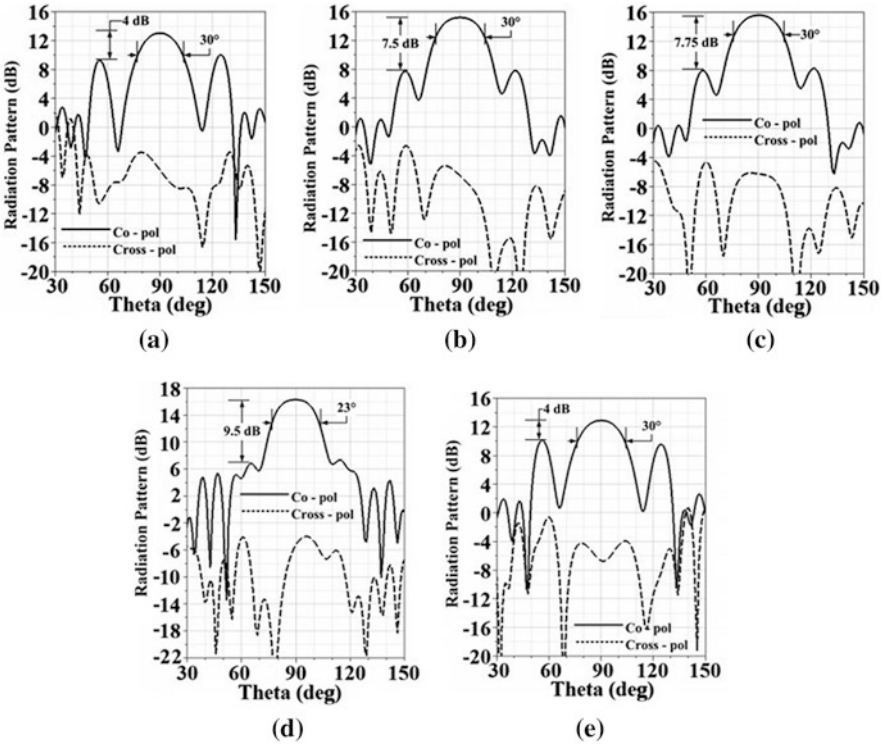

Fig. 15.21 Simulated 2D radiation pattern in elevation plane (ϕ = constant) from 17 PLPDA feeds integrated with Luneburg lens. (**a**) Feed 1 (ϕ = 173°), (**b**) feed 5 (ϕ = 131°), (**c**) feed 9 (ϕ = 90°), (**d**) feed 13 (ϕ = 49°), (**e**) feed 17 (ϕ = 8°)

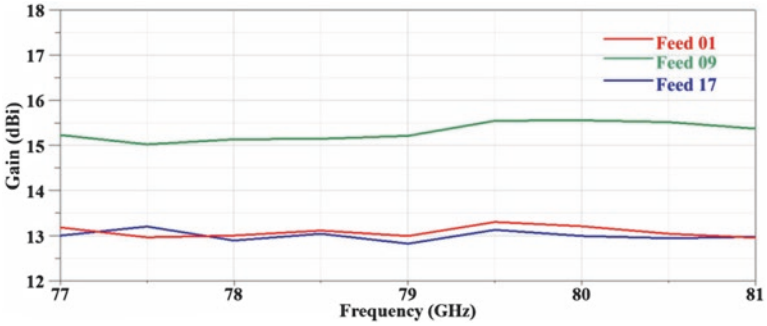

Fig. 15.22 Simulated maximum realized gain versus frequency from PLPDA feed 1, 9, and 17 of 17 PLPDA feed integrated with Luneburg lens

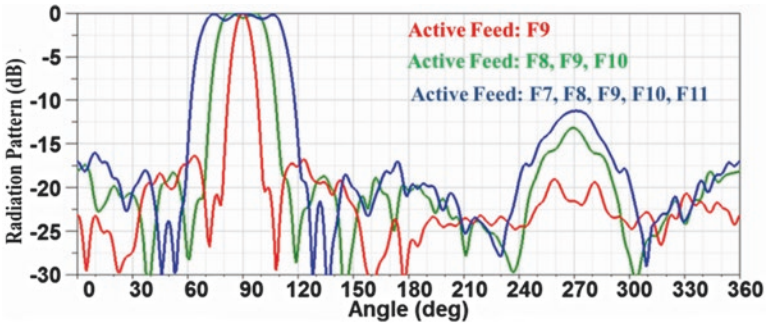

Fig. 15.23 Beam width control by activating multiple feeds at the same time

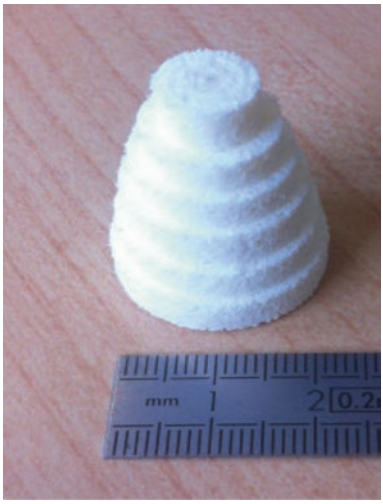

Fig. 15.24 Basic foam material in raw form for Luneburg lens fabrication

Table 15.3 Six-Layer Luneburg lens parameter values

	1	2	3	4	5	6
Radius	4.65	6.60	8.06	9.31	10.4	11.4
Permittivity	1.92	1.77	1.62	1.46	1.31	1.15
Loss tangent	0.015	0.014	0.013	0.01	0.008	0.007
$\xi = H_i/H_f$	8	6.5	5.35	4.2	2.75	1.5
H_i mm	28	22.75	18.725	14.7	9.625	5.25
H_{mf} mm	3.5	3.5	3.5	3.5	3.5	3.5

loss tangent of pressed foam have been measured using a characterization free space measurement setup composed of an AB Millimeter VNA and lens-horns antennas [18].

The fabricated six-layer Luneburg lens is shown in Fig. 15.25a. In Fig. 15.25b, the fabricated 17-element PLPDA array on quartz substrate is shown. To support the

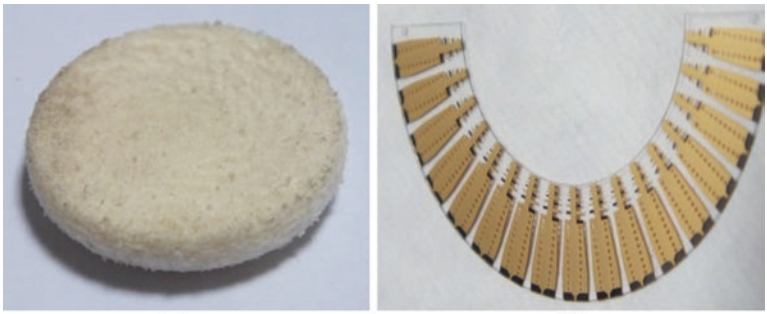

Fig. 15.25 Prototype fabrication. (**a**) Fabricated 6-layer Luneburg lens, (**b**) fabricated 17-element PLPDA array PCB on quartz substrate

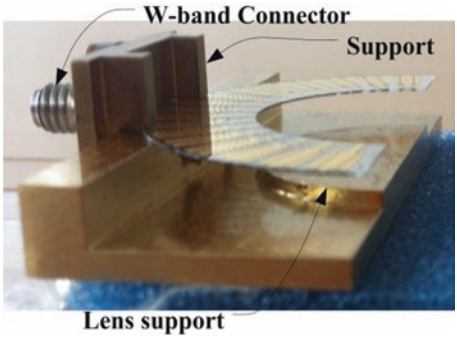

Fig. 15.26 Support for 17-element PLPDA array and Luneburg lens

17-element PLPDA array quartz PCB and align it with the six-layer Luneburg lens, a support is made, as shown in Fig. 15.26. The W-band connector is also included in the support to take measurements.

The 6-layer Luneburg lens and the 17-element PLPDA array on quartz substrate are integrated together, as illustrated in Fig. 15.27. The W-band connector is utilized for measurements and each PLPDA feed is activated individually by rotating the semicircular quartz PCB, as highlighted in Fig. 15.27a (feed 8 is active) and Fig. 15.27b (feed 17 is active).

It is important to mention that the inner connector of the W-band connector cannot be soldered to the antenna feed on quartz PCB. Furthermore, the substrate is quartz, which is highly rigid, and an excess pressure cannot be applied. During the measurement process, the inner connector of W-band connector is just barely touching the antenna feed on quartz substrate. The above-mentioned points can be considered for a small variation observed in measurements of return loss and radiation patterns. The return loss measurements are carried out by Vector Network Analyzer. The comparison between simulated and measured return loss for the three middle feeds (i.e., F_8, F_9, and F_{10}) is shown in Fig. 15.28. It is clearly evident that the antenna covers the required frequency band (77–81 GHz) of operation.

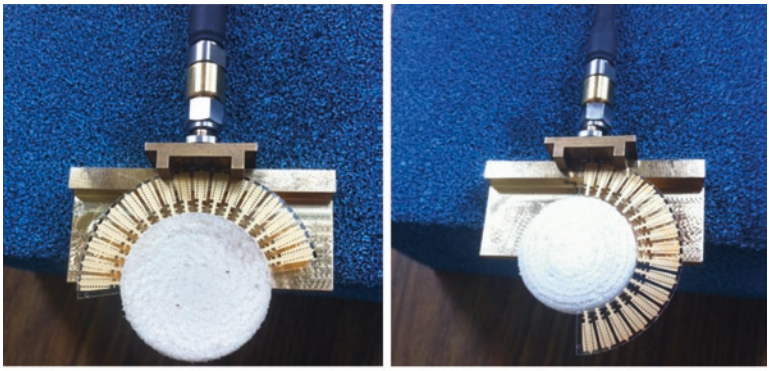

Fig. 15.27 The 17-element PLPDA array on quartz substrate integrated with Luneburg lens and W-band connector. (**a**) Feed 8 is active, (**b**) feed 17 is active

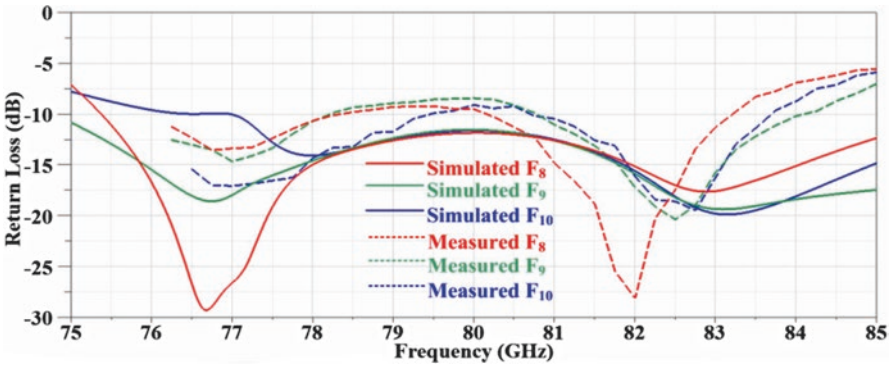

Fig. 15.28 Comparison between simulated and measured return loss for the three middle feeds (i.e., F_8, F_9, and F_{10})

The comparison between the simulated and measured co-pol radiation patterns at 79 GHz and 82.5 GHz is shown in Fig. 15.29. For clarity, the comparison is given for the three middle and two edge feeds (i.e., F_1, F_8, F_9, F_{10}, and F_{17}). A drop of approximately 2 dB is observed between simulated and measured radiation patterns at 79 GHz; whereas, for the comparison shown in Fig. 15.29b at 82.5 GHz, the simulated and measured radiation patterns are found to be in good agreement.

For a better understanding, the measured radiation patterns for all feeds (i.e., F_1, F_2, F_3, …, F_{17}) are shown in Fig. 15.30 at 79 GHz and 82.5 GHz. As shown in Fig. 15.30a, the worst-side lobe level of 10.51 dB below peak is found for the center feed (F_9), whereas, as shown in Fig. 15.30 b, the worst-side lobe level of 12.53 dB below peak is found for feed (F_{15}).

Finally, the gain measurements are done for the center feed (F_9) and a comparison between the simulated and measured realized gain is illustrated in Fig. 15.31.

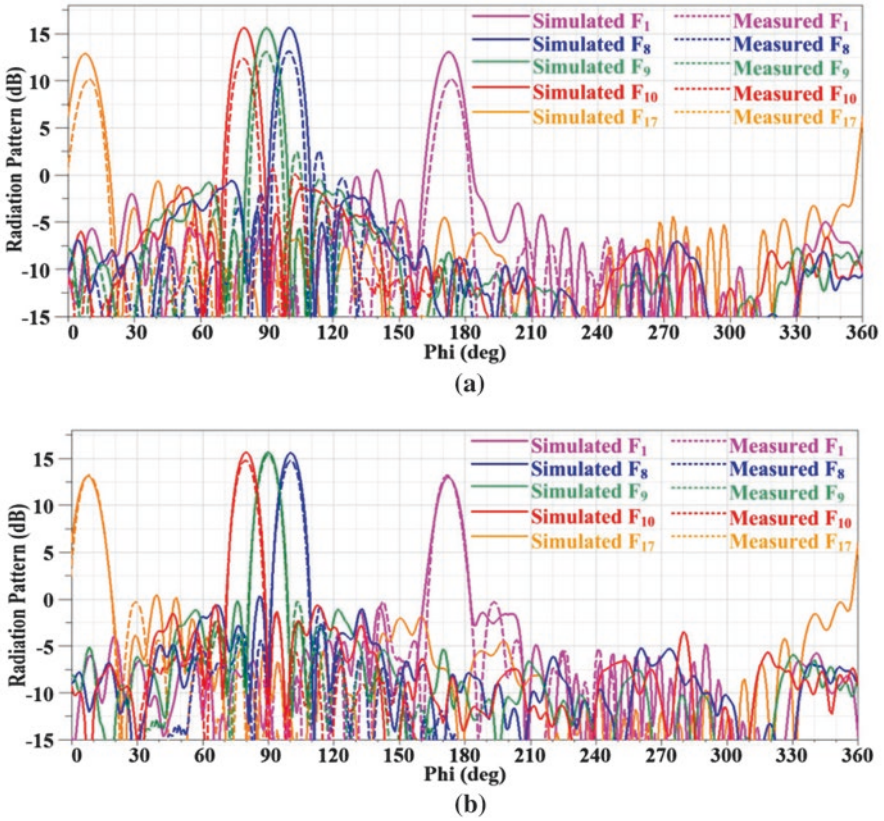

Fig. 15.29 Comparison between simulated and measured co-pol radiation pattern. (**a**) 79 GHz, (**b**) 82.5 GHz

15.7 Conclusion

This chapter presents the design and experimental results of an array of 17-element PLPDA integrated with Luneburg lens for 79 GHz beam scanning for automotive radar applications. The Luneburg lens is comprised of six cylindrical layers, with outer diameter and thickness of 22.8 mm and 3.5 mm, respectively. The source antenna array placed in close proximity of Luneburg lens consists of 17-element PLPDs integrated with SIW. The SIW is contacted to microstrip line through a triangular transition. The beam scanning can be accomplished by switching between the antenna elements in the array. The measured impedance bandwidth of the proposed antenna array is found to be 76–83 GHz, which is well in excess of the required 77–81 GHz frequency band allocated for 79 GHz radar applications. The maximum gain is achieved for the center feed (F_9), which is experimentally found to be 13.05 dB and 15.38 dB at 79 and 82.5 GHz, respectively. The minimum gain

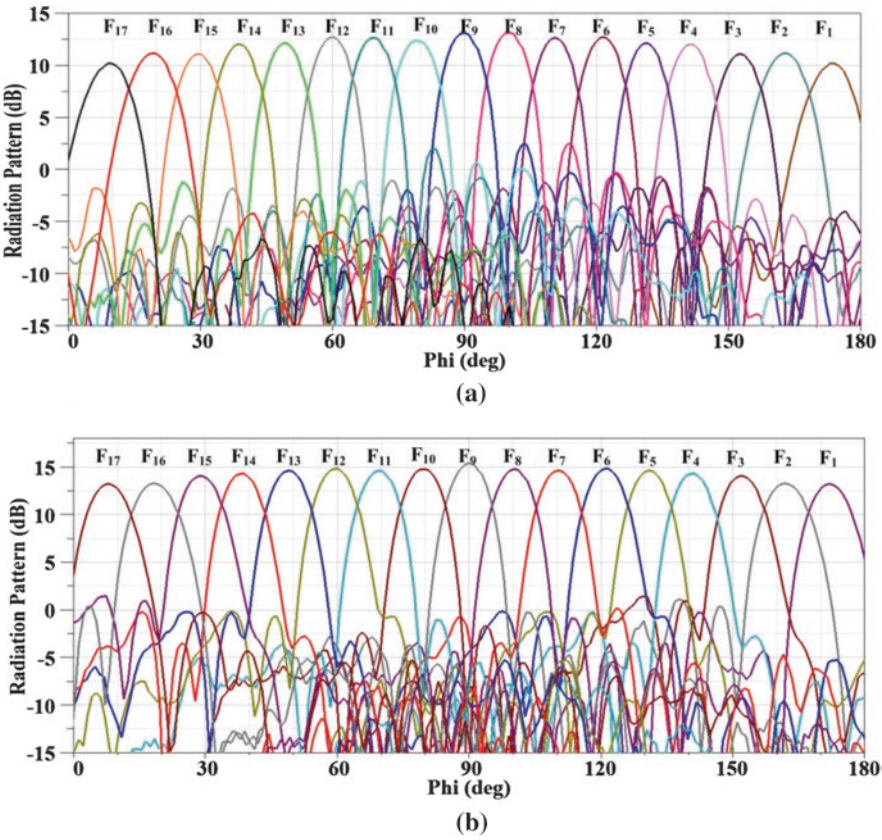

Fig. 15.30 Measured radiation pattern of all feeds F_1, F_2, F_3,…, F_{17}). (**a**). 79 GHz, (**b**) 82.5 GHz

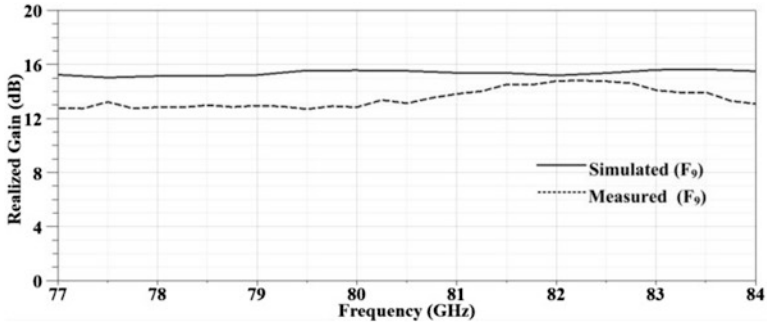

Fig. 15.31 Comparison between simulated and measured gain for center feed (F_9)

is found to be for the feeds at the edges (F_1 and F_{17}), which is experimentally found to be 10.15 dB and 13.2 dB at 79 GHz and 82.5 GHz, respectively. The obtained results demonstrate that the proposed antenna array integrated with Luneburg lens can be utilized as steerable directional antenna for 79 GHz radar applications.

References

1. R.H. Rasshofer, K. Gresser, Automotive radar and lidar systems for next generation driver assistance functions. Adv. Radio Sci. **3**, 205–209 (2005)
2. S. K. P. Zador , R. Vocas, Final Report-Automotive Collision Avoidance (ACAS) Program, Tech. Rep. DOT HS 809 080, NHTSA, U.S. DOT, Aug. (2000)
3. J.L. Kuo, Y.F. Lu, T.Y. Huang, Y.L. Chang, Y.K. Hsieh, P.J. Peng, H. Wang, 60-GHz four-element phased-array transmit/receive system-in-package using phase compensation techniques in 65-nm flipchip CMOS process. IEEE Trans. Microw. Theory Tech. **60**(3), 743–756 (2012)
4. H. Kirino, K. Ogawa, A 76 GHz multi-Layered phased array Antenna using a non-metal contact metamaterial waveguide. IEEE Trans. Antennas Propag. **60**(2), 840–853 (2012)
5. K.A. Zimmerman, D.L. Runyon, Luneburg lens and method of constructing same, U.S. Patent 5 677 796, 14 Oct 1997
6. K. Strohm, H.-L. Bloecher, R. Schneider, J. Wenger, Development of future short range radar technology. IEEE Trans., in *European Radar Conference* (Paris, France, Oct 2005), pp. 165–168
7. J. Hasch, E. Topak, R. Schnabel, T. Zwick, R. Weigel, C. Waldschmidt, Millimeter-wave technology for automotive radar sensors in the 77 GHz frequency band. IEEE Trans. Microw. Theory Tech. **60**(3), 845–860 (2012)
8. B. Schoenlinner, X. Wu, J.P. Ebling, G.V. Eleftheriades, G.M. Rebeiz, Wide-scan spherical-lens antennas for automotive radars. IEEE Trans. Microw. Theory Tech. **50**(9), 2166–2175 (2002)
9. O. Lafond, M. Himdi, H. Merlet, P. Lebars, An active reconfigurable antenna at 60 GHz based on plate inhomogeneous l ens and feeders. IEEE Trans. Antennas Propag. **61**(4), 1672–1678 (2013)
10. C. Hua, X. Wu, N. Yang, W. Wu, Air-filled parallel-plate cylindrical modified Luneberg lens antenna for multiple-beam scanning at millimeter-wave frequencies. IEEE Trans. Microw. Theory Tech. **61**(1), 436–443 (2013)
11. Y.S. Zhang, W. Hong, A millimeter-wave gain enhanced multi-beam antenna based on a coplanar cylindrical dielectric lens. IEEE Trans. Antennas Propag. **60**(7), 3485–3488 (2012)
12. C.A. Balanis, *Antenna Theory: Analysis and Design* (John Wiley & Sons, New York, 2012)
13. C. Campbell, I. Traboulay, M. Suthers, H. Kneve, Design of a strip line log periodic dipole antenna. IEEE Trans. Antennas Propag. **25**, 718–721 (1977)
14. R. Carrel, The design of log-periodic dipole antennas, in *IRE International Convention Record*, vol. 9, (IEEE, New York, USA, 1966), pp. 61–75
15. Ansys HFSS, v14, ANSYS Corporation Software, Pittsburgh, PA, USA, 2014
16. B. Fuchs, L. Le Coq, O. Lafond, S. Rondineau, M. Himdi, Design optimization of multishell Luneburg lenses. IEEE Trans. Antennas Propag. **55**(2), 283–289 (2007)
17. M. Kamran Saleem, H. Vettikaladi, A.S. Majeed, Alkanhal, M. Himdi, Integrated lens antenna for wide angle beam scanning at 79 GHz for automotive short range radar applications. IEEE Trans. Antennas Propag. **65**(99), 2041–2046 (2017)
18. H. Merlet, P. LeBars, O. Lafond, M. Himdi, Manufacturing method of a dielectric material and its applications to millimeter-waves beam forming antenna systems, U.S. Patent App.14/362,901, 7 Dec 2012

Chapter 16
Terahertz Communications for 5G and Beyond

Nadeem Naeem, Sajida Parveen, and Alyani Ismail

16.1 Terahertz Waves

There is no exact designation of what characterizes as terahertz (THz) frequency [1]. The terahertz frequency band of the electromagnetic spectrum is mostly defined as the higher frequency range starting from 0.1 to 10 THz, as illustrated in Fig. 16.1. Common considerations are that such frequency region for terahertz is bounded between 100 GHz and 10 THz, which is more or less equal to wavelength of 10^{12} cycles per second with the quantum energy between 0.4 meV and 0.4 eV [2].

There are several properties of THz electromagnetic waves that could promote their use as an effective sensing and imaging tool. Since terahertz wave has no ionization effect, it is useful for biological tissue and other radiations including Rayleigh scattering of electromagnetic radiation, which is many orders of magnitude less for THz waves than for the neighboring infrared and optical regions of the spectrum. THz radiation is highly useful in security screening for concealed weapons and it can also penetrate nonmetallic materials such as fabric, leather, and plastic. The molecular rotations and vibrations of DNA and proteins, as well as explosives, have energy levels corresponding to THz waves and can provide characteristic distinctive signatures to separately identify biological tissues in a region of the frequency spectrum that is not previously researched for medical use or for detection and identification of trace amount of explosives.

N. Naeem (✉)
Department of Electronic Engineering, QUEST, Nawabshah, Pakistan
e-mail: nadeemnaeem@yahoo.com

S. Parveen
Department of Computer Systems Engineering, QUEST, Nawabshah, Pakistan

A. Ismail
Department of Computer and Communication Systems Engineering, Universiti Putra, Serdang, Malaysia

I. Elfergani et al. (eds.), *Antenna Fundamentals for Legacy Mobile Applications and Beyond*, DOI 10.1007/978-3-319-63967-3_16

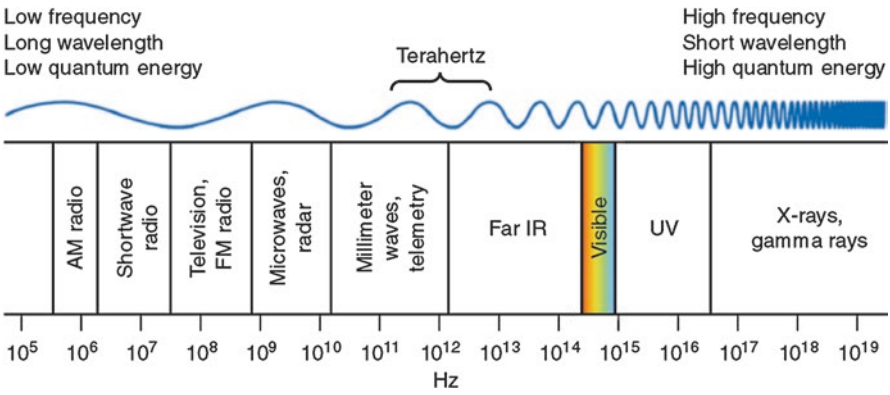

Fig. 16.1 Electromagnetic spectrum showing THz Frequency band [2]

THz wavelengths are particularly sensitive to water and they can demonstrate an absorption peak, which makes this technique very sensitive to hydration state and can indicate tissue condition. Characterization of semiconductor materials has been used in the THz radiation and in testing and it is also used in failure analysis of integrated circuits [3].

A photon is characterized by either a wave length λ or photon energy denoted by E [4]. The wavelength (or frequency) and energy are related with each other through an inverse relationship provided in Eq. (16.1):

$$E = \frac{hc}{\lambda} \tag{16.1}$$

where E is the energy of the photon, the Planck's constant is $h = 6.626 \times 10^{-34}$ J/s, and the speed of light is denoted as $c = 2.998 \times 10^{8}$ m/s.

The common measuring unit of energy is electron-Volt (eV) rather than Joule (J) when dealing with particles like photons or electrons. The electron-Volt is the energy required to raise an electron by 1 Volt, therefore, a photon has energy equal to 1.602×10^{-19} J. The product of $hc = 1.99 \times 10^{-25}$ J/m. This hc product can be written in electron-Volt as $hc = (1.24 \times 10^{-25}$ J/m) $\times$ (1 eV/1.602×10^{-19} J) = 1.24×10^{-6} eV/m. The link between frequency, wavelength, and quantum energy is shown in the electromagnetic spectrum in Fig. 16.1.

Terahertz frequency band has been ignored in the electromagnetic frequency spectrum that later realized to be explored through scientific research. This was due to the fact that there was limited handling capability of the existing microwave and infrared technology at that time. Nowadays, the rapid progress in the field of terahertz science is greatly contributed by increasing nanotechnology. Many applications that require advanced level of handling expertise find their way in terahertz. This is because of the electromagnetic characteristics inherited by terahertz from millimeter and infrared waves.

16.2 Applications of Terahertz

With lower quantum energy of terahertz frequency in the electromagnetic spectrum compared to infrared and higher frequency, calls for many potential applications that are unique to them. Some aspects of potential applications are discussed in this chapter. The major application category of today's THz technology focuses on spectroscopic analysis, sensing, imaging, and in antennas. Near-field imaging for subwavelength-scale small features is a remarkably fast advancing field in this category. Communication is also one of the promising applications for THz frequency band.

16.2.1 Terahertz Spectroscopy

Spectroscopy is one vital application of terahertz innovation that emerged from the qualities of the emanation or assimilation details for the rotational and vibrational excitations of the particles. To create diverse strategies to straightforwardly screen out the complex real-time molecular dynamics, it has been proposed that atom level picture of the deliberate movements of polypeptide chains and DNA can be open through precise estimation of low-frequency vibrational spectra. These vibrations are trusted to occur in the terahertz spectrum regime. Identification of DNA signatures through dielectric resonance is an alternate intriguing consequence that has got to be feasible because of possible estimation and quickly recognizable proof of diverse spectral signatures by terahertz spectroscopy instruments [5]. The frequencies of THz are of great important for biosensing applications since numerous characteristic vibrational modes of macromolecules such as proteins and DNA are placed in this frequency range. This coincidentally opens up the possibility for label-free biosensing [5]. THz time-domain spectroscopy (THz-TDS) has been the primary and key technique for demonstrating the potential applications of THz technology. A typical THz-TDS system, as depicted in Fig. 16.2, includes an ultrafast laser (e.g., Ti-Sapphire laser) that produces optical pulses in femtosecond (10^{-15} s) durations. Each pulse is separated into two optical paths. One path travels through a time delay stage and hits the emitter, such as a photoconductive antenna or a nonlinear crystal, at which point the optical pulses are converted into ultrashort electromagnetic pulses. The generated electromagnetic (EM) pulses are focused onto the sample under test and collimated again so that they are focused onto the detector. The other part of the pulse is also delivered onto the detector directly. The detector measures the amplitudes of the electromagnetic waves in order to evaluate the change in the waveform due to the sample. By altering the delay time between the two beams, it will be feasible to scan the THz pulse and construct its electric field as a function of time. Consequently, in order to extract the frequency spectrum from time-domain data, a Fourier transform may be exploited. Comparison of the waveforms with and without the sample allows the estimation of the complex refractive

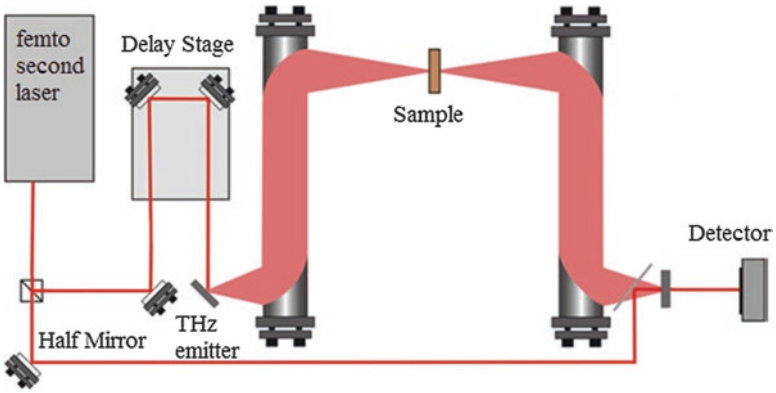

Fig. 16.2 Simplified schematic of a typical THz-TDS system [2]

index of the material, which yields other parameters, such as the dielectric constant, conductivity, and surface impedance. Regardless, this system has been largely utilized in research facilities. However, due to its complexity and size, this results in preventing widespread deployment particularly in out-of-lab applications [2].

16.2.2 Terahertz Imaging

Terahertz has increasingly attracted the attention of scientists in the field of imaging. There are some significant reasons, the biggest being that the terahertz wave is a nonionizing radiation. It also actuates the rotational or vibrational aspect of a molecule but does not disturb its electronic state. This means that terahertz radiation is more secure than other radiations. Terahertz radiations are able to infiltrate a wide assortment of nonconducting materials. Numerous materials, for example, plastics, cardboard, fabrics, and biological tissue are transparent to terahertz radiation and these materials leave spectral fingerprints when terahertz radiation passes through them [6]. In comparison to the wavelengths of visible spectrum, the wavelengths related to the terahertz frequency could reduce Rayleigh scattering. There exists plenty of information on the reflection, absorption, and transmission of distinctive materials. It is commonly considered that transmission response diminishes as the resonant frequency increases, but the measurable readouts for distanced items can still be determined. The discovery of hidden objects is possible with terahertz radiation. Light waves and terahertz radiation possess the same electromagnetic properties, which is how terahertz waves propagate through space.

Terahertz radiation can be reflected and refracted with the help of terahertz devices. In imaging applications, a high spectral resolution can be achieved with shorter terahertz wavelengths than other radiations. The other applications of terahertz imaging are the discovery of hidden fire arms, land mines and bombs, medical imaging, and the study of human cell tissues, real-time monitoring of biological

and chemical concealed weapons and checking of luggage at the airport, as well as quality control checking of semiconductors [7]. Calculation of refractive index, amplitude and phase, biological sample thickness, and monitoring of signal strength using imaging based on transmitted or reflected terahertz waves from a considered sample can be done with the help of terahertz time-domain spectroscopy.

The operation of imaging involves the generation and then detection of the terahertz electromagnetic signal. An intense femtosecond optical laser produces this signal. The pulses generated energize the charge carriers so much that they overcome their energy band gap and pairing thus occurs. The pairing causes static current to flow. If the drift time is further shortened, then the flowing current will generate waves. The image of the sample can be observed with the help of an imaging system that uses a separate charge coupled device; each one gets a separate measurement of the primary colors that are red, green, and blue [2].

Terahertz radiations are very useful in pharmacological- and security-related applications because terahertz can penetrate many materials. Due to these characteristics, terahertz can be used to find hidden objects under clothes and packets of low-energy photons. The nonionizing characteristic of terahertz radiation allows THz waves to be used in noninvasive and nondestructive inspection via spectroscopy. Monitoring and maintaining quality control of goods is yet another application for terahertz imaging.

16.2.3 Terahertz Sensors

This section describes the basic understanding of terahertz sensors, which are an important part of T-wave technology. So, it is important to understand the sample deposition on terahertz sensors. There are three basic methods of depositing samples on the surface of sensors:

1. Under layer
2. Over layer
3. Split gap area

Almost all metamaterial terahertz sensors are designed to sense the presence of the samples in the methods mentioned earlier [8–10]. When the sensor that is composed of split-ring resonators is excited by external fields, the current flows on the surface of the sensor and surface electric field is established. The geometry of the resonator is such that it has gap areas at the splits of the rings. Some structures have single gap and others can have more than single split gaps, depending upon the geometrical structure of the sensor. The gap areas can be considered as analogous to the parallel plate capacitors where most of the electric field is localized in between them, as compared to the other parts of the sensor [11]. The longer continuous strips serve as inductive elements and they can be represented as inductors. The sensor operates at the frequency when energy stored in inductive element is in balance with the energy stored in capacitive element. The electric field changes itself when a

sample of different dielectric constant is inserted into the sensor, which causes the change in refractive index, which in turn changes the location of resonance frequency in terms of transmission (S_{21}) or reflection (S_{11}) coefficients of the sensor on the frequency domain [12]. This shift in the transmission is different from that of pure LC transmission resonance when the sample is not loaded on the sensor's surface or in the gap areas.

Generally, under layer loading takes place when the sample is deposited under the sensor's surface and above the substrate or base materials. Variations in sensors designs allow samples to be place under cuts with complementary structures also. Under layer sensing can be visualized in Fig. 16.2 and the shift in the resonance frequency in Fig. 16.3.

Over layer sensing method is widely used by planar terahertz sensors in which the sample under test is deposited above the substrate on the split-ring resonator. The thickness of the samples varies based on the geometric size of the resonators. This has been the popular method for getting high Q factor planar metamaterial sensors. The resonant frequency shifted down or upward on the frequency domain according to the dielectric constant of the sample to be tested. Figure 16.4 shows an example of sensing over layer through cross shaped and the complementary cross absorber as terahertz sensor.

The incident electric field and wave vector direction as shown in Fig. 16.5, the excited electric fringing fields above the absorber surfaces at resonance are schematically illustrated. When the lossless analyte of different refractive indices is deposited on the top surface of cross-sensor and complementary to cross, the change in electric and magnetic field distribution would lead to different frequency and amplitude response. The total frequency shift is about 130 GHz and the resonance amplitude change is 56.6% for the identical range of variation in the refractive index. The Q factor of the resonance reflection spectra for cross-absorber is 7.036 and for complementary to cross-absorber is 7.189.

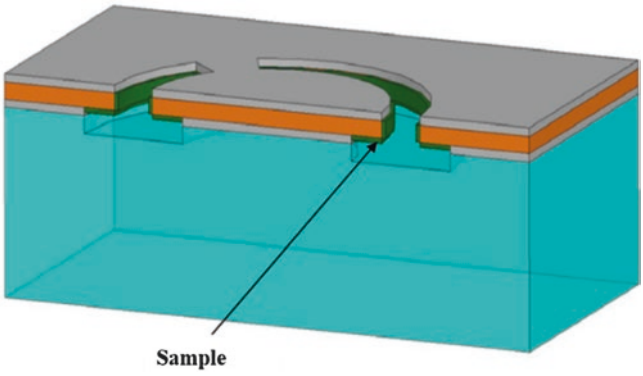

Fig. 16.3 Cross-section view of complementary asymmetric double split-ring resonator [8]

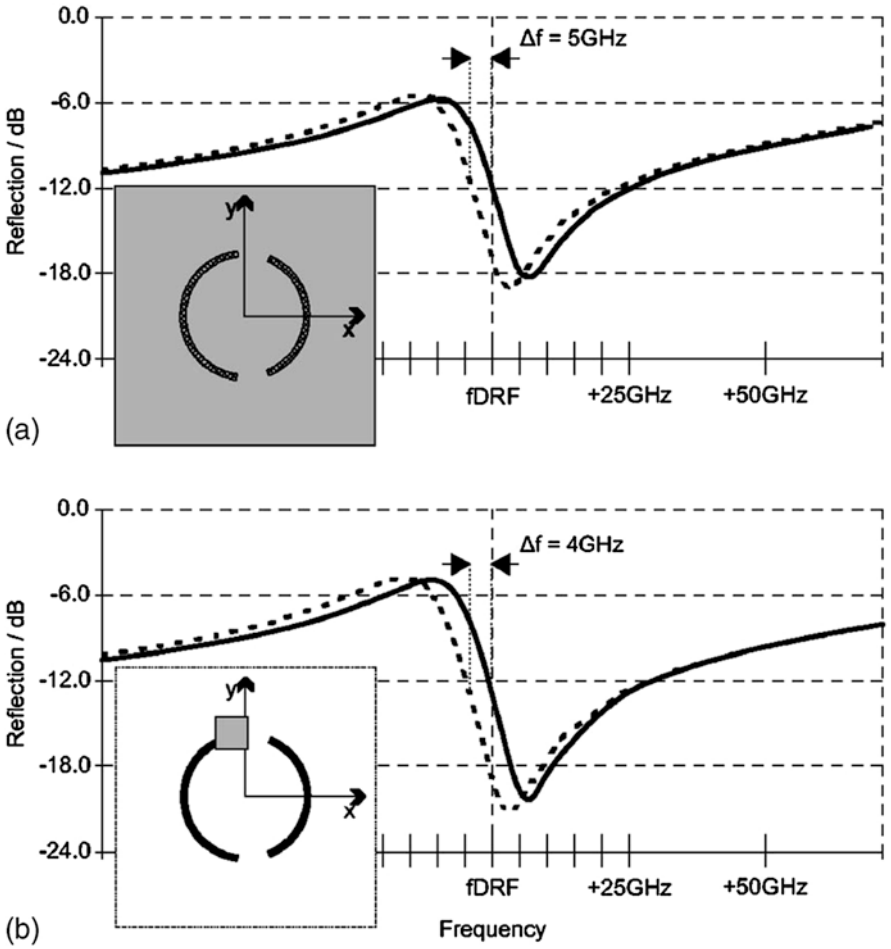

Fig. 16.4 Observed shift in resonance frequency after loading of sample [8]

Split gap sensing method is mostly used in sensor designs where surface electric field distribution is highly localized at split gaps of the sensors. The sample under test is placed near or in the gaps to interrupt the electric field, thereby causing it to change, which further shifts down the resonance frequency of the sensor. That frequency shift indicates the presence of the sample of particular dielectric characteristics. Successful implementation of terahertz sensors for sensing microorganisms and biomolecules are available in the literature. Figure 16.6 shows the terahertz sensor with gap sensing biomolecules with change in resonance.

In case of split gap sensing, the dielectric environment of small split gap area is important to consider here in this experiment. The frequency shift in terms of transmission change appears when the capacitance in between the split gap changes. This is because of filling up of the gap area, which alters the capacitance according

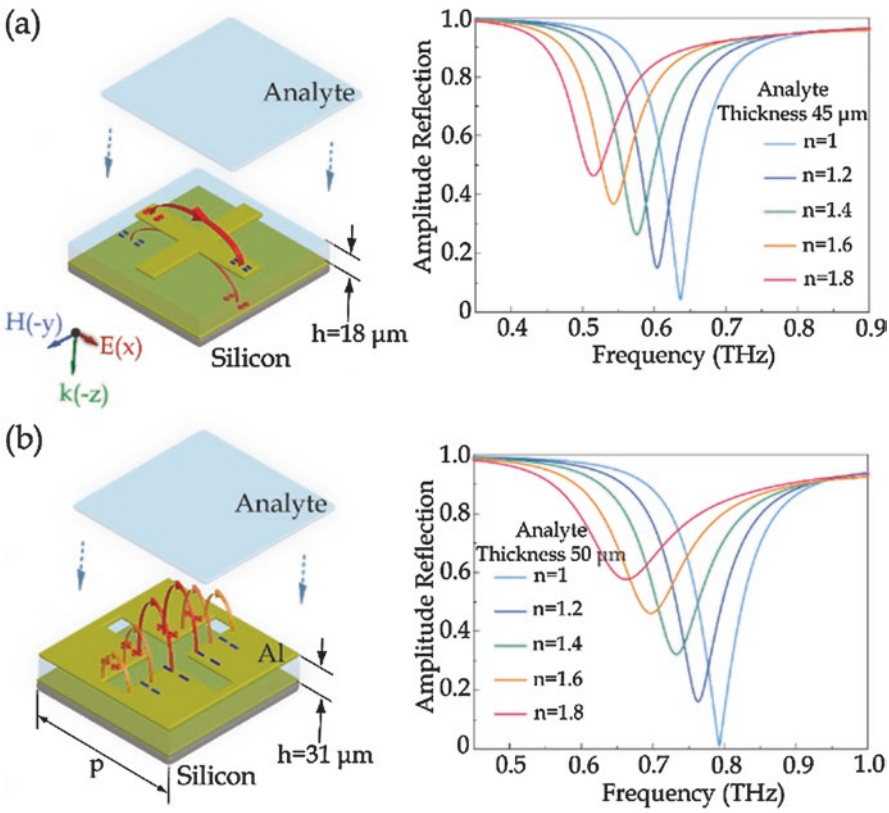

Fig. 16.5 (**a**) Cross-shape terahertz sensor. (**b**) Complementary cross-absorber [9]

to $C = \varepsilon A/d$, where A is the area of the strips, d is for the distance between the splits, and ε is dielectric constant of the capacitor. It can be observed that the presence of microorganisms in terms of testing sample increases the values of dielectric constant, which results in shifting of frequency response.

In recent years, metamaterials have proved their worth in terahertz frequency operated applications because of the nonionizing characteristic of terahertz radiation that makes it harmless when interacting with live cells or human body [13]. However, thin layer dielectric sensing in terms of resonant metamaterial structures denotes a promising direction, above all for high sensitivity recognition.

In general, metamaterial is prepared from a pool of subwavelength resonators; its frequency response is made according to its shape and geometrical dimensions [14]. This means that these are made resonant at terahertz frequencies mainly by simple scaling [9]. Additionally, these are organized in effectively homogeneous structures, easily explored with conventional THz-TDS having no adjustments to the system configuration. Therefore, metamaterials proposed a very much stretchy method as paired to new sensing schemes for instance waveguide sensors and resonator-based terahertz filters. Similarly, metamaterials are intended as three-dimensional (3D)

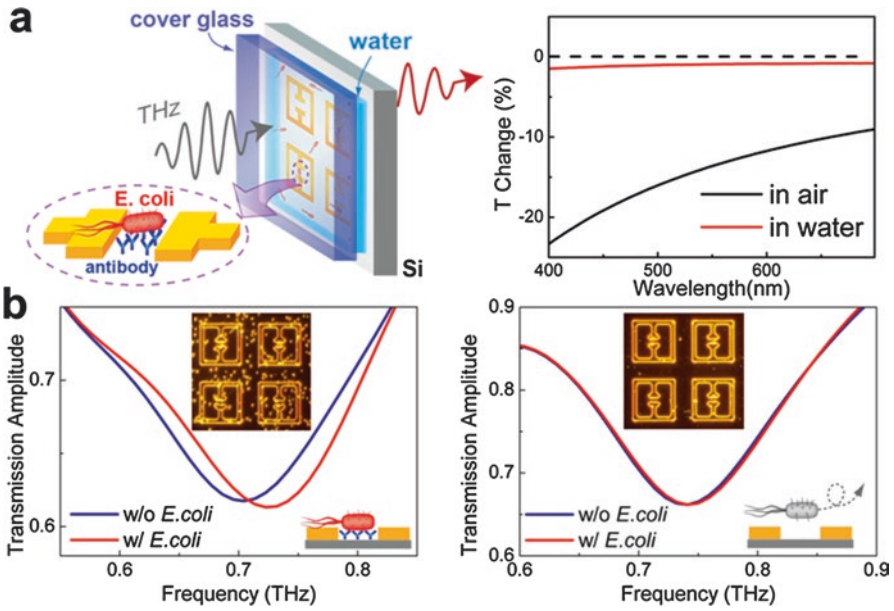

Fig. 16.6 Terahertz biosensor for detection of *Escherichia coli* bacteria (**b**) Transmission spectra of the quartz coated by *E. coli* [10]

structures completely discussed planar metamaterials as the advanced and further agreeable to thin-film sensing.

Planar metamaterials are considered as metafilms or metasurfaces that incorporate very much related technology of frequency selective surfaces (FSS). Metamaterials are intended either for bandstop or bandpass spectral reaction. It has been described that each resonator in a metamaterial is naturally composed of a metallic loop with a split [15]. This resonator reveals Lorentz resonance response over excitation due to an incident wave. This response is analogous and is accessible from a lumped *LC* circuit with capacitance *C* and inductance *L* resolute by the properties of the dielectric gap and the metallic loop. The corresponding relationship can be observed in Eq. (16.2):

$$f_r = \frac{1}{2\pi\sqrt{LC}} \tag{16.2}$$

16.3 Terahertz Biosensors

It was demonstrated that the ever-changing resonance frequency of a split-ring resonator array was developed to sense a silicon layer thinner as compared to the skin depth of terahertz radiation [16]. The sample comprised of silicon nanospheres based on the 50 nm in diameter put off in an ethanol solution which was dropped on

the metamaterial while the ethanol was evaporated by separating the silicon nanospheres. These produced a change of the ultimate resonance to lower frequencies at about 0.05 THz as compared to the original resonance of 1.2 THz. The experimentations presenting the impact of 50 nm shrill liquid layers (double-distilled water, ethanol, and chloroform) are also studied as the same [17]. These liquid layers produced red shifts in the resonant spectra signifying a positive demonstration of detection as was expected. Both fundamental resonances and higher-order SRR resonances expose these changes in order to be utilized. Additionally, multiple resonance effects were controlled in different SRR designs later to form super lattices by interposing SRRs of different size and shape into hexagonal and square unit cells [18]. Different under-patterns consisting of one, two, or three are used in the superpattern by allowing the same number of resonances to be excited consecutively by using resonant frequency shifts at three different frequencies, which expands the measurement accurately. This technique is used to rebut the possible false positive proof of identity. The constraints of this methodology are obviously significant in contemporary applications.

Successful demonstrations were conducted for detection of living organisms with the help of metamaterials operating in terahertz frequency [10]. A thin layer was set down in three separate places for sensitivity comparisons including the gaps of the SRRs, between the Si substrate and the SRR array as an intermediate layer, and on the SRR array as an over layer [19]. The detected percentage shifts include 0.71% with a 0.7 μm AZ6612 photoresist sample, 10.5% with a 1.7 μm SU-8 photoresist sample, and 1% with a 1.8 μm SU-8 photoresist sample. Moreover, the sensitivity is very high for the second case, which is not practical to keep the analyst under the metalized SRRs. The result indicates the importance of tuning the entire metamaterial to elevate sensing. It was revealed that paper metamaterials could be used as terahertz sensors [20]. The micrometer-sized metamaterial structures were placed straight onto 280 μm thick paper substrates with predefined microstencils. Glucose solutions with concentrations ranging between 3 and 30 millimoles per liter (mmol/L) were put on the paper. A maximum shift of about 300 GHz was observed in measuring the 30 mmol/L glucose solution coated sample. The minimum possible measurable frequency change for the experimental configuration was about 5 GHz and assuming a linear relationship between the frequency shift and the concentration of the glucose solution. It was estimated that a change of 0.35 mmol/L in glucose level can be identified with a base glucose level of 5.5 mmol/L. This is a medicine-related application. However, research showed that precision and sensitivity are vital at low glucose concentrations. Marketable glucose needs an accuracy of ±1 mmol/L for glucose levels less than 5.5 mmol/L typically meters. This specific approach to metamaterial sensing can be upgraded by assuming more innovative approaches utilizing different compositions and SRR geometries. This technique's sensitivity looks as if it is not too far uninvolved from real-world applicability.

All studies on metamaterial-based terahertz biosensors mostly emphasize on increasing the sensitivity by maximizing a change in the resonance frequency in terms of a deposited film. Biological sample thickness is considered due as small as hundreds

of nanometers. The spot size of the probing terahertz beam is restricted because of the total volume of the sample that is fundamentally limited by diffraction. The reduction in the amount of sample would be critical in some applications. A close-field source is used in conjunction with a metamaterial-based sensor to decrease the least spot size and the required sample volume [21]. A focused beam terahertz near-field system can narrow the sensing spot on an SRR-based metamaterial to 0.2λ in diameter or equivalently 3×3 resonators. Therefore, a number of stimulated resonators were reduced and the intercell couplings were also narrowed. This efficiently headed to a devepolment in achieving higher Q factor in comparison to the far-field measurement.

16.4 Terahertz Antenna

Due to the remarkable advancement of wireless communication network and system, the future wireless generation requires systems that have enormous wideband features in high mobility environment. To meet the requirements of such applications, ranging from personal communications to home, car, and office networking with high data rates, high spectral efficiencies and effective fading mitigation are required to be accomplished. Owing to its specific specification and roles, the type of microstrip antennas simultaneously satisfy the constraint requirements with regard to the geometrical features such as compact volume, light-weight, adaptability to actual platform and nonobstructive to user, broad bandwidth, radiation properties, high-efficiency, reconfigurability, suitability for diversity as well as the low cost of fabrication and packaging. To achieve a wireless communication system with several advantages such as wide bandwidth, high data rates, low latency, better directivity, and low potential interference with other systems, the frequencies higher than microwaves may meet these requirements. The THz electromagnetic spectrum may be considered a promising option to meet all the above-mentioned requirements for the envisaged and future communications.

Terahertz portion of electromagnetic spectrum is of vital interest to engineers and system designers due to the availability of broad bandwidth that plays important role in future communication. Moreover, with the main practical benefit of using the THz system in satellite communication systems, the THz regime has the capability to employ compact antennas in transmitter and receiver sides [22–27]. By definition, the spectrum of THz is the frequency range between the microwave and optical frequencies, which is defined as the band from 0.1 to 10 THz [22–24].

This radiation of THz spectrum is seen as a good candidate for use in several emerging technologies and applications. These include sensing, imaging and communication, with unique applications to screening for weapons, explosives, and biohazards, imaging of concealed object water contents and skin [23–26]. Despite the rapid exploitation of THz systems in various areas of research, the lack of practical and compact sources has led to the limitations of using the THz over a large scale. Several attempts have been made to get the practical sources operating at the

THz frequencies, but no THz sources currently satisfy size, output power level, and operating temperature requirements.

Microstrip antenna is key for the THz wireless communication system. Using carrier frequencies above 300 GHz, oscillator and amplifier sources with approximately 10% fractional bandwidth would enable very high data rate (>10 GB/s) wireless communications with high security protection [27]. Such features may be easily realized with tremendously simple and low-cost amplitude modulation schemes, when the sufficient, compact, and broadband sources are obtainable.

Photoconductive antennas are an alternative THz source due to their compact volume as well as broad configurability at room temperature [28, 29]. However, this type of antenna has the drawback of low output power, which is attributed to high impedance inherent to a photomixer.

For more clarification, while the antenna that has a moderate input impedance is joined to a photomixer, the power that is transmitted from the photomixer to this antenna will be poor because of the severe mismatching of the impedance. The mismatching that takes place between the photomixer and the antenna may be overcome if the resistance of the antenna increased; this will lead to enhancing the radiated power from the antenna [30–32].

Generally, the size of the microstrip patch antenna mainly depends on the frequency band of operation. However, there are many other parameters that may contribute to determining the geometrical dimension of the microstrip antenna and its behavior; these factors include the substrate material and the thickness of this substrate [33, 34]. The patch material influences the efficiency of the antenna, while the type of substrate plays a major role in the determination of the antenna dimensions [35, 36]. A common shape of the microstrip patch antenna is the rectangular shape. The rectangular microstrip patch antenna consists of a conductive rectangular patch on a dielectric substrate above a conductive ground plane, as shown in Fig. 16.7.

The microstrip patch antenna can be excited by using microstrip feed-line [37, 38]. This feeding-line approach provides the electrical signal to radiating patch, which will be converted into an electromagnetic wave. The geometrical structure of this THz rectangular microstrip patch antenna is as shown in Fig. 16.7. In this

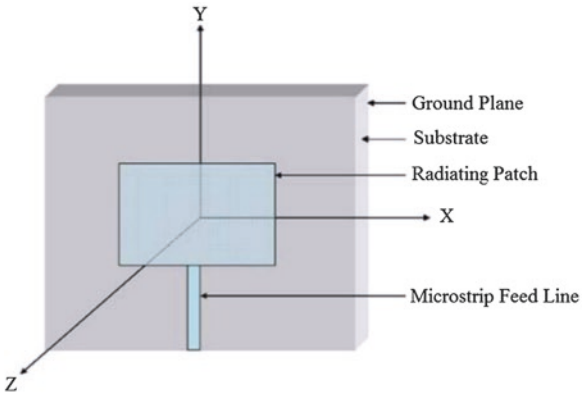

Fig. 16.7 Geometrical configuration of the rectangular microstrip patch antenna at THz frequency [39]

antenna, the substrate has length, width, and thickness of 1000 μm × 1000 μm × 200 μm, respectively. The substrate material is RT/Duriod 6006 with dielectric constant 6.15 with loss tan (δ) of 0.0019. The patch has length and width 600 μm × 400 μm, respectively. The microstrip feed line has the dimension 40 μm × 300 μm and thickness 40 μm. In this antenna design, microstrip line edge feeding technique and simulation has been performed by using CST Microwave Studio [39].

There is more attention paid to the short-range wireless communications, which in turn has led to increase in the demand of higher data rates, low transmit power, and secured wireless communication capability for numerous new multimedia broadbandwidth. On the other hand, the communications in THz frequency band should satisfy and comply with the aforementioned requirements. Thus, rectangular microstrip patch antenna with high-gain and ultra-broadband is discussed in this chapter. The aim of this antenna is to deal with the short-distance wireless communication systems at THz frequency, which would support multi-gigabit data rates transmission [40, 41]. The computed outcomes of the proposed THz rectangular microstrip patch antenna that operates over the frequency range of 0.7–0.85 THz is illustrated in Fig. 16.8. The size of the antenna was significantly reduced due to the close distance between the shorting pin and the feed point [42]. The return loss of the rectangular microstrip patch antenna with and without shorting pin is shown in Fig. 16.8.

It can be observed that the resonant frequency was shifted downward a bit in the presence of shorting pin in contrast to the case of without shorting pin. From the Fig. 16.9, the resonant frequency of the antenna without shorting pin structure is around 742.15 GHz, while the impedance bandwidth of the antenna is 17.76% with

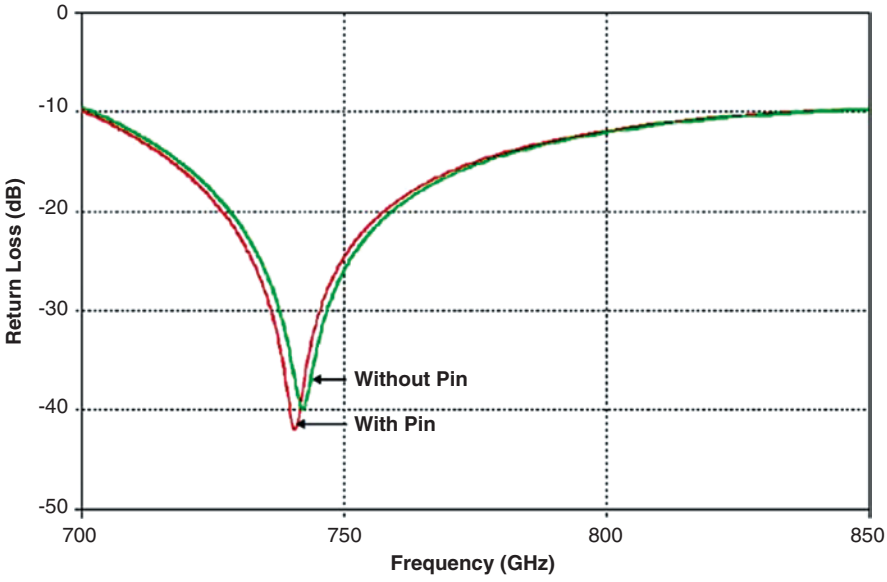

Fig. 16.8 Return losses of the rectangular microstrip patch antenna at THz frequencies with and without shorting pin

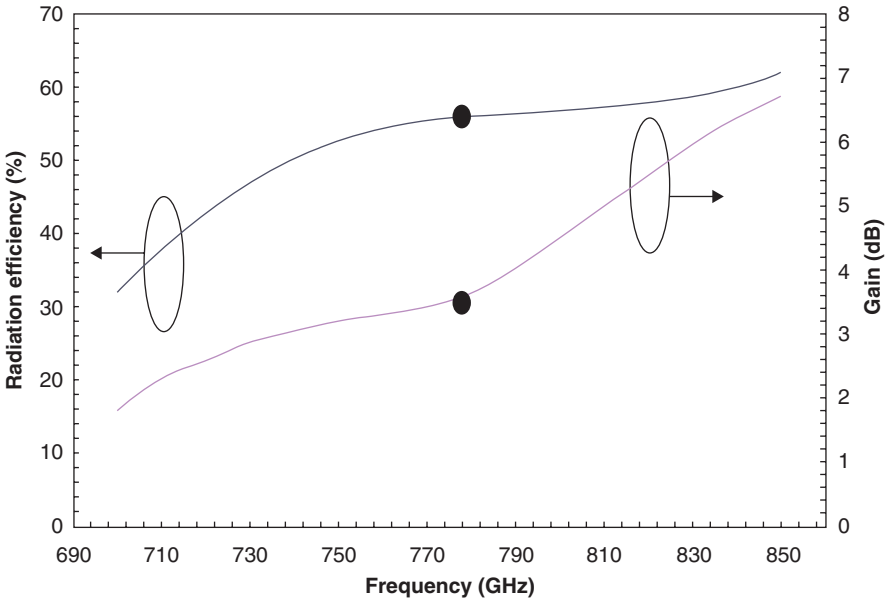

Fig. 16.9 Variation of the radiation efficiency and gain of the rectangular microstrip patch antenna at THz frequencies

respect to the center frequency of operation. Moreover, by examining Fig. 16.9, the radiation efficiency and gain of the antenna have been enhanced in the case of exploiting the shorting pin configuration compared to the one without shorting pin.

The gain, directivity, and radiation efficiency of the proposed THz antenna without shorting pin are 3.497 dB, 6.038 dBi, and 55.71%, respectively, whereas for the shorting pin structure, these parameters are 3.502 dB, 6.03 dBi, and 55.88%, which is quite high for proposed small antenna. One can note that usable impedance bandwidth of the antenna with shorting post is 17.27%, which decreases as compared to without shorting pin structure. Commonly, printing an antenna over a substrate with high dielectric constant is considered as promising and attractive candidate in size reduction; however, it creates strong surface wave modes, in which such surface waves may result in degrading the radiation pattern and reduce the radiation efficiency of the antenna. This is the basic reason behind the lesser efficiency and gain of the antenna without shorting post. For shorting post structure, the surface wave in the substrate will be discontinuous. Therefore, the electrical parameter of the antenna increases. In the proposed antenna structure, we have taken the shorting pin closer to the feed point, that is, 15 μm distance away from the feed point.

From Fig. 16.9, it is seen that the frequency the radiation efficiency of the antenna increases as the resonant frequency increases. Same finding was also envisaged regarding the antenna gain. From Fig. 16.9, the relation of the gain and resonant frequency is said to be proportional. The gain of the antenna increases with increase of the frequency.

The electrical parameters were adopted at the frequency of 742.15 GHz, which is a dip of the return loss of the antenna without shorting pin have radiation efficiency (50.74%) and gain (3.099 dB). Similarly with shorting pin at the frequency of 740.8 GHz the radiation efficiency and gain are 50.98% and 3.068 dB, respectively, which is smaller than the center frequency parameters.

Another analysis of the effect of the width of the microstrip line on the proposed antenna efficiency and gain was carried out, as in Fig. 16.10. The width of the feeding line shows remarkable influences of the antenna gain and efficiency, in which once the width of the strip-line increases, the radiation efficiency and gain decreases, as shown in Fig. 16.10, whereas the return loss decreases with the increase of the strip-line width.

As the variation of the width of the strip-line changes from 10 μm to 60 μm, the width of interest would be 40 μm, on which satisfactory radiation efficiency, gain, and return loss can be achieved. Due to this reason, there is no consideration about the point at which radiation efficiency and gain are high; instead the point of interest is at 40 μm width of strip-line. At this point balanced radiation efficiency, power gain return loss are all achieved. The overall volume of the proposed antenna design is compact and miniaturized, which makes it very suitable for satellite communication systems. One of the key challenges in realizing modern wireless communication links for long distances at THz frequency regime are phenomena occurring during electromagnetic wave propagating through atmosphere. For satellite-to-satellite communication, atmospheric absorption is not a problem.

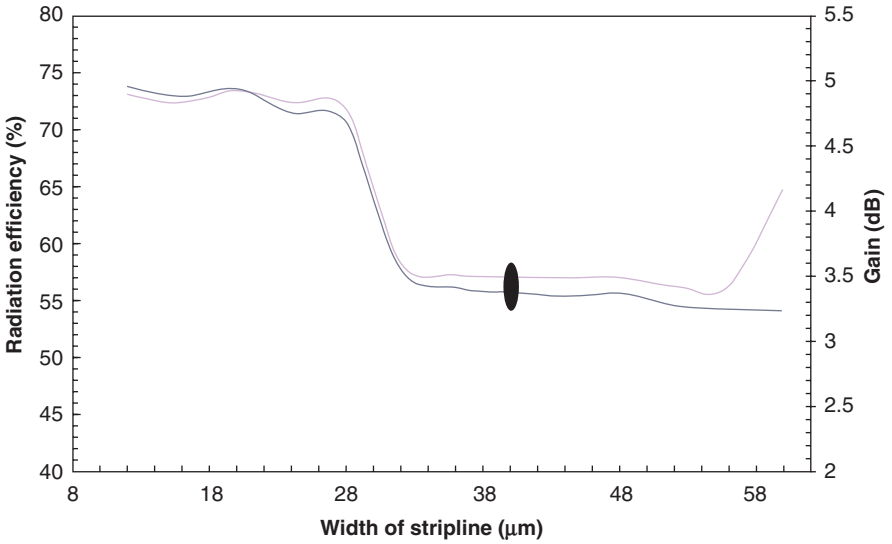

Fig. 16.10 The effects of variation of width of microstrip-line (feed-line) on the radiation efficiency and gain of the rectangular microstrip patch antenna

16.5 Conclusion

The definition of the terahertz frequency spectrum has been extended over a wide frequency bandwidth between 0.1 and 10 THz; however, generally it is confined by the ITU regulation between 300 GHz and 3 THz bandwidth. Known as Tera waves or T-waves rather than submillimeter wave, it has approximately a fraction of a wavelength less than 30 μm. T-wave is heavily used in sensing and imaging applications, and has no ionization hazards and is an excellent candidate frequency band to defeat the multipaths interference problems for pulse communications.

The lower quantum energy of T-waves identifies its potential applications toward near-field imaging, telecommunications, spectroscopy and sensing including medical diagnoses and security screening. Identification of DNA signatures including complex real-time molecular dynamics through dielectric resonance is a good example of terahertz spectroscopy instruments nowadays. Thin layer sensing approaches based on terahertz biosensors widely differ in various aspects. Some approaches are used to describe the broadband terahertz properties of samples, whereas others are appropriate only for the detection of such samples. There is a variety of such detection schemes that are based on the selectivity of the biosensors.

Practical applications of Terahertz communications are discussed in this chapter including research challenges that lie ahead in terms of antenna design for short distance wireless communication. The size of terahertz antenna is quite small compared to large conventional antennas, is portable, and can be deployed in different geological environments and for communication between satellite-to-satellite systems where atmospheric absorption is not an issue.

References

1. W. Withayachumnankul, D. Abbott, Metamaterials in the terahertz regime. IEEE Photonics J. **1**(2), 99–118 (2009)
2. N. Pala, A.N. Abbas, Terahertz technology for nano applications. Enc. Nanotechnol. **1**, 2653–2667 (2012)
3. S. Ergün, S. Sönmez, Terahertz technology for military applications. J. Mil. Inf. Sci. **3**(1), 13–16 (2015)
4. M. Planck (ed.), *The Theory of Heat Radiation*, 2nd edn. (P. Blakiston's Sons & Co., Philadelphia, 1914), pp. 180–181
5. D. Woolard, R. Kaul, R. Suenram, A.H. Walker, T.Globus, A. Samuels, Terahertz electronics for chemical and biological warfare agent detection. in *IEEE MTT-S International Microwave Symposium Digest* (Anaheim, 1999), pp. 925–928
6. K. Kawase, Y. Ogawa, Y. Watanabe, H. Inoue, Non-destructive terahertz imaging of illicit drugs using spectral fingerprints. Opt. Express **11**(20), 2549–2554 (2003)
7. M. Yamashita, K. Kawase, C. Otani, T. Kiwa, M. Tonouchi, Imaging of large-scale integrated circuits using laser terahertz emission microscopy. Opt. Express **13**(1), 115–120 (2005)
8. C. Debus, P.H. Bolivar, Frequency selective surfaces for high sensitivity terahertz sensing. Appl. Phys. Lett. **91**(18), 184102 (2007)
9. L. Cong, R. Singh, Sensing with THz metamaterial absorbers. arXiv Preprint- arXiv **1408**, 3711 (2014)

10. S.J. Park, J.T. Hong, S.J. Choi, H.S. Kim, W.K. Park, S.T. Han, J.Y. Park, S. Lee, D.S. Kim, Y.H. Ahn, Detection of microorganisms using terahertz metamaterials. Sci. Rep. **4**, 4988 (2014)
11. C. Sabah, Tunable metamaterial design composed of triangular split ring resonator and wire strip for S-and C-microwave bands. Prog. Electromagn. Res. B **22**, 341–357 (2010)
12. H. Torun, F.C. Top, G. Dundar, A.D. Yalcinkaya, An antenna coupled split-ring resonator for biosensing. J. Appl. Phys. **116**(12), 124701.1–124701.6 (2014)
13. W. Guo, L. He, H. Sun, H. Zhao, B. Li, X.W. Sun, A dual-band terahertz metamaterial based on a Hybrid'H'-shaped cell. Prog. Electromagn. Res. M **30**, 39–50 (2013)
14. Z. Jakšić, S. Vuković, J. Matovic, D. Tanasković, Negative refractive index metasurfaces for enhanced biosensing. Dent. Mater. **4**(1), 1–36 (2010)
15. J.B. Pendry, A.J. Holden, W.J. Stewart, I. Youngs, Extremely low frequency plasmons in metallic mesostructures. Phys. Rev. Lett. **76**(25), 4773 (1996)
16. T. Driscoll, G.O. Andreev, D.N. Basov, S. Palit, S.Y. Cho, N.M. Jokerst, D.R. Smith, Tuned permeability in terahertz split-ring resonators for devices and sensors. Appl. Phys. Lett. **91**(6), 062511 (2007)
17. Y. Sun, X. Xia, H. Feng, H. Yang, C. Gu, L. Wang, Modulated terahertz responses of split ring resonators by nanometer thick liquid layers. Appl. Phys. Lett. **92**(22), 221101 (2008)
18. C.M. Bingham, H. Tao, X. Liu, R.D. Averitt, X. Zhang, W.J. Padilla, Planar wallpaper group metamaterials for novel terahertz applications. Opt. Express **16**(23), 18565–18575 (2008)
19. A. Elhawil, J. Stiens, C. De Tandt, W. Ranson, R. Vounckx, Thin-film sensing using circular split-ring resonators at mm-wave frequencies. Appl. Phys. A **103**(3), 623–626 (2011)
20. H. Tao, A.C. Strikwerda, M. Liu, J.P. Mondia, E. Ekmekci, K. Fan, D.L. Kaplan, W.J. Padilla, X. Zhang, R.D. Averitt, F.G. Omenetto, Performance enhancement of terahertz metamaterials on ultrathin substrates for sensing applications. Appl. Phys. Lett **97**(26), 261909 (2010)
21. W. Withayachumnankul, H. Lin, K. Serita, C.M. Shah, S. Sriram, M. Bhaskaran, M. Tonouchi, C. Fumeaux, D. Abbott, Sub-diffraction thin-film sensing with planar terahertz metamaterials. Opt. Express **20**(3), 3345–3352 (2012)
22. S. Galoda, G. Singh, Terahertz technology — an emerging electromagnetic spectrum, in *Proceedings of International Conference on Information and Communication Technology (IICT-2007)* (DIT Dehradoon, India, 26–28 July 2007), pp. 482–486
23. S. Galoda, G. Singh, Fighting terrorism with terahertz. IEEE Potential Mag. **26**(6), 24–29 (2007)
24. J. Grade, P. Haydon, D.V. Weide, Electronic terahertz antennas and probes for spectroscopic detection and diagnostics. Proc. IEEE **95**(8), 1583–1591 (2007)
25. P. Kumar, A.K. Singh, G. Singh, T. Chakravarty, S. Bhooshan, Terahertz technology – a new direction, in *IEEE International Symposium on Microwave, Bangalore, India* (2006), pp. 195–201
26. S. P. Mickan, X.-C. Zhang, in *Terahertz Sensing Technology*, ed. by D. L. Woolard, W. R. Loerop, M. S. Shur (Eds), (World Scientific, Singapore, 2003)
27. D.R. Vizard, Millimeter-wave applications: from satellite communications to security systems. Microw. J. **49**(7), 22–36 (2006)
28. E.R. Brown, K.A. McIntosh, K.B. Nichols, C.L. Dennis, Photo mixing upto 3.8 THz in low temperature grown GaAs. Appl. Phys. Lett. **66**, 285–287 (1995)
29. S. Verghese, K.A. McIntosh, E.R. Brown, Optical and terahertz power limits in the low temperature GaAs photomixer. Appl. Phys. Lett. **71**, 2743–2745 (1997)
30. R. Mendis, C. Sydlo, J. Sigmund, M. Feiginov, P. Meissnev, H.L. Hastnagel, Spectral characterization of broadband THz antennas by photoconductive mixing; towards optimal antenna design. IEEE Antenna Wirel. Propag. Lett. **4**, 85–88 (2005)
31. I.G. Gregory, W.R. Tribe, B.E. Cole, M.J. Evans, E.H. Linfield, A.G. Davies, M. Missons, Resonant dipole antennas for continuous wave terahertz photomixers. Appl. Phys. Lett. **85**, 1622–1624 (2004)
32. M. Matsuura, M. Tani, K. Sakai, Generation of coherent terahertz radiation by photomixing in dipole photoconductive antennas. Appl. Phys. Lett. **70**, 559–561 (1997)

33. F.K. Schwering, Millimeter wave antenna. Proc. IEEE **80**(1), 92–102 (1992)
34. T. Seki, N. Honma, K. Nishikawa, K. Tsunekawa, Millimeter-wave high-efficiency multilayer parasitic microstrip antenna array on Teflon substrate. IEEE Trans. Microwave Theory Tech. **53**(6), 2101–2106 (2005)
35. D.M. Pozar, Microstrip antennas. Proc. IEEE **80**(1), 79–91 (1992)
36. A.A. Abdelaziz, Bandwidth enhancement of microstrip antenna. Prog. Electromagn. Res. **63**, 311–317 (2006)
37. R. Garg, V.S. Reddy, Edge feeding of microstrip ring antennas. IEEE Trans. Antennas Propag. **51**(8), 1941–1946 (2003)
38. M. Saed, R. Yadla, Microstrip-fed low profile and compact dielectric resonator antenna. Prog. Electromagn. Res **56**, 151–162 (2006)
39. A. Sharma, G. Singh, Rectangular microstirp patch antenna design at THz frequency for short distance wireless communication systems. J. Infrared Millim. Terahertz Waves **30**, 1–7 (2009)
40. A. Sharma, V.K. Dwivedi, G. Singh, THz rectangular patch microstrip antenna design using photonic crystal as substrate, in *Proceedings of Progress in Electromagnetic Research Symposium (PIERS 2008)*, (Cambridge, USA, 2–6 July 2008), pp. 161–165
41. R. Piesiewicz, T. Kleine-Ostmann, N. Krumbholz, D. Mittleman, M. Koch, J. Schoebel, T. Kurner, Short-range ultra-broadband terahertz communications: concept and perspectives. IEEE Antennas Propag. Mag. **49**(6), 24–38 (2007)
42. A. Sharma, G. Singh, Design of single pin shorted three dielectric layered substrates rectangular patch microstrip antenna for communication systems. Prog. Electromag. Res. Lett. **2**, 157–165 (2008)

Index

I. Elfergani et al. (eds.), *Antenna Fundamentals for Legacy Mobile Applications and Beyond*, DOI 10.1007/978-3-319-63967-3